17th INTERNATIONAL CONGRESS
of the Geological Society of Greece

BULLETIN OF THE GEOLOGICAL SOCIETY OF GREECE, SP. PUBL.

EXTENDED ABSTRACT 201

An example of DsGSDs in Abruzzo Region (Central Italy): the complex case of Civitella del Tronto

Mangifesta M.[1], Scalella G.[2], Sciarra N.[1]
(1) Science Department, University of Chieti-Pescara, 66100 Chieti, Italy, mmangifesta@unich.it
(2) Special Office for the Reconstruction-Earthquake 2016 Extraordinary Commissary, Bureau of the Council of Ministers, 00187 Rome, Italy

Abstract

Deep gravitational slope deformations (DsGSDs) are geological and engineering challenge with important implications for slope stability, reliability of existing infrastructures, land use and, above all, the safety of settlements. This work focuses on the DsGSD (Cappadonia *et. al.,* 2024) phenomenon that affects a large part of the Borrano hamlet, located in the municipality of Civitella del Tronto (Teramo, Abruzzo, Italy). In the area a monoclinal structure of the Laga Formation (Casero *et. al.* 2006) is present, with dips towards the north-east (Artoni, 2013). The terrigenous fill sediments were generated by turbiditic currents, creating characteristic stratified deposits. The deposits consist mainly of marly clays and clayey marls alternating with pelitic-arenaceous intervals with a thickness of about 1500 m. They are characterised by structures elongated in a north-south direction to the east of the main carbonate-covered fronts of the Central Apennine chain. This process is visible within the Teramo Flysch (Artoni, 2003), where two distinct lithostratigraphic units can be observed (figure 1):

- Arenaceous facies: the structural framework shows a trending monocline, with dips ranging from 38° to 60°. The arenaceous component increases the resistance to erosion, allowing these formations to define the geological subsoil.
- Pelitic facies: they are constituted by marly clays, with intercalations of thin layer arenaceous; the structural arrangement follows that of the predominantly arenaceous interval (higher stiffness), with the direction of the layers approximately N-N-E, but with extremely variable dip of the layers.

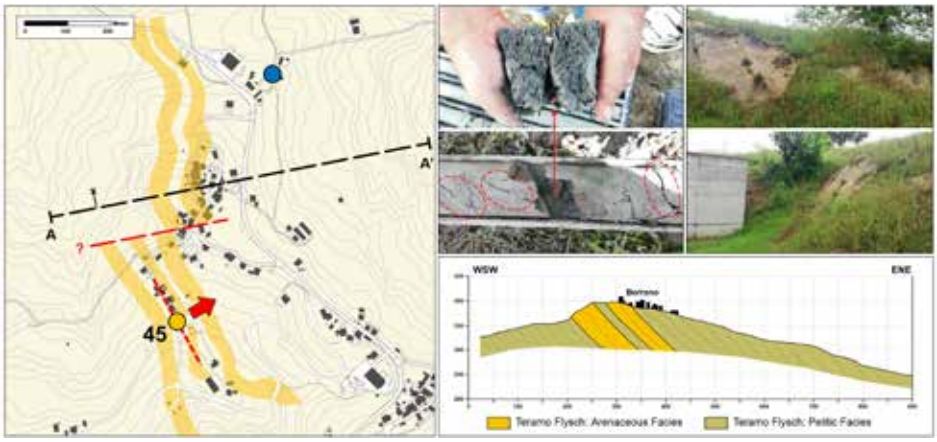


Figure 1. Detail of the Teramo Flysch in predominantly pelitic facies identified in the drill hole at depths of over 30 metres.

In the Borrano area, the identified landslides are of variable extension and mainly consist of slow movements of roto-translative type. The study of the area was carried out using aerial-photographs and Lidar data (Höfle *et al.,* 2011, Gaidzik *e. al.,* 2017) to identify shapes and structural features. The morphology of the terrain, shaped over time by geological processes, reflects the lithological nature of the materials present. The analysis showed that the slopes in the study area are dominated by values between 10° and 30°, with only a few local parts exceeding this range, and the energy of the survey is useful for identifying areas of greater erosion potential and instability. Following the seismic events of 2016/2017, the Borrano area was subjected to a detailed geognostic survey to evaluate slope stability and the vulnerability of existing structures. The damage observed to several local buildings and infrastructure raised significant concerns, indicating the presence of active or potentially reactivatable landslide movements triggered by further seismic or meteorological events. For this, the need arose for a continuous monitoring system capable of detecting any acceleration of the landslide phenomenon in real time and issuing timely warnings to the population to mitigate risk and ensure effective emergency response. A surface monitoring system, shown schematically in figure

2, was installed throughout the area, providing an integrated and technologically advanced system for detecting and analysing the site deformations.



Figure 2. Detail of the installation of the superficial monitoring instruments.

The geognostic survey was realized by boreholes and installed inclinometers and piezometers to a depth of 80 meters. The drilled material shows a complex stratigraphic sequence typical of geological contexts influenced by tectonic and depositional dynamics. The photo-interpretation study has shown a significant evolution of the area. Since the 2000s, it is evident that the entire built-up area was progressively affected by slope movement, indicating a state of activity over time. Significant deformations were identified by deep inclinometers. The image in figure 3 shows the inclinometric analysis (Allasia *et. al.*, 2020) carried out in the area, which provides a complete understanding of the dynamics of the system. It is possible to define a progressive intensification of movements, with significant displacements concentrated at very high depths, suggesting that the deep slip surfaces are active.

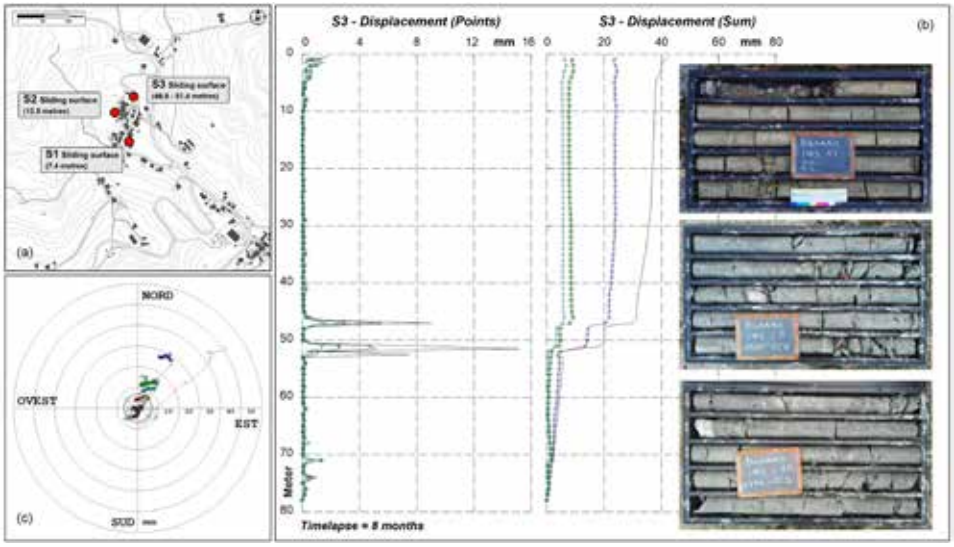


Figure 3. Detail of the inclinometric monitoring.

The successive numerical analyses (Borgatti, 2024) established a good correlation with the monitoring data, revealing in detail the instability of both local and territorial processes. A two-dimensional numerical analysis was carried out in the most critical part of the area to simulate the behaviour of the soil under different loading and saturation conditions. The model parameters (table 1) were calibrated using geognostic data obtained during the investigations, allowing the determination of deformations and stresses at different soil depths.

Table 1. Geotechnical parameters used in numerical analysis.

	Cover Layer	Subsoil	Weakness Planes
Unit weight	19.0 kN/m^3	20.0 kN/m^3	--
Friction angle (j′)	22°	24°	12°
Cohesion (c′)	10.0 kPa	100.0 kPa	0.0 kPa
Elastic modulus	0.01GPa	1.0 GPa	--

The map in figure 3b shows a zone of maximum displacement at the most superficial part, where the alteration cover with less mechanical properties encounters the more compact geological substrate. This transition zone may be affected by alteration, erosion or frictional forces that facilitate movement of the overlying material. At greater depths, secondary failure surfaces develop, which may result from fractures or structural deformation caused by tectonic forces or excessive increase pore pressure. These planes, although less visible on the surface, are critical to the stability of the overall system as they can determine the intensity and direction of deeper and more complex movements of large masses of material. In addition, the graph in figure 3c can be used to identify areas in critical condition where the applied stress exceeds the strength of the material along weakness planes, resulting in creep to failure.

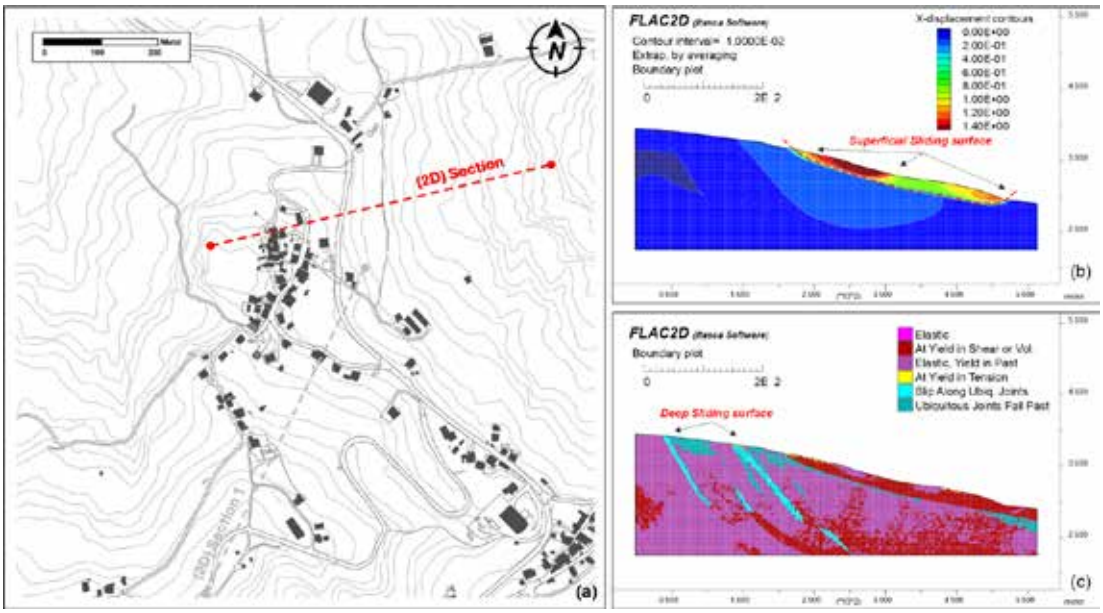


Figure 3. Two-Dimensional Numerical modelling of the section-2.

Because the extent of the potentially unstable area, a three-dimensional numerical model was developed to integrate all the available data and to represent in detail the stress-strain behaviour of the entire analysed area. The model was constructed by incorporating two fundamental components: the surface layers, identified in all the boreholes, and the substrate layer. Particular attention was paid to the modelling of the deep layers, by implementing a constitutive Ubiquitous Joint Plasticity Model (Yang, 1998), capable of describing in three dimensions both the overall mechanical behaviour of the mass (Mohr-Coulomb) and the internal planes of weakness (Zhou *et. al.,* 2018, Azadi *et. al.* 2024). In this specific case, these planes were schematized with a 45° inclination and a preferential north-north-east direction, in accordance with the stratigraphic and structural information obtained from the geological investigations. The mechanical parametrization and the definition of the boundary conditions followed the same criteria as in the two-dimensional model, to ensure consistency and comparability with the real conditions. The three-dimensional approach allowed a detailed analysis of the plastic deformations and their evolution on a local scale, highlighting that a significant part of the inhabited area is affected by widespread plastic deformations, indicating an active instability process. The map of SSI shear rate increments (figure 4) shows red areas of maximum deformation that are large, continuous and characterized by an elongated north-north-east trend. This configuration reflects the geometry of the fracture system and the assumed planes of weakness within the substrate, suggesting significant structural control over the way the ground deforms and slides. These planes of weakness act as stress concentration surfaces, promoting material movement along predefined directions. The results of the three-dimensional model (figure 4) also show good agreement with the real conditions. There is a good comparison with inclinometer measurements (fig. 3), both for deep deformations (inclinometer S3) and surface deformations (inclinometer S1).

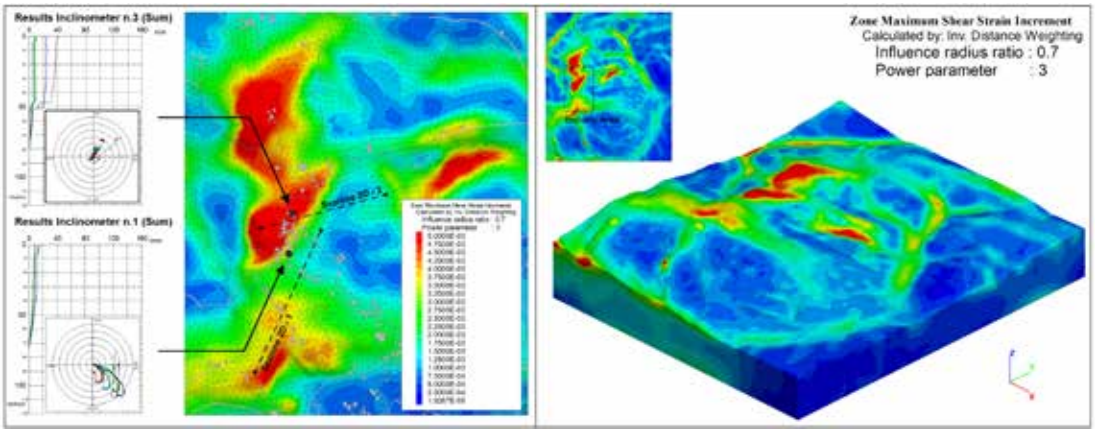


Figure 4. Three-Dimensional Numerical modelling: Shear Strain Increment map.

One crucial aspect is certainly the need to refine the hypotheses on the distribution of water saturation, a parameter that decisively influences the mechanical response of the materials and the local stability conditions. A better understanding of the spatial and temporal variations of saturation could significantly improve the predictive capacity of the models, especially in contexts characterized by intense rainfall or significant seasonal variations. In addition, the detailed study of the local responses of the weakening planes is another fundamental topic of investigation. A more accurate characterization of the geotechnical properties of these surfaces, such as residual shear strength or cohesion under partially saturated conditions, could allow a more realistic representation of the natural processes involved. This would be particularly relevant for improving predictions of surface instabilities, which are often more difficult to model due to their sensitivity to local parameters and variations in environmental conditions. The results of the study provide an essential basis for the development of strategies aimed at planning mitigation and/or relocation measures, which are crucial for the protection of infrastructure and the safety of local communities. The work also highlights the importance of integrated spatial planning, which can combine innovative detection technologies with traditional methods. This approach also makes it possible to optimize land management, making it more effective and sustainable, especially in geologically complex and vulnerable contexts.

Acknowledgements

The Authors thank the Special Office for Reconstruction of the Italian Government's for providing funds for the geognostic surveys.

References

Allasia, P., Godone, D., Giordan, D., Guenzi, D., Lollino, G. 2020. Advances on Measuring Deep-Seated Ground Deformations Using Robotized Inclinometer System. Sensors 2020, 20, 3769. https://doi.org/10.3390/s20133769

Artoni, A. 2003. Messinian events within the tectono-stratigraphic evolution of the Southern Laga Basin (Central Apennines, Italy). Boll. Soc. Geol. Ital.

Artoni A. 2013. The Pliocene-Pleistocene stratigraphic and tectonic evolution of the Central sector of the Western Periadriatic Basin of Italy. Marine and Petroleum Geology: 42, 82-106.

Azadi, A., Momayez, M. 2024. Review on Constitutive Model for Simulation of Weak Rock Mass. Geotechnics 2024, 4, 872-892

Borgatti, L., Donati, D., Hu, L., Landi, G., Zama, F. 2024. A Regularization Method for Landslide Thickness Estimation. J. Imaging 2024, 10, 314.

Cappadonia, C., Confuorto, P., Di Martire, D., Calcaterra, D., Moretti, S., Rotigliano, E., & Guerriero, L. 2024. Geomorphological Insights to Analyze the Kinematics of a DSGSD in Western Sicily (Southern Italy). Remote Sensing, 16(21), 4040. https://doi.org/10.3390/rs16214040.

Casero, P., and Bigi, S., 2006. Deep structure of the Laga Basin. Poster session TS7.2 - XY0591, EGU General Assembly 2006.

Gaidzik, K., Ramírez-Herrera, M. T., Bunn, M., Leshchinsky, B. A., Olsen, M., & Regmi, N. R. 2017. Landslide manual and automated inventories, and susceptibility mapping using LIDAR in the forested mountains of Guerrero, Mexico. Geomatics, Natural Hazards and Risk, 8 (2), 1054–1079.

Höfle, B., & Rutzinger, M. 2011. Topographic airborne LiDAR in geomorphology: A technological perspective. Zeitschrift Fur Geomorphologie , 55 , 1–29.

Yang, Z., Chen, J., Huang, T. 1998. Effect of joint sets on the strength and deformation of rock mass models. Int. J. Rock Mech. Min. Sci. 1998, 35, 75–84.

Zhou, X., Tang, C.A., Li, W. 2018. Modeling the mechanical behavior of jointed rock masses with the synthetic rock mass approach. Eng. Geol. 2018, 110, 136–148.

17th INTERNATIONAL CONGRESS of the Geological Society of Greece

BULLETIN OF THE GEOLOGICAL SOCIETY OF GREECE, SP. PUBL.

EXTENDED ABSTRACT 202

The 'treasure' of aeolianites on the coastal front of Marathopoli Dialiskari, Messinia, Western Coast of the Peloponnese: rhizoliths petrified forest and historical abandoned quarries

Manoutsoglou Emmanouil

Technical University of Crete, School of Mineral Resources Engineering, University Campus, 73500 Akrotiri, Chania, Greece, emanoutsoglou@tuc.gr

Introduction

Aeolianites and rhizoliths are geological structures that occur rarely in spatially limited coastal areas along the coasts of our country (Moraiti & Alexopoulos, 2019; Manoutsoglou, 2022; Μανούτσογλου, 2023). Aeolianites and rhizoliths are associated with the action of natural factors, such as marine activity, wind and vegetation. As fossil dune deposits with carbonate cement mainly of Quaternary age, aeolianites provide key clues for understanding sea-level fluctuations from the Late Quaternary to the Holocene and the dynamic transport of sediments by wind in coastal environments. Since their characteristics are similar to those of recent coastal dunes, such as cross-bedded structures, sand-dominated grain size, and long parallel axes on the shore, these rocks provide records of both past coastal wind-driven dynamics and the complex interactions between aeolian and colluvial river depositional processes in coastal environments. Generally, the morphology of aeolianites reflects the marine dynamics of the region combined with wind direction and changes in climatic conditions during their deposition (Brooke, 2001). Similarly, rhizoliths record the geochemical interaction of soil roots with their environment, indicating the presence of plants and the environmental conditions that prevailed during their formation (Alonso-Zarza, 1999). The description and detailed study of rhizoliths in coastal aeolianites can provide crucial information on the paleoenvironmental conditions of the western coast of the Peloponnese, particularly in the Marathopoli – Dialiskari area (Municipality of Trifylia, Messinia). This study represents one of the first comprehensive attempts to document these features in the region, contributing to a broader understanding of the dynamics of Mediterranean coasts and the interaction between biological and sedimentary processes. While the aeolianites tell a story of natural processes, the historically abandoned quarries in the area, carved into these formations, speak of human ingenuity and resourcefulness. Historically, aeolianite deposits have been exploited as a source of building stone, particularly in coastal areas where other durable rock types are rare. The soft, flexible nature of freshly cut aeolianites makes it an ideal construction material, while its hardening over time ensures the durability of structures built from it. This work aims to highlight the significance of coastal aeolianite rhizoliths forest and abandoned quarries, which represent natural and historically technological 'treasures' for the broader region.

Geological outline

The SW Peloponnese, mainly Messinia, located in the western part of the Aegean arc system, represents one of the most tectonically and seismically active areas of the Africa-Eurasia collision zone. The topographic relief of the SW Peloponnese is characterized by the presence of several mountains and drainage basins with a trend mainly NW-SSE and E-W (Figure 1). The outer part of the western Peloponnese is dominated by extensional tectonics as expressed by the normal faults oriented E-W in its central-western part (Fountoulis *et al*., 2014). According to Αθανασάς (2010), typical marine sedimentation in the submarine areas of Western Messinia seems to start in the Lower Pliocene with a large surface spread. It consists mainly of sandstone formations whose thickness varies. They mainly occupy the plateau between the Pylos-Gargaliannoi-Filiatra heights in the west and the Kyparissia Mountains in the east. They also occur in isolated locations south of Pylos. However, disagreement exists regarding the partial division of the sand-margin formations into Pliocene and Pleistocene. Older stratigraphic studies of the area indicate that this sedimentation began in the Lower Pliocene and became generalized in the Upper Pliocene. Marine deposits consist of calcitic sandstones, marly sandstones, marls and conglomerates of different thicknesses from place to place. Φυτρολάκης (1980) in the geological map (Koroni – Pylos – Skhiza Sheet) considers the calcitic sandstones in the area north of the Romanos to be of Tyrrhenian age, while Αντωνίου και Φυτρολάκης (1988) recognize within the calcareous sandstones of the Petrochori-Romanos coastal front both the aeolian and marine phases and relate them to eustatic events of the Late Pleistocene (Eu- and Neo- Tyrrhenian). Terrestrial deposits consist mainly of conglomerates, red-coloured siliceous sands and sandstones. The multi-coloured sandstones above the marine post-alpine deposits are likely from the Middle and Upper Pleistocene.

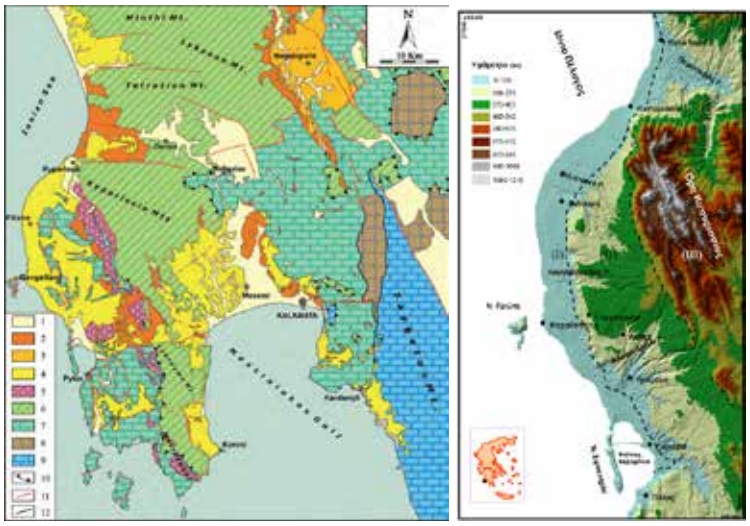


Figure 1. Left, Map depicting the geotectonic units and the post-Alpine deposits of the study area. 1: Holocene deposits; 2: continental deposits; 3: lacustrine deposits; 4: marine deposits; 5: conglomerates of Messinia (molasse); 6: Pindos Unit; 7: Gavrovo-Tripolis Unit; 8: Arna Unit (Phyllites-Quartzites); 9: Mani Unit; 10: thrust; 11: fault zone; 12: detachment fault zone [from Fountoulis et al., 2014]. Right, Three-dimensional visualization of the study area in Western Messinia using ArcGIS. Three basic physical geographical units are distinguished. A smooth surface west of the locations Gialova-Gargalianoi-Filiatra (I), a second, equally smooth but of higher altitudeseast of the previous one (II), which is interrupted by a third even further east that includes the Kyparissia Mountains (III). The altitudes are provided as a graduated color scale every 135 m. The coordinates (top left and bottom right) are given in the EGSA '87 system (from Athanasas, 2010). The study area is in the red boxes.

Sandstones appear in a relatively narrow coastal zone of 50-100 meters that starts north of the Bay of Navarino and extends up to Kyparrissia. Within these sandstones, aeolian deposits were found over a length of approximately two kilometres, spanning from the area north of Marathopolis to the south of Dialiskari. Numerous sites featuring extensive occurrences of rhizoliths were identified within these aeolianites, confirming the presence of a fossilized rhizolith forest in the region. In addition, four abandoned historical quarries were identified nearby, along with the well-known historical salt pan at Dialiskari.

Objectives

According to Brooke (2001), Aeolianite is a type of limestone found in coastal areas, demonstrating the reworking of vast amounts of carbonate sediments of biogenic origin from shallow marine environments into coastal sand dunes. Most aeolianites are calcareous sandstones originating from the biogenic carbonate sediments of shallow marine environments formed through the diagenesis of coastal sand dunes. The cementation of Quaternary-period dunes is the primary source of the aeolianites observed today in numerous island regions of both the northern and southern hemispheres. Most aeolianites consist of multiple generations of older dunes that have undergone diagenesis. When these dunes are cemented (lithified), they preserve the structures imparted by aeolian processes, often retaining their cross-bedded, parabolic, or barchanoid forms. While aeolianites are typical sedimentary deposits of the Quaternary period, instances of Paleozoic and Mesozoic carbonate aeolianites have also been documented (Brooke, 2001). Segments of sand dunes have been identified as distinct due to their association with well-developed paleosols, correlating with sea-level changes driven by glacial cycles. Geochronological records of extensive aeolianite deposits in both hemispheres indicate that eustatic sea-level changes largely controlled the timing of large-scale coastal carbonate dune formations. For an extended period, interpretations of coastal carbonate dunes were limited to their formation during glacial periods, with the majority dating to the Late Tertiary and Quaternary periods. Recent discoveries of aeolianites from interglacial periods challenge the belief that aeolianite formations are exclusive to glacial periods. Instead, these findings highlight the impact of large sea-level fluctuations, which reflect the cyclical growth and melting of continental ice sheets (Frébourg *et al*., 2008).

In the studied region, aeolianites are extensively developed in a relatively narrow coastal zone of 50-100 meters over a length of approximately two kilometres, spanning from the area north of Marathopolis to the south of Dialiskari. These deposits exhibit prominent and distinctive cross-bedding and served historically as a source of quarry material. The study of ancient quarries has evolved from a historical focus in the 19th century to a multidisciplinary field involving archaeologists, geologists, and engineers. Initially perceived as secondary production sites, quarries gained importance with the realization that their technical and economic aspects were crucial to understanding ancient construction. The late 20th century saw systematic excavation methods and geochemical analyses enhancing research. Today, quarry studies integrate archaeological surveys, geological

mapping, and digital tools, providing insights into ancient economies and craftsmanship. Despite challenges, interest persists in medieval quarries, revealing their cultural and economic significance (Lamesa *et al*., 2021). The historical abandoned quarries described for the first time in this work in the area are not registered in the databases and catalogues of historical quarries in Greece (Κουκουβού, 2010; Κοκκορού-Αλευρά κ.α., 2014; Τσιλιγκάκη, 2014). The only historical abandoned quarry in the area has been recorded in the corpus of ancient quarries with number 713. ''location: Pylos, Dialiskari-Marathoupoli". At the same location (Figure 2), a possible salt marsh has been described from the first excavations of the Swedish archaeological mission about a century ago in the area: "..On the rock they have carved half a meter above the sea a 6mx3m. On two sides a groove allows the tank to communicate with the sea. It is probably a salt marsh.." (Valmin, 1930).



Figure 2. Left is the place where the ancient salt lake was built. On the right, you can still see the excavation of the seawater supply channel.

The first quarry that bears traces of recent exploitation (Figure 3) is the largest in dimensions and is located north of Marathopolis, where the coastal aeolianites have the greatest width and width in front of the coast, exceeding one hundred meters. What is left is an abandoned ancient quarry with rugged and uneven terrain filled with large rocks and boulders. The quarry is surrounded by steep, weathered rock walls, which appear eroded over time. There are no exploitation levels, only a front located on the east side, as opposed to the coastal front located on the west side of the site. The quarry's remnants highlight the historical stone extraction, possibly for construction or other purposes, with evidence of human intervention still visible in the surrounding formations.



Figure 3. The first and largest abandoned quarry is located north of Marathopolis.

The second quarry (Figure 4) is located about 500 meters south of the Church of Agios Nikolaos, which was built in the small bay of Dialiskari. The second quarry is an abandoned ancient quarry with visible layers of stone extraction. The quarry's rock face is marked by precisely cut, rectangular sections, indicating past human activity and extraction methods. The ground appears rugged and uneven, strewn with smaller rocks and debris, characteristic of a long-abandoned excavation site. On the right, the image displays visible wedge marks on the rock surface, indicating the stone extraction techniques used in antiquity. These wedge marks appear as small, evenly spaced holes or indentations, likely created by inserting wooden or metal wedges to split the stone. Over time, natural weathering and erosion have partially obscured some of these marks, but their distinct pattern remains visible. The presence of these wedge marks provides valuable insight into the methods employed by ancient quarry workers to extract large stone blocks for construction and other purposes.



Figure 4. Left, the second abandoned quarry is located about 500 meters south of the Church of Agios Nikolaos, which was built in the small bay of Dialiskari; on the right, traces of wasps associated with the method of exploitation.

The third quarry is located next to Barlas beach, 4 km from Marathopoli (Figure 5) and is approximately 10 m above sea level. The colour of the aeolianites without containing layers of paleo-soil is red. However, the colour of the extracted material is uniform throughout the quarry. The surface of the rocky aeolianites shows distinct cutting marks and stepped formations, indicating systematic quarrying techniques. The surrounding area consists of weathered stone with patches of sand and small debris. The layout of the quarry suggests that it was used for the quarrying of large stones, with clear signs of chiselling and splitting methods. Throughout the quarry surface, there are characteristic residual cut marks and grooves indicating wedging techniques, where wooden or metal wedges were inserted into pre-cut grooves to split the stone. These grooves, often arranged in parallel, herringbone, or lattice patterns, suggest a systematic technique in stone quarrying. In addition, the presence of tool marks, such as chisel marks and wedge holes, provides valuable information about the methods used by ancient workers to extract large stones with precision. The creation of stepped steps during quarrying suggests an excavation process preserved to this day, where successive layers of stone were removed. The surrounding environment, with scattered debris and partially worked boulders, reflects the operational phases of the quarry, from initial extraction to preparation for transport. The erosion and weathering of the exposed rock faces suggest that the quarry has been abandoned for a long time. The 1 m wooden stick has been placed on the surface for scale reference.



Figure 5. The third quarry is located by Barlas Beach, 4 kilometres from Marathopoli. On the right, the image shows a close-up view of an abandoned ancient quarry with clear signs of quarrying activity. The rock face exhibits distinct vertical and horizontal tool marks, likely created using chisels and wedges to extract stone blocks. The marks are characterized by parallel grooves and stepped formations, which indicate a systematic quarrying process used to detach large stone blocks from the bedrock.

Comparing the image with documentation and visual records from ancient quarries, the quarrying methods shown here are consistent with those used in classical antiquity. In this era, a combination of hand tools and water-based wedge techniques was employed to split the rock along desired lines. These techniques allowed for the efficient production of stone blocks for construction purposes, such as temples, fortifications, and public buildings.

As well as building material mined in many places, the aeolianite formations along the Marathopoli – Dialiskari coastline exhibit well-preserved examples of fossilized root structures, i.e. rhizoliths, indicative of ancient dune stabilization by vegetation. These features were mapped and analyzed to determine their spatial distribution and morphological characteristics. The fossilized roots appear as vertical to sub-vertical tubular structures, often branching, which are associated with paleo-vegetation that thrives under specific climatic and geomorphic conditions. Rhizoliths, formed by the mineralization of root systems, were observed in association with paleosol layers within the aeolianite sequence, reflecting periods of dune stability and soil development. Klappa (1980) identified five primary types of rhizoliths: (1) root molds, which are tubular cavities left by roots that no longer exist; (2) root casts, formed by the infilling of root molds with sediment and/or cement; (3) root tubules, which are cemented cylindrical structures surrounding root molds; (4) rhizocretions, representing pedo diagenetic mineral accumulations around plant roots; and (5) root petrifactions, involving the mineral impregnation or replacement of organic material, preserving root anatomical features either wholly or partially.

Dozens of rhizoliths were counted in a relatively small area of a few hundred square meters. The first rhizoliths in the area were found within the first quarry north of Marathopolis. The second place is located in Dialiskari (Figure 6). Rhizoliths are visible as irregular, branching grooves and cavities, creating a rugged and porous texture across the terrain. Like many other fossils in the study area, rhizoliths in full development can be observed on aeolianite surfaces formed by marine erosion. The erosion has exposed these rhizoliths, revealing their complex network, which likely developed through the gradual dissolution of sandstone. The excellent preservation of a multitude of roots of various sizes indicates that most rhizoliths in the study area possess greater resistance to marine mechanical erosion compared to the surrounding aeolianites. This observation serves as an initial indication that the majority of the rhizoliths are not mere “root casts” but are very likely mineralized, fossilized roots. If they were simply root casts filled with the surrounding sediment of the aeolianites, they would not have withstood marine mechanical erosion. Detailed mapping has revealed that the distribution of rhizoliths corresponds to distinct stratigraphic horizons, suggesting episodic phases of vegetation growth and sediment stabilization. These intervals are interspersed with layers of reworked aeolian sands, indicative of dune reactivation during climatic aridity or increased wind intensity. The stratigraphic position of the rhizoliths provides a valuable framework for reconstructing the paleoecological and climatic history of the region.



Figure 6. Extensive surface with rhizoliths within the quarry at the Dialiskari location. The settlement and the bay are clearly visible.

Apart from the root system, they were distinguished by positions and remains of fossilized tree trunks (Figure 7). The fossilized tree trunks exhibit significant erosion, with their surfaces marked by deep grooves and cavities resulting from prolonged exposure to marine erosion. Despite the wear, the cylindrical shape and woody texture remain discernible, indicating their origin as tree trunks. The size and orientation of these trunks suggest they were once part of a forested landscape, subsequently buried and preserved through geological processes. Surrounding and connected to the fossilized trunks are rhizoliths.



Figure 7. The provided images depict heavily eroded fossilized tree trunks accompanied by rhizoliths, showcasing the intricate interplay between ancient vegetation and sedimentary processes.

Rhizoliths occur and spread on the flat erosional surfaces of aeolianites (Figure 8 and Figure 9). At the same time, they start from the underlying paleosoil that appears by position. The various rhizoliths differ in size (length, diameter, branching, etc.). Mega-rhizoliths and biokarst dissolution pipes were recognized.



Figure 8. A coastal landscape is characterized by a dense network of rhizoliths and mineralized root structures formed through the diagenetic processes of ancient vegetation. These rhizoliths are visible as elongated, branching, and interconnected features across the eroded limestone surface.



Figure 9. A more detailed look at the rhizolith structures reveals intricate branching patterns with visible root voids and mineralized traces. The rhizoliths exhibit a well-preserved morphology, retaining their cylindrical and tapered shapes

Conclusions

The coexistence of rhizoliths and historical abandoned quarries within aeolianites presents an intriguing juxtaposition: on the one hand, fossilized roots offer a glimpse into ancient ecosystems shaped by natural forces; on the other, quarries stand as monuments to human adaptation and transformation of the landscape. These elements underscore the dynamic relationship between nature and culture, revealing how landscapes evolve under the combined influence of environmental change and human activity. Studying this intersection enhances our understanding of past environments and societies and has contemporary relevance. Understanding how ancient communities adapted to their environments can offer valuable lessons as we face ongoing climate change and increasing pressure on natural resources.

References

\Αθανασάς, Κ., 2010. Νεοτεκτονική εξέλιξη της Μεσσηνίας κατά το ανώτερο τεταρτογενές, βασισμένη σε γεωχρονολογήσεις με τη μέθοδο της φωταύγειας: συμβολή στην αρχαιομετρία. Διδακτορική διατριβή, ΕΚΠΑ, Σχολή Θετικών Επιστημών, Τμήμα Γεωλογίας και Γεωπεριβάλλοντος. Τομέας Δυναμικής, Τεκτονικής και Εφαρμοσμένης Γεωλογίας, σελ.264.

Αντωνίου, Μ., Φυτρολάκης, Ν., 1988. Ιζηματολογικές και νεοτεκτονικές παρατηρήσεις σε νεοπλειστοκαινικούς και ολοκαινικούς σχηματισμούς της Νότιας και Δυτικής Πυλίας (Δυτική Μεσσηνία), Μεταλλειολογικά και Μεταλλευτικά Χρονικά, 85-66.

Κοκκορού-Αλευρά, Γ., Πουπάκη, Ε., Ευσταθόπουλος, Α., Χατζηκωνσταντίνου, Α., 2014. Corpus αρχαίων Λατομείων, ΕΛΚΕ ΕΚΠΑ, Ερευνητικό πρόγραμμα «ΚΑΠΟΔΙΣΤΡΙΑΣ», Αθήνα.

Κουκουβού, Α., 2010. Λατομεία πωρόλιθου στην περιοχή της αρχαίας Βέροιας: μελέτη για την λατομία οικοδομικού λίθου στην αρχαιότητα. Διδακτορική διατριβή, ΑΠΘ, Σχολή Φιλοσοφική, Τμήμα Ιστορίας και Αρχαιολογίας, Τομέας Αρχαιολογίας, σ. 546.

Μανούτσογλου, Ε., 2023. Χαρτογραφώντας το απολιθωμένο δάσος στον Σταυρό Ακρωτηρίου στα Χανιά. Πρακτικά 16ου Εθνικού Συνεδρίου Χαρτογραφίας “Η Χαρτογραφία στον σύγχρονο πολυθεματικό κόσμο” Αιγάλεω, 2/11- 4/11/2023, 819-833.

Τσιλιγκάκη, Ε., 2014. Τα αρχαία λατομεία της Κρήτης, Διδακτορική διατριβή, Παν. Κρήτης, Τμήμα Ιστορίας και Αρχαιολογίας, σ. 937.

Φυτρολάκης, Ν., 1980. Γεωλογικός χάρτης Ελλάδας 1:50,000, Φύλλο Κορώνη-Πύλος-Σχίζα, Ι.Γ.Μ.Ε..

Alonso-Zarza, A.M., 1999. Initial stages of laminar calcrete formation by roots: examples from the Neogene of central Spain. Sedimentary Geology 126, 177-191.

Brooke, B., 2001. The distribution of carbonate eolianite, Earth-Science Reviews, 55, 135-164.

Fountoulis, I., Mariolakos, I., Ladas, I., 2014. Quaternary basin sedimentation and geodynamics in SW Peloponnese (Greece) and late stage uplift of Taygetos Mt., Bollettino di Geofisica: teorica ed applicata, (55), 303-324, 2014, Istituto Nazionale di Oceanografia e di Geofisica Sperimentale, 0006-6729.

Frébourg, G., Hasler, C., Le Guern, P., Davaud, E., 2008. Facies characteristics and diversity in carbonate eolianites, Facies, 54(2), 175-191.

Klappa, C.F., 1980. Rhizoliths in terrestrial carbonates: classification, recognition, genesis, and significance, Sedimentology, 26, 613-629.

Lamesa, A., Bessac, J.-C., Sciuto, C., 2021. The archaeology of quarries and rock-cutsites. In: Claudia Sciuto, Anaïs Lamesa, Katy Whitaker and Ali Yamaç, .Carved in Stone. The Archaeology of rock-cut sites and stones quarries, BAR Publishing, pp. 1-8.

Manoutsoglou, E,. 2022. Rhizoliths within aeolianites at the ancient quarry of Stavros Akrotiri Chania Greece, 16th International Congress of the Geological Society of Greece 17-19 October, 2022 - Patras, Greece, Bulletin of the Geological Society of Greece, Sp. Publ. 10 Ext. Abs., GSG2022-193, 2022.

Moraiti, E., Alexopoulos, A., 2019. Geopark of Aghios Nikolaos–Neapolis, Lakonia, Peloponnese, 15th International Congress of the Geological Society of Greece Athens, 22-24 May, 2019, Harokopio University of Athens, Greece Bulletin of the Geological Society of Greece, Sp. Pub. 7 Ext. Abs. GSG2019-376.

Valmin, N., 1930. Etudes topographiques sur la Messénie ancienne, Lund. 1931. Aten genom tiderna, Stockholm.

17th INTERNATIONAL CONGRESS of the Geological Society of Greece

BULLETIN OF THE GEOLOGICAL SOCIETY OF GREECE, SP. PUBL.

EXTENDED ABSTRACT 203

Monitoring sea water intrusion at Samaria gorge National Park

Manoutsoglou E.[1], Andronikidis N.[1], Lazos I.[1], Kritikakis G.[1], Steiakakis E.[1], Xirouchakis, G.[1] and, Vafidis A.[1]

(1) School of Mineral Resources Engineering of the Technical University of Crete, Chania, Greece, emanoutsoglou@tuc.gr

Introduction

Samaria gorge National Parks is located at the White Mountains mass, at the southwestern part of Crete (Figure 1). It is one of the most significant geomorphological structures in the Mediterranean region globally recognized by numerous international distinctions: 1) UNESCO Man and the Biosphere Reserve, 2) European Diploma of Protected Areas, awarded by the Council of Europe, 3) European Biogenetic Reserve of the Council of Europe, 4) Important Bird Areas by the Birdlife international, 5) NATURA 2000 protected area, under code GR4340014 (Zone of Special Protection: ZSP). The wider area of White Mountains belongs to the Natura 2000 European Network of Protected Areas (under code GR4340008H) and it is certified as a Place of Universal Importance (PUI).

Among geophysical methods, electrical resistivity tomography (ERT) has become a valuable tool for imaging seawater intrusion due to its low cost in combination with the effectiveness and quick interpretation. Automated data collection using multi-electrode resistivity surveying instruments, made the electrical tomography ERT method one of the most widely used geophysical methods for near-surface investigations. Fast acquisition 3D data instruments and inversion algorithms enhance the reliability of the method (Hamdan and Vafidis, 2009).

This study employs the ERT and seismic tomography geophysical methods for sea water intrusion imaging and monitoring at Samaria gorge. The geophysical survey conducted in the National Park of Samaria gorge employed the 3D ERT method which is more efficient due to the 3D nature of this geological structure. Dipole-dipole and gradient arrays were chosen to detect both lateral and vertical resistivity variations.

Geological setting

Crete located just over the active subduction zone of the eastern Mediterranean oceanic plate beneath the Eurasian one, exhibits a gradual uplift and complicated active tectonics (Pavlaki and Perleros, 2015; Manoutsoglou, et al., 2022) The Alpine tectonostratigraphic regime indicates compression tectonics, such as folding. The major tectonic units of Crete (stratigraphically from the lower to the upper one) are:

i) Plattenkalk Group (para-autochthonous),
ii) Phyllite Nappe,
iii) Tripolis Nappe,
iv) Pindos Nappe and
v) Uppermost Nappe.

Various lithological formations, composing these nappes, tectonically overlie different parts of the Plattenkalk Group formations. Plattenkalk Group is predominantly structured by HP/LT affected metamorphic rocks. Furthermore, the Ravdoucha (slate-carbonate) beds tectonically overlie the dynamo-metamorphic sequence in different parts of Western Crete, constituting the lower part of Tripolis Zone, while its upper part includes the carbonate sequence and flysch.

Considering the model relating geological processes and geomorphological features, the following remarks arise for the Samaria gorge area:

1. The entire region is a part of mega structure, consisting of metamorphic unsorted stromatolite limestones (Mt Gigilos). On either side of this mountain, the dip direction of the formations is differentiated, maintaining the same NNE-SSW striking and indicating that Mt Gigilos is a tectonic window.
2. The Trypali Unit occurs at the southwestern part of Samaria gorge according to field observations (Figure 1c).
3. The formations inclination is directly associated with the tectonic processes and the geomorphological evolution of the region.
4. The phyllites and slates (Gigilos formation) are characterized by medium dip angles and smooth relief. On the contrary, the meta-carbonate formations with cherts of Plattenkalk Group are accompanied by high (up to vertical) dip angles. These formations exhibit sharp slopes with height up to 300 m in some locations on both sides of the stream that crosses Samaria gorge.
5. Overall, Samaria gorge constitutes a typical catchment area, in which the surface runoff is favored at the northern part, due to outcropping lithological formations, while the underground one is favored at the southern part.

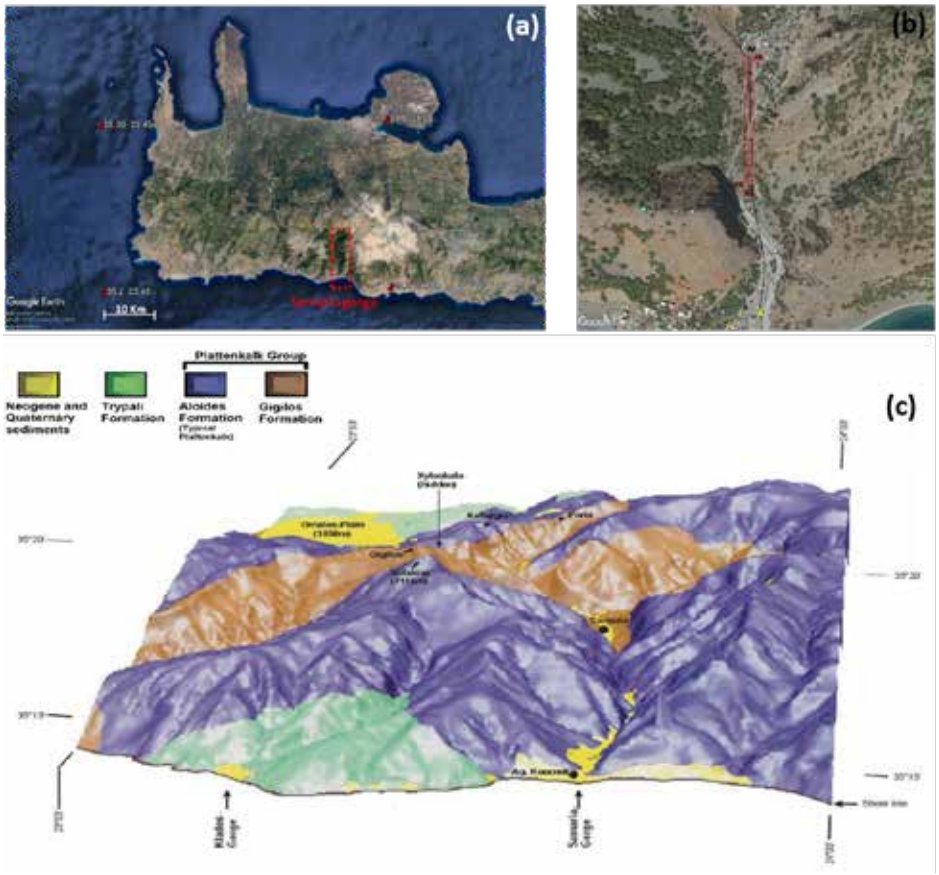


Figure 1. (a) Aerial photograph of Western Crete indicating in red dotted box the Samaria gorge area, (b) South portion of Samaria gorge wherein red are the geophysical lines and (c) the geological model for the wider region of Samaria gorge (modified from Manoutsoglou, et al., 2001).

Electrical tomography survey

The electrical tomography survey scanned the Samaria gorge area during four periods (October 2022, September 2023, June 2024 and October 2024) with 2 ERT lines and a grid (900 m x 30 m) consisting of 4 lines (A0, A1, A2 and A3 from east to west) to inspect seawater intrusion at different time periods. ERT data were acquired using Dipole-Dipole and Gradient arrays and 21 electrodes. The electrode spacing ranges from 10m to 45m. Apparent resistivity data were collected with a 10-channel SYSCAL Pro Switch™, IRIS Instruments system at 19-30 depth levels per line. Resistivity data were processed using the RES2Dinv™ software. Outliers from the original 2D data were removed by trimming data which contributed to high errors. Trimmed data were used for 3D inversion using both the RES3Dinv™ and EarthImager3D™ software packages resulting to a volume of electrical resistivity for the surveyed grid.

The inversion technique gives reasonably accurate images of three-dimensional structures, enabling the 3D imaging of the subsurface using cost–effective 2D electric tomography techniques (Dahlin and Loke, 1997). Since the inversion results deduced from 2 different software packages were similar, the EarthImager3D™ software was utilized for the visualization of 3D data.

The geoelectrical sections (Fig. 2) and the 3D geoelectrical model (Fig. 3) exhibit a lower resistivity zone with resistivity values between 5-40 Ohm.m attributed to sea water intrusion. The geoelectric section along Line A1, acquired during 2022 (Fig. 2a), exhibits lower resistivity values in this zone indicating that the seawater intrusion front extents to more than 650 m from the beginning of the line. Comparing the geoelectrical section Line A1 with the one acquired during 2023, (Fig.2b), the lower resistivity zone is reduced to approximately 600 m from the beginning of the 2023 lines. Finally, the geophysical survey of 2024 (June and October, Fig.2c-d) has shown that the sea water intrusion front is withdrawn to 550m of line A1 on June (Fig.2c), while on October, extents again to more than 650 m from the beginning of the line. The absolute altitude of the sea water intrusion front in the hinterland ranges from -50 to -120 meters.

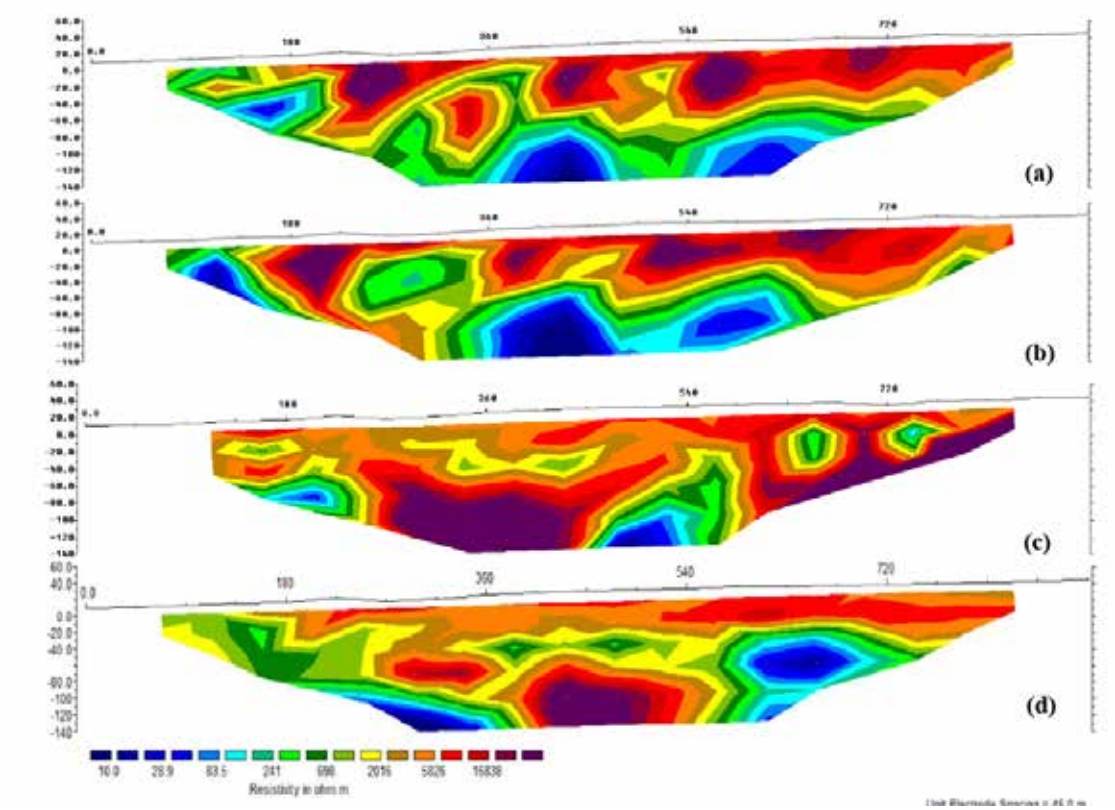


Figure 2. 2D geoelectrical sections along Line A1 surveyed using Gradient electrode array. Data collected during (a) 2022, (b) 2023 and (c-d) 2024 survey (June and October, respectively).

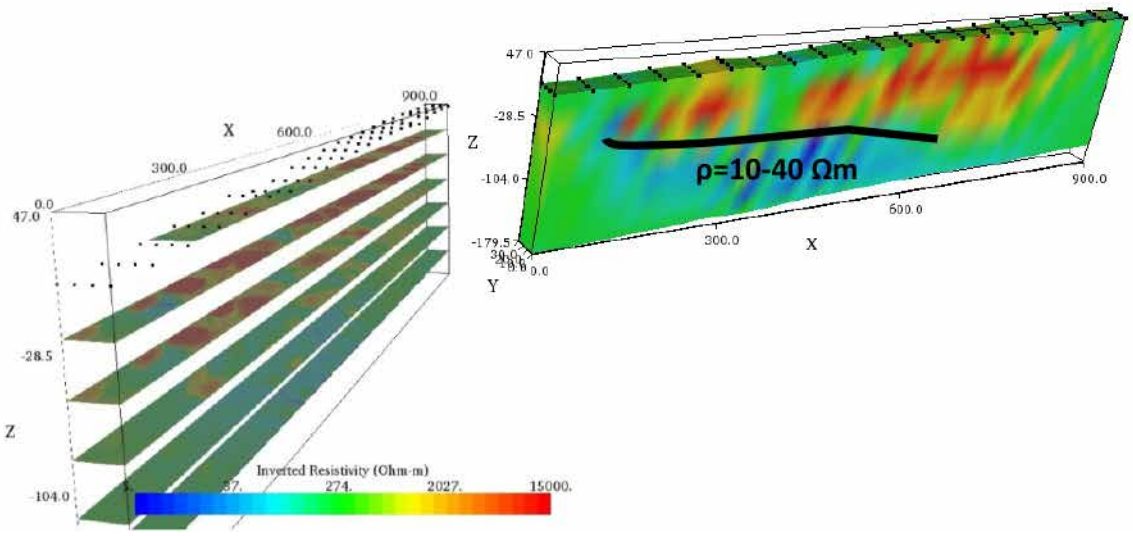


Figure 3. (a) 3D resistivity model (c) Horizontal slices from 3D model for the grid scanned during the 2023 survey.

Seismic tomography survey

The seismic refraction tomography (SRT) survey was conducted at Samaria gorge area during two periods (June and October of 2024) with 2 lines at different positions along ERT line A1. The main target of SRT survey was to delineate the interface between the alluvial deposits and the carbonate bedrock, as well as to estimate the depth to the healthy (unfractured) limestone (with Vp ≥ 3500m/s). SRT data were acquired using 24 geophones in 5m spacing and an 8gk sledgehammer as seismic source. The seismic section acquired on June of 2024 shown that alluvial deposits do not

exceed the thickness of 3-4m, while the fractured limestone appears up to the depth of 20m at the northern part of the section (Fig. 4).

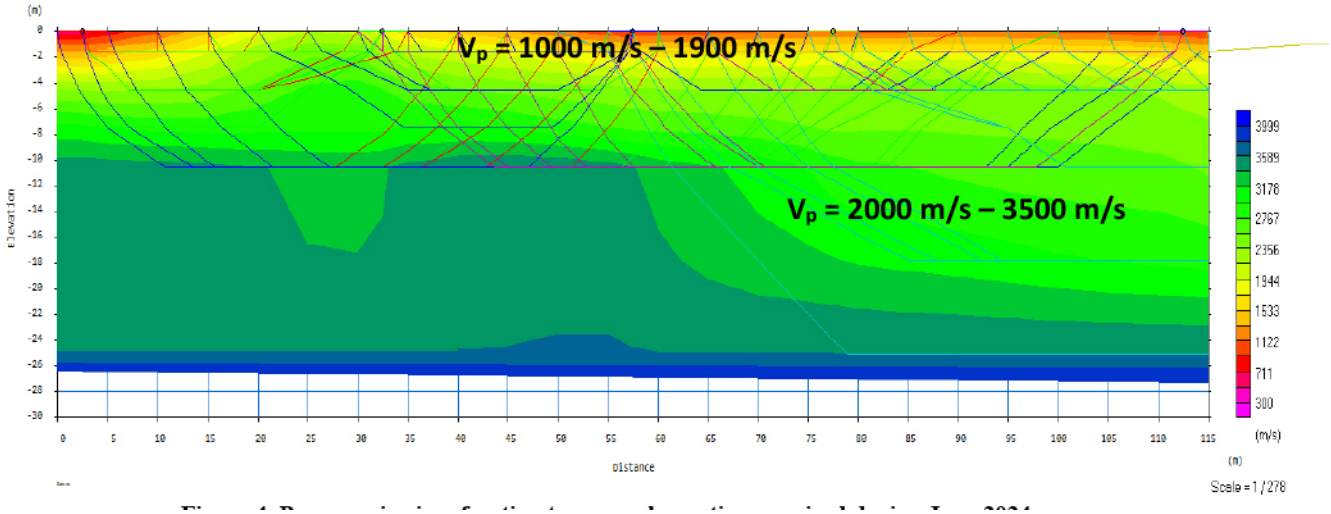


Figure 4. P-wave seismic refraction tomography section acquired during June 2024 survey.

Conclusions

A geophysical survey conducted during two periods namely 2022 and 2023 in the National Park of Samaria gorge employed the ERT method and dipole-dipole and gradient arrays to image the intrusion of sea water whose front appeared at 600 m from the beginning of the scanned lines during the 2023 survey and more than 650 m from the beginning of the scanned lines during the 2022 survey. The geophysical survey of 2024 (June and October) has shown that the sea water intrusion front was withdrawn to 550m of line A1 on June, while on October, extended again to more than 650 m from the beginning of the same line. This rapid change between June and October 2024 can be explained by the fact that infiltration of seawater into the hinterland is performed through the existing faults of the studied area.

Acknowledgements

This research was funded by the Applied Research Project “3D geological structure modeling of Samaria Gorge, aiming at the investigation of hydrogeological conditions and water reservoir levels in the core of Samaria National Park (Lefka Ori), Western Crete” (funding number: 82230), which is financially supported by the Green Fund “Forest Protection and Upgrading 2019” under “Other Nationals. Green Fund”.

References

Dahlin, T. and Loke, M. H., 1997, Quasi-3D resistivity imaging - mapping of three dimensional structures using two dimensional DC resistivity techniques, 3rd EEGS Meeting, Aug 1997, cp-95-00037, DOI: https://doi.org/10.3997/2214-4609.201407298.

Hamdan, H. and Vafidis, A., 2009, Inversion techniques to improve the resistivity images over karstic structures, Proceedings of the «15th European Meeting of Environmental and Engineering Geophysics», 3–5 September, Dublin, Ireland.

Manoutsoglou, E., Lazos, I., Steiakakis, E. And Vafeidis, A., 2022, The Geomorphological and Geological Structure of the Samaria Gorge, Crete, Greece – Geological Models Comprehensive Review and the Link with the Geomorphological Evolution. Applied Sciences, 12(20), 10670.

Manoutsoglou, E.; Spyridonos, E.; Soujon, A.; Jacobshagen, V., 2001, Revision of the Geological Map and 3D Modelling of the Geological Structure of the Samaria Gorge Region, W. Crete. Bulletin of the Geological Society of Greece, 34, 29–36, doi:10.12681/bgsg.16940.

Pavlaki, A., and Perleros, V., 2015. Updated Geological Map of the Lefka Ori National Park with Determination and Mapping of Geotope Locations (in greek). Development Organization of Crete S.A.

17th INTERNATIONAL CONGRESS of the Geological Society of Greece

BULLETIN OF THE GEOLOGICAL SOCIETY OF GREECE, SP. PUBL.

EXTENDED ABSTRACT 204

Preliminary results on sedimentological characteristics of Mass Transport Deposits (MTDs) during the Amorgos tsunami 1956: sediment provenance and geochemical elements.

Manta K.[1,2], Rousakis G.[1], Geraga M.[2], Papatheodorou G.[2], Sakellariou D.[1], Karageorgis A.P[1]

[1] Institute of Oceanography, Hellenic Centre for Marine Research (HCMR), 46.7 km Athens-Sounion, Greece, kmanta@hcmr.gr, [2] Department of Geology, University of Patras, 26504 Rio, Greece

Introduction

On July 9, 1956, two earthquakes struck in the central Aegean Sea (Perissoratis and Papadopoulos, 1999; Okal et al., 2009; Friederich et al., 2014; Brüstle et al., 2014)in Greece and adjacent regions, constitute the most tsunamigenic areas in Europe. The most recent large tsunami was a 20 m high wave that generated on 9 July 1956 in the Amorgos Basin, South Aegean Sea, in association with a M(s. The first earthquake had a magnitude of Ms = 7.4 and was located SE of Amorgos Is. (Fig 1) and occurred at 25 km depth. The second earthquake, M_S= 7.2 occurred just 13 min later close to Anafi Is. at more than 100 km depth. The tsunami that followed reached run-up heights of up to 30 meters along the southern coast of Amorgos marking the highest run-up value in the 20th century in the Mediterranean Basin (Soloviev et al., 2000). Detailed investigation of the run-up values along the Cyclades, Crete, Dodecanese Islands and the Turkish shoreline and propagation modeling by Okal et al. (2009) showed that the tsunami can't be explained by the co-seismic fault-rupture alone. These authors suggested that submarine landslide(s) must have been triggered by the earthquake(s) and contributed to the generation of the tsunami.

The sea floor between Amorgos and Astypalaia Islands is underlain by thick sediments, primarily due to the deposition of slumps debris and mass flows, which mostly consist of fine sand and silt, with occasional coarse sand present (Perissoratis and Papadopoulos, 1999; Tsampouraki-Kraounaki et al., 2021)in Greece and adjacent regions, constitute the most tsunamigenic areas in Europe. The most recent large tsunami was a 20 m high wave that generated on 9 July 1956 in the Amorgos Basin, South Aegean Sea, in association with a M(s. Sakellariou et al. (2021) and Manta et al. (2022) have shown high-resolution seafloor mapping, sub-bottom profiling, and sediment coring descriptions, which provide clear evidence of recent mass transport deposits below the seafloor in the area triggered by the 1956 earthquake(s).

This study provides new sedimentological and geochemical evidence derived from two gravity cores collected south of Amorgos and Anafi Islands, respectively, which confirm the occurrence of submarine landslide deposits linked to the 1956 earthquake(s). The 1956 Mass Transport Deposits (MTDs) vary in thickness from 55 to 100 cm. They are characterized by a gray color, calcite dilution, higher gamma density values, a terrestrial origin, sharp boundaries, and a mixture of cohesive and non-cohesive flows. Additionally, they contain lower amounts of phosphorus (P), calcium (Ca), magnesium (Mg), cobalt (Co), chromium (Cr), iodine (I), manganese (Mn), nickel (Ni), and strontium (Sr). The differences in sedimentological characteristics of the MTDs are attributed to their proximity to the seismic event. The rapid deposition during the seismic shaking preserved the old seafloor, maintaining its physical and chemical characteristics. The predominant fraction of the sediments is clay, followed by sand, while silt is negligible.

Methods

Two sediment cores (Fig. 1) retrieved from water depths between 720 and 1,030 meters. The core from the Amorgos basin (SA-1B: 25°52.974' E, 36°40.304 N) was obtained from a depth of 320 meters and has a length of 144 cm. The second core, SA-4 (26°00.835 E, 36°04.873 N), with a total length of 133 cm and was collected from the South East Aegean Sea. Initially, both cores were scanned using a multi-sensor core logger (Geotek) at 1 cm sample intervals to determine key attributes such as magnetic susceptibility, gamma-ray density, and P-wave velocity. Subsequently, the cores were longitudinally split into two halves. One half was photographed and described macroscopically, and samples were collected for grain size analysis, total organic carbon (TOC), total carbon (C), nitrogen (N), and both major and minor elements. In total, 83 samples were collected from core SA-1B, and 62 samples were obtained from core SA-4. The second half of each sediment core subjected to X-radiography using a Faxitron apparatus (cabinet X-ray). Grain size analysis was performed using a SediGraph device (Micromeritics SediGraph III Plus). Textural sediment classification followed the criteria established by Folk (1974). For carbon and TOC measurements, samples were processed in a CHN Elemental Analyzer (Fisons Elemental Analyzer EA1108) according to standard analytical procedures. The C/N ratios were calculated to estimate terrestrial organic matter inputs, according to Meyers (1994). The chemical composition of major and trace elements was analyzed through fuse beads in an X-ray fluorescence spectrometer (Phillips PW–2400). Terminology that used in this study follows Shanmugam and Wang (2015).

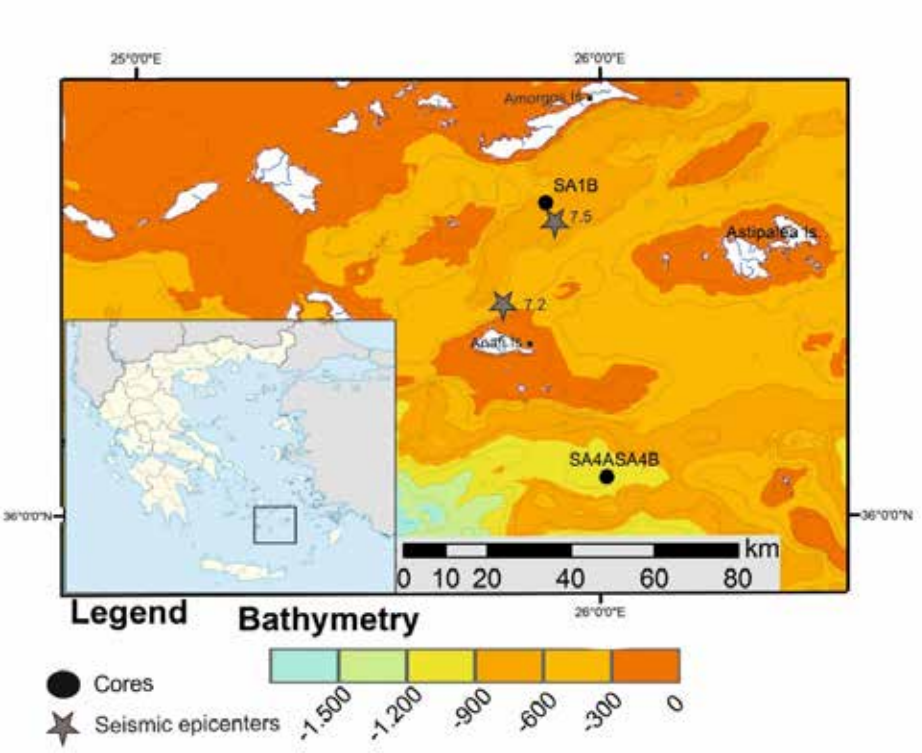


Figure 1. Location and bathymetry (in meters; grid interval of100 m) of the study area. Black circles show the location of the cores. Brown stars show the proposed epicenters for the two seismic events with their magnitude from Perissoratis and Papadopoulos (1999) and Okal et al., 2009.

Results

In core SA-1B, the uppermost 10 cm are characterized by a dull yellow color. Below this layer, the sediment transitions to a light gray hue, extending to a depth of 88 cm. Between 88 cm and 110 cm, the sediment exhibits a gray coloration. From 110 cm to 117 cm, the sediment is light yellow, followed by a dull yellow interval. Finally, the lowermost 19 cm (126–145 cm) of the core are composed of yellowish-gray sediment. The core is mostly composed of clay fractions except for some centimeters wherein sand fractions are dominant. X-radiographic analysis reveals a diagonal erosional surface with pumice at 2–5 cm, and a sandy horizon with pumice at 9 cm. At 79–82 cm, undisturbed sediment is observed at the bottom with an intrusion of sand, while the upper section of this interval is distorted. Hummocky cross-stratification is identified at 85 cm, and horizontal laminations are evident from 95–100 cm. These sediments exhibit high water content. Mud clasts and bioturbation are observed between 33–103 cm, while sand injection and erosional surfaces are present from 105–120 cm. Physical properties, including P-wave velocity and fractional porosity, exhibit similar downcore distributions, with maximum values recorded at 93–94 cm. In contrast, gamma density demonstrates an inverse trend. Total Organic Carbon (TOC) values and calcium carbonate ($CaCO_3$) exhibit parallel downcore trends, while the C/N ratio indicates a mixture of marine and terrestrial input, with the highest value (55) at 10 cm and the lowest (6.2) at 40 cm. Major element profiles reveal abrupt changes at key depths. Elements such as Al, Ba, Si, and K show significant declines at 115 cm, whereas P, Ca, Ti, Fe, Co, Cr, I, Ni, Sr, and V display pronounced increases at the same depth. Maximum values for As, Bi, Br, Sb, and Te occur at 119 cm, while Ce, Ga, and La reach their lowest values at the same depth. Proxies including Fe/Al, Mg/Al, Ca/Al, Br/Al, and Mn/Al show minimum values between 15 and 115 cm, whereas Zr/Sr peaks in this interval (Fig.3).

The uppermost section of the core represents the modern seafloor, consisting of a mixture of hemipelagic sediment and turbidites. Between 10 and 110 cm, mass transport deposits (MTDs) dominate, likely triggered by the 1956 earthquake. Below this, from 110 to 130 cm, the core records ‘old’ seafloor processes. The final section, from 130 to 144 cm, also reflects MTD deposition (Fig. 2).

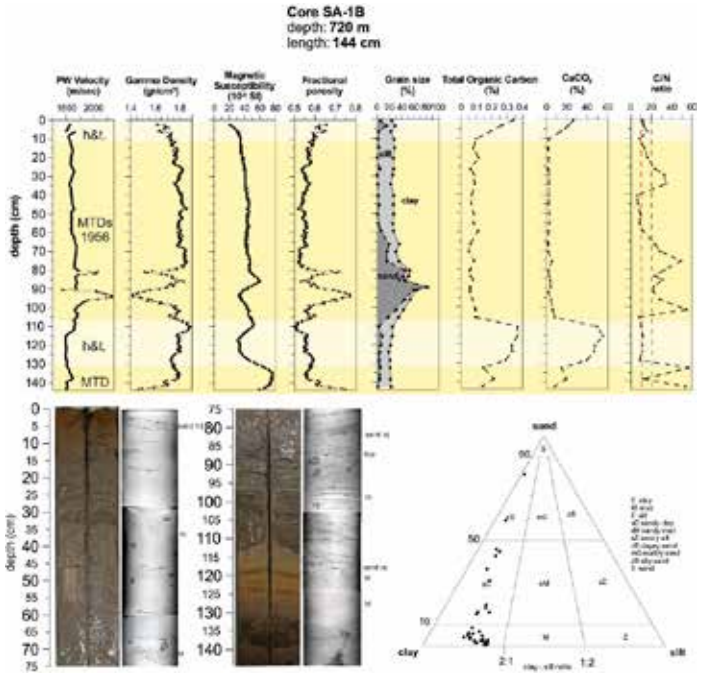


Figure 2. Downcore of plots: P Wave Velocity (m/s), Gamma-ray Density (g/cm³), Magnetic Susceptibility (10^{-5}), Fractional Porosity, Grain size distribution (dw%), Total Organic Carbon (dw%), CaC03 (dw%) and, C/N ratio, with red lines being discriminator between marine or terrigenous origin according to Meyers (1994). Photographs and X-radiographs (negative), as well as the Folk classification of grain assemblages. With light pink the sea floor is noted (h&t) and with pale yellow are marked the MTDs.

In core SA-4, the upper 18 centimeters exhibit a dull yellow-orange coloration (Fig. 4). Between 18 and 28 centimeters, the sediment transitions to a grayish-yellow hue. From 30 to 81 centimeters, the sediment is predominantly gray. The color reverts to dull yellow-orange from 81 to 89 centimeters before darkening further between 89 and 98 centimeters. From 98 to 123 centimeters, the sediment is characterized as grayish yellow, while the final 9 centimeters (123–132 cm) are dark grayish yellow. The core is primarily composed of clay, with the exception of the interval between 30 and 38 centimeters, which consists of sandy clay. Limited occurrences of broken shell fragments are found in the uppermost centimeters and at 95–96 centimeters. Small amounts of sand and pebbles are present at 4–5 centimeters and 90–91 centimeters. Pumice fragments are observed at 20–21 centimeters and 119–120 centimeters, along with volcanic sand identified at 130–131 centimeters. X-radiography of the core reveals a diagonal erosional surface at 3–5 centimeters, accompanied by a few pebbles and mud clasts. Another erosional surface is noted at 18–20 centimeters. Changes in sediment stiffness are observed at depths of 25 and 126 centimeters. P-wave velocity values generally increase downcore, reaching a depth of 77 centimeters, except for an anomaly at 24 centimeters where a value of 1500 m/s is recorded. Gamma density values range between 1.71 and 1.92 g/cm³, showing an overall increase downcore until 80 centimeters, where a local decrease to 1.65 g/cm³ is observed. Magnetic susceptibility values demonstrate an increasing trend, ranging from 23 × 10^{-5} at 1 centimeter to 143 × 10^{-5} at 59–60 centimeters. Fractional porosity displays an inverse relationship with gamma density, decreasing with depth. Total Organic Carbon (TOC) and calcium carbonate diagrams exhibit similar trends, with both showing decreasing values until 80 centimeters, followed by a peak and subsequent decline at greater depths. The C/N ratio indicates that sediments in the upper 30 centimeters and between 80 and 120 centimeters are of marine origin, while the rest of the core is composed of terrestrial material. Major element trends reveal an increase in aluminum (Al), silicon (Si), and potassium (K), from 27 to 75 centimeters. In contrast calcium (Ca), phosphorus (P), magnesium (Mg), manganese (Mn), and sulfur (S) show a decline over the same interval, with Ca and Mg reaching their lowest values. Trace elements such as arsenic (As), cobalt (Co), chromium (Cr), copper (Cu), iodine (I), nickel (Ni), antimony (Sb), and strontium (Sr) display reduced concentrations between 25 and 82 centimeters. Elements such as gallium (Ga), molybdenum (Mo), rubidium (Rb), zirconium (Zr), and yttrium (Y) increase until 40 centimeters, followed by a minor decline and subsequent increase at greater depths. Fe/Al, Mg/Al, Ca/Al, Br/Al, Mn/Al, and Zn/Al ratios decrease between 27 and 75 centimeters, while the Zr/Sr ratio exhibits an opposite trend (Fig. 3).
The uppermost centimeters of the core represent the seafloor and consist of a mixture of hemipelagic sediment

and turbidites. Between 25 and 80 centimeters, mass transport deposits (MTDs), triggered by the 1956 earthquake, dominate the stratigraphy. Below 80 centimeters, extending to 102 centimeters, the “old” seafloor processes are evident. The final section from 102 to 134 centimeters is composed of MTDs, reflecting both marine and terrestrial contributions (Fig. 4).

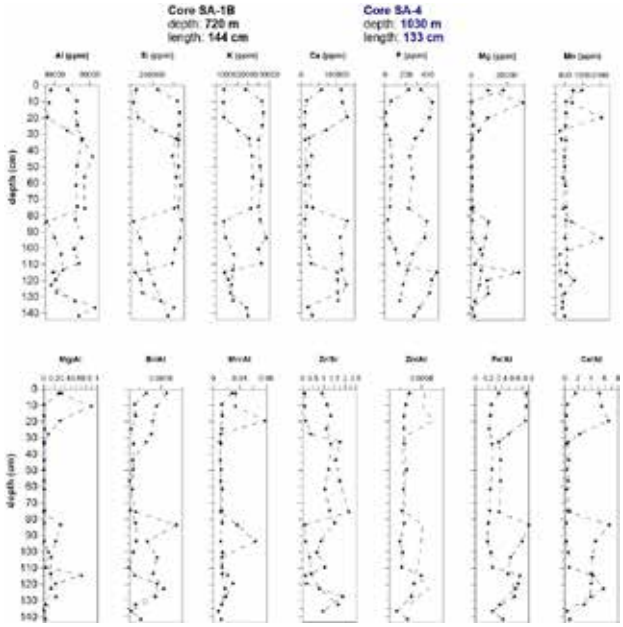


Figure 3. Downcore of plots: Al (ppm), Si (ppm), K (ppm), Ca (ppm), P (ppm), Mg (ppm), Mn (ppm), Mg/Al, Br/Al, Mn/Al, Zr/Sr, Zn/Al, Fe/Al, Ca/Al. Black dashed line are values of core SA-1B and blue dashed line for core SA-4.

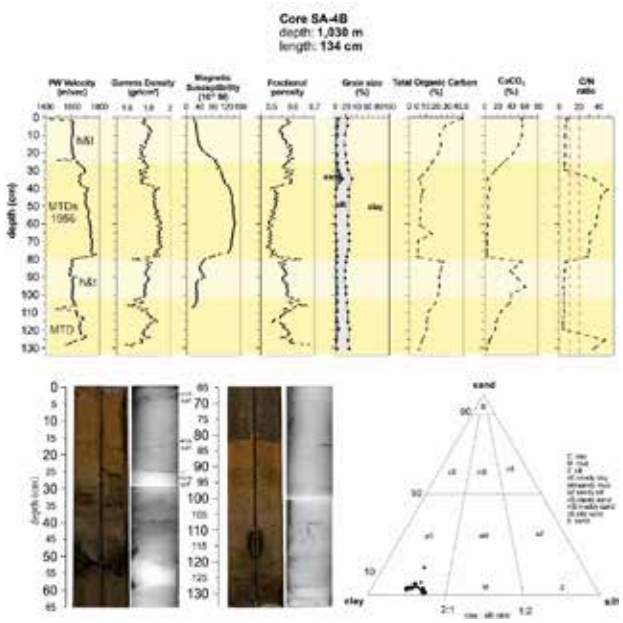


Figure 4. Downcore of plots: P Wave Velocity (m/s), Gamma-ray Density (g/cm^3), Magnetic Susceptibility (10^{-5}), Fractional Porosity, Grain size distribution (dw%), Total Organic Carbon (dw%), CaC03 (dw%) and, C/N ratio, with red lines being discriminator between marine or terrigenous origin according to Meyers (1994). Photographs and X-radiographs (negative), as well as the Folk classification of grain assemblages. With light pink the sea floor is noted (h&t) and with pale yellow are marked the MTDs.

Synthesis

The sediment cores in this study consist of mass transport deposits (MTDs), hemipelagites and turbidites, focusing on MTDs triggered by the 1956 Amorgos earthquakes. The MTDs identified in the cores are classified as debris flows, which can exhibit both cohesive and cohesionless behaviors. In core SA-4, the clayey debris flows are structure-

less, while in core SA-1B from the Amorgos Basin, mud clasts and sedimentary structures are observed. Notably, in core SA-1B, the flow demonstrates a mix of cohesive and non-cohesive behavior, featuring approximately 20 cm of non-cohesive sandy debris flows at depths ranging from 80 to 100 cm. This core also exhibits soft-sediment deformation structures (SSDS), including hummocky cross-stratification, which indicate liquefaction processes potentially triggered by seismic events such as the 1956 earthquake. Both cores share similarities in their sedimentological facies, as illustrated in Figures 2 and 4. The uppermost sections of both cores represent the “present” seafloor, followed by the deposition of large gravity flows (debrites and sandy debrites) during the 1956 earthquake(s). Beneath these layers lies the “old” seafloor, containing older MTDs that predate the 1956 earthquake. These findings align with the work of Perissoratis and Papadopoulos (1999), who reported that sediments between Amorgos and Astypalaia Islands predominantly consist of mass flows, slumps, and debrites.

Core SA-1B, retrieved from the Amorgos Basin, shows a significantly high sand content, reaching up to 80%. This elevated sand fraction is likely attributed to two factors: a) the proximity to Amorgos Island, contributing coarser material to the basin, and b) the location near the epicenter of the 1956 seismic event. The currents generated by the earthquake are believed to have flowed into several channels on the seafloor, resulting in high-energy flows that deposited thick sediment layers. Near the epicenter, MTDs reach up to 1 meter in thickness, while nearly 50 km away measure about 55 cm thick.

The MTDs in both cores consist of a mixture of marine and terrestrial material, as confirmed by various geochemical indicators. The C/N ratio in these sediments shows values up to 60, and a clear decrease in CaCO3 content correlates with the dilution of the sediments by terrigenous material. Additional proxies, such as the calcium-to-aluminum (Ca/Al) ratio (Rothwell and Croudace, 2015), along with elevated levels of silicon (Si), aluminum (Al), potassium (K), and rubidium (Rb), further corroborate this observation. These deposits exhibit high gamma density values and lower fractional porosity, which can serve as diagnostic criteria for classifying similar deposits in the region.

The rapid deposition of MTDs in the study area enabled the underlying sediments to retain their original characteristics. The “old” seafloor layers in both cores are composed of oxidized clay, marked by a distinct color change at the transition to these deposits. Although some differences exist between the two cores, the overall trends remain consistent. Both cores display marine-origin sediments in the present and old seafloor layers, as indicated by the C/N ratio, bromine (Br), and total organic carbon (TOC) values. Furthermore, calcium (Ca) in these deposits is primarily sourced from biogenic CaCO3, as evidenced by the co-variation of calcium (Ca) and strontium (Sr). Manganese (Mn) values tend to be higher in the upper layers than underlying sediments, decreasing downcore. Nevertheless, distinct peaks in Mn concentrations are observed at the same depth intervals where the “old” seafloor is found.

These findings enhance our understanding of the sedimentological and geochemical features of mass transport deposits (MTDs) in the central Aegean Sea, particularly those associated with the 1956 Amorgos earthquakes. The characteristics of these deposits can serve as diagnostic criteria for identifying similar deposits in the surrounding area. By applying the thickness of these facies to a model alongside other numerical calculations, we can gain insights into the volume and direction of the flows generated during these seismic events. Furthermore, numerical modeling of the 1956 tsunamis, combined with the sediment characteristics, is essential for evaluating the impact of tsunamis and providing predictive insights for future seismic events.

Conclusion

- The mass transport deposits resulting from the twin earthquakes exhibit similar characteristics. These deposits consist of both cohesive and cohesionless flows, show a gray color, and vary in thickness from 55 cm to 1 m. They are primarily composed of a very high clay content and possess similar chemical properties. The variation in thickness is attributed to their proximity to the epicenter of the main earthquake.
- The chemical signatures reveal that core SA-4 contains terrestrial materials, while core SA-1B consists of a mixture of terrestrial and marine origins. This suggests that most deposits have traveled from shallower depths and undergone intense remobilization.
- During the seismic shaking and the rapid deposition of these mass transport deposits (MTDs), the old seafloor remains intact, preserving its physical characteristics, color, and geochemical composition. The seafloors before and after the deposition of the MTDs in 1956 show similar characteristics.
- The sedimentological and geochemical signatures of the aforementioned deposits are reliable criteria for distinguishing similar deposits from the 1956 twin earthquakes in the central Aegean Sea.

References

Brüstle, A., Friederich, W., Meier, T., Gross, C., 2014. Focal mechanism and depth of the 1956 Amorgos twin earthquakes from waveform matching of analogue seismograms. Solid Earth 5, 1027–1044. https://doi.org/10.5194/se-5-1027-2014

Friederich, W., Brüstle, A., Küperkoch, L., Meier, T., Lamara, S., 2014. Focal mechanisms in the southern Aegean from

temporary seismic networks – Implications for the regional stress field and ongoing deformation processes. Solid Earth 5, 275–297. https://doi.org/10.5194/se-5-275-2014

Manta, K., Tsampouraki-Kraounaki, K., Sakellariou, D., Rousakis, G., Chiocci, F., Casalbore, D., Migeon, S., Estrada, F., Alonso, B., Gross, F., Morfis, I., Livanos, I., Panagiotopoulos, I., Kalaitzis, M., 2022. Marine geophysical & sedimentological data reveal multiple submarine landslides triggered by the July 1956 Amorgos earthquake in the South Aegean Sea, Greece. Int. Conf. Seafloor Landforms, Processes and Evolution, Valetta, Malta, 4-6 July 2022.

Meyers, P.A., 1994. Preservation of elemental and isotopic source identification of sediemntary organic matter. Chem. Geol. 114, 289–302. https://doi.org/10.1016/0009-2541(94)90059-0

Okal, E.A., Synolakis, C.E., Uslu, B., Kalligeris, N., Voukouvalas, E., 2009. The 1956 earthquake and tsunami in Amorgos, Greece, in: Geophysical Journal International. John Wiley & Sons, Ltd (10.1111), pp. 1533–1554. https://doi.org/10.1111/j.1365-246X.2009.04237.x

Perissoratis, C., Papadopoulos, G., 1999. Sediment instability and slumping in the southern Aegean Sea and the case history of the 1956 tsunami. Mar. Geol. 161, 287–305. https://doi.org/10.1016/S0025-3227(99)00039-0

Rothwell, R.G., Croudace, I. w., 2015. Twenty Years of XRF Core Scanning Marine Sediments: What Do Geochemical Proxies Tell Us? Springer, Dordrecht, pp. 25–102. https://doi.org/10.1007/978-94-017-9849-5_2

Sakellariou, D., Manta, K., Rousakis, G., Tsampouraki-Kraounaki, K, Chiocci, F., Casalbore, D., Migeon, S., Estrada, F., Alonso, B., Gross, F., Morfis, I., Livanos, I., Panagiotopoulos, I., Kalaitzis, M., 2021. Multiple, earthquake-triggered, submarine landslides generated the July 1956 devastating tsunami(s) in the South Aegean Sea, Greece. General Assembly European Seismological Commission, ESC2021, 19-24 Sept. 2021

Shanmugam, G., Wang, Y., 2015. The landslide problem. J Palaeogeogr 4: 109–166. https://doi.org/10.3724/SP.J.1261.2015.00071

Soloviev, S.L., Solovieva, O.N., Go, C.N., Kim, K.S., Shchetnikov, N.A., 2000. Tsunamis in the Mediterranean Sea 2000 B.C.-2000 A.D. https://doi.org/https://doi.org/10.1007/978-94-015-9510-0

Tsampouraki-Kraounaki, K., Sakellariou, D., Rousakis, G., Morfis, I., Panagiotopoulos, I., Livanos, I., Manta, K., Paraschos, F., Papatheodorou, G., 2021. The Santorini-Amorgos Shear Zone: Evidence for Dextral Transtension in the South Aegean Back-Arc Region, Greece. Geosciences 2021, 11, 216, https://doi.org/10.3390/ geosciences11050216

17th INTERNATIONAL CONGRESS of the Geological Society of Greece

BULLETIN OF THE GEOLOGICAL SOCIETY OF GREECE, SP. PUBL.

EXTENDED ABSTRACT 205

Increased preparedness in anticipation of an imminent disaster: actions during the early 2025 Santorini – Amorgos (Aegean Sea, Greece) earthquake crisis and lessons learned

Mavroulis S.[1], Sarantopoulou A.[1], Mavrouli M.[2], Antonarakou A.[3], Lekkas E.[1,4]

(1) Department of Dynamic Tectonic and Applied Geology, Faculty of Geology and Geoenvironment, School of Sciences, National and Kapodistrian University of Athens, Athens, Greece, smavroulis@geol.uoa.gr

(2) Department of Microbiology, Medical School, National and Kapodistrian University of Athens, Athens, Greece

(3) Department of Historical Geology and Palaeontology, Faculty of Geology and Geoenvironment, School of Sciences, National and Kapodistrian University of Athens, Athens, Greece

(4) Earthquake Planning and Protection Organization, Athens, Greece

1. Introduction

Seismic waves from earthquakes propagate quickly, impacting natural and built environments before emergency measures can be implemented, posing challenges for Civil Protection authorities. Earthquake early warning systems (EEWS), which detect primary seismic waves and issue alerts, help mitigate damage and casualties by enabling timely precautionary actions (Cremen and Galasso, 2020). Despite their benefits, EEW systems are not universally applicable due to the complex geodynamic and seismotectonic characteristics of many regions. In such cases, seismic risk reduction depends largely on preparedness actions taken during standard operational phases, as reliable short-term earthquake forecasts remain elusive. Therefore, for most seismic events, the transition from standard preparedness to emergency response is immediate, making the enhanced preparedness phase impractical. In case of experiencing increased seismic activity, Civil Protection authorities may implement increased preparedness actions through public risk communication, structural assessments, and stakeholder engagement, aiming to enhance awareness, influence behavior, and improve community resilience (Musacchio et al., 2023). A notable case occurred during the early 2025 seismic sequence between the Santorini and Amorgos Islands in the southern part of the Aegean Sea (Greece), a rare and unprecedented event globally. This sequence raised significant concerns regarding its evolution, duration, and potential link to magmatic and volcanic activity. It affected mainly the daily activities of the population, affecting services, and economic sectors such as tourism and transportation. This event marked the first instance in Greece where increased preparedness measures were activated in anticipation of a potential major earthquake. This study examines the measures implemented by the Greek Civil Protection authorities and operational agencies in response to the ongoing and escalating seismic sequence. Emphasis is placed on safeguarding both residents and visitors, while proactively reducing the potential risks associated with the occurrence of a more powerful earthquake that could have significant consequences for both the natural and built environments.

2. Disaster Prevention and Management Framework in Greece

Civil Protection in Greece is primarily governed by Law 4662/2020 (Government Gazette of the Hellenic Republic - GGHR, 2020), as amended by Law 5075/2023 (GGHR, 2023), which enhance disaster management and reorganize operational structures. These laws define the roles and coordination mechanisms among key agencies, including the General Secretariat for Civil Protection (GSCP), Fire Service, Hellenic Police, and Armed Forces, across all disaster phases. The GSCP, under the Ministry of Climate Crisis and Civil Protection (MCCCP), coordinates emergency responses for natural and technological hazards at all levels of administration. Strategic disaster management is guided by the national “Xenocrates” Plan, which ensures interagency coordination for disaster risk reduction and response (GGHR, 2003). Earthquake management is outlined in the “Enceladus” Plan, initially issued in 2020 and then updated in the version “Enceladus 2” (GSCP, 2022), while the “Talos 2” Plan focuses on volcanic hazards, particularly for the Santorini volcanic complex (GSCP, 2023). These earthquake plans have been tested through operational exercises (Mavroulis et al., 2025) and real events, including the 2020 Samos (eastern Aegean) earthquake and the 2021 Thessaly (central Greece) and Crete (southern Greece) earthquakes (Mavroulis et al., 2022).

The earthquake contingency plan outlines a four-phase disaster management framework: (i) standard prevention and preparedness measures, (ii) heightened preparedness in anticipation of an imminent earthquake, (iii) emergency response involving immediate mobilization and impact management, and (iv) short-term relief and rehabilitation of affected populations (GSCP, 2022). However, due to the unpredictability of seismic events and the absence of reliable short-term forecasting, the second phase has never been activated. In practice, the standard preparedness before a strong earthquake is followed by emergency response and subsequent relief and recovery after its generation. Notably, the second phase was conceived as an enhancement, not an acceleration, of standard preparedness activities.

2.1. Standard Preparedness Prevention Actions

During the prevention phase of standard preparedness, all involved stakeholders implement measures aimed at enhancing preparedness for earthquake emergencies and the rapid management of their effects. These actions include pre-seismic building inspections, contingency plan revisions, development of action memoranda, and allocation of financial resources. The functionality of emergency communication systems and the efficiency of information exchange are assessed to support coordinated decision-making. Maintenance of emergency equipment, identification of assembly sites and waste disposal areas, and readiness of shelters are also prioritized. Memoranda of understanding with private entities are established to secure additional resources, while public awareness campaigns promote self-protection. Local and regional Coordination Bodies convene to strengthen interagency collaboration, supported by structured training programs and operational exercises for Civil Protection personnel.

2.2. Enhanced Earthquake Preparedness Actions

Given the limitations of short-term earthquake forecasting, early warning systems are not included in Greece's seismic risk management framework. Nonetheless, the Secretary General of Civil Protection may increase operational readiness based on evaluations from the specialized seismic hazard committees of the Earthquake Planning and Protection Organization (EPPO). In response, Municipal and Regional authorities are responsible for implementing or accelerating preventive actions, while local coordination bodies, convened by Mayors or Deputy Mayors, facilitate interagency collaboration. Simultaneously, Civil Protection operational structures review and update emergency plans, enhance capabilities in high-risk zones, and actively participate in coordination efforts at both local and regional levels.

2.3. Emergency response and short-term earthquake impact management

Upon a strong earthquake, the Civil Protection mobilization system is activated under the "Enceladus 2" Plan, coordinating response actions across six areas: (i) search and rescue (SAR) and emergency medical services, (ii) restoration of critical infrastructure and essential services, (iii) protection of affected populations, (iv) operational coordination and administrative measures, (v) public communication and awareness, and (vi) international cooperation (Mavroulis et al., 2022, 2025). The Fire Brigade leads SAR, provides medical aid, and oversees evacuations. Authorities collect real-time data for decision-making, while infrastructure rehabilitation includes inspections, debris clearance, and restoration of utilities. Civil Protection Coordination Bodies manage response efforts locally and regionally, with support from the Armed Forces, volunteers, and public communication initiatives. If needed, evacuations are organized, and international support is requested through the European Civil Protection Mechanism

.

2.4. Immediate relief and rapid rehabilitation actions

In the post-earthquake relief phase, immediate recovery efforts focus on supporting affected populations, conducting damage assessments, and facilitating efficient administrative response. Priority is given to assisting homeless and displaced individuals through municipal welfare services, which provide financial aid for basic needs and essential household replacements. Concurrently, damage to buildings is documented, affected zones are delineated, and housing assistance is granted based on official decisions. Financial support is also extended to impacted businesses, including industrial, commercial, agricultural, and non-profit entities. Restoration of critical infrastructure, such as water, electricity, telecommunications, and road networks, is undertaken by the responsible technical services.

3. The early 2025 Santorini – Amorgos Earthquake Swarm and its Impact

3.1. Seismotectonic Setting of Santorini-Amorgos Area

The central Aegean region, dominated by the Cyclades islands, is geologically defined by the NE-SW trending Anydros, Santorini-Anafi, and Amorgos grabens, within the Santorini-Amorgos Tectonic Zone, an extensional structure 60-70 km long and 20-25 km wide between the Cyclades and Anafi-Astypalaea Plateaus (Tsampouraki-Kraounaki et al., 2021). These grabens, bounded by major faults and separated by horsts, exhibit NW-ward tilt and reach depths of up to 755 m. The area has a history of destructive seismicity, most notably the 9 July 1956 Amorgos earthquake, the strongest in 20th-century Greece. It caused widespread damage across several islands, resulting in 53 fatalities and 100 injuries (Papazachos and Papazachou, 2003). It also triggered the largest tsunami reported in the 20th century over the whole Mediterranean Basin with run-up values up to 30 m in several islands of the southern Aegean Sea (Okal et al., 2009). It was triggered either by offshore landslides (Ambraseys, 1960) or large seafloor rupture (Leclerc et al., 2024).

3.2. Evolution, Seismological Properties and Environmental Effects of the 2025 Earthquake Swarm

After the first significant episode since 2011-2012, seismic activity reemerged between June 2024 and January 2025 within the Santorini caldera, with intensification observed from mid-September. Over 1,200 earthquakes were detected in the Santorini–Kolumbo area using machine-learning-based methods, with the largest event (M=3.8) occurring off Thirassia Island on 25 January

(Interdisciplinary Risk and Crisis Management Committee of the University of Athens, 2025). A new seismic cluster emerged east of Kolumbo on 26 January, with activity peaking on 3 and 4 February at 136 and 140 events, respectively (Seismological Laboratory of the National and Kapodistrian University of Athens – SL-NKUA, 2025) (**Figure 1**). Earthquakes with M ≥ 4.0 were most frequent between 1–12 February, particularly on 4–5 February (19 events per day), and the strongest event (M 5.2) was recorded on 10 February (SL-NKUA, 2025). Seismic activity gradually declined after mid-February, with no M ≥ 4.0 earthquakes after 27 February (SL-NKUA, 2025).

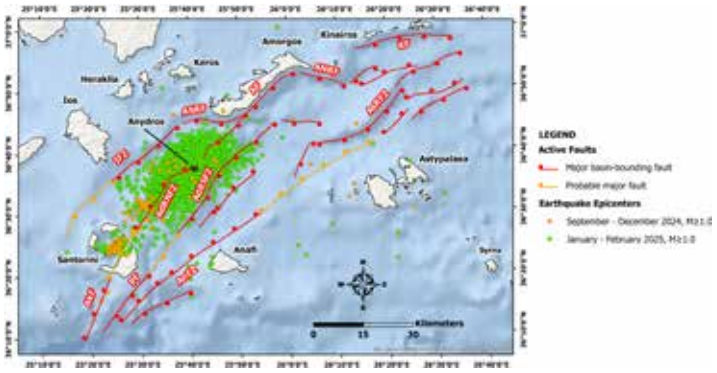


Figure 1. The Santorini – Amorgos area that was mainly affected by the early 2025 earthquake swarm along with the major basin bounding faults and the probable major faults based on Tsampouraki-Kraounaki et al. (2021). The epicenters in the affected area from September 2024 to February 2025 were recorded from the SL-NKUA (2025). AdRNFZ: Anydros Ridge North Fault Zone; AdRSFZ: Anydros Ridge South Fault Zone; AF: Amorgos Fault; AkF: Akrotiri Fault; AnFZ: Anafi Fault Zone; ANRF: Amorgos North Relay Fault; ASRF: Amorgos South Relay Fault; AsRFZ: Astypalaea Ridge Fault Zone; IFZ: Ios Fault Zone; KF: Kinairos Fault; PF: Perissa Fault.

Spatially, initial epicenters were located northeast of Santorini and east of the offshore Kolumbo volcano, later migrating toward and around Anydros islet (SL-NKUA, 2025). Most seismicity occurred southwest of Anydros, though epicenters periodically shifted northeast or appeared simultaneously on both sides of the islet (SL-NKUA, 2025). This pattern highlights a dynamic and evolving seismic sequence concentrated within the Santorini – Amorgos area.
The early 2025 earthquake swarm triggered landslides in three areas: the southern coastal zone (e.g., Red and Vlichada beaches), the central-eastern caldera slopes (e.g., Athinios, Alonaki, Fira, Imerovigli and Skaros), and the northern part of the island along the Fira-Oia road (**Figure 2**).



Figure 2. The spatial distribution of the landslides in Santorini triggered by the 2025 earthquake swarm.

Common geomorphological features at these sites include steep slopes, unstable volcanic formations, and landslide deposits. Impacts varied from debris accumulation at Red beach to sediment mobilization at Vlichada. Minor landslides in the Athinios area posed no threat to infrastructures, while rockfalls near Fira occurred downslope of residential zones without damage. In the north, rockfalls along the Fira-Oia road created hazardous conditions, requiring caution for drivers.

4. Increased preparedness actions for anticipation of an imminent earthquake

4.1. Joint meetings of seismic and volcanic risk assessment committees and public information dissemination

In response to ongoing seismic activity in the Santorini–Anydros–Amorgos region, the EPPO's Permanent Scientific Committees for Seismic Hazard Assessment and Volcanic Arc Monitoring convened to analyze the evolving seismic sequence. Official communications from the MCCCP summarized their findings, noting potential links between seismicity, offshore faults, and magmatic and volcanic processes. Recommended preventive measures included suspending educational activities, avoiding gatherings in unstable structures, restricting port access, removing hazardous building elements, selecting safer routes near landslide-prone areas, and evacuating coastal zones. Key meetings took place in January and February 2025, including a major session on 5 February chaired by the Prime Minister and Minister for Climate Crisis and Civil Protection, followed by a public broadcast featuring experts from the National and Kapodistrian University of Athens and Aristotle University of Thessaloniki, discussing related hazards and risks.

4.2. Awareness raising efforts

The EPPO, Greece's authority on earthquake policy implementation, also plays a vital role in public education and awareness to reduce seismic risk and assess seismic hazard. Its initiatives target diverse groups, including professionals, educators, Civil Protection personnel, tourism workers, and vulnerable populations such as individuals with disabilities. In response to the 2025 seismic sequence, and alongside committee meetings and official announcements on risk reduction, the EPPO conducted awareness and training activities for the affected population. Notably, it organized a webinar titled "Experiencing an Earthquake Period: Earthquake Protection of School Units" in collaboration with the Municipality of Thira, which was attended by local school directors, kindergarten heads, and nursery managers.

4.3. Strengthening security forces in affected islands

In response to the seismic sequence in Santorini and the surrounding islands, multiple Greek authorities coordinated efforts to increase preparedness and public safety. The Hellenic Fire Service deployed specialized disaster management units (EMAK in Greek), rescue dogs, drones, forest operations teams, and a mobile operations center ("Olympos") equipped with advanced technology to monitor and manage disaster response. Additional search and rescue teams were stationed across nearby islands, with aerial rescue teams on standby. Concurrently, the Hellenic Police reinforced local law enforcement with personnel and vehicles from Athens, the capital of Greece, implementing nightly patrols and security checks to prevent criminal activity and safeguard abandoned properties, ensuring public order and a sense of security amid widespread evacuations. The Hellenic Coast Guard implemented strict emergency measures in Santorini's ports, including restricted access, vessel movement controls, and safety protocols for mooring and navigation, backed by enforcement of legal sanctions. The Coast Guard also instructed vessel operators to maintain high alert for both seismic and potential hydrometeorological hazards. Meanwhile, the Hellenic Armed Forces remained on standby, deploying essential logistics infrastructure such as cranes, lighting systems, tents, portable kitchens, and liaison officers to coordinate with Civil Protection authorities. Strategic naval assets, including a tank landing ship and a support vessel, were positioned near Santorini to enable rapid response capabilities across the affected island region.

4.4. Strengthening health services in affected islands

In response to the ongoing seismic activity, all leaves for medical, nursing, and support staff at Santorini Hospital were revoked to ensure full operational readiness. The National Center for Emergency Assistance, under the MCCCP, reinforced its teams on Santorini, Amorgos, and Ios with personnel from the Special Department of Disaster Medicine, including doctors, rescuers, medical equipment, and additional ambulances. The Health Operations Centre and the Unified Coordination Operations Centre maintained high alert for continuous coordination. The 2nd Health Region of Piraeus and Aegean also enhanced readiness by deploying medical teams from "Attikon" General University Hospital and Naxos General Hospital – Health Center, and a psychological support unit from "Dafni" Psychiatric Hospital of Attica. Plans were in place to mobilize all private doctors in the affected islands if needed. Additionally, an evacuation exercise was conducted at Thira General Hospital, supervised by the Deputy Minister of Health and hospital leadership, reflecting the elevated state of preparedness.

4.5. Contribution of public utilities

To mitigate the risk of a widespread blackout during a major earthquake, the Hellenic Electricity Distribution Network Operator deployed generator-equipped trucks to Santorini, while the Municipality enhanced the island's electrical infrastructure by reinforcing networks and installing additional poles and conductors. Simultaneously, the Ministry of Digital Governance, in collaboration with mobile and satellite communication providers, ensured the deployment of mobile units and generators across the affected islands to maintain uninterrupted telecommunications during potential power failures. In response to the increasing number of residents leaving Santorini due to escalating seismic activity, and following a request from the MCCCP, airlines introduced extra flights, offering free tickets to children and teachers, along with a free return ticket valid until 20 August 2025 for those who had evacuated. Ferry companies also initiated emergency services and committed to adjusting schedules as needed to support residents and visitors departing the island.

4.6. Notifying the population via European Emergency Number 112

During the January – February 2025 seismic sequence, Greece's 112 emergency warning system was activated for the first time in response to landslide hazard. On 3 February, a geotargeted alert was issued to Santorini residents warning of landslides due to seismic activity and prohibiting access to Ammoudi and Armeni ports and the old port of Fira, while urging compliance with official instructions. A second message followed, sent to residents of Ios, Amorgos, Santorini, and Anafi, advising heightened alertness and adherence to Civil Protection directives amid ongoing seismic activity.

4.7. Municipal authorities' coordination with Civil Protection agencies

In February 2025, the Municipality of Thira issued the updated Civil Protection plan "Thiras 2" (Municipality of Thira, 2024) emphasizing preventive evacuation of at-risk populations. The plan featured thematic maps identifying emergency shelters, coastal embarkation points, and airdrop zones, selected based on terrain, accessibility, evacuation routes, and minimal tsunami risk. Designated pick-up points for vulnerable groups and students were included, and shelter locations were widely shared through social media and local announcements. To support seismic risk management, the municipality ensured continuous public communication in line with EPPO guidelines. Pre-seismic inspections by the Ministry of Infrastructure confirmed the structural safety of schools. Following landslides in Santorini and, to a lesser extent, in Amorgos, causing limited disruption, authorities enforced access restrictions and installed warning signs near hazardous areas and unstable structures to protect residents.

4.8. Municipality of Thira emergency declaration

On 6 February 2025, the MCCCP declared a State of Emergency in Civil Protection for the Municipality of Thira (MCCCP, 2025a), within the Regional Unit of Thira in the South Aegean Region. This measure was taken to address emergency needs and manage the impact of seismic activity that occurred between January and February in the study area. The declaration was in effect from February 1 to March 1. This action primarily facilitates the bypassing of bureaucratic procedures in public administration to ensure a more efficient response to the seismic crisis.

4.9. Ministerial decisions on earthquake impact mitigation and risk reduction

To mitigate the risks associated with seismic activity and secondary hazards such as landslides, preventive measures were enacted on Thira and Thirassia Islands through a ministerial decision (GGHR, 2025), co-signed by key governmental bodies including the MCCCP. In force from March 14 to May 14, 2025, these temporary restrictions targeted high-risk zones, particularly those with frequent tourist activity or proximity to landslide-prone areas. Measures included limitations on access to ports and adjacent offshore areas without port authority approval, restricted movement on selected roadways and footpaths, controlled access within specific settlement zones, suspension of operations in residential, hospitality, and healthcare facilities, and a ban on vehicular traffic in designated road sections.

4.10. Voluntary team actions for the public and vulnerable groups

During the earthquake swarm in the southern Aegean, the Hellenic Red Cross (HRC) played a crucial role by deploying specialized volunteer teams to Santorini, including Samaritan-Rescuers, psychosocial health professionals, and trained K9 units. These teams provided psychological support to vulnerable populations such as the elderly, chronically ill, and disabled individuals, conducting home visits and counseling for 60 families to address uncertainties regarding emergency contacts and shelter. Additionally, the HRC organized mental health first aid courses, training 198 residents in crisis-response skills, and conducted an evacuation exercise at the Elderly Care Center. On Amorgos, HRC teams collaborated with local Civil Protection agencies to provide community-wide psychosocial support and established a temporary Operations Center in Aegiali area. Volunteers also led awareness campaigns in schools to improve seismic preparedness. These efforts enhanced local capabilities for psychological support, emergency readiness, and resilience.

4.11. Web platform for emergency shelter dissemination

Amid the ongoing seismic activity, the Ministry of Digital Governance, in collaboration with the National Observatory of Athens, launched a web platform to inform and guide citizens on the location of safe assembly points across Greece (MCCCP, 2025b), including seismically affected islands of Santorini, Amorgos, and Ios. The platform ensures user-friendly, real-time access to officially approved assembly points without requiring application installation, and is progressively updated with additional information tailored to various natural hazard scenarios.

5. Discussion

5.1. Adequacy of implemented measures during the early 2025 seismic sequence

During the early 2025 crisis, Civil Protection authorities focused on institutional preparedness through infrastructure assessments, operational readiness, and public announcements. However, community engagement was limited, with minimal participation of

residents and visitors in preparedness actions. Although seismic inspections and safety measures were implemented, the lack of inclusive actions reduced the overall effectiveness of public preparedness efforts. This gap was addressed by the HRC, which deployed trained volunteers to provide psychosocial support, first aid training, and mental health awareness programs, particularly to vulnerable groups such as people with disabilities and the elderly. These interventions played a critical role in enhancing individual psychological preparedness and social resilience, complementing the institutional response and filling crucial gaps in community-level risk reduction. Holistic preparedness also included physical measures like retrofitting and emergency planning for key infrastructure, alongside campaigns promoting risk awareness. The integration of psychological and physical preparedness, as seen in both Civil Protection and HRC efforts, underlines the importance of multi-dimensional strategies for enhancing resilience.

5.2. Further proposed measures to reduce risk

To reduce risks in the Santorini volcanic complex and surrounding areas, early actions are vital, particularly through continuous geophysical, seismological, and geochemical monitoring. Predictive models, combined with real-time data, enable authorities to issue timely warnings and initiate preparatory actions to mitigate human and economic losses. Risk communication, including regular exercises and training for Civil Protection authorities and the public, is crucial for effective disaster preparedness. However, challenges remain, as no full-scale exercises have been conducted since the approval of the “Enceladus” and “Talos” plans in 2020. While awareness efforts are important, they must be more frequent, especially for vulnerable populations. Infrastructure improvements, including safe evacuation routes and emergency ports, are essential, as delays during the 2025 crisis hindered timely responses. Pre-seismic inspections and strengthening critical infrastructure, such as schools and healthcare facilities, are necessary for long-term resilience.

6. Conclusions

The unpredictability of early 2025 Santorini-Amorgos seismic sequence emphasized the need for increased preparedness actions. In response, the authorities and the operational structures of the Civil Protection system in Greece implemented unprecedented preparedness measures, marking the first time in the country that proactive actions were taken in anticipation of an imminent earthquake. These included strengthening security and health services, activating the European Emergency Number 112, enhancing infrastructure resilience, updating emergency plans, and launching public awareness campaigns. Volunteer groups also provided support to vulnerable populations. This comprehensive practice, tailored to the specific geological conditions of the region, can be considered a model approach for managing seismic emergencies and offers valuable lessons for other areas with similar geodynamic risks.

References

Ambraseys, N.N., 1960. The seismic sea wave of July 9th 1956, in the Greek Archipelago. Journal of Geophysical Research 65, 1257–1265. https://doi.org/10.1029/JZ065i004p01257

Cremen, G., Galasso, C., 2020. Earthquake early warning: Recent advances and perspectives. Earth-Science Reviews 205, 103184. https://doi.org/10.1016/j.earscirev.2020.103184

General Secretariat for Civil Protection, 2022. General Plan for Emergency Response and Immediate/Short-Term Management of the Earthquake Impact, Code-Named “Enceladus 2”. Ministry of Climate Crisis and Civil Protection, General Secretariat of Civil Protection, Directorate of Emergency Response Planning.

General Secretariat for Civil Protection, 2023. General Plan for Emergency Response and Immediate/Short-Term Management of the Impact of Volcanic Activity in the Volcanic Complex of Santorini, Code-Named “Talos 2”. Ministry of Climate Crisis and Civil Protection, General Secretariat of Civil Protection, Directorate of Emergency Response Planning.

Government Gazette of the Hellenic Republic, 2003. Ministerial Decision No. 1299/2003. Approval of the 7.4.2003 General Civil Protection Plan with the Keyword “XENOCRATES”. Second Volume, Sheet No. 423.

Government Gazette of the Hellenic Republic, 2020. Law No. 4662/2020. National Mechanism for Crisis and Risks Management and Risk Management, Restructuring of the General Secretariat for Civil Protection, Upgrading of the Civil Protection Volunteer System, Reorganization of the Fire Service and Other Provisions. First Volume, Sheet No. 27.

Government Gazette of the Hellenic Republic, 2023. Law No. 5075/2023. Restructuring of Civil Protection—National Air Rescue and Air Ambulance Mechanism and Other Urgent Provisions on State Aid. First Volume, Sheet No. 206.

Government Gazette of the Hellenic Republic, 2025. Emergency Civil Protection measures in the Island Complex of Santorini. Second Volume, Sheet No. 1267.

Interdisciplinary Risk and Crisis Management Committee of the University of Athens, 2025. Special Announcement, Tuesday 4-2-25 at 9.00 am. Available online: https://hub.uoa.gr/diepistimoniki-epitropi-diacheirisis-kindynon-kai-kriseon-ekpa-ektakto-deltio-typou-triti-4-2-25-kai-ora-9-00/ (accessed on 04/02/2025).

Leclerc, F., Palagonia, S., Feuillet, N., Nomikou, P., Lampridou, D., Barrière, P., Dano, A., Ochoa, E., Gracias, N., Escartin, J., 2024. Large seafloor rupture caused by the 1956 Amorgos tsunamigenic earthquake, Greece. Communications Earth & Environment 5, 663. https://doi.org/10.1038/s43247-024-01839-0

Mavroulis, S., Lekkas, E., Grambas, A., Mavrouli, M., Mokos, V., Kourou, A., Thoma, T., Karagiannis, F., Stamati, E., Kaviris, G., et al., 2025. Enhancing Preparedness and Resilience for Seismic Risk Reduction: The "Minoas 2024" Full-Scale Exercise for Earthquakes and Related Geohazards in Crete (Southern Greece). Geosciences 15, 59. https://doi.org/10.3390/geosciences15020059

Mavroulis, S., Mavrouli, M., Kourou, A., Thoma, T., Lekkas, E., 2022. Multi-Hazard Emergency Response for Geological Hazards Amid the Evolving COVID-19 Pandemic: Good Practices and Lessons Learned from Earthquake Disaster Management in Greece. Sustainability 14, 8486. https://doi.org/10.3390/su14148486

Musacchio, G., Saraò, A., Falsaperla, S., Scolobig, A., 2023. A scoping review of seismic risk communication in Europe. Frontiers in Earth Science 11, 1155576. https://doi.org/10.3389/feart.2023.1155576

Ministry for Climate Crisis and Civil Protection, 2025a. Declaration of State of Emergency for the Municipality of Thira. General Secretariat for Civil Protection, Athens, Greece. Document No. A479.

Ministry for Climate Crisis and Civil Protection, 2025b. Map of safe assembly points – mySafetyPlan. Available online: https://mysafetyplan.gov.gr (accessed on 06/04/2025).

Municipality of Thira, 2024. Second Issue of the Special Civil Protection Plan for the Preventive Organized Evacuation of the Citizens of the Municipality of Thira with the Code Word "THIRAS 2".

Okal, E.A., Synolakis, C.E., Uslu, B., Kalligeris, N., Voukouvalas, E., 2009. The 1956 earthquake and tsunami in Amorgos, Greece. Geophysical Journal International 178, 1533–1554. https://doi.org/10.1111/j.1365-246X.2009.04237.x

Papazachos, B., Papazachou, C., 2003. The earthquakes of Greece. Ziti Publications, Thessaloniki, 286 p.

Seismological Laboratory of the National and Kapodistrian University of Athens. Earthquake Catalogue Search. Available online: http://www.geophysics.geol.uoa.gr/stations/gmapv3_db/index.php (accessed on 10/01/2024).

Tsampouraki-Kraounaki, K., Sakellariou, D., Rousakis, G., Morfis, I., Panagiotopoulos, I., Livanos, I., Manta, K., Paraschos, F., Papatheodorou, G., 2021. The Santorini-Amorgos Shear Zone: Evidence for Dextral Transtension in the South Aegean Back-Arc Region, Greece. Geosciences 11, 216. https://doi.org/10.3390/geosciences11050216

17th INTERNATIONAL CONGRESS of the Geological Society of Greece

BULLETIN OF THE GEOLOGICAL SOCIETY OF GREECE, SP. PUBL.

EXTENDED ABSTRACT 206

Application of GIS-Based Multicriteria Decision Analysis and Analytic Hierarchy Process for Flood-Hazard Mapping in the Messapios River Basin, Central Evia Island, Greece

Mazarakis V.[1], Tsanakas K.[1], Greenbaum N.[2], Batzakis D.-V.[1], Sorrentino A[3], Tsodoulos I.[1], Valkanou K.[1], Karymbalis E.[1]

(1) Department of Geography, Harokopio University, Athens, Greece, karymbalis@hua.gr (2) School of Environmental Sciences, University of Haifa, Israel (3) Department of Science and Technology, Parthenope University of Naples, Italy

Introduction

Floods are among the most frequent and devastating natural hazards worldwide, causing widespread fatalities, significant property damage, and environmental degradation. In recent decades, the occurrence of extreme flood events has risen dramatically, leading to both immediate impacts, such as loss of life, property and infrastructure destruction, and longer-term effects, including health issues caused by pollution and financial difficulties for individuals and communities. Statistics emphasize the scale of the issue, with floods consistently accounting for a large proportion of natural disasters, deaths, and economic losses globally (CRED, 2023). The increasing frequency and intensity of floods highlight the pressing need to understand their underlying causes and implement effective strategies for risk mitigation. Flood-hazard assessment and mapping have become essential tools for prevention and spatial management. A widely used approach involves integrating GIS-based Multi-Criteria Decision Analysis (MCDA) with the Analytic Hierarchy Process (AHP), which allows for a systematic evaluation of multiple factors contributing to flooding and their relative importance (Ouma & Tateishi, 2014; Gigovic *et al*., 2017; Das, 2018; Radwan *et al*., 2019).

This study applies a GIS-based MCDA methodology in combination with AHP to assess and map flood hazard in the Messapios River catchment, a flood-prone area in Central Evia Island, Greece. The analysis incorporates critical factors influencing flooding, including those that affect water flow during extreme runoff events, and assigns weights to these factors based on expert input. This approach aligns with similar studies conducted across Greece, indicating its effectiveness in flood-hazard assessment and providing significant insights for spatial planning and disaster prevention.

Study Area

The Messapios River, an ephemeral stream in central Evia Island, is approximately 34 km long with a catchment area of 216 km² (Figure 1).

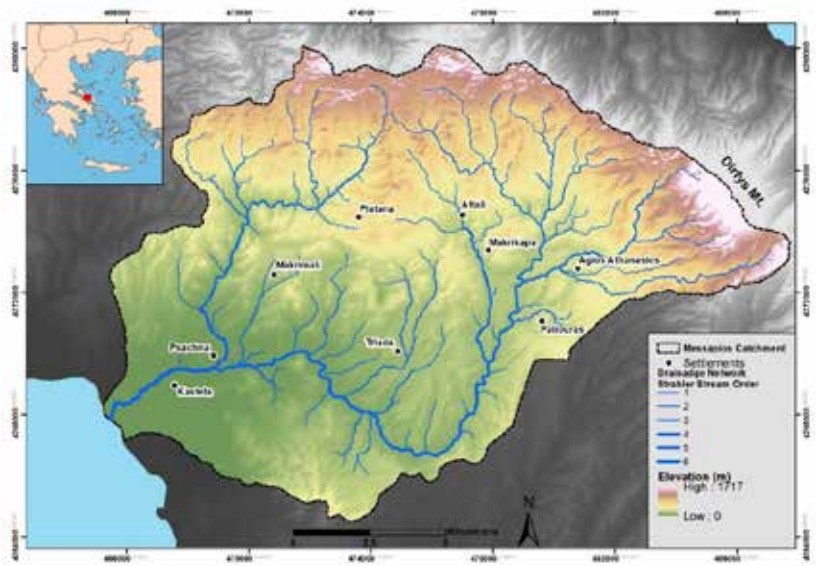


Figure 1. Map of the Messapios River drainage network and catchment.

The drainage network drains a rugged mountainous area, reaching elevations of up to 1,743 m on Mount Dirfys, with steep slopes averaging 24.1% that promote surface runoff. The lowland fan delta near the river's mouth, characterized by gentle slopes, enhances sediment deposition and rainwater infiltration. The catchment consists of geological formations of the Sub-Pelagonian geotectonic zone, including ophiolites, limestones, and flysch, as well as Neogene sedimentary rocks, and Holocene

alluvial deposits.
The climate of the study area is subtropical Mediterranean with hot, dry summers and mild, wet winters, with annual precipitation averaging 450 mm. Hydrologically, the Messapios River catchment falls within the Eastern Sterea Hellas Water District, which recorded 181 flood events between 1939 and 2018. Severe floods in 2006 and 2020 caused significant damage to settlements, infrastructure, and farmland, particularly during the 2020 "Thalia" storm, which resulted in eight fatalities and extensive property destruction.
Administratively, the catchment is part of the Municipality of Dirfys-Messapia, with 15,934 residents, half of whom live in the low-lying plains. Key settlements include Psachna, Kastella, Triada, and Makrykapa. The rural economy relies heavily on agriculture, with 35% of the population engaged in farming, supported by the fertile soils over the plains, and olive cultivation.

Methodology
This study aims to assess and map flood risk within the Messapios River catchment using a model that integrates Multi-Criteria Decision Analysis (MCDA) and the Analytic Hierarchy Process (AHP). This approach enabled the selection, calibration, and integration of five critical factors: slope, elevation, proximity to higher-order stream channels, land cover, and hydro-lithological characteristics of the geological formations. These factors, identified from a review of established methodologies in the literature (Haan *et al*., 1994; Kazakis *et al*., 2015; Bathrellos *et al*., 2016; Patrikaki *et al*., 2018; Skilodimou *et al*., 2021; Feloni *et al*., 2020; Karymbalis *et al*., 2021), influence water flow when drainage systems are overwhelmed by high runoff. A single-level hierarchy was used to maintain a straightforward weighting process for each factor's impact on flood hazard, avoiding potential subjectivity in grouping criteria and following the approach used in similar studies.
Each factor was initially divided into five classes with defined boundaries and then reclassified on a standardized scale from 1 to 5, representing increasing flood hazard levels, as shown in Table 1. A rating of "1" corresponds to a very low flood hazard level, while a rating of "5" represents a very high flood hazard level. The spatial distribution of each factor was visualized through thematic maps, where the values were classified and standardized to ensure consistency in assessing overall flood hazard.
The slope analysis for the study area was conducted using ArcGIS/ArcMap ESRI® software, utilizing a high-resolution 5-meter Digital Elevation Model (DEM) provided by the Hellenic Cadastre (Ktimatologio S.A.). This DEM also served to derive the elevation grid for the area and to extract the drainage network. The stream channels were ranked according to Strahler's stream order system (Strahler, 1957) using ArcGIS/ArcMap. To determine the "proximity to the stream channel" factor, buffer zones were created in ArcMap, generating polygons around both sides of stream channels with a Strahler order greater than 3, at specified distances. A Strahler order greater than 3 was chosen to prioritize larger channels that have a greater potential to contribute to flood hazards due to their size and drainage capacity. Land cover data was obtained from the Copernicus CORINE Land Cover database (Copernicus CORINE Land Cover, 2018) and the Agricultural Blocks dataset (ILOTS 2012) provided by the Ministry of Rural Development and Food. Geological formations in the catchment were sourced from the 1:50,000 scale geological map provided by the Institute of Geology & Mineral Exploration of Greece (IGME, 1981).
The AHP was employed to assign weights to each criterion (Saaty, 1990a; Saaty, 1990b). A pairwise comparison was conducted by the authors based on their expertise in flood hazard assessment from similar studies to assess and rank the criteria based on their relative significance. After determining the weights, the overall flood-hazard score for the Messapios River catchment was calculated by linearly combining the weighted criteria. This process involved overlaying the thematic maps of the factors, each assigned a specific weight, within a vector-based GIS environment. The criteria were integrated using the Weighted Linear Combination (WLC) method, expressed by the formula:

$$H = \sum_{i=1}^{n} w_i X_i$$

where H represents the flood hazard degree, n is the number of criteria, w_i is the weight of criterion i, and X_i is the rating of criterion i.
The result was a final thematic layer depicting the flood hazard across the entire catchment. A sensitivity analysis was also conducted to assess the robustness of the model. This involved applying a slight adjustment to the weight of the most influential criterion while proportionally modifying the weight of the second most influential criterion, ensuring that the changes did not undermine the model's effectiveness.
To validate the flood hazard map, it was compared with the Zoning of Flood-Prone Areas established by the Special Secretariat of Water, Ministry of Environment and Energy, as well as with past flood records in the study area. This comparison helped to assess the consistency of the results. Additionally, to provide an initial estimate of the catchment's vulnerability to flooding, the spatial distribution of settlements and critical infrastructure—such as roads, bridges, schools, industrial facilities, and electricity substations—was analyzed in relation to the mapped flood hazard zones.

Table 1. Classification matrix for flood-hazard criteria, detailing the assigned rating categories and the corresponding area covered by each category for every criterion.

Flood-hazard Criterion	Class	Rating	Area (km^2)	Area (%)
Slope (°)	>40	1	10.03	4.65
	25–40	2	50.42	23.35
	15–25	3	45.01	20.24
	5–15	4	61.06	28.27
	<5	5	49.44	22.89
Elevation (m a.m.s.l.)	901-1717	1	14.97	3.93
	501-900	2	39.29	18.19
	301-500	3	27.92	12.93
	151-300	4	55.58	25.74
	<150	5	78.20	39.21
Proximity to the stream channels (m)	>80 for the 3rd order streams, >100 for 4th order streams, >120 for 5th order streams, and >150 for 6th order stream	1	205.03	94.94
	60-80 for the 3rd order streams, 80-100 for 4th order streams, 100-120 for 5th order streams, and 130-150 for 6th order stream	2	1.88	0.87
	40-60 for the 3rd order streams, 60-80 for 4th order streams, 80-100 for 5th order streams, and 100-130 for 6th order stream	3	2.15	0.99
	20-40 for the 3rd order streams, 30-60 for 4th order streams, 40-80 for 5th order streams, and 50-100 for 6th order stream	4	3.15	1.46
	<20 for the 3rd order streams, <30 for 4th order streams, <40 for 5th order streams, and <50 for 6th order stream	5	3.75	1.74
Land cover	Forests (broad-leaved, coniferous, mixed), Sclerophyllous vegetation, Transitional woodland-shrub	1	129.90	60.13
	Olive groves, natural grasslands, shrub and/or herbaceous vegetation associations	2	16.15	7.47
	Complex cultivation patterns, and principally occupied by agriculture, with significant areas of natural vegetation	3	23.54	10.90
	Non-irrigated arable land, sparsely vegetated areas	4	41.38	19.19
	Discontinuous urban fabric, industrial or commercial units,	5	4.99	2.31
Geological formations	Permeable alluvial deposits	1	49.85	23.08
	Permeable carbonate rocks	2	103.44	47.90
	Semi-permeable alternations of conglomerates, marls, clays, sandstones	3	20.91	9.68
	Semi-permeable igneous and metamorphic rocks	4	27.79	12.87
	Flysch formation	5	13.97	6.47

Results

The thematic maps in Figure 2 illustrate the spatial distribution of the five criteria employed in flood hazard assessment, categorized into five hazard levels according to their respective impact on flooding. The slope in the study area ranges from 0° to 76°, with 51% (~110 km^2) of the catchment categorized as "highly" or "very highly" susceptible to flooding, primarily in the central, southern, and western plains of Psachna and Triada. Steeper slopes with "low" to "very low" flood risk are located in the northern and eastern mountainous regions, including Mount Dirfys (Figure 2a). Regarding the elevation criterion, approximately 65% of the area (~137 km^2), which includes most settlements and all documented flood events, lies below 300 m and falls within the "high" and "very high" flood hazard susceptibility zones (Figure 2b). Based on the classification used for the "proximity to the stream channels" criterion, flood-prone zones are primarily along the 6th order Messapios River main channel, as well as along its major 5th order tributaries, the Mantania and Vailelekas streams (Figure 2c). Regarding the "land cover" criterion, areas covered by forests and semi-natural vegetation, which have "very low" flood susceptibility, account for approximately 60% of the catchment. The highly susceptible areas (~19%) with arable land and sparse vegetation are concentrated in the central and

western parts of the catchment, while less resistant agricultural land and artificial surfaces account for approximately 18% and 3.5% of the catchment area, respectively (Figure 2d). Finally, substantial portions of the catchment are occupied by permeable carbonate rock formations (~48%) and highly permeable alluvial deposits (~23%), which reduce flood susceptibility (Figure 2e).

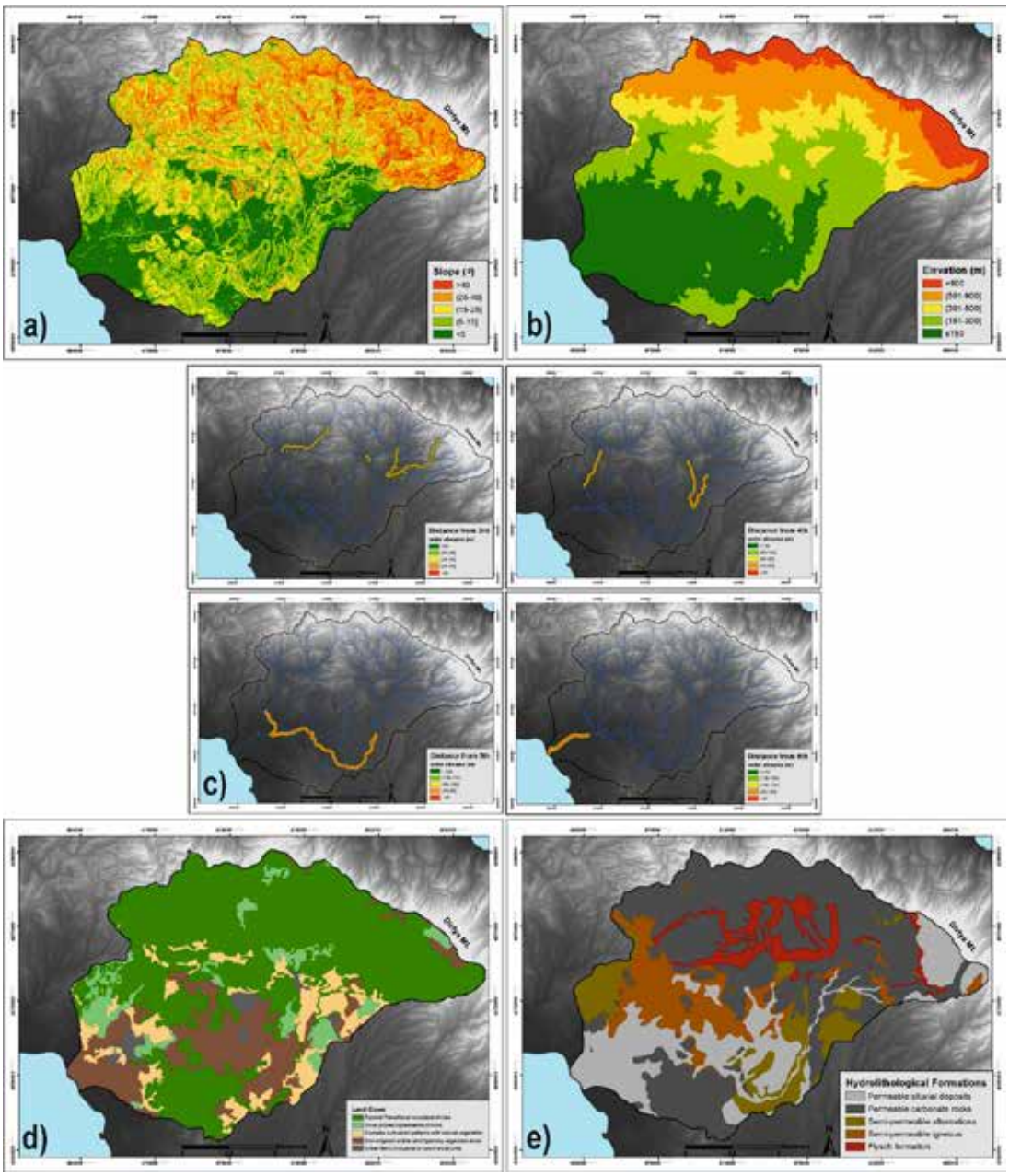


Figure 2. Maps of the Messapios River catchment illustrating the classification of: a) slope values, b) elevation, c) proximity to the stream channel, d) land cover, and e) geological formations into five categories. The rating for each criterion class is presented in Table 1.

The results of the AHP, including the pairwise comparisons matrix and the criteria weights, are given in Table 2. The estimated value of the Consistency Ratio is 0.0296, which is well below the 0.1 threshold, confirming that the hierarchy and pairwise comparisons of the criteria exhibit an acceptable level of consistency.

Two scenarios were considered for the sensitivity analysis: in Scenario 1, the weight of Slope was increased by 0.05, and the weight of Elevation was decreased by 0.05; in Scenario 2, the adjustments were reversed. The updated weights resulted in minimal deviations between the scenarios and the original AHP model, with the largest deviation being -1.57% in Scenario 1 and +1.71% in Scenario 2. These small variations indicate that the model is stable and significantly not affected by minor

changes in the weights.

Table 2. Pairwise comparison values, derived from expert insights grounded in experience with fluvial geomorphology and flood-hazard analysis, reflecting a consensus of their recommendations. W represents the relative weight of the criteria.

	Slope	Elevation	Proximity to the stream channel	Land cover	Geological formations	W
Slope	1.00	2	3	3	4	0.395
Elevation	0.50	1.00	2	2	3	0.239
Proximity to the stream channel	0.33	0.50	1.00	2	3	0.173
Land cover	0.33	0.50	0.50	1.00	2	0.119
Geological Formations	0.25	0.33	0.33	0.50	1.00	0.073
Sum	2.41	4.33	6.83	8.50	13	

To validate the results, the AHP-based flood hazard map, produced using the WLC method, was compared with the Flood Prone Zones from Greece's Special Secretariat of Water and with past flood event locations within the Messapios River catchment (Figure 3). The comparison revealed strong alignment between "high" and "very high' flood hazard areas obtained using the AHP method and the Flood Prone Zones provided by the Special Secretariat of Water of the Ministry of Environment and Energy of Greece. In addition, all past flood events (5 in total) have occurred within the "very high" flood hazard zone. This confirms that the model is reliable for flood risk assessment and management in the Messapios River catchment.

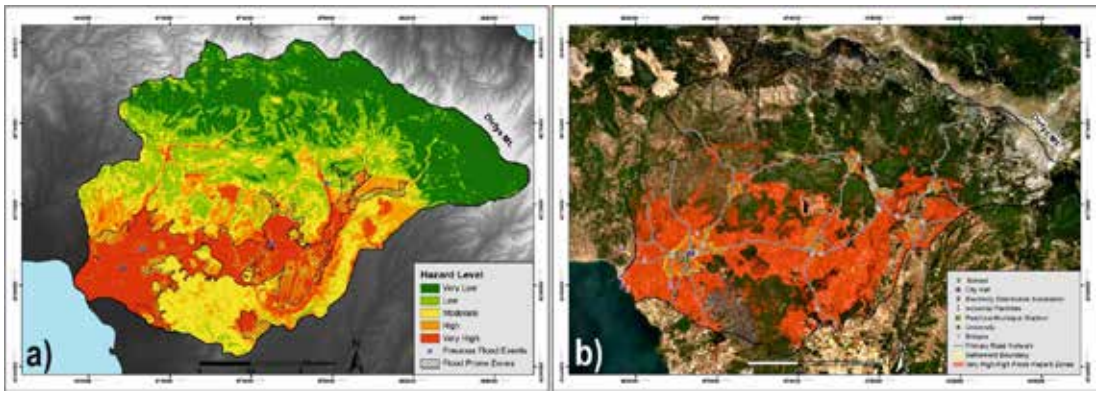


Figure 3. a) Flood hazard map of the Messapios River catchment, which also includes the Flood Prone Zones delineated by the Special Secretariat of Water of the Ministry of Environment and Energy of Greece, as well as the locations of past flood events. b) A comparative map showing the flood hazard zones identified in this study, juxtaposed with the distribution of settlements and critical infrastructure, including the primary road network, bridges, schools, industrial facilities, and electricity distribution substations.

Table 3 summarizes the areas corresponding to each of the five flood susceptibility zones from the flood hazard assessment map of Figure 3a. Approximately one-third of the catchment is classified as "very high" (17.86%) and "high" (18.02%) flood hazard areas. These zones are primarily concentrated in the central, southern, and western parts of the study area, primarily along the channels of the main streams (Messapios, Mantania, Makrimalli, Vailelekas, Makrikapiatiko), in the lower reaches of the catchment, and at the fan delta near the mouth of the river. In contrast, the "very low" and "low" flood-hazard areas are found in the northern and eastern parts, characterized by a rough mountainous relief with steep slopes and dense vegetation.

Table 3. Area (in km² and percentage) of the Messapios River catchment classified by flood-hazard levels, as determined through the Weighted Linear Combination (WLC) method using criteria weights derived from the AHP approach.

Flood Hazard Ranking	Area (km²)	Area (%)
Very low	47.14	21.83
Low	44.85	20.77
Moderate	46.48	21.52
High	38.91	18.02
Very high	38.58	17.86

The spatial comparison of settlements and critical infrastructure—such as roads, bridges, schools, industrial facilities, and power substations—with flood hazard zones highlights the area's significant vulnerability to flooding (Figure 3b). Nearly all settlements, except Platana, are in "high" or "very high" flood-prone areas, exposing approximately 9,000 residents. Psachna and Makrykapa are at greatest risk due to their proximity to major rivers with a history of severe flooding, including recent events like the "Elias" storm on September 27, 2023. Key infrastructure is also at risk: a substantial portion of the road network (~60 km) and all bridges are in "high" and "very high" flood hazard zones, as well as five major industrial facilities in the Messapios River fan delta. The General High School of Psachna, attended by students from across the municipality, and the adjacent municipal stadium are also within this zone, while the Psachna and Triada plains, vital for local agriculture, lie almost entirely in the "very high" flood hazard area, posing severe economic risk. Additionally, the Public Power Corporation substation's location in this zone signifies the potential for widespread disruption during floods.

The flood-hazard assessment map is a crucial tool for regional land-use planning, helping identify areas suitable for development while guiding long-term policies. This is particularly relevant in the study area, where ongoing land cover changes, primarily due to wildfires, have enlarged flood risk.

Concluding Remarks

This study led to the following conclusions:

- The MCDA approach effectively assessed flood hazard in the Messapios River catchment, integrating factors like topography (slope, elevation, and proximity to stream channels), land cover, and hydro-lithological characteristics of the geological formations.
- About one-third of the catchment, primarily its central, southern, and western parts, is classified as "high" or "very high" flood hazard zones, while the mountainous northern and eastern regions are less susceptible.
- Approximately 9,000 residents, key settlements (Psachna, Triada, Kastella, Makrykapa), critical infrastructure (five industrial facilities, one school, one stadium, and the power substation), and vital agricultural plains are situated in highly flood-prone zones.
- The findings emphasize the need for targeted flood mitigation measures and strategic land-use planning to reduce risk and safeguard lives, infrastructure, and economic assets.
- MCDA offers a structured, objective framework to prioritize vulnerable areas, optimize resource allocation, and guide efficient flood management strategies.
-

References

Bathrellos, G., Karymbalis, E., Skilodimou, H., Gaki-Papanastassiou, K., Baltas, E., 2016. Urban flood hazard assessment in the basin of Athens Metropolitan city, Greece. Environmental Earth Science 75, 319.

Centre for Research on the Epidemiology of Disasters (CRED) (2023) 2023 Disasters in Numbers available at: https://files.emdat.be/ reports/2023_EMDAT_report.pdf

Copernicus CORINE Land Cover, 2018. https://land.copernicus.eu/en/products/corine-land-cover

Das, S., 2018. Geographic information system and AHP-based flood hazard zonation of Vaitarna basin, Maharashtra, India. Arabian Journal of Geosciences 11, 1–13.

Feloni, E., Mousadis, I., Baltas, E. 2020. Flood vulnerability assessment using a GIS-based multi-criteria approach–The case of Attica region. Journal of Flood Risk Management 13, e12563.

Gigovic, L., Pamucar, D., Bajic, Z., Drobnjak, S., 2017. Application of GIS-Interval Rough AHP Methodology for Flood Hazard Mapping in Urban Areas. Water 9(6), 360.

Haan, C.T., Barfield, B.J., Hayes, J.C., 1994. Design Hydrology and Sedimentology for Small Catchments; Elsevier: San Diego, CA, USA, p. 608.

Institute of Geology and Mineral Exploration of Greece (IGME), 1981. Geological Map of Greece, in scale 1:50,000, Prachna and Steni Sheets.

Karymbalis, E., Andreou, M., Batzakis, D., Tsanakas, K., & Karalis, S., 2021. Integration of GIS-Based Multicriteria Decision Analysis and Analytic Hierarchy Process for Flood-Hazard Assessment in the Megalo Rema River Catchment (East Attica, Greece). Sustainability 13(18), 10232.

Kazakis, N., Kougias, I., Patsialis, T., 2015. Assessment of flood hazard areas at a regional scale using an index-based approach and Analytical Hierarchy Process: Application in Rhodope-Evros region, Greece. Science of the Total Environment 538, 555–563.

Ouma, Y.O., Tateishi, R., 2014. Urban flood vulnerability and risk mapping using integrated multi-parametric AHP and GIS: Method ological overview and case study assessment. Water 6, 1515–1545.

Patrikaki, O., Kazakis, N., Kougias, I., Patsialis, T., Theodossiou, N., Voudouris, K., 2018. Assessing Flood Hazard at River Basin Scale with an Index-Based Approach: The Case of Mouriki, Greece. Geosciences 8, 50.

Radwan, F., Alazba, A.A., Mossad, A., 2019. Flood risk assessment and mapping using AHP in arid and semiarid regions. Acta

Geophysica 67, 215–229.
Saaty, T.L., 1990a. An exposition of the ahp in reply to the paper remarks on the analytic hierarchy process. Management Science 36, 259–268.
Saaty, T.L., 1990b. How to make a decision: The analytic hierarchy process. European Journal of Operational Research 48, 9–26.
Skilodimou, H.D., Bathrellos, G.D., Alexakis, D.E., 2021. Flood Hazard Assessment Mapping in Burned and Urban Areas. Sustainability 13, 4455.
Special Secretariat of Water, Ministry of Environment and Energy, Greece. Flood Risk Management Plan for the East Sterea Hellas River Basins, Stage I, 1st Phase—Deliverable 1, Analysis of the Areas' Features and Flood Mechanisms; The Hellenic Government: Athens, Greece, 2017. 46.
Strahler, A.N., 1957. Quantitative analysis of watershed geomorphology. Eos, Transactions American Geophysical Union 38, 913–920.

17th INTERNATIONAL CONGRESS of the Geological Society of Greece

BULLETIN OF THE GEOLOGICAL SOCIETY OF GREECE, SP. PUBL.

EXTENDED ABSTRACT 207

Indium and tellurium enrichment in sulfides and sulfosalts at the Pefka high- to intermediate-sulfidation epithermal deposit, Rhodope, Greece

Melfou M.[1], Voudouris P.[2], Klemd R.[3], Keith M.[3], Melfos V.[1], Tarantola A.[4], Papadopoulou L.[1], Kantiranis N.[1]

(1) Faculty of Geology, Aristotle University of Thessaloniki, Greece, melfoumv@geo.auth.gr (2) Faculty of Geology and Geoenvironment, National and Kapodistrian University of Athens, Greece (3) GeoZentrum Nordbayern of Friedrich-Alexander-Universität (FAU) Erlangen-Nürnberg, Germany (4) Université de Lorraine, CNRS, GeoRessources Laboratory, France

Introduction / Background

Indium and tellurium are critical metals for renewable energy and advanced technologies. Tellurium is essential for cadmium telluride (CdTe) solar cells, while indium is vital for indium tin oxide (ITO) coatings used in displays and solar panels (Müller et al. 2025). Both elements are primarily obtained as by-products of base-metal mining (e.g., zinc and copper refining), making their production highly dependent on these industries. Understanding their geological occurrences is crucial for enabling more targeted exploration and efficient extraction, thereby reducing reliance on imports. This is of high significance, as China dominates global production, creating supply chain vulnerabilities (Müller et al. 2025). The Pefka high- to intermediate-sulfidation deposit hosts the highest indium and tellurium grades in Greece (1160 ppm In and >1000 ppm Te), making it an ideal case to study the enrichment processes of these metals in an epithermal environment (Voudouris et al. 2022; Melfou et al. 2023). Studies on the distribution of elements like In and Te in multi-mineral assemblages, where sphalerite is rare, remain scarce, despite their importance (Cook and Ciobanu 2015). The objective of this study is to investigate the capacity of minerals to incorporate indium and tellurium at various stages of mineralization and the processes that control their enrichment. These particularly include roquesite for indium and tellurides/goldfieldite for tellurium, but also in minor proportions galena, luzonite, chalcopyrite, and Cu-rich varieties of tennantite-tetrahedrite. This study also aims to assess the potential of pyrite to provide insights into ore-forming conditions within a deposit characterized by a complex paragenetic sequence with numerous mineral phases.

Geological context

The Rhodope metallogenic province in Greece (Fig. 1a), located within the broader Western Tethyan metallogenic belt, is a highly productive district for epithermal mineralization hosted in Oligocene-Miocene volcanic rocks (Melfos and Voudouris 2017; Voudouris et al. 2019). This region is characterized by metamorphic core complexes exhumed during the Late Cretaceous and Tertiary, as well as supra-detachment sedimentary basins, and mafic to felsic magmatism dating from the Late Eocene to Early Miocene (Marchev et al. 2005; Voudouris et al. 2022). The Pefka-Loutros area, as part of the supra-detachment northern Hellenic Thrace basin, is associated with both sedimentary and calc-alkaline to locally shoshonitic volcanic rocks. These formations are linked to the Tertiary syn- to late-orogenic extensional processes in the Rhodope province (Kilias et al. 2013). The Pefka deposit, located within this area, is one of many high- (HS) and intermediate-sulfidation (IS) epithermal mineralizations hosted in hydrothermally altered volcanic rocks and tuffs, which exhibit intermediate argillic to sericitic-argillic and locally adularia alteration (Fig. 1b). The HS to IS epithermal Pefka deposit is structurally controlled and is characterized by multistage quartz and quartz-carbonate veins and breccias with a complex ore mineralogy. This includes sulfosalts (e.g., enargite, luzonite, tennantite), sulfides (e.g., pyrite, chalcopyrite, galena), and tellurides (e.g., hessite, altaite, coloradoite). The mineralization is enriched in base, rare, and critical metals (e.g., Cu, Fe, Au, Ag, Pb, Zn, Bi, Sn, Ge, Ga, In, Mo, V, As, Hg, Te, and Se), exhibiting an exceptional ore mineralogy that includes a wide variety of sulfides, sulfosalts, tellurides, and native metals (Dimou et al. 1994; Voudouris 2006; Melfos and Voudouris 2012; Repstock et al. 2015; Voudouris et al. 2019, 2022). Bulk ore concentrations in rock chips reach up to 2300 ppm Se, 1160 ppm In, >1000 ppm Te, 390 ppm Ag, 345 ppm Au, and 250 ppm Bi, making the deposit the richest one in Te and In grades in Greece (Melfou et al. 2023). The deposit displays at least three distinct mineralization styles. The early NNW-trending Se-rich galena-quartz vein system crosscuts the altered host rocks. This early stage is followed by an NE-trending HS vein system composed of quartz, enargite/luzonite, goldfieldite, watanabeite (Biagioni et al. 2024), colusite, chalcopyrite, roquesite, tennantite/tetrahedrite-(Cu), tennantite-(In), and native gold (Voudouris 2006; Repstock et al. 2015; Voudouris et al. 2022). Tennantite-(Cu) marks the transition from the HS to the IS stage (Voudouris et al. 2022). The late-stage mineralization is characterized by a NE-trending IS vein system primarily composed of carbonates, tellurides, and tetrahedrite-(Zn), tetrahedrite/tennantite-(Fe) (Voudouris 2006; Repstock et al. 2015; Voudouris et al. 2022). The galena-bearing assemblages are the most In-rich, while the samples with carbonate gangue are the most Te-rich.

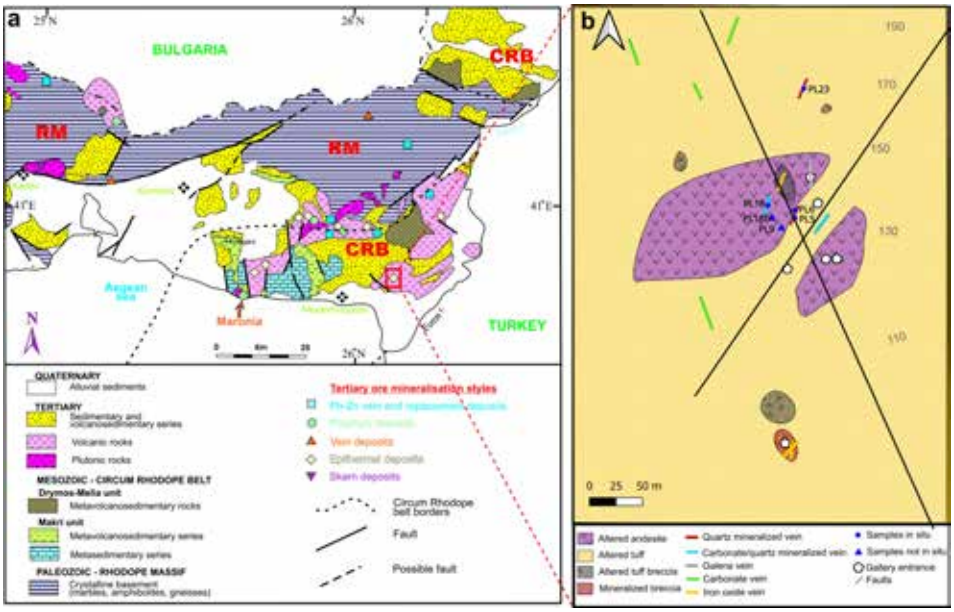


Figure 1. Regional and local simplified geological maps of the study area. (a) Geological map of the Rhodope Metallogenic Province in northern Greece, highlighting the different styles of mineralization (Melfos and Voudouris 2012). (b) Local lithological map of the Pefka HS-IS epithermal deposit, showing the locations of the samples used in this study.

Methods

Ore samples were collected from outcrops of the vein systems in the Pefka deposit and from piles outside abandoned galleries (Fig. 1a, b). Six polished sections and three polished mounts were analyzed using Electron Microprobe Analysis (EMPA) to determine the major and minor element composition of various sulfide and sulfosalt minerals. The analyses were performed with a JEOL JXA-8200 Superprobe equipped with five wavelength-dispersive X-ray spectrometers (WDS) at the GeoZentrum Nordbayern, Germany. The trace element content of sulfide and sulfosalt grains from the Pefka deposit was further analyzed by Laser Ablation Inductively Coupled Plasma Mass Spectrometry (LA-ICP-MS), which was conducted at the GeoZentrum Nordbayern, Germany. An Analyte Excite 193 nm laser (Teledyne Photon Machines) coupled to an Agilent 7500a ICP-MS was used for this purpose, using beam diameters of 20 to 35 µm. Data processing for LA-ICP-MS measurements were performed using GLITTER. Where significant interferences were observed, such as between ^{115}In and ^{115}Sn or between ^{74}Ge and ^{74}Se, mathematical corrections were applied. Due to reduced accuracy in ^{74}Ge measurements on most analytical days, only ^{73}Ge was used.

Results

A modified paragenetic sequence of ore formation at the Pefka deposit, compared to that of Voudouris et al. (2022), is presented in Figure 2a. This study focuses on the most abundant minerals analyzed using LA-ICP-MS to link the petrographic and geochemical observations. The mineralization was divided into three main stages: Pb-Se stage 1, Cu-As-Au-In-V-Sn stage 2a and 2b, and Zn-Te-Sb stage 3 (Fig. 2b-m). Stage 1 is characterized by massive Se-rich galena veins. Stage 2a hosts luzonite and enargite that are typical for high-sulfidation (HS) environments, while Stage 2b (tennantite/tetrahedrite-(Cu) and -(Fe), watanabeite, goldfieldite, colusite) marks the transition from high- (HS) to intermediate-sulfidation (IS) conditions. Stage 3 is characterized by chalcopyrite, tellurides, tetrahedrite-(Zn) that are associated with IS environments. Galena (Fig. 2b, f, g) commonly has enargite and tetrahedrite-(Cd) inclusions in Stage 1, which is accompanied by gangue quartz, forming massive 1–2 cm thick veins. Roquesite forms at the edges of the galena (Fig. 2g), suggesting their close genetic relation (Fig. 2f). The galena is crosscut by Stage 2a-b enargite, bournonite, tennantite-(In), tennantite-(Fe), and tennantite-(Cu) (Fig. 2f). The Stage 2a mineralization predominantly consists of luzonite (Fig. 2c) or enargite, often associated with pyrite. However, the enargite and luzonite of this stage are replaced and usually appear as tennantite-(Cu) of stage 2b (Fig. 2j). Pyrite occurs in two varieties, including py_{1a} that is bright in BSE images and inclusion-rich py_{1b} that is darker in BSE mode. Py_{1a} forms thin semi-massive veins (up to 0.5 cm) (Fig. 2d) and microscopically consists of anhedral grains surrounded by tennantite-(Cu) (Fig. 2i). $Pyrite_{1a}$ usually hosts large luzonite inclusions (Fig. 2h). $Pyrite_{1b}$ is found as disseminations in quartz veins related to sericite or along with barite, sometimes enclosing py_{1a} (Fig. 2i). Chalcopyrite (ccp_1) accompanies enargite in this stage. This stage includes gray quartz containing native gold grains associated with subhedral

py_2, goldfieldite, or tennantite-(Fe) (Fig. 2k). Other sulfosalts, such as colusite and watanabeite, hosting metals like V and Sn, are part of the sulfosalt assemblage in this stage (Fig. 2j). Quartz veins from Stages 2a and 2b are associated with sericite and minor APS (aluminum phosphate-sulfate) minerals, including svanbergite ($SrAl_3(PO_4)(SO_4)(OH)_6$).

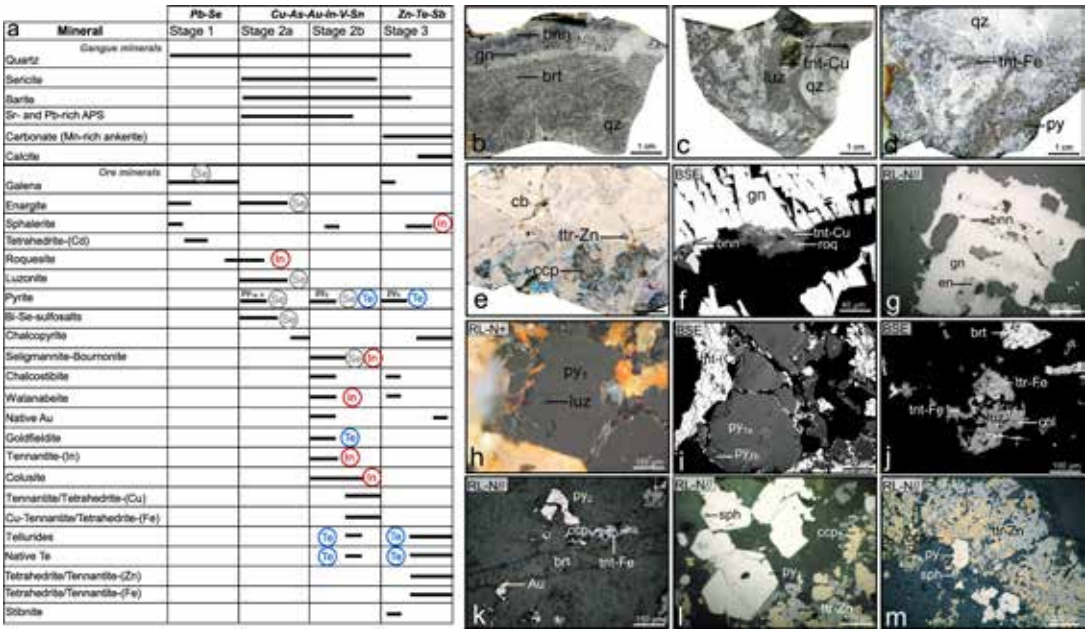


Figure 2. Simplified paragenetic sequence and macroscopic/microscopic photographs of the high-grade ore at the Pefka deposit. (a) Simplified paragenetic sequence of the Pefka deposit, focusing on analyzed sulfides and sulfosalts. (b) Galena (gn)-quartz (qz) vein of stage I, replaced by bournonite (bnn) and crosscut by an Au-rich quartz (qz) vein with barite (brt) grains. (c) Quartz vein with massive luzonite (luz), surrounded by tennantite-(Cu) (tnt-Cu). (d) Quartz vein from HS stage 2a with massive pyrite (py_{1a}) surrounded by tennantite-(Fe) (tnt-Fe) and disseminated pyrite (py_{1b}) within a sericite-rich matrix. (e) Carbonate (cb) vein of the IS stage, containing minor quartz, chalcopyrite (ccp), tetrahedrite-(Zn) (ttr-Zn), tellurides, and pyrite (py_3). (f) Galena replaced by bournonite, tennantite-(In) (tnt-In), and roquesite (roq). Remnants of galena are observed between roquesite and tnt-In. (g) Galena replaced by bournonite and enargite (en). (h) Subhedral py_1 containing luzonite mineral inclusions. (i) Anhedral, bright (in BSE) inclusion-poor py_{1a} and darker, inclusion-rich py_{1b} at the rims, surrounded by tennantite-(Cu). (j) Luzonite crosscut by barite and replaced by tetrahedrite-(Fe) (ttr-Fe) and colusite (col), accompanied by barite veins. (k) Native Au at the rims of a barite grain, accompanied by subhedral py_2 and tennantite-(Fe). (l) Euhedral py_3 hosting sphalerite (sph) and tetrahedrite-(Zn) inclusions in contact with chalcopyrite and tetrahedrite-(Zn) (m) Euhedral py_3 surrounded by chalcopyrite and tennantite-(Zn), which hosts telluride inclusions and minor sphalerite.

Stage 3 represents the IS stage, characterized by quartz and carbonate veins (Fig. 2e) comprising chalcopyrite, tetrahedrite-(Zn) and -(Fe), sphalerite, and tellurides. These are associated with euhedral pyrite (py_3), which contains numerous mineral inclusions (Fig. 2l-m). This stage is also accompanied by sericite and barite.

Variations in the elemental composition of the different pyrite generations, combined with the presence of other elements, offer valuable insights into the physico-chemical conditions of ore formation (Fig. 3a). Selenium and Te concentrations have high median values of 113 ppm and 2 ppm, respectively in py_2, while Ge is higher in py_1, with median at 2 ppm. Silver concentrations are elevated in py_1, with median values at 5 ppm, while Co is elevated in py_2, reaching 150 ppm (Fig. 3a).

Indium and Te concentrations obtained from LA-ICP-MS analyses vary among the sulfide groups, including pyrite (py_1–py_3), chalcopyrite (ccp_1-ccp_2), and galena. In pyrite, In and Te reach up to 0.5 ppm and 22 ppm, respectively, while in galena, they reach up to 30 ppm and 20 ppm, and in chalcopyrite ccp_2, up to 500 ppm and 100 ppm, respectively (Fig. 3b). LA-ICP-MS analyses of sulfosalts include luzonite from Stage 2a and bournonite, colusite and watanabeite from Stage 2b. Luzonite exhibits high Te contents of up to 3000 ppm. Luzonite is In-depleted, while bournonite of stage 2b hosts up to 30 ppm In. Colusite and watanabeite contain up to 550 ppm In and 7000 ppm Te (Fig. 3c). Indium in tennantite and tetrahedrite species reaches up to 2 wt% in the analyzed data, while previous reports noted up to 6 wt% In in the tennantite-(In) (Voudouris et al. 2022). Stage 2b tennantite/tetrahedrite-(Cu) and -(Fe) ranges from In- and Te-poor to In- and Te-rich, with tennantite/tetrahedrite-(Zn) reaching up to 1500 ppm In and 1.3 wt% Te (Fig. 3d). A slight positive correlation between In and Te content ($R^2 = 0.5$) is observed in these minerals.

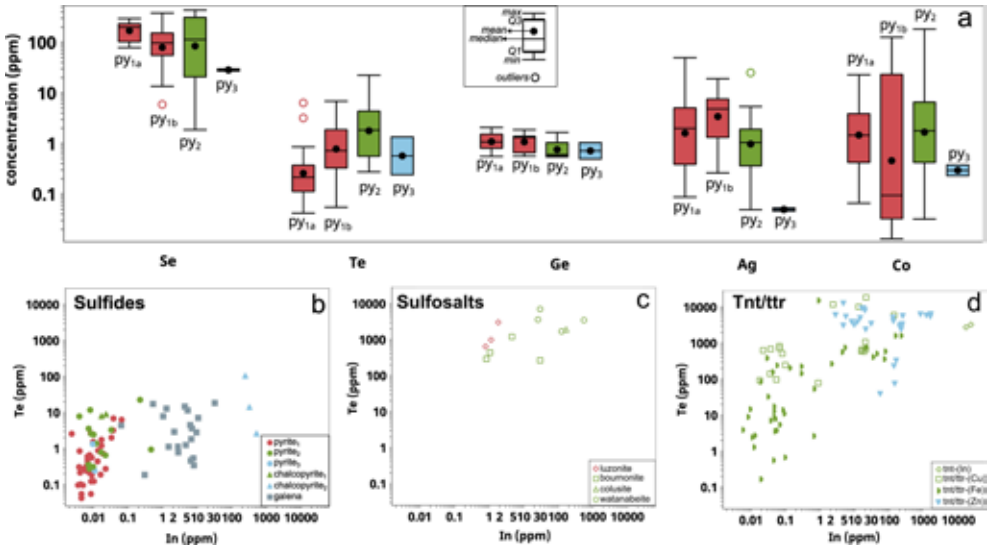


Figure 3. Geochemical variations analyzed with LA-ICP-MS from the Pefka deposit across different stages of pyrite (a), sulfides (b), sulfosalts (c), and varieties of tennantite and tetrahedrite (tnt/ttr) (d). (a) Selenium, Te, ^{73}Ge, Ag, and Co variations in the different pyrite generations. (b) In versus Te contents in different types of pyrite, chalcopyrite, and galena. (c) Indium versus Te contents in stage 2a minerals (luzonite) and stage 2b minerals (bournonite, colusite, watanabeite). (d) In versus Te contents in tennantite/tetrahedrite varieties from stage 2a (tennantite-(In), tennantite/tetrahedrite-(Cu) or -(Fe), and stage 3 (tennantite/tetrahedrite-(Zn)). Colors are indicative of the different stages: Stage 1 is grey, stage 2a is red, stage 2b is green and stage 3 is pale blue.

LA-ICP-MS profiles focusing on In and Te patterns (Fig. 4) in the different minerals suggest either micro-inclusions or the presence of these elements in solid solution. Other elements, such as Cu, Au, Ag, and Pb, were monitored to detect inclusions potentially forming phases with In and Te. Notably, only galena shows evidence of inclusions in the LA-ICP-MS patterns (Fig. 4a). In contrast, sulfosalts display smooth patterns for In and Te, suggesting that In and Te are within the mineral structures (Fig. 4b-h). However, Pb exhibits spiky patterns in tennantite-(In) and tetrahedrite-(Zn) (Fig. 4d, g), likely due to remnants of earlier galena.

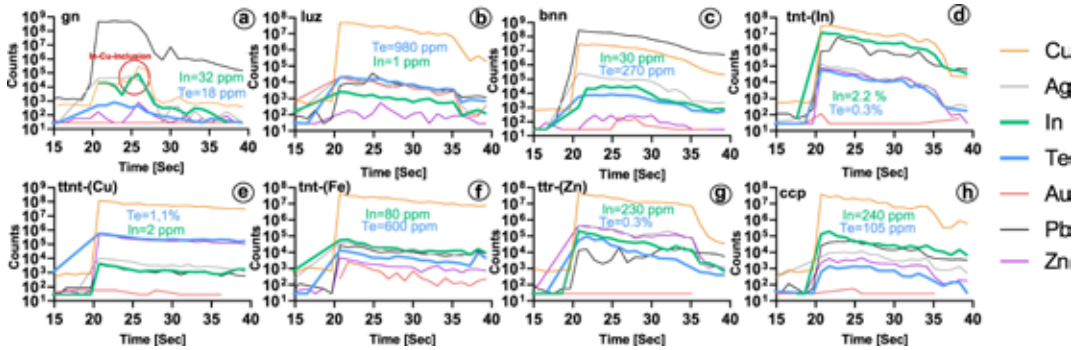


Figure 4. LA-ICP-MS time patterns of (a) galena (gn), (b) luzonite (luz), (c) bournonite (bnn), (d) tennantite-(In) (tnt-In), (e) tennantite-(Cu) (tnt-Cu), (f) Tennantite-(Fe) (tnt-Fe), (g) tetrahedrite-(Zn) (ttr-Zn), and (h) chalcopyrite (ccp). Indium and Te are illustrated with thick green and blue lines, respectively, and their concentrations after data reduction are stated. These patterns are also accompanied by those of Cu, Ag, Au, Pb, and Zn to highlight the presence of mineral inclusions or zonation.

Discussion

The Pefka deposit hosts, to our knowledge the most In and Te rich mineralization in Greece, with the presence of these two metals in a variety of minerals. The main carriers of In are roquesite that hosts 48 wt% In and tennantite-(In) that hosts up to 6 wt% In (Voudouris et al. 2022, 2023). Both minerals belong to stage 2, while roquesite also appears at the end of stage 1. Indium is also present in sphalerite of stage 3 (up to 0.31 wt%; Voudouris et al. 2022). The main carriers of Te are stage 2b goldfieldite that host up to 23 wt% Te and stage 3 tellurides (e.g., hessite, petzite, coloradoite, native Te, etc), in which Te is the main constituent of the minerals. The tellurides also occur in minor amounts in stage 2b in association with goldfieldite. The in-situ LA-ICP-MS analyses revealed the ability of sulfides, including pyrite, galena, and chalcopyrite, as well as sulfosalts like tennantite-tetrahedrite, enargite, colusite, bournonite, and watanabeite to host In and Te in their

structure or in the form of micro-inclusions. Galena shows a moderate enrichment of In, but as revealed by the LA-ICP-MS spectra, this is related to the presence of micro-inclusions, probably of roquesite. Stage 2a minerals like luzonite show no enrichment in In (up to 2 ppm) and a moderate enrichment in Te (up to 3000 ppm) (Fig. 4c and 5b). The sulfosalts of stage 2b, excluding the main carriers (i.e. roquesite), host up to 550 ppm In and 1.9 wt% Te. Stage 3 of the mineralization hosts up to 2500 ppm of In and 2 wt% of Te. Therefore, it is indicated that all stages host In, while Te is mainly hosted in stages 2b and 3. Higher In grades in global epithermal/polymetallic deposits have been detected in Sn-rich systems (Mejías et al. 2023). This fact is also seen at the Pefka deposit with the co-occurrence of In-rich minerals of stage b like tennantite-(In)/bournonite and Sn-rich minerals like colusite that have also high In-contents.

Pyrite, a well-studied and ubiquitous mineral in epithermal deposits, serves as a valuable indicator of ore-forming conditions throughout the different mineralization stages. Different pyrite generations in the Pefka deposit show a progressive evolution in chemistry, particularly in specific elemental ratios, which provide insights into processes like cooling, fluid mixing, and boiling (Keith et al. 2022; Falkenberg et al. 2024). The Se/Te ratio has been used to indicate temperature changes (Keith et al., 2022; Falkenberg et al., 2024). Pyrite data from the Pefka show that py_{1a} formed at higher temperatures, with median Se/Te ratios around 1000, while py_3 exhibits median Se/Te ratios closer to 1, suggesting lower temperatures of formation (Fig. 5a). Other pyrite generations fall progressively between these values: py_{1b} has a median ratio of ~100, while py_2 displays median values around 10. In the Koloula (Solomon Islands) and Maronia (Greece) porphyry-epithermal systems, pyrite formed above 350 °C has median Se/Te ratios >50, while lower-temperature pyrite shows ratios <50 (Keith et al., 2022; Falkenberg et al., 2024). This aligns with mineralogical evidence from Pefka, suggesting its initial HS sulfidation occurred above 300 °C (Voudouris et al., 2022).

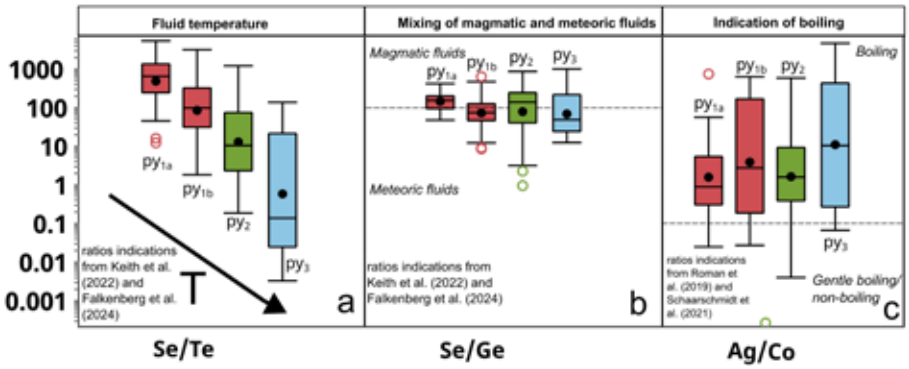


Figure 5. Boxplots from ratios derived from in-situ LA-ICP-MS data in pyrite from the Pefka deposit, used to infer physicochemical parameters of the ore-forming conditions. (a) The Se/Te ratio, which indicates cooling of the fluid temperature (Keith et al., 2022; Falkenberg et al., 2024). (b) The Se/Ge ratio, which reflects the mixing of magmatic and meteoric fluids (Keith et al., 2022; Falkenberg et al., 2024). (c) The Ag/Co ratio, that reflects boiling or non-boiling conditions (Román et al., 2019; Schaarschmidt et al., 2021). Colors are indicative of the different stages: Stage 1 is grey, stage 2a is red, stage 2b is green and stage 3 is pale blue.

The Se/Ge ratio has been applied to indicate fluid mixing, particularly between magmatic and meteoric fluids (Keith et al. 2022; Falkenberg et al. 2024). $Pyrite_{1a}$ and py_2, have median Se/Ge ratios that fall within the magmatic fluid field while the Se/Ge ratio of py_{1b} and py_3 points towards ore fluids with a mixed magmatic and meteoric fluid component (Fig. 5b). It is notable that the high-In stage 2b shows elevated Se/Ge ratios, suggesting important contribution of the magmatic fluids at the In-rich stage. The Ag/Co ratio of pyrite has been used in studies to differentiate boiling from non-boiling environments (Román et al. 2019; Schaarschmidt et al. 2021). At Pefka, all pyrite grains have Ag/Co ratios above 1, indicative of boiling conditions (Fig. 5c). Evidence for boiling at Pefka is also provided by the telluride mineralogy and the presence of adularia alteration in the surrounding rocks, including the andesitic host rock (i.e. Voudouris et al., 2022).

Conclusion

The outcome of this study is the In and Te partitioning in a multi-mineral assemblage where sphalerite is volumetrically rare, providing valuable insights into their distribution in various sulfide and sulfosalt species. Early-stage galena shows moderate enrichment, with In and Te concentrations reaching up to 30 ppm and 20 ppm, respectively, possibly because of the presence of inclusions. In contrast, later-stage tetrahedrite-tennantite varieties exhibit significantly higher concentrations, with up to 6 wt% In and 1.9 wt% Te. Pyrite, analyzed across multiple generations, provides valuable insights into the evolution of the hydrothermal system. A systematic decrease in the Se/Te ratio of pyrite—from magnitudes around 1000 to values close to 1—indicates progressive cooling of the ore-forming fluids. Additionally, Ag/Co ratios in pyrite suggest boiling conditions during both the high-

sulfidation (HS) and intermediate-sulfidation (IS) stages. The LA-ICP-MS analyses reveal that sulfosalts play a critical role in hosting In and Te, from HS, during the transition and final IS stages. Minerals such as tennantite-tetrahedrite, colusite, and watanabeite act as significant carriers, with In and Te present both in solid solution and as inclusions. These findings underscore the importance of sulfides and sulfosalts not only as repositories of critical metals but also as proxies for reconstructing the physicochemical processes that governed ore deposition in the Pefka deposit. Future research will focus on the distribution of other elements in sulfosalts and sulfides, such as Se, Ag, and Au, which are particularly enriched at Pefka. Additionally, pyrite trace element ratios, which provide insights into ore-forming conditions, will be compared with those from similar systems.

Acknowledgements

Dr. H. Brätz is thanked for her assistance during the LA-ICP-MS analyses and data processing. Boliden Mineral AB is gratefully acknowledged for providing financial support to the PhD thesis of M. Melfou entitled “Mineralogy geochemistry and ore genesis of the critical and rare metals enrichment in the high- to intermediate-sulfidation epithermal systems at the Pefka-Loutros area, Rhodope, Greece”.

References

Biagioni, C., Voudouris, P., Moëlo, Y., Sejkora, J., Dolníček, Z., Musetti, S., and Mauro, D., 2024, Crystal structure of Pb-bearing watanabeite from Pefka, Greece: Mineralogical Magazine, v. 88, no. 3, p. 218–227.

Cook, N.J., and Ciobanu, C.L. (2015) Mineral hosts for critical metals in hydrothermal ores. In Mineral Resources in a Sustainable World, Proceedings of the 13th SGA Biennial Meeting, Nancy, France. 24-27

Dimou, E., Michael, C., and Serment, R., 1994, Mineralogical composition of epithermal polymetallic mineralization at Pefka. Rhodope., in Bull. Geol. Soc. Greece. 30, 553–1550.:, p. 553–1550.

Falkenberg, J.J., Keith, M., Melfos, V., Hohl, M., Haase, K.M., Voudouris, P., Höss, A., Wenske, J., Klemd, R., Beier, C., Kutzschbach, M., and Strauss, H., 2024, Insights into fluid evolution and Re enrichment by mineral micro-analysis and fluid inclusion constraints: Evidence from the Maronia Cu-Mo±Re±Au porphyry system in NE Greece: Mineralium Deposita.

Keith, M., Haase, K.M., Chivas, A.R., and Klemd, R., 2022, Phase separation and fluid mixing revealed by trace element signatures in pyrite from porphyry systems: Geochimica et Cosmochimica Acta, v. 329, p. 185–205.

Kilias, A., Falalakis, G., Sfeikos, A., Papadimitriou, E., Vamvaka, A., and Gkarlaouni, C., 2013, The Thrace basin in the Rhodope province of NE Greece — A tertiary supradetachment basin and its geodynamic implications: Tectonophysics, v. 595–596, p. 90–105.

Marchev, P., Kaiser-Rohrmeier, M., Heinrich, C., Ovtcharova, M., von Quadt, A., and Raicheva, R., 2005, 2: Hydrothermal ore deposits related to post-orogenic extensional magmatism and core complex formation: The Rhodope Massif of Bulgaria and Greece: Ore Geology Reviews, v. 27, no. 1, p. 53–89.

Mejías, O., Parbhakar-Fox, A., Jackson, L., Valenta, R., and Townley, B., 2023, Indium in ore deposits and mine waste environments: Geochemistry, mineralogy, and opportunities for recovery: Journal of Geochemical Exploration, p. 107312.

Melfos, V., and Voudouris, P., 2017, Cenozoic metallogeny of Greece and potential for precious, critical and rare metals exploration: Ore Geology Reviews, v. 89, p. 1030–1057.

Melfos, V., and Voudouris, P.Ch., 2012, Geological, Mineralogical and Geochemical Aspects for Critical and Rare Metals in Greece: Minerals, v. 2, no. 4, p. 300–317.

Melfou, M., Voudouris, P., Klemd, R., Keith, M., Melfos, V., and Kantiranis, N., 2023, In-situ trace element analyses of pyrite from the Pefka epithermal Cu-Au-Te-In-Se deposit, Rhodope, Northern Greece, in 17th Biennial SGA Meeting, Minerals in a changing world, Zurich.

Müller D, Groves DI, Santosh M, Yang C-X (2025) Critical metals: Their applications with emphasis on the clean energy transition. Geosystems and Geoenvironment 4:100310.

Repstock, A., Voudouris, P., and Kolitsch, U., 2015, New occurrences of watanabeite, colusite, “arsenosulvanite” and “Cu-excess” tetrahedrite-tennantite at the Pefka high-sulfidation epithermal deposit, northeastern Greece: Neues Jahrbuch für Mineralogie - Abhandlungen, v. 192, no. 2, p. 135–149.

Román, N., Reich, M., Leisen, M., Morata, D., Barra, F., and Deditius, A.P., 2019, Geochemical and micro-textural fingerprints of boiling in pyrite: Geochimica et Cosmochimica Acta, v. 246, p. 60–85.

Schaarschmidt, A., Haase, K.M., Klemd, R., Keith, M., Voudouris, P.C., Alfieris, D., Strauss, H., and Wiedenbeck, M., 2021, Boiling effects on trace element and sulfur isotope compositions of sulfides in shallow-marine hydrothermal systems: Evidence from Milos Island, Greece: Chemical Geology, v. 583, p. 120457.

Voudouris, P., 2006, A comparative mineralogical study of Te-rich magmatic-hydrothermal systems in northeastern Greece: Mineralogy and Petrology, v. 87, nos. 3–4, p. 241–275.

Voudouris, P., Mavrogonatos, C., Spry, P.G., Baker, T., Melfos, V., Klemd, R., Haase, K., Repstock, A., Djiba, A., Bismayer, U., Tarantola, A., Scheffer, C., Moritz, R., Kouzmanov, K., et al., 2019, Porphyry and epithermal deposits in Greece: An overview, new discoveries, and mineralogical constraints on their genesis: Ore Geology Reviews, v. 107, p. 654–691.

Voudouris, P., Repstock, A., Spry, P., Frenzel, M., Mavrogonatos, C., Keith, M., Tarantola, A., Melfos, V., Tombros, S., Zhai, D., Cook, N., Ciobanu, C., Schaarschmidt, A., Rieck, B., et al., 2022, Physicochemical constraints on indium-, tin-, germanium-, gallium-, gold-, and tellurium-bearing mineralizations in the Pefka and St Philippos polymetallic vein- and breccia-type deposits, Greece: Ore Geology Reviews.

Voudouris P., Biagioni C., Sejkora J. and Musetti S. (2023) Tennantite-(In), IMA 2023-011. In: CNMNC Newsletter, 73. European Journal of Mineralogy, 35, 397–402.

17th INTERNATIONAL CONGRESS of the Geological Society of Greece

BULLETIN OF THE GEOLOGICAL SOCIETY OF GREECE, SP. PUBL.

EXTENDED ABSTRACT 208

An Overview of Geological Map Sheets of Crete by HSGME.

I. Michalakis[1], A. Photiades[2], Sp. Staridas[1]

(1) Hellenic Survey of Geology and Mineral Exploration, Regional Branch of Crete, Rethymno, Greece, michalakis@eagme.gr (2) Hellenic Survey of Geology and Mineral Exploration, Department of General and Applied Geology, Acharnes, Greece, afotiadis@eagme.gr

Research Highlights

The geological mapping of Crete, undertaken over several decades, represents a monumental effort to document the island's complex and diverse geology. However, the varying methodologies, technologies, and scientific approaches employed during different survey periods have resulted heterogeneity in the maps produced. This paper highlights advancements in the visualization and integration of geological data within a GIS environment, providing new opportunities for cohesive and comprehensive geological interpretations of Crete.

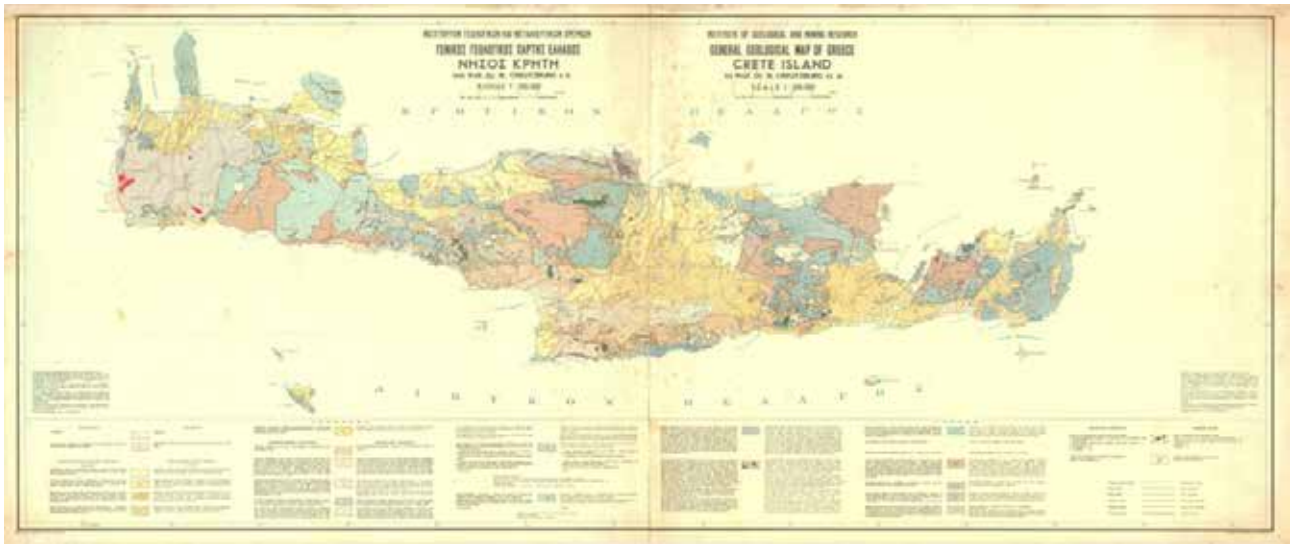


Figure 1. The General Geological Map of Greece / Island of Crete, published by the Institute of Geological and Mining Research (IGMR) in 1977, at a scale of 1:200k (*Commonly known as the Geological Map of Crete by Creutzburg et al.*).

Introduction / History of Publication of Geological Maps of Crete

The geological framework of the island of Crete is extensively documented in the General Geological Map of Greece / Island of Crete, published in 1977 by the Institute of Geological and Mining Research (IGMR), at a scale of 1:200k (Figure 1). This foundational and legacy map represents one of the most significant milestones in capturing the geological complexities of the island. Crete (including Gavdos island) is covered by 24 map sheets (Figure 2) that form part of the Basic Geological Map of Greece (BGMG), produced by the Institute for Geology and Subsurface Research (IGSR)—later renamed the Institute of Geology and Mineral Exploration (IGME), and now known as the Hellenic Survey of Geology and Mineral Exploration (HSGME). These maps, published at a scale of 1:50k between 1956 and 2013, provide a more detailed account of Crete's geological units and structures. The geological mapping of Crete reflects a systematic and iterative process spanning several decades, undertaken by HSGME and its predecessor organizations (IGSR, IGMR, and IGME).

Background / Geological Map Sheets of Crete

The geological mapping of Crete has undergone remarkable advancements over decades of systematic surveys, as summarized in Table 1 and illustrated in Figure 2. The need for a detailed geological map to capture the island's complex geological framework became evident as early as the mid-20th century (Aronis, 1949). In the following years, the IGSR focused on extensive fieldwork, resulting in foundational geological maps at a scale of 1:50k. Notable examples include the Alikianos (Vatolakkos) map sheet in Western Crete (Christodoulou & Tataris, 1969; Figure 4.2) and the Kato Chorio (former Ierapetra) map sheet in Eastern Crete (Papastamatiou et al., 1959; Figure 4.1). These pioneering efforts provided critical insights into the geological structure of the island and paved the way for future

advancements. Figures 4.1 and 4.2 depict the updated versions of these map sheets—soon to be released by the HSGME—showcasing significant progress in geological mapping techniques and visualization. These updates are part of the BGMG series, reflecting the integration of modern methodologies and technologies focused on creating a more cohesive and accurate geological framework for the region.

In 1977, the IGMR published the General Geological Map of Crete at a scale of 1:200k, consolidating decades of geological research (Creutzburg & Papastamatiou, 1966; Creutzburg et al., 1977) and serving as a foundational resource for understanding the island's geology. In the subsequent decades, the IGME (now the HSGME) advanced this work by completing the island's detailed geological framework as part of the BGMG series (Table 1). These endeavors were concentrated on diverse methodologies and advancements in earth science techniques, including petrographic and micropaleontological analyses. The historical evolution of geological mapping in Crete reflects monumental scientific labor, laying the groundwork for modern geological studies while addressing the challenges of heterogeneity in methodologies and outputs over time.

Table 1 (as a reference) provides an overview of the geological map context of Crete (including Gavdos sheet), summarizing critical data such as map sheets, scales, publication bodies, years of publication, and survey periods. This information underscores the extensive involved effort in documenting the island's complex geological framework (Figure 2). The figure effectively organizes these map sheets across the region, optimized by their publication years, showcasing the chronological progression of geological surveys. This dataset highlights the evolution of geological documentation in Crete, beginning with foundational surveys in the mid-20th century and advancing to modern updates that incorporate sophisticated methodologies. However, despite these extensive efforts, several objective difficulties and challenges remain. These include the integration and evaluation of historical and modern bibliographic data, georeferencing older map sheets to contemporary grids, and homogenizing geological data across varied methodologies and periods. Addressing these challenges is critical for achieving a cohesive and accurate geological framework for the region.

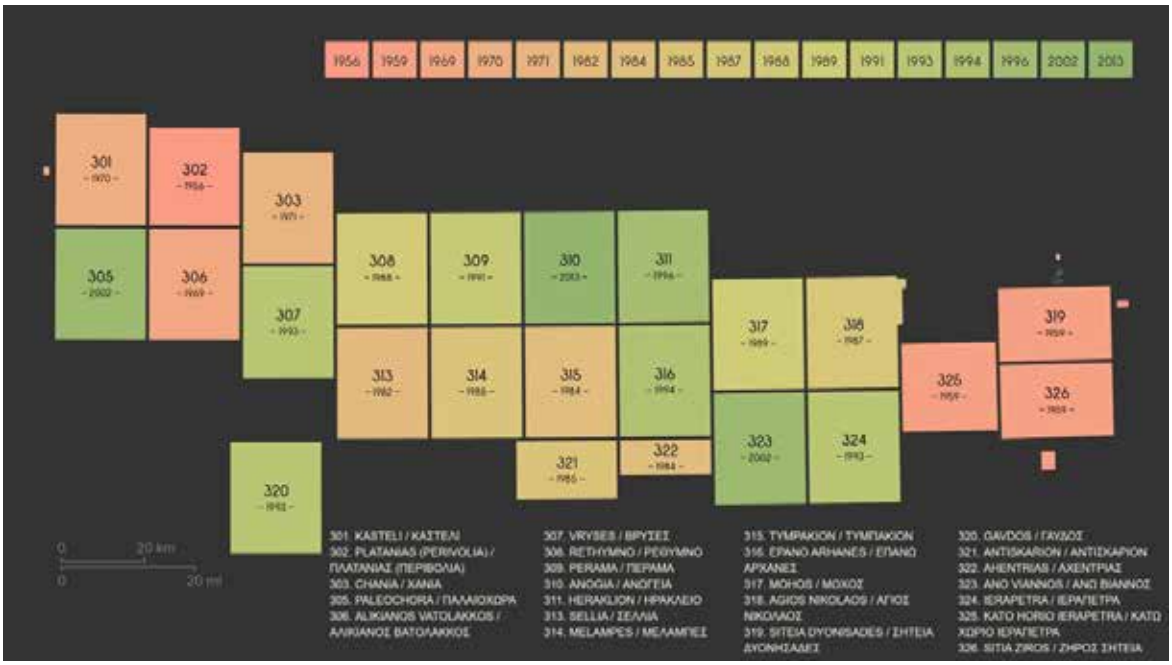


Figure 2. The spatial distribution of the 24 map sheets of the BGMG series, covering the region of the island of Crete (and Gavdos). Optimization based on the publication year.

Objectives

The geological mapping of Crete, conducted over several decades, represents a monumental effort to document the island's intricate and diverse geology. However, the use of varying methodologies, technologies, and scientific approaches during different survey periods has introduced heterogeneity into the resulting maps. This study aims to provide an overview of the Geological Map Sheets of Crete produced by IGME, as well as the ongoing progress by HSGME in advancing this work. A critical focus is on the integration of these maps within a GIS environment, which represents a significant step toward achieving a comprehensive and cohesive geological understanding of Crete.

Table 1. The geological context of the island of Crete is documented in the "General Geological Map of Greece / Island of Crete", published by the IGMR in 1977 at a scale of 1:200k. Additionally, the region of Crete is covered by 24 map sheets from the BGMG series produced by the IGSR (later IGME and now known as HSGME) between 1956 and 2013.

s/n	Code	Scale	Geological Sheet	Geological Sheet (Name after ELOT 743)	by	Year	Period of Survey
1	-	200k	GENERAL GEOLOGICAL MAP OF GREECE / CRETE ISLAND (CREUTZBURG)	CREUTZBURG	IGMR	1977	PRE-NEOGENE 1957-1973, NEOGENE 1961-1974
2	301	50k	KASTELLI	KASTELLI	IGSR	1970	1968
3	305	50k	PALAEOHORA	PALAIOCHORA	IGME	2002	1984, 1994-1995
4	302	50k	PLATANIAS	PLATANIAS	IGSR	1956	1950
5	306	50k	ALIKIANOS VATOLAKKOS	ALIKIANOS VATOLAKKOS	IGSR	1969	1960-1961
6	303	50k	KHANIA	CHANIA	IGSR	1971	1951, 1969
7	307	50k	VRISSES	VRYSES	IGME	1993	1985-1987
8	320	50k	GAVDOS	GAVDOS	IGME	1993	1988
9	308	50k	RETHYMNO	RETHYMNO	IGME	1988	1980-1984
10	313	50k	SELLIA	SELLIA	IGME	1982	1977-1978
11	309	50k	PERAMA	PERAMA	IGME	1991	1982-1987
12	314	50k	MELAMBES	MELAMPES	IGME	1985	1972-1974
13	310	50k	ANOGHIA	ANOGEIA	IGME (IGMEM)	2013	2005-2007
14	315	50k	TIMBAKION	TYMPAKION	IGME	1984	1973-1977
15	321	50k	ANTDISKARION	ANTISKARION	IGME	1985	1970-1972
16	311	50k	HERAKLION	IRAKLEIO	IGME	1996	ALPINE 1983, POST-ALPINE 1973
17	316	50k	EPANO ARCHANAE	EPANO ARCHANAI	IGME	1994	ALPINE 1983, POST-ALPINE 1973-1977
18	322	50k	AKHENDHRIAS	ACHENTRIAS	IGME	1984	1970-1974
19	317	50k	MOCHOS	MOCHOS	IGME	1989	ALPINE 1982-1983, POST-ALPINE 1973-1977
20	323	50k	ANO VIANNOS	ANO VIANNOS	IGME	2002	ALPINE 1975, 1987, POST-ALPINE 1987 (WEST SECTION), 1976 (EAST SECTION)
21	318	50k	AYIOS NIKOLAOS	AGIOS NIKOLAOS	IGME	1987	1976, 1977, 1981
22	324	50k	IERAPETRA	IERAPETRA	IGME	1993	ALPINE 1982, POST-ALPINE 1976
23	325	50k	KATO CHORIO IERAPETRA	KATO CHORIO IERAPETRA	IGSR	1959	1955
24	319	50k	SITIA DIONYSSIADES	SITEIA DYONISADES	IGSR	1959	1953, 1954
25	326	50k	ZIROS SITIA	ZIROS SITEIA	IGSR	1959	1954

Methods and Challenges

The revision of the geological mapping of Crete and its tectono-stratigraphic structure of alpine and post-alpine formations involved a combination of intensive field mapping, field tectonic measurements, sampling, and laboratory analysis. These efforts were further supported by the application of remote sensing techniques and Geographic

Information Systems (GIS) methods (Figures 3.1 & 3.2). The integration of these tools allowed for detailed geological cartographic results, which were subsequently homogenized and correlated with neighboring geological map sheets. This ongoing process (as part of the projects referenced in the Acknowledgements), has contributed to the development of the BGMG at a scale of 1:50,000, accompanied by a detailed explanatory document for each map sheet.

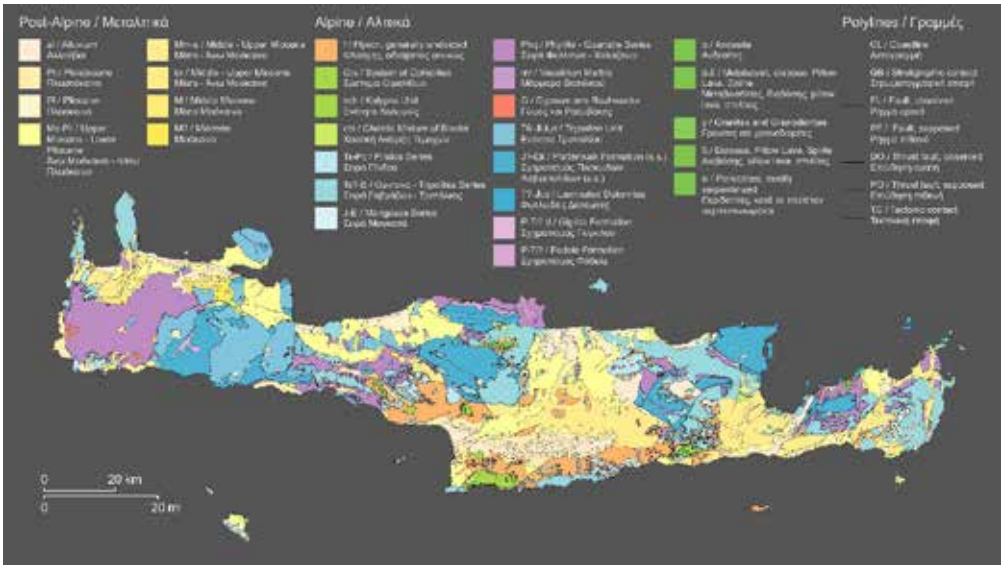


Figure 3.1. The geological setting of the island of Crete, as depicted in the 1:200k Geological Map by Creutzburg et al. (1977), has been further optimized and refined through the application of GIS for enhanced spatial analysis and accuracy.

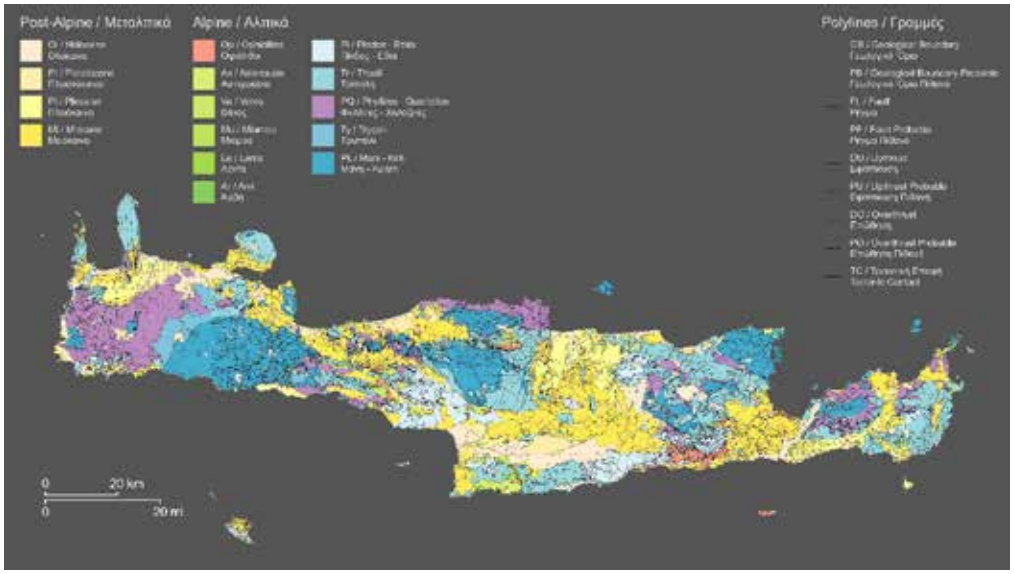


Figure 3.2. The geological setting of the island of Crete, as depicted by the 24 map sheets of the BGMG series, produced by the IGME (1956-2013).

Over the decades, numerous researchers contributed to geological maps of Crete, but these were often based on different methodologies and topographic bases. As a result, discontinuities emerged in the positioning of geological boundaries, in the classification of lithological formations, and in the depiction of tectonic elements, leading to problems, not only in the margins of adjoining map sheets. Various researchers from various schools of thought have carried out geological maps over extended periods, and their results have consequently been projected on different topographic maps. This resulted in the accommodation of geological boundaries in the exact locations and content of the lithological formations with tectonic elements, not coinciding with neighboring sheets.

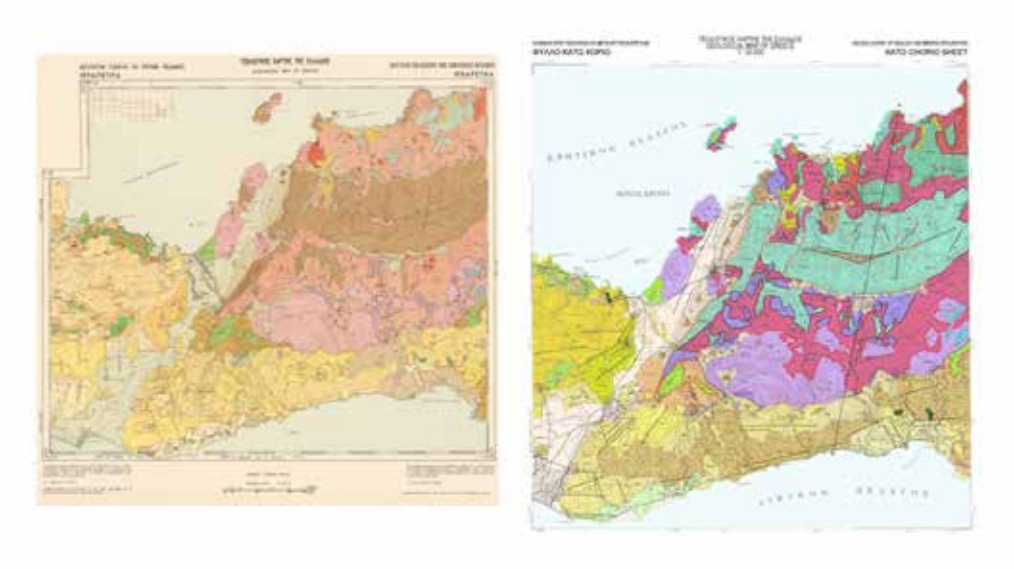


Figure 4.1. The evolution of geological mapping for the Kato Chorio (Ierapetra) map sheet in Eastern Crete. On the left is a segment of the original map, published in 1959 by IGSR, representing one of the foundational efforts in geological documentation. The right panel presents the updated version of the same sheet—soon to be released by HSGME.

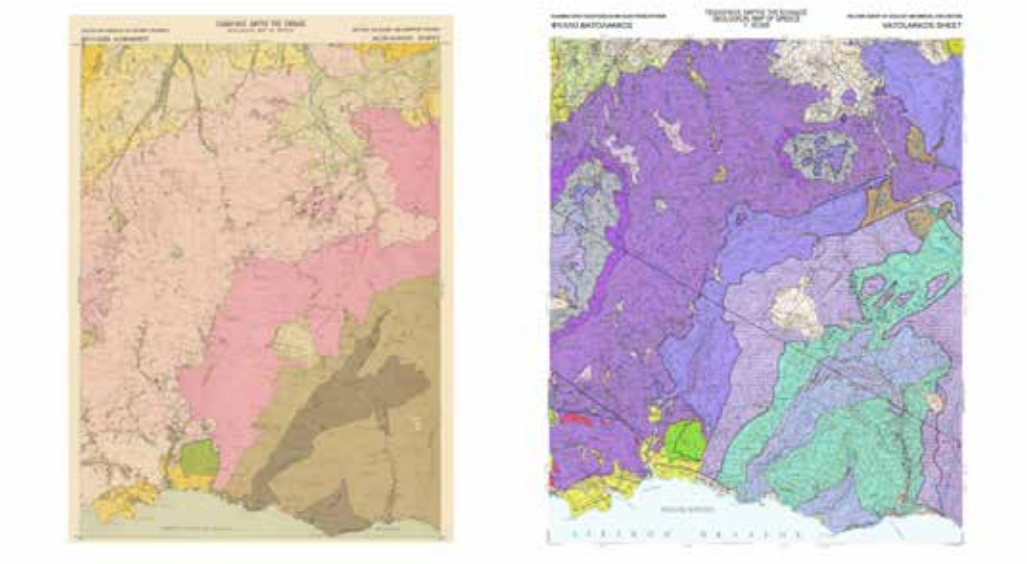


Figure 4.2. The evolution of geological mapping for the Alikianos (Vatolakkos) map sheet in Western Crete. On the left is a segment of the original map, published in 1969 by the IGSR, showcasing one of the foundational efforts in documenting the region's geology. On the right is the updated version of the same sheet—soon to be published by the HSGME.

Addressing these challenges required a multifaceted approach including collection, evaluation, and utilization of bibliography, georeferencing of older maps, grouping and homogenization of geological data, integration of modern geological perspectives, field mapping and data collection, physical and logistical barriers, GIS and cartographic optimization. To meet the objective difficulties and challenges, the fieldwork mapping effort was based on sampling and evaluation of on-site data along with parallel laboratory information and using broadly a modern bibliography. With the georeferencing of older map sheets in Greek Grid (*in Greek EGSA 87'*), in the documentation and appropriate interpretation, grouping-homogenization of geological elements, significant problems were identified within the boundaries of the formations, in the compilation and integration of new data (e.g. geochronological data) and tectonostratigraphic views on the geological structure of Greece. All observations and correlations were focused on the grouping and differentiation of geological formations, primarily categorized into basic lithostratigraphic sequences.

Results

Significant progress has been achieved in revising and homogenizing the 24 geological map sheets of Crete, including Gavdos. Two prominent examples illustrate this advancement: the geological map sheets of Vatolakkos (Western Crete) and Kato Chorio (Eastern Crete). These revised maps (Galanakis et al., 2024; Photiades & Kalogiannis, 2024) incorporate detailed geological cross-sections and tectonostratigraphic unit columns (pre-alpine and post-alpine formations), all compiled using a unified legend. Comparative analyses of these sheets highlight significant differences in both cartographic quality and geological structure (Figures 4.1 and 4.2). For instance, the Vatolakkos sheet in Western Crete extensively represents the full Plattenkalk sequence, ranging from the Upper Triassic to the Eocene, overlain by a meta-flysch formation dated to the Upper Eocene–Lower Oligocene (Figure 4.2). In contrast, the Kato Chorio sheet in Eastern Crete depicts only the uppermost members of the Plattenkalk sequence (Eocene) and the meta-flysch formation (Figure 4.1). Based on these maps, a new comprehensive geological map of Crete has been compiled. This updated map addresses many of the interregional inconsistencies and challenges that arose due to temporal and methodological gaps in the historical geological mapping of Crete (Table 1). The systematic revision and digitization of geological maps provides a valuable foundation for addressing modern challenges. These maps contribute substantially to sustainable development by enabling better planning for large infrastructure projects, optimizing the utilization of natural resources, and improving the management of natural hazards associated with the climate crisis.

Conclusions

The historical progression of geological mapping in Crete represents a monumental scientific endeavor, highlighting decades of systematic surveys that have substantially advanced knowledge of the island's intricate geology. Despite these achievements, challenges such as inconsistencies in methodologies, outdated bibliographic data, and issues in georeferencing older map sheets must be addressed to achieve a unified and accurate representation of Crete's geological context. Moving forward, continued efforts to integrate, update, and modernize the island's geological data are essential. These initiatives will not only build upon the foundational work of past surveys but also ensure that the resulting geological framework supports future research and contributes to the sustainable management of Crete's natural resources.

Acknowledgements

The authors would like to express their sincere gratitude to the personnel of the HSGME who contributed to *the Hydrogeological Mapping at a Scale of 1:100,000: Case Study of the Island of Crete* (part of the National Development Programs for the period 2021–2025, Ministry of Environment & Energy) and to the personnel involved in the revision and homogenization project of the Basic Geological Map of Greece (2019–2023), carried out within the framework of Project GEOINFRA: *Geological Mapping of Greece towards Support of Innovation and Entrepreneurship* (NSRF 2014–2020).

References

Aronis, G. (1949). *General Hydrological Survey of the Island of Crete (Includes Geological Map of Crete, Scale 1:500,000)*. Institute for Geology and Subsurface Research (IGSR), Athens.

Christodoulou, G., & Tataris, A. (1969). *Geological map of VATOLAKKOS sheet (1st ed., scale 1:50,000)*. Institute for Geology and Subsurface Research (IGSR), Athens.

Creutzburg, N., & Papastamatiou, J. (1966). *New Contribution to the Geology of the Island of Crete*. Institute for Geology and Subsurface Research (IGSR), Athens.

Creutzburg, N., Drooger, C. W., Meulenkamp, J. E., Papastamatiou, J., Sannemann, W., Seidel, E., & Tataris, A. (1977). *The General Geological Map of Greece: Island of Crete*. Institute of Geological and Mining Research (IGMR), Athens.

Galanakis, D., Moforis, L., & Carras, N. (2024). *Geological map of VATOLAKKOS sheet (2nd ed., scale 1:50,000)*. Hellenic Survey of Geology and Mineral Exploration (HSGME), Acharnes.

Papastamatiou, J., Vetoulis, D., Tataris, A., Bornovas, J., Christodoulou, G., & Katsikatsos, G. (1959). *Geological map of KATO CHORIO sheet (1st ed., scale 1:50,000)*. Institute for Geology and Subsurface Research (IGSR), Athens.

Photiades, A., & Kalogiannis, N. (2024). *Geological map of KATO CHORIO sheet (2nd ed., scale 1:50,000)*. Hellenic Survey of Geology and Mineral Exploration (HSGME), Acharnes.

17th INTERNATIONAL CONGRESS
of the Geological Society of Greece

BULLETIN OF THE GEOLOGICAL SOCIETY OF GREECE, SP. PUBL.

EXTENDED ABSTRACT 209

Water Wells in Crete: Distribution by Municipality, Use, and Ownership—Results of a Systematic Inventory in Greece.

I. Michalakis[1], E. Tsolaki[1]
(1) Hellenic Survey of Geology and Mineral Exploration, Regional Branch of Crete, Rethymno, Greece, michalakis@eagme.gr

Research Highlights

One of the recent projects undertaken by the Department of Hydrogeology at the Hellenic Survey of Geology and Mineral Exploration (HSGME), co-financed under the European Union's Corporate Regional Development Agreement for the 2014-2020 period, involved a systematic inventory of water wells (boreholes) throughout the country of Greece. In Crete and the island of Gavdos, extensive fieldwork conducted by experienced personnel from HSGME spanned from July 2019 to January 2023, lasting a total of 43 months. This comprehensive effort resulted in the identification and documentation of 5,349 water wells (boreholes) across the 24 municipalities of the region (Figure 1).

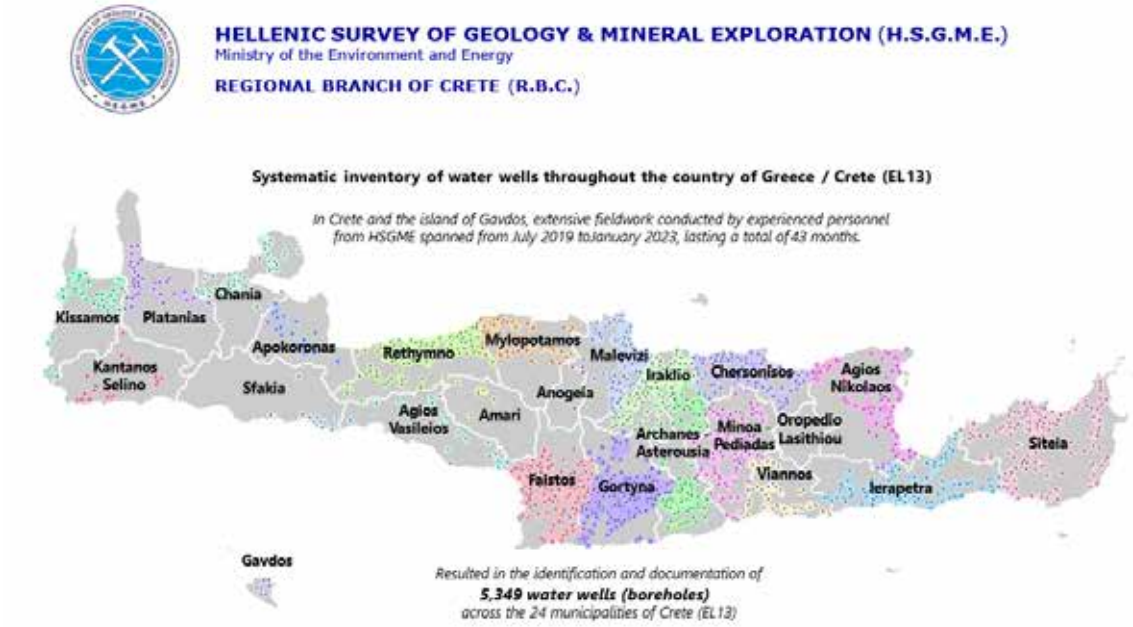


Figure 1. Results of a systematic inventory of water wells (boreholes) conducted across Water District EL13, which identified and documented 5,349 water wells within the 24 municipalities of the region. Different colored dots represent boreholes categorized by their respective municipalities, while white lines delineate municipal boundaries.

Introduction

Since the early 2000s, the European Union has implemented transformative water resource management policies, most notably the Water Framework Directive (Directive 2000/60/EC). Effective from 22 December 2000, this Directive establishes integrated quality, ecological, and quantitative targets for the protection of aquatic ecosystems, aiming to achieve "*good status*" for all water resources through a holistic, basin-scale approach. The Directive expands the definition of a River Basin to include inland surface waters (e.g., rivers, lakes), groundwater, and transitional and coastal ecosystems (e.g., deltas and estuaries). To realize its objectives, the Directive mandates the development and implementation of Management Plans at the River Basin level, as outlined in Article 13 and Annex VII. These plans incorporate Programs of Measures for the Protection and Rehabilitation of Waters, as specified in Article 11 and Annex VI.

In Greece, River Basin Management Plans have been developed in alignment with Directive 2000/60/EC and formalized through Law 3199/2003 and Presidential Decree 51/2007. These plans provide comprehensive details on River Basin Districts, River Basins, and surface and groundwater bodies.

As a complement to the "*Groundwater Monitoring Network of Greece*" (HSGME/RBC, 2019-2023), the Department of Hydrogeology at HSGME initiated the "*Systematic Inventory of Water Wells for All Uses Throughout the Country of*

Greece" (HSGME, 2019-2023). Co-financed under the European Union's Corporate Regional Development Agreement for the 2014–2020 period, this project sought to address critical gaps in groundwater data and understanding. The outcomes of this project directly support the initiatives of the General Directorate of Water within the Ministry of Environment and Energy, strengthening national water policies. These efforts ensure the protection of both the quality and quantity of Greece's water resources, fulfilling obligations under European Union Directives 2000/60/EC, 2006/118/EC, and 91/676/EEC. The project's functionality is integrated with the geospatial database and services system of the National Register of Water Abstraction Points (*in Greek: "EMSY"*). Established in January 2014, EMSY is an electronic register maintained by the General Directorate of Water (formerly the Special Secretariat for Water) in compliance with Greek Law 3882/2010, which was adopted following Directive 2007/2/EC.

Background / Project Overview (EL13)

For Water District EL13, which includes the Island of Crete and the Island of Gavdos, the majority of water needs are met through water wells (boreholes) and the exploitation of groundwater reserves (IGME, 2009). Groundwater management in Crete poses significant challenges, as it requires the collaboration of multiple stakeholders. Various authorities are involved in managing groundwater resources, including municipalities, municipal enterprises for water supply and sewerage, local land reclamation organizations, and the Water Directorate of the Decentralized Administration of Crete, alongside numerous individual stakeholders. This multiplicity of actors complicates coordination efforts and hinders effective management. The widespread prevalence of illegal water wells (boreholes) further exacerbates these challenges, making it increasingly difficult to achieve sustainable groundwater resource management. Despite significant progress made by the Department of Water Management within the Decentralized Administration of Crete in implementing the River Basin Management Plan and its updates, several obstacles persist (General Directorate of Water, 2024).

Between July 2019 and January 2023, extensive fieldwork conducted by experienced HSGME personnel across Crete and the island of Gavdos yielded valuable insights (HSGME/RBC, 2019–2023). This systematic inventory not only documented the distribution and status of water wells (boreholes) but also enhanced understanding of the geological and hydrogeological conditions of the region. These findings establish a robust foundation for future investigations and make a significant contribution to the sustainable management of groundwater resources on the island.

Objectives

This study aims to present aggregate data on the spatial and percentage distribution of water wells by municipality, use, and ownership, derived from a systematic inventory conducted across Water District EL13 (Island of Crete and Island of Gavdos). Site inspections, carried out in collaboration with local authorities—including municipalities, local communities, municipal water and sewerage enterprises, local land reclamation organizations, and the Water Directorate of the Decentralized Administration of Crete—as well as with individual stakeholders. These efforts resulted in the identification and documentation of 5,349 water wells (boreholes) across the 24 municipalities of the region.

Methods

To implement the objectives of the project *"Systematic Inventory of Water Wells for All Uses Throughout the Country of Greece*" (Subproject 1: "*On-site inspections, direct inventory of water wells and completion of inventory forms*") in Crete (Water District EL13), the Regional Branch of Crete, in collaboration with the Hydrogeology Directorate of HSGME, was designated as the responsible department.

The project commenced with organizational meetings at the Water Directorate of the Decentralized Administration of Crete, followed by the coordination efforts of the Regional Branch to conduct on-site visits municipality by municipality. Initial meetings were held with key local stakeholders, including mayors, deputy mayors responsible for water management, presidents and directors of municipal water and sewerage enterprises, presidents of local communities, local water distributors, and presidents and staff of local land reclamation organizations. Following these discussions, field campaigns were organized to carry out the inventory (Figure 5). To guide field inspections, all available datasets from local authorities were collected, compiled into geodatabases, and thoroughly reviewed. These geodatabases served as a critical resource for planning and optimizing fieldwork efforts. For instance, the geodatabase of the Water Directorate of the Decentralized Administration of Crete recorded 3,657 boreholes as of July 2019 and 3,884 boreholes as of October 2021 (Water Directorate of Crete, accessed: July 2019; October 2021; December 2024).

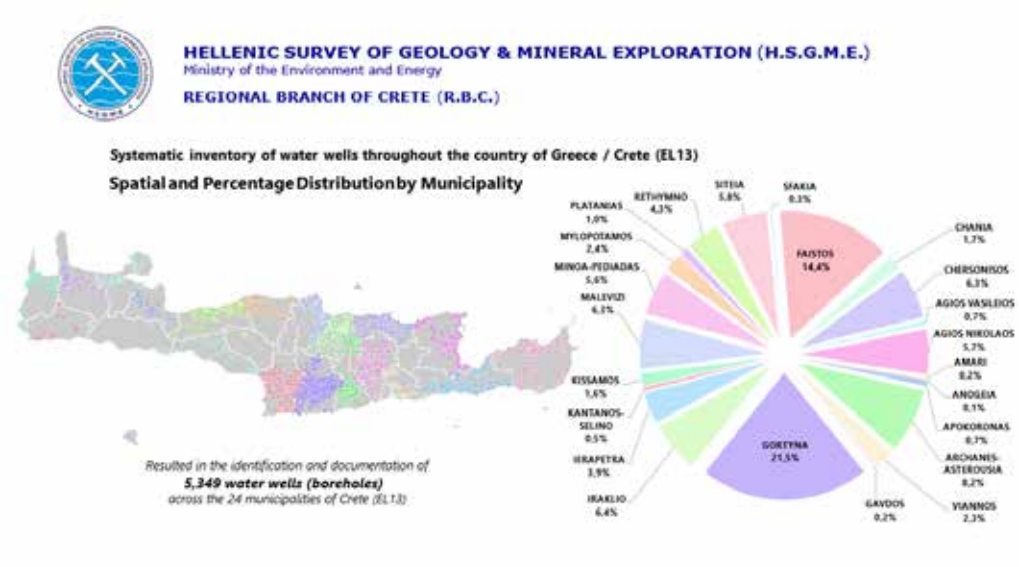


Figure 2. Spatial and Percentage Distribution of Water Wells (Boreholes) in Water District EL13 (Island of Crete and Island of Gavdos). This figure presents the results of a systematic inventory of water wells (boreholes) conducted across Water District EL13, documenting a total of 5,349 wells within the region's 24 municipalities. Colored dots represent boreholes associated with individual municipalities, while white lines delineate municipal boundaries. The accompanying pie chart illustrates the percentage distribution of boreholes by municipality within the district.

Experienced personnel from HSGME were organized into teams of two for field inspections, collaborating with available staff from local authority stakeholders. With their assistance, field inspections were conducted in coordination with individual stakeholders within their respective areas of responsibility.

The on-site inventory of water wells involved completing inventory forms with technical data (e.g., depth, pump specifications), informational details (e.g., ownership, location, coordinates in the Greek Grid), usage information (e.g., irrigation, drinking, period and hours of pumping), and field measurements (e.g., depth of water level, discharge, physicochemical parameters).

All collected data was entered into the project's geodatabase, providing a critical resource for assessing water balances, evaluating the status of the island's groundwater systems, and estimating the pressures exerted on them. This comprehensive data supports the development of appropriate measures aimed at achieving rational and sustainable groundwater management.

As part of the project, Technical Reports on Groundwater Systems within Water District EL13 are being prepared in alignment with the requirements outlined in Greece's River Basin Management Plans.

Results

Aggregate data on the spatial and percentage distribution of water wells (boreholes) by municipality, use, and ownership, derived from a systematic inventory conducted across Water District EL13 (Island of Crete and Island of Gavdos), are presented in Table 1 and Figures 2–4. The inventory resulted in the identification and documentation of **5,349 water wells (boreholes)** across the **24 municipalities** of the region (Table 1; Figures 1 and 2).

The **Municipality of Gortyna** accounts for **21.5%** of all water wells in Crete, followed by the **Municipality of Faistos** with **14.4%** and the **Municipality of Archanes-Asterousia** with **8.2%** (Figure 2). Notably, **52% of all water wells in Crete** are located within the municipalities of Faistos, Gortyna, Archanes-Asterousia, Minoa-Pediadas, and Viannos (Michalakis et al., 2022; HSGME/RBC, 2019–2023). Within the **wider area of the Messara Basin, 46.3%** of all water wells in Crete are concentrated (Michalakis, I., 2024).

Regarding usage, **79.4% of the wells on the Water District EL13 are designated for irrigation**, while **10.5% are used for water supply (drinking water)**. A further **7.6% of the wells are abandoned or no longer in use** (Figure 3).

Ownership data indicate that **68.6% of water wells are privately owned**, followed by **16.4% owned by municipalities**, **9.4% by municipal water and sewerage enterprises**, and **4.6% operated by local land reclamation organizations** (Figure 4).

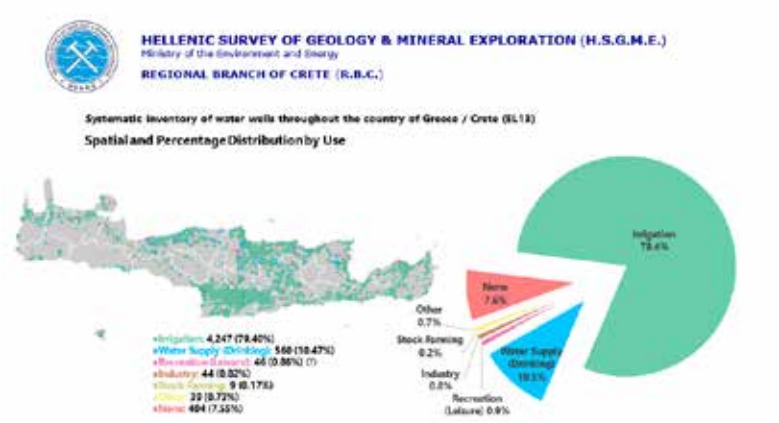


Figure 3. Spatial and Percentage Distribution by Use of Water Wells (Boreholes) in Water District EL13 (Island of Crete and Island of Gavdos) and corresponding pie chart. Different colored dots on the map represent boreholes categorized by specific usage, as detailed in the map legend.

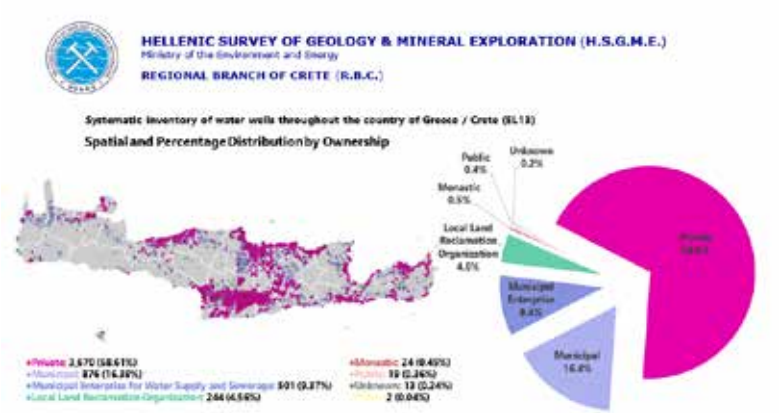


Figure 4. Spatial and Percentage Distribution by Ownership of Water Wells (Boreholes) in Water District EL13 (Island of Crete and Island of Gavdos) and corresponding pie chart. Different colored dots on the map represent boreholes categorized by ownership type, as detailed in the map legend.

Table 1 presents aggregate data by municipality, classified according to the respective main use and ownership of water wells (boreholes). Numeric values indicate the total number of wells, with corresponding percentages (%) shown in parentheses, and are provided for reference.

Table 1. Aggregate data by municipality, main use, and ownership derived from the inventory of water wells (boreholes) conducted across Water District EL13.

		Main Use		Main Ownership			
Municipality	**Total Number of Water Wells (%)**	**Irrigation (%)**	**Water Supply (%)**	**Private (%)**	**Municipal (%)**	**Municipal Enterprises (%)**	**Local Land Reclamation Organization (%)**
Agios Vasileios	35 (0.65)	28 (93.3)	2 (6.7)	16 (45.7)	18 (51.4)	-	1 (2.9)
Agios Nikolaos	306 (5.72)	169 (67.9)	49 (19.7)	200 (65.4)	33 (10.8)	39 (12.7)	27 (8.8)
Amari	10 (0.19)	4 (57.1)	3 (42.9)	-	10 (100.0)	-	-
Anogeia	4 (0.07)	-	4 (100.0)	-	2 (50.0)	2 (50.0)	-
Apokoronas	39 (0.73)	20 (83.3)	3 (12.5)	3 (7.7)	34 (87.2)	2 (5.1)	-
Archanes-Asterousia	440 (8.23)	300 (92.0)	25 (7.7)	341 (77.5)	94 (21.4)	1 (0.2)	-
Viannos	123 (2.30)	106 (88.4)	13 (10.8)	60 (48.8)	54 (43.9)	-	8 (6.5)
Gavdos	9 (0.17)	1 (20.0)	4 (80.0)	1 (11.1)	8 (88.9)	-	-

Gortyna	1,151 (21.52)	800 (95.2)	37 (4.4)	962 (83.6)	157 (13.6)	1 (0.1)	28 (2.4)
Iraklio	341 (6.38)	283 (87.1)	36 (11.1)	256 (75.0)	6 (1.8)	78 (22.9)	-
Ierapetra	209 (3.91)	161 (89.0)	13 (7.2)	144 (68.9)	48 (23.0)	-	15 (7.1)
Kantanos-Selino	26 (0.49)	15 (62.5)	9 (37.5)	9 (34.6)	-	5 (19.2)	4 (15.4)
Kissamos	87 (1.63)	61 (80.3)	15 (19.7)	20 (23.0)	-	4 (4.6)	9 (10.3)
Malevizi	335 (6.26)	169 (70.4)	58 (24.2)	213 (63.6)	22 (6.5)	80 (23.9)	-
Minoa-Pediadas	297 (5.55)	202 (89.9)	21 (9.3)	166 (55.9)	105 (35.4)	24 (8.1)	-
Mylopotamos	127 (2.37)	70 (68.6)	28 (27.5)	56 (44.1)	36 (28.3)	33 (26.0)	1 (0.8)
Oropedio Lasithiou	-	-	-	-	-	-	-
Platanias	55 (1.03)	42 (82.4)	9 (17.6)	8 (14.5)	-	38 (69.1)	9 (16.4)
Rethymno	232 (4.34)	126 (63.0)	47 (23.5)	144 (62.1)	1 (0.4)	86 (37.1)	-
Siteia	309 (5.78)	242 (91.3)	18 (6.8)	183 (59.2)	61 (19.7)	33 (10.7)	24 (7.8)
Sfakia	15 (0.28)	9 (75.0)	3 (25.0)	2 (13.3)	11 (73.4)	-	2 (13.3)
Faistos	770 (14.40)	555 (96.6)	14 (2.4)	585 (76.0)	64 (8.3)	2 (0.3)	115 (14.9)
Chania	92 (1.72)	63 (79.7)	12 (15.2)	69 (75.0)	1 (1.1)	17 (18.5)	1 (1.1)
Chersonisos	337 (6.30)	209 (77.7)	50 (18.5)	232 (68.9)	49 (14.5)	56 (16.6)	-

Conclusions

This study provides a comprehensive overview of the systematic inventory of water wells conducted across Water District EL13. The identification and documentation of **5,349 water wells (boreholes)** across **24 municipalities** represent a significant milestone in understanding the spatial and functional distribution of groundwater abstraction points. The findings reveal key insights into the distribution and use of water wells. The **wider area of the Messara Basin**, a critical agricultural and hydrogeological region in central-southern Crete, accounts for **2,474 wells** (**46.3% of the island's total**), highlighting the region's significant dependency on groundwater for irrigation.

Irrigation dominates water use, representing **79.4% of all wells**, followed by **water supply** (**10.5%**) and a smaller fraction of wells (**7.6%**) that are abandoned or not in use. Ownership patterns indicate a high prevalence of **private wells** (**68.6%**), highlighting the challenges of regulatory oversight and sustainable resource management.

The geodatabases developed as part of this inventory serve as a vital tool for planning and decision-making. They provide a foundation for assessing water balances, evaluating groundwater pressures, and formulating appropriate management strategies. By integrating technical, informational, and usage data, the inventory supports compliance with Greece's River Basin Management Plans and aligns with the European Union's Water Framework Directive and related policies.

The successful implementation of this project demonstrates the importance of collaboration among stakeholders, including local authorities, municipal enterprises, land reclamation organizations, and individual users. Despite challenges such as the prevalence of illegal wells and the complexity of coordinating multiple actors, this initiative contributes significantly to improving the management and sustainability of Crete's groundwater resources.

Future efforts should focus on strengthening the monitoring of groundwater systems, enforcing regulations on illegal wells, and promoting sustainable water use practices. These actions are crucial to safeguarding groundwater resources and addressing the growing pressures of agricultural demand, climate variability, and population growth in the region.



Figure 5. Random photographs from fieldwork conducted during the systematic inventory across Water District EL13.

Acknowledgements

Fieldwork was conducted by the executive staff—Athanasouli Elpida, Davrados Michalis, Lionakis Ioannis, Papanikolaou Kassiani, Pavlidou Saia, Tsolaki Eleni, Zourmpakis Evangelos, and the first author—from the Regional Branch of Crete and the Department of Hydrogeology of HSGME as part of the project "*Systematic Inventory of Water Wells for All Uses Throughout the Country of Greece"*. The authors express their gratitude to the personnel of local authorities, including mayors, deputy mayors responsible for water management, presidents and directors of municipal water and sewerage enterprises, presidents of local communities, local water distributors, presidents and staff of local land reclamation organizations, as well as the personnel of the Water Directorate of the Decentralized Administration of Crete. The authors also express their sincere gratitude to all individuals who provided their cooperation, particularly during field activities.

References

Council Directive 91/676/EEC of 12 December 1991 concerning the protection of waters against pollution caused by nitrates from agricultural sources, 1991. [http://data.europa.eu/eli/dir/1991/676/oj].

Directive 2000/60/EC of the European Parliament and of the Council of 23 October 2000 establishing a framework for Community action in the field of water policy, 2000. [http://data.europa.eu/eli/dir/2000/60/oj].

Directive 2006/118/EC of the European Parliament and of the Council of 12 December 2006 on the protection of groundwater against pollution and deterioration, 2006. [http://data.europa.eu/eli/dir/2006/118/oj].

Directive 2007/2/EC of the European Parliament and of the Council of 14 March 2007 establishing an Infrastructure for Spatial Information in the European Community (INSPIRE), 2007. [http://data.europa.eu/eli/dir/2007/2/oj].

General Directorate of Water, 2024. 2nd Revision of the River Basin Management Plan of the Water District of Crete and the corresponding Strategic Environmental Impact Assessment. Ministry of Environment and Energy. [https://wfdver.ypeka.gr/wp-content/uploads/2024/07/EL13_2REV_sdlap.pdf].

General Directorate of Water, 2025. National Register of Water Intake Points (in Greek: *EMSY*). Ministry of Environment and Energy. [http://lmt.ypeka.gr/].

HSGME/RBC, 2019-2023. Systematic inventory of water wells of every use throughout the country of Greece. (Municipalities of Crete. Preliminary Technical Reports, Rethymno, Greece.

HSGME/RBC, 2018-2023. Groundwater Monitoring Network of Greece, Preliminary Reports, Rethymno, Greece.

IGME, 2009. Project: "Recording and Evaluation of the Hydrogeological Characteristics of the Groundwater and Aquifer Systems of Greece. Water District EL13". Rethymno, Greece.

Michalakis, I., Tsolaki, E., Loupasakis, C., Voudouris, K., Kontoes, Ch., 2022. Groundwater level dynamics of the Messara Basin, Crete Island [Bulletin of the Geological Society of Greece, Special Publication 10, Ext. Abs. GSS2022-162, pp 553-554].

Michalakis, I., 2024. Hydrogeological Conditions and Sustainability Challenges in the Messara Basin. Agia Pelagia, Crete. [SIPS 2024. 10th Intl. Symp. on Sustainable Mineral Processing].

Water Directorate of Crete, (2019; 2021; 2024). Decentralized Administration of Crete [Retrieved from https://data.apdkritis.gov.gr/el].

17th INTERNATIONAL CONGRESS of the Geological Society of Greece

BULLETIN OF THE GEOLOGICAL SOCIETY OF GREECE, SP. PUBL.

EXTENDED ABSTRACT 210

Preliminary Results on Land Subsidence Induced by Groundwater Overexploitation Using Copernicus Sentinel Data: Insights from the Messara Basin, Crete

Michalakis I.[1,2], Tsolaki E.[2], Loupasakis C.[1], Voudouris K.[3], Kontoes Ch.[4]

(1) Laboratory of Engineering Geology and Hydrogeology, School of Mining and Metallurgical Engineering, National Technical University of Athens, Athens, Greece, michalakis@eagme.gr, (2) Hellenic Survey of Geology and Mineral Exploration, Regional Branch of Crete, Rethymno, Greece, (3) Aristotle University of Thessaloniki, Dept. of Geology, Thessaloniki, Greece (4) National Observatory of Athens, Institute for Astronomy and Astrophysics, Space Applications and Remote Sensing, BEYOND Center for EO Research and Satellite RS, Athens, Greece.

Research Highlights

Areas of significant groundwater depression have been identified, alongside potential geohazards linked to land subsidence resulting from excessive groundwater withdrawal and significant level decline. Data from the European Ground Motion Service (EGMS) were analyzed to detect land subsidence induced by groundwater exploitation, with findings subsequently validated through site inspections.

Introduction / Background

In cases of overpumping with significant lowering of the piezometric surface across large aquifers subsidence phenomena are often observed (Zhang et al., 2008; Loupasakis et al., 2014; Raspini et al. 2014; Svigkas et al., 2016; Papoutsis et. al., 2020; Kamali et al., 2021). The Messara Basin, a key agricultural and hydrogeological region in central-southern Crete (Figure 2), is characterized by complex geological formations, intensive agricultural activities, and increasing water demand. Geodetic satellite measurements for the period 2007-2009 indicate a subsidence rate of approximately 2 cm per year in the central part of the Messara Plain (Mertikas et al., 2010).

Groundwater demand has approximately doubled the number of recorded boreholes in the area over the past decades. By 2007, the number of boreholes was estimated at 1,400. Recent data from a systematic inventory of water wells (boreholes) in Greece, documented 2,474 boreholes in the Messara Basin (Figure 1), accounting for 46.3% of all water wells in Crete (H.S.G.M.E./ R.B.C., 2023; Michalakis, 2024).



Figure 1. The Spatial Distribution of 2,474 water wells across the broader area of Messara Basin. Results from Project: Systematic inventory of water wells (boreholes) throughout the country of Greece / Crete (EL13). This comprehensive effort resulted in the identification and documentation of 2,474 boreholes across Messara Basin. This represents 46.3% of all water wells in Crete.

Groundwater levels in the Messara Basin exhibit notable seasonal fluctuations (Michalakis, 2024), primarily driven by overexploitation for irrigation, particularly in the aftermath of a prolonged drought. This unsustainable usage raises significant concerns regarding the sustainability of water resources and heightened the basin's vulnerability to climate-induced stresses. Remote sensing technologies, such as the Copernicus Sentinel satellite program, provide valuable tools for monitoring environmental changes and guiding field inspections (Delgado Blasco et al., 2019). This study outlines the integration of Sentinel data with site inspections to address potential geohazards identifying notable displacements and detect induced land subsidence associated with groundwater over-exploitation.

Objectives

This study presents preliminary results from site inspections conducted using Copernicus ground motion data from EGMS. The results highlight the utility of Sentinel data in enhancing field observations and addressing potential geohazards by identifying notable displacements and detecting induced land subsidence associated with groundwater overexploitation.

Methods

Groundwater levels in the basin exhibit significant seasonal variations, largely due to over-exploitation for irrigation, raising critical sustainability concerns. Effective groundwater management requires systematic data collection and precise utilization of primary data. Changes in groundwater head within the Messara Basin were studied from May 2021 to October 2023, leading to the identification of areas with generalized groundwater depressions (Michalakis et al., 2022; Michalakis, 2024). During this period, field observations were conducted, and local authorities and civilians were engaged to assist in identifying notable displacements in their respective areas, with particular emphasis on those linked to groundwater overexploitation. It is worth noting that deformation phenomena occur in several areas; however, as these areas are under cultivation, such phenomena often go unnoticed due to erosion and plowing or are not given adequate consideration.

Following, mean vertical velocities (weekly measurements) from two datasets (80,014 Persistent Scatterers -PSs-) —ORTHO (Level 3) Vertical for 2016–2021 (spanning 5 January 2016 to 22 December 2021) and 2018–2022 (spanning 6 January 2018 to 23 December 2022)—were analyzed using geostatistical methods to identify regions of significant subsidence (Figure 2). Subsequently, an analysis of the ORTHO (Level 3) Vertical dataset for 2019–2023 (spanning 13 January 2019 to 18 December 2023), obtained from the European Ground Motion Service (EGMS) Explorer (accessed on 30 October 2024), led to the selection of 86 PSs for site inspections (EGMS Data Explorer, 2024).

Finally, targeted site inspections at the narrow areas surrounding the 86 selected EGMS PSs were conducted from 11 to 29 November 2024.

Figure 3 presents a plot of vertical displacements and vertical mean velocities for the 86 PSs selected for site inspections in the Messara Basin. In the plot, vertical displacement values range from +48.10 mm (EGMS_08) to -152.40 mm (EGMS_82), while vertical mean velocities range from +9.8 mm/year to -30.80 mm/year, respectively.



Figure 2. The Spatial Distribution of the Mean Vertical Velocities (weekly measurements spanning from 5 January 2016 to 22 December 2021) from dataset: [ORTHO (Level 3) Vertical for 2016–2021 / 80,014 PSs]

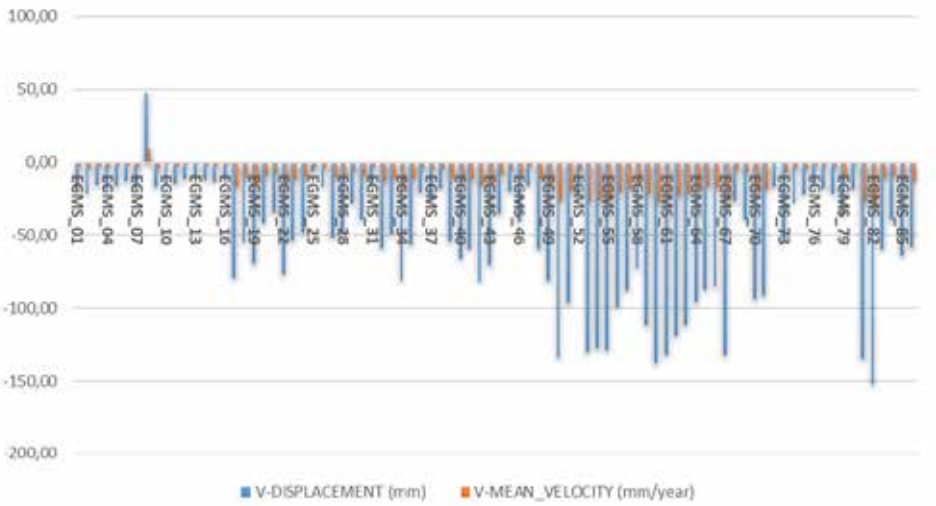


Figure 3. Plot of Vertical Displacements and Vertical Mean Velocities of the 86 PSs selected for site inspections in the Messara Basin.

These values were derived from the ORTHO (Level 3) Vertical dataset for 2019–2023 (spanning 13 January 2019 to 18 December 2023), obtained from the European Ground Motion Service (EGMS) Explorer (accessed on 30 October 2024).

Description and Documentation: An Example

The applied method highlights the utility of Sentinel data in complementing field observations and addressing potential geohazards by identifying displacements and detecting induced land subsidence associated with groundwater overexploitation. Preliminary findings indicate that areas of significant displacement can be identified, while the study of geological and hydrogeological conditions provides a valuable tool for evaluating ongoing geohazards.

An example of the inventory form designed for reporting the findings of the 86 selected sites is presented in figure 3, referring to a Location Southwest of Moires (Kalamiari) (Date of site inspection: 09 December 2024). In Figure 4, embedded Figure 86.1 shows a snapshot from the EGMS Data Explorer, incorporated into the inventory form of EGMS_86.

The reference measurement point (10HQYNAEOU, EGMS_86) is located southwest of Moires, within an olive grove (Figure 4; embedded Figure 86.1). At the reference point and within a radius of ~30m, significant ground ruptures were identified, both within the olive grove and on the paved road to the east. Openings due to pipe-laying phenomena are observed within the olive grove, which are related to underlying deformations (Figure 4; embedded Figure 86.2a). Ground ruptures were observed to the west and at a distance of ~20m, on the eastern margin of the road (Figures 4; embedded Figures 86.2b and 86.2c). Significant deformations and ruptures (Figure 4; embedded Figure 86.2d) are observed over a length of ~70m of the eastern road and are located mainly east and south of the reference point. Two more reference points (EGMS_19 and EGMS_22, shown in figures 5.1 and 5.2) in a short distance gave similar phenomena after site inspections helping to identify an area of high geohazard risk.

Geological Setting. The geological framework of the area is presented in figure 5.2. where **alluvium (al) deposits** comprising unconsolidated sediments such as sands, silts, clays, and gravels deposited by rivers and streams during the Quaternary (thickness up to 20m) overlaying **Pleistocene (Pt) deposits** consisting of marine terraces (typically composed of consolidated beach deposits such as sand, gravel, and occasionally shells) and non-marine clastics including fluviatile beds and fans (consist of coarse-grained materials like sand and gravel).

Hydrolithological Setting.

Alluvium deposits typically form highly permeable and productive aquifer systems where variable yet generally favorable conditions for groundwater storage and movement within these deposits can create a heterogeneous permeability profile. The hydrogeological behavior of alluvial deposits is influenced by the sorting, size distribution, and interbedding of the different sediment types. These factors contribute to a complex and layered aquifer system where hydrological properties can vary significantly over short distances. The hydrogeological properties can vary based on the clast size, sorting, and degree of cementation. This complexity can lead to heterogeneous aquifer properties within short distances, influenced by changes in sediment characteristics and depositional processes (Michalakis et al., 2024).

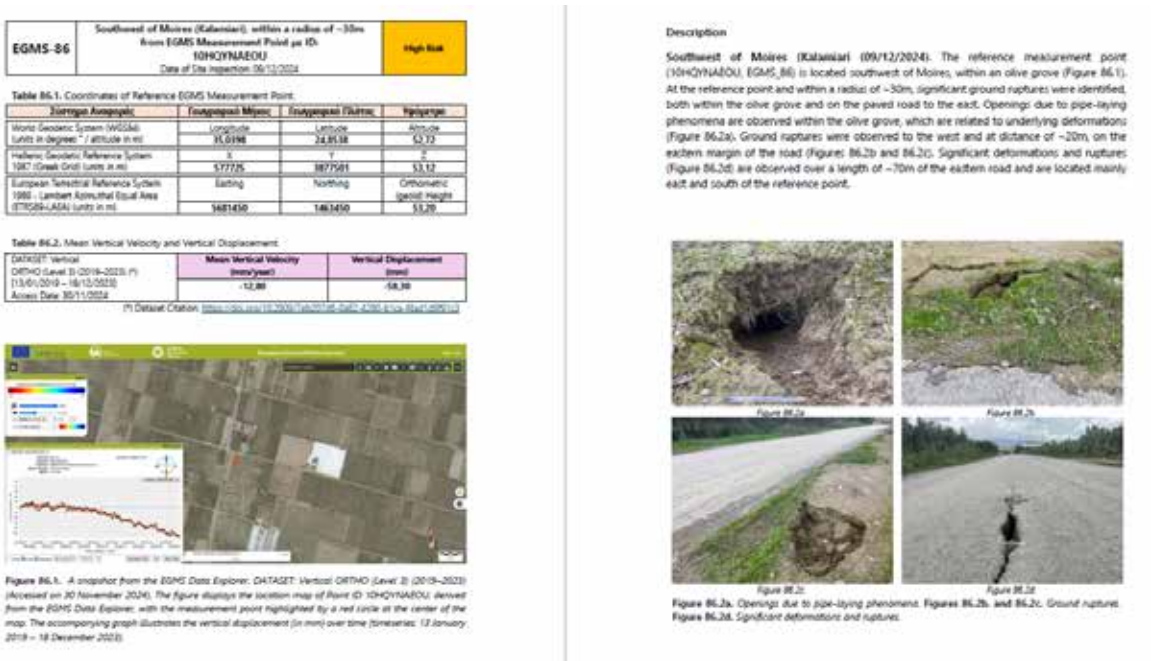


Figure 4. Inventory Form of EGMS Measurement Point: 10HQYNAEOU (EGMS-86).

Pleistocene deposits, presents a stratified aquifer system where the lithological diversity significantly influences hydrogeological properties. Marine terraces, typically composed of consolidated beach deposits such as sand, gravel, and occasionally shells. The degree of cementation varies, but where less consolidated, these terraces often exhibit high porosity and permeability, conducive to effective groundwater storage and flow. The porosity and permeability in marine terraces depend on the degree of lithification. In areas where the terrace deposits are less cemented, they can exhibit high porosity and permeability. Non-marine clastics (fluviatile beds and fans) formed from river and alluvial fan processes, generally consist of coarse-grained materials like sand and gravel. The sorting and layering of these materials can significantly affect their hydrogeological characteristics. Typically, these materials have high porosity due to the loose packing of coarse grains, coupled with high permeability that facilitates effective water infiltration and movement. The hydrogeological properties can vary based on the clast size, sorting, and degree of cementation. The unit exhibits a complex hydrogeological behavior due to the mixture of marine and non-marine depositional environments. This complexity can lead to heterogeneous aquifer properties within short distances, influenced by changes in sediment characteristics and depositional processes. The groundwater flow in these areas is generally robust, especially in regions where the sediments are coarse and well-sorted. The yield from these aquifers can vary depending on local conditions such as sediment depth, degree of consolidation, and the presence of impermeable layers or lenses within the deposits (Michalakis et al., 2024).

Hydrogeological Setting and Deformations

Hydrogeological conditions in the Messara Basin were studied from May 2021 to October 2023, resulting in the identification of areas with generalized groundwater depressions (Michalakis et al., 2022; Michalakis, 2024). Potentiometric data, collected during wet and dry seasons in 2021 and 2023, were derived from an extensive network of 767 measurement points across the basin. These data allowed for the analysis of groundwater head changes, leading to the documentation of significant depressions.

Groundwater overexploitation near the reference measurement point has created a cone of depression, with groundwater levels dropping to negative elevations (below mean sea level). Figure 5.1 illustrates this phenomenon, where the purple-shaded area represents a cone of depression with groundwater head values reaching as low as -31.08 m by the end of the dry season in 2023. Within this zone of excessive groundwater withdrawal (Figures 5.1 and 5.2) lies reference measurement point 10HQYNAEOU (EGMS_86), along with EGMS_19 and EGMS_22, where notable deformations and ruptures were observed.

During the wet season, groundwater levels in alluvial deposits rise to +50 m, influenced by the Geropotamos River located approximately 550 m to the north. However, significant seasonal fluctuations—up to 85 m in vertical water level—are observed in the area, which has an altitude of 53.12 m (EGMS_86). These fluctuations are exacerbated by extensive groundwater overexploitation and occur within highly permeable hydrolithological units that facilitate rapid water infiltration and movement. Embedded Table 86.2 in Figure 3 presents the mean vertical velocity and total vertical displacement of EGMS_86, as derived from the EGMS Data Explorer (accessed on 30 October 2024).

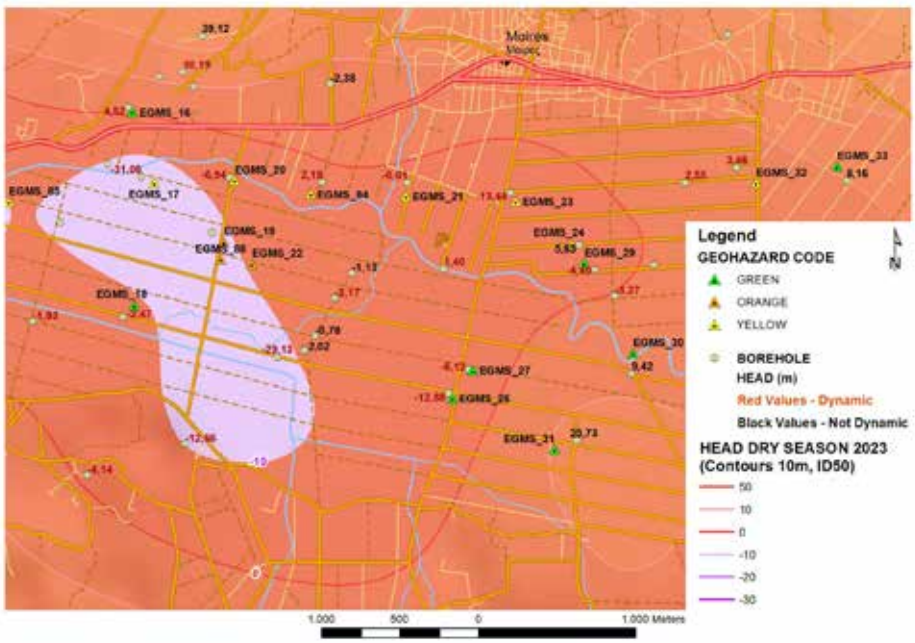


Figure 5.1. Groundwater overexploitation near the reference measurement point has created a cone of depression, with groundwater levels dropping to negative altitude.

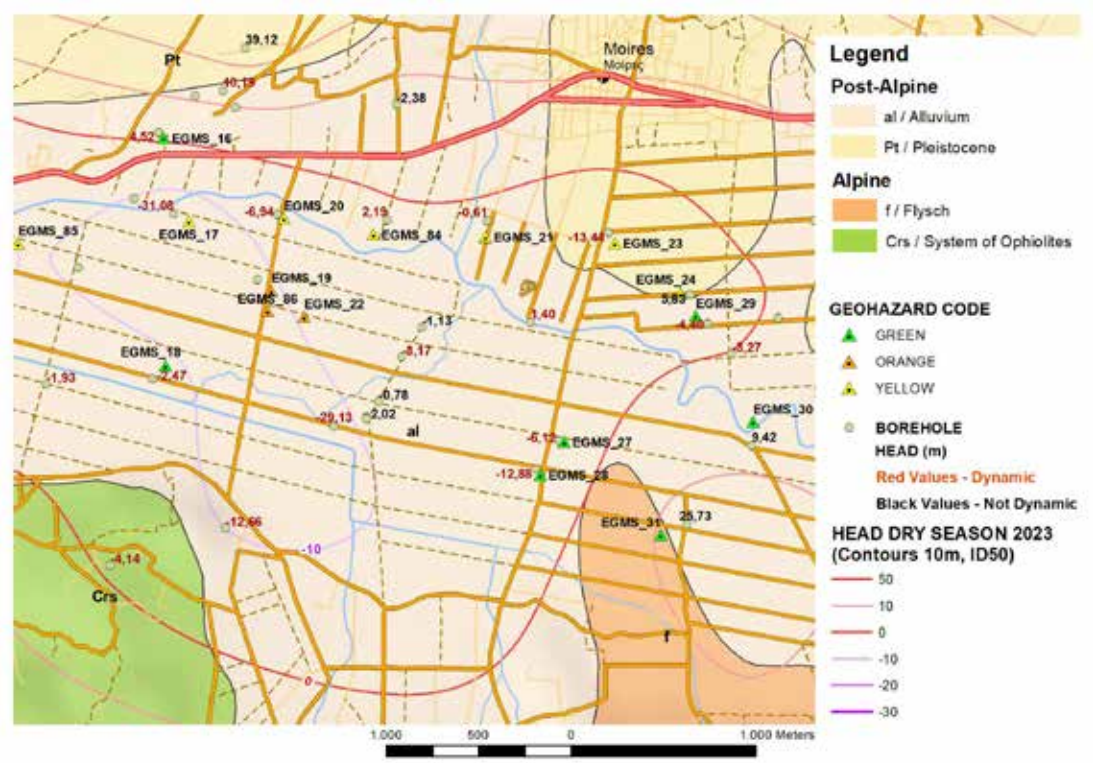


Figure 5.2. The geological framework of the area, illustrating potentiometric contours and head values.

The loose packing of alluvial deposits in the upper layers and the unconsolidated Pleistocene deposits (e.g., sand and gravel) beneath them are particularly affected by these changes. This interaction leads to significant ground ruptures and openings due to pipe-laying phenomena, which are attributed to underlying deformations caused by groundwater-level fluctuations.

It is worth noting that similar phenomena (subsidence - ground movements due to groundwater depletion) occur in other comparable areas; however, because these areas are under cultivation, deformation phenomena often go unnoticed due to erosion and plowing or are not given sufficient consideration. Documenting these areas where such phenomena occur can enhance the understanding of the geological background's response in regions affected by overexploitation and contribute to the assessment of existing or potentially emerging geohazards, ultimately aiding in risk reduction. In addition, it will help in the design of mitigation measures, such as the application of artificial recharge.

Conclusions

Ground movements caused by groundwater decline are an increasingly significant issue worldwide, often due to excessive water extraction and pronounced rainfall seasonality. In agricultural and peri-urban areas, such as the Messara Basin on the island of Crete, these drawdowns are predominantly anthropogenic, with excessive groundwater extraction for agriculture leading to land subsidence. Understanding the geological and hydrogeological conditions of an area, combined with the use of satellite data, offers a critical tool for mitigating risks and minimizing the impacts of potential geohazards. Such integration is particularly valuable for civil engineering applications, including the structural assessment of buildings and infrastructure, detection of differential displacements, evaluation of terrain stability, and other related challenges.

Acknowledgements

Field surveys have been conducted within the framework of the PhD thesis assigned to the first author at the N.T.U.A. We acknowledge the use of data from the European Ground Motion Service (EGMS) Data Explorer in this study. The datasets provided valuable insights for analyzing induced land subsidence and geohazards. We gratefully acknowledge the European Environment Agency (EEA) for maintaining and providing access to the EGMS data, which significantly contributed to the outcomes of this research.

References

Delgado Blasco, J.M., Foumelis, M., Stewart, C., Hooper, A., 2019. Measuring Urban Subsidence in the Rome Metropolitan Area (Italy) with Sentinel-1 SNAP-StaMPS Persistent Scatterer Interferometry. Remote Sensing 11, 129. [https://doi.org/10.3390/rs11020129].

European Ground Motion Service / Land Monitoring / EGMS Explorer. Dataset: ORTHO (Level 3) East/West (2019–2023) & Vertical (2019–2023) [https://doi.org/10.2909/7eb207d6-0a62-4280-b1ca-f4ad1d9f91c3EGMS-01].

H.S.G.M.E./R.B.C., 2023. Project: "Systematic inventory of water wells of every use throughout the country of Greece" of the Municipalities: Phaistos, Gortyna, Archanon Asterousion, Minoa Pediadas, Viannos (Period: 2020-2022). Preliminary Technical Reports, Rethymno, Greece.

Kamali, M., Papoutsis, I., Loupasakis, C., Abuelgasim, A., Omari, K., Kontoes, C., 2021. Monitoring of land surface subsidence using persistent scatterer interferometry techniques and ground truth data in arid and semi-arid regions, the case of Remah, UAE, Science of The Total Environment, Volume 776 [https://doi.org/10.1016/j.scitotenv.2021.145946].

Loupasakis, C., Angelitsa, V., Rozos, D., Spanou, N., 2014. Mining geohazards—land subsidence caused by the dewatering of opencast coal mines: The case study of the Amyntaio coal mine, Florina, Greece. Natural Hazards, vol. 70(1), pages 675-691.

Mertikas, S., Papadaki, E., Paleologos, E., 2010. Radar interferometry technique for monitoring subsidence induced by excessive groundwater pumping in Crete, Greece. ESA Proceedings for the Living Planet Symposium, pp. 6, Bergen, Norway.

Michalakis, I., Tsolaki, E., Loupasakis, C., Voudouris, K., Kontoes, Ch., 2022. Groundwater level dynamics of the Messara Basin, Crete Island. [Bulletin of the Geological Society of Greece, Sp. Publ. 10. Ext. Abs. GSS2022-162. 553-554 p.].

Michalakis, I., Staridas Sp., Tsolaki, E., 2024. Hydrolithological Classification of the Island of Crete: Based on the 1:200,000 Geological Map by Creutzburg et al. (1977) / First Report on the Hydrolithological Properties and Spatial Distribution of Geological Units on the Island of Crete. Rethymno [H.S.G.M.E./R.B.C. Library Code: 377/HG231].

Michalakis, I., Staridas Sp., Tsolaki, E., 2024. Hydrolithological Classification of the Island of Crete: Based on the 1:200,000 Geological Map by Creutzburg et al. (1977) / Second Report on the Hydrolithological Properties and Spatial Distribution of Geological Units on the Island of Crete / Hydrolithological Classification of the Island of Crete. Rethymno [H.S.G.M.E./R.B.C. Library Code: 379/HG233].

Michalakis, I., 2024. Hydrogeological Conditions and Sustainability Challenges in the Messara Basin, Crete. [SIPS 2024. 10th Intl. Symp. on Sustainable Mineral Processing. Paper ID: 493].

Papoutsis, I., Kontoes, C., Alatza, S., Apostolakis, A., Loupasakis, C., 2020. InSAR Greece with Parallelized Persistent Scatterer Interferometry: A National Ground Motion Service for Big Copernicus Sentinel-1 Data. Remote Sensing 12, no. 19: 3207. [https://doi.org/10.3390/rs12193207].

Raspini, F., Loupasakis, C., Rozos, D., Adam, N., Moretti, S., 2014. Ground subsidence phenomena in the Delta municipality region

(Northern Greece): Geotechnical modeling and validation with Persistent Scatterer Interferometry. International Journal of Applied Earth Observation and Geoinformation, Volume 28, Pages 78-89, [https://doi.org/10.1016/j.jag.2013.11.010].

Svigkas, N., Papoutsis I., Loupasakis C., Tsangaratos P., Kiratzi, A., Kontoes C., 2016. Land subsidence rebound detected via multi-temporal InSAR and ground truth data in Kalochori and Sindos regions, Northern Greece. Engineering Geology, Volume 209, Pages 175-186, ISSN 0013-7952, [https://doi.org/10.1016/j.enggeo.2016.05.017].

Zhang, Y., Xue, Y.Q., Wu, J.C., Yu, J., Wei, Z.X., Li, Q.F., 2008. Land subsidence and earth fissures due to groundwater withdrawal in the southern Yangtse Delta, China. Environmental Geology 55, No 4, 751-762.

17th INTERNATIONAL CONGRESS of the Geological Society of Greece

BULLETIN OF THE GEOLOGICAL SOCIETY OF GREECE, SP. PUBL.

EXTENDED ABSTRACT 211

Application of geochemical indices for heavy metal evaluation in the Pinios Dam, Greece

Michalopoulou M.[1], Depountis N.[1], Zagana E.[1], Avramidis P.[1]
(1) Department of Geology, University of Patras, Patra, Greece, maria_michalopoulou@ac.upatras.gr

Research Highlights: Application of geochemical indices for the evaluation of sediment and water samples in the Pinios Dam drainage basin in Western Greece

Introduction

Reservoirs are essential for water supply and flood management; yet numerous reservoirs encounter quality challenges caused by heavy metal concentration. This study investigates the extent of heavy metal concentration in the Pinios Dam drainage basin in the Ilia Regional Unit in Western Greece by analyzing sediment and water samples from the dam reservoir as well as water samples from the river tributaries. The main focus is to evaluate heavy metal concentration levels using established geochemical indices. The indices that were used for this purpose include the Geo-Accumulation Index (Igeo), the Contamination Factor (CF), the Pollution Load Index (PLI), and the Heavy Metal Pollution Index (HPI).

Study area

The Pinios Dam is an earth-filled structure characterized by a heterogeneous design, standing 50 meters high and spanning a length of 2,175 meters, with a final crest elevation of 100 meters. Constructed in 1968, the reservoir associated with the dam covers a total surface area of 19.87 km² and it collects surface runoff from a catchment area of 673.41 km². The water that is collected serves dual purposes, supplying both drinking and irrigation needs (Michalopoulou et al., 2024). Geologically, the catchment area is predominantly underlain by Alpine bedrock, which includes formations from the Ionian, Gavrovo-Tripolis, and Pindos geotectonic zones. These formations primarily consist of flysch and limestone. Additionally, the area features Neogene and Quaternary sediments. To provide a detailed representation of the area's geological framework, a geological map was developed using ArcGIS Pro 3.4.0. This map integrates unified data from four geological sheets produced by the Hellenic Survey of Geological and Mineral Exploration and presents the sampling points of this research (Figure 1).

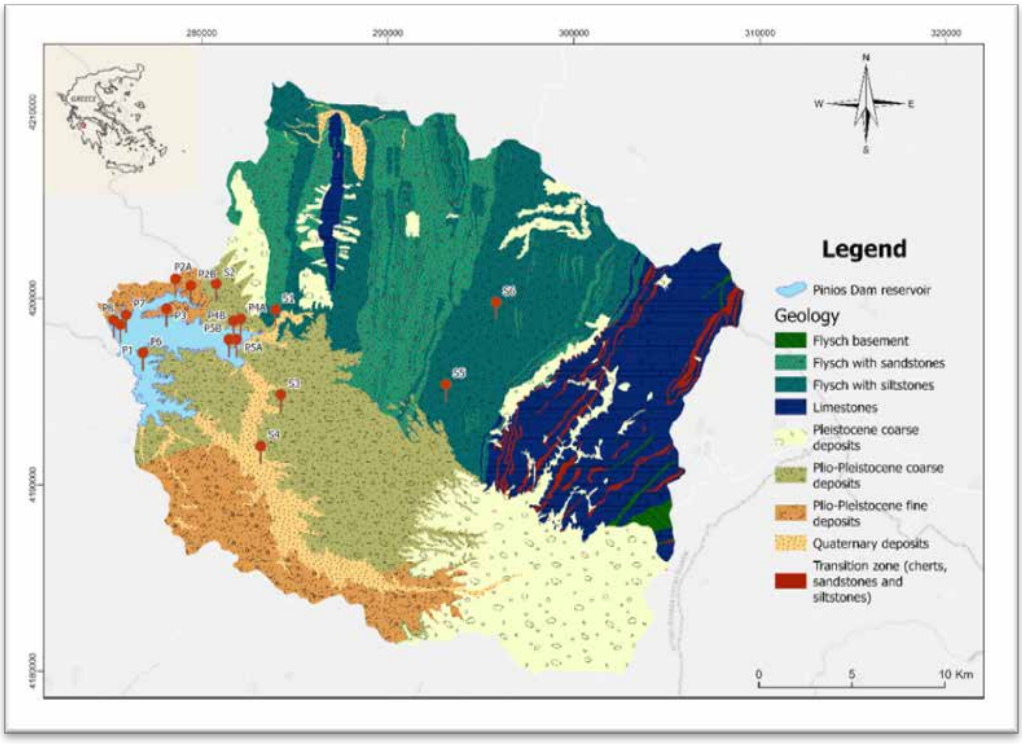


Figure 1. The sampling points and the geological formations of the research area (modified from Michalopoulou et al., 2024).

The surrounding region has experienced high rates of soil erosion and shallow landslide activity in recent decades, largely attributed to the extensive wildfires that have occurred over the past 20 years (Depountis *et al.*, 2020; Lainas *et al.*, 2021; Michalopoulou *et al.*, 2022). These processes have accelerated sediment deposition within the reservoir, significantly influencing the distribution and concentration of heavy metals in the water body and the deposited sediments; thus, altering the geochemical dynamics of the artificial lake.

Methods

Within the research area, monitoring and sampling stations (Figure 1) were established for the analysis of sediments, as well as the incoming and stagnant water. Sediment samples were obtained from the reservoir's bottom using a Van Veen grab sampler at seven stations (P1-P7), covering a collection area of 0.04 m². At locations P3 and P7, in situ measurements were performed during the autumn and winter seasons to record the physicochemical properties of the water column. Both sediment and water samples were transported to the laboratory in a portable refrigerator. Sediment samples were stored at −4 °C to ensure preservation, while water samples were analyzed within 24 hours for nutrient content and acidified for subsequent heavy metal analysis. Regarding the sediment analysis, major elements were analyzed using WD-XRF (Rigaku ZSX PRIMUS II), and the total organic carbon was quantified using the potassium dichromate oxidation method. Fe and Mn in water samples were measured via atomic absorption spectroscopy (Perkin Elmer Pinacle 900). pH, Eh, and other parameters were recorded in situ with a YSI 63 multiparameter probe.

Runoff water sampling was carried out at six sites (S1–S6), representing the tributaries and the main branch of the Pinios River basin. Samples were collected in two polyethylene bottles, one with a capacity of 1 L and the other 100 mL. The 100 mL samples were filtered on-site through a 0.45 μm filter to remove particles, followed by acidification with HNO_3. Following each sampling, water samples were transported to the laboratory for chemical analysis using atomic absorption spectroscopy. The elements analyzed in the sediments are Fe, Mn, Ni, Cr, Pb, Zn, Cu, Co, and Zr. The water samples were analyzed for Fe, Mn and major cations/anions Ca^{2+}, Mg^{2+}, Na^{+}, K^{+}, HCO_3^{-}, SO_4^{2-}, Cl^{-}, NO_3^{-}, NO_2^{-}, PO_4^{3-}, NH_4^{+}.

The Geo-Accumulation Index (Igeo) was used for the assessment of heavy metal enrichment in sediments and soil as suggested by Muller (1969), Sojka *et al.* (2022), Wu *et al.* (2022), and Wang *et al.* (2023) from another similar research. According to Muller (1969), the Igeo index is calculated by the following formula.

$$I_{geo} = \log_2\left(\frac{C_n}{K * B_n}\right), \quad (1)$$

The Cn value represents the measured heavy metal concentrations of the sediment samples (mg/kg), the K coefficient is typically equal to 1.5 and demonstrates the adjustment of the standard variation of heavy-metal concentrations during diagenesis (Wu *et al.*, 2022) and the Bn is the background concentrations of each heavy metal (mg/kg) displaying the composition of the upper continental crust (Taylor *et al.*, 1985; McLennan, 2001). The classes of the Igeo index describing the level of contamination are the following: Igeo ≤ 0: uncontaminated, 0 < Igeo ≤ 1: uncontaminated to moderately contaminated, 1 < Igeo ≤ 2: Moderately contaminated, 2 < Igeo ≤ 3: Moderately to heavily contaminated, 3 < Igeo ≤ 4: Heavily contaminated, 4 < Igeo ≤ 5: Heavily to extremely contaminated and Igeo > 5: Extremely contaminated sediment sample.

The Contamination Factor (CF) is an index proposed by Hakanson (1980) and is widely used for the evaluation of the contamination level of sediments by metals and it is calculated by dividing the measured heavy metal concentration (C_{metal}) with their corresponding background value ($C_{background}$). CF values below 1 show low contamination, values between 1 and 3 show moderate contamination, values between 3 and 6 indicate considerable contamination and values higher than 6 show very high contamination.

$$CF = \frac{C_{metal}}{C_{background}} \quad (2)$$

The Pollution Load Index (PLI) is another index suggested by Tomlinson *et al.* (1980), that intends to evaluate the degree of heavy metal enrichment in sediment samples, and it is calculated by the following formula (Tomlinson *et al.*, 1980).

$$PLI = \sqrt[n]{CF_1 \times CF_2 \times \cdots \times CF_n} \quad (3)$$

The CF component refers to the calculated contamination factor for each element mentioned above. The PLI is

estimated as the n root of the n contamination factors multiplied together. The classifications of the PLI values are the following: no pollution for PLI ≤1, moderate pollution for 1 <PLI ≤2, strong pollution for 2 <PLI ≤3, and extremely strong pollution for PLI ≥3.

The Heavy Metal Pollution Index (HPI) is suggested by Mohan *et al.* (1996) for the assessment of the water quality. In this study, HPI is used for the examination of lake and stream surface water quality concerning Fe and Mn concentrations. The formulas for the estimation of this index are presented below (Mohan *et al.*, 1996; Moldovan *et al.*, 2022; Sur *et al.*, 2022).

$$Q_i = \frac{M_i}{S_i} \times 100 \quad (4)$$

$$W_i = \frac{1}{S_i} \quad (5)$$

$$HPI = \frac{\sum_{i=1}^{n} W_i Q_i}{\sum_{i=1}^{n} W_i} \quad (6)$$

The Q_i refers to the sub index of the *i*th parameter, the W_i is the unit weightage of the *i*th parameter, the n is the number of the examined heavy metals, the Si demonstrates the standard permissible values of the examined heavy metals, and the Mi presents the measured heavy metal concentrations of the water samples. Concerning the Si values for Fe and Mn, the European Directive 2020/2184 on water quality was assessed. When the HPI is less than 100, it indicates low levels of heavy metal concentrations; when it is estimated to be more than 100, it indicates that the water is unsafe for consumption and can have adverse health implications.

Results

The indices that were chosen for the pollution assessment are Igeo, CF, PLI for sediments and HPI for water samples. The values of Igeo for all sampling sites are shown in Figure 2. For most heavy metal elements, the Igeo values are calculated below 1 in every station which means that the samples are practically uncontaminated. Igeo values above unity indicate moderate heavy metal enrichment and were calculated for Ni in all stations (range: 1.02-1.44) except P5 (0.67), and for Cr only in station P2 (1.05). The average Igeo values were ranked as: Ni> Cr> Pb> Zn> Cu> Co> Zr. The Igeo values suggest a heterogeneous distribution of heavy metal enrichment, which is related to natural geological processes as the metal concentrations could be influenced by natural mineral deposits, or even historical land use patterns.

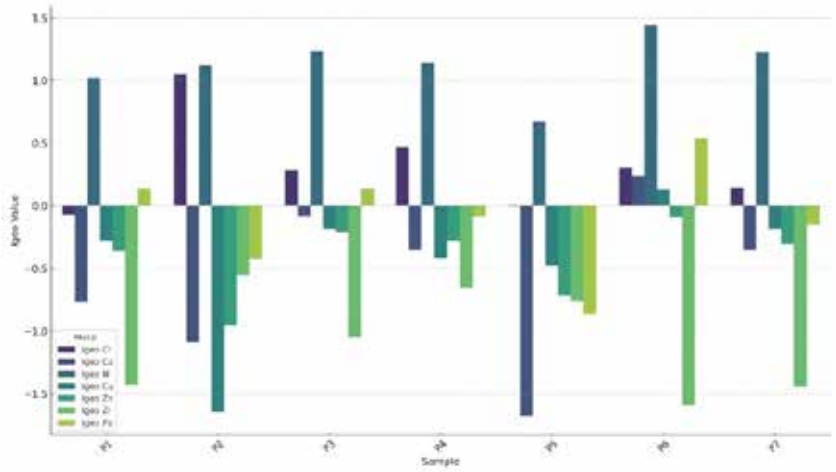


Figure 2. Bar chart of the Igeo values of the examined heavy metals for each station.

The Contamination Factor (CF) values for heavy metals offer insight into the degree of heavy metal enrichment in the examined samples. The ranges of the CF values for Zr, Co, Zn, Cu, Pb, Cr and Ni are 0.50 to 1.02, 0.47 to 1.76, 0.77 to 1.41, 0.48 to 1.64, 0.82 to 2.18, 1.43 to 3.11 and 2.39 to 4.07, respectively. Average CF values for all metals were ordered as presented in the following sequence Ni>Cr>Pb>Cu>Zn>Co>Zr. Low to moderate contamination based

on CF values was calculated for Cu, Zn, Pb, Zr, Co and Cr. The CF values for Ni showed moderate to considerable contamination with a minimum value of 2.39 and a maximum value equal to 4.07. The CF concentrations for all samples indicate varying degrees of heavy metal enrichment, with certain metals like Ni showing consistently higher levels across all samples reflecting mainly natural geological variations (Figure 3).

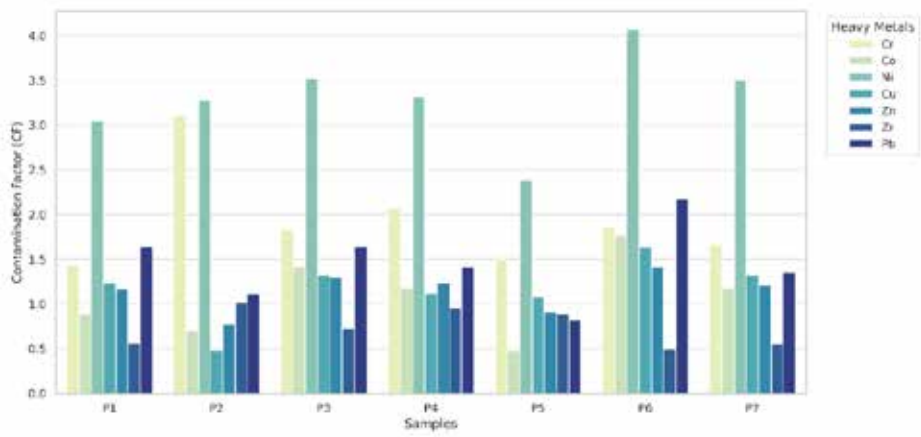


Figure 3. Bar chart of the CF values of the examined heavy metals for each station.

The Pollution Load Index (PLI) for heavy metals offers insight into the degree of contamination in each of the reservoir stations where samples were collected. PLI values below 1 show negligible concentrations while values greater than 1 suggest significant concentrations. The calculated PLI values range between 1.03 to 1.65, indicating moderate degrees of heavy metal enrichment across the stations. The bar graph below visualizes the PLI values across the different stations with the red dashed line representing the PLI threshold (Figure 4).

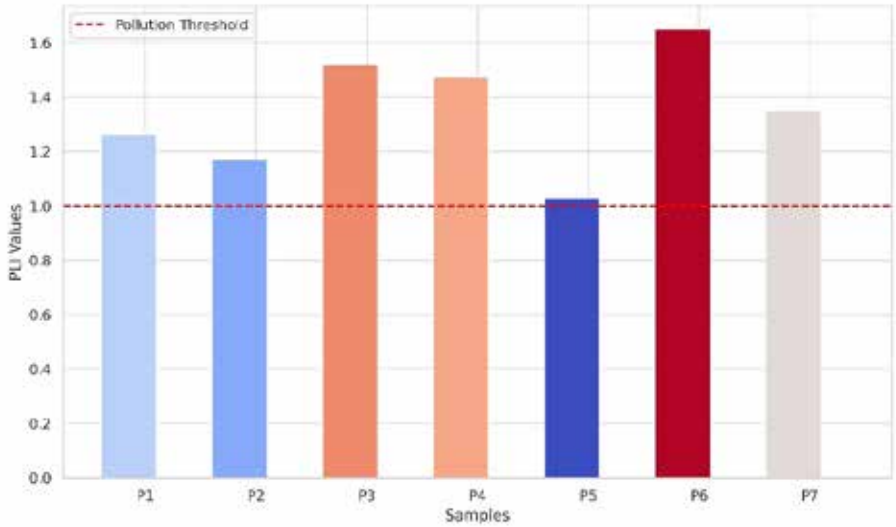


Figure 4. Bar chart of the PLI values of the examined heavy metals for each station.

The Heavy-Metal Pollution Index (HPI) is a vital index for evaluating heavy metal concentrations in water sources as it assesses several heavy metals in the water and their combined effects on water quality in a thorough manner. Each heavy metal is given a weighting factor according to its toxicity and possible health effect in order to calculate the HPI (Badeenezhad *et al.*, 2023). The HPI index was calculated for lake and stream samples for different periods of time. The bar charts for each type of sample are presented in Figure 5. The results showed that the surface lake water samples exceed the threshold of 100 in 22/02/2019 in stations P1, P2, P5, P6, P7 and P8, where in 09/10/2018 the HPI value is considerably high mainly because of the high measured concentration of Mn (226 μg/l). This is likely due to seasonal redox cycling and stratification, which influence metal mobility in the hypolimnion.

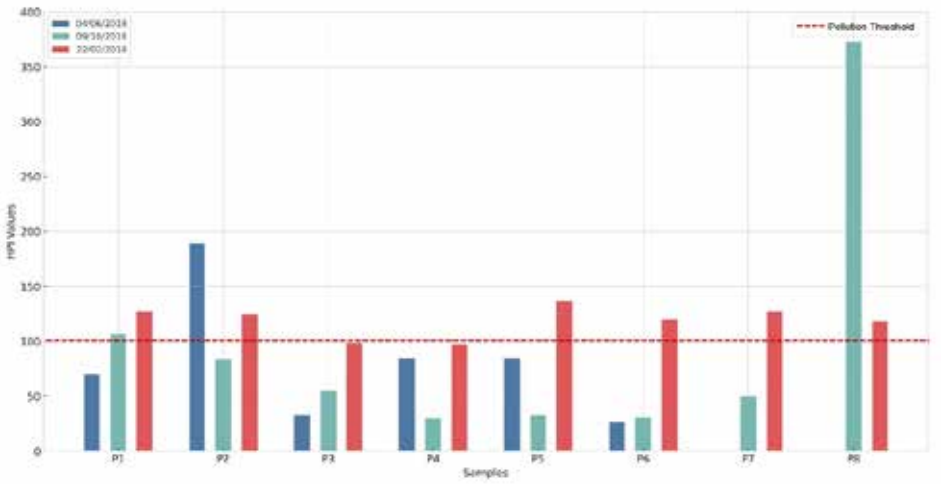


Figure 5. Bar chart of the HPI values of the lake samples for different dates.

Concerning the stream water samples (Figure 6), stations S2, S3, S4 and S6 presented HPI values above the threshold 100. The S2 station is the one with the highest values which exceeded the threshold in almost all samples except for the ones that were taken on 29/11/2018 and at 22/02/2019.

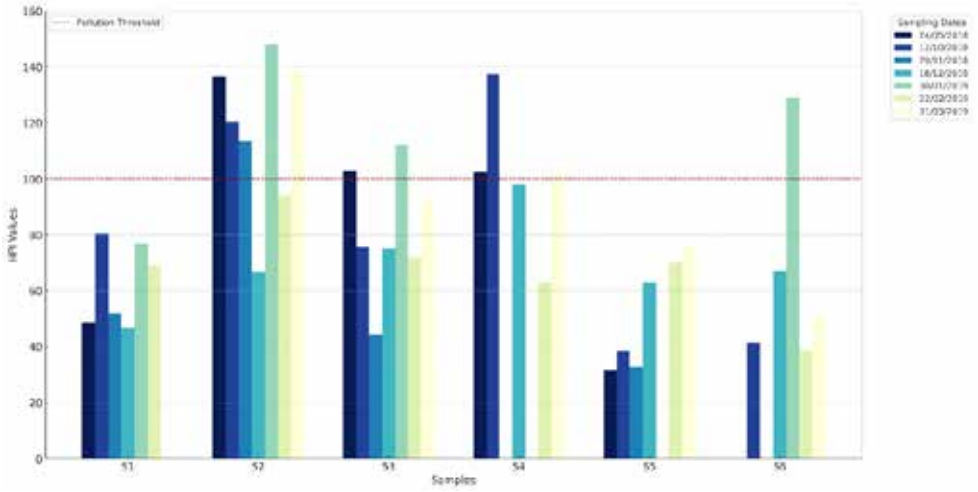


Figure 6. Bar chart of the HPI values of the stream samples for different dates.

Discussion & Conclusions

The application of geochemical indices in the Pinios Dam drainage basin provided valuable insights into the extent and distribution of heavy metal enrichment in sediments and concentrations in water. Regarding the evaluation of sediments, the Igeo values indicate that most heavy metals in the sediment samples are within uncontaminated to moderately contaminated levels, with exceptions observed for Ni and Cr in specific stations. The CF values further suggest low to moderate contamination for most metals, with Ni showing moderate to considerable concentrations, likely due to natural enrichment. The PLI values, ranging from 1.03 to 1.65, point to moderate pollution levels in the sediments across the study area. The examination of the water quality was based on the HPI index which reveals that lake and stream water samples frequently exceed the pollution threshold, primarily due to elevated Fe and Mn concentrations. Temporal variations suggest that certain periods are more prone to higher Fe and Mn concentrations, potentially due to hydrological or seasonal factors. More specifically, in this case, seasonal stratification plays a crucial role in shaping the distribution and mobility of Fe and Mn within the water column of the reservoir, as seasonal fluctuations in their concentrations were evident, with higher levels of these elements observed in the hypolimnion during the autumn/dry season (Michalopoulou *et al.,* 2024).The observed heavy metal indices strongly reflect the strong influence of natural geological processes, such as weathering of metal-rich formations, erosion,

and sediment deposition. These processes dominate the geochemical dynamics of the study area as the observed metal enrichment in the examined sediments originated from natural processes as well as the high concentration of organic carbon and the clayey composition of the fine sediments. So, the geoaccumulation in sediments occurs due to the ability of organic matter and clay minerals to adsorb trace element cations. Anthropogenic activities, such as agriculture, appear to have a secondary role, as suggested by the localized and relatively moderate contamination levels for most metals, and needs further investigation to better quantify their impact. Evaluating pollution levels using multiple indices for the same region can yield varying pollution classifications and lead to different interpretations as these discrepancies arise from the distinct mathematical formulations of each index (Karaouzas et al., 2021). Thus, to ensure effective management, it is essential to prioritize continuous monitoring and utilize modeling techniques to better understand the long-term behavior of metals in the system and to mitigate the potential environmental impacts of metal enrichment.

Acknowledgements

The authors are grateful for the financial and administrative support of the research by the Region of Western Greece and the Municipality of Ilida (project contract 82334).

References

Badeenezhad, A., Soleimani, H., Shahsavani, S., Parseh, I., Mohammadpour, A., Azadbakht, O., ... & Babakrpur Nalosi, K., 2023. Comprehensive health risk analysis of heavy metal pollution using water quality indices and Monte Carlo simulation in R software. Scientific Reports, 13(1), 15817.

Depountis, N., Michalopoulou, M., Kavoura, K., Nikolakopoulos, K., Sabatakakis, N., 2020. Estimating Soil Erosion Rate Changes in Areas Affected by Wildfires. *ISPRS Int. J. Geo-Inf.*, *9*, 562.

Directive (EU) 2020/2184 of the European Parliament and of the Council of 16 December 2020 on the quality of water intended for human consumption. Available online: https://eur-lex.europa.eu/eli/dir/2020/2184/oj. (accessed on 11 November 2024).

Hakanson, L., 1980. An ecological risk index for aquatic pollution control. A sedimentological approach. Water research, 14(8), 975-1001.

Karaouzas, I., Kapetanaki, N., Mentzafou, A., Kanellopoulos, T. D., & Skoulikidis, N., 2021. Heavy metal contamination status in Greek surface waters: A review with application and evaluation of pollution indices. *Chemosphere*, *263*, 128192.

Lainas, S., Depountis, N., Sabatakakis, N., 2021. Preliminary Forecasting of Rainfall-Induced Shallow Landslides in the Wildfire Burned Areas of Western Greece. *Land*, *10*, 877.

McLennan, S. M., 2001. Relationships between the trace element composition of sedimentary rocks and upper continental crust. Geochemistry, Geophysics, Geosystems, 2(4).

Michalopoulou, M., Depountis, N., Nikolakopoulos, K., Boumpoulis, V., 2022. The Significance of Digital Elevation Models in the Calculation of LS Factor and Soil Erosion. *Land*, *11*, 1592.

Michalopoulou, M., Depountis, N., Zagana, E., Avramidis, P., 2024. Investigation of the Origin of Elevated Amounts of Iron and Manganese in a Dam Reservoir. Geosciences, 14, 336.

Mohan, S. V., Nithila, P., & Reddy, S. J., 1996. Estimation of heavy metals in drinking water and development of heavy metal pollution index. Journal of Environmental Science & Health Part A, 31(2), 283-289.

Moldovan, A., Török, A. I., Kovacs, E., Cadar, O., Mirea, I. C., & Micle, V., 2022. Metal contents and pollution indices assessment of surface water, soil, and sediment from the Arieș River Basin Mining Area, Romania. Sustainability, 14(13), 8024.

Muller, G. M. M. G. M. G. M. G. P., 1969. Index of geoaccumulation in sediments of the Rhine River. Geojournal, 2, 108-118.

Sojka, M., Jaskuła, J., Barabach, J., Ptak, M., & Zhu, S., 2022. Heavy metals in lake surface sediments in protected areas in Poland: concentration, pollution, ecological risk, sources and spatial distribution. Scientific Reports, 12(1), 15006.

Sur, I. M., Moldovan, A., Micle, V., & Polyak, E. T., 2022. Assessment of surface water quality in the Baia Mare area, Romania. Water, 14(19), 3118.

Taylor, S. R., & McLennan, S. M., 1985. The continental crust: its composition and evolution. Blackwell, Malden, Mass.

Tomlinson, D. L., Wilson, J. G., Harris, C. R., & Jeffrey, D. W., 1980. Problems in the assessment of heavy-metal levels in estuaries and the formation of a pollution index. Helgoländer meeresuntersuchungen, 33, 566-575.

Wang, M., Wang, M., Yang, L., Yang, T., Li, J., & Chen, Y., 2023. Distribution Characteristics and Genesis of Iron and Manganese Ions in Groundwater of Eastern Sanjiang Plain, China. Water, 15(11), 2068.

Wu, D., Liu, H., Wu, J., & Gao, X., 2022. Spatial distribution, ecological risk assessment and source analysis of heavy metals pollution in urban lake sediments of Huaihe River Basin. International Journal of Environmental Research and Public Health, 19(22), 14653.

17th INTERNATIONAL CONGRESS of the Geological Society of Greece

BULLETIN OF THE GEOLOGICAL SOCIETY OF GREECE, SP. PUBL.

EXTENDED ABSTRACT 212

The impact of aquaculture units on Copper (Cu) concentrations in marine sediments

Michalopoulou S.[1], Faulwetter S.[1], Christodoulopoulos D.[1], Ramfos A.[2], Avramidis P.[1]
(1) Department of Geology, University of Patras, Greece, mich.sofi6@gmail.com (2) Department of Biology, University of Patras, Greece

Introduction / Background

Copper (Cu) is a trace element commonly found in various rocks and minerals, well known for its antimicrobial properties (Wang et al. 2022). Due to these properties, copper is widely used in aquaculture nets to control biofouling (e.g. Nikolaou et al. 2014). More specifically, it is applied in the form of copper sulfate (CuSO□), which dissolves in water and eventually settles on the seabed. However, at elevated concentrations, copper becomes toxic, particularly in marine sediments where the accumulation of heavy metals is significantly elevated and therefore poses a serious threat to aquatic organisms (Emenike et al. 2022). The effects of fish farm operations on copper concentrations have been the focus of several studies worldwide (e.g. Dean et al. 2007) but in Greece, research has focused mainly on individual fish farms (e.g. Farmaki et al. 2014), and overall knowledge on copper concentrations, their spatial distributions and their accumulation processes in the sediment near fish farms in Greece is limited.

Objectives

While the fate and consequences of organic wastes for the benthic ecosystem are relatively well understood worldwide, less attention has been given to metallic wastes from fish farms and to the changes in marine sediments from copper concentrations. Therefore, the main objectives of our study are:

- To determine the impact of copper originating from marine fish farms on marine sediments
- To examine which environmental and farm parameters influence the copper concentration in marine sediments in different regions of Greece.
- To determine the spatial extent of the impact of fish farms of copper concentration in the sediment
-

Methods

We examined the impact of aquaculture activities across four different regions: Aegean Sea, Corinthian Gulf, Euboea and Ionian Sea (Fig. 1). Sediments were collected from 32 fish farms at 50 m distance from the cages, in accordance with the Greek legislation, as well as from reference stations. In addition, we used a dataset assembled between 2020 and 2023 that included samples collected at distances of approximately 0, 25, 50 and 100 m from the cages, as well as reference samples (Fig. 1). Sediment samples were analyzed for total organic carbon (TOC) and total nitrogen (TN) using a Shimadzu TOC-VCSH TOC/TN analyzer. Total phosphorus (TP) was measured with a Hach photometer according to the APHA 2005-4500-P method. Sediment grain size was determined through dry sieving for coarser materials and with a Malvern Mastersizer 2000 Hydro for the finer fractions. Heavy metal content in the sediment was determined (Cu, Mn, Pb, Zn, Fe) using a Bruker Handheld X-ray Fluorescence Analyzer (Titan S1).
For the dataset from 2024, we assembled additional information on the surface area of the farm, the geomorphology of the coastline (farm located within open or closed embayment) and the distance from the coast.
To test the effects of various environmental parameters on the copper concentration in marine sediments two different analyses were performed, using a general linear model (GLM) with a gamma distribution and inverse link function. For the dataset from 2020-2023, the model included the distance from the farm, depth of the seafloor, percentage of sand, sediment type and geographical region as explanatory variables. For the dataset from 2024, the model included the distance from the farm, depth of the seafloor, percentage of mud, sediment type, geographical region, surface area of the farm, distance from the coast, and bay type (open or enclosed) as explanatory variables. The significance level for all tests was set to α=0.05 and all analysis were performed in R (R Core Team 2024).
Two geochemical indices- Contamination Factor (CF), and the Geo-Accumulation Index (Igeo)- were calculated to identify the enrichment or depletion of metal distribution in sediment samples. The calculation of the CF values contacted using the following equation:

$C_F = \bar{c}_s / C_b$

where the $\bar{c}_s$ represents the mean copper concentration from positions (0, 25, 50, 100m) around the cages and C_b is the background concentration from reference data for each region. The Igeo was calculated using the following equation:

$Igeo=\log_2(Cs /1.5\times Cb)$

where the $\overline{c_s}\overline{c_s}$ represents the mean copper concentration from positions (0, 25, 50, 100m) around the cages, C_b is the background concentration of the same metal in an uncontaminated environment and the factor 1.5 is used as a correction factor to account for natural variability in background levels.



Figure 1. Sampling stations.

Results

The results of the analysis indicated a decrease in copper concentrations with increasing distance from the fish cages (Fig.3a,b). Specifically, the highest concentrations of copper were found directly beneath and around the fish farm cages, but significantly elevated concentration (in comparison to the reference stations) were still found at distances of up to 100 m from the farms (Fig. 2). The dataset from 2024 which included only stations from 50 m distance as well as reference stations showed likewise significantly elevated concentrations at 50 m distance compared to the reference stations.

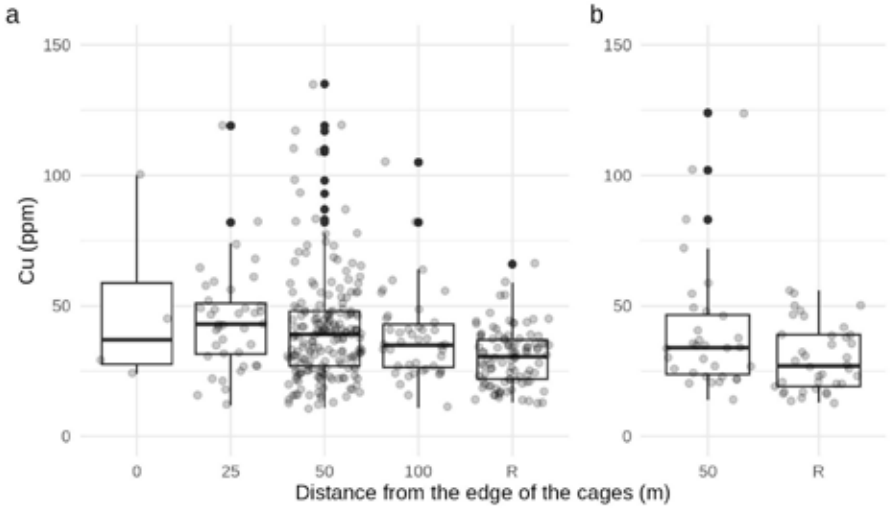


Figure 2. Copper concentration for different distances from the farm distance from the farm. R = Reference station. a) Dataset of 2020-2023, b) Dataset of 2024.

The sediment type was also associated with copper absorption, as finer-grained sediments exhibited a higher capacity for copper absorption in both datasets (Fig. 3). This correlation was weak but statistically significant.

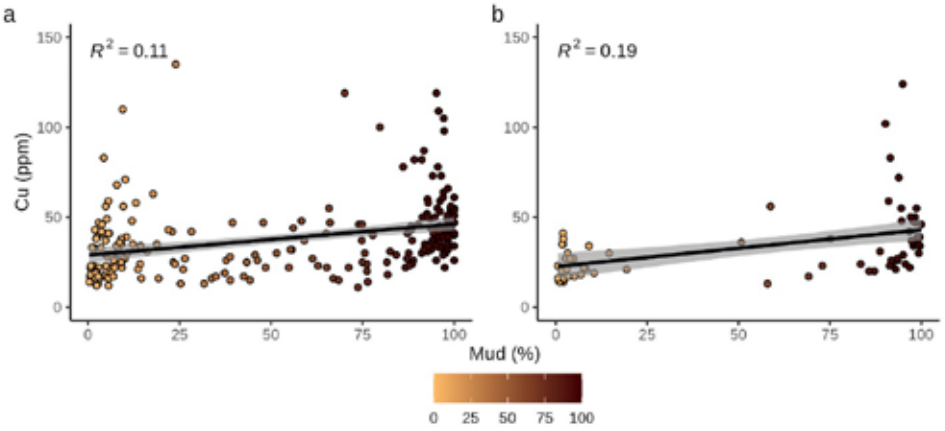


Figure 3. Copper concentration vs percentage of mud in the sediment. a) Dataset of 2020-2023, b) Dataset of 2024.

Additionally, there was an association between copper (Cu) concentration and the geographical region (Fig. 4) Copper concentrations were notably higher in the Ionian region compared to other regions. The Ionian exhibited the highest copper concentrations across all distances from the farm, including reference samples that reflected the natural copper levels of the area. The general pattern of decreasing copper concentrations with increasing distance from the cages was consistent across most regions. However, slight exceptions were observed in regions like Euboea and the Ionian Sea, likely due to a limited number of samples at certain distances.

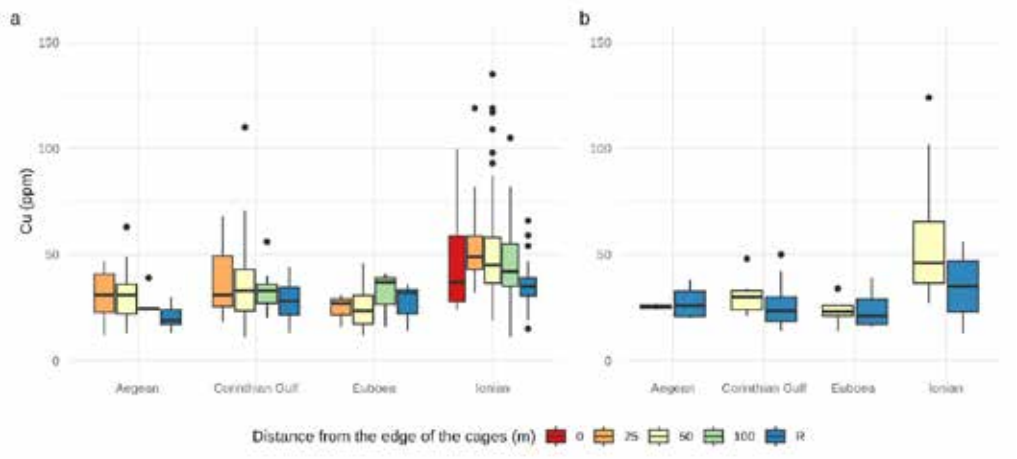


Figure 4. Copper concentration at different distances from the farm, across different regions of Greece. R = Reference station. a) Dataset of 2020-2023, b) Dataset of 2024.

The other variables included in the statistical models (depth of the sea floor, surface area of the farm, the distance from the coast and the bay type (open or enclosed)) did not show any statistically significant effects on copper concentrations.

Overall, the dataset for 2024 confirmed the results of the 2020-2023 dataset. Similar factors were identified to play an important role for copper concentrations in marine sediments.

The contamination factor (CF) provides insight into the extent of pollution in each region. As shown in Table 1, all regions exhibit moderate contamination ($1 \leq CF < 3$), except for Euboea, which falls slightly below this threshold (CF = 0.97), indicating low contamination. Among the regions, the Ionian Sea displays the highest CF value (1.46), suggesting a relatively greater pollutant concentration compared to its natural background levels.

The geoaccumulation index (Igeo) results suggest that all regions are classified as uncontaminated (Igeo<0). The lowest Igeo value was recorded in Euboea (-0,62), significantly lower than the other regions, indicating a natural background concentration very close to or even higher than the sample concentration. The Ionian Sea had the highest Igeo value (-0.04) but still remained within the uncontaminated category.

Table 1. Contamination Factor (CF) and Geoaccumulation Index (Igeo) in Four Study Areas

Region	Sample Concentration (Cs) ppm	Background Concentration (Cb) ppm	CF	Igeo
Aegean	29,4	21,57	1,36	-0,14
Corinthian Gulf	34,81	27,61	1,26	-0,25
Euboea	25,55	26,25	0,97	-0,62
Ionian	51,34	35,13	1,46	-0,04

Conclusions

The present study shows that the determining factors for copper concentration are related to certain individual characteristics of the environment of each farm, such as sediment type and the geographical region. Findings of the present study are of great interest as it highlights that copper concentration is not only determined by the aquaculture activities but also by local environmental conditions.

In both datasets, 2020-2023 and 2024, the results of the analysis indicated that the highest copper concentrations were found directly beneath and around the fish farm cages, within a range of at least 100 m from the cages (no distances further than that were examined). Greek legislation mandates regular environmental monitoring at a distance of 50m from the cages, and while no thresholds or allowed limits for copper concentrations exist in Greece, it is implied that the environmental impact of the farms should overall be limited to this distance. The elevated concentrations found here indicate an effect of the farm on the surrounding marine environment and highlights the impact of feed and faecal inputs as well as the footprint of antifouling products in aquaculture. The spatial extent found in this study is in line with the literature, where effects have been found up to several hundred meters (e.g. Farmaki *et al.* 2014).

The correlation between sediment type and copper concentration in both datasets indicated a weak but significant association, with finer-grained sediments exhibiting a higher capacity for copper absorption. This can be attributed to the solid physio-chemical properties, as smaller particles provide larger surface area per unit mass, facilitating greater adsorption of copper ions.

The spatial differences in copper concentration, particularly in the Ionian region, may be linked to the natural copper concentrations of the area and the geological features, such as inflowing river waters, seasonal variations, hydrodynamic conditions, the rather sheltered conditions of many of the farms and sediment type. In addition, the Ionian region hosts a high number of large fish farms, and cumulative and far-field effects that could even affect the reference stations might likewise play a role and are in need of investigation.

Copper thresholds in marine sediments are crucial for assessing the environmental impacts of aquaculture activities. These thresholds can vary depending on factors such as sediment characteristics, the local species, and environmental conditions. As no copper thresholds have been established by the National or EU Legislation for marine sediments, as well as with SQGs recommended by the Canadian Council of Minister of the Environment (Farmaki et al., 2014), direct comparison of our findings is rather difficult. We found that mean copper concentrations near the cages (42.67 ppm) including extreme values, exceed the Canadian guidelines, set at 18.7 ppm and remain below the Probable Effects Level (PEL=108 ppm). While levels below the PEL suggest that severe biological effects are unlikely, exceeding the ISQGs indicates potential risks to benthic organisms, particularly with prolonged exposure. Additionally, the mean copper concentration in Greece is below 65 ppm, aligning with the threshold set by the Australian & New Zealand Guidelines for Fresh & Marine Water Quality. These findings underscore the need for regular monitoring and targeted mitigation measures.

Other studies in the Mediterranean Sea have found that there is a definite enrichment for copper under the cages, up to 28 ppm in Gulluk Bay in the southeastern Aegean Sea (Dalman et al., 2006). In E. Aegean Sea, Balci Küçüksezgin (1994) found copper concentrations from 8 to 29 ppm and lower copper levels of 15 ppm have been reported in the Bay of Cádiz in Spain, by Mendiguchía et al. (2006) . Outside the Mediterranean, significantly higher copper concentrations were documented in areas with intense industrial activity, such as the mining and smelting region of Rouyn-Noranda, Quebec in Canada (216–2984 ppm) (Borgmann et al., 2004). According to another Canadian study (Brooks and Mahnken, 2003) that compared surface sediment samples from salmon farms that (a) were using copper anti-foulant products, (b) used no copper-based anti-foulant and (c) from reference stations remote from fish farms, concluded that sediment copper levels were higher at farms using copper based anti-foulants.

Overall, this study is an important contribution to the understanding of the impact of fish farms on copper concentrations in the marine sediments and the results should be taken into account for designing environmental monitoring

programs and adopting sustainable farming practices.

Acknowledgements
The authors would like to thank the personnel of all involved fish farms for assistance in field work as well as the personnel of the Research Group for the Environmental Monitoring of Aquaculture of the Department of Geology, University of Patras, for support in sampling and laboratory analyses.

References
Borgmann, U., Nowierski, M., Grapentine, L.C., Dixon, D.G., 2004. Assessing the cause of impacts on benthic organisms near Rouyn-Noranda, Quebec. Environmental Pollution 129, 39–48. https://doi.org/10.1016/j.envpol.2003.09.023

Brooks, K.M., Mahnken, C.V.W., 2003. Interactions of Atlantic salmon in the Pacific Northwest environment. Fisheries Research 62, 295–305. https://doi.org/10.1016/S0165-7836(03)00065-1

Dalman, Ö., Demirak, A., Balcı, A., 2006. Determination of heavy metals (Cd, Pb) and trace elements (Cu, Zn) in sediments and fish of the Southeastern Aegean Sea (Turkey) by atomic absorption spectrometry. Food Chemistry 95, 157–162. https://doi.org/10.1016/j.foodchem.2005.02.009

Dean, R.J., Shimmield, T.M., Black, K.D., 2007. Copper, zinc and cadmium in marine cage fish farm sediments: An extensive survey. Environmental Pollution 145, 84–95. https://doi.org/10.1016/j.envpol.2006.03.050

Emenike, E.C., Iwuozor, K.O., Anidiobi, S.U., 2022. Heavy Metal Pollution in Aquaculture: Sources, Impacts and Mitigation Techniques. Biol Trace Elem Res 200, 4476–4492. https://doi.org/10.1007/s12011-021-03037-x

Farmaki, E.G., Thomaidis, N.S., Pasias, I.N., Baulard, C., Papaharisis, L., Efstathiou, C.E., 2014. Environmental impact of intensive aquaculture: Investigation on the accumulation of metals and nutrients in marine sediments of Greece. Science of The Total Environment 485–486, 554–562. https://doi.org/10.1016/j.scitotenv.2014.03.125

Mendiguchía, C., Moreno, C., Mánuel-Vez, M.P., García-Vargas, M., 2006. Preliminary investigation on the enrichment of heavy metals in marine sediments originated from intensive aquaculture effluents. Aquaculture 254, 317–325. https://doi.org/10.1016/j.aquaculture.2005.10.049

Nikolaou, M., Neofitou, N., Skordas, K., Castritsi-Catharios, I., Tziantziou, L., 2014. Fish farming and anti-fouling paints: a potential source of Cu and Zn in farmed fish. Aquaculture Environment Interactions 5, 163–171. https://doi.org/10.3354/aei00101

R Core Team, 2024. R: A Language and Environment for Statistical Computing_. R Foundation for Statistical Computing, Vienna, Austria. https://www.R-project.org

Wang, Y., Li, H., Yuan, X., Jiang, Y., Xiao, Z., Li, Z., 2022. Review of copper and copper alloys as immune and antibacterial element. Transactions of Nonferrous Metals Society of China 32, 3163–3181. https://doi.org/10.1016/S1003-6326(22)66011-4

17th INTERNATIONAL CONGRESS of the Geological Society of Greece

BULLETIN OF THE GEOLOGICAL SOCIETY OF GREECE, SP. PUBL.

EXTENDED ABSTRACT 213

Spatiotemporal diffusion variability in seismic swarms

Michas G.[1]
(1) Institute of Geodynamics, National Observatory of Athens, Athens, Greece, gmichas@noa.gr

Research Highlights

- The spatiotemporal diffusion properties of seismic swarms can well be reproduced with the Continuous Time Random Walk (CTRW) model and the fractional diffusion equation
- The results show intrinsic variability in earthquake diffusion that may highlight the physical mechanisms at play

Introduction

Seismic swarms are characterized by intense seismic activity strongly clustered in time and space and without the occurrence of a major event that can be considered as the mainshock. Such intense seismic activity is most commonly associated with external aseismic factors, as pore-fluid pressure diffusion, aseismic creep, or magmatic intrusion that can perturb the regional stresses locally triggering the observed seismicity (Vidale & Shearer, 2006). These factors can control the spatiotemporal evolution of seismic swarms, frequently exhibiting spatial expansion and migration of event hypocenters with time (Michas *et al.*, 2021). This phenomenon, termed as earthquake diffusion, can be highly anisotropic and complex, with earthquakes occurring preferentially along fractures and zones of weakness within the heterogeneous crust, presenting anisotropic diffusivities that may locally vary over several orders of magnitude (Michas & Vallianatos, 2018a). The efficient modelling of the complex spatiotemporal evolution of seismic swarms, thus, represents a major challenge.

Herein, we apply a stochastic framework based on the well-established Continuous Time Random Walk (CTRW) model, to map the spatiotemporal evolution of seismic swarms. The CTRW model is a well-established stochastic framework for modelling anomalous diffusion phenomena in complex heterogeneous media (Berkowitz *et al.*, 2006), including fluid flow in fault zones (O'Brien *et al.*, 2003; Brixel *et al.*, 2020) and seismicity (Sotolongo-Costa *et al.*, 2000; Helmstetter & Sornette, 2002; Michas & Vallianatos, 2018a; 2024) among others. The term "anomalous" is used to signify the deviation of the triggered earthquake diffusion from linear diffusion equations and normal (Gaussian) diffusion. Within this context, earthquake occurrence is considered as a point- process in space and time, with jump lengths and waiting times between successive earthquakes drawn from a joint probability density function. The spatiotemporal evolution of seismicity is then described with an appropriate master equation and the time-fractional diffusion equation (TFDE). The applicability of the model is herein demonstrated for the 2014 Long Valley Caldera (California) seismic swarm that has been associated with pore-fluid pressure diffusion at depth (Shelly *et al.*, 2016) and the results are compared with seismic swarms that have occurred in the Corinth Rift (Greece) (Michas & Vallianatos, 2018a; Michas *et al.*, 2021; 2022) and elsewhere, including injection-induced seismicity (Michas & Vallianatos, 2024) and the 2025 seismic crisis in the offshore area between Santorini and Amorgos.

Methods

Within the CTRW context, we consider seismicity as a point-process in time and space, marked by the magnitude of the event. Starting from an origin, seismicity undergoes a random walk in space and time, where the hypocenter of each new event is the new position of the random walk that occurs after waiting some time τ in the previous position. This process can be described with the joint probability density $\psi(x, t)$, which, in the case of seismicity, expresses the probability of an earthquake to occur at some position x after some time t (Michas & Vallianatos, 2018a). By further considering that jump lengths and waiting times between the successive earthquakes are independent random variables, the probability densities of jump lengths $\lambda(x)$ and waiting times $\varphi(t)$ can be deduced from $\psi(x, t)$. In this case, finite or divergent moments of $\lambda(x)$ and $\varphi(t)$ determine the type of the diffusive process. If both are finite, then the random walk corresponds to the well-known Brownian motion (normal diffusion). If, however, $\lambda(x)$ and $\varphi(t)$ present broad distributions with power-law scaling behavior that signifies long-range interactions, then anomalous diffusion arises (e.g., Metzler & Klafter, 2000). In this case, the mean squared distance (MSD) $\langle x^2(t) \rangle$ of seismicity deviates from its linear growth with time t, a function that characterizes normal diffusion. Instead, for various complex systems that present anomalous diffusion, MSD frequently takes the mathematical form:

$$\langle x^2(t) \rangle \propto t^a. \quad (1)$$

The latter equation manifests the power-law growth of the MSD with time, with the diffusion exponent a characterizing

the various domains of anomalous diffusion. Thereby, for $a > 1$ we get superdiffusion, for $0 < a < 1$ subdiffusion, while for $a = 1$ normal (Gaussian) diffusion is recovered.
In the case of seismicity, the diffusion exponent a can provide a proxy for the rate of triggered earthquake diffusion (McKernon & Main, 2005). The MSD is estimated from an origin that is considered to be the mean position of the first ten events in the beginning of each seismic sequence. Then, $x(t)$ is the 3D Euclidean distance between each event and the origin. The MSD is then calculated from the following equation (Michas & Vallianatos, 2018a):

$$\langle x^2(t)\rangle = \frac{1}{N}\sum_{n=1}^{N} x_n^2(t), \quad (2)$$

where N is the total number of events and $x_n(t)$ the distance of the nth event from the origin that have occurred at time t.
In addition, subdiffusion in terms of the probability density function (pdf) $P(x,t)$ to find the variable under observation (e.g., an earthquake) at some position x after some time t, is interchangeable with the time-fractional diffusion equation (TFDE) (Metzler & Klafter, 2000):

$$\frac{\partial}{\partial t}P(x,t) = {}_0D_t^{1-a} K_a \frac{\partial^2}{\partial x^2}P(x,t), \quad (3)$$

where K_a is the generalized diffusion coefficient and ${}_0D_t^{1-a}$ is the Riemann – Liouville fractional operator of order $1 - a$ ($0 < a < 1$) applied to $P(x,t)$. The standard approach to find the position of the propagator $P(x,t)$ is the Fourier-in-space Laplace-in-time transform (Metzler & Klafter, 2000). In terms of $F(x,t)$, i.e. the pdf of the number of earthquake events having just occurred at some position x after some time t, the solution of the TFDE can be found by using the Riemann – Liouville derivation and in terms of the Fox hypergeometric functions, providing the asymptotic behavior of $F(x,t)$ for large x (Helmstetter & Sornette, 2002; Michas & Vallianatos, 2024):

$$F(x,t) \sim \frac{(\tau')^{-a}}{\sqrt{K_a}t^{1-(a/2)}}\left(\frac{|x|}{\sqrt{K_a t^a}}\right)^{d(1-a)/(2-a)} \times \exp\left[-\left(1-\frac{a}{2}\right)\left(\frac{a}{2}\right)^{a/(2-a)}\left(\frac{|x|}{\sqrt{K_a t^a}}\right)^{2/(2-a)}\right], \quad (4)$$

where $\tau' = T\left(\Gamma(1-a)\right)^{1/a}$ ($a < 1$) and d the spatial dimensions. The latter equation manifests a power-law increase of the earthquake density for short distances from the origin and an exponential decay of seismicity as distance increases.

Results

First, we consider the probability distribution of waiting times τ between the successive events with magnitude $M \geq -0.4$ for the 2014 Long Valley Caldera seismic swarm (Shelly *et al*., 2016). The probability density $p(\tau)$ is calculated by counting the number of τ that fall into logarithmically spaced bins and then normalized by the bin width and by the total number of counts (Michas & Vallianatos, 2018b). In Fig. 1b the probability density $p(\tau)$ is shown that presents asymptotic power-law behavior with exponent -1.51. For comparison, the probability density $p(\tau)$ of the waiting times τ ($M \geq 0$) for the 2020 Perachora (Corinth Rift) seismic swarm (Michas *et al*., 2022) is shown in Fig. 1a, using a seismic catalogue enriched more than thirty-fold with template-matching (Kapetanidis *et al*., 2023). In this case, $p(\tau)$ shows an almost flat regime for short τ and a rapid decay for larger τ, exhibiting a bimodal behavior. This trend is approximated with the q-generalized gamma function (Michas & Vallianatos, 2018b):

$$f(\tau) = C\left(\frac{\tau}{\tau_0}\right)^{\gamma-1}\exp_q\left(-\frac{\tau}{\tau_0}\right), \quad (5)$$

where C is a normalization constant, τ_0 a positive scaling parameter and γ the scaling exponent. The last term in the right-hand side is the q-exponential function:

$$\exp_q(x) = [1 + (1-q)x]^{1/(1-q)}. \quad (6)$$

For $q > 1$, the q-exponential function exhibits asymptotic power-law behavior, while in the limit of $q \to 1$ it exactly recovers the exponential function and the q-generalized gamma the ordinary gamma function, respectively (Michas & Vallianatos, 2018b).

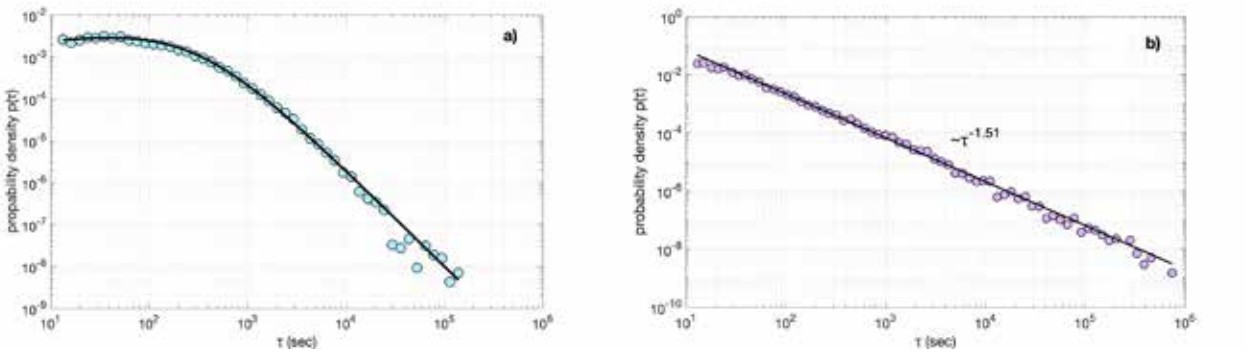


Figure 1. a) Probability density $p(\tau)$ of the waiting times τ (symbols) for the 2020 Perachora swarm according to a template matching catalogue. The solid line represents the q-generalized gamma function fitted to the data, with parameter values C = 0.0012, γ = 1.33, τ_0 = 105.37 and q = 1.38. b) Probability density $p(\tau)$ of the waiting times τ (symbols) for the Long Valley Caldera swarm. The solid line represents a power-law function fitted to the data.

As observed in Fig. 1a, the q-generalized gamma function fits rather well the normalized probability density $p(\tau)$ for the 2020 Perachora swarm, indicating clustering effects in the long-term occurrence of seismicity at breaking asperities that interact with each other. Similar scaling behavior was found for multiplet families during the Perachora swarm (Kapetanidis *et al*., 2023), for the Agios Ioannis seismic swarm that occurred in the western Corinth rift in 2001 (Michas & Vallianatos, 2018a), as well as for injection-induced seismicity in Enhanced Geothermal Systems (Michas & Vallianatos, 2024; Michas, 2025).

Next, the mean squared distance (MSD) $\overline{\langle x^2(t)\rangle}\overline{\langle x^2(t)\rangle}$ of seismicity, as estimated from Eq. 2, is analyzed. For the 2014 Long Valley Caldera swarm, the MSD scales according to Eq. 1 (R^2=0.97), for a diffusion exponent a=0.34 ±0.03 (Fig.2b), showing subdiffusion. The 2020 Perachora swarm presents the higher diffusion exponent of a=0.89 ±0.06 (R^2=0.98), still lower than unity, indicating once more subdiffusion of seismicity (Michas *et al*., 2022). Similar behavior and subdiffusion have also been found for other seismic swarms in the western Corinth rift (Michas *et al*., 2021) and for injection-induced seismicity during hydraulic stimulations in EGS (Michas & Vallianatos, 2024; Michas, 2025). However, diffusion exponents higher than unity and superdiffusion have also been found in seismic sequences and injection-induced seismicity, as for the 2006 hydraulic stimulation in Basel (Michas, 2025) and the 2025 seismic sequence in Anydros, in the Santorini-Amorgos tectonic zone, where a rapid diffusive regime with diffusion exponent >3 is encountered during the first days of intense activity. Such diffusion exponents, close to or even greater than unity, are consistent with pore-fluid pressure diffusion phenomena in fractured media and fault zones (Berkowitz *et al*., 2006; O'Brien *et al*., 2003), implying fluid diffusion as the dominant triggering mechanism. In addition, aftershock sequences associated with stress transfer effects show considerably lower diffusion exponents, generally lower than 0.1 (Huc & Main, 2003; Helmstetter *et al*., 2003; Michas *et al*., 2021), suggesting that diffusion variability may be used to infer the main triggering mechanism of seismicity.

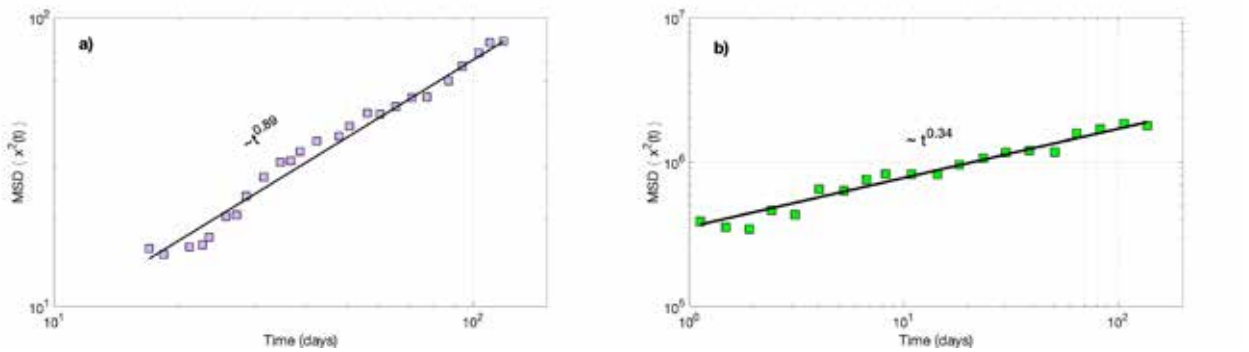


Figure 2. Mean squared distance (MSD) of seismicity with time for a) the Perachora (modified from Michas *et al*., 2022) and b) the Long Valley Caldera seismic swarms (filled squares). Solid lines represent the best-fitting solutions according to Eq. 1 for the diffusion exponents shown in the image.

Furthermore, as discussed previously, the subdiffusive regime of the CTRW model is interchangeable with the time-

fractional diffusion equation (TFDE). Fig. 3 shows the application of its asymptotic solution (Eq. 4) to the observed concentration profiles of seismicity for the Long Valley Caldera swarm for two time periods. In practice, the concentration profile shows the histogram of the absolute 3D distances between each event (for $M \geq M_c$) and the origin. Then, $F(x,t)$ is normalized such that $\int dxF(x,t) = 1$. $F(x,t)$ shows a peak closer to the origin and a tail that stretches towards greater distances. For comparison, the concentration profiles of seismicity for the 2001 Agios Ioannis swarm (Corinth Rift) (Michas & Vallianatos, 2018a) is also shown in Fig. 3 for two time periods. The model successfully captures the main features of earthquake occurrence regarding the peak of concentration close to the origin, the narrowing down and broadening of the peak with time and the stretched relaxation of seismicity with distance.

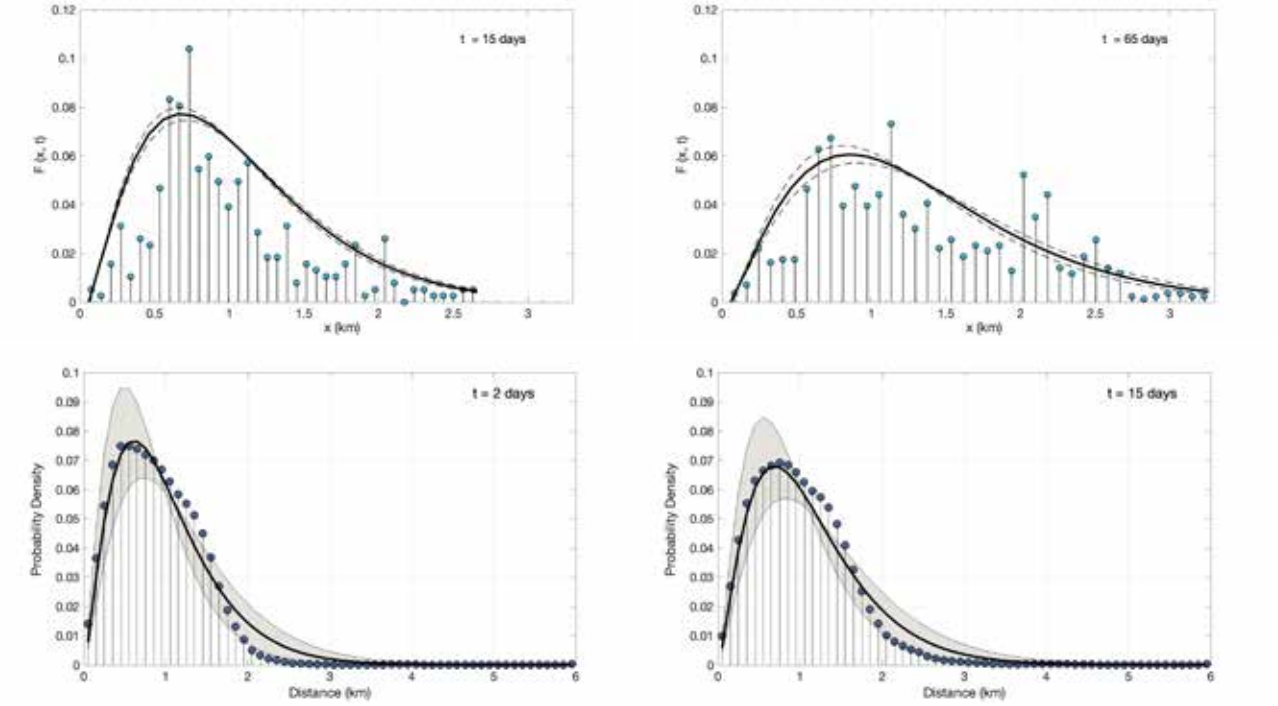


Figure 3. Concertation profiles of seismicity for two time periods, for the 2001 Agios Ioannis seismic swarm (top) (modified from Michas & Vallianatos, 2018a) and the 2014 Long Valley Caldera swarm (bottom). The solid line and the shaded area, or the dashed lines, indicate the asymptotic solution of the TFDE (Eq. 4) and the corresponding confidence intervals, respectively.

Conclusions

Statistical analysis of the studied cases in the light of the CTRW model shows that the mean squared distance of event hypocenters from an origin departs from its linear growth with time, while the temporal occurrence of seismicity exhibits broad waiting times distributions with asymptotic power-law behavior, indicating long-term inter-erathquake interactions. Such properties are intrinsic characteristics of anomalous earthquake diffusion. In such cases, the asymptotic solution of the TFDE can successfully capture the main features of earthquake progression in time and space, showing a peak of event concentration close to the initial source of the stress perturbation and a stretched relaxation of seismicity with distance. Furthermore, the spatiotemporal diffusion variability encountered in various seismic swarms, as well as in injection-induced seismic sequences associated with hydraulic stimulations in EGS, may highlight the main triggering mechanims at play, showing higher diffusion exponents for fluid-related sequences. Overall, the results demonstrate that the CTRW model and the TFDE can efficiently be used to decipher the complex spatiotemporal evolution of seismicity.

References

Berkowitz, B., Cortis, A., Dentz, M., Scher, H., 2006. Modeling non-Fickian transport in geological formations as a continuous time random walk. Reviews of Geophysics, 44, RG2003.

Brixel, B., Klepikova, M., Lei, Q., Roques, C., Jalali, M.R., Krietsch, H., Loew, S., 2020. Tracking fluid flow in shallow crustal fault zones: 2. Insights from cross□hole forced flow experiments in damage zones. J. Geophys. Res. Solid Earth, 125(4), e2019JB019108.

Helmstetter, A., Sornette, D., 2002. Diffusion of epicenters of earthquake aftershocks, Omori's law, and generalized continuous-time random walk models. Physical Review E, 66(6), 061104.

Helmstetter, A., Ouillon, G., Sornette, D., 2003. Are aftershocks of large Californian earthquakes diffusing? J. Geophys. Res. Solid Earth, 108, 2483.

Huc, M., Main, I.G., 2003. Anomalous stress diffusion in earthquake triggering: Correlation length, time dependence, and directionality. J. Geophys. Res. Solid Earth, 108, 2324.

Kapetanidis, V., Michas, G., Spingos, I., Kaviris, G., Vallianatos, F., 2023. Cluster Analysis of Seismicity in the Eastern Gulf of Corinth Based on a Waveform Template Matching Catalog. Sensors, 23, 2923.

McKernon, C., Main, I.G., 2005. Regional variations in the diffusion of triggered seismicity. J. Geophys. Res. Solid Earth, 110, 1–12.

Metzler, R., Klafter, J., 2000. The random walk's guide to anomalous diffusion: A fractional dynamics approach. Physics Reports, 339, 1–77.

Michas, G., 2025. Spatiotemporal Diffusion Variability of Injection-Induced Seismicity in Enhanced Geothermal Systems. Pure and Applied Geophysics, 182, 405–417.

Michas, G., Vallianatos, F., 2018a. Modelling earthquake diffusion as a continuous-time random walk with fractional kinetics: the case of the 2001 Agios Ioannis earthquake swarm (Corinth Rift). Geophysical Journal International, 215(1), 333-345.

Michas, G., Vallianatos, F., 2018b. Stochastic Modeling of Nonstationary Earthquake Time Series with Long-Term Clustering Effects. Physical Review E, 98, 042107.

Michas, G., Vallianatos, F., 2024. Stochastic modeling of injection induced seismicity based on the continuous time random walk model. Scientific Reports, 14(1), 4951.

Michas, G., Kapetanidis, V., Kaviris, G., Vallianatos, F., 2021. Earthquake diffusion variations in the Western Gulf of Corinth (Greece). Pure and Applied Geophysics, 178(8), 2855-2870.

Michas, G., Kapetanidis, V., Spingos, I., Kaviris, G., Vallianatos, F., 2022. The 2020 Perachora peninsula earthquake sequence (East Corinth Rift, Greece): spatiotemporal evolution and implications for the triggering mechanism. Acta Geophysica, 70(6), 2581-2601.

O'Brien, G.S., Bean, C.J., McDermott, F, 2003. A numerical study of passive transport through fault zones. Earth Planet. Sci. Lett., 214, 633–643.

Shelly, D.R., Ellsworth, W.L., Hill, D.P., 2016, Fluid-faulting evolution in high definition: Connecting fault structure and frequency-magnitude variations during the 2014 Long Valley Caldera, California, earthquake swarm. J. Geophys. Res. Solid Earth, 121, 1776–1795.

Sotolongo-Costa, O., Antoranz, J.C., Posadas, A., Vidal, F., Vazquez, A., 2000. Levy flights and earthquakes. Geophysical Research Letters, 27, 1965–1968.

Vidale, J.E., Shearer, P.M., 2006. A survey of 71 earthquake bursts across southern California: Exploring the role of pore fluid pressure fluctuations and aseismic slip as drivers. J. Geophys. Res. Solid Earth, 111(B5), B05312.

17th INTERNATIONAL CONGRESS of the Geological Society of Greece

BULLETIN OF THE GEOLOGICAL SOCIETY OF GREECE, SP. PUBL.

EXTENDED ABSTRACT 214

Hellenic Landslide Platform (He.L.P.): A Geospatial Landslide Inventory for Western Greece.

Misiri Z.[1], Lainas S.[1], Depountis N.[1]
(1) University of Patras, Department of Geology, Patra, Greece, geo07060@ac.upatras.gr

Research Highlights: **Development of a comprehensive landslide inventory for Western Greece**

Introduction

Landslides pose a significant risk to communities, infrastructures, and the natural environment throughout Europe and worldwide. Driven by complex geological settings, increasing urban development, and infrastructure expansion, as well as the occurrence of extreme climatic events, landslides are becoming more frequent and severe. This presents a growing hazard for both human activities and economic assets.

Landslides are widely spatially distributed across Europe, with their occurrence influenced by various topographic and geo-environmental factors, often dictated by each Country's unique geological, geomorphological, and environmental conditions. In Greece, landslides are predominantly associated with mountainous and hilly areas, road network, coastal regions, and riverbanks. Specific site conditions, such as lithology, hydrology, hydrogeology, active tectonics, as well as slope gradient and directionn, are critical in determining landslide susceptibility, hazard and risk status.

The complex geological and tectonic settings in Greece contribute to the complexity and variety of landslide types observed. The classification of landslides in the country generally follows established international standards, including those by Varnes (1978), Cruden *et al.* (1996), and Hungr *et al.* (2014). These classifications are based on the type of movement and the material involved. According to these classifications, the most identified landslide types in Greece include earth slides (rotational and translational), earth flows, debris flows, rockfalls, rockslides, and complex landslides.

While the aforementioned conditions predispose areas to landslides, external triggers serve as the immediate causes of landslide activation. In Greece, the most frequent triggers are related to increasingly extreme weather events, such as intense or prolonged rainfalls, often associated with floods. Other natural triggers include earthquakes, as well as natural erosion along coastlines and riverbanks. Human activities also significantly contribute to landslide initiation, as any interference with a slope influences its equilibrium.

Given for certain that landslides triggered by extreme rainfall events will increase in the future due to climate change, there is an urgent need for landslide recording, enhanced monitoring, risk assessment, and predictive capabilities in affected areas to protect communities, infrastructures, and preserve human activities.

To address this, landslide inventories and susceptibility maps have been developed in many countries worldwide, including at small-scale European and Global levels. A European Landslide Susceptibility Map (ELSUS v2) developed by Günther *et al.* (2014) and Wilde *et al.* (2018) is already available at the European Soil Data Centre (ESDAC) web page. Furthermore, a Global Landslide Catalog (GLC), published in 2019, which includes NASA's landslide datasets and other reports contributed by scientists, is available on-line, but should be updated in the future and with other available landslide datasets.

According to the definition given by Fell *et. al.* (2008) a landslide inventory is an inventory of the location, classification, volume, activity and date of occurrence of landsliding. So far in Greece there is no web application with the of landslide inventory in Greece. However, a national landslide inventory is under construction by the Hellenic Survey of Geology and Mineral Exploration (H.S.G.M.E.), which is the competent authority for the identification, recording, investigation and study of geohazards, as well as for the preparation of susceptibility, hazard and risk maps.

The presented in this work Landslide Inventory Platform named as He.L.P. (Hellenic Landslide Platform) is a first attempt to publish a web-based GIS platform that provides information on landslide phenomena which have been recorded over time in the geographic territory of Western Greece, as defined by the administrative regions of Western Greece, Epirus, and Ionian Islands.

The aim of the platform is to manage geographic information from multiple sources that can be applied to administrative departments and agencies, scientific and general applications, with the management of the volume of information having multiple feed points.

Presentation of the platform

The design and development of HeLP (Hellenic Landslide Platform) (Figure 1) is the achievement of many years of effort by all the members of the Laboratory of Engineering Geology of University of Patras (Professors, PhDs,

Postgraduate students) and was prepared after years of collection, processing and analysis of data from landslide surveys and studies performed by the Laboratory members, satellite images, historical records, as well as studies from Public Authorities, Organizations, Institutes, as well as Technical and Engineering Consulting Companies. Moreover, the possibility for continuous completion and updating with additional records, gives the Platform a "dynamic" character with the prospect of its expansion throughout Greece.



Figure 1: The HeLP (Hellenic Landslide Platform) developed by the EnGeo lab. The red dots represent the landslide events

The Platform draws all its data from geographic databases maintained by the Laboratory of Engineering Geology. In this way, the end user has at his disposal the satellite image of the area with information such as, inventory code, geographical location based on the administrative division of Greece, coordinates in GGRS87, type of landslide and a Landslide Inventory Form (LIF) as a pdf sheet.
In a more advanced process, the platform can display various lists of layers concerning a) the administrative boundaries of a region or a municipality, b) the elevation, c) geological data (engineering-geological units, etc), d) the land use patterns, e) boreholes, f) information on geotechnical monitoring, etc. (Figure 2)

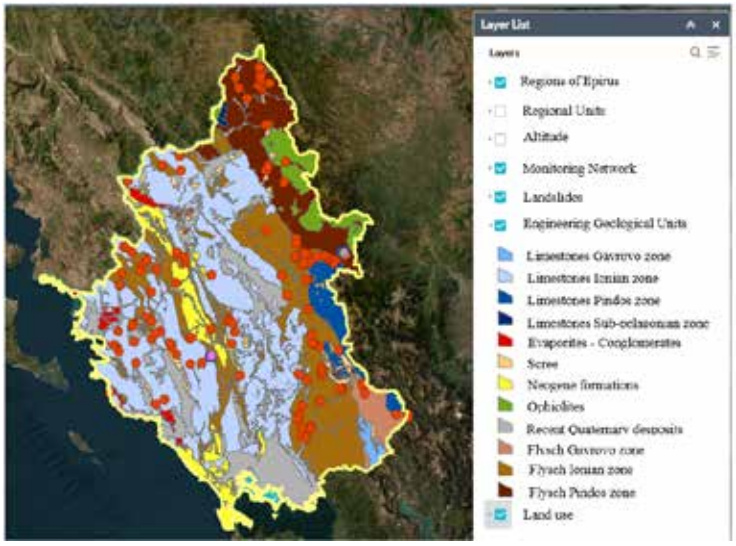


Figure 2. Display of He.L.P. (https://gis.geodory.gr/) for the Region of Epirus. The red dots represent landslide events.

The platform presently includes 1176 landslides. The detailed inventory and the corresponding descriptive data are stored in a database, separately from the graphical part of the inventory map in the form of tables, which allows the visualization of queries and analysing.

The main requirement for predicting future landslides is a well-documented Landslide Inventory Form (LIF). LIF has as its main purpose the recording of all landslides under a common code to achieve an objective in comparison between them and to make it easier to register a new landslide. The design of LIF, used in the He.L.P. platform, was based on the landslide report (WP/WLI, 1990), summary (WP/WLI, 1991), activity (WP/WLI, 1993), landslide causes (WP/WLI, 1994), and rate of movements (WP/WLI, 1995) as well as on corresponding forms of international organizations (United States Geological Survey) and the experience of the Laboratory's staff in the field of landslides. The presented LIF (Figure 3) provides all the necessary information in a condensed form so that it can be easy to rapidly assess the possible risk of each landslide to the natural and man-made environment. It includes seventeen (17) basic fields of information, some of which are subdivided into other categories, as described below.

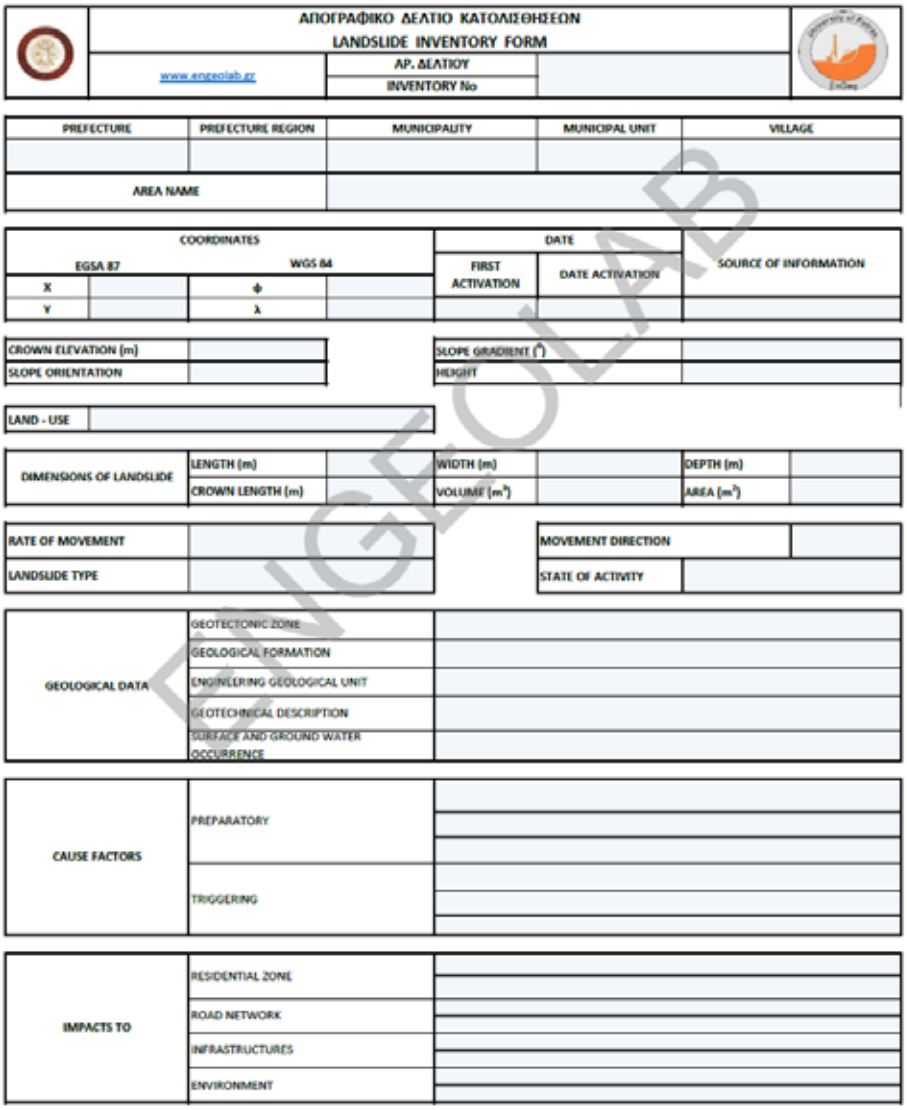


Figure 3. The Landslide Inventory Form used in the He.L.P. platform

Land use classification was based on the Corine Land Cover 2018 project, which is part of the Pan-European Land Use Database and includes residential areas, cultivated areas, forest areas, wetlands and fire-affected areas.

Landslide type was indicated according to the classification of Varnes (1978), whose main criteria are the type of movement and the type of material (Figure 4).

TYPE OF MOVEMENT		TYPE OF MATERIAL		
		BEDROCK	ENGINEERING SOILS	
			Predominantly coarse	Predominantly fine
FALLS		Rock fall	Debris fall	Earth fall
TOPPLES		Rock topple	Debris topple	Earth topple
SLIDES	ROTATIONAL	Rock slide	Debris slide	Earth slide
	TRANSLATIONAL			
LATERAL SPREADS		Rock spread	Debris spread	Earth spread
FLOWS		Rock flow (deep creep)	Debris flow (soil creep)	Earth flow
COMPLEX		Combination of two or more principal types of movement		

Figure 4: Classification of landslides according to Varnes (1978)

The geological data are a decisive factor for the likelihood of a landslide occurrence. In the LIF Geotectonic Zone refers to the Geotectonic Zones of Greece, for example Ionian, Sub-pelagonian, Pelagonian, Paxon zone, while the Engineering Geological Unit describes the lithology, and the properties of the materials involved in the movement.
The landslide causal factors are divided into preparatory and triggering factors (Varnes 1978). A preparatory factor can act for years preparing the conditions for the occurrence of a landslide, while a triggering is the factor that under certain conditions can shift the slope from a marginally stable to an actively unstable state. Some of the preparatory factors are surface erosion, annual or seasonal rainfall, slope and tectonics, while triggering factors are earthquakes, volcanic action, and intense or prolonged rainfall.
Landslides have various effects on both the natural and human environment. Effects can be quantitative or qualitative, extensive or not. Table 1 lists examples of the landslide impacts in Residential Zones, Road Network, Infrastructures and the Environment.

Table 1. Impacts of landslides

IMPACTS	RESIDENTIAL ZONE	Damage to buildings
	ROAD NETWORK	Failure of embankments
	INFRASTRUCTURES	Failure of public service networks
	ENVIRONMENT	Loss of arable land

Conclusions

Landslides are a major geohazard, as they are widespread and rank high on the list of natural disasters. In Greece, their occurrence is frequent and controlled mainly by geomorphology, geological structure, seismicity and rainfall. Therefore, their recording is of utmost importance and aims to process their data for scientific and civil protection purposes.
The grouping of the most important parameters describing landslides from a huge number of different information sources created the need for the creation of the presented in this paper Hellenic Landslide Platform names as He.L.P., and the creation of a Landslide Inventory Form (LIF) for each landslide. The design of the Landslide Inventory Form as well as the selection and grouping of its parameters (geological conditions, type of landslides, causative factors, etc.) was made according to the current International Standards and guidelines for landslide recording.
The main objective of this work is the presentation of He.L.P., which is a web-based GIS platform, and by today includes 1176 landslides that have occurred in the regions of Western Greece, Epirus, and Ionian Islands. The simplicity of the platform as well as its accompanying LIF, gives to the Platform a “dynamic” character of continuous completion and updating with additional landslide records, with the prospect of its expansion throughout Greece.

References

Cruden, D.M., Varnes D.J., 1996. Landslides Types and Processes. In: Turner A.K. & Schuster R.L. (Eds.) Landslides: Investigation and Mitigation. Transportation Research Board, Special Report 247, p.36-72, National Academy Press, Washington D.C

Fell, R., Corominas, J., Bonnard, C., Cascini, L., Leroi, E., Savage, W.Z. on behalf of the JTC-1 Joint Technical Committee on Landslides and Engineered Slopes, 2008. *Guidelines for landslide susceptibility, hazard and risk zoning for land use planning*. Engineering Geology, 102: 85-98. doi: 10.1016/j.enggeo.2008.03.022

Günther, A., Van Den Eeckhaut, M., Malet, J.-P., Reichenbach, P., Hervás, J., 2014. *Climate-physiographically differentiated Pan-European landslide susceptibility assessment using spatial multi-criteria evaluation and transnational landslide information*. Geomorphology, 224: 69-85. doi: 10.1016/j.geomorph.2014.07.011

Wilde, M., Günther, A., Reichenbach, P., Malet, J.-P., Hervás, J., 2018. *Pan-European landslide susceptibility mapping: ELSUS Version 2.* Journal of Maps, 14(2): 97-104 and supplemental map. doi: 10.1080/17445647.2018.1432511

Varnes, D.J., 1978. Slope Movement Types and Pro*cesses. In Special Report 176: Landslides: Analysis* and Control (R.L. Schuster and R.J. Krizek, eds.), TRB, National Research Council, Washington, D.C., pp. 11-33.

Hungr, O., Leroueil, S. & Picarelli, L., 2014. The Varnes classification of landslide types, an update. *Landslides 11: 167–194* . https://doi.org/10.1007/s10346-013-0436-y

Varnes, D.J., 1978. Slope movement types and processes. In: Schuster R.L. & Krizek R.J. (Eds.) Landslides: Analysis and control. Transportation Research Board, Special Report 176, p.11–33, National Research Council, Washington D.C.

WP/WLI. 1990. A suggested method for reporting a landslide. International Geotechnical Societies' UNESCO Working Party on World Landslide Inventory (Chairman D Cruden), Bull Eng Geol Env, 41(1), 5–12, doi:10.1007/BF02590201.

WP/WLI. 1991. A suggested method for a landslide summary, International Geotechnical Societies' UNESCO Working Party on World Landslide Inventory (Chairman D Cruden), Bull Eng Geol Env, 43, 101–110, doi:10.1007/BF02590177.

WP/WLI. 1993. Multilingual landslide glossary. International Geotechnical Societies' UNESCO Working Party on World Landslide Inventory (Chairman D Cruden), BiTech, Richmond, p p 59.

WP/WLI. 1994. International Geotechnical Societies' UNESCO Working Party on World Landslides Inventory. Working group on Landslide causes (Chairman: Popescu ME) "A Suggested Method for Reporting Landslide Causes". *Bull IAEG 50:71-74*.

WP/WLI. 1995. A suggested method for describing the rate of movement of a landslide. International Geotechnical Societies' UNESCO Working Party for World Landslide Inventory (Chairman ME Popescu), Bull Eng Geol Env, 52(1), 75–78 doi:10.1007/BF02602683.

17th INTERNATIONAL CONGRESS
of the Geological Society of Greece

BULLETIN OF THE GEOLOGICAL SOCIETY OF GREECE, SP. PUBL.

EXTENDED ABSTRACT 215

Biostratigraphy, Sedimentary Microfacies, and Depositional Environment of the Paleocene-Early Eocene Calciturbidites in Gardiki Section (Epirus, Western Greece)

Moforis L.[1], Kontakiotis G.[1], Antonarakou A.[1], Zambetakis-Lekkas A.[1], Ahmad S.[2], Paschos P.[3], Galanakis D.[3], Kanellopoulos C.[3], Sboras S.[4], Janjuhah H.T.[5], Lazos I.[4], Karakitsios V.[1]

(1) National and Kapodistrian University of Athens, Faculty of Geology and Geoenvironment, Department of Historical Geology and Paleontology, Panepistimiopolis, Zografou, 15784, Athens, Greece, leonidasmoforis@gmail.com (2) Department of Geology, University of Peshawar, Peshawar, Pakistan (3) H.S.G.M.E., Hellenic Survey of Geology and Mineral Exploration, Athens, Greece (4) Institute of Geodynamics, National Observatory of Athens, Lofos Nymphon, Thesio, 11810 Athens, Greece (5) INTI International University, Nilai, Negeri Sembilan, 170000, Malaysia

Introduction

The present study examines the depositional processes as well as the sedimentary microfacies types of the Paleocene-early Eocene carbonates of the Gardiki section, situated in Epirus region (western Ionian basin, Paramythia, Greece). This study defines the Paleocene-early Eocene depositional evolution of the area, based mainly on litho-stratigraphic characteristics in the external Ionian domain, which is regarded as a significant hydrocarbon prolific basin in western Greece. This work was accomplished by an extensive sedimentological analysis of the carbonate succession, alongside a synthetic paleoenvironmental reconstruction of the study area. Furthermore, the results provide valuable insights into regional geology and contribute to a deeper understanding of the Ionian basin in western Greece.

Study area

The study area is situated in the Ionian zone, a key element of the fold-and-thrust belt of the External Hellenides orogenic belt in western Greece. The External Hellinides are divided into three tectonostratigraphic zones, namely the pre-Apulian, Ionian, and Gavrovo-Tripoli tectono-stratigraphic zones. At a regional scale, this Alpine belt records the initiation, development, and final destruction of the southeastern margin of the Tethys Ocean and the consequent continent-to-continent collision between the Apulian and the Pelagonian micro-continents to the east. On a local scale, the various sub-basins of the Hellenic Tethys margin have been inverted to produce the main Hellenic thrust sheet folded zones. The Ionian zone, bounded westwards by the Ionian thrust and eastwards by the Gavrovo thrust, extends from Albania to the north most of the Epirus region and parts of the Ionian islands and continues southwards to Central Greece, Crete, and the Dodecanese. According to Auboin (1959) and IGRS-IFP (1966), the Ionian zone is subdivided into the Internal, Middle and External sub-basins (Figure 1a).

Materials and methods

A total of 126 samples were systematically collected from Gardiki area (lat: 39°20′22,08′′ N, long: 20°33′5,63′′ E) (Figure 1b), covering the Paleocene-early Eocene carbonate formations. The fieldwork included detailed logging, measurements and sampling, along with additional observations made on the litho-stratigraphic properties of the limestones, such as colour, lithological and textural variations, bed thickness, syn- and post-depositional features etc. Sampling resolution varied along the section, influenced by outcrop conditions, thickness and the lateral extend of each carbonate unit.

All samples undergone microfacies analysis, focusing mainly on lithofacies and biofacies, to ascertain their age and depositional environment. Thin sections were prepared at the Hellenic Survey of Geology and Mineral Exploration (H.S.G.M.E.) and examined biostratigraphically and sedimentologically using a polarized LEICA DM LP microscope, with photographs captured via an OLYMPUS UC30 microscope digital camera.

The microfacies description and textural characters analysis of the limestones were defined according to Dunham (1962) classification scheme, which was later modified by Embry and Klovan (1971) and Flügel (2004), based on the Standard Microfacies Types (SMF) in the Facies Zone (FZ) of the rimmed carbonate platform model. Depositional paleoenvironments were reconstructed by analyzing sedimentological characteristics observed during the fieldwork and interpreted sedimentary facies analysis. This analysis was supplemented by comparing additional data from existing time-equivalent sections of the same formation known from the literature.

Finally, the basic geological information was provided by the geological map (PARAMYTHIA SHEET 1:50.000) of the Hellenic Survey of Geology and Mineral Exploration (H.S.G.M.E.).

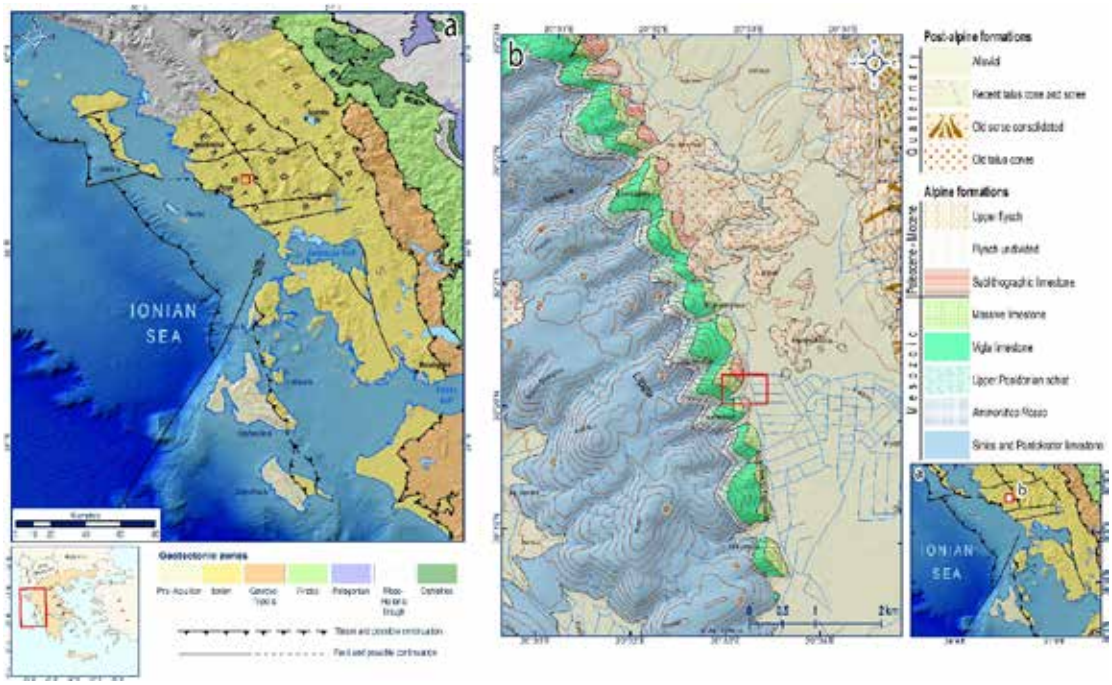


Figure 1(a,b). a) Geological map of the External Hellinides in NW Greece, illustrating the principal tectono-stratigraphic zones: Pre-Apulian, Ionian, Gavrovo, Pindos. b) Geological map of the study area. The red square shows the location of the study area. Legend interpretations are presented in the inset.

Biostratigraphy

The biostratigraphic analysis based on planktonic foraminifera presented in Table 1, revealed that the study part of Gardiki section covers the Paleocene-early Eocene time span based on the existence of *Morozovella* sp., *Operculina* sp., *Miscellanea* sp., *Melobesia* sp., Globorotaliidae and Globigerinidae. In addition, the appearance of radiolarians, rudist fragments, Dasycladacea algae, Siderolites spicules, Globotruncanidae, *Orbitoides* fragments, Miliolidae, *Idalina sp.*, supports their transportation form the underlying Upper Cretaceous Senonian limestones.
The age determination is in partial accordance with the geological map (PARAMYTHIA SHEET 1:50.000) concerning the Ionian rock exposures in Epirus area.

Sedimentary Microfacies Analysis

The key textural and compositional attributes, along with the sedimentary features of the identified microfacies are outlined in Table 1, corresponding to various depositional environments or facies zones. More specifically, within the studied carbonate succession, we observed 4 distinct sedimentary microfacies (Figure 2), which correspond to environments ranging from the upper part of the slope to the deep shelf. They mostly include in-situ wackestone-packstone lithofacies enriched in keeled planktonic foraminifera of Paleocene age, accompanied by faunal fragments indicative of shallower conditions due to their erosion and transportation by turbiditic currents along the slope, e.g., from the nearby platform to the basin. Within these deposits, the presence of bioclasts like the pelagic Globotruncanids in the micritic matrix of the basal samples was interpreted that they have been transferred from the underlying Upper Cretaceous strata. In the Ionian zone, such “clastic limestones” are usually alternated with sub-lithographic pelagic limestones reflected mostly by bioclastic mudstone facies (Kontakiotis *et al.*, 2020; Bourli *et al*., 2021; Moforis *et al.*, 2022).
More explicitly, the lower part of the succession was characterized by alterations of a pelagic biomicrite mudstone mostly with planktonic foraminifera and more rarely radiolarian (SMF 2-3) with a bioclastic biomicrite wackestone-packstone with abundant planktonic foraminifera (SMF 3-4), reflecting deposition in a low energy, relatively deep environment such as the toe of slope (FZ3) and/or the deep shelf (FZ2). A microbreccia bioclastic rudstone enriched in planktonic foraminifera along with fragments of shallow water fauna (benthic foraminifera, rudists, echinoderms and algae) (SMF 5), represents deep slope depositional conditions (FZ 4). A biomicrite packstone-grainstone (SMF 5) with mixed fauna and reworked lithoclasts was also observed and could be considered as indicative of a medium to high energy environment in the upper part of the slope close enough to the platform.

Samples	Description of Microfacies Analysis	Facies Zone	Lithology	Age
K69-K126	Biomicrite packstone-grainstone (SMF 5) Biomicrite mudstone (SMF 2-3)	Slope (FZ 4) Deep shelf (FZ 2)	Turbiditic limestone	Paleocene-early Eocene
K60-K68	Bioclastic rudstone (SMF 5)	Slope (FZ 4)	Micro-brecciated limestones	Paleocene
K1-K59	Bioclastic biomicrite wackestone-packstone (SMF 3-4) Biomicrite mudstone (SMF 2-3)	Toe of slope (FZ 3) and/or Deep shelf (FZ 2)	Turbiditic limestone	Paleocene

Table 1. Description of microfacies analysis of samples from Gardiki section (Epirus, western Greece).

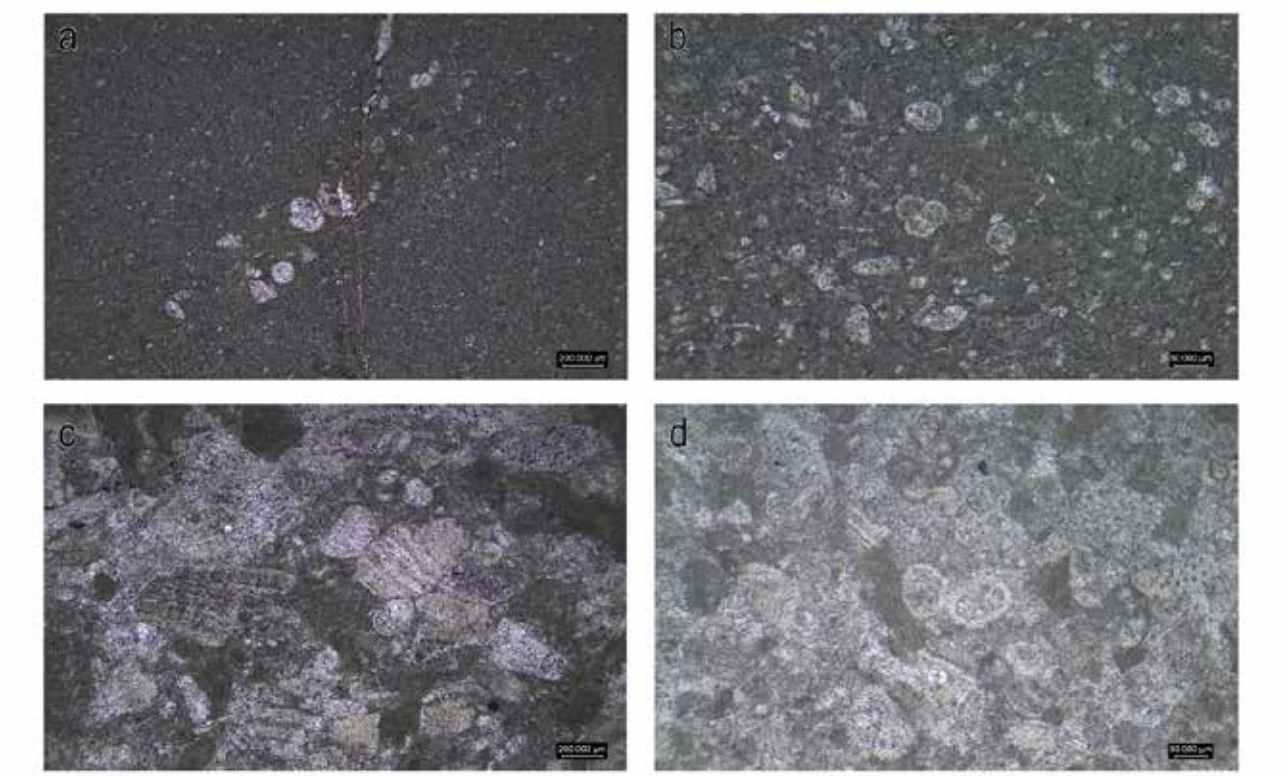


Figure 2. Representative figures of the 4 distinct sedimentary facies. a) Biomicrite mudstone with planktonic foraminifera, b) bioclastic biomicrite wackestone-packstone, c) bioclastic rudstone with planktonic and benthic foraminifera and rudist fragments, d) biomicrite packstone-grainstone with planktonic and benthic foraminifera

References

Aubouin, J.; Le Pichon, X.; Winterer, E.; Bonneau, M. Les Hellénides dans l'optique de la tectonique des plaques, 6th Colloquium on the Geology of the Aegean Region, Athens, 1977; Reprinted from proceedings vol. III; IGME: Athens, Greece, 1979; Volume 3, pp. 1333–1354

Bourli, N., Pantopoulos, G., Maravelis, A.G., Zoumpoulis, E., Iliopoulos, G., Pomoni-Papaioannou, F., Kostopoulou, S., Zelilidis, A., 2018. Late Cretaceous to early Eocene geological history of the eastern Ionian Basin, southwestern Greece: A sedimentological approach. Cretaceous Research 98, 47-71

Bourli, N., Iliopoulos, G., Papadopoulou, P., Zelilidis, A., 2021. Microfacies and Depositional Conditions of Jurassic to Eocene Carbonates: Implication on Ionian Basin Evolution. Geosciences 11 (7), 288]

Dunham, R.J. Classification of Carbonate Rocks According to Depositional Textures; American Association of Petroleum Geologists: Tulsa, OK, USA, 1962

Embry, A.F., Klovan, J.E., 1971 A late Devonian reef tract on northeastern Banks Island, NWT. Bull. Can. Pet. Geol., 19, 730–781

Flügel, E., 2004. Microfacies analysis of carbonate rocks. In Analysis, Interpretation and Application; Springer: Berlin/ Heidelberg, Germany

IGRS-IFP., 1966. Étude Géologique de l'Epire (Grèce Nord—Occidentale); Technip & Ophrys Editions: Paris, France]

IGME., 1966. Geological Map of Greek Series, Paramythia Sheet, Scale 1:50.000; Institute for Geology and Subsurface Research: Athens, Greece,

Karakitsios, V., 1995. The influence of pre-existing structure and halokinesis on organic matter preservation and thrust system evolution in the Ionian basin, northwestern Greece. AAPG Bulletin 79, 960-980

Kontakiotis, G., Moforis, L., Karakitsios, V., Antonarakou, A., 2020. Sedimentary Facies Analysis, Reservoir Characteristics and Paleogeography Significance of the Early Jurassic to Eocene Carbonates in Epirus (Ionian Zone, Western Greece). Journal of Marine Science and Engineering 8 (9), 706

Moforis, L., Kontakiotis, G., Janjuhah, T.H., Zambetakis-Lekkas, A., Galanakis, D., Paschos, P., Kanellopoulos, C., Sboras, S., Besiou, E., Karakitsios, V., Antonarakou, A., 2022. Sedimentary and Diagenetic controls across the Cretaceous-Paleogene Transition: New Paleoenvironmental Insights of the External Ionian Zone from the Pelagic Carbonates of the Gardiki Section (Epirus, Western Greece). Journal of Marine Science and Engineering 10 (12)

17th INTERNATIONAL CONGRESS of the Geological Society of Greece

BULLETIN OF THE GEOLOGICAL SOCIETY OF GREECE, SP. PUBL.

EXTENDED ABSTRACT 216

The geospatial characteristics of island beaches: the case of Kos, Greece

Monioudi I.N.[1], Chatzistratis D.[1], Velegrakis A.F.[1], Rigos A.[1], Chatzipavlis A.E.[1,2], Nikolaou A.[1,3], Andreadis O.P.[1]
(1) Department of Marine Sciences, University of the Aegean, University Hill, 81100 Mytilene, Greece, imonioudi@marine.aegean.gr (2) Department of Physics and Earth Sciences, University of Ferrara, Ferrara, Italy (3) ROGAN ASSOCIATES S.A., Athens, Greece

Research Highlights

Acquisition analysis of widely available geospatial information to assess the state and dynamics of island beaches.

Introduction

Assessing the state and dynamics of sandy shorelines (beaches) is vital for developing efficient management strategies (e.g. Karditsa *et al*., 2024; Chalazas *et al*., 2024), with the approaches used depending on their spatio-temporal scales and the available information and resources. In regional (island) scales, the extensive scope of studies and the high potential costs of adaptation (Narayan *et al*., 2016) may require prioritization of responses and efficient allocation of the (mostly) limited resources. This requires, among others, information of the geospatial characteristics and their interrelationships which may provide much needed information and identify potential controls of beach dynamics. Therefore, the objective of this short contribution is to present an approach that could acquire such information at a regional (island) scale on the basis of widely available geospatial data; the approach is demonstrated for the island of Kos, South Aegean Sea, Greece (Fig.1).

Study area

Kos has an area of about 295 km^2, a coastline length of 112 km and a resident population of about 37,100. Kos is a highly touristic island: in 2023, 1.3 million passengers arrived at the island of Kos. There are > 57,000 hotel beds in Kos, tourism density and intensity being very high (28,917 tourist nights/km^2). Most of this infrastructure and the tourist activities are associated with the island's beaches, as Kos is a global tourist destination for Sea-Sand-Sun - 3S tourism (SETE, 2024). Kos coast is microtidal (0.1 m astronomical tidal range). In the north NNW waves dominate with the largest waves showing heights Hs of 3.8 m and periods Tp of 7.5 s. Energetic waves occasionally impinge on western and southern coasts, with the largest waves having heights of 4–5 m and periods of 9–10 s (Monioudi *et al*., 2025). Kos is a part of the easternmost South Aegean volcanic arc. Its northeastern part is mostly formed on Plio-Quaternary sediments, whereas its southeastern highlands are made mostly of alpine and pre-alpine metamorphics and some Miocene volcanics (Pe-Piper *et al*., 2024). Following a hiatus, volcanism, resumed 3 million years ago (mostly) in the island's west; the large eruption of the Kos Plateau Tuff volcano (161 ka BP) deposited pyroclastics up to 15 m thick that covered most of the western Kos and the adjacent islands (Piper and Pe-Piper, 2020). Most large/wide beaches are found in the low-relief, sedimentary northeastern Kos (Fig. 1), indicating a potential geological control.

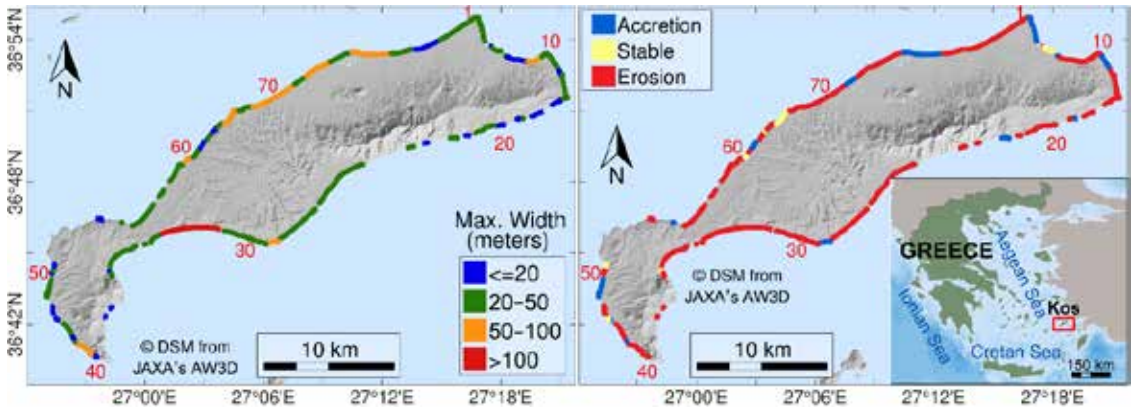


Figure 1. Kos: Beach maximum width (BMW) and long-term beach erosion trends. Numbers refer to the ID of the 78 beaches of Kos (after Monioudi *et al*., 2025).

Methods

The compiled inventory of the Kos beaches provides information on the dimensions, sediment types and the presence of outflowing streams, coastal defenses or artificial and natural features. Using satellite images available in the Google Earth Pro application, subaerial (dry) beaches were digitized as polygons based on clearly visible boundaries: natural features like vegetated dunes or cliffs and permanent artificial structures such as embankments, seawalls, or buildings and the shoreline define the landward and seaward limits, respectively. To ensure consistency, all digitization was conducted by a single analyst adhering to strict delimitation rules. The database was constructed through the digitization of beach polygons from selected images obtained in the period 2003–2021, which allowed an estimation of the recent historical changes. The beach (CNES/Airbus and Maxar) imagery has a spatial resolution about 0.5 m, but its results are constrained by the image accuracy; comparison of satellite images with concurrent RTK-DGPS ground observations showed an RMSE of about 2 m. Moreover, although tidal effects on the shoreline position are very small care was taken to analyze satellite images from the same season and under low hydrodynamic conditions; however as the available images along the islands' coasts have been collected at different times and under different preceding hydrodynamic conditions, recorded beach dimensions may not represent synoptic conditions at the island scale. Such limitations, however, cannot be avoided in the analysis of (historical) satellite imagery at large spatial scales (Monioudi *et al*., 2023). Following these procedures, the characteristics of 78 (Kos) beaches (Fig. 1) were identified, recorded and compared.

Results

The majority of beaches (53%) were found to have maximum widths (BMWs) of 20-50 m, 35% had widths < 20 m and 10 beaches had widths > 50 m (Fig. 1); the average maximum width was found to be 31 m. Despite the higher wave energy of the north- and west-facing beaches, a clear trend was observed in the development of northwest-facing beaches (303.75°- 348.75°). Fewer beaches were found to develop with southeast (16%) and south (12%) orientations, with the remaining beaches exhibiting other orientations (Fig. 2). This supports the hypothesis that the development of the Kos beaches is not controlled by the hydrodynamics, but is mainly subject to geological controls.

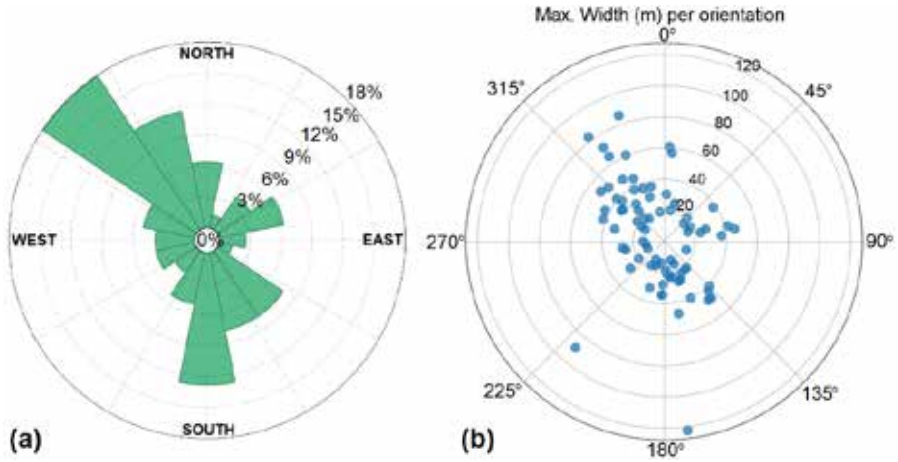


Figure 2. (a) Distribution of the Kos beach orientation. (b) Rose diagram of the beach maximum widths.

The relationship between orientation and the BMWs was further investigated using Angular-Linear correlation (Mardia, 1976; Zar, 2014) was used. This statistical test assesses the null hypothesis H_0 of no correlation between the two variables against the alternative hypothesis H_1 of a significant correlation. The results showed an $R^2 = 0.0327$ and $p = 0.279$, suggesting rejection of the H_0 hypothesis as $p > 0.05$; thus, there is no statistically significant correlation between the two variables.

There are outflowing streams in many Kos beaches (49%), indicating (potential) terrestrial sediment supply. Comparison of the BMWs with the occurrence of streams, shows that stream presence affects the beach size. In 2021, beaches with streams were found to have an average maximum width of 40.4 m which was almost double the

width of beaches without streams (22.8 m). In order to examine the potential correlation between stream presence and BMWs it was checked whether the BMWs follow a normal distribution. Using the Shapiro-Wilk regularity test (Shapino and Wilk, 1965), it was found that the BMWs do not show 'normality' in terms of distribution (the Shapiro-Wilk regularity control gave W = 0.772, p <0.001); thus, the non-parametric Mann-Whitney test was used. Its result showed that these two types of beaches differ (U = 307.5, p <0.001), i.e., there is a correlation between beaches without streams and smaller BMWs with a median width of 22 m (Fig. 3a).

Regarding beach sediments, the majority of Kos beaches (53%) form on sandy sediments, whereas 32 % of the beaches on mixed sediments (gravels/sands) and 15% on pebbles. Comparison of the BMWs with the different sediment types showed good correlations; sandy beaches had an average BMW of 40.8 m (standard deviation 20), i.e. they are significantly wider than mixed sediment beaches and pebble beaches which showed average BMWs of 23.4 m (10.8 standard deviation) and 16 m (7.3 standard deviation), respectively. Even when the mixed sediment and pebble beaches were grouped together, their comparison with the sandy beaches showed a clear difference. Sandy beaches were found to have significantly greater BMWs (40.8 m) compared to the grouped mixed sediment/pebble beaches (21 m). It appears that the coarse sediment beaches attain BMWs 10-25 m, whereas the sand beach BMWs 30-50 m and 50-80 m (Fig. 3b).

In addition, it appears that about 60% of sandy beaches are also associated with outflowing streams, compared with those beaches forming on mixed sediments (45%) and pebbles (17%). To check this hypothesis the non-parametric Kruskal-Wallis test was used (the BMWs do not follow a normal distribution). The test checked the hypotheses: H_0, no correlation between the BMWs and the local sediment; and H_1, correlation between BMWs and the local sediments. The test showed that there is a clear difference between the maximum widths of beaches forming on sand and those forming on mixed/coarse sediments (H_1 = 25.911, p < 0.001). Beaches forming on pebbles have a median BMW of 14.9 m, whereas those formed on mixed sediments and sands 22.6 m and 40.5 m, respectively. A Kruskal-Wallis test (Kruskal and Wallis, 1952) was also applied in the case that beaches divided into two classes: those with sand sediments and those with mixed sediments and pebbles. The test showed a clear difference between these beach classes (H_1 = 25.090, p <0.001).

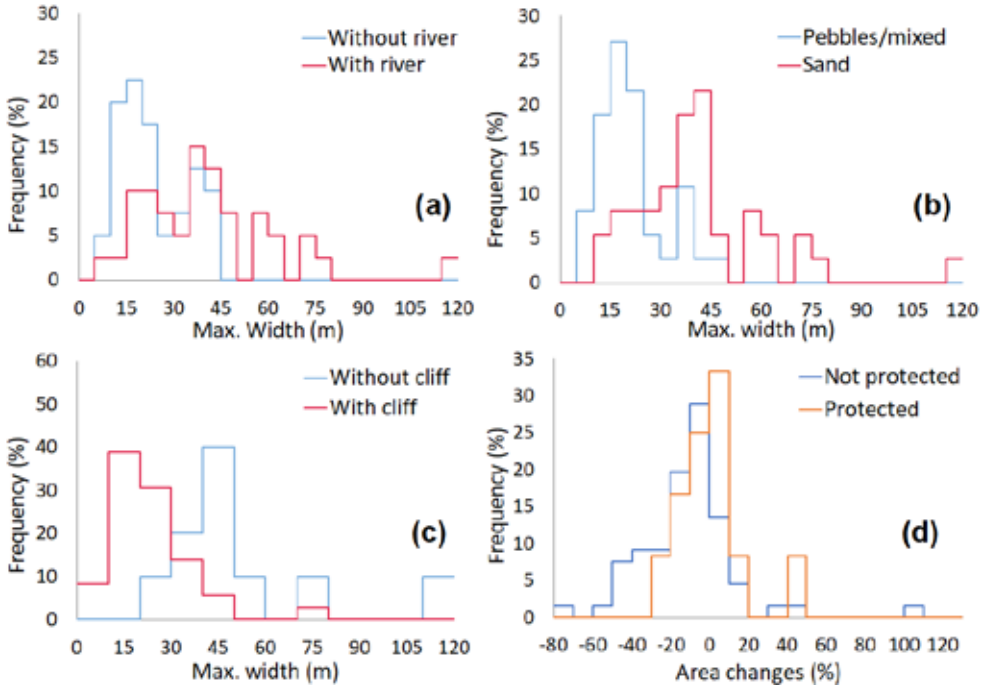


Figure 3. (a) Beach maximum widths (BMW) and the presence of beach streams (5 m steps), (b) BMWs and sediment texture (2 categories), (c) BMWs with the presence of backshore cliffs (10 m steps) excluding beaches with backshore infrastructure, and (d) Histogram of frequencies of areal changes.

A total of 50% of the island's beaches are characterized by the presence of backshore coastal cliffs. An initial investigation of the potential correlation with the BMWs did not reveal a significant relationship. However, as the presence of infrastructure/assets along the immediate backshore might affect the BMWs and other beach dimensions due to e.g., reduction/interruption of the land sediment supply and, thus, the correlation. Excluding beaches where there are backshore infrastructure/assets (about 50% of the total), a significant relationship is apparent (Fig. 3c). Many beaches with cliffs show BMWs of 10-20 m (and up to 30-50 m), whereas the beaches without cliffs attain obviously greater BMWs. The relationship was tested using the Mann-Whitney method excluding beaches with backshore infrastructure/assets. It appears that there is a statistically significant relationship ($U = 34$, $p < 0.001$). Those beaches without a backshore cliff are larger (a median BMW of 46 m) than those with a backshore cliff (median of 22 m). It seems that the coastal topography controls beach formation and size.

To assess the impact and effectiveness of coastal protection schemes, the areal changes between the beach polygons obtained from older imagery (2004-2009) and 2021 were considered which was preferred over more recent ones, as images were taken in spring/summer months (Fig. 3d). The Shapiro-Wilk regularity test for the variable 'beach area change' yielded results $W = 0.889$ and $p < 0.001$ showing that the data do not follow a normal distribution. Thus, the non-parametric Mann-Whitney control was also applied by controlling the following assumptions: H_0, the distribution of the continuous variable "percentage of change of beach area" is similar between beaches with coastal protection works and beaches without protection works; and H_1, the distribution of the continuous variable "percentage of change of beach area" differs between beaches with protection works and beaches without works. The test results show there is a significant areal difference ($U= 260$, $p=0.050$) between beaches with and without coastal works.

Discussion and Conclusions

The analysis of the geo-spatial data using both basic statistical metrics and more complex parametric and non-parametric tests, led to interesting findings regarding the Kos beaches. Comparison of the digitized polygons of the beaches showed erosion trends (Fig. 1) with the average BMW having decreased in 76% of the beaches compared to the period 2004-2009 (average decrease of 3 m). In addition, the area was reduced in 61 beaches out of the 78 beaches of the island, with an average decrease of 15% per beach. As the maximum dry width is considered a relatively conservative indicator of beach erosion (Monioudi and Velegrakis, 2022), the estimation of the areal reduction offers a more comprehensive picture. The analysis also showed that the detection of long-term erosive trends requires availability of time series of data with spatio-temporal resolution better than that currently available in open source imagery. In the near future, when it is expected that the availability of such data will increase significantly (Velegrakis *et al*., 2024), the approach developed/applied in the present study can be used more for the detection (and management) of coastal morphodynamics (erosion). In Kos, the orientation of the beaches does appear to affect the size of the beach, which on the contrary is related to stream presence and sediment texture size. In addition, the presence of backshore cliffs is correlated with small BMWs. Generally, it appears the Kos beach dimensions are primarily controlled by the geology rather the hydrodynamics.

Acknowledgements

This research was supported by the Hellenic Foundation for Research and Innovation (H.F.R.I.) under the '2nd Call for H.F.R.I. Research Projects to Support Post-Doctoral Researchers' (MARICC, Project Number: 211).

References

Chalazas, T., Bove, G., Chatzistratis, D., Monioudi, I.N., Velegrakis, A.F., 2024. A system for the management of sandy shorelines under climate change: United States Virgin Islands (USVI). Ambio 53, 406 - 420. https://doi.org/10.1007/s13280-023-01946-w

Karditsa, A., Niavis, S., Paramana, T., Monioudi, I, *et al*., 2024. Is the insular coastal tourism of western Greece at risk due to climate induced sea level rise? Ocean & Coastal Management 251, 107088. https://doi.org/10.1016/j.

ocecoaman.2024.107088.
Kruskal, W.H., Wallis, W.A., 1952. Use of ranks in one-criterion variance analysis. Journal of the American statistical Association 47(260), 583-621. https://doi.org/10.1080/01621459.1952.10483441
Monioudi I.N., Velegrakis, A.F., 2022. Beach Carrying Capacity at Touristic 3S Destinations: Its Significance, Projected Decreases and Adaptation Options under Climate Change. Journal Of Tourism and Hospitality 11, 500.
Monioudi, I.N., Velegrakis, A.F., Chatzistratis, D. *et al*., 2023. Climate change—induced hazards on touristic island beaches: Cyprus, Eastern Mediterranean. Front. Mar. Sci. 10, 1188896. https://doi.org/10.3389/fmars.2023.1188896
Monioudi, I.N., Chatzistratis, D., Chalazas, T. *et al*. 2025. A prioritization framework for adaptation responses for climate change-induced erosion in island beaches—Cases from the Aegean islands, Greece. J. Mar. Sci. Eng. 13, 491. https://doi.org/10.3390/jmse13030491
Mardia, K., 1976. Linear-Circular Correlation Coefficients and Rhythmometry. Biometrika 63 (2), 403–405, https://doi.org/10.2307/2335637
Narayan, S., Beck, M.W., Reguero, B.G. *et al*., 2016. The effectiveness, costs and coastal protection benefits of natural and nature-based defences. PLoS ONE 2016, 11, e0154735. https://doi.org/10.1371/journal.pone.0154735
Pe-Piper, G., Piper, D.J., Tsoukalas, N., 2024. Mineralogy and Geochemistry of Upper Miocene Igneous Rocks, Kos Island, Greece: Extension during Strike-Slip Faulting and Subduction Rollback. Minerals 14(10), 989. https://doi.org/10.3390/min14100989
Piper, D.J.W., Pe-Piper, G., 2020. A reworked isolated deposit of the Kos Plateau Tuff and its significance for dating raised marine terraces, Kos, Greece. Geol. Mag. 157, 2021–2032. https://doi.org/10.1017/S0016756820000254
SETE, 2024. Annual Report of Competitiveness and Structural Adjustment in the Touristic Sector for 2023: South Aegean. https://insete.gr/wp-content/uploads/2024/12/24-12_South_Aegean-1.pdf (in Greek)
Shapiro, S.S., Wilk, M.B., 1965. An analysis of variance test for normality (complete samples). Biometrika 52(3–4), 591–611. https://doi.org/10.1093/biomet/52.3-4.591
Velegrakis, A.F, Chatzistratis, D., Chalazas, T., *et al*., 2024. Earth observation technologies, policies and legislation for the coastal flood risk assessment and management: a European perspective. Anthropocene Coasts 7, 3. https://doi.org/10.1007/s44218-024-00037-x
Zar, J.H., 2014. Biostatistical Analysis. Pearson Education Limited

17th INTERNATIONAL CONGRESS of the Geological Society of Greece

BULLETIN OF THE GEOLOGICAL SOCIETY OF GREECE, SP. PUBL.

EXTENDED ABSTRACT 217

Innovative educational programs at the Lavreotiki UNESCO Global Geopark: the ERASMUS+ "ARTeMIS" Program Action for Research and Teaching Mineral exploration Inclusive School, Greece

Moraiti E.[1], Voudouris P.[2], Tarantola A. & Barsaki V.

(1) Lavreotiki UNESCO Global Geopark, Lavrion, Greece, eugeniamoraiti@gmail.com (2) National and Kapodistrian University of Athens, Ilissia, Greece

Introduction

UNESCO Global Geoparks (UGGp) are single, unified geographical areas where sites and landscapes of international geological significance are managed with a holistic concept of protection, education and sustainable development. Their bottom-up approach of combining conservation with sustainable development while involving local communities is a fundamental principal and is becoming increasingly popular.

The UNESCO Global Geoparks are ideal destinations that can support local communities and serve the 17 goals of the United Nations' Green Agenda in various ways.

In particular geoparks educate and prepare societies and youths for the new challenges that climate crisis has triggered. Education holds a pivotal role in the operation and management of a geopark. Every member is obliged to implement educational programs based on its geodiversity and biodiversity wealth. Geosites function as experiential laboratories, welcoming students, educators, and visitors to offer them unique experiences and communicate a sustainable way of living.

The ARTeMIS ERASMUS+ program

In the frame of collaboration and the accomplishment of the 17, Lavreotiki UNESCO Global Geopark has joined the ARTeMIS Erasmus + project. This project (funded with 385.000 euros per year and three years duration in total) is led by Alexandre Tarantola, Professor (Associate), head of the first year of the Master's degree in "Earth and Planetary Sciences, Environment", "Earth-Resources System" course of the University of Lorraine, Nancy. Its objective is to develop the methods and tools of geoscience professions through a research-based training approach. It aims to allow students to confront the realities and expectations of the field in geology, to complete their academic career and to broaden their horizons by allowing collaboration with students from other European Universities. This approach brings together various players working on the theme of mineral exploration such as the Friedrich-Alexander-University of Erlangen-Nuremberg, the National and Kapodistrian University of Athens (Scientific Responsible, Professor Panagiotis Voudouris), the Aristotle University of Thessaloniki (Scientific Responsible, Professor Vassilis Melfos) as well as Hellas Gold SA, a subsidiary of the Canadian company Eldorado Gold Corporation, which specializes in the exploration and exploitation of mines worldwide and the Lavreotiki UNESCO Global Geopark with its famous deposits. The Lavrion deposit comprises five different styles of related deposits, a unique geological phenomenon recorded only in Greece and in the Lavreotiki UGG's territory.

Its minerals contain the highest number of different elements (48) of any known mining district and thus more diverse than anywhere else in the world. Lavrion area offers the best opportunity to study the interplay between large-scale tectonic processes which took place during earlier Alpine collision and compression, followed by Miocene extension in the back-arc region of the Hellenic subduction zone; magmatic activity, expressed by emplacement of various igneous rocks in a syn- to post-tectonic regime; hydrothermal activity and fluid circulation within various lithologies, resulting in enormous quantities of ore deposition and related base and precious metal mineralization, later supergene weathering processes, resulting in a unique zone of supergene ore oxidation, which contains, in addition to the primary ores, the most mineral species ever found on a single mining district on earth and the way, geological processes have profoundly influenced ore deposition and the course of human history and technology.

Among many courses and actions, the "ARTeMIS" program includes a 4-days training course in the field (at the geopark's mining galleries) for teachers and students, using spectroscopic analysis tools and the implementation of classroom lessons in mineral resource geochemistry. These actions provide an opportunity to carry out exercises in the use of spectroscopic analysis tools, mapping and reflection on the establishment of metallogenic systems on geological objects that are at the heart of the research carried out by the various partners. The 4-days training course took place in April with great success.



Figure 1. Photography captions during the 4-day training course in the field, at the Lavreotiki UGGp geosites / sites of mining heritage.

Results

The expected results of the "ARTeMIS" ERASMUS+ program are:

- The creation of complementary teaching units for teachers and second-cycle university students engaged in an "exploration and mineral resources" course.
- The use and development of portable field tools suitable for mineral exploration.
- The application of an ergonomic approach to training and research in geology.
- The publication of an educational field guide dedicated to the mineral resources of northeastern Greece.
- The creation of a logistics preparation methodology.

Last but not least, an important aspect of the ARTeMIS project also aims to promote the integration of students with disabilities by making training accessible in order to offer them new opportunities for professional integration. To this end, a collaboration has been initiated with occupational therapists from the Lorraine-Champagne-Ardennes Occupational Therapy Training Institute with a view to identifying avenues for improvement and proposing alternatives. Workshops will be held, bringing together teachers, students, Earth Sciences stakeholders and occupational therapists. In the long term, these solutions will lead to a diversification of jobs and the development of processes that are more in line with the specificities of field geology.

Such substantive partnerships become models of good practices for the adaptation and sustainability of the local communities and the organizations involved in education. These partnerships foster interdisciplinarity and communicate science and universal values, such as collaboration, respect, inclusion, and quality education, to the youth and the next generations. These values are included and promoted by the United Nations Sustainable Development Goals (such as SDG 4, SDG 11, SDG 12, SDG 13, and SDG 17).



Figure 2. SDG 4: Ensure inclusive and equitable quality education and promote lifelong learning opportunities for all, SDG 12: Ensure sustainable consumption and production patterns, SDG 16: Promote peaceful and inclusive societies for sustainable development, provide access to justice for all and build effective, accountable and inclusive institutions at all levels & SDG 17: Strengthen the means of implementation and revitalize the Global Partnership for Sustainable Development.

References

Voudouris, P., et al. 2008. Mineralogical and fluid inclusion study of the Kamariza carbonate-replacement deposit, Lavrion, Greece. **[Mineralogy and Petrology, 94, 85–106.]**

Rieck B. (2024) Lavrion Mining District, Lavreotiki, East Attica, Attica, Greece https://www.mindat.org/loc-1942.html

https://hub.uoa.gr/erasmus-artemis/

https://master-stpe.formation.univ-lorraine.fr/projet-erasmus-artemis-terrain-en-grece-m2-smge/

17th INTERNATIONAL CONGRESS of the Geological Society of Greece

BULLETIN OF THE GEOLOGICAL SOCIETY OF GREECE, SP. PUBL.

EXTENDED ABSTRACT 218

Empowering Future Generations: Incorporating Geo - Environmental Education on Climate Change into Greek Compulsory Education

Moshou H., Drinia H.

Department of Geology and Geoenvironment, National and Kapodistrian University of Athens, Panepistimiopolis, 15784 Athens, moshouhara@geol.uoa.gr

Introduction

The urgent need to address climate change has never been more critical, as its impacts are being felt globally, with severe consequences for ecosystems, economy, and human communities. Adapting to a rapidly changing world is equally essential. Climate change poses one of the greatest challenges of our era, making immediate action imperative. Education, including geoeducation, can serve as a key tool in preparing future generations to mitigate and adapt to these challenges. Geoeducation, enriched with geoconservation principles, emphasizes the importance of protecting geological heritage while fostering an understanding of Earth's processes and their relevance to the climate crisis. Therefore, it provides a unique opportunity to equip students with the knowledge and skills to grasp the complexities of climate change and its impact on our planet.

This paper underscores the significance of education, particularly environmental education and geoeducation, in addressing the climate crisis, while also exploring obstacles and challenges regarding the implementation of climate change education in Greece. Additionally, it proposes general strategic approaches for systematically integrating climate change education into the compulsory education system, with the objective of fostering both mitigation and adaptation in response to the climate crisis. The study employs a mixed-method approach to explore integrating climate change education (CCE) into Greek compulsory education. A systematic review of national and international studies identifies best practices, challenges, and gaps in implementing CCE. SWOT analysis evaluates internal factors like teacher preparedness and resources, while PEST examines external political, economic, social, and technological influences.

The Importance of Geo - Environmental Education in Addressing the Climate Crisis

Recognizing the critical role of education in addressing climate change is essential. Environmental education fosters ecological awareness and equips citizens with the skills and attitudes necessary to adopt sustainable practices and social responsibility (Damoah, 2023; Daskolia, 2023; Nantsopoulos & Mogias, 2020). Geoeducation, with its emphasis on understanding Earth's systems, geological processes, and their interaction with the environment, complements this effort by providing a scientific foundation for grasping the complexities of climate change. Together, environmental education and geoeducation not only raise public awareness but also encourage proactive behavior, leading to significant behavioral shifts. Coupled with effective government policies (see Figure 1), they can mitigate climate impacts and enhance societal resilience to environmental challenges.

Georgousis et al. (2021) emphasize that geoeducation, or geoenvironmental education, plays a pivotal role in connecting students with Earth's dynamic processes, promoting a deeper understanding of the natural environment, and fostering sustainable attitudes. They argue that integrating geoenvironmental education into curricula can bridge the gap between theoretical knowledge and practical applications, empowering learners to critically assess and address environmental issues such as climate change. Geoeducation, coupled with geoconservation, not only deepens students' understanding of Earth's dynamic systems but also emphasizes the preservation of geosites, which serve as critical records of past climatic conditions. This dual approach empowers learners to appreciate the interplay between geological heritage and environmental sustainability. By focusing on interdisciplinary learning, geoeducation highlights the interplay between geology, geography, and environmental science, making it an essential component of climate-focused education.

The urgency for climate-focused education is greater than ever, as new generations face complex challenges from the climate crisis. Integrating climate change into school curricula fosters early environmental and geoscientific awareness, shaping responsible citizens (Nantsopoulos & Mogias, 2020). Early education is vital, as misconceptions formed in childhood can persist into adulthood (Boyes & Stanisstreet, 1993). Geoeducation is particularly valuable in helping students understand how climate change affects Earth's physical processes and ecosystems, fostering a holistic perspective. Preparing students with solid knowledge and its geological dimensions about climate change enhances their willingness to act and fosters active participation in addressing future challenges (Lester et al., 2006)..

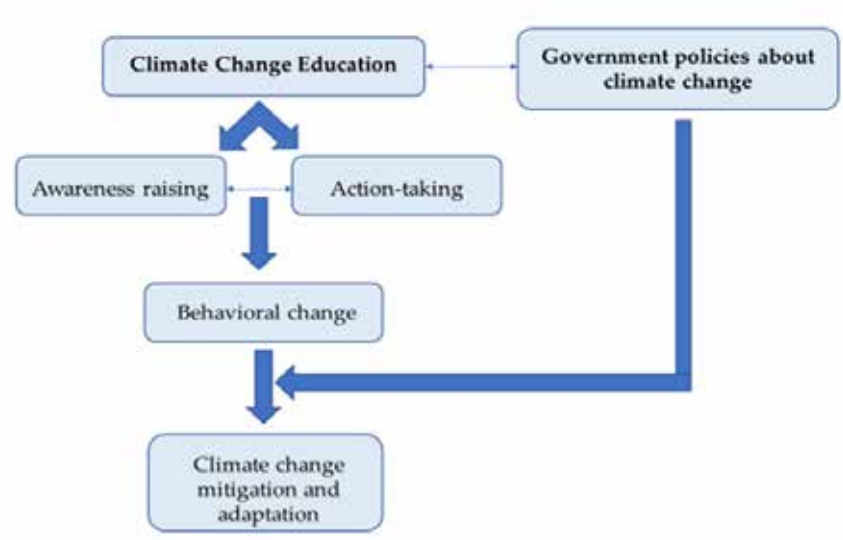


Figure 1. Climate change education as an important part of climate change mitigation and adaptation. (Figure from Moshou & Drinia, 2023)

Challenges and Barriers in Implementing Climate Change Education in Greece

The implementation of climate change education in Greece encounters significant challenges linked to social, political, economic, and educational factors. Although 83% of Greeks recognize climate change as a critical issue of the 21st century (EIB, 2021), integrating environmental education into the national curriculum remains problematic. Since its introduction in 1987, environmental education has been optional and limited to specific programs (Farangitakis & Sbarounis, 2020). Textbooks present environmental topics in a fragmented way, leading to knowledge gaps and misconceptions, such as confusion between the greenhouse effect and ozone layer depletion (Nantsopoulos & Mogias, 2020). Incorporating geoconservation into environmental education could bridge gaps in understanding Earth's history and its relevance to climate change, while fostering a sense of responsibility for preserving unique geological sites as natural laboratories for scientific inquiry. Additionally, inadequate teacher training exacerbates the issue, as many educators lack sufficient preparation in environmental topics (Moshou & Drinia, 2023). These deficiencies are further illustrated in Figure 2, which highlights how early misconceptions formed in childhood persist into adulthood, impacting future educational efforts.

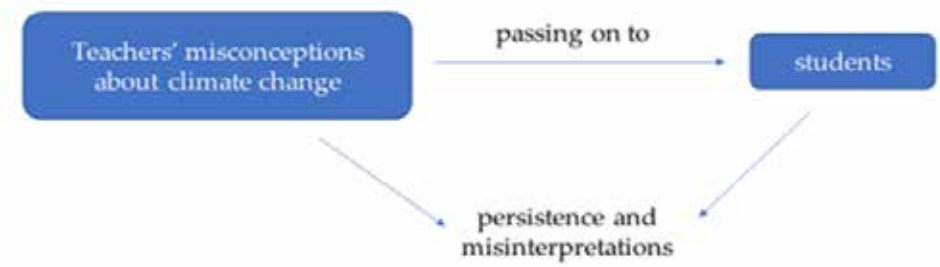


Figure 2. Teachers' misconceptions pass on to students and lead to misconceptions' persistence and misinterpretations (Figure from Moshou & Drinia, 2023)

Further challenges are rooted in Greece's prolonged economic crisis, which limits funding for programs, infrastructure, and teacher training. Environmental Education Centers, critical for raising awareness, face resource shortages, reducing their ability to operate effectively (Farangitakis & Sbarounis, 2020). Psychological distance also plays a role, as many Greeks have yet to experience direct impacts of climate change, diminishing the urgency and public engagement necessary to address the issue. Additionally, unclear legislation and delays in decision-making, coupled with insufficient collaboration among stakeholders, hinder progress. Figure 3 presents a SWOT analysis summarizing these barriers, categorizing them as weaknesses and threats while identifying opportunities for improvement through international best practices and stronger political support.

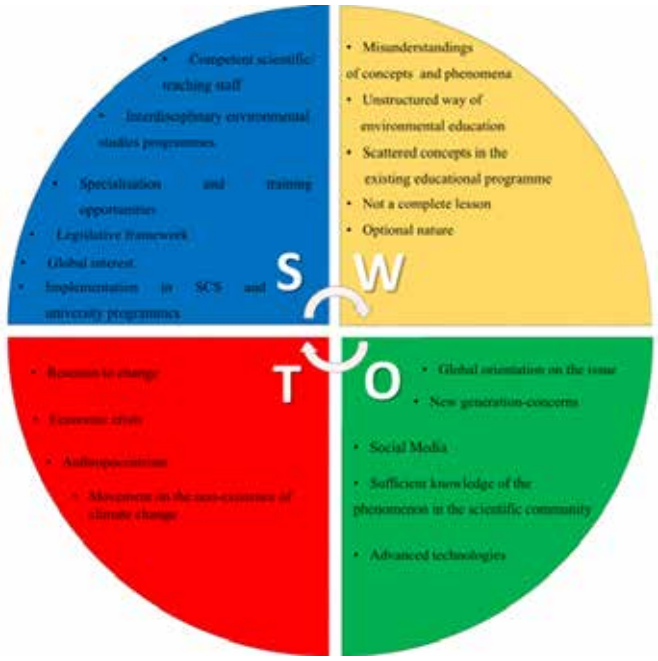


Figure 3. SWOT analysis of environmental education for climate change in Greek Compulsory Education (Figure from Moshou & Drinia, 2025)

Strategic Guidelines for the Effective Integration of Climate Change Education in Greece

The integration of climate change education (CCE) into Greece's educational framework demands a well-structured approach addressing existing challenges. Based on a thorough analysis, including literature reviews, SWOT, and PEST analyses (Moshou & Drinia, 2023; 2025), the following strategic framework is proposed to enhance CCE in Greece:

- Mandatory Environmental Education. CCE must be incorporated as a compulsory subject at all levels of education, ensuring that all students acquire essential knowledge about the environment and climate change. The purpose of this initiative is to provide both theoretical and practical knowledge for reducing environmental risks in the short term and to strengthen students' connection with nature, fostering a lasting environmental consciousness, as well as addressing the main goal of mitigating and adapting to climate crisis.
- Cross-Disciplinary Integration. Given the multidimensional nature of climate change, its integration across various school subjects can promote a holistic understanding of its impact on different aspects of daily life, such as health, the economy, and social equity (Damoah, 2023). While embedding climate change education into existing subjects can be beneficial, it should complement, rather than replace, a distinct compulsory course on environmental education (Moshou & Drinia, 2025). Moreover, it is proposed the inclusion of geoconservation as a key topic within cross-disciplinary education, linking geology, geography, and environmental science to highlight the significance of preserving geosites and their role in understanding climate change.
- Teaching by Specialized Educators. Environmental education, particularly on complex topics like climate change, should be taught by educators with specialized environmental scientists with pedagogical competence. These professionals possess the interdisciplinary knowledge needed to convey accurate information and minimize misconceptions (Moshou & Drinia, 2023).
- Comprehensive Teacher Training. Specialized training programs for teachers are essential to equip them with the necessary knowledge and skills to teach environmental education effectively. Continuous professional development, even for specialized educators, is equally critical to keep pace with the latest scientific developments and pedagogical practices.
- Collaboration with Key Stakeholders. Strengthening collaboration between schools, universities, and local communities is vital for developing innovative educational programs. Partnerships with research institutions can facilitate the design of advanced curricula and educational tools, fostering a culture of environmental responsibility. The collaboration with geologists, conservationists, and UNESCO Global Geoparks to create programs that promote geoconservation and its connection to climate change education aims to foster a deeper

understanding of how geological heritage can play a crucial role in mitigating and adapting to climate change, while also raising awareness about the sustainable management and protection of these invaluable resources for future generations.

- Reducing Psychological Distance. CCE must address the psychological distance that prevents students from relating to climate change. Incorporating local issues and tangible examples into the curriculum can bridge this gap, making the topic relevant and engaging. Emotional and personal connections can motivate students to participate in advocacy and sustainability initiatives actively.
- Utilizing Technology. Technology can play a pivotal role in enhancing environmental education. Digital platforms, interactive applications, and multimedia learning tools can make learning more engaging and effective for students (Nantsopoulos & Mogias, 2020). Moreover, the use of simulations can help reduce psychological distance, allowing learners to better grasp complex environmental issues by visualizing potential outcomes and real-world scenarios.
- Policy Recommendations and Curriculum Policymakers should collaborate with universities and research centers to revise educational frameworks. A clear national framework must outline goals, objectives, and action plans for integrating CCE, alongside timelines and regular program evaluations. The incorporation of geoconservation into national educational policies as a framework to protect geological heritage while enhancing students' understanding of climate and environmental challenges seeks to empower future generations with the knowledge and skills needed to address pressing global issues. By integrating geoconservation into curricula, students can develop a greater appreciation for the role of Earth sciences in tackling climate change and promoting sustainable environmental practices.
- Developing a National Strategy for Climate Change Education. A comprehensive national strategy should be created, taking into account Greece's international obligations and promoting a holistic approach to understanding the climate crisis. This strategy should aim to elevate environmental education as a core component of the educational system, fostering both knowledge acquisition and behavioural change towards sustainability.

Conclusion

Environmental education for climate change is one of the most essential pillars for shaping responsible citizens and fostering a sustainable society. Despite the challenges, integrating environmental education into greek educational system can play a decisive role in developing active and responsible citizens who will be equipped to face and adapt to future environmental challenges.

Developing a cohesive strategy, investing in well-trained educators, and enhancing appropriate teaching methods are key priorities for advancing environmental education. Only through coordinated actions and collaborations can we hope for a sustainable future for the next generations.

Emphasizing sustainable development, cultivating critical thinking, and encouraging active student participation are crucial for achieving this goal. Greece has the potential to become a model country in climate change education if it invests in the appropriate resources and strategies.

Moreover, integrating geoconservation into climate change education not only protects our geological heritage but also provides students with tangible examples of climate change's impact over time, fostering a deeper connection to Earth's history and its future.

Acknowledgements

References

Boyes, E., Stanisstreet, M., 1993. The "greenhouse effect": Children's perceptions of causes, consequences and cures. International Journal of Science Education 15, 531–552.

Damoah, B., 2023. Reimagining climate change education as a panacea to climate emergencies. International Journal of Environmental, Sustainability & Social Science 4, 977–987.

Daskolia, M., 2023. The climate crisis as a "wicked" problem and a learning subject: Theoretical, research, and teaching insights with a focus on education for climate change. Environmental Education for Sustainability 5, 48–65.

EIB (European Investment Bank)

Farangitakis, G., Sbarounis, Th., 2020. SWOT analysis of education for environmental citizenship — Country report: Greece, in: Hadjichambis, A.Ch., Reeis, P., Paraskeva-Hadjichambi, D. (Eds.), European SWOT analysis on education for environmental citizenship. European Network for Environmental Citizenship (ENEC) COST Action Report, 137–148.

Georgousis, E., Savelides, S., Mosios, S., Holokolos, M.-V., & Drinia, H., 2021. The Need for Geoethical Awareness: The Importance of Geoenvironmental Education in Geoheritage Understanding in the Case of Meteora Geomorphes, Greece. Sustainability, 13(12), 6626.

Lester, B.T., Ma, L., Lee, O., Lambert, J., 2006. Social activism in elementary science education: A science, technology, and society approach to teach global warming. International Journal of Science Education 28, 315–339.

Moshou, H., Drinia, H., 2023. Climate Change Education and Preparedness of Future Teachers—A Review: The Case of Greece. Sustainability 15, 1177.

Moshou, H., Drinia, H., 2025. Strategic Insights for Environmental Education in Greece: SWOT & PEST Analyses in the Context of the Climate Change Crisis. Sustainability 17, 2633.

Nantsopoulos, M., Mogias, A., 2020. Climate change and the role of education: The case of environmental study textbooks in primary education. Environmental Education for Sustainability 2, 1–15.

17th INTERNATIONAL CONGRESS
of the Geological Society of Greece

BULLETIN OF THE GEOLOGICAL SOCIETY OF GREECE, SP. PUBL.

EXTENDED ABSTRACT 219

Slope stability rehabilitation in the traditional settlement of Chora, Andros Island, Greece

Mourtzas N.[1], Gkiolas A.[2], Papacharalambous G.[2], Tsakonas A[2]., Kolaiti E.[3]
(1) Society for the Study of Ancient Coastlines - AKTES NPO; University of Nottingham, Department of Classics and Archaeology, Kefallinias 18, 15231 Chalandri, Athens, Greece, nikosmourtzas@gmail.com (2) ATENEIA Geotechnical Consultants Private Technical Company (ATENEIA P.C.), Athens, Greece (3) Society for the Study of Ancient Coastlines - AKTES NPO; National Hellenic Research Foundation, Institute of Historical Research; University of Nottingham, Department of Classics and Archaeology, Chalandri, Athens, Greece

Research Highlights

Engineering geological and geotechnical design for slope stability to ensure the long-term protection of the overlying buildings and footpath along a coastal slope in a traditional settlement in the Cyclades, including design implementation, rehabilitation works, and aesthetic interventions.

Introduction - Project area

The failed slope is located in the traditional settlement of Chora on Andros Island, on the northern side of the Chora peninsula, along the southern coast of Nimporio Bay, in the Plakoura area, and approximately 75m southwest of the church of Agia Thalassini. It extends from an elevation of between +2.60m and +3.80m at the slope toe to between +16.80m and +17.40m at the crest, with an average height of 15m. The sickle-shaped slope features a 30m-long arch and a corresponding 25m-long chord, trending NE-SW with a plunge of 85° towards the NW (Fig. 1).



Figure 1. Satellite images of the project area (Google Earth Pro, v. 7.3.4., accessed on 3 October 2021). The yellow outline indicates the location of the failed slope.

Description of the failure

In March 2021, a large volume of rock detached from the central part of the slope, between elevations +9.50m and +14.70m. This event created unsafe conditions for the buildings immediately above the slope's crest and posed a risk of accidents in case of additional rockfalls along the footpath, which runs close to the slope's base. The failed area, measuring approximately 30m^2, is located in the central part of the slope. The failure occurred along a weakness zone in the schist formation, resulting in an 8m-wide, 5m-high and approximately 3m-deep caving (Fig. 2). Moreover, three older, smaller-scale slides, ranging in size from 2m^2 to 4.5m^2, are observed in the central part of the slope at lower elevations, between +4m and +7m (Fig. 2).



Figure 2. General view of the failed slope, the overlying buildings along the slope crest, and the footpath along the slope toe. The location of the failure is indicated by a red outline.

Geology of the landslide area

The slope consists of mica schists (Mehl *et al.*, 2007; Höhn *et al.*, 2022) that are moderately, and in some zones, intensely tectonized. Tectonization of the rock occurred due to four major inverse shear zones (R1, R2, R3, and R4), as well as additional zones parallel to these (R5, R6, and R7), which can be observed on the adjacent property slope (Fig. 3A, 3B). The shear zones extend for several meters, trending NW with plunges ranging from 15° to 25°, and are associated with a compressive tectonic regime, oriented NE-SW. The four major shear zones divide the slope area into five zones, one of which is where the recent slide occurred, while smaller failures have occurred in the other zones in the past.

To investigate the stability conditions, engineering geological characteristics, and properties of the rock mass along the slope, a comprehensive microtectonic analysis was conducted in order to form a complete picture of the tectonism of the rock mass (Fig. 3C). Subsequently, to examine the tectonism of the individual sections of the slope, it was divided into eight sub-sectors: two sectors at the NE end (sectors A and B), one at the SW end (sector H), and five sectors between the faults with a slope direction parallel to that of the slope (sectors C, D, E, F, G, and H). In each sector, a microtectonic analysis was performed (using the software DIPS, v. 5.1, Rocscience) to assess the stability and support of the rock mass (Hoek and Bray, 1981; ISRM Suggested Methods, 1981) (Fig. 3C).

The schistosity is well-developed, showing dips towards the SW in the NE part of the slope, towards the SE to SSW in the central part, and towards the SW to WSW in the SW part, with dips ranging from 15° to 30°. The general dip of the schistosity is oriented towards the SW, with an average dip of 20° (Fig. 3A, 3B). The main joint systems crossing the slope are two: one trending NE-SW with dips towards the NE, and the other trending NNE-SSW with dips towards the ENE. A third, less frequent joint system, with a dip direction parallel to the slope, trends ENE-WSW and dips towards the NNE (Fig. 3A, 3B).

Stability analyses of the slope against wedge and planar failure were conducted (using the software Swedge, v. 5.01 for wedge failures and RocPlane, v. 2.029 for plane failures, Rocscience), based on conservative assumptions (Norrish and Wyllie, 1996; Wyllie and Mah, 2004). Discontinuities were considered planar and of infinite length. The length of the slope was assumed to be L=20m and the rock mass unit weight was taken as γ=26 kN/m^3. Regarding the angle of internal friction, taking into account the characteristics of the schist formation, the condition of discontinuities, and based on literature, a range of values from 25° to 30° was considered (Wyllie and Norrish, 1996). The minimum value of 25° was conservatively selected for the analyses. Regarding cohesion, a value of zero was conservatively assumed, considering the possibility of infilling material being washed out due to groundwater circulation. Analyses were performed for static loading, static loading with hydrostatic pressure on the discontinuities for a 50-year return period (even though a permanent water table was not encountered), assuming partial filling of the discontinuities with water for short periods following intense rainfall, in cases where infiltrating water does not dissipate quickly to lower elevations, and seismic loading.

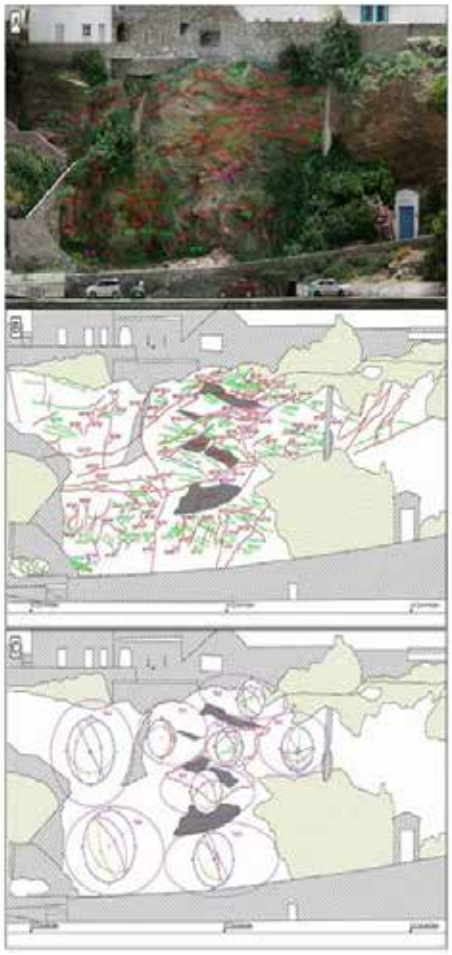


Figure 3. (A, B): View and front view of the failed slope, indicating joints (red lines), schist planes (green lines) and their geometric features. (C): Stereonets of the eight sub-sectors into which the slope was divided. The grey areas in 3B and 3C indicate the locations of recent and older failures.

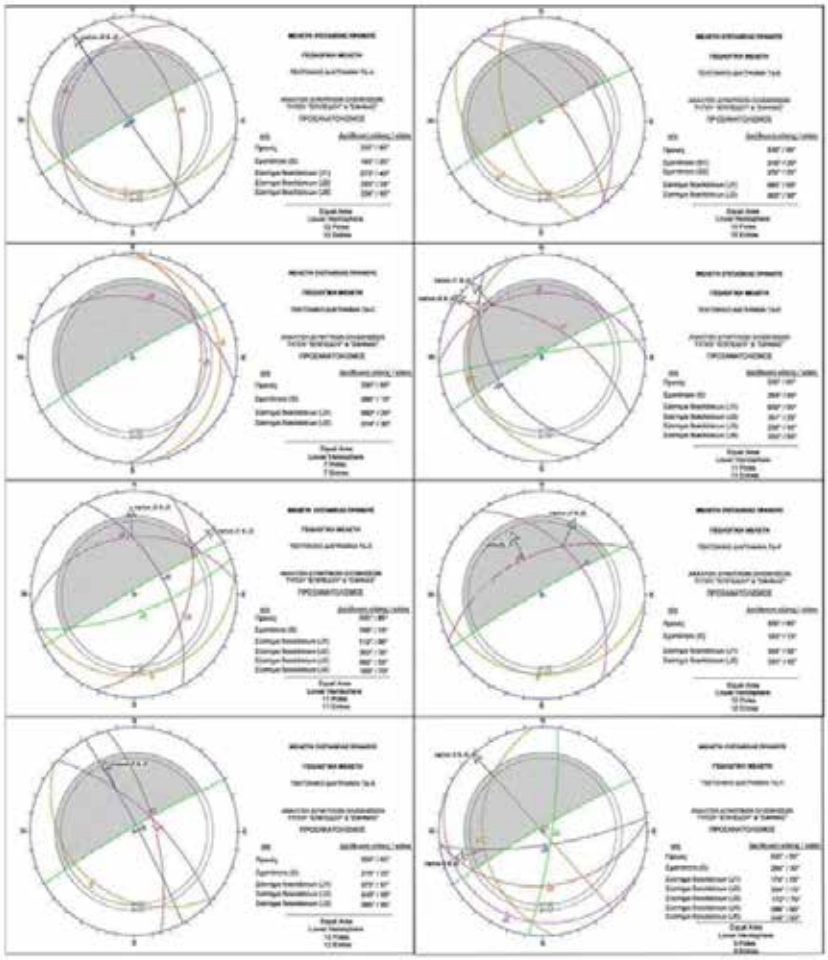


Figure 4. Stereonets of the eight sub-sectors into which the slope was divided. Sliding Kinematic Analysis

Based on the results of the analysis of wedge failure for the overall discontinuity stereonet, as well as for the stereonets of the individual zones of the slope (TΔ-A to TΔ-H, Fig. 3C, Fig. 4), it is inferred that achieving slope stability requires the application of 6m-long rock bolts in a 3m x 3m (v:h) pattern. Furthermore, based on the results of the analysis against planar failure, it is concluded that stabilize the upper six meters of the slope, where planar failures may occur, 6m-long rock bolts in a 2m x 2m (v:h) pattern are needed.

Therefore, from the results of both wedge and planar failures analyses, a rock bolt pattern of 2m x 2m (v:h) was selected for the upper part of the slope, above elevation +9.80m (the higher six meters), and a 2m x 2.50m (v:h) pattern for the lower part of the slope. A rock bolt length of L=6m was chosen for both areas to ensure sufficient anchoring depth (Fig. 5).

Rehabilitation of the slide area

In order to ensure the stability of the slope and provide long-term protection of the rock mass against wedge and planar failure, erosion induced from water runoff, coastal erosion due to the slope's proximity to the sea, and its continuous exposure to wind and waves, as well as to rehabilitate the caving and overall geometry of the slope from both recent and older failures, the most efficient and aesthetically acceptable rehabilitation scheme comprises the combination of rock bolts, shotcrete, and wire mesh across the entire slope surface. The proposed shotcrete coverage aims to provide long-term protection of the rock mass against both surface and in-depth erosion of schist,

while also rehabilitating the slope geometry in areas of failure (recent and older), where cavings and locally negative slope gradients develop. Furthermore, shotcrete in combination with steel wire mesh effectively retain smaller-scale structural failures that may occur between the rock bolts (Fig. 5).



Figure 5. Front view of the slope showing the support and protection measures.

Specifically, the construction of seven rows of rock bolts was proposed for the section of the slope between cross-sections S3 and S12, and six rows for the section beyond cross-section S12 (Fig. 5, 6). In all rows, a horizontal distance of 2m between consecutive bolts is foreseen. The rock bolts are fully grouted steel bars, 24mm or 25mm in diameter, made of S650 steel (for □24mm) or S500 steel (for □ 25mm), with nominal tensile capacity of 200kN, 6m in length, and installed with a downward inclination of 15°. The drillhole diameter for the rock bolts was proposed at least 100mm. Continuous threaded steel bars will be used to ensure good bonding with the grout and also to allow easy screwing of the nut and cutting of any possibly protruding parts of the bars. Additionally, given the proximity of the slope to the sea, all steel bars and relevant materials (e.g. nuts, rock bolt plates) will be hot-dip galvanized to ensure resistance to corrosion.

For the environmental integration of shotcrete, appropriate pigments will be used during mixing, based on relevant in-situ test, to match the natural color of the slope's rock mass. A minimum structural thickness of 10cm of shotcrete was proposed, applied in two layers of 5cm each, with one layer of steel wire mesh placed between them.

In areas of the slope where relatively deep cavings have occurred, consecutive layers of shotcrete will be applied, with additional layers of steel wire mesh installed every 20-30cm of shotcrete thickness. For the first layer of steel wire mesh, to be installed on top of the first five centimeters of shotcrete across the entire slope, T131 wire mesh will be used to provide enough flexibility to conform to the rough slope surface. In areas with extensive and/or deep cavings, the wire mesh layers in between the shotcrete layers will be made of T188 type wire mesh and steel grade B500C. For fixing the additional steel wire mesh layers, bolts consisting of □16mm or □18mm solid steel bars will be used, arranged in an appropriate configuration.

To prevent pore pressure build-up behind the shotcrete facing, drilling of three rows of weep holes (water pressure relief holes), was proposed, each with a diameter of 3'' and ranging from 0.50m to 1.50m in length, depending on the local thickness of the applied shotcrete, and spaced every 2m horizontally. Specifically, the lower row of weep holes was proposed at approximately elevation +7.80m, the second row at +9.80m and the upper row at +13.80m. In addition to the weep holes, two rows of raking drains, transverse to the slope, were proposed, spaced every 2m horizontally. The raking drains will have a diameter of 3'', a length of 6m, and a slight upward inclination of 5° to relieve water pressure in case of a seasonal groundwater table. Inside the raking drains drillholes, □2'' perforated PVC tubes will be installed, coated with separation geotextile to prevent clogging by fines from the surrounding eroding schist rock mass. The lower row of raking drains was proposed at approximately elevation +11.80m (Fig. 6).

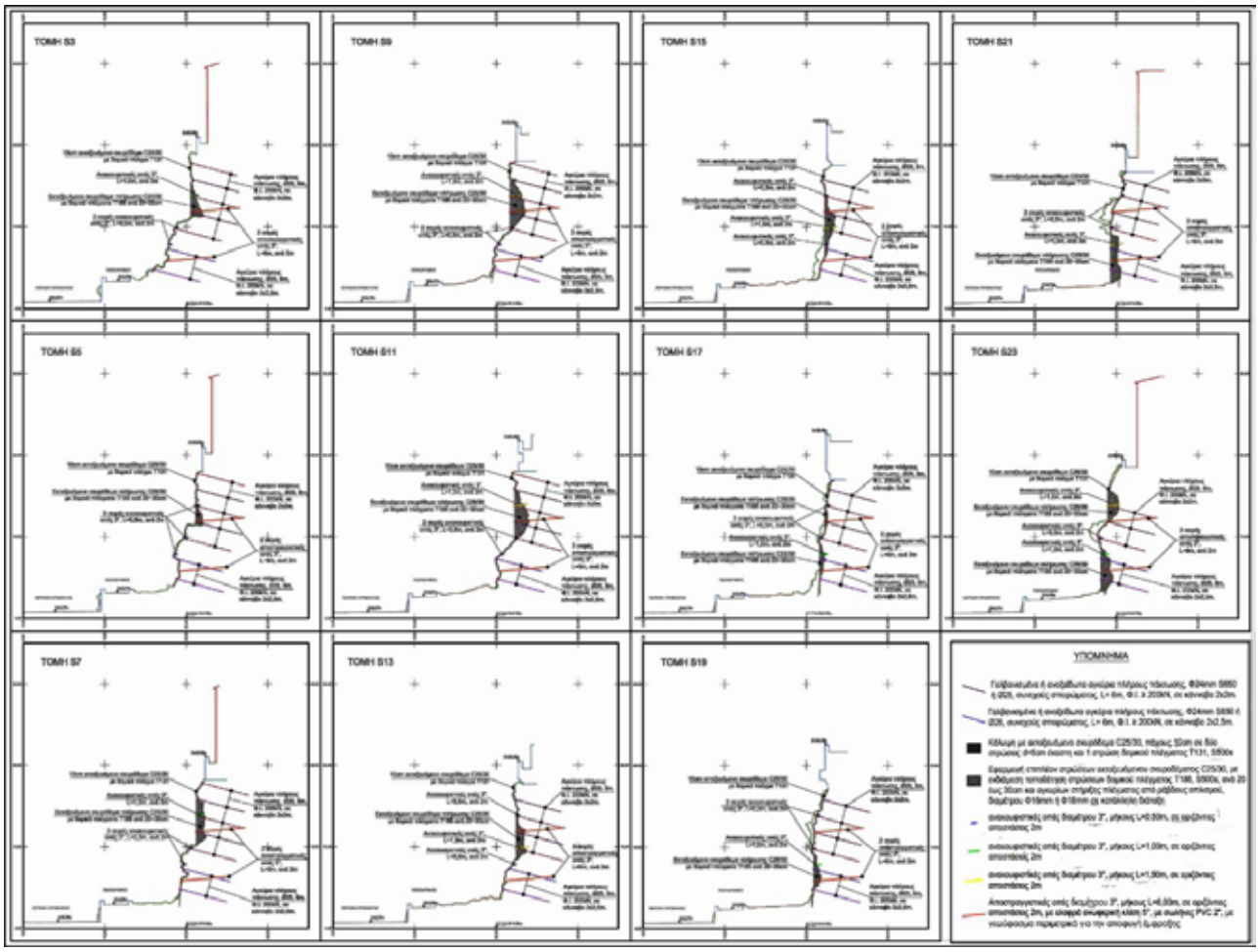


Figure 6. Cross-sections of the failed slope showing the support and protection measures.

Design Implementation

Stabilization and rehabilitation works on the rock slope began in October 2023, following the end of the summer tourist season, to minimize disruption and inconvenience to the visitors of the Agia Thalassini church and those visiting the Andros Chora Castle area, on the northern side of the Chora peninsula (Fig. 7).



Figure 7. Views of the slope after the application of the support and protection measures, before (left) and after (right) the final aesthetic interventions.

Special attention was given to shaping the final slope surface to closely resemble its condition prior to the rehabilitation works, with aesthetic interventions made in consideration of the features of the traditional settlement. Therefore, the shotcrete layers followed the natural slope surface, in accordance with the approved design. Final coloring of the

slope was carried out after the winter of 2024, allowing time for precipitation, sea spray from waves, intense winds, and storms in the area, as well as water seepage (both groundwater and surface water), to naturally balance the color of the shotcrete, which had been already pigmented during shotcreting. An aesthetic intervention followed, involving planting at the slope toe and the reconstruction of the low wall on the footpath side, which was damaged by the slide (Fig. 7).

References

Hoek, E., Bray, J.W., 1981. Rock Slope Engineering, Revised 3rd ed. Institution of Mining and Metallurgy, London.
Höhn, M., Bröcker, M., Berndt, J., 2022. The Jurassic meta-ophiolitic rocks of Cape Steno, Andros, Greece: a high-pressure/low-temperature mélange with Pelagonian affinity in the Cycladic Blueschist Unit? International Journal of Earth Sciences 111, 949-968.
ISRM Suggested Methods, 1981. Rock Characterization Testing & Monitoring, E.T. Brown (ed.), Pergamon Press.
Mehl, C., Jolivet, L., Lacombe, O., Labrousse, L., Rimmele, G., 2007. Structural evolution of Andros (Cyclades, Greece): a key to the behaviour of a (flat) detachment within an extending continental crust, in: Taymaz, T., Yilmaz, Y., Dilek, Y. (Eds), The Geodynamics of the Aegean and Anatolia. Geological Society, London, Special Publications, 291, 41-73.
Norrish, N.I., Wyllie, D.C., 1996. Rock slope stability analysis. in: Turner, A.K., Schuster, R.L. (Eds), Landslides: Investigation and Mitigation, Transportation Research Board, Special Report 247, 391-425.
Wyllie D.C., Norrish N.I., 1996. Rock Strength Properties and their Measurement, in: Turner, A.K., Schuster, R.L. (Eds), Landslides: Investigation and Mitigation, Transportation Research Board, Special Report 247, 372-390.
Wyllie, D.C., Mah, C.W., 2004. Rock Slope Engineering – Civil and Mining, 4th ed. Spon Press.

17th INTERNATIONAL CONGRESS of the Geological Society of Greece

BULLETIN OF THE GEOLOGICAL SOCIETY OF GREECE, SP. PUBL.

EXTENDED ABSTRACT 220

The Horizontal-to-Vertical Spectral Ratio Method for Underground Voids Detection: Testing Over Mycenaean Tombs

Moustakas H. I.[1], Roumelioti Z.[1], Sokos E.[1], Evangelidis Ch.[2]

(1) Department of Geology, University of Patras, Patras, Greece, up1060600@upnet.gr (2) Institute of Geodynamics, National Observatory of Athens, Athens, Greece

Abstract

This study investigates the potential of the Horizontal-to-Vertical (H/V) spectral ratio method, a technique typically used for site characterization, as a complementary tool for detecting underground voids. We leverage ambient noise measurements conducted at the Mycenaean cemetery of Voudeni, Peloponnese, Greece, utilizing the site's numerous underground tombs as test targets. We analyzed the H/V spectral amplitudes above the centers of various sized tombs and the spatial variation of horizontal and vertical spectral amplitudes and of their ratio along trial linear arrays. We verify the suggestion of previous research that over voids the H/V curve shows a characteristic drop below unity at high frequencies (in our test cases, typically >20Hz), which remains below unity for a considerable frequency interval. This phenomenon is attributed to a velocity reversal caused by the void within the surrounding rock. We attempt a first-order comparison of the void size and frequency of initiation of the characteristic drop and conclude that larger subsurface voids tend to affect the H/V curve at lower frequencies compared to smaller voids, exhibiting an exponential relationship. We also observe that the H/V drop over our test voids is primarily driven by the amplification of the vertical component rather than de-amplification of the horizontal component and this suggests that using linear arrays of vertical component geophones alone could be effective for void detection, particularly as a complement to other geophysical methods. We demonstrate this possibility through trial linear arrays of vertical sensors. We conclude that the H/V method and linear arrays of vertical sensors hinder promising advancements as void detection techniques, especially considering their readily deployable and cost-effective character, although theoretical modeling and extensive testing in various geological settings and void characteristics are required to better understand the observed phenomena.

Background and Objective

The Horizontal to Vertical Spectral Ratio (H/V or HVSR) method (Nogoshi and Igarashi, 1971; Nakamura, 1989) involves the analysis of earthquakes or microtremor (ambient noise) records to compute the ratio of the spectral amplitudes of the horizontal components to the vertical component. It was originally proposed as a method to calculate the local amplification and resonance frequency resulting from sedimentary layers overlying the bedrock. For the simplified case of a viscoelastic sedimentary soil layer of thickness h and shear wave velocity Vs, over a viscoelastic bedrock, the resonance frequency f_n is calculated by the formula:

$$f_n = (2n+1)\frac{V_s}{4h}, (n = 0,1,2,\dots)$$

Empirical data have shown that the lowest frequency at which the maximum value of the H/V curve is observed at a site, is identical or very close to the resonance frequency, f_0, of the soil by shear waves SH. In addition to f_0, the method can provide information on the thickness of the soil over bedrock, the presence of high density layers, lateral discontinuities of the subsoil layers from variations of the curves at different locations and velocity reversals (e.g. from natural or artificial hard layer over softer soil) (e.g., Field and Jacob 1993; Lermo and Chávez-García 1994a; Bonilla et al. 1997; Bour et al. 1998; Bard 1998; Fäh et al. 2001; Woolery and Street 2002; Molnar and Cassidy 2006; Haghshenas et al. 2008).

As the popularity of the H/V method increases, several aspects of its practical application are being examined in more detail. One such aspect involves the performance of the method at sites where there is a strong velocity reversal very close to the ground surface. This situation often arises when measurements are collected on top of concrete slabs, asphalt, etc, as discussed in detail in Castellaro and Mulargia (2009). A special case falling under this category is the presence of underground voids close to the surface, either natural or man-made (e.g., cellars, underground parking spaces). Castellaro and Mulargia (2009) present H/V curves for several example cases and discuss that under the absence of shallow velocity reversals, the common plot of the spectra of the horizontal and vertical components presents a characteristic oval shape around f_0, what the authors describe as 'eye shape'. According to the same study, the appearance of this feature suggests that the H/V peak is of stratigraphic origin. Also, when there are no velocity reversals the vertical component remains less than or equal to the horizontal component at all frequencies, hence H/V≥ 1, except for a small range near $2\times f_0$ where it can drop below unity due to the elliptic motion of Rayleigh waves (Fäh et al., 2001). In contrast, if the amplitudes of the H/V curve fall below 1 in regions distant from $2\times f_0$ and remain below 1 for a considerable range of frequencies, this may be evidence for a velocity reversal.

In this work, we further investigate the suggestion of Castellaro and Mulargia (2009) that the H/V curve over voids is expected to show characteristic drops below unity. More generally, we examine the working hypothesis that the method could be useful, at least as a complementary method, in the detection of underground voids. For this purpose, we have chosen as test site the Mycenaean cemetery of Voudeni in the Peloponnese, ~4 km east-northeast of the city of Patras. The archaeological site contains

numerous underground tombs that the Mycenaeans constructed more than 3000 years ago by carving into the soft rock (marl) of the area. Many tombs of different sizes and depths have been excavated and their geometry has been studied in detail by Turner (2020), making them ideal targets for our study.

Our study included three phases of ambient noise data collection and processing, which will be presented sequentially in the following. Data collection was conducted during daylight hours and when the archaeological site was not in operation to minimize nearby anthropogenic noise.

Three-Component Single-Point Ambient Noise Measurements Over Voids of Various Dimensions

In the first phase of our study, we performed single-point H/V measurements over several tombs of different dimensions targeting to 1) identify a characteristic imprint of voids on the shape of the H/V curves, as suggested by previous researchers, and 2) identify a possible correlation between the dimensions of the voids on the characteristics of this imprint. Data were collected using a Geometrics Atom-3C seismic acquisition unit with a 2Hz, three-component (3C) geophone and sampling rate of 4 ms (Nyquist frequency of 125 Hz). The sensor was placed over the centers of several ancient burial chambers, i.e. our target underground cavities, it was oriented to the North and was left to record ambient noise for at least 15 minutes. Since all targets are located at shallow depths (<1m to a maximum of 7-8m), longer recordings were not considered necessary.

Figure 1 shows an example measurement setting. The upper part of the Figure contains the plan view of a measured tomb (a; circled in red) and the side view of its detailed reconstruction (b; wireframe from photogrammetry) by Turner (2020). The lower part of Figure 1 (c-d) contains photographs of the tomb. In general, Mycenaean tombs include an entrance passage or “dromos”, a threshold or “stomion”, and the burial chamber/vault or “thalamos”. The facets of excavated tombs extend from the stomion floor to the ground, and we used them as reference planes to measure the distance to the center of the void chamber, first underground and then on the ground surface.

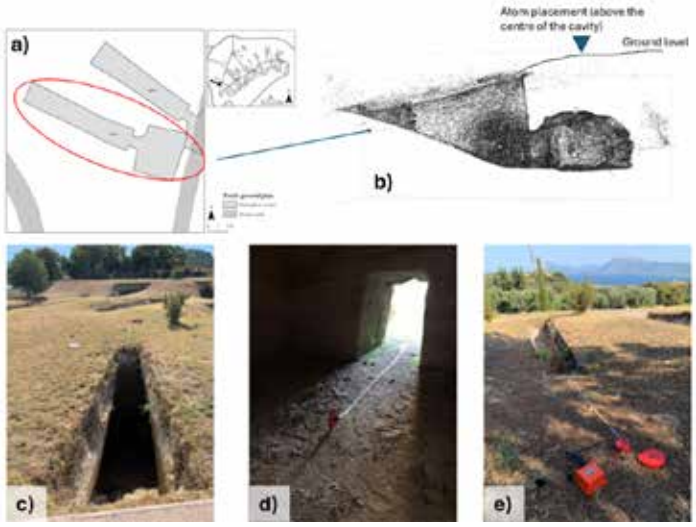


Figure 1. Example measurement setting: a) tomb (circled in red) ground plan and b) side view of its textured photogrammetric model by Turner (2020), c) photograph of the entrance pathway (dromos), d) photograph from the inside of the tomb (thalamos) looking at the stomion and e) photograph of the Atom-3C on the ground surface, over the void chamber.

Although our test site includes 78 excavated burial monuments, we were only able to measure 24, mostly because many chamber tops collapsed over the years or access to their tops was dangerous. Some geometric characteristics of these tombs, as provided by Turner (2020), are summarized in Table 1. The difference between the height of the dromos and the height of the vault is often a good proxy for the depth of the vault top.

The collected data were processed using using SPACPlus module of the SeisImager-sw software from Geometrics Inc. (https://www.geometrics.com/software/seisimager-sw/). Ambient noise time histories were trimmed at the beginning and end of each measurement to remove noise during instrument installation and removal. The common recording for the three components was then divided into segments of 512 samples, i.e. ~ 2 s duration, with an overlap of 50%. Fourier amplitude spectra were computed for each component and each recording segment, and the horizontal component spectra were geometrically averaged. Finally, the H/V ratio was computed for each segment and the results were visually inspected (both in terms of H/V curve shape and directly on the ambient noise records) to remove irregularly noisy segments and spectra. The remaining measurements were used to derive the mean H/V curve for each measured location.

Table 1. Geometric characteristics of the 24 Mycenaean tombs (after Turner, 2020, except those with * vault volume measured in the frame of this study) over which we performed ambient noise measurements.

Tomb Code	Vault Volume (m^3)	Dromos Height (m)	Vault Length (m)	Vault Width (m)	Vault Heigh (m)	Tomb Code	Vault Volume (m^3)	Dromos Height (m)	Vault Length (m)	Vault Width (m)	Vault Heigh (m)
01	20.63	2.33	2.47	2.94	2.05	34	32.9	3.16	3.16	3.09	2.33
02	17.42	2.36	2.2	4.04	1.83	42	18.7	2.11	2.48	2.66	1.71
06	16.98	2.24	2.16	2.51	1.76	43*	13.1	-	2.8	2.6	2.5
07	47.03	3.47	3.21	1.11	1.14	53	65.5	4.34	3.57	3.71	2.79
08	21.9	2.84	2.79	2.73	1.79	54	81.4	5.09	3.15	4.55	2.87
09	27.3	2.71	3.01	2.96	2.4	55	-	3.89	-	-	-
16	11.14	2.37	1.96	2.82	1.36	60	18.9	2.61	2.69	2.62	1.96
22	42.6	4.5	3.37	3.36	2.91	64	40	2.85	3.25	3.27	2.41
23*	20.4	-	2.3	2.3	1.8	71	28.3	3.64	3.18	3.15	2.7
25	126.3	4.29	4.79	3.9	4.09	72	17.11	2.92	2.63	2.71	2.21
28	13.49	2.21	2.39	2.65	1.96	75	257	6.6	5.08	7.6	4.57
29	82.1	3.93	3.66	4.7	3.29	78	106	5.47	3.8	4.58	3.23

Figure 2a shows an example output for the measurement over tomb 78 (Table 1). In the upper part of Figure 2a, the horizontal and vertical component spectra are compared, and it is clearly seen that, for a significantly wide range of frequencies (~22-38Hz), the vertical spectral amplitudes are larger than the horizontal, i.e., opposite to what is usually expected. This results in a drop of the H/V curve in the corresponding frequency range, as shown in the lower part of Figure 2a. The H/V returns to amplitude >1 at frequencies ~>35Hz.

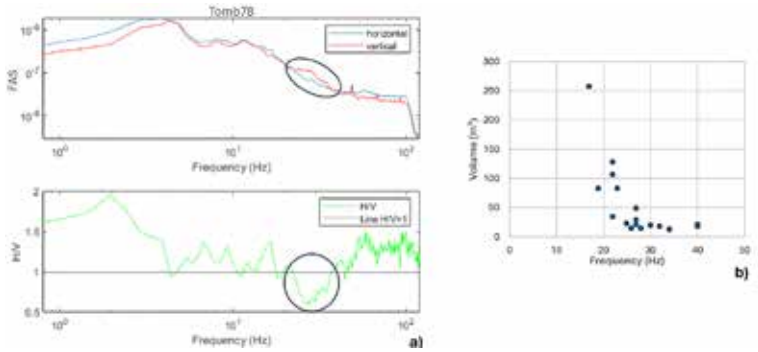


Figure 2. a) Example results of the H/V analysis of data over tomb 78. Upper part: Fourier amplitude spectra (FAS) of the horizontal and vertical components (in blue and red, respectively). The circled area is where the vertical component spectral amplitudes appear larger than the horizontal. Lower part: H/V spectral ratio. The circle marks the characteristic drop of the H/V ratio below unity, at high frequencies and for a significantly wide range. b) Underground void volume (in m^3) with respect to f_{DL} the frequency of initiation of the persistent H/V drop below 1Hz.

We define f_{DL} as the frequency above which we observe a sustained drop in H/V amplitude below 1, and we examined whether this discrete frequency is related to the volume of the underground void. The corresponding plot is shown in Figure 2b and implies an exponential relationship between the compared quantities, i.e. as the void volume increases, the frequency where H/V first drops below 1, in a clear and systematic manner, shifts to lower frequencies. This suggests that larger subsurface voids, at least at the shallow depths investigated here, affect the H/V curve at lower frequencies compared to smaller voids. However, this relationship appears to saturate (flattens) as void volumes become smaller (~<20-30m^3). A similar examination with respect to the depth of the tomb ceilings did not provide evidence for a clear relation, most probably because most ceilings are at very shallow depths of 0.5-1.5m and their geometry varies.

Three-Component Linear Array Ambient Noise Measurements Over a Large Void

One question raised by the previous measurements is how the persistent H/V drop varies spatially, and whether an underground void can be detected even if the ambient noise measurement is not taken directly over its center. Therefore, in the second part of our study, we collected data along a line over one example tomb to investigate, to some extent, the spatial variability of the shape of the H/V curve over a void. The test was conducted on tomb 75, which is the largest of the tombs examined in terms of volume (Table 1). The measurements were made in a linear arrangement across the center of the tomb. The total number of measuring

points was 13, with 2 m between successive measurements. The first was placed 6 m from the north side of the chamber and the last 10 m from the south side (Figure 3a, b).
Examples of results for two of the 13 sites are shown in Figure 3c, d. Specifically, results are shown for location S6, just above the center of the tomb (Figure 3c), and for S12, 5-6 m south of the tomb (Figure 3d). Focusing on the high frequency part of the results, the differences are quite pronounced with a very wide H/V drop below unity at S6 and a flat H/V curve around 1 at S12. Looking at the corresponding results for all 13 sites (not all are shown for reasons of space), the drop of the H/V curve below 1 clearly occurs at sites S4, S5, S6, S7, and S8 (Figure 3b), while at the remaining sites either no drop below 1 or drops within quite short ranges are observed.

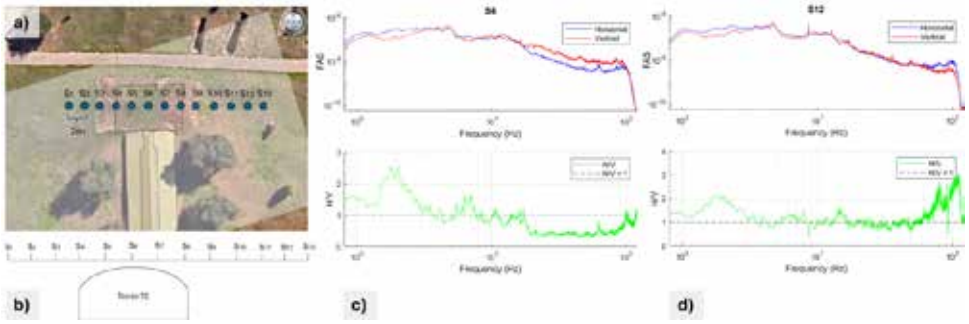


Figure 3. Linear array of 3C measurement points over one of the largest tombs (codenamed 75) in the Mycenaean Park of Voudeni a) in plan view and b) in cross section (depth and volume not to scale); c) Results for the example locations S6 right over the tomb and d) for S12, several meters to the south of the tomb. Top panels in c, d show the Fourier amplitude spectra of the horizontal and the vertical components and bottom panels the H/V curves.

From plots such as those in Figure 3c, d, it is difficult to understand the spatial variability of the results and even more difficult to understand whether the H/V drop is mostly due to de-amplification of the horizontal signal or amplification of the vertical signal. To better demonstrate the spatial variability of our results, we created spectrogram-like plot, but instead of time in the horizontal axis, we plotted the distance of each spectrum or H/V curve from S1. This creates a pseudo-2d spatial variation, which we show in Figure 4 in separate subplots for the amplitudes of the horizontal and vertical Fourier spectra and the H/V curve. The subplots for the horizontal and vertical components (Figure 4a, b) have the same color scale and are directly comparable. Note that since the horizontal axis shows the distance from S1, the measurements directly above the tomb are in the range of 6-14 m. This exact range is clearly colored differently in the H/V subplot (cool colors, mostly <1), starting from frequencies close to 20 Hz and continuing to much higher frequencies. This means that the changes in the wavefield due to the underground void are clearly imprinted on the spatial variability of the H/V amplitudes at high frequencies over the entire structure and not just over its center. In fact, the lateral extent of the structure is well captured in this subplot. By examining the individual component plots, we conclude that the H/V variation is mostly due to a corresponding spatial variation in the vertical component amplitudes (circled areas in Figure 4b). This means that the H/V drop over the studied underground void is mostly due to an increase of the vertical component amplitudes at high frequencies rather than a decrease of the horizontal component spectral amplitudes in the same range.

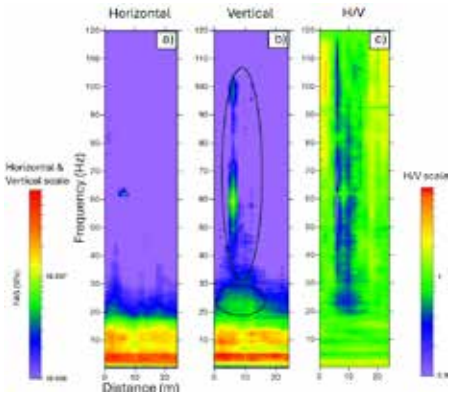


Figure 4. Pseudo-2D plot of results (spectral amplitudes or amplitude ratio vs distance from the starting measurement in the linear array) over tomb 75 for a) the horizontal Fourier amplitude spectra, b) the vertical Fourier amplitude spectra and c) the H/V amplitude. In the central plot for the vertical component, two prominent areas of spectral amplitude amplification are circled.

Vertical Component Linear Array Measurements Over Selected Voids

The preceding results indicated that it is possible to detect the presence of underground voids just by using the vertical component of ambient noise measurements. We further examined this potential by conducting measurements along a second linear array above two adjacent, smaller tombs. In this third phase of our work, we used 6 2Hz, 1-component geophones (Atom-1C, Geometrics), spaced every 1m along a line crossing over the chambers of tombs 28 and 29 (Table 1, Figure 5). The chambers of these two tombs are right next to each other and their separating "wall" was so thin that a small part collapsed, partly joining the two void spaces. It should also be noted that the chamber of tomb 29 is about 6-7 times larger in volume than the chamber of tomb 28 and that their floor depths differ by ~1.5m (Table 1). Fourier amplitude spectra for each recording were computed following the same processing steps as before and plotted against distance. The exact geometry and location of the linear array and the pseudo-2D variation of spectral amplitudes are shown in Figure 5. Distances are measured from geophone A1 (Figure 5a, b). At high frequencies (i.e., >~20Hz) in Figure 5b, we can clearly observe higher spectral amplitudes at distances corresponding to the locations of geophones A1 and A3-A5. A1 was placed exactly over the centre of tomb 28, whereas A3-A5 were over the chamber of tomb 29. A2 and A6 are close to the boundaries of the voids and although they also present elevated amplitudes at high frequencies, these are not as high, either because they are not directly over the voids or because of the lateral deepening of the vaulted tombs ceilings.

Another interesting observation in Figure 5b is that the spatial variation of the elevated spectral amplitudes suggests both the existence of two different voids (lower high frequency amplitudes at the location of A2 compared to those to the left and right of it) and their different dimensions (stronger imprint for tomb 29 and for a larger distance, comparable to the length of its chamber, ~4m). This suggests that denser measurements could provide an even better description of the geometry of the voids as well as their separation.



Figure 5. a) Geophones (A1-A6) placement over the void chambers of tombs codenamed 28 and 29 in the Mycenaean Park of Voudeni. b) Spatial variability of the spectral amplitudes of the vertical component of ambient noise recordings. Black frames mark the interpreted imprints of the two voids in the form of elevated amplitudes at high frequencies.

Conclusions/Discussion

We have tested the H/V method for its ability to contribute to the detection of underground voids as suggested by Castellaro and Mulargia (2009), using as test targets the chambers of Mycenaean tombs of various sizes in the archaeological park of Voudeni in the Peloponnese. We performed single point measurements over the center of the chambers as well as linear arrays over selected chambers using both 3C and 1C geophones. We have shown that the detection and even mapping of the lateral extent of voids by the H/V method is feasible considering the persistent drop of the H/V curve below 1 at high frequencies (in our test cases generally >20Hz). We also showed a correlation between void size and the frequency above which the H/V curve drops below 1. By separately examining the spatial variation of the horizontal and vertical spectral amplitudes over the voids, we concluded that the H/V drop below 1 is mostly due to an amplification of the vertical component rather than a de-amplification of the horizontal. This motivated us to further investigate the potential of detecting subsurface voids based on array measurements with 1C, vertical sensors alone, and we concluded that such an approach is indeed feasible.

Of the 24 single point measurements of ambient noise that we made over voids, 17 of them showed the expected drop in the H/V curve at high frequencies. The reason why the method "failed" in some cases is not yet understood and requires theoretical modelling beyond the scope of this initial feasibility study. It should be noted that although our test site is ideal in terms of the variety of void target sizes, it is also very complicated due to the density and often close proximity of tombs of different sizes, as well as the different shapes of chamber roofs (pyramidal, hipped, vaulted, arched). This was partly demonstrated in the third phase of our measurements, where we measured along a line over two adjacent tombs of different sizes.

Contrary to the preferred interpretation of Castellaro and Mulargia (2009), our results suggest that the drop of the H/V curve below 1 over voids is mainly due to increased spectral amplitudes in the vertical component. This does not mean that the horizontal component is not de-amplified, as would be expected above such an extreme velocity reversal (void within rock), but

that the amplification of the vertical component is more distinct, localized, and easier to detect in terms of its spatial variation. A possible explanation for why the vertical component is amplified above a void was proposed by Kolesnikov and Fedin (2017), who studied an experimental model and proposed the occurrence of standing P waves between the ground surface and the top of the void. This implies a vertical amplification at higher frequencies for shallower voids compared to deeper ones.

In conclusion, our tests support the findings and suggestions of the work of Castellaro and Mulargia (2009) that the H/V curve has special characteristics over voids. This means that the H/V method could be used in the geophysical prospection of underground voids, at least as a complementary method to other more tested and robust methods. Considering that the method is gaining popularity due to its ease of use and cost-effectiveness, it is important for the community to further investigate this possible additional use for void detection, a very common need in geophysical exploration with diverse applications such as archaeological prospection, geological hazard assessment, and infrastructure monitoring.

Our work also suggests that linear array measurements of the vertical component alone may be equally useful. Such measurements are routinely performed by most research groups for site characterization with low-cost equipment, and only require some targeted additional processing to be useful for void detection.

It should be emphasized that, as with all geophysical methods, the interpretation of the results of the proposed methods outside the geological context of a studied site is insecure, and there is always the potential - if not the certainty - that multiple other factors influence the measurements. Several such factors are reviewed and discussed in detail in Castellaro and Mulargia (2009), particularly in relation to the topic discussed here. H/V results can be useful for void detection but should always be corroborated with other geophysical methods for accurate subsurface characterization.

Acknowledgements

The study was carried out in the framework of the research project “UNMASK”, supported by the Hellenic Foundation for Research and Innovation (H.F.R.I.) under the “2nd Call for H.F.R.I. Research Projects to support Faculty Members & Researchers” (Project Number: 2724). We are greatly indebted to the Ephorate of Antiquities of Achaea, and more specifically to its director Dr. A. Koumousi and the archaeologists K. Aktypi and M. Gkazis, for providing the permit and facilitating us in every possible way to perform our measurements in the Mycenaean Park of Voudeni. We also thank them for providing us with supporting archaeological material.

References

Bard, P.-Y. (1998). Microtremor measurements: A tool for site effect estimation? In H. Irikura, K. Kudo, H. Okada, & T. Sasatani (Eds.), The Effects of Surface Geology on Seismic Motion (pp. 1251–1279). A.A. Balkema.

Bonilla, L. F., Steidl, J. H., Lindley, G. T., Tumarkin, A. G., & Archuleta, R. J. (1997). Site amplification in the San Fernando Valley, California: Variability of site effect estimation using the S-wave, coda, and H/V methods. Bulletin of the Seismological Society of America, 87(3), 710–730.

Bour, M., Fouissac, D., Dominique, P., & Martin, C. (1998). On the use of microtremor recordings for site effects studies: Application to the city of Nice (France). Pure and Applied Geophysics, 152(2), 275–288.

Castellaro S., Mulargia, F., 2009. The effect of velocity inversions on H/V. Pure appl. Geophys. 166, 567-592

Chen, Q.-F., Wang, W., & Zhao, J.-X. (2014). Ambient noise as the new source for urban engineering seismology and earthquake engineering: A case study from Beijing metropolitan area. Earthquake Science, 27(1), 89–100. https://doi.org/10.1007/s11589-013-0052-x

Fäh, D., Kind, F., & Giardini, D. (2001). A theoretical investigation of average H/V ratios. Geophysical Journal International, 145(2), 535–549.

Field, E. H., & Jacob, K. H. (1993). The theoretical response of sedimentary layers to ambient seismic noise. Geophysical Research Letters, 20(24), 2925–2928. https://doi.org/10.1029/93GL03168

Haghshenas, E., Bard, P.-Y., & Theodulidis, N. (2008). Empirical evaluation of microtremor H/V spectral ratio. Bulletin of Earthquake Engineering, 6(1), 75–108.

Kolesnikov Yu.I., Fedin K.V., 2017. Detecting underground cavities using microtremor data: physical modelling and field experiment. Geophysical Prospecting, 66, 342–353

Lermo, J., & Chávez-García, F. J. (1994). Are microtremors useful in site response evaluation? Bulletin of the Seismological Society of America, 84(5), 1350–1364.

Molnar, S., & Cassidy, J. F. (2006). A comparison of site response techniques using weak-motion earthquakes and microtremors. Earthquake Spectra, 22(1), 169–188.

Molnar S., Cassidy J. F., Castellaro S., Cornou C., Crow H., Hunter J. A., Matsushima S., Sánchez-Sesma F. J., Yong A., 2018. Application of Microtremor Horizontal-to-Vertical Spectral Ratio (MHVSR) Analysis for Site Characterization: State of the Art. Surv. Geophys. 39 ,613-631.

Nakamura, Y. (1989). A method for dynamic characteristics estimation of subsurface using microtremors on the ground surface. Quarterly Report of Railway Technical Research Institute (RTRI), 30(1), 25–33.

Nogoshi, M., & Igarashi, T. (1971). On the amplitude characteristics of microtremor (Part 2). Journal of Seismological Society of Japan, 24, 26–40.

Turner R. D., 2020. Grave reminders: Comparing Mycenaean tomb building with labour and memory, Sidestone Press.

Woolery, E. W., & Street, R. L. (2002). 3D near-surface soil response from H/V ambient-noise ratios. Soil Dynamics and Earthquake Engineering, 22(9–12), 865–876.

17th INTERNATIONAL CONGRESS of the Geological Society of Greece

BULLETIN OF THE GEOLOGICAL SOCIETY OF GREECE, SP. PUBL.

EXTENDED ABSTRACT 221

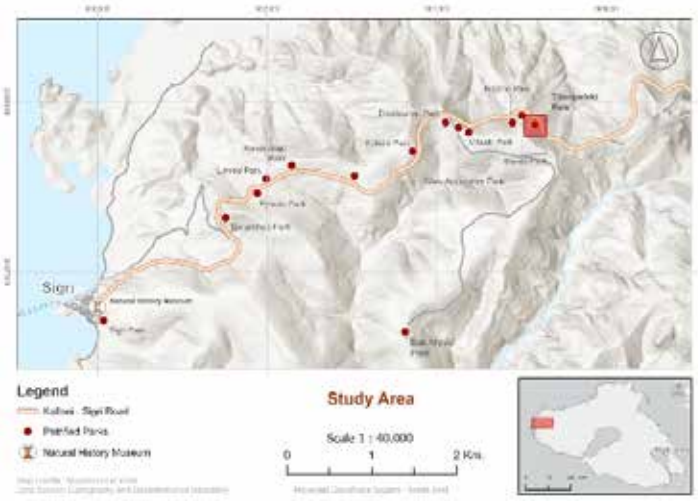
Multiscale 3D mapping and Geovisualization of a Petrified Forest Park in Lesvos, Greece, using UAV.

Moysidou L.[1], Papadopoulou E.E.[1], Proestakis S.[1], Zouros N.[1], Soulakellis N.[1]
(1) Cartography and Geoinformation laboratory, Department of Geography, University Of the Aegean, Mytilene, Greece.

Introduction / Background

The Petrified Forest of Lesvos, located in the western region of Lesvos Island, Greece, represents a unique petrified ecosystem that encompasses a significant number of fossilized tree trunks and animal remains. This exceptional natural monument was formed approximately 20 million years ago when volcanic activity covered the area in volcanic material, preserving the organisms in ashes. The volcanic deposits revealed an extensive array of fossils, including standing and recumbent fossilized trunks and petrified branches. (Natural History Museum of the Lesvos Petrified Forest, 2020)
To ensure the protection and systematic study of the Petrified Forest, the Natural History Museum of the Lesvos Petrified Forest was established in Sigri in 1994. The museum manages the petrified forest protected area, which spans an area of 15,000 hectares (Geo-Naturpark Bergstrasse-Odenwald., 2022). The Lesvos Petrified Forest was a founding member of the European Geoparks Network in 2000 and was later designated a Global Geopark in 2004, underscoring its geological and cultural significance (Zouros, 2007). Since 2015 the Lesvos island, is recognized as a UNESCO Global Geopark, including the Lesvos Petrified Forest as the geological heritage area of international significance.
Recent infrastructure projects, including the construction of the Kalloni-Sigri road, led to the discovery of numerous fossiliferous sites, including hundreds of fossilized tree trunks, branches, leaves and cones. The research activities for the excavation, conservation and protection of these findings as well as the presentation, interpretation and promotion of this important site facilitated by the integration of innovative geoinformation technologies, using unmanned aerial vehicles (UAVs), for multiscale and multitemporal 2D and 3D mapping.
This study specifically describes the 3D mapping methodology used for the Ioannis Toumpelekis Park (*Map 1*), a fossil site located in Akrocheiras hill, which comprises 212 fossilized tree trunks and branches (Apostolopoulou, 2024). The fossils within the park are categorized into two distinct stratigraphic sections. The lower section predominantly contains lying fossilized trunks, while the upper section is characterized by standing fossilized trunks belonging primarily to the hardwood tree family. The 3D mapping of the fossiliferous area of I. Toumpelekis park provides critical insights into the paleoenvironmental and geological conditions that contributed to the preservation of the forest.

This research emphasizes the use of advanced geoinformation technologies to study and visualize the fossilized ecosystem comprehensively. A multi-scale 3D geovisualization workflow is employed, encompassing data acquisition, processing, modeling, and visualization. UAV technology plays a central role in data acquisition, delivering high-resolution imagery that forms the foundation for detailed 3D models. By integrating UAV-derived images, photogrammetric 3D models, and panoramic imagery, this study creates an immersive and interactive virtual environment, enhancing the understanding and presentation of this unique paleontological and geological heritage.



Map 1. Study Area located at the western part of Lesvos island, North Aegean, Greece

Objectives

The primary objective of this research is to explore and implement multi-scale 3D mapping and geovisualization methods for the study area. To achieve this goal, a comprehensive methodology was developed, encompassing both data acquisition and the presentation of findings. This approach involves the following key steps:

1. Data acquisition: High-resolution data were collected at two different ground sampling distances (GSD) using the DJI Mavic 3E, ensuring the accuracy and detail required for subsequent analysis.
2. 2D thematic orthophoto map construction: The collected data were processed to generate detailed thematic orthophoto maps, providing a georeferenced representation of the study area.
3. Development of a multiscale 3D model: A multi-scale 3D model of the study area was created, enabling a detailed representation of both park and fossil-scale features.
4. Creation of 3D animated maps: Animated visualizations were developed to enhance the communication of spatial and temporal data, offering dynamic perspectives of the study area.
5. Construction of an immersive virtual reality (VR) application: A VR application was designed to provide an interactive and immersive experience, allowing users to explore the fossilized park in a virtual environment.

This methodology integrates state-of-the-art geoinformation technologies to advance the study and presentation of complex fossilized ecosystems. The resulting outputs contribute to a deeper understanding of the site and demonstrate the potential of innovative mapping and visualization tools in geoscientific research.

Materials and Methods

In the following workflow, all the stages of the methodology are presented in detail, structured into three (3) main stages: 1. Data Acquisition, 2. Data Processing, and 3. Geovisualizations. (*Figure 1.*):

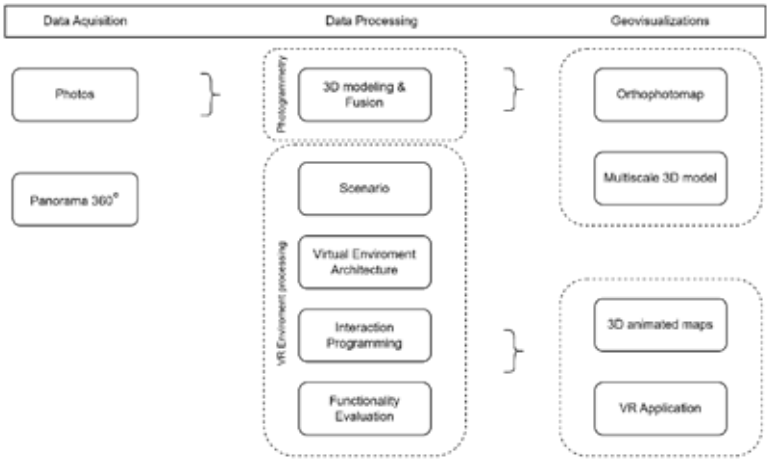


Figure 1. Methodology workflow.

Data Collection

The dataset for the present study was acquired through the deployment of unmanned aerial vehicles (UAVs) for the cartographic documentation of Ioannis Toumpelekis Park and its fossilized tree trunks at two different mapping scales. Specifically, a DJI Mavic 3 Enterprise UAV, featuring a 48 MP camera and a Real-Time Kinematic (RTK) positioning system, was employed to ensure the collection of high-precision spatial data.

Flight operations were carried out in two sessions, on May 1, 2023, and August 31, 2023, at flight altitudes of 70 meters and 2 meters, respectively. These sessions were planned under favorable weather conditions and optimal sunlight to reduce shadow interference and enhance the quality of the captured data. The utilization of the RTK system facilitated positional accuracy, achieving precision of up to 1 cm horizontally and 1.5 cm vertically, thereby obviating the requirement for ground control points. The data acquisition was conducted at two different scales: 1. park-scale (1:150) and 2. petrified tree trunk-scale (1:10). Overlap parameters were set at 80% frontally and horizontally to optimize the creation of image based 3D models and the orthophoto-map. Additionally, 360° panorama was captured at 50m height of flight, providing contextual visuals of the study area for VR geovisualization. (*Table 1.*)

Date	Height of flight	Type of data	Gimbal pitch	Scale	Type of flight
01/05/2023	70m.	Photos	Nadir	Park	Flight plan
	60m.	Photos	Oblique	Park	Manual
	50m.	Panorama	-	Broader Study area	Automatic
	2m.	Photos	Oblique	Fossil 109	Manual
				Fossil 111	
				Fossil 116	
				Fossil 117	
				Fossils F1-F9	
31/08/2023	2m.	Photos	Oblique	Fossil 105	Manual
				Fossil 119	

Table 1. Data acquisition information

Image based 3D Modelling

The 3D models for this study were constructed using a systematic workflow designed to ensure high precision and photorealistic outputs. The process began with the generation of a sparse point cloud, followed by the creation of dense point clouds from UAV imagery utilizing the Structure from Motion (SfM) algorithm (Papadopoulou et al., 2022). The sparse point cloud provided an initial geometric framework, while the dense point cloud added detail, accurately capturing surface features essential for realistic modelling.

.

Subsequently, a total of thirteen (13) 3D models were generated by interpolating the dense point cloud data. Twelve (12) of these 3D models were the fossilized trees within the study area and one (1) 3D model depicting the entirety of the park. Textures were then applied to the meshes, ensuring photorealistic visual fidelity. The fusion approach was employed to refine and fuse the models, maintaining high accuracy across both park-scale and tree trunk-scale. This process involved extracting areas containing fossilized tree trunks from the park-scale model and replacing them with high-detail fossil 3D models derived from data captured at a 2-meter flight altitude. (*Figure 2*). The resulting multiscale 3D model of the park enabled seamless transitions between different scales, providing detailed visualizations of the fossilized tree trunks while retaining the broader contextual information of the park.

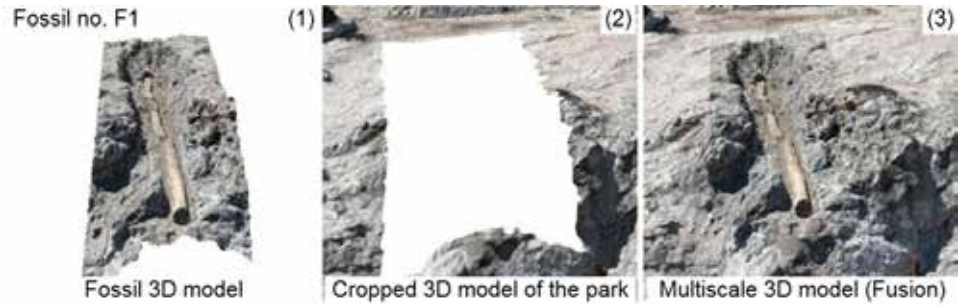


Figure 2. Multi-scale 3D model.

Geovisualization Methods

In the final stage, the 3D models were integrated into a virtual reality (VR) environment utilizing Twinmotion, a real-time 3D visualization software powered by Unreal Engine. This integration facilitated the development of an immersive and interactive experience, enabling users to virtually explore the park. Key features included 3D animated maps, interactive hotspots, and supplementary information highlighting the park's petrified tree trunks.

The development of the VR environment required the establishment of a structured methodology to define the content and features to be presented within the application (Papadopoulou et al., 2022). The process involved the following stages:.

- Scenario Design.
- Virtual Environment Architecture.
- Interaction Programming.
- Functionality Evaluation.

The Virtual Reality (VR) application integrated a 360° panoramic backdrop to enhance spatial awareness and realism within the virtual environment. The incorporation of thematic maps, dynamic animations, and supplementary 3D models—such as fences, staircases, animated human figures, vehicles, and vegetation—further enriched the immersive experience. By adhering to interactive design principles, the application facilitated both free exploration and structured, guided tours, offering users an engaging and intuitive navigation experience.

Results – Discussion

Multiscale 3D Model

The multiscale 3D model was developed through the integration of twelve (12) high level of detail 3D models of fossilized tree trunks with a single (1) overarching model representing the entire Park. This multiscale 3D modeling approach was employed to enhance the overall quality and accuracy of the park's virtual representation by incorporating detailed reconstructions of the petrified tree trunks. The seamless integration of these models enabled a comprehensive visualization of the fossils within their broader natural environment, supporting both interpretative analysis and educational outreach. *(Table 2)*

Fossilized Tree Trunks	Points	Surfaces	Photos	Quality
Fossil no. 105	1,176,473	78,431	53	medium
Fossil no. 109	352,540	47,428	16	medium
Fossil no. 111	552,250	26,381	26	medium
Fossil no. 116	563,681	144,295	35	medium
Fossil no. 117	1,745,749	349,149	57	medium
Fossil no. 119	3,095,251	619,049	76	medium
Fossil no. F1	777,563	200,155	20	medium
Fossil complex no. F2, F3	1,822,312	424,745	23	medium
Fossil complex no. F4, F5	167,888	75,720	38	medium
Fossil no. F6	2,440,954	162,185	103	medium
Fossil complex no. F7, F8	12,488,838	2,102,240	24	High
Fossil F9	1,032,177	203,383	82	medium
Multiscale 3D model	**24,497,102**	**4,835,635**	**594**	**medium**

Table 2. 3D models information

3D Animated Maps

To further enhance the visualization of the park's multiscale 3D model, a series of 3D animated maps were developed. These maps provided detailed visual representations, accurately depicting both standing and lying petrified tree trunks in their natural positions. The implementation of 3D animated maps offers significant potential as an educational tool for students, researchers, and educators, facilitating a deeper understanding of complex geological processes associated with the evolutionary history of the Petrified Forest of Lesvos.

A total of nine (9) 3D animated maps were generated utilizing two specialized software platforms: Agisoft Metashape and Twinmotion. Of these, seven (7) animations focused on individual petrified tree trunks, while two (2) provided comprehensive visualizations of the entire park. To enhance accessibility, these animations have been made available via the YouTube platform and can also be accessed through QR codes embedded within the park's orthophoto map, offering user-friendly experience. (link : https://www.youtube.com/watch?v=GwVFHR6T2EY&t=150s)

Virtual Reality Application

A virtual reality (VR) application was developed to present the multiscale 3D model of the park and to highlight the high level of detail 3D models of petrified trunks in their natural environment. This application also provides users with information A Virtual Reality (VR) application was developed to showcase the multiscale 3D model of the park, emphasizing the high level of detail in the 3D representations of the petrified tree trunks within their natural environment. In addition to immersive visualization, the application provides users with valuable information regarding: (1) the Petrified Forest of Lesvos, (2) the newly established petrified parks along the Kalloni–Sigri road, and (3) the specific study area. This interactive platform enhances user engagement and serves as an educational tool for exploring the geological and cultural significance of the site.

In the Virtual Reality (VR) application, users commence their experience at the entrance of I. Toumpelekis Park, where an introductory series of maps provides insights into the park's geological significance and spatial context. The application incorporates dynamic interactive features, such as the automatic opening of the park gate and the exploration of a detailed 3D animated map—developed in Twinmotion—that illustrates the walking paths and the distribution of petrified tree trunks. A key feature of the experience is the interactive engagement with tree trunk no. 105, which, when approached, activates a 1:1 scale visualization of the fossil's current state. The immersive journey concludes with a 360° panoramic view, offering users a comprehensive spatial perception of the site. (Figures 3-4)

.



Figure 3-4. VR application contents

Conclusions.

.The development of a multiscale 3D model and its integration into a virtual reality (VR) application for the Park, demonstrated both the potential and challenges associated with employing advanced geospatial technologies for the geovisualization of geosites.

Multiscale 3D model:.

1. The multiscale 3D model successfully combined detailed reconstructions of the petrified tree trunks with a broader, lower-level of detail 3D model of the park, enhancing visual fidelity while preserving environmental context. However, challenges were encountered during the management of the multi scale 3D model within platforms such as Twinmotion and Blender. Issues such as the misalignment of models required manual adjustments, including relocating pivot points and realigning coordinates, to ensure seamless integration.
2. **3D animated maps**:.
3. The 3D animated maps provided an innovative way to visualize the multi-scale 3D model, delivering significant educational value. Nevertheless, certain limitations emerged, including incomplete models and texture distortions caused by insufficient image overlap during UAV data acquisition. Furthermore, user interactivity was constrained to predefined perspectives, limiting the ability to explore specific points of interest freely.
4. **VR application**:.
5. The VR application offered an immersive and educational experience, enabling users to explore the park and visualize the detailed petrified tree trunks in their natural environment at a 1:1 scale. Despite its potential, the implementation revealed technical challenges, including scaling 3D models accurately and managing panoramic displays without distortion. Additionally, the requirement for high-performance computational systems imposed financial constraints, potentially limiting accessibility for institutions with restricted resources.

These findings highlight the potential of multiscale 3D modeling and VR applications to revolutionize geovisualization in geosites while emphasizing the need for further advancements in technology to overcome existing limitations.

References

The Forest under the Road, 2020. Natural History Museum of the Lesvos Petrified Forest. https://www.lesvosmuseum.gr/en/exhibitions/forest-under-road [Online Resource]

Lesbos Island UNESCO Global Geopark, 2022. Geo-Naturpark Bergstrasse-Odenwald. https://geo-naturpark.net/en/network/geopark-partnerships/lesbos-island-unesco-global-geopark/ [Online Resource]

Zouros, N., 2007. Geomorphosite assessment and management in protected areas of Greece: Case study of the Lesvos island – coastal

geomorphosites. Geographica Helvetica 62(3), 169–180. https://doi.org/10.5194/gh-62-169-2007 [Journal Article]

Apostolopoulou, N., 2024. Στρωματογραφική αποτύπωση των πυροκλαστικών αποθέσεων του όρους Ακρόχειρας (Λέσβος) με τη χρήση ψηφιακών μέσων. University of Patras, Patras, Greece.

Papadopoulou, E.-E., Papakonstantinou, A., Kapogianni, N.-A., Zouros, N., Soulakellis, N., 2022. VR multiscale geovisualization based on UAS multitemporal data: The case of geological monuments. Remote Sensing 14(17), 4259. https://doi.org/10.3390/rs141742590 [Journal Article]

17th INTERNATIONAL CONGRESS of the Geological Society of Greece

BULLETIN OF THE GEOLOGICAL SOCIETY OF GREECE, SP. PUBL.

EXTENDED ABSTRACT 222

Investigating Drought Dynamics in Greece Using Climate and Meteorological Indicators

Mpakopoulou Ch.[1], Tsesmelis D.[2], Kalogeropoulos K.[3], Vasilakou K.[4], Feloni E.[3,*], Zervas E.[5], Tsatsaris A.[3]

(1) Laboratory of Technology and Policy of Energy and Environment, School of Applied Arts and Sustain-able Design, Hellenic Open University, 26335 Patras, Greece

(2) Department of Agriculture, University of Patras, Messolonghi Campus, 30200 Messolonghi, Greece

(3) Department of Surveying and Geoinformatics Engineering, University of West Attica, 28 Ag. Spiridonos, 12243 Egaleo, Athens, Greece; efeloni@uniwa.gr

(4) Department of Natural Resources Development and Agricultural Engineering, Agricultural University of Athens, 11855 Athens, Greece (5) Laboratory of Technology and Policy of Energy and Environment, School of Applied Arts and Sustainable Design, Hellenic Open University, 26335 Patras, Greece

Background

This study investigates droughts in Greece based on the meteorological relative humidity index (Tsesmelis *et al.*, 2019, 2021, 2022). Droughts, temporary natural conditions tied to water availability, result from low regional rainfall (Karavitis, 1996; Lujala *et al.*, 2015; Feloni *et al.*, 2017). Their frequency, duration, and severity vary, impacting water resources and ecosystem recovery (Fleming-Muñoz *et al.*, 2023; Pizzorni *et al.*, 2024). Relative humidity (RH) measures air moisture relative to its maximum capacity under the same temperature and pressure (Kiem *et al.*, 2016). Using RH data from 42 Hellenic National Meteorological Service (HNMS) stations (1971–2004), the Standardized Relative Humidity Index (SRHI) was calculated at 1, 3, 6, 9, and 12-month intervals. Diagrams illustrated index changes, while drought maps, created via Inverse Distance Weighting, visualized annual SRHI12 and SRHI6 values. Analysis identified 1989–1990 as the most severe drought, followed by 2000–2001. Additionally, this study explores climate variability in Greece through statistical analysis of RH data from the same stations (1975–2004).

RH measures water vapor in relation to air temperature (US Department of Commerce, n.d.). It is the most used humidity index. It is defined as the ratio of the actual amount of water vapor in the air to the maximum amount it can hold under the same temperature and pressure conditions. In other words, it is defined as the ratio of hydrometric parameters to their corresponding values at saturation, as follows:

$$RH = mv/mvs \text{ } or \text{ } RH = e/es \text{ } or \text{ } RH = r/rs \text{ } or \text{ } RH = q/qs$$

Where: RH: relative humidity, m and mvs: mass of water vapor and the corresponding value at saturation, e and es: vapor pressure and the corresponding value at saturation, r and rs: mixing ratio of air and the corresponding value at saturation, q and qs: specific humidity and the corresponding value at saturation.

Relative humidity is expressed as a percentage (%) and always has a value ≤1. In practical terms, its value indicates how far the current state is from the corresponding saturation state, which occurs when there is fog or rain.

Drought is a complex climatic phenomenon that often occurs over large spatial and temporal scales. It is frequently accompanied by severe social impacts resulting from the reduction in the available quantity of water for human consumption, as well as for agricultural and livestock activities. The attempt to find a precise definition has led to the conclusion that it is a temporary natural phenomenon related to water availability, which usually results from low average rainfall values. It has an uncertain frequency, duration, and severity, causing significant impacts on water availability and the ability of the ecosystem to recover to its original state (Stathopoulos *et al.*, 2018).

Objectives

This study aims to investigate the impact of climate change (CC) in Greece by analyzing climate indices using meteorological data. The primary research question focuses on determining whether and to what extent global CC has influenced the climate of Greece. The literature offers a wide range of indices for assessing both qualitative and quantitative changes in climate. Through the processing and statistical analysis of carefully selected and formatted indices, a more in-depth analysis will be conducted compared to previous reports and records (Tsesmelis, 2017; Tsesmelis *et al.*, 2022, 2023). This study can comprehensively define the key elements related to climate, CC and drought phenomena.

Methods

The lack of studies correlating humidity with the occurrence of potential drought phenomena was the impetus for

further study and analysis in this work. In the first stage, humidity measurement data were collected from 42 HNMS stations across the country. These values were processed to produce daily and then monthly data. For each station, a file was created using a spreadsheet program (Excel) in which the minimum, maximum, mean, median, and standard deviation for each month of each year (from 1971 to 2004) were recorded, in order to make an initial estimate of the general trend of humidity measurements. The same process was followed again after the humidity measurements for each station were grouped to obtain the above statistical values for each study year. Subsequently, the monthly humidity values for each station were entered into a suitable programming language where the SRHI (Standardized Relative Humidity Index) was calculated for each station separately. The index was calculated for all time steps: one month (SRHI1), three months (SRHI3), six months (SRHI6), nine months (SRHI9), and twelve months (SRHI12). Using the values obtained from the program, graphs were created to depict the monthly variations of the indices for all years. In this way, an initial qualitative check of the processed data was performed. In order to study, understand, and interpret the results of the above analysis more extensively and ultimately draw conclusions, the creation of maps was initiated in the next stage. Using the spreadsheet program (Excel) again, a workbook was created in which the codes and names of the stations, the coordinates of each station (x and y in EGSA 87), and the results of SRHI6 and SRHI12 were recorded. Subsequently, 3 maps were created for each year based on the values of SRHI6 for the 6th and 12th month and SRHI12 for the 12th month, respectively. The creation of the maps using the geostatistical method of Inverse Distance Weighting, in which both the extreme values and the colors that represent them with blue (wet period) and red (dry period) were defined. The index used for the analysis is the Standardized Relative Humidity Index (SRHI). The SRHI uses a non-parametric standardization approach. First, the empirical probabilities of the relative humidity data are calculated using the empirical plotting position of Gringorten (Farahmand *et al.*, 2015).

$$p(RHi) = (i-0,44)/(n+0,12)$$

where i: the rank of the relative humidity data from the smallest, n: the sample size
The empirical probabilities of the relative humidity data are standardized as follows:

$$SRHI = \Phi\text{-}1(p(RHi))$$

where: Φ-1 is the inverse standard normal distribution function with mean zero and standard deviation one. The standardization is based on the following approximation:

$$SRHI = \begin{cases} \\ \end{cases} \quad 1+d_1t+d_2t^2+d_3t^3$$

where: c_0=2,52, c_1=0,80, c_2=0,01, d_1=1,43, d_2=0,19, d_3=0,00
and:

$$t = \begin{cases} \sqrt{\quad p(RHi)^2} \\ \end{cases}$$

Negative values of the SRHI index indicate relative humidity below the average and are suggested as a measure of dryness according to climatology. The following table (Table 1) presents the scale of the index values.

Table 1. Categorization of SRHI index values.

SRHI values	Category
> 2.00	Extremely Wet
1.50 to 1.99	Very Wet
1.00 to 1.49	Moderate Wet
0.50 to 0.99	Mild Wet
-0.49 to 0.49	Normal Conditions
-0.50 to -0.99	Mild Drought
-1.00 to -1.49	Moderate Drought
-1.50 to -1.99	Severe Drought
<-2.00	Extreme Drought

The HNMS operates 178 surface stations across Greece and three upper-air stations (Elliniko, Heraklion, Macedonia-Mikra). These stations record primary climate data every three hours, 24/7, for analysis and processing. This study utilized humidity data from 42 stations nationwide.

Results and Discussion

Although the index was analyzed at 1-, 3-, and 9-month intervals, SRHI6 was emphasized in diagrams and maps due to Greece's typically high humidity from October to March. Since humidity varies across regions, SRHI12 was also included. Calculating SRHI at these intervals produced 42 diagrams, with two representative examples shown (Figure 1).

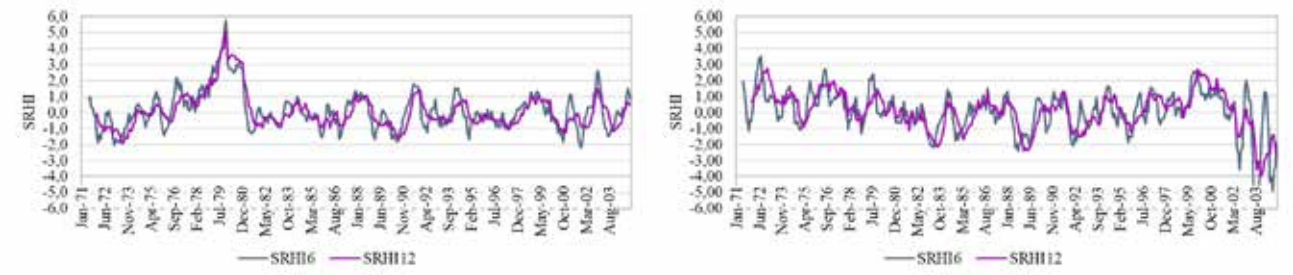


Figure 1. The SRHI index with a time scale of 6 and 12 months for the Lemnos meteorological station where a period of exceptional humidity is observed (left panel) and Methoni where a period of extreme drought is observed (right).

Analysis of the diagrams reveals multiple instances of low index values, indicating past droughts, even before rapid urbanization and increased water consumption. To better visualize drought periods nationwide, 102 maps were generated using Inverse Distance Weighting (IDW) in ArcGIS Pro 3.3—one for SRHI12 and two for SRHI6 annually. Drought patterns varied over the years. Severe droughts affected Arta, southern Peloponnese, Rhodes, and Sitia in 1971–1973, culminating in an extreme nationwide drought in 1974. Another severe drought occurred in 1977, mainly impacting Central Greece and Sitia. From 1979 to 1982, conditions were mostly normal, with localized wet and dry periods. Moderate droughts emerged in southeastern Greece in 1983, followed by a wet phase in 1984, which ended in late 1984 with recurring droughts through 1986, particularly in northern and western Central Greece. A significant shift began in 1988 with moderate drought across western Greece (SRHI12) and nearly the entire country (SRHI6). The most extreme drought occurred in 1989–1990, affecting almost the entire country, with SRHI6 showing more intensity than SRHI12. After milder droughts in 1992–1993, Crete (1995) and Evros (1996) faced localized dry conditions. In 1997, severe drought impacted Epirus, western Macedonia, Thira, and Rhodes. Moderate to severe drought appeared in central Peloponnese (1999), escalating nationwide in 2000–2001, especially in eastern Greece and later across nearly the entire country. In 2002, while Evros faced mild drought, much of Greece experienced unusually wet conditions, particularly Central Greece and Crete. By 2003, extreme drought was again localized in western Peloponnese, Evros, and the Cyclades. This study highlights key drought years: 1974, 1977–1978, 1983–1984, 1985–1986, 1989–1990, 2000–2001, and 2003. In contrast, 2002 was a year of high humidity. Notably, Pyrgella recorded extreme drought values of -6.60 in 1974 and an unprecedented -7.86 in 1975, despite the latter year not being generally dry (Figure 2).

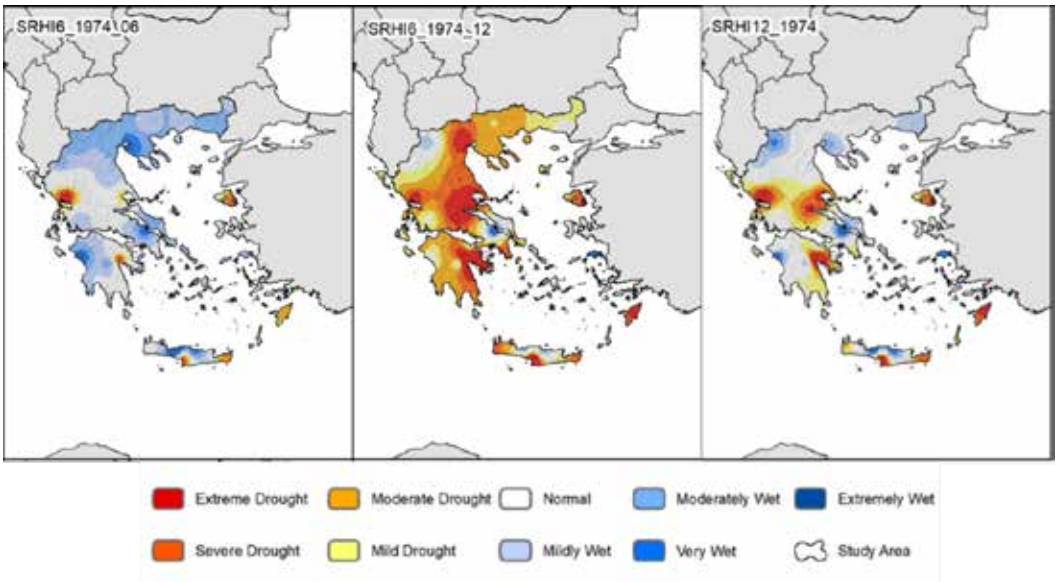


Figure 2. SRHI6 and SRHI12 maps for the year 1974.

The 1977–1978 drought was severe in many regions but not the most extreme recorded. This was followed by 1983–1984, when SRHI6 indicated moderate to high humidity across much of Greece, while SRHI12 showed a milder trend. A similar pattern occurred in 1985–1986, with severe to extreme drought in some areas (SRHI6), but a less intense picture from SRHI12.

In 1988, an extreme drought began, culminating in the devastating 1989–1990 drought—one of Greece's longest and most intense. Nearly the entire country experienced extreme drought, severely impacting agriculture and the economy. June 1990 was the worst month (SRHI6) (Figure 4). To mitigate the crisis, authorities explored solutions, including a proposal by the National Technical University of Athens to transport water by ship, prompting immediate government action (Tsesmelis, 2010).
The next significant drought occurred in 1993, though milder than previous events. It affected much of Northern Greece, Thrace, the Aegean islands, and the Dodecanese. Islands faced heightened drought issues in summer due to increased water consumption from tourism.
In 2000, Greece experienced the most severe drought since 1990, initially impacting Central Greece and northeastern Aegean islands. By year's end, drought spread across the country, with severe crop damage in northern Greece (Figure 5).
In 2001, drought conditions persisted, notably affecting central Peloponnese, Central Greece, and Thrace, but weakened towards the end of the year, returning the country to normal conditions.
Although 2003 had minimal drought issues, localized extremes were observed, such as in Methoni, where SRHI6 recorded the study's most extreme value of -8.11 in August (Figure 6).
Notably, unlike the recorded droughts, 2002 saw exceptionally wet conditions across most of Greece (Figure 7).
Monthly relative humidity analysis revealed two distinct periods: October–March, characterized by high humidity, and April–September, when levels are generally lower. This pattern is evident in station diagrams, though more pronounced in some locations than others.

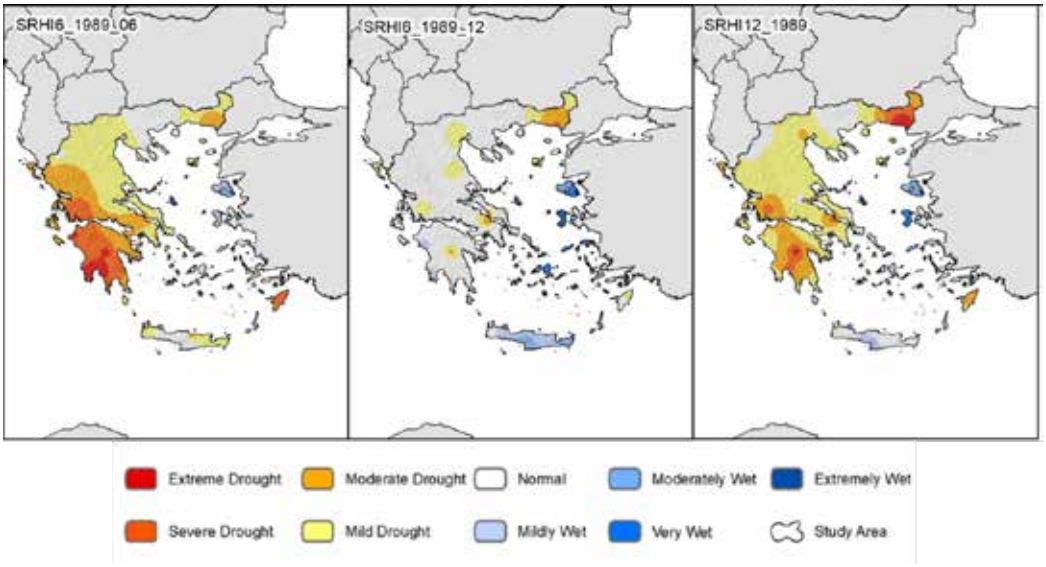


Figure 3. SRHI6 and SRHI12 maps for the year 1989.

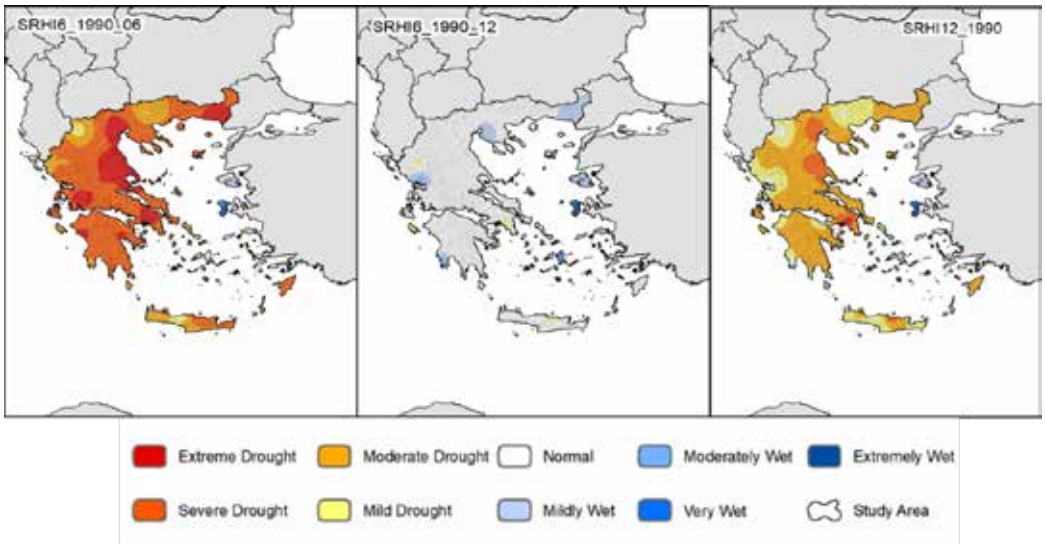


Figure 4. SRHI6 and SRHI12 maps for the year 1990.

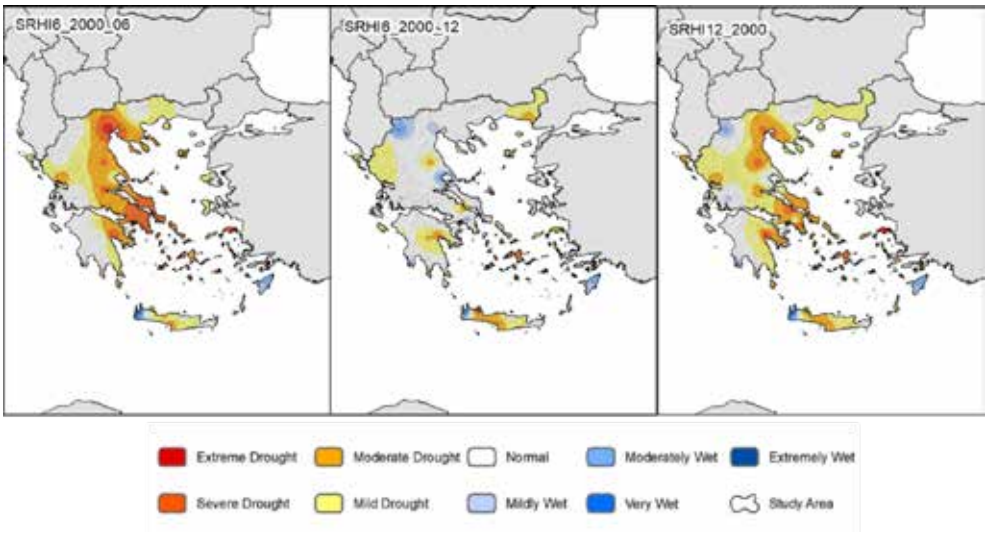


Figure 5. SRHI6 and SRHI12 maps for the year 2000.

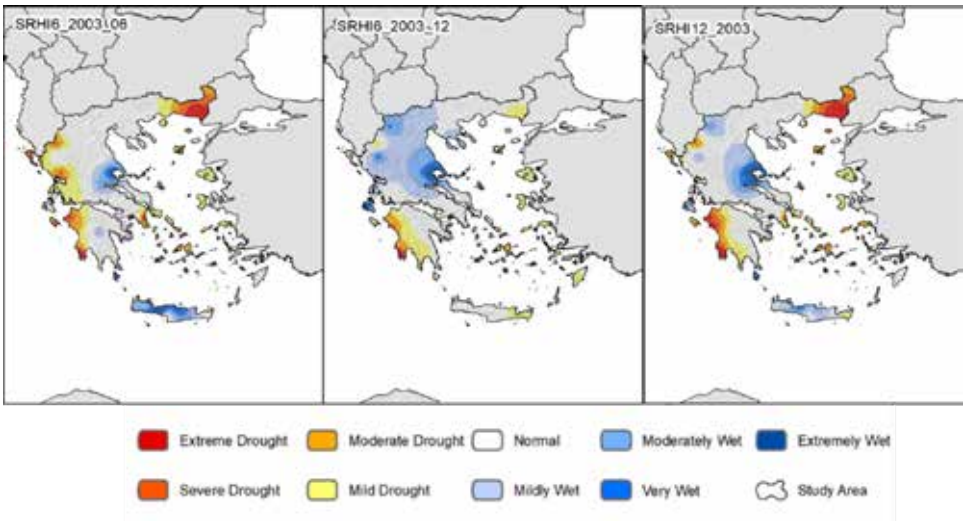


Figure 6. SRHI6 and SRHI12 maps for the year 2003.

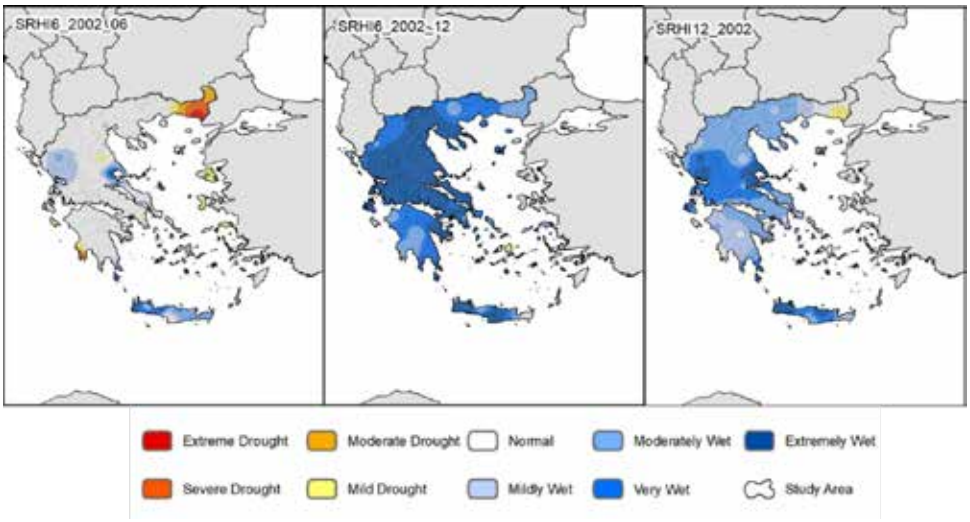


Figure 7. SRHI6 and SRHI12 maps for the year 2002.

Conclusions

This study investigates the drought phenomena in Greece from 1971 to 2004 to assess the long-term variability of climate over the years. Using humidity data from 42 HNMS stations across the country, the Standardized Relative Humidity Index (SRHI) was employed for analysis, with results presented through diagrams and maps. The findings highlight the widespread impact of droughts, particularly in island regions, which face unique challenges due to their geographic and socio-economic characteristics. Island areas, especially during the summer months, are particularly vulnerable to droughts. The increased influx of tourists significantly raises water consumption, exacerbating the already limited water resources available. This effect was observed notably in the Aegean islands and the Dodecanese, where droughts became more severe during peak tourist seasons. The study showed that, while mainland regions experience droughts of varying severity, the islands are often at greater risk due to their dependence on limited freshwater supplies, which are further strained by seasonal population increases.

The severe droughts of 1993, 2000, and 2001 particularly impacted the eastern islands, such as those in the northeastern Aegean. These regions experienced significant agricultural losses, which were compounded by the added strain of water scarcity caused by tourism. The 2000–2001 drought was among the most severe since 1990, with widespread consequences for both agriculture and the local economy, disproportionately affecting northern Greece and the islands. This pattern underlines the critical importance of addressing the unique vulnerabilities of island areas in future drought management strategies.

The overall trend shows that Greece's vulnerability to droughts has intensified, driven by both global CC and the substantial increase in water use. The combination of rising temperatures and heightened water consumption calls for immediate and proactive measures to mitigate drought impacts. The study underscores the urgent need for comprehensive drought prevention and management plans, tailored to both mainland and island regions, to minimize the economic and ecological consequences of future droughts. Given the significant challenges posed by droughts, particularly in island areas, further research is essential to develop more robust strategies for water conservation, sustainable tourism, and regional drought preparedness. With proper planning and management, the impact of droughts can be better mitigated, making their management more effective and less disruptive.

References

Farahmand, A., AghaKouchak, A., & Teixeira, J. (2015). A Vantage from Space Can Detect Earlier Drought Onset: An Approach Using Relative Humidity. *Scientific Reports*, *5*(1), 8553. https://doi.org/10.1038/srep08553

Feloni, E.G., Kotsifakis, K.G., Nastos, P.T. & Baltas, E.A. (2017). SPI analysis over Greece using high resolution precipitation gridded datasets. Eur. Water, 60, pp.319-326.

Fleming□Muñoz, D. A., Whitten, S., & Bonnett, G. D. (2023). The economics of drought: A review of impacts and costs. *Australian Journal of Agricultural and Resource Economics*, *67*(4), 501–523. https://doi.org/10.1111/1467-8489.12527

Karavitis, C. A. (1996). Regional Water Transfers and Drought Management Strategies. In J. Ganoulis, L. Duckstein, P. Literathy, & I. Bogardi (Eds.), *Transboundary Water Resources Management* (pp. 451–457). Springer Berlin Heidelberg. https://doi.org/10.1007/978-3-642-61438-5_29

Kiem, A. S., Johnson, F., Westra, S., Van Dijk, A., Evans, J. P., O'Donnell, A., Rouillard, A., Barr, C., Tyler, J., Thyer, M., Jakob, D., Woldemeskel, F., Sivakumar, B., & Mehrotra, R. (2016). Natural hazards in Australia: Droughts. *Climatic Change*, *139*(1), 37–54. https://doi.org/10.1007/s10584-016-1798-7

Lujala, P., Lein, H., & Rød, J. K. (2015). Climate change, natural hazards, and risk perception: The role of proximity and personal experience. *Local Environment*, *20*(4), 489–509. https://doi.org/10.1080/13549839.2014.887666

Pizzorni, M., Innocenti, A., & Tollin, N. (2024). Droughts and floods in a changing climate and implications for multi-hazard urban planning: A review. *City and Environment Interactions*, *24*, 100169. https://doi.org/10.1016/j.cacint.2024.100169

Stathopoulos, N., Skrimizeas, P., Kalogeropoulos, K., Louka, P., & Tragaki, A. (2018, October). *Statistical Analysis and Spatial correlation of rainfall in Greece for a 20-year time period*.

Tsesmelis, D. E. (2017). *Development, implementation and evaluation of drought and desertification risk indicators for the Integrated Management of Water Resources* [Ph.D. Dissertation, Department of Natural Resources Management & Agricultural Engineering, Agricultural University of Athens]. http://hdl.handle.net/10329/6743

Tsesmelis, D. E., Karavitis, C. A., Kalogeropoulos, K., Tsatsaris, A., Zervas, E., Vasilakou, C. G., Stathopoulos, N., Skondras, N. A., Alexandris, S. G., Chalkias, C., & Kosmas, C. (2021). Development and Application of Water and Land Resources Degradation Index (WLDI). *Earth*, *2*(3), 515–531. https://doi.org/10.3390/earth2030030

Tsesmelis, D. E., Karavitis, C. A., Kalogeropoulos, K., Zervas, E., Vasilakou, C. G., Skondras, N. A., Oikonomou, P. D., Stathopoulos, N., Alexandris, S. G., Tsatsaris, A., & Kosmas, C. (2022). Evaluating the Degradation of Natural Resources in the Mediterranean Environment Using the Water and Land Resources Degradation Index, the Case of Crete Island. *Atmosphere*, *13*(1), 135. https://doi.org/10.3390/atmos13010135

Tsesmelis, D. E., Karavitis, C. A., Oikonomou, P. D., Alexandris, S., & Kosmas, C. (2019). Assessment of the Vulnerability to Drought and Desertification Characteristics Using the Standardized Drought Vulnerability Index (SDVI) and the Environmentally Sensitive Areas Index (ESAI). *Resources*, *8*(1), Article 1. https://doi.org/10.3390/resources8010006

Tsesmelis, D. E., Leveidioti, I., Karavitis, C. A., Kalogeropoulos, K., Vasilakou, C. G., Tsatsaris, A., & Zervas, E. (2023). Spatiotemporal Application of the Standardized Precipitation Index (SPI) in the Eastern Mediterranean. *Climate*, *11*(5), 95. https://doi.org/10.3390/cli11050095

17th INTERNATIONAL CONGRESS
of the Geological Society of Greece

BULLETIN OF THE GEOLOGICAL SOCIETY OF GREECE, SP. PUBL.

EXTENDED ABSTRACT 223

Density modeling based on gravity survey at faulted area around Aigion, Gulf of Corinth, Greece

Mrlina J.[1]
(1) Institute of Geophysics CAS, Prague, Czechia, jan@ig.cas.cz

Introduction and objectives

This paper is based on the gravity survey data and highlights a quite important difference between former geological models and the new density/gravity model along two NNE-SSW oriented profiles crossing three principal normal faults in the Aigion area of the Gulf of Corinth.

The geological models were presented by Ghisetti *et al.* (2001), Ghisetti and Vezzani (2005), and Moretti *et al*. (2003).The current gravity model actually comprises much less conglomerate formations between the Helike and Pirgaki faults.

For this study, a new gravity map of the area was needed, so a gravity survey was carried out in a few steps, and the data were processed into the Bouguer gravity anomaly values. Then a gravity map and a residual gravity maps were constructed as a base for gravity field evaluation. As well, extensive rock sampling of the principal rock types was performed, as no such data were available from former investigations, as stated by Mrlina (2001). Rock densities and porosity were measured in a laboratory in Czechia.

The principal objective of the gravity surveying was to determine tectonic and structural setting of the area which forms the southern side of the Corinth Rift. The principal tectonic features are the WNW-ESE trending normal faults expressed in the topography of the region (Armijo *et al*., 1996, Rigo *et al.,* 1996). The region is prone to strong earthquakes (Bernard *et al.,* 1997). The target was to perform 2D and 2.5D gravity/density modeling to constrain existing tentative geological profiles. No such gravity models had been published in literature to that date.

The location of the study area is presented in Fig. 1

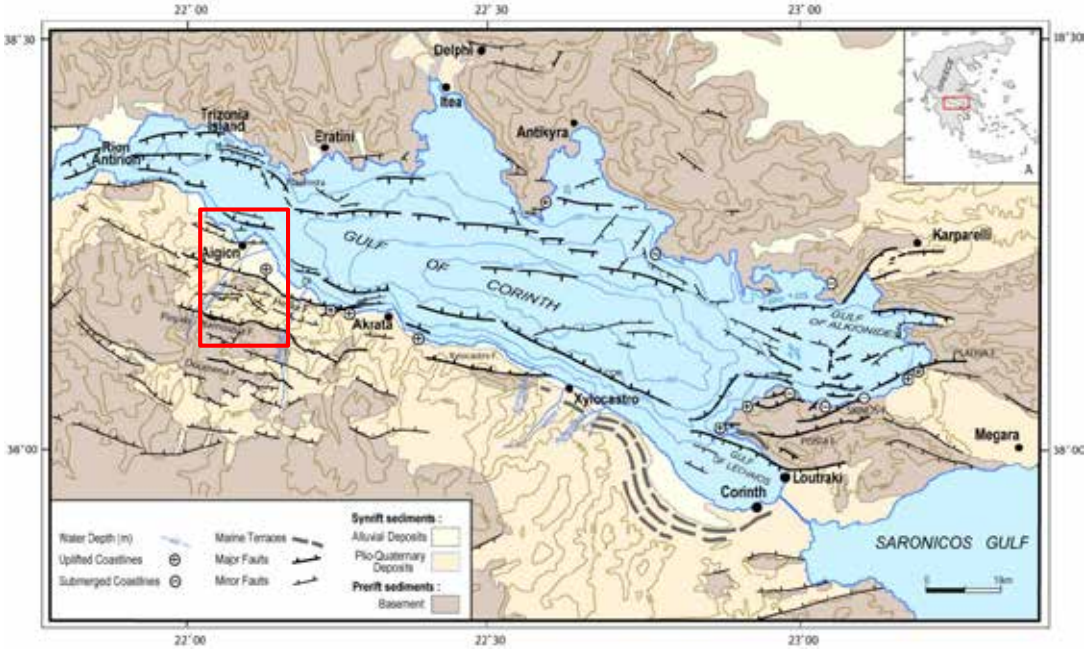


Figure 1. Tectonic map of Gulf of Corinth (after Moretti *et al.,* 2003). The study area around Aigion is marked by a red rectangle. Principal normal WNW-ESE faults are presented in the map.

Methods

The gravity survey was performed using the LaCoste&Romberg D-188 and LCR Graviton-EG gravimeters supported by the Trimble GNSS instrumentation. GNSS survey was connected to a few local Greek geodetic network stations (Lagios *et al.,* 1994), while the gravity measurements were referenced to relative gravity bases. One such base was established in the drill site of the AG10 well (see Fig. 2 for location) that was bored within the EC project Corinth Rift Laboratory.

Daily gravity loops included a few repeated points in order to define an accurate secular drift of a gravimeter. Also, independent control points were observed in order to define the repeatability of the gravity measurements that was evaluated to 0.010 mGal (1 mGal = 10^{-5} m/s^2). The rms of the Complete Bouguer anomaly values was 0.017 mGal. The final range of the gravity field within the gravity map in Fig. 2 was 17 mGal.
The Complete Bouguer anomaly (CBA) was calculated with a traditional formula with normal gravity field correction, elevation correction and Bouguer plate reduction for density of 2.50 g/cm3. Terrain corrections were computed to the distance of 167 km from each point. Terrain model included both onshore and offshore topography. The gravity map is shown in Fig. 2.

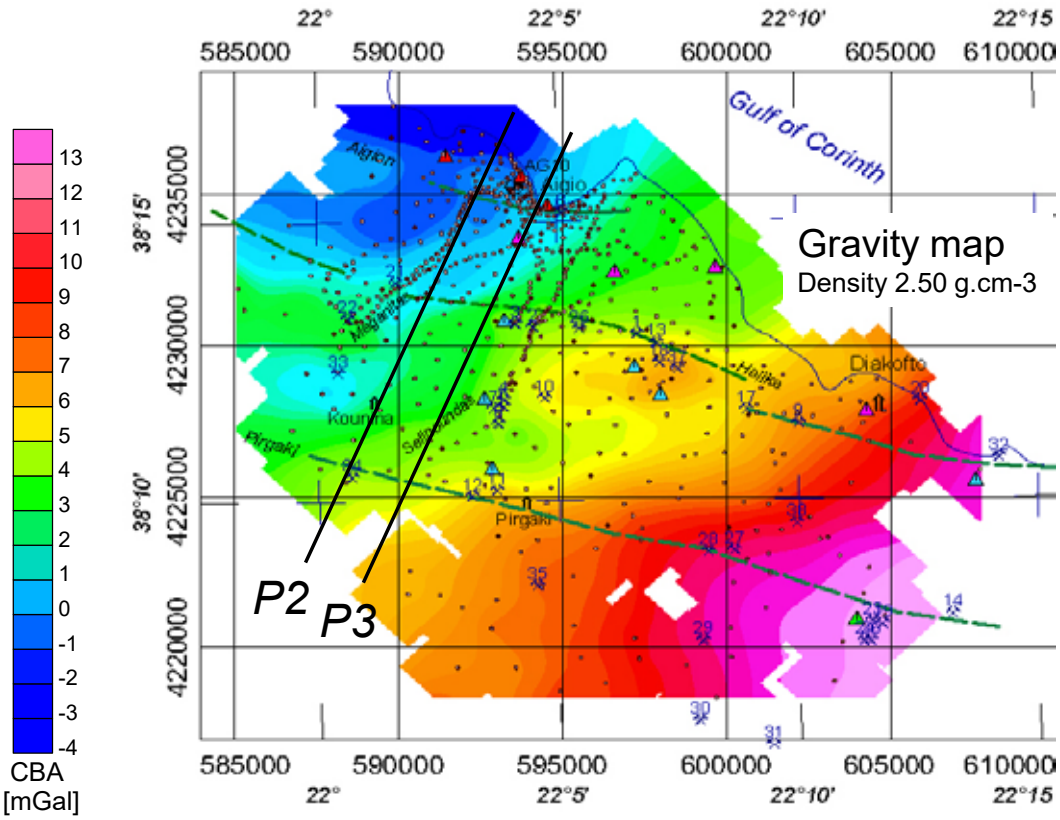


Figure 2. Gravity map of the Aigion area for reduction density 2.50 g/cm3. The total range of the map is 17 mGal. Principal faults are presented as green dashed lines. Two geological profiles P2 and P3 are located in western side of the map. Rock sampling locations are marked by crossed-hammers (mining) symbols. Blue triangles show gravity monitoring stations. Coordinates are WGS84 (degrees) and UTM34N (meters).

Density analysis was performed based on 135 rock samples collected during the field work. Sampling locations are shown in Fig. 2 as 'mining' symbols with numbers; each number represents a few samples from the given location (a,b,c, etc.). Relatively fresh samples were attempted in order to represent respective rock type as well as possible. Still, it is necessary to keep in mind that the samples cannot provide a complete idea on real rock fracturing inside a rock massif. Therefore, they provide approximate values of densities of the given rock types and keep certain freedom for the gravity/density modeling.
In the laboratory, five parameters were determined: bulk (volume), wet (saturated) and grain densities, porosity, and magnetic susceptibility.
The first collection of samples focused on the two principal rock types – limestone and conglomerate. The respective values are presented in Fig. 3, where wet (saturated) density is used, as it represents the most probable status of rocks in the natural conditions inside rock formations. There are 31 samples in the graph showing also average values for limestones and conglomerates, respectively.
As the sampling was further extended, the final collection contained 135 samples. They were separated into 8 groups, while limestone and conglomerate were still the most frequent rock types, see Fig. 4

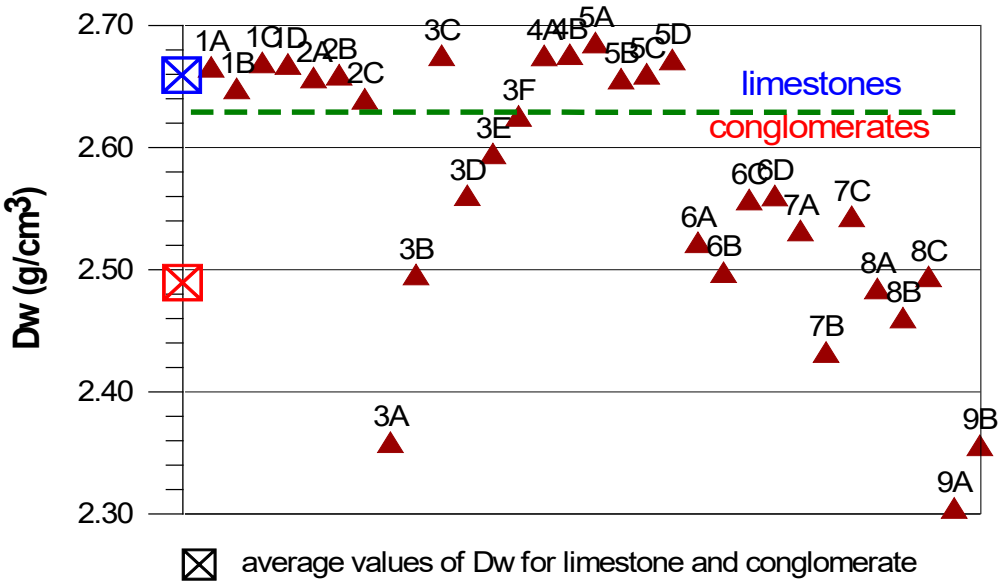


Figure 3. Collection of 31 rock samples (14 samples of limestone, and 17 of conglomerates). Average values of both groups are shown on wet density axis, blue for limestone, red for conglomerate.

rock	n	Db	range	Dw	range	Dg	range	P	range	MS	range
		g.cm-3		g.cm-3		g.cm-3		%		10-6 SI	
L	50	2.66	2.43-2.71	2.67	2.53-2.71	2.70	2.66-2.74	1.6	0.1-10.0	58	5-256
LB	6	2.56	2.45-2.65	2.61	2.55-2.67	2.70	2.65-2.74	5.4	2.0-9.8	71	32-157
R	15	2.58	2.43-2.73	2.61	2.49-2.73	2.66	2.53-2.73	2.9	0.2-10.5	152	30-342
Cst	11	1.82	1.50-2.10	2.14	1.94-2.32	2.70	2.64-2.74	32.7	21.9-43.3	81	18-126
C	39	2.46	2.11-2.66	2.55	2.30-2.68	2.68	2.62-2.76	8.5	5.5-27.2	89	18-353
S	8	2.55	2.42-2.66	2.60	2.51-2.68	2.69	2.67-2.71	5.2	1.9-9.7	244	205-296
GW	3	2.62	2.61-2.63	2.65	2.64-2.66	2.70	2.69-2.70	2.7	2.6-3.0	0	no data
Cal	3	2.66	2.61-2.68	2.67	2.65-2.69	2.70	2.70-2.70	1.7	0.9-3.3	12	7-17

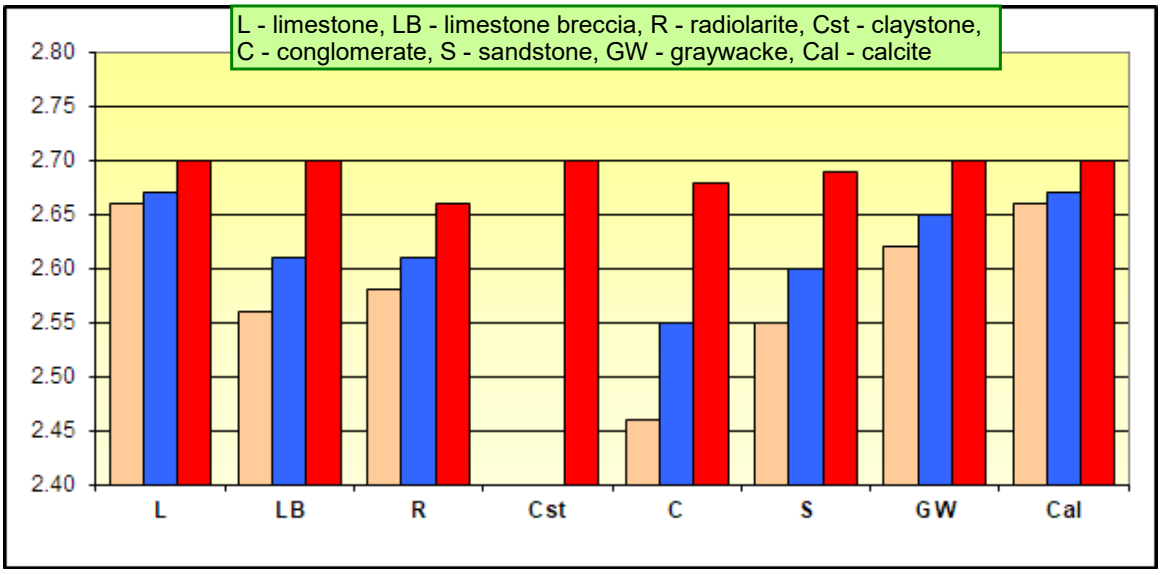


Figure 4. Up: Database of 135 rock samples and respective average values of particular density parameters, as well as porosity and magnetic susceptibility. Each parameter has also respective range of values. Down: Column graph of 3 density parameters for all 8 rock types. It is evident, that grain density Dg has a quite small range (red column), while bulk/volume (Db, orange) and wet/saturated (Dw, blue) densities show much larger differences. Rock type abbreviations are explained in the green window between the two parts of the figure.

Results and discussion

The analysis preceding the gravity modeling focused on the existing geological models. Average density values were attributed to particular formations present in the geological model. The density model was simplified into just two formations – limestone basement, and young rift-related sediments formed mainly by conglomerates (marls, claystones, radiolarites were neglected). Two differential densities were used to calculate these geological models – 0.11 and 0.18 g/cm^3, respectively. The calculated gravity response curves were printed on top of the models.

An example of this procedure is given in Fig. 5. Profile P2 is shown in color where green is limestone formation (basement) and yellow to brown formations are the young sediments. The two calculated gravity curves for both differential densities are presented above the geological model. The general trend is the gravity decrease from south to north due to increase of the thickness of the young sediments. The important features on the calculated curves are the local positive spikes related to fault zones, where the basement is elevated towards the surface – the best example is related to the Helike fault.

However, on top of the figure there are two other lines which show the real observed gravity data on P2 and P3. It is evident that theoretically calculated curves of the model do not fit with the observed data. Therefore, a new density model was developed with certain significant changes with respect to the original geological model, see Fig. 6.

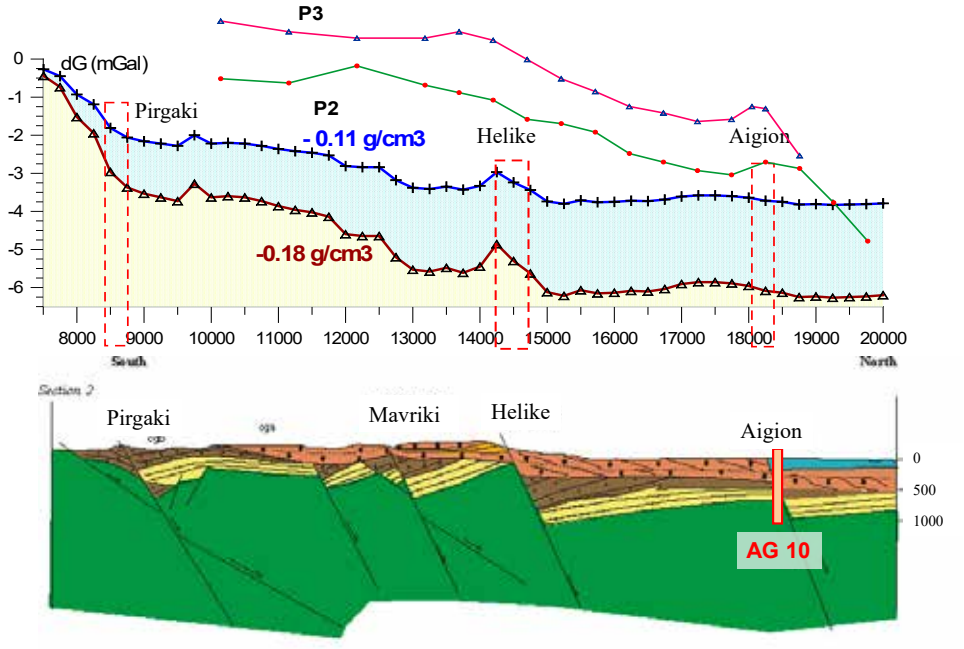


Figure 5. Geological tentative Profile 2 by Ghisetti *et al.* (2001). 2D gravity modeling performed for two differential densities between conglomerates and limestones (0.11 and 0.18 g/cm^3). Residual anomalies based on real observed Bouguer gravity values are different, as shown by two colored lines on top (for both P2 and P3). This justified significant changes in the models, as demonstrated on P3 in Fig. 6.

In the complex Fig. 6 there are actually 4 partial figures. At the bottom (D) the original geological model of Profile P3 (location in Fig 2) is presented. It is evident that all the section between the Pirgaki fault and the Gulf of Corinth is covered by the young sediments of variable thickness which is reaching even more than 1000 m in a few places. The smallest thickness is near the Helike fault where the blocks of the young sediment are strongly tilted to the south.

However, the gravity modelling could not fit the data until in the central part of the profile was completely changed and almost all young sediment removed. Like this the basement has only shallow cover of those young sediments. In part C a simple sketch of the density model is presented so that the descriptions are better visible, contrary to B where the geological formations are presented with raster and colors.

During the modeling process it was necessary to introduce two densities for the limestone formation – 2.70 g/cm^3 at deeper section, and 2.67 g/cm^3 in the upper parts. As well, within young sediments also claystone was incorporated (beside conglomerates) with low density of about 2.35 – 2.40 g/cm^3.

The A part shows observed and calculated gravity curves. In the substantial part of the profile the fit of the two curves is perfect, just in the southern end the data deviated from each other. This may be due to limited extend of the profile,

but also due to too high thickness of conglomerates on the hanging wall side of the Pirgaki fault.
It should be mentioned that the geological and gravity profiles are not completely identical in the field and they differ as for morphology, especially near the Helike fault, where the gravity survey avoided the steep slope of this fault. However, this does not affect the existence of the evaluated difference of the geological and gravity models.

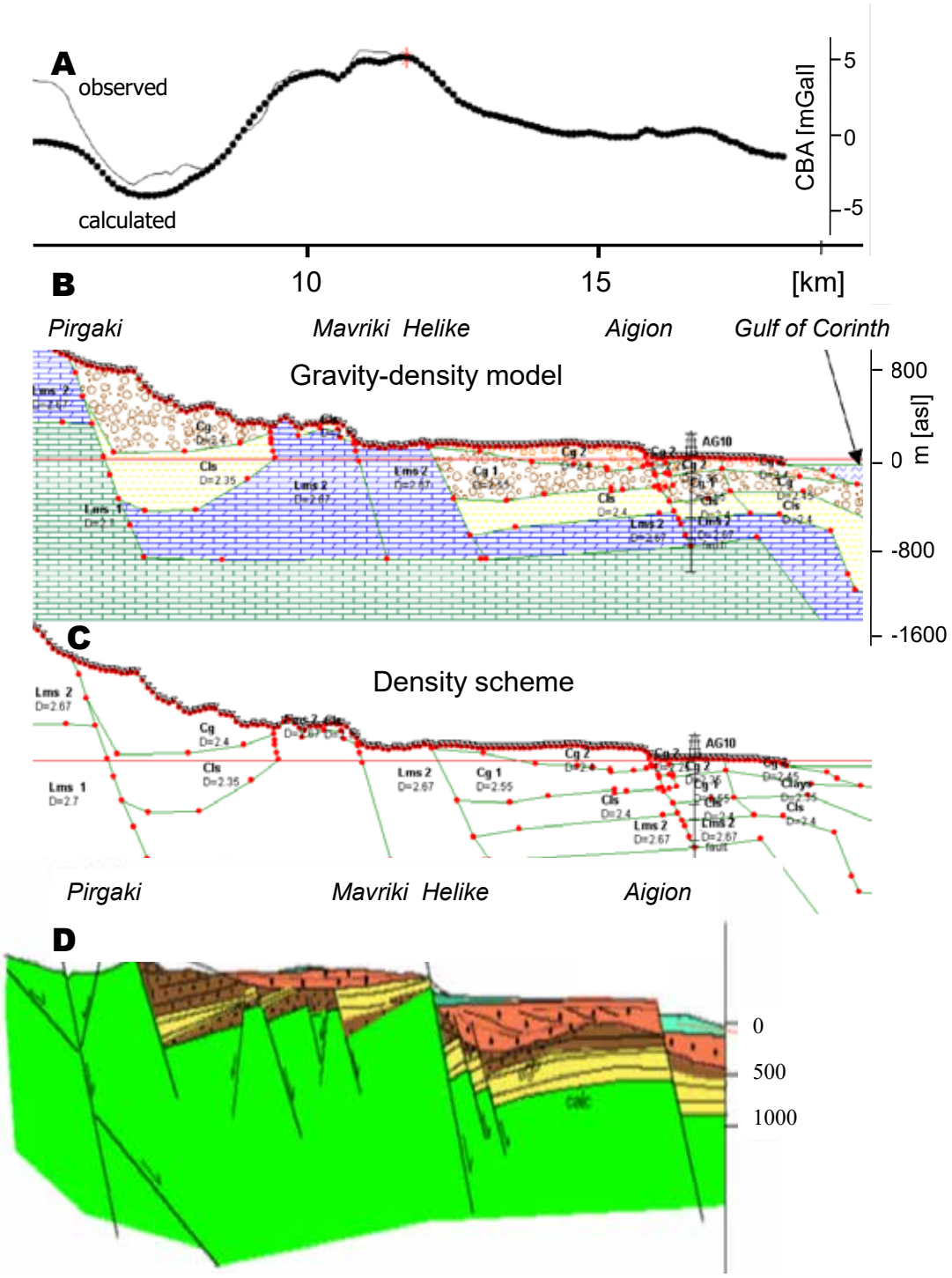


Figure 6. Residual (observed) and calculated gravity (A) for the new model of P3 shown in (B). In (C) simplified density model with rock types (Lms = limestone, Cg = conglomerate) is presented. Gravity/density model (B) is confronted with structural geological model (D) of Ghisetti et al. (2001). The principal difference of the models is exhibited between Helike and Pirgaki faults.

Conclusion

The presented work showed that the geological tentative profiles in complex tectonic and structural setting may suffer from inaccuracies. Therefore, some constraining techniques are recommended to be applied. For geological structures study the gravity method is a suitable geophysical tool.

It is also important to evaluate the rock densities for correct interpretation of the data. In this study we determined the difference between the two principal rock types, limestone and conglomerates, to range from 0.11 to 0.18 g/cm^3. In the Gulf of Corinth rift region it was found (by the gravity surveying and modeling) that the volumes (blocks) of particular formations significantly differ from the geological idea. Along the given NNE-SSW profiles P2 and P3, passing around Aigion city, especially in their central part between the Helike and Pirgaki faults, the volume of young rift-related sediments is much smaller than previously expected. Even if the density difference between basement (limestone) and young sediments cannot be perfectly determined, despite extensive sampling and laboratory work, the density models fit the observed data. In Fig. 6 such a result is presented.

Acknowledgements

The author wishes to appreciate I. Moretti for supporting the idea of a field gravity investigation, F. Ghisetti for sharing geological knowledge of the area, the assistance of M. Seidl with GNSS measurements during the gravity survey, and E. Lagios for providing information on geodetic/gravity networks in Greece. Field operation was supported by the EC project Corinth Rift Laboratory ENK6-CT2000-00056 NAS-3F-CORINTH.

References

Armijo R., Meyer B., King G.C.P., Rigo A., and Papanastassiou D., 1996. Quaternary evolution of the Corinth Rift and its implication for the Late Cenozoic evolution of the Aegean. Geophys. J. Int., 126, 11-53.

Bernard, P. et al., 1997. The Ms=6.2, June 15, 1995 Aigion earthquake (Greece): evidence for low angle normal faulting in the Corinth rift. J. Seism., 1, 131-150.

Ghisetti, F.C. and Vezzani, L., 2005. Inherited structural controls on normal fault architecture in the Gulf of Corinth (Greece). TECTONICS, Vol. 24, TC4016, doi:10.1029/2004TC001696

Ghisetti, F.C., Vezzani, L., Agosta, F., Sibson, R. and Moretti, I., 2001. Tectonic setting and sedimentary evolution of the south-west margin of the Corinth rift (Aigion – Xylokastro area). Report 56 207, IFP Paris, 22 p.

Lagios, E., Chailas, S., Hipkin, R.G. and Drakopoulos, J., 1994: Gravity and topographic data banks of Greece. NKUA, Publ. 4/94, 1-38.

Moretti, I., Sakellariou, D., Lykousis, V. and Micarelli, L., 2003. The Gulf of Corinth: an active half graben? J. Geodynamics, 36, 323-340.

Mrlina, J. (2001): Density measurements and plans for gravity survey and monitoring in the Aigion area. Corinth Rift Laboratory Workshop, Aigion, 2001.

Rigo, A., Lyon-Caen, H., Armijo, R., Deschamps, R., Hatzfeld, D., Makropoulos, K., Papadimitriou, P. and Kassaras, I., 1996. A micro-seismic study in the western part of the Gulf of Corinth (Greece): implication for large-scale normal faulting mechanisms. Geophys. J. Int., 126, 663-688.

17th INTERNATIONAL CONGRESS of the Geological Society of Greece

BULLETIN OF THE GEOLOGICAL SOCIETY OF GREECE, SP. PUBL.

EXTENDED ABSTRACT 224

Gravity monitoring at Santorini volcanic island, Greece

Mrlina J.[1]
(1) Institute of Geophysics CAS, Prague, Czechia, jan@ig.cas.cz

Introduction and objectives

Santorini island in the Aegean Sea is a famous volcanic structure, not only because of its beauty, but mainly for its catastrophic eruption about 3500 years ago. This eruption eliminated the Minoan civilization in Crete, and caused the volcano collapse forming the current day caldera. The volcano is one of the principal volcanoes of the Greek volcanic arc related to the collision of the African and Eurasian plates. The arc comprises also Kos-Nisyros volcanic system, the Milos island, and the Methana peninsula, see Fig. 1.
This volcano is still active, with the last lava flow in the central island of Nea Kameni in 1950. The island hosts numerous population and therefore is a subject of multiparameter control, starting with seismological permanent observations, GNSS (Global Navigation Satellite System) with permanent and campaign-style stations, gas monitoring, etc.
This situation was a motivation of introducing repeated gravity monitoring campaigns in 2013, after the volcano increased activity in 2011-2012. There was no lava eruption, however, the signals from GNSS were showing the inflation of the caldera with the central point in Nea Kamenni. Previously, there was an attempt of such research, but actually only two campaigns could be compared – the one in the 1970s, and the other in 2012-2014 (Paraskevas et al., 2021). Such gravity monitoring was applied e.g. in the Merapi volcano area (Indriana et al., 2023).
IGCAS (Institute of Geophysics, Czech Academy of Sciences) could support and perform this 4D gravity investigation thanks to the EPOS/CzechGeo project, see Acknowledgement. The objective was to indicate possible changes in the gravity field that may be related to mass changes and/or fluids movements inside the caldera.

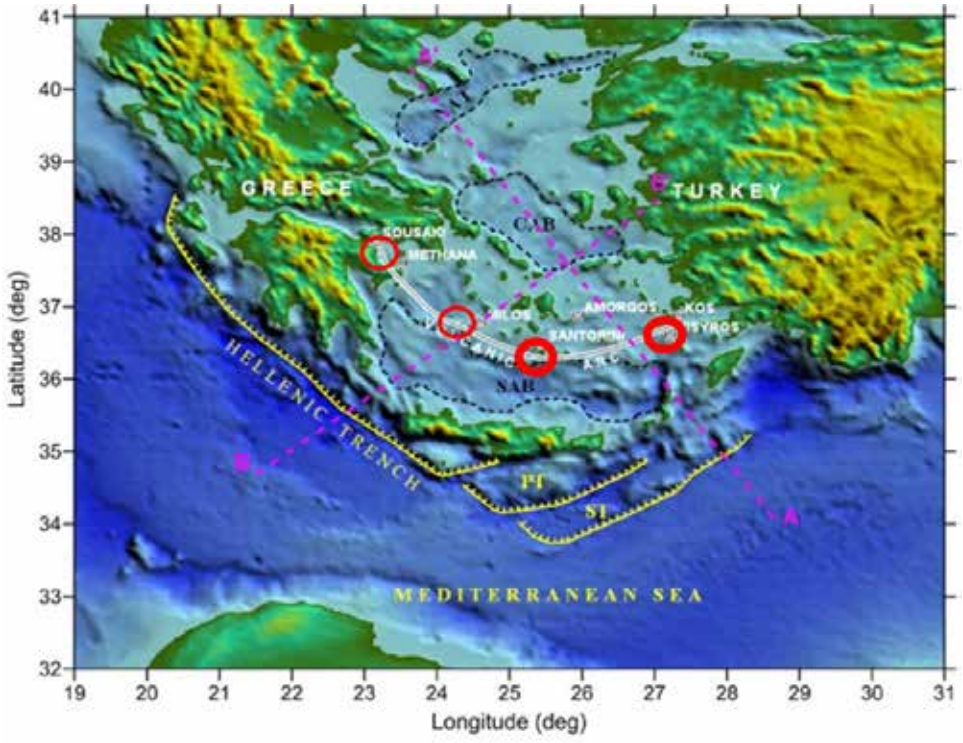


Figure 1. Position of Greek volcanic arc with four principal volcanic edifices – from left to right – Methana, Milos, Santorini, Nisyros.

The island is formed by lava extrusions of dacite, ryodacite, andesit and basalt, but the surface is covered mainly by pyroclastic formations of various composition, see Fig. 2. There are also outcrops of basement formed by carbonates (E, SE), but also metamorphics (slope to the new port) on the western side of Thira (Thera in Fig. 2). Tectonic zones are marked by white lines, as the principal ones of Columbo and Kammeni ones.

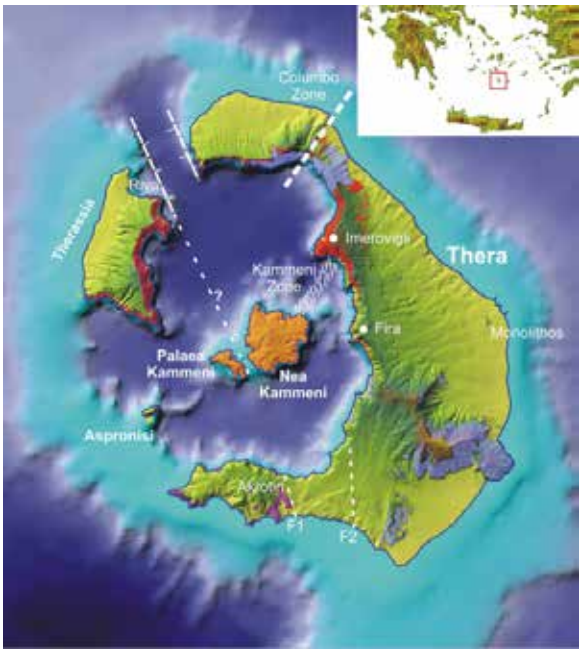


Figure 2. Position of principal tectonic features (Kammeni zone, Columbo zone) in Santorini, and principal lava flows (brown – dacite, ryodacite, andesite; light violet – basalts; medium violet – carbonate basement; green – various pyroclastic formations); after Lagios et al. (2013) and Druitte et al. (1999). Bathymetry after Nomikou et al. (2012).

The primary geophysical method for monitoring volcanoes and active faults is seismology, showing the active regions within the Earth crust. In Santorini two areas of different type of seismicity are located in the center of the caldera, and to the NE of Thira part of Santorini, see Fig. 3. Around Nea Kameni the epicenters are concentrated to a small area of about 5 x 3 km, actually along the Kammeni fault zone (see Figs. 2, 3), while in the NE they are spread on a large area with a diameter of more than 10 km.

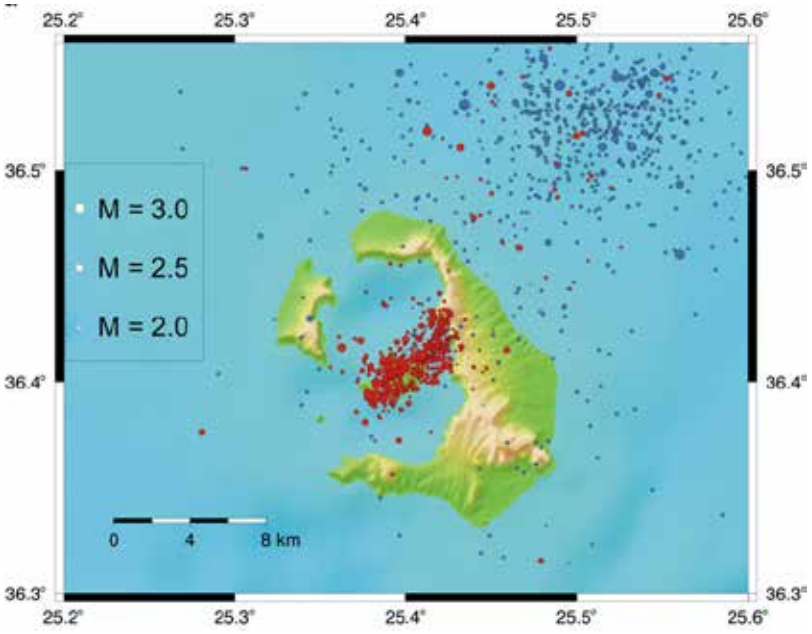


Figure 3. Seismicity around Santorini volcano in 1990-2010 (Lagios et al., 2013). It is evident that many events were recorded inside the caldera where Nea Kameni island is located. Earthquakes epicenters are accumulated within quite small elliptical area with longer axis less than 5 km. On the other side, in the area NE of Santorini seismicity shows much larger spread of epicenters around submarine volcano Kolumbos.

Gravity monitoring

The gravity monitoring is based on repeated measurements of gravity at a fixed network of stations. The observations at each station consist of a set of gravimeter readings, when a homogenous set has to be achieved (outlying readings are cancelled), as presented e.g. by Mrlina (2009, 2024).

Most, or all stations of the daily observation loop are measured three to five times in order to evaluate daily drift of the gravimeter. In this project one LaCoste&Romberg D-188 was used (2013-2021), later the Scintrex CG-6 gravimeter (2019-2024) was used, while in 2019 and 2021 both gravimeters were used simultaneously to provide enough overlap, see Fig. 4.

The network was based on the stations of NKUA (National Kapodistrian University of Athens) with the reference base stations No. 20, see the photos in Fig. 4. This base seems to be a reference point also for other gravity surveys in the Santorini island.

The old stations were continuously supplemented by new stations, as the author wished to cover some areas more densely, or to focus on some areas of higher interest, see Fig. 5. These new stations were selected in stable locations near churches, or similar, to ensure stable gravity observations. However, due to the general noise from the sea and from the volcano itself, exceptionally also of vehicles/people movement, some disturbed readings had to be eliminated. Some stations are increasingly difficult to operate due to difficult access in towns with enormous traffic (Fira, Oia).

The gravity campaigns usually lasted 9-13 days and also included one or two days to connect to Nea Kameni island stations by boat.

Each tie between any two stations was measured normally four times, which required a lot of driving by car (about 4 – 5 thousand km), or, in some cases, walking.

All these measurements, even simultaneous with two gravimeters, were performed as a single-man-job by the same operator (author), with the same gravimeters, and in the same period of a year.



Figure 4. Position of the principal reference base station in Monolithos to NE of the airport. It is a solid pillar with concrete filling at the parking near Monolithos church, built on the limestone basement block (see the hill behind the base). Gravity readings were always stable at this base. Gravimeter Scintrex CG-6 is presented at the bottom photo, LaCoste&Romberg D-188 gravimeter is inside to black box to stay protected from sunshine.

Some ties were repeated in other days in order to evaluate the repeatability. Standard deviation of the measurements was usually better than 4 uGal.
Each campaign was processed and the differences (ties) between stations were calculated. Then these differences were compared between any couple of campaigns. In this way the temporal changes of gravity field were evaluated. Then, the changes for each point were obtained and could be interpolated into a map. Such differential map is presented in Fig. 6 for the years 2013 versus 2021.

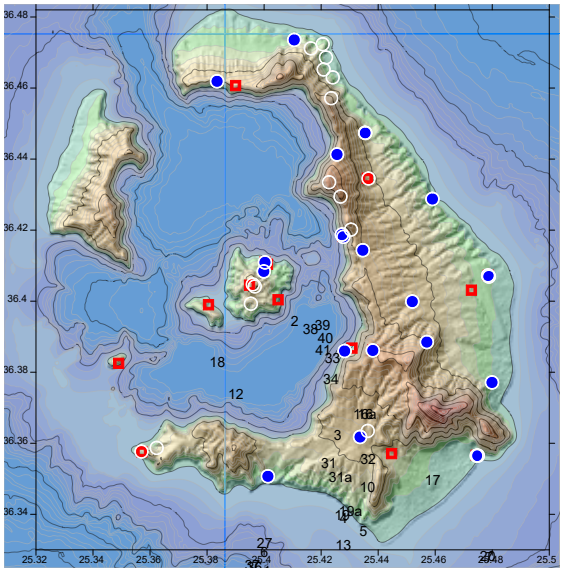


Figure 5. Position of the gravity monitoring network. Red rectangles are the old stations of the 1970s, full blue circles are the stations established by NKUA (Lagios et al., 1988), and white circles are stations used and established by author (IGCAS). Reference base station is No. 20 located in Monolithos to NE of the airport.

Results and discussion

The analysis of the data was focused on the temporal gravity difference between 2013 and 2021 (as in 2021 the campaign was performed with the LaCoste&Romberg D-188 gravimeter for the last time).
As mentioned above, the gravity differences at each station were used to interpolate all the differential values and the differential map was obtained, see Fig. 6.
There are two principal features in the map. The negative gravity changes in the northeastern side of Thira at the stations 3 and 16, and the positive change at the station 26 in the new port.
Most important is the negative change. It can be caused by continuous extension along the Kolumbo fault zone, which may decrease the volume density of the rocks within this zone. At the same time it may be responsible for the development of the Kolumbo submarine volcano with huge amount of fluids emissions through the opening fractures.
In order to exclude the impact of elevation change (that affect gravity values), the vertical component of the permanent GNSS station SANT was checked (courtesy of V.Sakkas). It is clear that within the period under study there was just a slight uplift 2013-2015 of less than 10 mm. Such value cause a gravity change of 2 uGal, which is almost negligible in respect to the amplitude of the negative zone (-50 uGal). Therefore the vertical displacement cannot be responsible of that significant decrease of gravity.
Another potential cause of the gravity decrease could be the emissions of fluids, but this is less probable as the released fluids would be substituted by water or other fluids coming from the deeper subsurface.
On the other hand, the old data 1976-2012 were showing the principal gravity increase in Nea Kameni (evaluated from data of Paraskevas et al., 2021), which was probably related to the magma and fluids rising to surface before the 2011-2012 crisis. During this crisis no lava erupted to surface, but the GNSS data showed inflation of the caldera and active fluid emissions were also encountered. In the NE there was also relative gravity decrease recorded.
This may justify the hypothesis that in the NE side of Santorini there may be an ongoing extension process.
For this reason the Author established another four new gravity monitoring stations 38-41 in the northeastern side of the island, see the white circles 38-41 in Fig. 5 and dark red triangles in Fig. 6. These stations were observed in 2023 and 2024, which is too short period for making any conclusions. The stations will be repeated in each potential future gravity monitoring campaign in the Santorini caldera.

The sharp gravity change between two nearby stations 10 and 26 (Fig. 6) can be affected by very sharp vertical difference, as 10 is located on the top of the cliff, while 26 is down in the new port. Here more investigation is needed to evaluate the impact of enormous change of air pressure during the measuring of this tie.

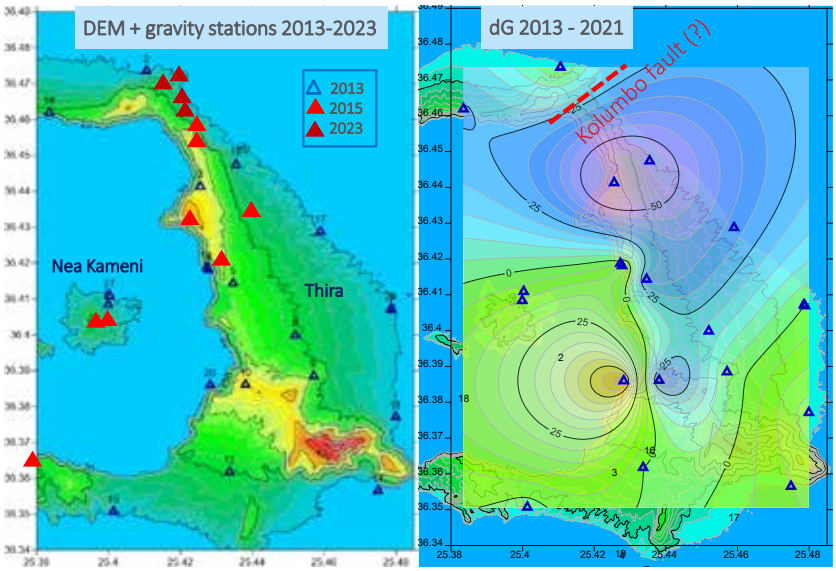


Figure 6. Left: Gravity monitoring stations used by IGCAS in 2013 (blue triangles established by Lagios et al., 1988), and established by IGCAS in later years 2015 and 2023 (red and brown triangles) for 4D gravity measurement campaigns. Right: Gravity difference between 2013 to 2021 in uGal (10^{-8} ms^{-2}) - principal feature is the gravity decrease in NE part of Thira (over -50 uGal) at stations 3 and 16.

Conclusion

This paper documents that the gravity monitoring of the Santorini volcanic island shows temporal gravity changes. As the vertical surface displacements play negligible role in affecting the gravity changes in the study period 2013 – 2021, the changes must be explained by geological/geodynamic processes.

Most significant is the temporal gravity decrease in the northeastern side of Santorini (Thira) where a long-term extension process in the underground may be causing the decrease of the volume density of the rock massif. Such extension within the Kolumbo fault zone also enables the opening for the currently active volcanic process around the Kolumbo underwater volcano with active fluids emissions.

In order to investigate this feature of the gravity field change, dense network of the monitoring stations was established in 2023 around the assumed Kolumbo fault zone.

Additional Comments

- In 2024 the author performed a small gravity survey in the NE part of Thira in order to investigate the Kolumbo fault zone which is related to the Kolumbo underwater volcano. This volcano has been recently very active with a lot of gas emissions. Seventy gravity stations were measured and data processed into the Complete Bouguer anomaly (CBA) with a traditional formula with normal gravity field correction, elevation correction and Bouguer plate reduction for density of 2.50 g/cm3. Terrain corrections were computed to the distance of 167 km from each point. Terrain model included both onshore and offshore topography. The gravity map has to be enlarged during next campaigns so that the tectonic pattern of this part of Thira can be updated.
- Similar gravity monitoring is performed by Author in Kos- Nisyros caldera, to be presented next time.

Acknowledgements

The author appreciates the financial support of the EPOS/CzechGeo project No. LM2015089. As well, Author thanks E.Lagios for introducing the existing stations in 2013 and V.Sakkas for performing random GNSS campaigns in Santorini and providing info on vertical movement trend from the permanent GNSS station SANT.

References

Druitt, T.H., Edwards, L., Mellors, R.A., Pyle, D.M., Sparks, R.S.J., Lanphere, M., Davies, M., Barriero, B., 1999. Santorini Volcano. Geological Society Memoir 19, 165.

Indriana, R. D., Nurwidiyanto, M. I. and Mrlina, J. 2023. Merapi complete Bouguer anomaly changes based on gravity data of Merapi in 2020-2019. AIP Conference Proceedings. Vol. 2738. Melville: American Institute of Physics, 2023 DOI: 10.1063/5.0140956.

Lagios, E., Drakopoulos, J., Hipkin, R.G. and Gizeli, C., 1988. Microgravimetry in Greece: applications to earthquake and volcano-eruption prediction. Tectonophysics, 152, p.197-207.

Lagios, E., Sakkas, V., Novali, F., Bellotti, F., Ferretti, A., Vlachou, K. and Dietrich, V., 2013. SqueeSAR™and GPS ground deformation monitoring of Santorini Volcano (1992–2012): Tectonic implications. Tectonophysics, TECTO-125831, 22p. http://dx.doi.org/10.1016/j.tecto.2013.03.012.

Mrlina, J., 2009. 4D Gravity – fluids monitoring in reservoirs. – Proc. Int. Petroleum Technology Conf., Doha, Qatar, 7-9 Dec., 6 pp., ISBN 978-1-55563-272-4.

Mrlina J., 2024. Application of Gravimetry to Investigation of Volcanism – Examples from West Bohemian Massif and Greece. Int. Journal of Geology and Earth Sciences (IJGES), Vol 10, No. 2, p.38-42. doi: 10.18178/ijges.10.2.38-42.

Nomikou, P., Carey, S., Papanikolaou, D., Croff Bell, K., Sakellariou, D., Alexandri, M., Bejelou, K., 2012. Submarine volcanoes of the Columbo Volcanic Zone NE of Santorini Caldera, Greece. Global and Planetary Change. http://dx.doi.org/10.1016/j.gloplacha.2012.01.001.

Paraskevas, M., Paradissis, D., Raptakis, K., Nomikou, P., Hooft, E. and Bejelou, K., 2021. Gravity observations on Santorini island (Greece): Historical and recent campaigns. Contributions to Geophysics and Geodesy Vol. 51/1, 1–24.

17th INTERNATIONAL CONGRESS of the Geological Society of Greece

BULLETIN OF THE GEOLOGICAL SOCIETY OF GREECE, SP. PUBL.

EXTENDED ABSTRACT 225

Ostracod-based environmental reconstruction of Lake Koronia, (Central Greece) during the Holocene

Navrozidou, V.[1,5], Koukousioura, O.[1,2], Doani, S.[1], Frenzel, P.[3], Triantaphyllou, M.[4], Albanakis, K.[1], Syrides, G.[1]

(1) Aristotle University of Thessaloniki, Thessaloniki, Greece, vnavrozi@geo.auth.gr (2) University of Cologne, Cologne, Germany (3) Institute of Earth Sciences, Friedrich-Schiller-Universität Jena, Jena, Germany (4) National and Kapodistrian University of Athens, Athens, Greece (5) The Goulandris Natural History Museum – Greek Biotope/Wetland Centre Thermi, Greece

Introduction

Lake Koronia is located in the western lowland area of the Mygdonia Basin, northeast of the city of Thessaloniki in northern Greece (40° 41′ N, 23° 09′ E, 75 m a.s.l.). It is the remnant of a once larger lake in the region (Psilovikos, 1977), but is now a shallow, hypertrophic and heavily polluted water body (Moustaka-Gouni *et al.*, 2012). It has experienced substantial degradation over time due to human activities, but has also dried up several times in the past two decades (2002, 2007, 2009 and 2014), resulting in its current state, formerly the fourth largest lake in Greece (Demertzioglou *et al.*, 2022). Despite its current ecological challenges, Lake Koronia is recognized as a protected wetland under international and national legislation, highlighting its importance (Malamataris *et al.*, 2017).

The aim of the present study was to investigate the paleoenvironmental evolution of Lake Koronia and the distribution of ostracod assemblages through time using a combination of core and recent surface sediment samples.

Methods

The KOR core (40°41'45.4" N, 23°11'08.8"E; Fig. 1) was drilled at 71 m b.s.l. and reached a depth of 368 cm. A total of 36 sediment samples were studied in order to reconstruct the paleoenvironmental evolution of the lake. In addition, two sediment samples were collected by boat, using an Ekman grabber from the upper 1 cm of the lake bottom for the analysis of the recent ostracod fauna. For ostracod analysis, 50 ml of each surface bottom sediment sample was wet sieved with tap water through a 125 μm pore size standard sieve. For core samples, 10 g of dried sediment was treated with hydrogen peroxide (H_2O_2) and wet sieved as described above. The residue was oven dried at 60°C and all ostracod valves over the >125 μm fraction were hand-picked under a Zeiss Stemi 305 binocular stereoscope. Species were identified, counted, and stored in microslides. Taxonomic identification of the species was based on the morphological features of the carapace using several published works, ostracod atlases and ostracod databases. In addition, radiocarbon dating was performed using accelerator mass spectrometry (AMS ^{14}C; Beta Analytic USA laboratory). Finally, a Q-mode cluster analysis was performed for the sediment samples of the core.

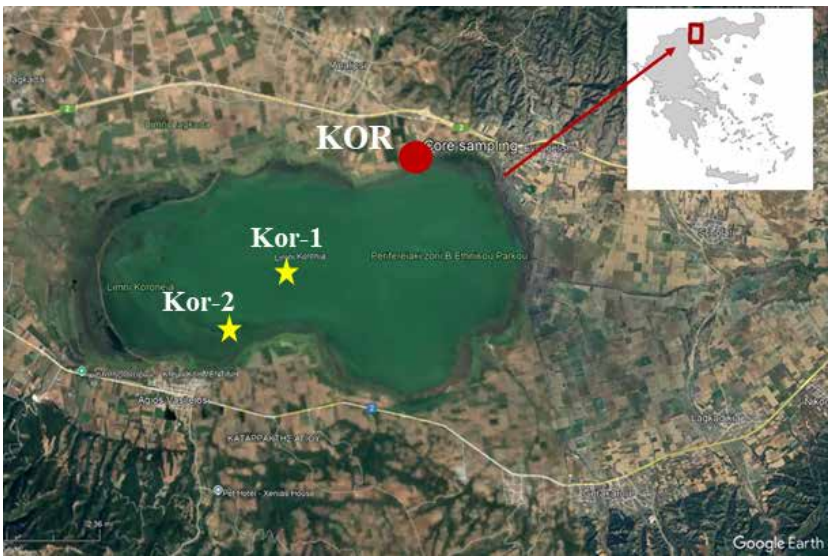


Figure 1. Sampling stations of surface sediments and the location of KOR core in Lake Koronia (modified from Google Earth).

Results and conclusions

The ostracod assemblage of Lake Koronia, both in the surface sediments and in the KOR sedimentary sequence, consisted of five taxa: ex gr. *Candona* juveniles, *Cyprideis torosa*, *Darwinula stevensoni*, *Heterocypris salina* and *Limnocythere inopinata*. In the recent surface sediments, station Kor-1 had a significantly higher abundance compared to station Kor-2. The *Candona* species dominated the assemblage, while *L. inopinata* was the second most abundant species of the total ostracod fauna recorded in the lake, with all other taxa showing relatively low abundances.

The ostracod valves obtained from the core (KOR) were well preserved and relatively abundant, with the number of valves/g reaching high values in some intervals, while the diversity indices showed relatively low values. The species *L. inopinata* dominated the assemblages, reaching even 100% in several intervals, followed by ex gr. *Candona* juveniles and *H. salina*. The species *D. stevensoni* and *C. torosa* accompanied the assemblage with lower but significant values.

The resulting dendrogram of the Q-mode cluster analysis performed on the KOR core sedimentary sequence, pointed out three distinct groups of samples associated with different assemblages and thus different paleoenvironmental conditions. The paleoenvironmental record of Lake Koronia revealed conditions of slightly elevated salinity between 2752-1437 cal. yr BP, occurring in a shallow environment with clear water and the absence of benthic macrophytes. The presence of *Cyprideis torosa*, a true brackish species (Meisch, 2000), further confirmed the elevated salinity during this period. After 1437 cal. yr BP, the fauna diverged significantly, and the environment transitioned to a purely lacustrine system, extremely shallow and with extensive macrophyte vegetation. At the top of the sedimentary sequence, the environment undergoes a further change, characterized by a significant increase in diversity, a deepening of the environment, and the establishment of well-oxygenated water conditions. This interval is comparable with the recent surface sediments in terms of faunal composition and diversity, but not in terms of abundance which was significantly higher at the recent stations.

Lake Koronia is a severely impacted lake that has faced significant degradation over the past few decades. Over the last 20 years, the lake has experienced a dramatic decrease in volume, surface area, and maximum depth (currently almost 2 meters) due to unsustainable water resource management. Further investigation of the benthic conditions and biota, coupled with the paleoenvironmental record of the lake, will be invaluable in this important biotope ecological assessment.

Acknowledgements

Sampling support for the recent sediment samples was provided by the Greek Biotope Wetland Centre.

References

Demertzioglou, M., Genitsaris, S., Mazaris, A.D., Kyparissis, A., Voutsa, D., Kozari, A., Kormas, K.A., Stefanidou, N., Katsiapi, M., Michaloudi, E., Moustaka-Gouni, M., 2022. A catastrophic change in a European protected wetland: From harmful phytoplankton blooms to fish and bird kill. Environmental Pollution 312, 120038.

Malamataris, D., Kolokytha, E., Mylopoulos, I., Loukas, A., 2017. Critical review of adaptation strategies for the restoration of Lake Koronia. European Water 58, 203-208.

Meisch, C., 2000. Freshwater Ostracoda of Western and Central Europe. In Schwoerbel, J. and P. Zwick (eds), Süßwasserfauna von Mitteleuropa 8/3, Spektrum Akademischer Verlag, Heidelberg, Berlin, 522 pp.

Moustaka-Gouni, M., Michaloudi, E., Kormas, K.A., Katsiapi, M., Vardaka, E., Genitsaris, S., 2012. Plankton changes as critical processes for restoration plans of lakes Kastoria and Koronia. European Water 40, 43-51.

Psilovikos, A., 1977. Paleogeographic development of the basin and lake of Mygdonia (Langada-Volvi area) GreecePh.D. Thesis, Aristotle University of Thessaloniki, Thessaloniki, 156 p.

17th INTERNATIONAL CONGRESS of the Geological Society of Greece

BULLETIN OF THE GEOLOGICAL SOCIETY OF GREECE, SP. PUBL.

EXTENDED ABSTRACT 226

Rapid Detection of Landslides Triggered by Mediterranean Cyclones Using Google Earth Engine and Open-Access Data

Nefros C.[1], Kitsara G.[2], Loupasakis C.[1], Giannakopoulos C.

(1) Laboratory of Engineering Geology and Hydrogeology, School of Mining and Metallurgical Engineering, National Technical University of Athens, Athens, Greece, email: kostasnefros@central.ntua.gr

(2) Institute for Environmental Research and Sustainable Development, National Observatory of Athens, Athens, Greece

This research introduces a methodological framework integrating Google Earth Engine and open-access data, to rapidly detect landslides triggered by Mediterranean Cyclones, which nowadays pose an increasing threat for the eastern Mediterranean region. This framework aims to enhance the timely identification and management of these hazards.

Introduction / Background

Medicanes or Mediterranean Cyclones are extreme meteorological phenomena, characterized by intense rainfall and winds speeds approaching hurricane strength (Lagouvardos et al., 1999). Their intensity and duration are expected to increase, along with a spatial shift toward the Ionian Sea and the eastern coasts of southern Italy (González□Alemán et al., 2019). Beyond causing floods and coastal waves, medicanes can trigger a series of landslide events within a short timeframe. These landslides often affect extensive areas and have impacts on various sectors (social, economic, transportation), making their management challenging for local authorities. This study introduces a methodological framework that integrates open access data, including Sentinel-2 and Google Earth imagery, combined with the computational power of Google Earth Engine (GEE), for the rapid identification and mapping of landslides activated by medicanes. The frequent revisit times of Sentinel-2 satellites over Europe and the high processing capabilities of GEE make this framework a valuable tool for the timely mapping of landslides. By enabling authorities to quickly assess the extent of landslide activity, following a medicane, the framework facilitates more effective management. The Ianos medicane, which struck the Cephalonia Island, Greece, in September 2020, was selected as a case study. Using the proposed approach, the activated landslides were identified and mapped. Moreover, the framework proved particularly effective in detecting landslides in remote, mountainous regions, underscoring its potential in difficult to reach areas.

Methods

The proposed framework is illustrated in Figure 1 and it leads to the creation of a comprehensive landslide inventory after a medicane, by using remote sensing techniques and open access data. The data used in the proposed methodology is derived exclusively from open-access or publicly available databases.

Case Study – Ianos Medicane

A medicane named Ianos by the National Observatory of Athens (NOA), struck Greece between 17 to 19 September 2020, severely impacting areas such as Cephalonia Island, Karditsa, and Fthiotida (Lekkas et al., 2020; Zekkos et al., 2020). According to Lagouvardos et al. (2022), the daily accumulated rainfall at the “Antipata” meteorological station in northern Cephalonia reached 644.7mm, which is the highest ever recorded value during a medicane and among the highest ever recorded in Greece. This extreme precipitation significantly exceeded the local precipitation thresholds for landslide activation across the Cephalonia Island, triggering widespread landslides. These landslides caused numerous damages to buildings, bridges, the local road network and other critical infrastructure. The large number of the activated landslides, combined with their extensive distribution, including remote and mountainous areas, posed significant challenges for local authorities in promptly documenting and mapping these events for their effective management. Cephalonia Island, situated in the Ionian Sea, in the west Greece, is characterized by steep terrain, limestone-dominated geology prone to karstification, and a dynamic hydrological network. These features, along with its history of frequent landslide activity, render Cephalonia particularly susceptible to landslides during heavy rainfall events. For these reasons, the island of Cephalonia was selected as a case study to examine the landslides activated by Ianos, highlighting the potential of the proposed framework.



Figure 1. Proposed Framework

Results and Discussion

As illustrated in Figure 2, by using the GEE, the Cephalonia Island was established as the Area of Interest (AoI) along with the time period before and after Ianos medicane. Sentinel-2 images were downloaded for the AoI.



Figure 2. GEE Environment

Cloud cover was mitigated in the Sentinel-2 images using the QA60 band. Specifically, bit 10 (value 1), was used to detect opaque clouds, while bit 11 (value 1) identified cirrus clouds, ensuring clearer imagery for analysis. The Normalized Difference Vegetation Index (NDVI) was then calculated for pre and post Ianos conditions, using the following equation:

$$NDVI = \frac{NIR-R}{NIR+R} \quad (1)$$

where the R factor corresponds to the red band, and NIR the near infrared band of the electromagnetic spectrum. NDVI values range between -1 and 1, reflecting vegetation health and coverage. Slope information was assessed using the Shuttle Radar Topography Mission (SRTM) Digital Elevation Model (DEM) provided by the of the United States Geological Survey (USGS). The SRTM DEM is version GL1, obtained from OpenTopography (portal.opentopography.org). This version provides a 30-meter resolution, ensuring reliable topographic representation. Potential landslide areas were identified based on two criteria: NDVI differences greater than 0.2 between pre and post Ianos, and slope angles exceeding 15°.

Subsequently, CHIRPS (Climate Hazards Group InfraRed Precipitation with Station data) precipitation data provided by the University of California, Santa Barbara (UCSB), were integrated into GEE to estimate the local/regional precipitation values that activated the landslides. CHIRPS were used to generate a raster file representing rainfall distribution over the AOI on the date medicane Ianos impacted Cephalonia. This dataset enables the spatial correlation of each detected landslide with the precipitation values, responsible for its activation. Thus, it facilitates the creation of a comprehensive landslide inventory, which

can be further used during the assessment of the local precipitation Intensity Duration (ID) thresholds.
Figure 3, illustrates the areas identified as potential landslides using the proposed framework, focusing on the Myrtos Beach area in north-western Cephalonia.

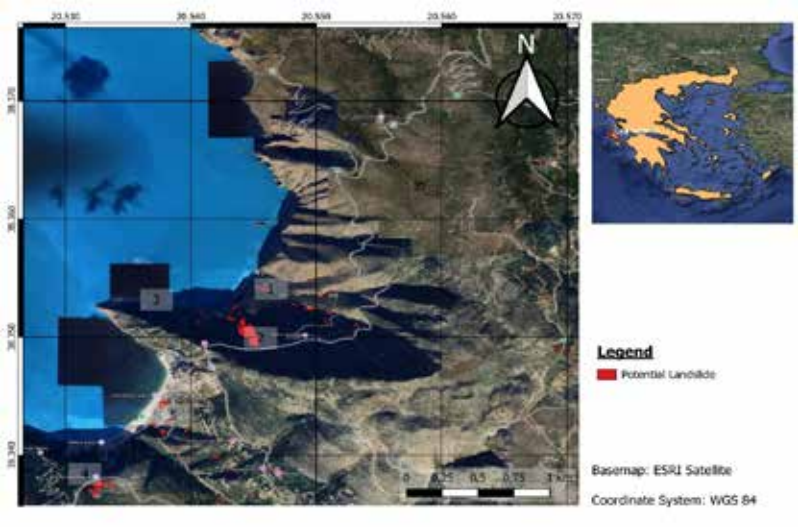


Figure 3. Potential Landslides according to GEE

Verification of these areas was conducted using high-resolution Google Earth imagery, as shown in Figure 4.



(a) (b)

Figure 4. Validation of the landslides using Google Earth Images before Ianos (a) (14-5-20) (Google Earth a) and after Ianos (b) (26-6-2021) (Google Earth b).
Results verification was also achieved using open-access landslide inventories derived from in situ investigations carried out after Medicane Ianos (Lekkas et al., 2020; Zekkos et al., 2020). These independent datasets provide ground-truth validation, supporting the accuracy and reliability of the detected landslides.
As it was revealed, the framework did not provide sufficient results in areas with sparse or absent vegetation, due to its reliance on NDVI changes. To address this issue, the landslide inventory was enriched with additional open access data and advanced remote sensing techniques, such as Persistent Scatterers Interferometry (PSI) processed using SNAP software provided by ESA. Specifically, PSI derived ground displacement velocities were analyzed, and a threshold of -2 mm/year was applied to identify areas exhibiting significant motion, improving landslide detection in non- vegetation regions.
The proposed framework introduces an efficient and rapid methodology for landslide detection by integrating GEE. Nevertheless, it has limitations, particularly in areas with sparse or absent vegetation, as it relies primarily on two criteria: slope angle and NDVI change. In the current study, this limitation was mitigated by incorporating supplementary open -access data and additional remote sensing techniques. However, future studies could address this issue further by enriching the GEE code with additional criteria, improving the framework's performance in diverse landscapes and enhancing its applicability. The final landslide inventory containing more than 600 landslides, is presented in Figure 5

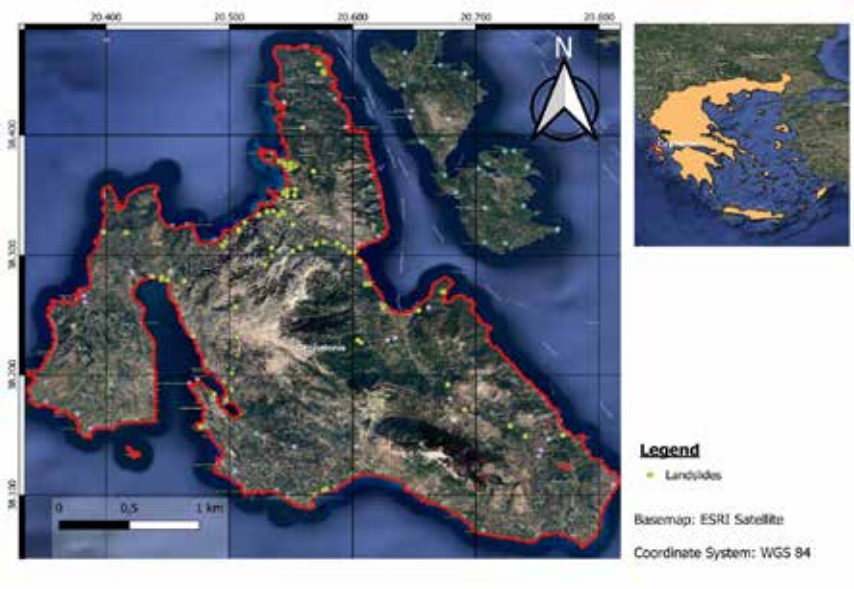


Figure 5. Landslide Inventory Map

These findings confirm the high intensity of the Ianos medicane and provide insight into the exceptionally large number of landslides it triggered. As illustrated in Figure 5, the activated landslides are distributed widely across the island. This widespread impact underscores the challenge of relying solely on in situ investigations for their identification and mapping, which require significant resources, time, and effort, particularly in remote and difficult to access areas.

The proposed framework, integrating open-access data and the computational power of Google Earth Engine (GEE), emerged as an effective, low-cost solution to tackle these challenges. By automating and accelerating the identification and mapping process, this framework minimizes the reliance on extensive field surveys while maintaining accuracy and spatial coverage.

Furthermore, this study highlights the potential of GEE, as a fundamental component of the proposed framework, demonstrating its ability to rapidly process and analyze large volumes of geospatial data. This capability is critical for the prompt identification and mapping of landslides, enabling authorities to respond more effectively. By facilitating timely decision-making and resource allocation, the framework contributes to the broader goal of efficient disaster management and mitigation, even to such extreme events, as the medicanes.

Conclusions

Medicanes are extreme phenomena that, due to climate change, pose nowadays a significant threat to regional or/and local communities in the Mediterranean region. Their destructive impact, including landslides activation, underscores the urgent need for effective disaster management strategies. This study not only highlights the severity of this threat but also introduces a practical solution through the proposed framework.

By leveraging the computational capabilities of GEE and open-access data, the framework offers a cost-effective solution that can assist authorities in promptly identifying regions most vulnerable to landslides. This enables them to implement promptly the necessary mitigation and civil protection measures and apply the necessary recovery measures.

References

Google Earth image (a), received at 14 May 2020. Publicly available at: https://earth.google.com/web/@38.35289638,20.54812259,137.18058809a,4112.50825678d,35y,120.97375048h,61.47762184t,-0r/data=ChYqEAgBEgoyMDIwLTA1LTE0GAFCAggBOgMKATBCAggASg0I_____ARAA (accessed 7 January 2025)

Google Earth image (b), received at 26 June 2021. Publicly available at: https://earth.google.com/web/@38.35289638,20.54812259,137.18058809a,4112.50825678d,35y,120.97375048h,61.47762184t,-0r/data=ChYqEAgBEgoyMDIxLTA2LTI2GAFCAggBOgMKATBCAggASg0I_____ARAA (accessed 7 January 2025)

González□Alemán, J. J. et al., 2019. Potential Increase in Hazard from Mediterranean Hurricane Activity with Global Warming,"

Geophys Res Lett, vol. 46, no. 3, pp.1754–1764, Feb.2019. https://doi.org/10.1029/2018GL081253

Lagouvardos, K., Kotroni, V., Nickovic, S., Jovic, D., Kallos, G. and Tremback, C.J., 1999. Observations and model simulations of a winter sub-synoptic vortex over the central Mediterranean. Met. Apps, 6: 371-383. https://doi.org/10.1017/S1350482799001309

Lagouvardos, K. et al., 2022. "Ianos—A Hurricane in the Mediterranean," Bull Am Meteorol Soc, vol. 103, no. 6, pp. E1621–E1636, Jun.2022. https://doi.org/10.1175/BAMS-D-20-0274.1

Lekkas, E. et al., 2020. "Impact of medicane IANOS on Cephalonia," Newsletter of EDCMS, National Kapodistrian University of Athens, Greece. ISSN 2653□9454.

Zekkos D., Zalachoris G., Alvertos, A. E., et al., 2020. "The September 18-20 2020 Medicane Ianos Impact on Greece - Phase I Reconnaissance Report". Geotechnical Extreme Events Reconnaissance Report, GEER-068, https://doi.org/10.18118/G6MT1T.

17th INTERNATIONAL CONGRESS of the Geological Society of Greece

BULLETIN OF THE GEOLOGICAL SOCIETY OF GREECE, SP. PUBL.

EXTENDED ABSTRACT 227

Integrating Volcanic Geoheritage and Community Engagement: The Case of Nisyros aspiring UNESCO Global Geopark

Nikoli E.[1], Nomikou P.[2], Tasioulas E.[1], Koroneos C.[3], Sakkali K.[1], Koukourakis G.[1], Nastos P.[2], Antoniou V[2], Emmanouloudis D.[3], Pehlivanides G.[4], Batis A.[5]

(1) Municipal Public Benefit Enterprise of Nisyros (DIKEN) (2) National and Kapodistrian University of Athens, Athens, Greece, evinom@geol.uoa.gr (3) International Hellenic University, Drama, Greece (4) (hands-on studio), Research & Art Direction, Branding, UX/UI Design, Project Management (5) Econtent Systems P.C, Software, Website and Mobile application development, Athens, Greece

Nisyros Geopark, located in the Southeastern Aegean, is a candidate for inclusion in the UNESCO Global Geoparks Network, recognized for its exceptional volcanic heritage and its integration of geological, natural, and cultural elements. Covering 481 km², the geopark is centered on the active Nisyros volcano and nearby islands, forming a dynamic landscape shaped by the South Aegean Volcanic Arc. Among its 24 geosites are active hydrothermal craters, a collapse caldera, volcanic domes, and numerous coastal hot springs, all of which serve as key focal points for educational activities.

Education is a cornerstone of the Geopark's mission, with a range of ongoing programs designed to share its unique geological story with diverse audiences. Workshops, guided tours, summer schools and educational programs are regularly organized to connect participants—ranging from local students to international visitors—with the island's volcanic and cultural history (Fig. 1,2). These activities have yielded significant outcomes, including increased local awareness of geohazards, active participation from hundreds of students annually, and strengthened collaboration with academic institutions. Evaluations indicate that participants develop a deeper understanding of volcanic processes and their environmental implications, contributing to a broader appreciation of geoconservation. These activities aim to foster an understanding of the dynamic processes that shaped the island and their relevance to contemporary environmental issues.



Figure 1. CIVIS Summer School "NATRISKS", May 2024
"Vulnerability of the Eastern Mediterranean: Natural Processes and Climate Risks "

Modern communication tools further enhance the educational experience. The Geopark's official website (www.nisyrosgeopark.gr), along with dedicated mobile applications, provides accessible and engaging resources, enabling visitors to explore the region's geoheritage independently or as part of structured activities. Partnerships with schools, universities, and cultural institutions ensure that educational outreach is deeply integrated into the community, encouraging active participation and fostering a long-term appreciation of the island's natural and cultural heritage.

By combining hands-on experiences, innovative communication techniques, and collaborations with educational organizations, Nisyros Geopark is establishing itself as a hub for learning and discovery. These efforts position the Geopark as a model for integrating education with the preservation and celebration of volcanic heritage, ensuring its significance is understood and valued by future generations.



Figure 2. European Geoscience Day 2023 in Nisyros Geopark

Acknowledgements
We sincerely thank the management body of Nisyros Geopark (DIKEN) and the Mayor of Nisyros, Mr. Koroneos Christofis, for their invaluable contributions and steadfast support. Their dedication has been pivotal in fostering sustainable development, preserving the region's unique geological and cultural heritage, and enriching its educational activities. These efforts have greatly enhanced the geopark's role as a center for learning and exploration, while also advancing its candidacy as a UNESCO Global Geopark.

17th INTERNATIONAL CONGRESS of the Geological Society of Greece

BULLETIN OF THE GEOLOGICAL SOCIETY OF GREECE, SP. PUBL.

EXTENDED ABSTRACT 228

The 2024 March 29, 5.9 M_L Strofades Earthquake (Greece) and its Seismic Sequence: Relocation, Focal Mechanism Solutions and Stress Inversion

Nikolopoulou I.[1], Bocchini G. M.[2], Roth M. P.[2], Essing D.[2], Harrington R. M.[2], Serpetsidaki A.[1], Fountoulakis I.[3], Evangelidis C.[3], Sokos E.[1]

(1) Seismological Laboratory, University of Patras, Patras, Greece, inikolopoulou@ac.upatras.gr

(2) Ruhr University of Bochum, Bochum, Germany

(3) National Observatory of Athens, Athens, Greece

Introduction

On March 29, 2024, a M_L 5.9 earthquake occurred offshore western Peloponesse, near the Strofades Islands in Western Greece. The region lies within the complex tectonic setting of the western segment of the Hellenic Subduction System (HSS), where the African plate is being subducted beneath the Aegean microplate with rates of 30-35 mm/yr (e.g., Chousianitis et al., 2015). The seismotectonic setting is controlled by the active subduction and the Kefalonia Transform Fault, which hosts the lateral transition from subduction to collision between Eurasian and Apulian plates. The mainshock was preceded by a M_L 4.1 foreshock and followed by an aftershock sequence consisting of hundreds of events that continued until June. The sequence occurred at depths ranging from 25 to 35 km, with the mainshock located at 33 km depth within the subducting slab.

The seismic sequence occurred in a region with limited station coverage, particularly offshore, where the azimuthal gap exceeds 180°. Onshore station coverage in western Peloponnese is adequate, but offshore seismic monitoring is significantly constrained. However, the mainshock and its aftershock sequence were well-recorded by the newly installed Pelops network (Harrington et al., 2023), consisting of eight broadband stations deployed by Ruhr University of Bochum in collaboration with the University of Patras and the Institute of Geodynamics of the National Observatory of Athens (NOA).

Using high-resolution seismic data from the Pelops, HUSN and Adria Array networks, we apply machine learning techniques to develop an enhanced catalog. We analyze the sequence through earthquake relocation, focal mechanism solutions, and stress tensor analysis, aiming to provide new insights into the seismic activity and fault dynamics in the western segment of the Hellenic Subduction System.

Data & Methods

To investigate the M_L 5.9 seismic sequence, we analyze the seismicity recorded across the broader region following the deployment of the Pelops network in December 2023. Seismic data include waveforms recorded from December 2023 to September 2024 by the Hellenic Unified Seismological Network (HUSN), Pelops, and Adria Array networks. Using machine learning techniques, we construct a joint catalog, by applying the PhaseNet picker (Zhu and Beroza, 2019) for automatic phase-arrival picking and the PyOcto associator (Münchmeyer, 2024) for correlating phase picks with corresponding events.

We obtain earthquake locations using NLLoc (Lomax et al., 2000) and achieve high-quality hypocentral solutions by applying Source-Specific Station Terms (SSST) travel-time corrections and a coherency analysis of earthquake waveforms (Lomax & Savvaidis, 2022). We use the 1D Vp velocity model of Sachpazi et al. (2020) that we edit by replacing the first two layers with those from the velocity model of Kassaras et al. (2014). We assume a Vp/Vs ratio of 1.81, derived from events in our catalog that have at least 10 reliable Vp/Vs pairs.

We further investigate the sequence by obtaining moment tensors for five events, consisting of the foreshock, mainshock and three larger aftershocks, through full-waveform inversion using the ISOLA code (Sokos & Zahradnik, 2008). We analyze 20 additional aftershocks of lower magnitudes and determine their focal mechanism solutions from first-motion polarity data using the FPFIT program (Reasenberg & Oppenheimer, 1985). Finally, we conduct stress tensor analysis with the StressInverse code (Vavryčuk, 2014) using moment tensor-solutions and well-constrained focal mechanisms.

Results & Discussion

The M 5.9 March 2024 Strofades earthquake ruptured a NE-SW left-lateral strike-slip fault. The distribution of relocated aftershocks aligns with the NE-SW strike inferred from the focal mechanism solution of the mainshock and delineates a structure approximately 10-12 km in length and 6-8 km in width (Figure 1). The foreshock and the mainshock occurred at 30 and 33km depth, respectively, while aftershocks were distributed between 25 to 35 km (Figures 1,3).

The top of the subducting slab in the region is estimated to lie at approximately 20 km depth (Makris & Papoulia 2014, Sachpazi et al. 2016, Bocchini et al. 2018), suggesting that the rupture occurred within the subducting slab.
Focal mechanism solutions derived from moment tensor inversion and first-motion polarities, predominantly indicate strike-slip and normal faulting (Figure 2). The moment tensor solutions of the foreshock, mainshock and largest aftershocks suggest NE-SW strike-slip faulting, with the exception of one event, which exhibits normal faulting with a significant strike-slip component (Figure 2). Focal mechanisms derived from first-motion polarities are compatible with the kinematics of the mainshock (Figure 2, inset).
The geometry of the ruptured area is well-constrained in the two cross-sections, which were constructed parallel and perpendicular to the strike of the aftershock sequence, in SW-NE and NW-SE directions, respectively (Figure 3). The spatial distribution of the sequence is evident in the A-A´ profile, showing the width and length of the ruptured area. The B-B´ cross-section reveals a well-constrained vertical structure, with hypocenters aligned with the dip inferred from the focal mechanisms (Figure 3). Stress tensor analysis indicates a σ_3 axis oriented in an E-W direction, σ_1 oriented horizontally in a N-S direction and a vertically oriented σ_2 (Figure 2). P- and T-axes azimuths are consistent with the inferred stress axes within the subducting plate (Shaw & Jackson, 2010).
The mainshock and its aftershock sequence are not related to any mapped faults at the surface, as their location, geometry and kinematics do not align with the observed spatial distribution of the sequnce (Figure 1). The rupture occurred within the subducting slab, with no evidence of slip along any mapped offshore structures, as further indicated by the cross-sections (Figure 3).
After the mainshock, a sequence consisting of numerous events was recorded onshore in the eastern part of the study area (Figure 1). Future work will assess any potential connection to the Strofades seismic sequence.

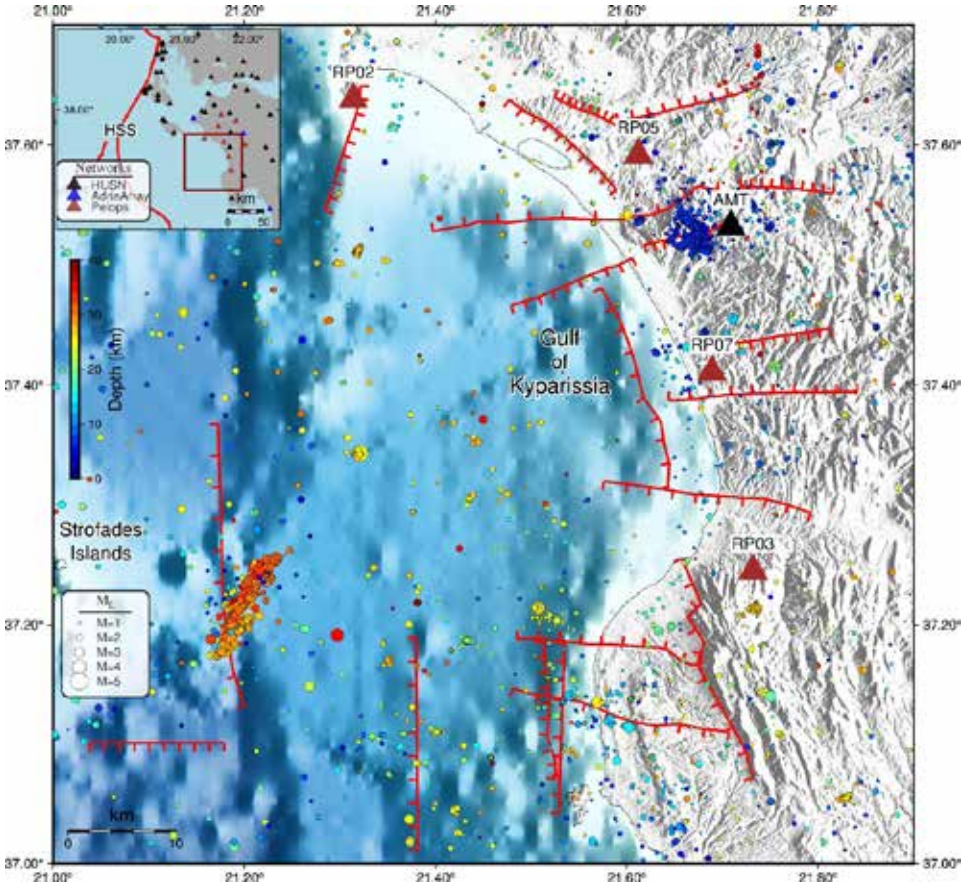


Figure 1. Seismicity map of the broader Gulf of Kyparissia region, showing relocated earthquakes of the M 5.9 earthquake sequence and regional seismicity recorded between December 2023 and September 2024. Earthquakes are depicted as circles, scaled by magnitude and color-coded by depth. Triangles denote the seismic stations operating within the study area. The inset map shows the location of the study area, station coverage across western Greece, and the Hellenic Subduction System (HSS), the main seismotectonic feature of the region. Mapped active faults (in red colour) from Ganas (2024).

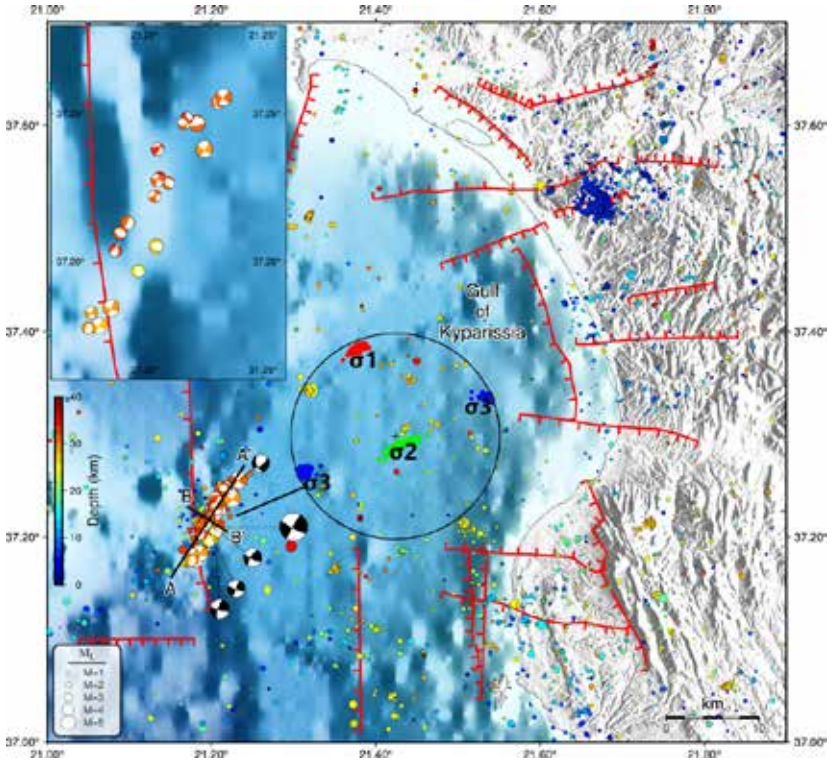


Figure 2. Focal mechanisms of the foreshock, mainshock and 23 major aftershocks of the Strofades sequence, polarity-based solutions are color-coded by depth, centroid moment tensors are the black beachballs, black lines connect the beachball with the centroid location. The location of the A-A´ cross-section and its perpendicular B-B´ cross-section is also shown. A zoomed-in view of the focal mechanisms of the aftershocks in the inset. Principal stress axes (σ1, σ2 and σ3) orientation is shown in the stereographic plot. Mapped active faults (in red colour) from Ganas (2024).

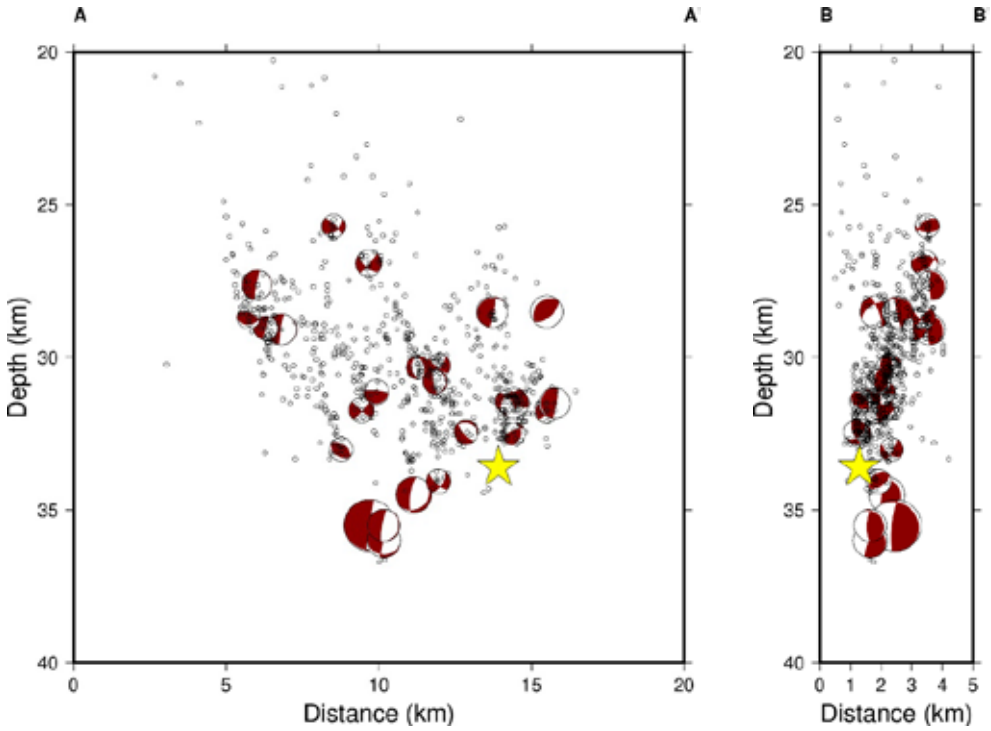


Figure 3. Distribution of the relocated hypocenters in A-A´ (along strike) and B-B´ (along dip) profiles. Beachballs are projected at the centroid location, yellow star denotes mainshock's hypocenter.

Acknowledgements

Waveforn seismic data were retrieved from EIDA@NOA (https://eida.gein.noa.gr/) and the following networks were used. HL (NOA, Hellenic Seismic Network), DOI:10.7914/SN/HL, HT (Aristotle University of Thessaloniki Seismological Network), DOI:10.7914/SN/HT, HP (University of Patras, Seismological Laboratory), DOI:10.7914/SN/HP, HA (National and Kapodistrian University of Athens, Seismological Laboratory), DOI:10.7914/SN/HA, HI (Institute of Engineering Seismology and Earthquake Engineering), DOI:10.7914/SN/HI, HC (TEI of Crete, Seismological Network of Crete), DOI:10.7914/SN/HC, 1Y (2022-2026) (Greece/North Macedonia Contribution to AdriaArray Temporary Network), DOI:10.7914/y0t2-3b67, 5B (2023-2027) (RUB Observational Geophysics Lab Deployment: Northwestern Peloponnese (Pelops), DOI:10.7914/pxkt-x819.

References

Bocchini, G. M., Brüstle, A., Becker, D., Meier, T., van Keken, P.E., Ruscic, M., Papadopoulos, G.A., Rische, M., Friederich, W., 2018. Tearing, segmentation, and backstepping of subduction in the Aegean: New insights from seismicity. Tectonophysics 734-735, 96-118.

Chousianitis, K., Ganas, A., & Evangelidis, C. P. (2015). Strain and rotation rate patterns of mainland Greece from continuous GPS data and comparison between seismic and geodetic moment release. Journal of Geophysical Research: Solid Earth, 120(5), 3909–3931.

Friederich, W., Evangelidis, C., Papazachos, C., Sokos, E., Kaviris, G., & Cernih, D. (2022). AdriaArray Temporary Network: Greece, North Macedonia [Data set]. International Federation of Digital Seismograph Networks.

Ganas, A. (2024). NOAFAULTS KMZ layer Version 6.0 (version 6.0) [Data set]. Zenodo.

Harrington, M., Bocchini, G. M., Roth, M., Sokos, E., & Evangelidis, C. (2023). RUB Observational Geophysics Lab Deployment: Northwestern Peloponnese [Data set]. International Federation of Digital Seismograph Networks.

Kassaras, I., Kapetanidis, V., Karakonstantis, A., Kaviris, G., Papadimitriou, P., Voulgaris, N., Makropoulos, K., Popandopoulos, G., Moschou, A., 2014. Journal of Geodynamics 73, 60-80.

Lomax, A., & Savvaidis, A., 2022. High-Precision Earthquake Location Using Source-Specific Station Terms and Inter-Event Waveform Similarity. Journal of Geophysical Research: Solid Earth 127, e2021JB023190.

Lomax, A., Virieux, J., Volant, P., Berge, C., 2000. Probabilistic earthquake location in 3D and layered models: introduction of a Metropolis-Gibbs method and comparison with linear locations, in: Thurber, C.H., Rabinowitz, N. (Eds.), Advances in Seismic Event Location. Kluwer, Amsterdam, 101–134.

Makris, J., & Papoulia, J., 2014. The backstop between the Mediterranean Ridge and western Peloponnese, Greece: its crust and tectonization. An active seismic experiment with ocean bottom seismographs. Bollettino di Geofisica Teorica ed Applicata 55(2), 249-279.

Münchmeyer J., 2024. PyOcto: A high-throughput seismic phase associator. Seismica 3.

Reasenberg, P. & Oppenheimer, D., (1985). FPFIT, FPPLOT and FPPAGE: Fortran computer programs for calculating and displaying earthquake fault plane solutions, Open-File Report, U.S. Geological Survey, 95-515.

Sachpazi, M., Laigle, M., Charalampakis, M., Diaz, J., Kissling, E., Gesret, A., Becel, A., Flueh, E., Miles, P., Hirn, A., 2016. Segmented Hellenic slab rollback driving Aegean deformation and seismicity. Geophysical Research Letters 43 (2), 651–658.

Sachpazi, M., Kapetanidis, V., Charalampakis, M., Laigle, M., Kissling, E., Fokaefs, A., Daskalaki, E., Flueh, E., Hirn. A., 2020. Methoni Mw 6.8 rupture and aftershocks distribution from a dense array of OBS and land seismometers, offshore SW Hellenic subduction. Tectonophysics (796) 228643.

Shaw B., & Jackson J. (2010). Earthquake mechanisms and active tectonics of the Hellenic subduction zone. Geophysical Journal International, 181(2), 966-984.

Sokos, E. N., & Zahradnik, J. (2008). ISOLA a Fortran code and a Matlab GUI to perform multiple-point source inversion of seismic data. Computers and Geosciences, 34(8), 967–977.

Vavryčuk, V. (2014). Iterative joint inversion for stress and fault orientations from focal mechanisms. Geophysical Journal International, 199(1), 69–77.

Zhu, W., Beroza, G.C., 2019. PhaseNet: a deep-neural-network-based seismic arrival-time picking method. Geophysical Journal International 216(1), 261-273.

17th INTERNATIONAL CONGRESS of the Geological Society of Greece

BULLETIN OF THE GEOLOGICAL SOCIETY OF GREECE, SP. PUBL.

EXTENDED ABSTRACT 229

Sinkholes, roads and exceptional transports, a risk to be assessed

Stefania Nisio[1], Sergio Madonna[2], Giancarlo Ciotoli[3], Francesco Gentili[2], Livio Ruggiero[3]
1 ISPRA – Dipartimento per il Servizio Geologico d'Italia , Via Vitaliano Brancati 48, 00144 Roma
2 Università degli Studi della Tuscia - Via San Camillo de Lellis, 01100 VITERBO (VT).
3 CNR – Consiglio Nazionale delle Ricerche, Italy Piazzale Aldo Moro 7 Roma

Introduction / Background

The Italian territory, characterised by its complex geological and geomorphological features, faces a unique combination of natural hazards, including volcanic activity, landslides, floods, sinkholes and seismic events.
These hazards, which affect nearly the entire country, pose significant challenges to the safety and resilience of transportation networks. Among these geohazards, natural and anthropogenic sinkholes represent a particularly insidious threat due to their sudden and unpredictable nature, often resulting in severe disruptions to road infrastructure.
This danger is further exacerbated by exceptional transports (ETs)—vehicles carrying oversized or heavy loads—which require stable and robust roadways to ensure operational safety.
Italy's urban centres' historical and archaeological richness introduces an additional layer of complexity. Many Italian cities, with their millennia-old history, rest on a network of underground cavities, often remnants of ancient quarries, tunnels, and cisterns. These subterranean voids, many of which remain undocumented, frequently intersect the modern road network, creating hidden vulnerabilities. In historical centres where traffic is already constrained, the passage
A critical dimension of this issue lies in Italy's current nuclear waste management challenges. The absence of a national repository for radioactive waste has necessitated the storage of such materials in numerous temporary facilities scattered across the country, many of which are considered suboptimal in terms of security and stability. Once a national repository is identified, extraordinary transport will play a central role in transferring these hazardous materials to a single site.
The combination of geohazards, infrastructure vulnerabilities, and the logistical demands of nuclear waste transport underscores the critical need for comprehensive risk assessment and mitigation strategies
Comprehending the relationship between sinkhole formation and the transportation of heavy loads is essential, as incidents can increase the risk of human life loss, environmental pollution problems, and significant economic and infrastructure damage.

Objectives

This study aims to raise awareness among public administrations, as well as public and private entities about the significant hazards posed by natural or anthropogenic sinkholes, particularly in the context of exceptional transport planning. The goal is to ensure that this geohazard is systematically accounted for in decision-making processes to mitigate potential safety threats and infrastructure damage.
The issue is especially critical in the historical centers of Italy's art cities, where intricate networks of underground cavities create hidden vulnerabilities that can be exacerbated by exceptional transports or by the placement of heavy temporary structures. The concentrated stress from such activities can trigger or accelerate sinkhole formation, posing a serious threat not only to the stability of the ground but also to the preservation of invaluable cultural and architectural heritage.
Beyond urban areas, this problem is equally relevant in sparsely populated rural and extra-urban regions. Here, the planning of exceptional transports—particularly those involving extremely heavy or high-risk cargo, such as nuclear waste. By highlighting these risks, this study seeks to provide a comprehensive framework for integrating sinkhole hazard assessments into the planning and execution of exceptional transports. This includes developing guidelines for evaluating subsurface stability, strengthening coordination between public and private stakeholders, and implementing preventive measures to enhance the resilience of both urban and rural infrastructures.
By emphasising the importance of continuously updating datasets and integrating diverse geospatial layers, this study seeks to establish a best-practice model for sinkhole risk assessment and mitigation, facilitating safer and more informed decision-making for exceptional transport and infrastructure planning.

Methods

The foundation of this study is the recently updated database of sinkholes and underground cavities developed as part of the PNRR Geosciences IR Project (figure 1A, B). This comprehensive dataset provides a crucial resource for understanding the spatial distribution of sinkholes across Italy and their potential impact on infrastructure. By leveraging Geographic Information System (GIS) technologies, it is now possible to overlay the mapped distribution of currently catalogued sinkholes (point vector layer) with the layout of primary and secondary road networks (line vector layer). The distance from each sinkhole to the nearest road segment can be calculated using GIS tools, such as QGIS's "Distance to Nearest Hub," ArcGIS's "Near" tool,

or GRASS GIS's v. distance. Specific sections of roads can be classified into hazard categories according to their distance from sinkholes. To refine this assessment, additional geospatial layers, including structural elements (e.g., tectonic features), gas emission distributions, geological (e.g., karst terrains, soluble rock types, etc.) or hydrogeological data (e.g., groundwater flow, water table fluctuations, etc.), historical variations of hydrography, land use, etc. can be integrated to identify areas where environmental, geological or anthropogenic conditions may exacerbate sinkhole hazard along specific road segments. Finally, thematic maps are created to visualise risk zones; statistical analyses can identify high-risk clusters, and the results with field data or expert knowledge to ensure accuracy and local relevance. This approach provides a comprehensive framework for evaluating sinkhole hazards near road networks while allowing for site-specific adjustments based on additional data.
Thematic maps, like susceptibility maps, could be created to visualise the likelihood of sinkhole occurrence across large hazard zones. Still, the results must be validated with field data, analysis, and expert knowledge to ensure accuracy and local relevance. Particularly, the development of susceptibility maps for major urban areas offers invaluable tools for planning exceptional transport and positioning temporary heavy loads, such as those used for events or maintenance activities on buildings and infrastructure.

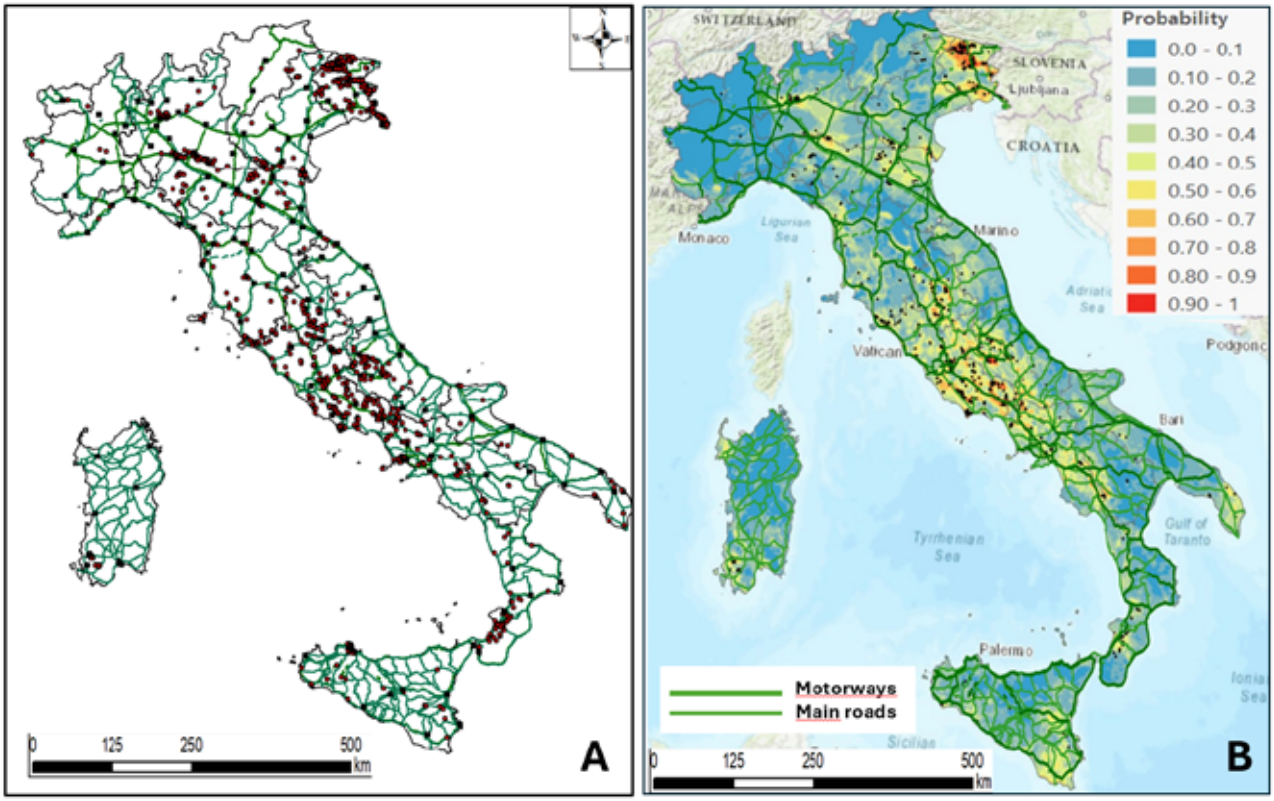


Fig. 1 - Main roads in Italy and: A) Natural sinkhole distribution B) susceptibility maps. From the GIS database PNNR-Geosciences-IR

The first phase of constructing an anthropogenic sinkhole susceptibility map involved constructing a conceptual model identifying potential predisposing factors for anthropogenic sinkholes in urban areas. All selected factors (independent variables), along with the sinkhole database (response variable), were entered into a geodatabase managed in a GIS environment in shapefile format (point, linear, and polygonal geometries) and/or raster format (grid). All grid layers (original and/or produced) were constructed with a resolution appropriate for the purpose of the study. The density analysis of event distribution is a fundamental and straightforward technique to determine the area most prone to a specific geographical phenomenon. The density model is based on the hypothesis that areas with a higher presence of events are more likely to experience additional occurrences. The density analysis was carried out using the "Kernel Density Estimation" (KDE) (Silverman, 1986). The KDE produces a density map representing the number of elements per unit area based on the neighbourhood distance around those elements. The neighbourhood distance is determined by the observed mean distance using the NNI. Density analysis can be calculated for both point and linear elements. Density maps provide preliminary zoning of the territory; a sinkhole density map constitutes an initial evaluation element of an area's susceptibility to this phenomenon.

Random forest regression, a supervised machine learning model that combines decision trees to make accurate predictions, was used to develop a sinkhole susceptibility map (figure.1B). Sinkhole presence, transformed into a binary variable (presence/absence), was used as target variable. Predisposing factors of various types were considered as predictors, organised into a national 10x10 km grid. These included geological variables (GEO, KA), geomorphological factors (DTM, TPI, HAND, Slope), hydrogeochemical indicators (DensGas, DistGasCat, DensSpring, DistSpringCat), seismic features (EQD) and structural parameters (FD). Both continuous and categorical variables were processed to capture detailed local environmental conditions. The supervised method split the data into training and test sets to ensure robust model evaluation and validation. With its ability to handle non-linear relationships and complex variable interactions, the Random Forest model was trained on these data to identify areas with higher susceptibility to sinkhole formation. In addition, the model provided insight into the key drivers of sinkhole susceptibility by providing a Receiver Operating Characteristic (ROC) curve to assess its predictive performance and quantify the importance of each variable.

Results and discussion

Sinkholes are large depressions that suddenly open in the ground catastrophically, with diameters and depths varying from a few to hundred of meters. They are divided into two main categories: natural sinkholes that mostly occur in plain areas and anthropogenic sinkholes affecting basically urban centres, particularly in large metropolitan areas. Natural sinkholes are related to the area's geological, structural, and hydrogeological context, while anthropogenic sinkholes are directly or indirectly related to human activities, particularly the presence of underground cavities.

In recent decades, many sinkholes have opened up in or near important road arteries in extra-urban (figure 2A, B) or urban (figure 2C, D) areas.



Fig. 2 - Examples of sinkholes affecting extra-urban and urban roads: A) provincial road near Ravenna; B) provincial road that crosses the Vepe-Latera caldera (Volsini Volcanic Complex - Latium); C) Viterbo - collapse of the vaults of underground environments under an urban road; D) Rome urban road Via Sestio Mensas.

The recent event that occurred inside the Latera-Vepe caldera (figure.2B) near (about 5m) from Provincial Road 118 leading to Lake Mezzano points out that even volcanic areas are not exempt from these phenomena, which are too often underestimated (Puzzilli et al., 2024). This case also shows that sinkholes are very easily filled with water almost simultaneously with their formation. It is common, after their formation, for groundwater or water rising from deep aquifers to flow into the cavity, turning it into a small lake, and this could lead to further complications in the sinkholes open in communication infrastructure.

The National Database of ISPRA is a fundamental tool for mitigating sinkhole hazards (Caramanna et al. 2008; Nisio et al.

2007; Nisio 2008). Among its various applications, we want to emphasise its usefulness in managing and planning exceptional transport and positioning temporary large loads. ISPRA's National Sinkhole Database was developed using ESRI's ArcGIS software with the WGS84/UTM Zone 33N reference system and has been updated to include further natural sinkhole inventory in the flat areas of Italy, plateau regions, and the transition zones between plains and slopes. The current census is up to date, with more than 6,000 sinkhole phenomena catalogued and classified according to the Italian case typology proposed by Nisio (2008) (Fig. 1A), creating a unique database in Italy.

More than 6000 cases of natural subsidence in plain or slope areas, attributed to natural sinkhole phenomena, have been catalogued and studied by ISPRA through field investigations and archival studies. Many of the catalogued phenomena are hypothesized to relate to the upward migration of aggressive fluids. The areas most susceptible to sinkholes are concentrated in the central Tyrrhenian slope, particularly in the regions of Friuli Venezia Giulia, Lazio, Puglia, Abruzzo, Campania, and Tuscany. Due to its geological-structural setting, the Adriatic side is not affected by these types of sinkholes, nor are the Alpine arc and the Dolomites.

The conditions are different in Northern Italy (where the census is still ongoing). Small diameter depressions with modest depth (known as "occhi pollini") are also widespread in the Po Valley and Lombard plains. The genetic mechanisms of these depressions, probably caused by surface suffusion phenomena, are currently being studied. In the plains and internal basins of Veneto, Friuli-Venezia Giulia (Calligaris 2019 a, b; 2020), Puglia, and Sicily, as well as the Autonomous Province of Bolzano, subsidence phenomena are closely controlled by the dissolution of evaporitic and carbonate lithotypes found beneath relatively thin covers, which are therefore attributable to cover-collapse sinkhole types.

On the other hand, the phenomena reported in Calabria are linked to small cavities, now filled in, whose location is difficult to pinpoint. These originated entirely during seismic events and are associated with liquefaction phenomena in the soils. The geological context appears substantially different in Sicily and Puglia, where subsidence cases are influenced by the presence of evaporitic (gypsum and salt) or calcareous soils and by thinner clayey or sandy covers.

Anthropogenic sinkholes typically occur in large metropolitan cities and are primarily associated with the presence of a complex network of underground cavities (figure 2C), many of which are still unknown. The cities most affected by this phenomenon are Rome, Naples, Cagliari, and Palermo (figure 3A), for which more detailed time series data is available (Ciotoli et al. 2013, 2015 a, b, c; Nisio et al. 2017; Tufano et al. 2022). Similarly, the regions with extensive outcrops of volcanic rocks, such as Lazio and Campania (figure 3B), are the most affected by anthropogenic sinkholes, given the millenary history of occupation and exploitation of its subsoil.

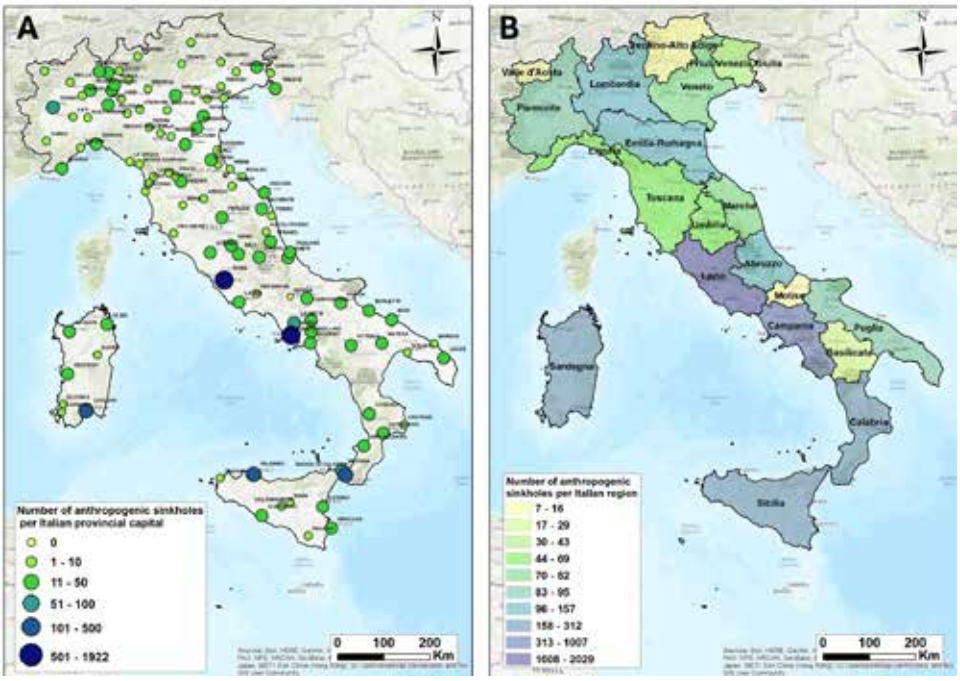


Figure 3-- - Number of anthropogenic sinkholes per Italian provincial capital A) and region B). From the database PNNR-Geosciences-IR.

These cavities have been created by human activity at various times over more than two thousand years. The presence of underground cavities can, under certain conditions, cause the more superficial soil layers to collapse, resulting

in sinkholes (anthropogenic sinkholes). An additional factor that contributes to the formation of such anthropogenic sinkholes is the malfunction, leakage and general dysfunction of the hydraulic network of the underground services. In the last forty years, the frequency of these phenomena has increased due to the denser and more indiscriminate urbanization of the area, and possibly also due to changes in rainfall patterns, which in recent years have led to very intense rainfall events and permanent flooding in certain areas of the city.

The application of the Random Forest Regression model provides a sinkhole susceptibility map, integrating predisposing factors such as geological, geomorphological, hydrogeochemical, and structural variables. The model achieved high predictive performance, as evidenced by the ROC curve with an AUC of 0.96 for the test data, indicating excellent discrimination between sinkhole-prone and non-prone areas. The variable importance analysis revealed that earthquake density (11.5%), gas emission density (11.4%), and karst areas (10%) were the most significant predictors, followed by fault density, mineral spring density, and slope.

The sinkhole susceptibility map (Fig. 1B) highlights areas of high probability, concentrated in karstic and faulted regions, as well as areas with high seismic activity or significant hydrogeochemical anomalies (Di Salvo et al.2024) The map provides valuable insights for land-use planning and risk mitigation, helping prioritise monitoring and intervention efforts in vulnerable areas. The updated sinkhole inventory, combined with this susceptibility analysis, represents a critical resource for understanding and managing sinkhole risks at a national scale.

The processes that create sinkholes are very complex and sometimes difficult to define, not solely attributed to gravity or karst dissolution but to a series of predisposing and triggering causes: liquefaction phenomena, the presence of cavities deep underground, easily erodible cover soils, tectonic features such as faults or fractures, CO_2 and H_2S upwelling, seismic events, heavy rainfall, and human activities like water extraction, mining, excavation, etc.

In urbanised areas, the most significant predisposing factor is generally related to the presence of pre-existing underground cavities, such as catacombs, hypogea, quarries, etc. The collapse or instability of these cavities can propagate to the surface, causing sudden collapses. Another critical element is associated with underground erosion processes caused by infiltration or exfiltration due to the deterioration of the sewer drainage system or underground water supply network. This progressive deterioration of underground cavities can lead to sudden collapses on the surface. Additionally, extreme meteorological events (prolonged or intense rainfall) can act as a triggering factor, especially in urban areas prone to flooding (Di Salvo et al., 2018).

In all these cases, however, the presence of heavy loads and vibrations caused by exceptional transports (ETs) can act as a significant triggering factor for sinkhole formation. These vibrations, combined with the concentrated weight of vehicles, can exacerbate the instability of subsurface voids or weakened geological structures, particularly in karst terrains or areas with soluble rock formations. Repeated mechanical stress from traffic can accelerate the collapse of cavities by dislodging loose sediment, compacting unconsolidated materials, or increasing subsurface pressure, leading to sudden subsidence. This effect is particularly pronounced in areas where groundwater flow or fluctuating water tables have weakened the subsurface, making it more susceptible to external forces. Such dynamics highlight the importance of monitoring high-traffic zones for sinkhole risks, especially in regions with vulnerable geological conditions.

Conclusion

In Italy, natural sinkholes predominantly affect extra-urban areas, while anthropogenic sinkholes are more prevalent in towns and cities. These phenomena pose significant dangers to road infrastructure, threatening public safety and causing substantial economic losses. Among the triggering factors for sinkholes, both natural and anthropogenic, are vibrations and overloads generated by human activities. Specifically, vibrations induced by heavy mechanical equipment used in construction or agriculture, as well as traffic from heavy vehicles, contribute to subsurface instability. Similarly, overloads from exceptional transports (ETs) or the temporary placement of very heavy loads create additional stress concentrations in the soil, further exacerbating pre-existing geological vulnerabilities.

These activities are particularly hazardous in areas prone to sinkhole formation, as they can destabilize subsurface structures and trigger collapses. In urban centres, most sinkholes occur on roadways due to the concentrated impact of traffic and infrastructure stress. In extra-urban areas, sinkholes are frequently found near major road infrastructures and railways, where the cumulative effects of vibrations and heavy loads are most pronounced. The hazard is heightened in regions with karst or pseudokarst formations, where underground cavities or soluble rock layers create a predisposition to collapse. Similarly, areas with unconsolidated soils or shallow water tables are at increased risk, as the additional stress from ETs can lead to soil liquefaction, suffusion, or piping phenomena. The impact of these overloads is not confined to natural sinkholes but extends to urban environments, where anthropogenic sinkholes are linked to underground cavities, failing hydraulic infrastructure or malfunctions of sub-service networks. Most Italian cities are built on a complex network of underground cavities, many of which are still unknown. In the last forty years,

the frequency of these phenomena has increased due to the denser and more indiscriminate urbanisation of the area and possibly also due to changes in rainfall patterns, which in recent years have led to very intense rainfall events and permanent flooding in certain areas of the city. Addressing these risks is essential to safeguard infrastructure, minimise hazards, and mitigate the socio-economic impacts associated with sinkhole formation.

The ISPRA dataset provides a crucial resource for understanding the spatial distribution of sinkholes across Italy and their potential impact on infrastructure. This has practical implications for improving the planning and management of exceptional transport and temporary heavy loads. The sinkhole susceptibility maps can guide decision-makers in prioritising monitoring efforts, implementing preventive measures, and mitigating risks associated with ETs and road infrastructure.

Integrating advanced modelling techniques, such as random forest regression, has proven essential for understanding and predicting natural sinkhole susceptibility. Through the combination of geological, geomorphological, hydrogeochemical and structural factors, the model provides a robust framework for assessing the likelihood of sinkhole formation across Italy. The model's high prediction performance (AUC of 0.96) demonstrates its reliability, while variable importance analysis identifies key drivers, including seismicity, gas emission densities and karst regions. These findings provide a better understanding of the sinkhole phenomenon and demonstrate the potential of machine learning to deal with complex geohazard scenarios.

Future work should focus on refining predictive models by incorporating time-series data, climate change projections, and emerging urbanisation trends. Enhancing these models will improve their reliability and applicability to complex geohazard scenarios. Ultimately, integrating advanced modelling techniques with historical and geospatial data provides a scalable and reproducible methodology for addressing sinkhole hazards.

Acknowledgements

This research was partially funded by PNRR—European Union—NextGenerationEU—Mission 4 "Education and Research"—Component 2 "From Research to Business"—Investment 3.1 "Fund for the realization of an integrated system of research and innovation infrastructures". CUP:I53C22000800006..

References

Calligaris C., Zini L., Nisio S., Piano C. (2019 a) - Sinkholes in the Friuli Venezia Giulia Region: state of the art of the of territorial analyses in the evaporites.Springer Book "Applied Geology: Approaches to Future Resource.

Calligaris C., Zini L., Nisio S., Piano C. (2019 b) - Sinkholes in the Friuli Venezia Giulia Region: state of the art of the of territorial analyses in the evaporites. Springer Book "Applied Geology: Approaches to Future Resource.

Calligaris, C., Zini, L., Nisio, S., & Piano, C. (2020). Sinkholes in the Friuli Venezia Giulia Region focus on the evaporites. Applied Geology: Approaches to Future Resource Management, 73-90.

Caramanna G., Ciotoli G., Nisio S. (2008) - A review of natural sinkhole phenomena in Italian plain areas. Journal of Natural Hazard, 45, 145- 172, DOI 10.1007/s, 11069-007-9165-7.

Ciotoli G. Corazza A., Finoia M.G., Nisio S. Succhiarelli C. (2013) – Gli sprofondamenti antropogenici nell'aria urbana di Roma. Mem. Descr. Carta Geol. D'IT. 93, 143-182.

Ciotoli G., Di Loreto E, Liperi L., Meloni F., Nisio S., Sericola A. (2015a) - Carta dei Sinkhole Naturali del Lazio 2012 e sviluppo futuro del Progetto Sinkholes Regione Lazio. Mem. Descr. Carta Geol. D'It. 99, 189-202.

Ciotoli G., Finoia m.G., Liperi L., Meloni F., Nisio S., Tonelli V., Zizzari P. (2015 b) - Sinkhole susceptibility map of the Lazio Region, central Italy. Journal of Maps 12-2, 287-294, 1/2015.

Ciotoli G., Nisio S., Serafini R. (2015 c) – Analisi della suscettibilità ai sinkholes antropogenici nel centro urbano di Roma: analisi previsionale. (2015) Mem. Descr. Carta Geol. D'IT. 99, 167-188.

Di Salvo, C., Ciotoli, G., Mancini, M., Nisio, S., & Stigliano, F. (2024) - Analysis of Geological Multi-Hazards in an Urban District. Geosciences, 14(2), 27.

Nisio S. (2008) - I fenomeni naturali di sinkhole nelle aree di pianura italiane. Monografia Memorie descrittive della Carta Geologica d'It. Vol. LXXXV; 475pp.

Nisio S., Caramanna G. & Ciotoli G. (2007) Sinkholes in Italy: First results on the inventory and analysis. Geological Society London Special Publications 279(1):23-45. DOI:10.1144/SP279.4

Nisio S., Allevi A., Ciotoli G., Ferri G., Fiore R., Pascucci R., Stranieri I., Succhiarelli C., (2017) Carta delle Cavità sotterranee di Roma. ISPRA

Puzzilli, L. M., Ruscito, V., Madonna, S., Gentili, F., Ruggiero, L., Ciotoli, G., & Nisio, S. (2024). Natural Sinkhole Monitoring and Characterization: The Case of Latera Sinkhole (Latium, Central Italy). Geosciences, 14(1), 18.

Silverman, B. W. (1986). Kernel density estimation technique for statistics and data analysis. *Monographs on statistics and applied probability*, *26*.

Tufano, R., Guerriero, L., Annibali Corona, M., Bausilio, G., Di Martire, D., Nisio, S., & Calcaterra, D. (2022). Anthropogenic sinkholes of the city of Naples, Italy: An update. Natural Hazards, 112(3), 2577-2608.

17th INTERNATIONAL CONGRESS
of the Geological Society of Greece

BULLETIN OF THE GEOLOGICAL SOCIETY OF GREECE, SP. PUBL.

EXTENDED ABSTRACT 230

Nisyros Geopark: A Living Laboratory of Volcanic Geoheritage in the South Aegean

Nomikou P.[1], Nikoli E.[2], Tasioulas E.[2], Koroneos C.[3], Sakkali K.[2], Koukourakis G.[2], Nastos P.[1], Antoniou V.[1], Emmanouloudis D.[3], Pehlivanides G.[4], Batis A.[5]

(1) National and Kapodistrian University of Athens, Athens, Greece, evinom@geol.uoa.gr (2) Municipal Public Benefit Enterprise of Nisyros (DIKEN) (3) International Hellenic University, Drama, Greece (4) (hands-on studio), Research & Art Direction, Branding, UX/UI Design, Project Management (5) Econtent Systems P.C, Software, Website and Mobile application development, Athens, Greece

Nisyros Geopark, a candidate for nomination as a UNESCO Global Geopark, is distinguished by its remarkable geological, natural, and cultural features. Situated in the Southeastern Aegean, it spans 481 km² and includes the active Nisyros volcano along with nearby islands (Fig. 1). Positioned at the southeastern edge of the South Aegean Volcanic Arc—one of the world's most significant active volcanic systems—the geopark offers a unique terrestrial and submarine landscape shaped by its volcanic origins. The geopark encompasses 24 geosites (Fig. 2), showcasing its rich geological history. Visitors can explore the impressive collapse caldera, hydrothermal craters and lava domes on the western side, stratified layers of lava, ash, and pyroclastics, which chronicle its extensive geological evolution (Parcharidis et al., 2018). Active hydrothermal craters and numerous coastal hot springs highlight ongoing hydrothermal activity, while the submarine aspects of the geopark are key to its formation and development. These features attract international scientific research, positioning Nisyros Geopark as a prominent natural geological laboratory in the Eastern Mediterranean. As part of the South Aegean Volcanic Arc, the geopark features a striking landscape shaped by five eruptive cycles over the past 160,000 years (Dietrich & Lagios, 2018). These cycles have left their mark on both the land and the seabed (Nomikou & Papanikolaou, 2011). The offshore region continues this volcanic landscape beneath the sea, hosting basins, underwater volcanic structures like craters and lava domes, fractures, and even a prehistoric caldera, Avyssos, located northeast of Strongyli islet (Tibaldi et al., 2008; Nomikou et al., 2021).



Figure 1. Nisyros Geopark location map

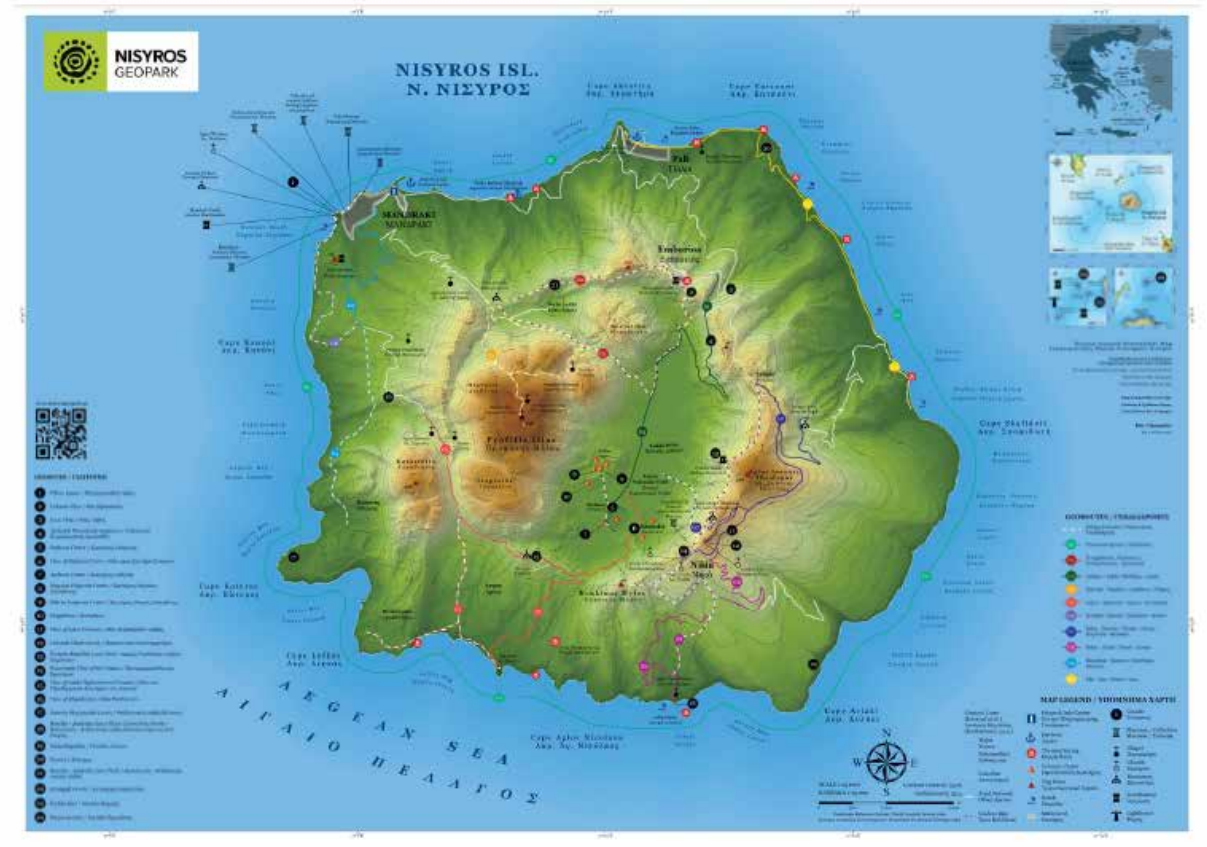


Figure 2. Nisyros Geopark geotouristic map

Beyond its geological wonders, the geopark is steeped in cultural heritage. Despite its modest size, the region has been continuously inhabited for millennia and is linked to the myth of Gigantomachy. The region's cultural heritage has stood steadfast through the ages, showcasing the brilliance of art and civilization through its prehistoric and historic sites and monuments. It is home to remarkable archaeological and cultural landmarks, including fortresses such as Paleokastro and the Mandraki castle, remnants of ancient settlements, numerous Byzantine-era churches and monasteries like the famous Panagia Spliani Monastery (Fig. 3), as well as thermal springs tied to its long-standing tradition of thermal baths. Together, these elements have shaped the region's history, fostering the traditions and preserving the tangible and intangible heritage cherished by its local communities today. Moreover, the Geopark features rich biodiversity protected by the two internationally designated Natura 2000 areas including its entire surface, as well as three wildlife refuge areas recognized at a national level. A great number of species of flora, avifauna and reptiles thrive within the geopark's area (Antoniou et al., 2019).



Figure 3. Panagia Spiliani Monastery (left) and ancient wall of Paleokastro (right)

To enhance visitor engagement and educational opportunities, Nisyros Geopark is upgrading its services. Current initiatives include the development of two free mobile applications, Nisyros Geopark App and Nisyros Volcano App, an informative website (www.nisyrosgeopark.gr) and a variety of educational materials. The geopark actively promotes awareness through talks, workshops, summer schools, and media campaigns, fostering an appreciation of its unique geological and cultural significance among residents and visitors alike.

Acknowledgements
We extend our heartfelt gratitude to the management body of Nisyros Geopark (DIKEN) and the Mayor of Nisyros, Mr. Koroneos Christofis, for their invaluable contribution, unwavering support, and dedication to the vision of the geopark. Their efforts have been instrumental in promoting the sustainable development of the region, preserving its unique geological and cultural heritage, and advancing its candidacy as a UNESCO Global Geopark.

References

Antoniou, V., Nomikou, P., Zafeirakopoulou E., Bardouli P., Ioannou T., 2019. Geo-biodiversity and cultural environment of Nisyros volcano, 15th International Congress of the Geological Society of Greece, Athens, 22-24 May, 2019 | Harokopio University of Athens, Greece. Bulletin of the Geological Society of Greece, Sp. Pub. 7 Ext. Abs. GSG2019-195.

Dietrich, V. and Lagios, E., 2018. Nisyros Volcano, The Kos - Yali - Nisyros Volcanic Field. 1st ed. Springer, Cham.

Nomikou P., Papanikolaou D. (2011). Extension of active fault zones on Nisyros volcano across the Yali-Nisyros Channel based on onshore and offshore data. Marine Geophysical Research 32 (1), pp.181. DOI 10.1007/s11001-011-9119-z.

Nomikou, P., Krassakis, P., Kazana, S., Papanikolaou, D. and Koukouzas, N., 2021. The Volcanic Relief within the Kos-Nisyros-Tilos Tectonic Graben at the Eastern Edge of the Aegean Volcanic Arc, Greece and Geohazard Implications. Geosciences, 11(6), p.231.

Parcharidis, I., Lagios, E. and Sakkas, V., 2018. Differential interferometry as a tool of an early warning system in reducing the volcano risk: the case of Nisyros volcano. Bulletin of the Geological Society of Greece, 36(2), p.913.

Tibaldi A., Pasquarè F.A., Papanikolaou D., Nomikou P. (2008). Tectonics of Nisyros Island, Greece, by field and offshore data, and analogue modeling. Journal of Structural Geology 30 (12), pp.1489.

17th INTERNATIONAL CONGRESS of the Geological Society of Greece

BULLETIN OF THE GEOLOGICAL SOCIETY OF GREECE, SP. PUBL.

EXTENDED ABSTRACT 231

Assessment of groundwater quality and seasonal dynamics in Chortiatis, northern Greece: Insights for sustainable resource management

Ntona Maria Margarita [1], Stavropoulou Vasiliki [2], Lampropoulou Dimitra [3], Zagana Eleni [2], Pouliaris Christos[2], Kazakis Nerantzis [2]

(1) Laboratory of Engineering Geology & Hydrogeology, Department of Geology, Aristotle University of Thessaloniki, 54124 Thessaloniki, Greece, margaritantona@yahoo.com (2) Laboratory of Hydrogeology, Department of Geology, University of Patras, Faculty of Natural Sciences, 26504 Rion, Patras, Greece, nkazakis@upatras.gr (3) Department of Chemistry, Aristotle University of Thessaloniki, 54124 Thessaloniki, Greece

Research Highlights:

- Groundwater samples are characterized by Ca-HCO□ water type.
- Seasonal groundwater level variations reveal various recharge patterns based on precipitation events.

Introduction / Background

Various geological formations and significant seasonal variability in precipitation influence complex hydrogeological environments (Luo *et al.*, 2023). In these cases, effective groundwater management requires a comprehensive understanding of both groundwater levels and quality parameters, especially under the pressures of the climate crisis (Davamani *et al.*, 2024). This study presents the results of field measurements as well as hydrochemical and statistical analysis to assess groundwater quality in the Chrotiatis region, Greece. By combining these methodologies, a comprehensive hydrogeological profile of the region is provided with valuable insights for future resource management. In this aspect, hydrochemical analyses of groundwater samples reveal potential sources of pollution, while groundwater level data provide insights into seasonal fluctuations and recharge patterns of the study area. Additionally, groundwater level measurements reveal temporal trends, including seasonal declines offering key insights into the dynamics of the region's water resources. The findings are expected to benefit water authorities and local stakeholders by offering reliable insights for sustainable groundwater management, protection strategies, and the mitigation of pollution risks.

Study area

The study area is located in northern Greece in the Central Macedonia region (Figure 1). The upper geological units in the area comprise alluvial deposits and red clays, while the Alpine formations, including clay schists, limestones, and igneous rocks, reflect significant tectonic and magmatic activity in the study area. The presence of quartzites and various igneous rocks, such as gabbros and peridotites indicates volcanic processes. These formations contribute to the area's aquifer systems and play a key role in water storage and water movement through the complex lithology. The presence of these diverse geological formations contributes to several types of aquifers in the area, namely alluvial, fractured, and karst aquifers. Based on the Copernicus database, the study area is occupied by transitional forested and shrubland (27.9%), agricultural activities with significant parts of natural vegetation (18.7%), and non-irrigated-arable land (15.7%). Mineral mining sites of limestones and mixed forests are also noted.

Methodology

The combination of qualitative and quantitative data can provide significant information about groundwater dynamics, the influence of local geological formations, and the potential sources of pollution in the aquifers (Kazakis *et al.*, 2015). In this study, monthly groundwater level measurements were obtained across the study area during the period of 2023-2024 to establish a hydrogeological framework using a judgmental sampling approach (Ntona *et al.*, 2023). Additionally, chemical analyses of sixteen (16) groundwater samples from deep boreholes were performed in June 2024 to assess the concentrations of major ions and trace elements, revealing mixing processes and ion exchange reactions in the study area. Piper and Durov diagrams are constructed in AquaChem software, while the maps were designed in ArcMap software. Precipitation data was obtained from the meteorological station Eptapurgio (meteo.gr), located near the study area. Raster file of digital elevation model (DEM) downloaded by NASA open data.

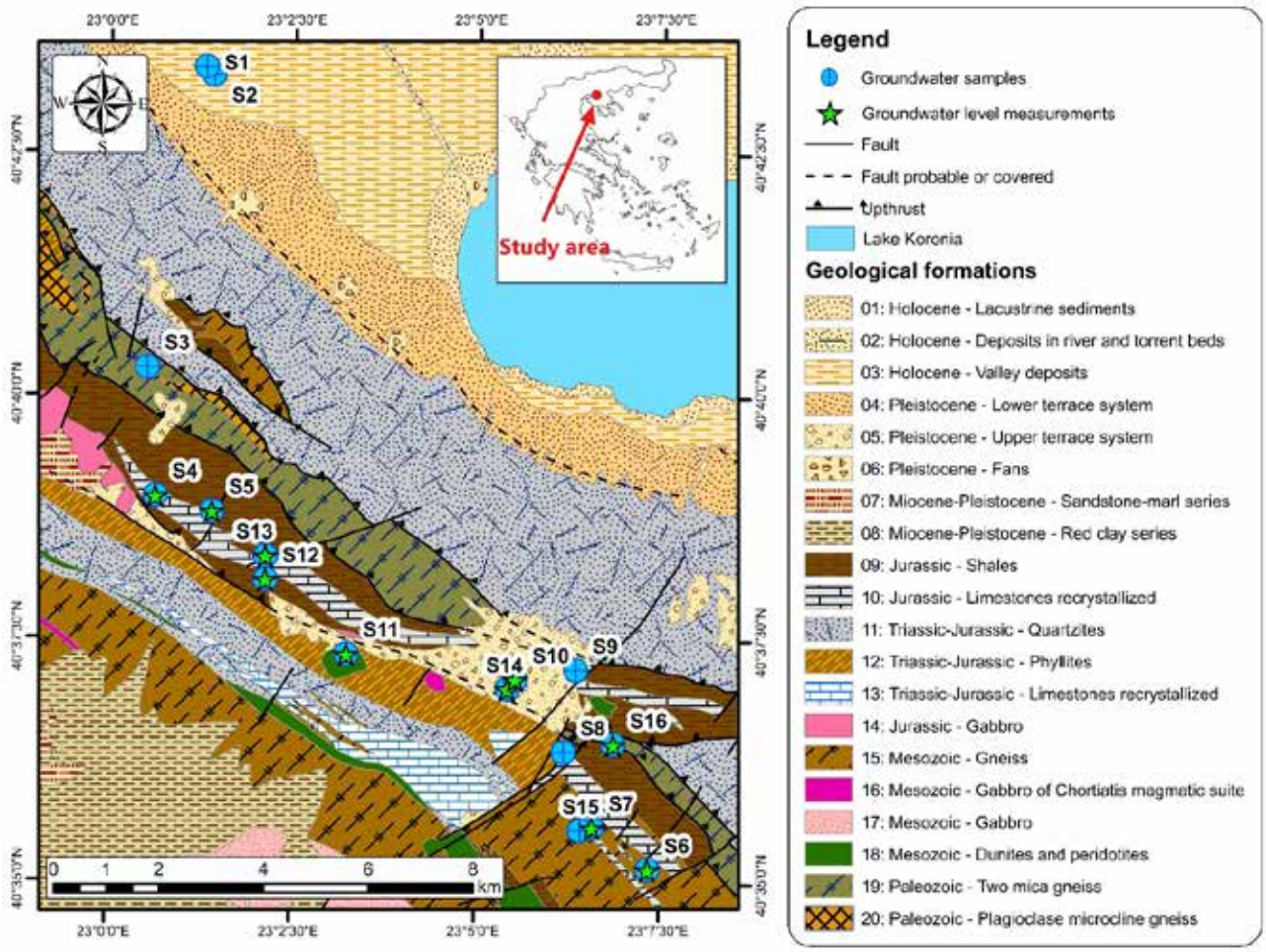


Figure 1. Geological map of the study area (HSGME with modifications, scale 1:50,000, sheets: Thessaloniki and Thermi).

Results and discussion

The chemical composition of all samples is shown in Table 1 and on Piper (Piper, 1944) and Durov (Durov, 1948) diagrams (Figure 2), which demonstrate the proportions between the major water components of the study area. The results of groundwater chemical analyses reflect both natural processes and some potential pollution sources. The pH levels range from 7.4 to 8.5, pointing to slightly alkaline conditions likely influenced by the local carbonate rocks. Electrical conductivity (EC) values vary from 525 to 1640 μS/cm with a mean value of 833 μS/cm (Figure 3a). High concentrations of calcium (Ca) and magnesium (Mg) indicate the presence of calcite and dolomite rocks. Sodium (Na) and chloride (Cl) concentrations vary from 3.7 to 63 mg/L and from 7.5 to 59 mg/L, respectively. These values indicate a mix of natural mineral dissolution and possible pollution from human activities in the area. Nitrate (NO_3) concentrations vary between 2.7 and 78.5 mg/L with a mean value of 18.6 mg/L, indicating agricultural or/and urban pollution. According to Piper and Durov diagrams, the most dominant water types are Ca-Mg-HCO_3, while samples S1 and S2 indicate Ca-Na-K-HCO_3 and sample S11 indicate Na-HCO_3 and Mg-Ca-HCO_3 water types, respectively. Samples S1 and S2 are projected at the center of the cations' triangle, indicating the groundwater origin from different sources of ion exchange processes.

The ratios of the major ions are provided in Table 2. The obtained proportions indicate insightful information about the geochemical characteristics of groundwater and potential sources of pollution in the study area. The results noted elevated Na/Cl and Mg/Cl ratios in several samples, suggesting varying degrees of cation exchange and mineral dissolution, possibly linked to carbonate geological formations (Figure 3b). High values of the ration (Ca+Mg)/(K+Na) in groundwater samples indicate a dominant presence of calcium and magnesium, which could be linked to natural mineralization processes from limestone and dolomite rocks. Within the study area the value of (Ca+Mg)/(K+Na) is higher than 1 highlighting the continuous recharge of the aquifer. On the other hand, values <1 of the Cl/SO_4 ratio observed in ten (10) samples highlight sulphate concentration, possibly from gypsum dissolution or agricultural activities.

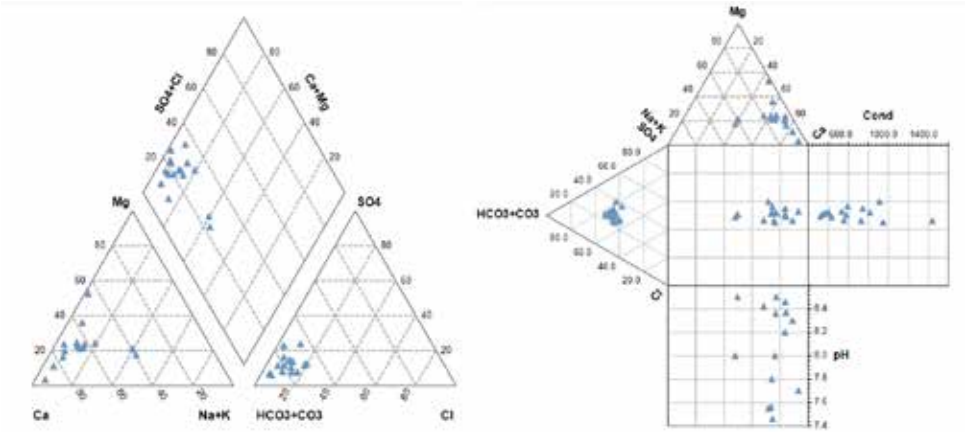


Figure 2. Classification of groundwater samples in Piper and Durov diagrams for the period of June 2024.

Table 1. Descriptive statistics of water quality parameters in the study area for the period of June 2024.

Parameter	Unit	Min value	Max value	Mean value	St.dev.
pH	-	7.4	8.5	8.0	0.4
T	°C	12.0	22.3	17.4	2.8
ORP	mV	-87.0	-20.0	-38.6	16.0
O_2	mg/l	0.0	9.9	4.6	3.3
EC	μS/cm	525.0	1640.0	833.5	295.0
Ca^{2+}	mg/l	50.0	124.0	95.8	25.0
Mg^{2+}	mg/l	2.7	56.8	21.3	13.1
Na^{+}	mg/l	3.7	63.0	21.9	17.2
K^{+}	mg/l	0.3	2.1	1.1	0.5
HCO_3^{-}	mg/l	272.1	451.4	335.7	51.8
SO_4^{2-}	mg/l	16.0	109.0	44.4	26.4
Cl^{-}	mg/l	7.5	59.0	27.8	14.5
NO_3^{-}	mg/l	2.7	78.5	18.6	20.6
NO_2^{-}	mg/l	0.0	0.0	0.0	0.0
NH_4^{+}	mg/l	0.0	0.1	0.1	0.0
PO_4^{2-}	mg/l	0.0	0.2	0.1	0.1

Table 2. Descriptive statistics of components ratios of groundwater samples in the study area.

Ion ratio	Min value	Average value	Max value	St.dev.
Mg^{2+}/Cl^{-}	0.5	3.0	14.4	3.2
Na^{+}/Cl^{-}	0.4	1.3	3.3	1.0
Cl^{-}/SO_4^{2-}	0.1	1.0	2.3	0.6
Mg^{2+}/Ca^{2+}	0.0	0.4	1.2	0.2
Na^{+}/K^{+}	12.7	39.1	148.8	33.5
$(Ca^{2+}+Mg^{2+})/(K^{+}+Na^{+})$	1.3	12.2	51.8	11.7

The trace element analysis of groundwater samples reveals a diverse chemical composition influenced by both the geological regime and possible pollution sources. The concentrations of iron (Fe) in the samples vary from 30.5 to 875.0 μg/L with a mean value of 141.9 μg/l, while the potable limit for Fe is 200 μg/L (EU Council directive 2020/2184). Strontium (Sr) concentrations vary from 52.1 to 581.3 μg/L with a mean value of 374.4 μg/L. High concentrations are also noted by the elements of boron (B) and zinc (Zn). It is worth noting that B element is only presented in the samples at the northern part of the sampling area, with a mean value of 216.7 μg/L and a maximum of 284.0 μg/L, potentially indicating anthropogenic activities such as agricultural fertilizers. Uranium (U) concentrations are below the potable limit of 30 μg/L and range from 0.1 μg/L to 12.7 μg/L.

Table 3. Descriptive statistics of trace element concentrations in groundwater samples of the study area (μg/L).

Trace elements	Min	Max	Mean	St.dev.
Al	ND	13.5	2.5	3.7
As	0.1	3.6	1.0	1.1
B	ND	284.0	216.7	95.2
Ba	8.3	212.5	70.6	56.9
Cr	5.9	42.4	11.0	8.6
Cs	0.0	0.2	0.1	0.1
Cu	1.3	15.8	4.7	4.3
Fe	30.5	875.0	141.9	209.0
Li	0.7	17.1	5.4	4.8
Mn	0.7	199.4	26.8	57.7
Mo	0.2	2.9	0.9	0.9
Ni	3.0	7.4	5.1	1.3
P	16.3	50.1	32.9	10.8
Rb	0.1	1.6	0.7	0.5
Se	ND	3.7	0.7	0.9
Sn	0.2	0.6	0.4	0.1
Sr	52.1	581.3	374.4	119.8
U	0.1	12.7	3.4	3.3
V	ND	4.7	0.8	1.7
Zn	ND	211.6	26.4	50.6

*ND: Not detected

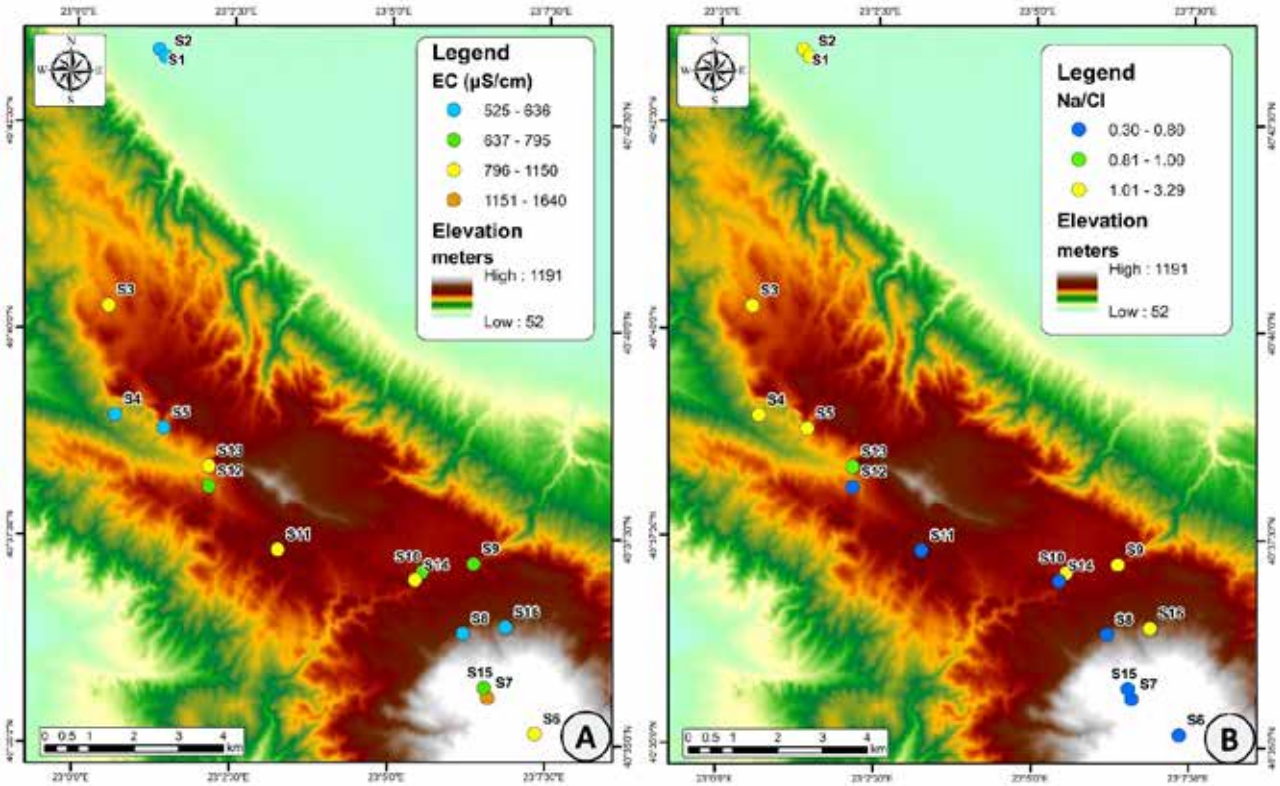


Figure 3. Spatial distribution of the (a) EC (μS/cm) and (b) Na/Cl ion ratio in the study area.

The monthly variation of precipitation and groundwater level for the monitoring wells are also provided in Figure 4, highlighting the groundwater dynamics and spatial heterogeneity of the aquifers. In the diagram of Figure 4a, the groundwater level exhibits a gradual decline over the year, despite a rainfall peak in March 2024. In Figure 4b, a marked rise in groundwater levels is noted following significant rainfall in March and April 2024. No significant variations are mentioned in the diagram of Figure 4c for a long period, on the contrary, low recharge and/or high groundwater exploitation values are noted during the period of June to September 2024. Higher groundwater levels, compared to the other wells, are noted in Figure 4d with a clear seasonal recharge pattern. It should be noted that this particular well has been out of operation for more than a year.

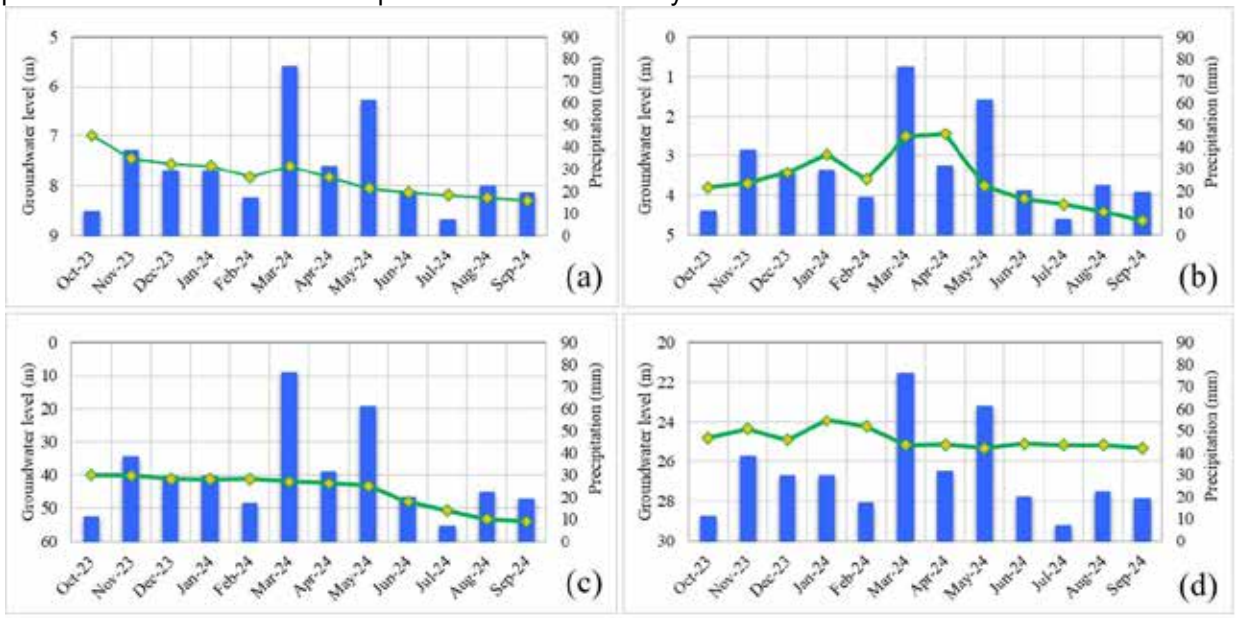


Figure 4. Groundwater level measurements in the hydrological year 2023-2024.

Conclusions

In this study, the hydrochemistry of major ions and trace elements is used to define the hydrochemical characteristics of groundwater in the Chortiatis region. Based on the results, the quality of groundwater is affected by geological regime and human activities. This research indicates that Ca-HCO_3 is the predominant groundwater type, with notable concentrations of sodium-chloride ions. Additionally, elevated concentrations of trace elements such as iron (Fe) and manganese (Mn) highlight the interactions with mineralized rock layers and potential contamination risks that require further monitoring. The results also reveal groundwater level variations across the hydrological year, characterized by seasonal recharge patterns following significant precipitation events and notable declines during dry months. Spatial heterogeneity among the monitoring wells highlights differences in recharge capacity and aquifer exploitation intensity, providing valuable insights for sustainable groundwater management.

Acknowledgment

This research was carried out within the framework of the project entitled “Development of a methodology for investigating the phenomenon of groundwater flooding and defining protection measures and zones for water abstraction projects and infrastructure in the Municipal Unit of Chortiatis.” with Scientific Coordinator Prof. Kazakis Nerantzis and was funded by the Water and Sewage Management Company of Pylaias-Chortiati (DEYA) and the Municipality of Pylaias-Chortiati.

References

Davamani, V., John, J.E., Poornachandhra, C., Gopalakrishnan, B., Arulmani, S., Parameswari, E., Santhosh, A., Srinivasulu, A., Lal, A., Naidu, R., 2024. A Critical Review of Climate Change Impacts on Groundwater Resources: A Focus on the Current Status, Future Possibilities, and Role of Simulation Models. Atmosphere 15(1), 122.

Digital Elevation Model (DEM), raster file downloaded by NASA open data. https://asterweb.jpl.nasa.gov/gdem.asp (accessed on 10 January 2024).

Durov, S.A., 1948. Natural Waters and Graphic Representation of Their Composition. Doklady Akademii Nauk

SSSR, 59, 87-90.
Hellenic Survey of Geology & Mineral Exploration (HSGME), 1978. Geological Map of Greece, Scale 1:50,000, Sheets: Thessaloniki and Thermi.
Kazakis, N., Oikonomidis, D., Voudouris, K., 2015. Groundwater vulnerability and pollution risk assessment with disparate models in karstic, porous and fissured rock aquifers using remote sensing techniques and GIS in Anthemountas basin, Greece. Environmental Earth Science 74(7), 6199-6209.
Luo, Y., Zhou, Q., Peng, D., Yan, W., Zhao, M., 2023. Key influence of hydrogeological, geochemical, and geological structure factors on runoff characteristics in karst catchments. Journal of Hydrology 623, 129852.
Ntona, M.M., Chalikakis, K., Busico, G., Mastrocicco, M., Kalaitzidou, K., Kazakis, N., 2023. Application of Judgmental Sampling Approach for the Monitoring of Groundwater Quality and Quantity Evolution in Mediterranean Catchments. Water, 15, 4018.
Piper, A.M., 1944. A graphic procedure in the geochemical interpretation of water analyses. Eos, Transactions American Geophysical Union 25(6), 914–928.

17th INTERNATIONAL CONGRESS
of the Geological Society of Greece

BULLETIN OF THE GEOLOGICAL SOCIETY OF GREECE, SP. PUBL.

EXTENDED ABSTRACT 232

Evaluation of National Groundwater Monitoring Network at the Peloponnese, Greece

Ntontos P.
Freelance Geologist, Naflpio, Greece, ntontosp@gmail.com

Abstract
The Water Framework Directive requires the establishment of monitoring programmes covering groundwater quantitative status, chemical status and the assessment of significant, long-term pollutant trends resulting from human activity. Greece has a significant disadvantage in developing such a monitoring programme because of its geological complexity. This disadvantage is further magnified by the obligatory choice of Greece, due to lack of data, to delineate «Groundwater Systems» and not «Groundwater Bodies» as Guidance Documents describes.
The basic principles that Guidance Documents suggest are not followed by the developed monitoring network in the region of the Peloponnese. There are fewer than the necessary number of monitoring sites, which are badly distributed over the area and, in many cases, not representative of the monitored aquifers. In contrast to the particularly costly and time-consuming solution of developing an adequate and representative ground water monitoring network, the alteration of all existing wells/boreholes to monitoring sites by establishing of institution of "Well Inspector" seems to be the only direct and sustainable solution to the problem.

Background
The WFD 2000/60/ec for groundwater aims to prevent further qualitative degradation, prevent or contain pollutants, restore groundwater quantity, restore groundwater quality by progressively reduce pollutants, and ensure a balance between abstraction and recharge of groundwater.
To achieve these objectives, the member-countries were obliged to describe "Groundwater Bodies" which are defined as "distinct volumes of groundwater within one or more aquifers". According to the specifications the GroundWater Bodies (GWBs) should be defined in all three dimensions. The GWBs are not necessarily homogenous in their natural characteristics or the concentration of pollutants in them. However, the GWBs should be defined in such a way that the definition of their qualitative and quantitative state is possible (Guidance Document No. 2).
For the accurate definition of the quantitative and chemical status of the GWBs, the appropriate selection of the measures necessary for the achievement of the environmental objectives of the directive, the evaluation of the effectiveness of these measures and the detection and reversal of the pollutants of human intervention in the groundwater, the member-countries should develop a monitoring programme. For this programme to be representative, it should be designed according to the theoretical model and the understanding of the general schema of "recharge-pathway-discharge" for each GWB. The determination of the monitoring sites in the design of the monitoring network should be made by taking into consideration the three-dimensional nature of the GWBs, as well as their spatial and temporal variability. The number of the monitoring sites and the frequency of the sampling procedure should be proportionate to the difficulty in evaluating the UWB status, the presence of pollutants, and the probability of wrongful estimations which the restoration measures may be based on. For GWBs which are at risk, a minimum number of 3 monitoring sites is recommended (Guidance Document No. 15).
The monitoring programmes comprise 3 network categories which are of quantitative monitoring, surveillance monitoring, and operational monitoring, The operational monitoring takes place in the GWBs that are at risk of not fulfilling or are already not fulfilling the objectives of the 2000/60 directive (Guidance Document No. 15). To implement this monitoring programme, Greece enforced the National Monitoring Water Network for the first time in 2011, which was amended in 2021. Groundwater is monitored by part of this network.

Delineation of the GWBs and the Groundwater Monitoring Network
In Greece, the implementation of the 2000/60 directive did not lead to the delineation of "GroundWater Bodies", but of "GroundWater Systems" (GWSs). This was according to the hydrolithological classification of the geological formations that accommodate the underground aquifers. The boundaries were determined according to the outcrop at the surface of these formations, without attempting to evaluate their three-dimensional development or the possible differentiation in the hydraulic behaviour of the formations.
The first River Basin Management Plans (RBMPs) of the 14 Water Districts of the country were conducted either through studies assigned to 5 different joint-venture study groups, or by studies of the Special Secretariat for Water itself. The weaknesses and errors that emerged during the process are the disagreement of the philosophy in the

determination of the GWSs according to the study group, the merging of different aquifers in a single GWS and the determination of the GWSs with geological and not hydrogeological criteria (Ntontos, 2022(a)).
In the first RBMPs, 539 GWSs were determined. Later, in their first revision in 2017, the GWSs were redefined, and the number reached 553, while in their second revision in 2024, the total number reached 598.
The complex and complicated structure of the GWSs which have been determined requires the development of a similarly complex and complicated monitoring network, so that it can be representative and adequate. It should be noted that for a GWS to be characterized as in poor quantitative status, the monitoring sites should present an established water level decline for more than a year, at a rate of at least 20% of the monitoring sites. For a GWS to be characterized as in poor chemical status, at least 20% of the monitoring sites should present exceedance (due to human activities) of the highest acceptable value regardless of the parameters measured. Both characterizations are valid on condition that monitoring sites are uniformly distributed in the whole area of the GWS and not locally placed.
The first governmental attempt to develop such a network was in 2011 with JMD 140384/2011, which included 1,392 groundwater monitoring sites. This network, which is in operation today, was enriched and slightly amended in 2021 with JMD 107168/1444/2021 and now includes 1,895 monitoring sites. The development and monitoring of this network was conducted by an informal assignment to H.S.G.M.E.

Adequacy Inspection Methodology of the Groundwater Monitoring Network

A statistical index, the Representative Index, Ru, has been developed (Grath et al., 2001) for the evaluation of the monitoring network with the following form:

$$R_U = \frac{37.7}{dist_{ave}\sqrt{k / Area}} \ [\%]$$

where

- $dist_{ave}$ is the minimum average distance of any site of the GWS from the closest monitoring site
- k the number of monitoring sites
- Area the area of the GWS

However, this index can be used only in hydrogeologically uniform GWSs. When they are heterogenous, the representation should be estimated solely on hydrogeological criteria. For this reason, the methodology for examining the network quantitative adequacy should abide by the following rules:

- The GWSs that are in a good quantitative and qualitative status, the minimum number is established at 3 monitoring sites (Guidance Document No 15).
- The GWSs that are in poor quantitative and/or chemical status and are hydrogeologically uniform, the minimum number is established at 5 monitoring sites so that 20% of these sites is at least 1 site.
- When the GWSs consist of different aquifer systems (karstic, granular, fissured), the minimum number is established at 3 monitoring sites for every type of significant aquifer. For an aquifer system to be considered as significant, we arbitrarily establish as the minimum area the 10% of the total area of the GWS, or it should accommodate at least 10% of the current productive wells/boreholes in the GWS.

For a monitoring network to be qualitatively adequate, the monitoring sites should be well distributed in the area, and, at the same time, they should be representative of the aquifer formations that form the GWSs. Furthermore, they should not be productive wells/boreholes, except if the measurement frequency is at least every hour (Guidance Document No. 15, ANNEX 2).

Groundwater Monitoring Network of the Peloponnese

According to the 2nd revision of the RBMPs, in the Peloponnese there are 90 Groundwater Systems or Subsystems. These systems have been separated into hydrolithological units, the surface area of which has been calculated. According to the quantitative and chemical status of the GWSs, 71 are in good quantitative and chemical status, 8 in poor quantitative and chemical status, 8 only in poor quantitative status, and 3 in only poor chemical status.
The Groundwater Monitoring Network as defined by the J.M.D. 140384/2011 (O.G.G. 2017/B΄/9-9-2011) included 294 monitoring sites in the Peloponnese. Of these sites, 198 were productive boreholes, 36 productive wells and 60 springs. After revising the network according to J.M.D. 107168/1444/2021 (O.G.G. 5384/B΄/19-11-2021) monitoring sites increased approximately 26%, to 371 sites. Of these sites, 270 are productive boreholes, 35 productive wells and 66 springs. In only 3 of the boreholes the measurement frequency is every hour.

Network Evaluation in the Peloponnese

According to the methodology developed, the first rule for the 71 GWSs that were of good quantitative and chemical status, and the second one for the 19 GWBs that were of bad quantitative and/or chemical status were examined. Table 1 presents the number of GWSs per number of monitoring sites. This table shows that 31 GWSs that are of good quantitative and chemical status, and 5 GWSs that are of poor quantitative and/or chemical status, do not have quantitative adequacy of monitoring sites.

Table 1. Number of GWSs with specific number of monitoring sites in them.

	Number of monitoring sites											
	0	**1**	**2**	**3**	**4**	**5**	**6**	**7**	**8**	**9**	**10**	**13**	**14**
GWSs of good quantitative and chemical status	10	7	14	14	10	3	2	5	1		2	2	1
GWSs of poor quantitative and/or chemical status	2	1		1	1	2	2	3	1	3	1	2	

The third rule was examined for the 14 GWSs that are in poor quantitative and/or chemical status (Table 2) and have more than 5 monitoring sites. It was found that GWSs comprised more than one significant hydrolithological systems, 4 of which have less than the minimum required monitoring sites.

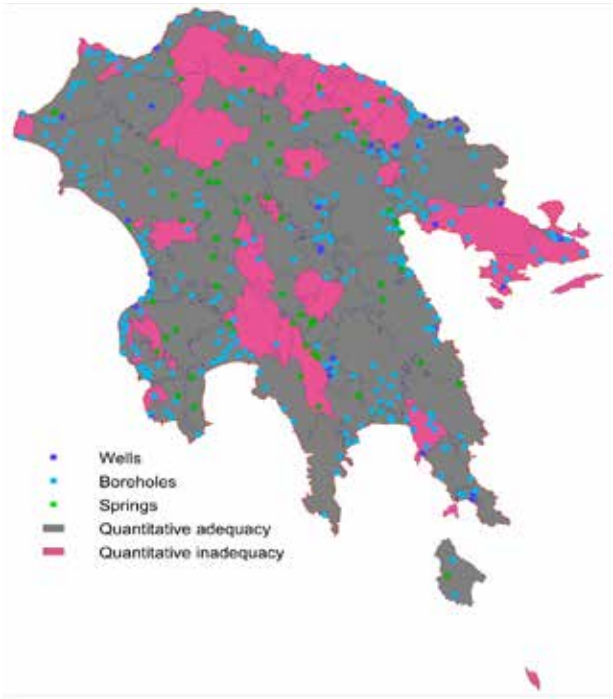


Figure 1. Illustration of the quantitative status of GWSs in the Peloponnese.

Table 2. Area of each significant hydrolithological system (%) of the total GWS area, and number of existing and required monitoring sites.

GWS's code	K1	P1	P2	P3	P4	A1	A2	Number of existing sites	Minimum number required
EL0100100		52,2		45,4				13	6
EL0100170		10,0		87,1				9	6
EL0200091		95,9						7	5
EL0200171		22,3	19,6	48,6				9	9
EL0200173		14,2	11	72,1				6	9
EL0200190		96,3						9	5
EL0300030		98,6						10	5
EL0300040		99,0						13	5
EL0300050	58,4	17,9				8,3*	6,9*	8	12
EL0300060		91,0						6	5
EL0300070	9,4*	9,7*				69,8	7,7*	5	12
EL0300090		71,5			26,2			7	6
EL0300130				95,0				5	5
EL0300150		15,9		43,8			30,2	7	9

K1: Calcareous formations of high to medium permeability. P1: Granular, mainly fluvial deposits of variable permeability. P2: Neogene/Pleistocene deposits of medium to low permeability. P3: Granular, non fluvial deposits of low to very low permeability. P4: Scree of variable permeability. A1:

Fissured formations of low to very low permeability (flysch). A2: Fissured formations of low to very low permeability (phyllites, quartzites, schists).
* Hydrolithological formation accommodating at least 10% of the current wells in the GWS

According to the previous evaluation, the 40 GWSs of good quantitative and chemical status, and the 10 GWSs of poor qualitative and/or chemical status that have quantitative adequacy of monitoring sites were examined for the good spatial distribution of the monitoring sites. Only 23 of them were found to have good spatial distribution of the monitoring sites, with 2 of them not presenting good representation of the aquifer formations. It should be noted that good spatial distribution of monitoring sites means not only to be spread in the area of GWS but mainly near clustered sites of productive wells/boreholes.

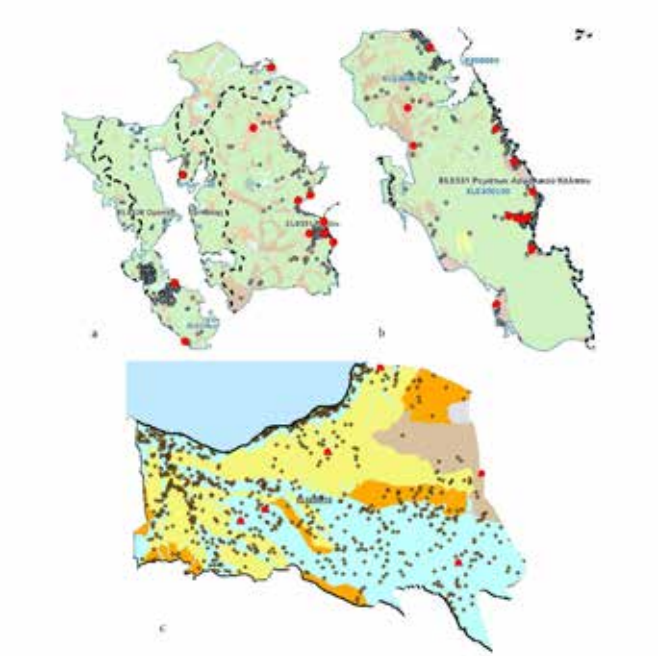


Figure 2. Example of poor (a) and good (b) spatial distribution of monitoring sites (red spots) that need to be not only spread but also near clustered sites of productive wells/boreholes (circles).

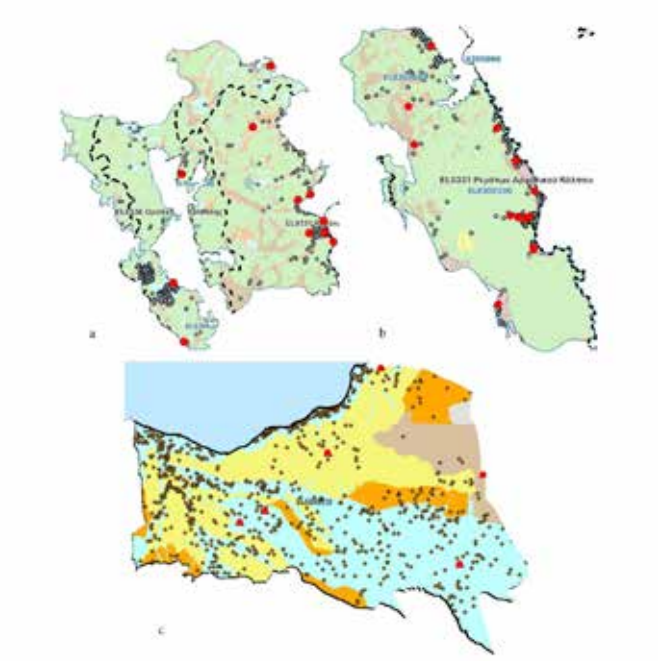


Figure 3. Example of poor representation of aquifer types, as monitoring sites (red spots) need to be not only spread in the area but also within significantly exploited hydrolithological units of the GWS.

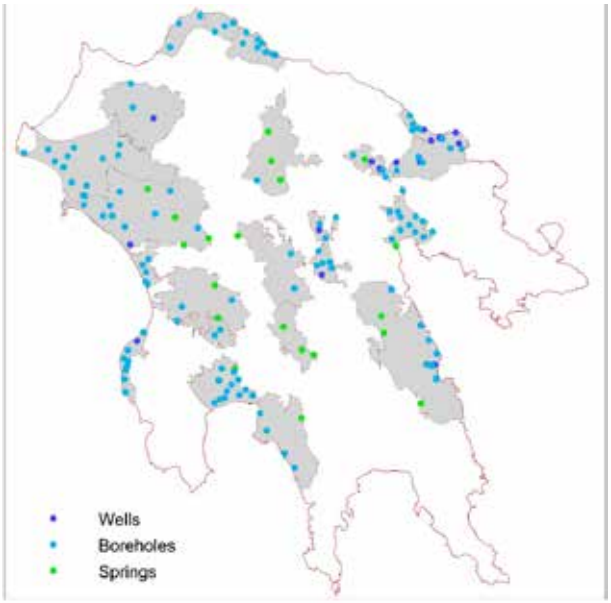


Figure 4. Three types of monitoring sites in 21 GWSs of good spatial and qualitative distribution. Only in 1 borehole measurements were conducted every hour.

Furthermore, 154 sites of the monitoring system were found in the 21 GWSs which were of good spatial and qualitative distribution of monitoring sites. Of those, 134 sites are productive wells/boreholes and only 20 of those sites are springs. However, only in 1 borehole measurements were conducted with the required frequency (eg hourly frequency). In only 4 GWSs the springs comprise the majority of the monitoring sites or are adequate in number (≥3). In the Peloponnese and Western Greece Prefectures, the number of existing productive wells/boreholes is estimated at 83,000 and in Greece at 250,000 respectively (Ntontos, 2017). These wells/boreholes can easily become unofficial monitoring sites for water level and water electric conductivity measurements. These measurements can be conducted twice a year or more frequently by geologists in the private sector who are paid by well/boreholes owners. Such an extended network, with no cost for the state, can contribute to the full understanding of the hydrogeological regime of every aquifer. This in turn can contribute to the appropriate selection of the measures necessary for the achievement of the environmental objectives of the directive.
This procedure is described in the Institution of Well Inspectors (Ntontos, 2022 (b)) and can produce hundreds or even thousands of work positions for geologists. According to the Geotechnical Chamber of Greece data for the year 2023, unemployment rates reach 40%.

Conclusions

According to the recommended methodology, after the examination of the qualitative and quantitative adequacy of the National Monitoring Network of Ground Water, it was found that, from the total of 90 GWSs that are found in the Peloponnese, only 4 of them have quantitatively adequate monitoring sites of good spatial and qualitative distribution. For it to be quantitative adequacy in all GWSs, the monitoring sites must increase in number by at 25%, selectively, and wherever this is imperative. The rearrangement of the monitoring sites is also of significance in many of the GWSs, so that they are distributed well, both spatially and quantitively. Finally, there should be water level loggers installed in all productive wells that are used as monitoring sites, to ensure the frequent monitoring of the water level according to the current European specifications.
It should also be noted that the existence of a minimum number of monitoring sites in each GWS does not, lead to the understanding of the hydrogeological status of the GWS by itself, nor does it contribute to the accurate determination of their quantitative and chemical status. Moreover, the development of a dense underwater monitoring system maintained by the state is extremely costly. Therefore, the implementation of the institution of the well inspector can contribute to the prompt development of an extensive monitoring network, which will consist of all the active wells/boreholes of the country estimated at more than 250,000. In this way, hundreds or even thousands of work positions will be created for geologists, thus the unemployment rates, which reach 40% according to Geotechnical Chamber of Greece data for the year 2023, will be reduced.

References

Ntontos, P., 2022 (a). Well Inspectors: Giving Greek Geologists a Chance. G.S.G. International Congress, Patras, Greece, p. 454 [Bulletin of GSG, Special Publication No. 10]

Ntontos, P., 2022 (b). River Water Management Plans: Weaknesses and Errors. Hellenic Chapter of IAH & CAGME International Hydrogeological Conference, Nicosia, Cyprus, p. 362.

Ntontos, P., 2017. Hydrowells permit issuing: Existing legislation, current situation and future prospects. Hellenic Chapter of IAH & CAGME International Hydrogeological Conference, Athens, Greece, p. 309.

Guidance Document No.15, 2007: Guidance on Groundwater Monitoring. European Communities [Guidance Document of CIS for the WFD 2000/60/EC]

Guidance Document No2, 2003. Identification of water bodies. European Communities. [Guidance Document of CIS for the WFD 2000/60/EC]

Grath, J., Scheidleder, A., Uhlig, S., Weber, K., Kralik, M., Keimel, T., Gruber, D., 2001: “The EU Water Framework Directive: Statistical aspects of the identification of groundwater pollution trends, and aggregation of monitoring results”. Final Report. Austrian Federal Ministry of Agriculture and Forestry, Environment and Water Management (Ref.: 41.046/01-IV1/00 and GZ 16 2500/2-I/6/00), European Commission (Grant Agreement Ref.: Subv 99/130794), in kind contributions by project partners. Vienna. [Technical Report of CIS for the WFD 2000/60/EC]

17th INTERNATIONAL CONGRESS of the Geological Society of Greece

BULLETIN OF THE GEOLOGICAL SOCIETY OF GREECE, SP. PUBL.

EXTENDED ABSTRACT 233

Characteristics of REE mineralization in bauxite strata and in bauxite residue deposited into the Corinth Gulf, Greece

Ntouros E. [1], Sofis N. [1], Damoulianou, M.E. [1], Iatrou M.[2,3], Grammatikopoulos T.[4], Papatheodorou G.[2], Kalaitzidis S.[1*]

(1) Laboratory of Economic Geology, Department of Geology, University of Patras, Rio-Patras Greece, skalait@upatras.gr (2) Laboratory of Oceanography, Department of Geology, University of Patras, Rio-Patras Greece (3) Institute of Oceanography Hellenic Centre for Marine Research (HCMR) (4) SGS Canada Inc.

Research Highlights

Authigenic cerianite mineralization and elevated REE values in b1 and b3 bauxites at the Parnassos-Ghiona Unit and bauxite residues from the Corinth Gulf

Introduction

The Mesozoic carbonate sequence of the Parnassus-Ghiona Unit mainly attracts research and economic interest, particularly around the three karstic-type bauxite strata it hosts, namely b1, b2, b3, which were deposited between Middle Jurassic and Upper Cretaceous times (e.g. Valeton *et al.*, 1987; Kalaitzidis *et al.*, 2010; Laskou & Economou-Eliopoulos, 2013; Economou-Eliopoulos *et al.*, 2016; Gamaletsos *et al.*, 2017). Nowadays mainly b3 horizon is exploited, b2 has been the subject of mining in the past, whereas b1 was never extracted, as it occurs sporadically, with limited quantities and low grade in terms of Al. Diaspore, boehmite and gibbsite are the main Al-minerals of interest, whereas the mineralogical composition frequently includes hematite, goethite, kaolinite, chlorite, anatase and pyrite (Mondillo *et al.*, 2022 and references therein).

Although bauxite mining in Greece takes place for almost a century, nowadays the focus shifts towards the REE, which occur either within the bauxite or the bauxite residues after metallurgical processes and are a key part of the EU Green Deal, in order to transit to a greener and more sustainable future for the EU (European Commission, 2020). REE are characterized by unique electrochemical and magnetic properties, thus making them “critical metals” for technological and industrial development for both developed and developing economies around the world (Borra et al., 2016; Panda et al., 2021). For the reasons above, REE are widely used in green technologies such as electric car batteries, solar panels, special magnets for wind turbines and others (Narayanan, 2019; Deady et al., 2016; Wall, 2014). The REE are traced within the bauxite residue (BR), being enriched in comparison to the bauxite with a factor of about two (Borra *et al.*, 2016; Ujaczki, 2017). In Greece, the bauxite residue is produced during the Bayer method by the alumina and aluminum production plant “Aluminum of Greece SA”(ATE) at Aspra Spitia of Boeotia, and for several decades it was disposed in the gulf of Antikyra in the northern and central part of the Corinthian Gulf. Its discharge began in the 1970s through a submarine pipeline and it ceased in 2012. In total, it is estimated that more than 20 Mt of bauxite residue have been discharged in the Corinthian Gulf, covering up to 12% of its total surface area (Iatrou, 2013). According to Ochsenkiihn-Petropulu et al. (1994) and Borra et al. (2015) the mean value of the ΣREE in the Greek BR is approximately 974 mg/kg. In this study bauxite, from the Parnassus-Ghiona Unit, and bauxite residue samples from the Corinth Gulf were examined in order to record and evaluate their main mineralogical, geochemical and mineral-chemical characteristics, with emphasis on the REE, which has not been systematically studied till now. The aim of this study is to assess the REE mode of occurrence in bauxites and wastes from the metallurgical process of bauxites (BR) and determine their origin.

Methods

Bauxite samples represent a b1 outcrop (EL2, EL3, EL3A and EL4 samples) (in total 17 samples) from Elateia site (near the small town of Elateia, Central Greece) and two b3 outcrops from Kardarrorahi (KR3 samples) (in total 3 samples) and Vargiani (PBF1-2-2 sample) (in total 1 sample) sites (near Delphi area), whereas samples of bauxite residue (RM samples) (in total 12 samples) represent deposition within Corinth Gulf; BR samples were obtained during a drilling campaign in 1994 and 2007 as part of an environmental study.

X-Ray diffraction analysis was performed in all samples, as well as geochemical analyses for major, minor and trace elements. SEM-EDS measurements were also conducted both in bauxite and bauxite residue samples.

Results

The b3 samples mainly consist of Al_2O_3 ranging between 36.81 and 51.55 wt.-%, Fe_2O_3 in a range of 11.26-28.33 wt.-% and SiO_2 fluctuating greatly from 4.23 to 23.97 wt.-%, while the b1 samples consist of Al_2O_3 ranging within

26.39 and 63.9 wt.-%, Fe_2O_3 in a range of 4.80-25.92 wt.-% and SiO_2 fluctuating greatly from 1.85 to 12.9 wt.-%. The bauxite residue samples mainly consisting of Fe_2O_3 (9.85-25.2 wt.-%), CaO (14.85-22.2 wt.-%), SiO_2 (14.2-23.9 wt.-%), and Al_2O_3 (9-11.1 wt.-%).

The ΣREE at the b3 samples vary greatly between 771.67-1961.8 mg/kg, while at the b1 samples varies between 510.23 and 1090.73 mg/kg. Finally, the total REE contents (ΣREE) of the bauxite residue samples vary between 484 and 771 mg/Kg.

The mineralogical examination of the bauxite samples presented similar mineralogical features in the bauxite samples (for both b1 and b3 samples), with small variations among diaspore, boehmite and gibbsite, as well as for the iron oxides and hydroxides. Furthermore, rutile concentration is always low between 1-3%, while Kaolinite seem to be more dominant in the b1 samples.

EDS analysis on individual particles in the bauxite residue samples, was challenging due to the small average size of the crystals. However, several mineral phases were identified with hematite, ilmenite, quartz and calcite being the predominant ones. Various accessory minerals were also rarely detected, including pyrite, and zircon. REE minerals were also found in bauxite and bauxite residues and more specifically individual cerianite crystals.

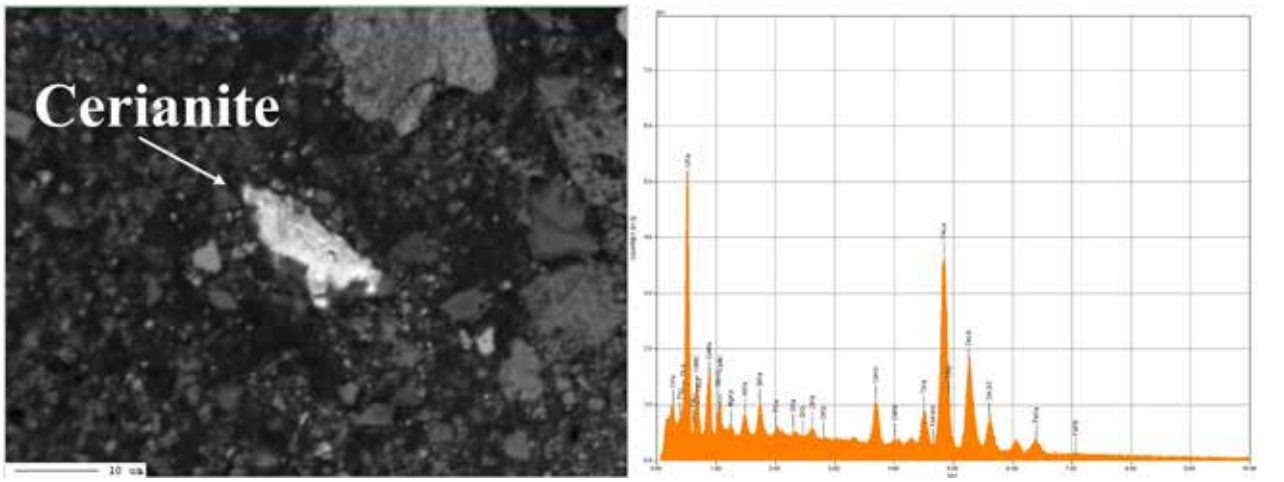


Figure 1. Back-scattered electron image of sample RM13 depicting cerianite in the bauxite residue and relative EDX spectra.

Conclusions

Both bauxite (b1 and b3) and bauxite residue samples seem to be enriched in REE, and show similar ranges in the total content of them. By comparing the ΣREE of the herein studied BR samples with those from previous studies of pure BR from Greece, the former values seem slightly decreased. This divergence is justified due to the mixing of the bauxite residue with the sediments of the Corinth Gulf. Authigenic REE-bearing minerals were identified in all samples and more specifically cerianite.

References

Economou-Eliopoulos, M., Frei, R., & Megremi, I., 2016. Potential leaching of Cr (VI) from laterite mines and residues of metallurgical products (red mud and slag): An integrated approach. Journal of Geochemical Exploration, 162, 40-49.

European Commission, 2020. Report on Critical Raw Materials Resilience: Charting a Path towards greater Security and Sustainability. https://ec.europa.eu/docsroom/documents/ 42849.

Borra, C.R., Blanpain, B., Pontikes, Y., 2016. Recovery of Rare Earths and Other Valuable Metals From Bauxite Residue (Red Mud): A Review. J. Sustain. Metall., 2, 365-386.

Borra C. R., Pontikes Y., Binnemans K., Gerven T. V., 2015. a Leaching of rare earths from bauxite residue (red mud), Minerals Engineering, Volume 76, 20-27

Deady, É, Mouchos, E., Goodenough, K., Williamson, B., & Wall, F., 2016. A review of the potential for rare-earth element resources from European red muds: Examples from Seydişehir, Turkey and Parnassus-Giona, Greece. Mineralogical Magazine, 80(1), 43-61.

Gamaletsos, P. N., Godelitsas, A., Filippidis, A., & Pontikes, Y., 2019. The rare earth elements potential of Greek bauxite active mines in the light of a sustainable REE demand. Journal of Sustainable Metallurgy, 5, 20-47.

Gamaletsos, P.N., Godelitsas, A., Kasama, T., Church, N.S., Douvalis, A.P., Gottlicher, J., Steininger, R., Boubnov, A., Pontikes, Y., Tzamos, E., Bakas, T., Filippidis, A., 2017. Nano-mineralogy and -geochemistry of high-grade diasporic karst-type

bauxite from Parnassos-Ghiona mines. Greece. 84, 228–244.
Iatrou. M., 2013. Oceanographic-Geomorphological surveys in the central Corinthian Gulf in relation to the dispersion of red mud. PhD thesis, University of Patras, Department of Geology.
Kalaitzidis S., Siavalas G., Skarpelis N., Araujo V., Christanis K., 2010. Late Cretaceous coal overlying karstic bauxite deposits in the Parnassus-Ghiona Unit, Central Greece: Coal characteristics and depositional environment. International Journal of Coal Geology, 81(4), 211-226.
Laskou, M. and Economou-Eliopoulos, M. 2013. Biomineralization and potential biogeochemical processes in bauxite deposits: Genetic and ore quality significance. Mineralogy and Petrology, 107, 471-486.
Mondillo, N., Di Nuzzo, M., Kalaitzidis, S., Boni, M., Santoro, L., Balassone, G., 2022. Petrographic and geochemical features of the B3 bauxite horizon (Cenomanian-Turonian) in the Parnassos-Ghiona area: A contribution towards the genesis of the Greek karst bauxites. Ore Geology Reviews, 143, 104759.
Mouchos, E., 2015. A Geological Study of the Potential for Rare Earth Element By-Product Recovery from Greek Bauxite Deposits. University of Exeter (United Kingdom).
Narayanan Remya P., 2019. Recovery of Rare Earth Elements from Bauxite Residue: A Comparative Economic Analysis. International Journal for Multidisciplinary Research, 1(2), 21-40.
Ochsenkühn-Petropulu, M., Lyberopulu, Th., Parissakis, G., 1994. Direct determination of landthanides, yttrium and scandium in bauxites and red mud from alumina production. Anal. Chim. Acta 296 (3), 305-313.
Panda S., Biancalana C. R., Sikandar S. S., Mishra S., Bevilaqua D., Akcil A., 2021. Biotechnological trends and market impact on the recovery of rare earth elements from bauxite residue (red mud) – A review, Resources, Conservation and Recycling, Volume 171, 105645.
Ujaczki, É., Zimmermann, Y.S., Gasser, C.A., Molnár, M., Feigl, V. and Lenz, M. 2017. Red mud as secondary source for critical raw materials – extraction study. J. Chem. Technol. Biotechnol, 92, 2835-2844.
Valeton, I., Biermann, M., Reche, R. and Rosenberg, F., 1987. Genesis of nickel laterites and bauxites in Greece during the Jurassic and Cretaceous, and their relation to ultrabasic parent rocks. Ore Geology Reviews, 2, 359-404.
Wall, F., 2014. Rare earth elements.: Critical Metals Handbook (G. Gunn, editor). First Edition. John Wiley & Sons, Ltd., 312-339.

17th INTERNATIONAL CONGRESS of the Geological Society of Greece

BULLETIN OF THE GEOLOGICAL SOCIETY OF GREECE, SP. PUBL.

EXTENDED ABSTRACT 234

Characterization and timing of charcoal in geoheritage sites preserved by major volcanic destructions – Geoarcheological and paleo-environmental considerations in Ecuador

Grace Tatiana Páez-Barrera[1] Karla Vizuete[1], Alexis Debut[1], Mario Cruz-D´Howitt, Juan José Ortiz-Aguilu, Theofilos Toulkeridis[3,4]

(1) Universidad de las Fuerzas Armadas ESPE, Sangolquí, Ecuador; (2) Universidad Técnica de Manabí, Portoviejo, Ecuador; (3) Aristotle University of Thessaloniki, Thessaloniki, Greece (4) Universidad UDET, Quito Ecuador

Research Highlights

The variety of microfossils identified allowed to reconstruct the original ecosystem of the lake areas of the Pululahua Volcano after its destructive volcanic events. Based on the characterization and timing of charcoal pebbles encountered within a distant but prominent ash-layer, it has been possible to identify how an ancient culture has been destroyed in coastal Ecuador, some 3,5 ka ago.

Introduction / Background

Throughout phanerozoic times, past botanic fossil records are often preserved when ironically huge catastrophic events take place, allowing the reconstruction of past evolutionary processes in the diversity and developments of plant life. These catastrophic events may include flooding of which newly deposited sedimentary material remains above previous existing vegetation, a number of volcanic events or hazards such as lava flows, ash and pyroclastic flows as well as avalanche deposits, ice or glacial deposits and also due to drought and landslides among many others (Ukraintseva *et al.*, 2014; Svoboda *et al.*, 2019; Vallé *et al.*, 2024). Nonetheless, there are a variety of studies where older plants and their corresponding flora and even fauna have been preserved in a variety of forms, due to severe volcanic events such as by even famous eruptive phases of the past (Ayala-Usma *et al.*, 2024).

As it is a challenge to encounter preserved paleoenvironmental areas with corresponding vegetation, it is even more difficult to find paleobotanic remains of wetlands, lagoonal or fluvial environments. Such environments not only preserve the flora and fauna of the given time of its existence, but they are also able to reveal the paleoclimatic and paleoecologic conditions of its time, allowing to reconstruct past events in order to understand the recent and future atmospheric behavior and their fluctuation. Such information may be reconstructed by the content of such wet environments which may include either macro or microfossils. Therefore, paleobotanic research of wet environments may be based on the findings of preserved macrofossil plants within sedimentary layers as impressions or compressions, as casts or molds, and also as petrification. However, many more details are preserved in form of microfossils, when looking with magnifying glasses, binoculars or microscopes of any kind. Such findings may be plants, algae, diatoms, fungi, pollen, spores, bacteria, biomass in general and other kind of microfossils of some animal remains. These discoveries are the basic results for a subsequent declaration of geoheritage sites.

Unfortunately, in Ecuador paleobotanic research is scarce, although there are many reports of charcoals inside of volcanic environments within a high amount of extinct and active volcanoes in the continental part of the country as well as on the Galapagos islands. However, such findings have been mostly used in past for carbon dating without further specification or characterization of the plant or wood fossil content. There are also petrified forests of the Mesozoic period, like the well-known in Puyango in the southern part of Ecuador, but also of limited information concerning paleobotanic findings (Cadena & Román-Carrión, 2018).

Based on the aforementioned context, the current study´s predominant aim has been to identify and characterize microfossil content of charcoal deposits of a fluvial-lagunar environment and a coastal site, being preserved by the volcanic activity of two volcanic complexes in north-central Ecuador. This shall be achieved by a detailed volcanic reconstruction of the catastrophic events of the past, in combination of a microscopic inventory of encountered charcoal horizons within the volcaniclastic deposits. As we deal with two different events in time, the first results may allow to establish the environmental conditions of a so far unknown humid landscape of local to regional importance within the Ecuadorian highlands, shortly after glaciation and almost simultaneously to the first appearance of human settlings, while the second results may allow to reconstruct the almost complete disappearance of a flourishing culture in the coast of Ecuador.

Geological background and study areas

The four Ecuadorian continental volcanic arcs are the result of the subduction of the Nazca oceanic plate below the Caribbean and South American continental plates. The NNE-SSW aligned volcanoes within these arcs correspond to the Western, Inter-Andean, Eastern and Subandean Volcanic Arcs or Cordilleras of Ecuador. In the central part of the Western Volcanic Arc is situated the Pululahua caldera and dome complex as well as the Pichincha Volcanic Complex (PVC), both being located just a few km outside of Ecuador´s capital Quito (Toulkeridis and Zach, 2017).

For the Pululahua volcano, at least 16 predominantly andesitic to dacitic domes have been identified, belonging to four different units (Units I-IV; Andrade *et al.*, 2021). The oldest domes are heavily eroded, porphyritic amphibole-bearing dacitic pelean lava domes of unknown emplacement ages belong to the so-called Unit I. Some further older domes (La Marca among others), belong to the Unit II yielded ages of 18 to 10 ka, while later single or major events took place at 6.75 ka, 2.6 – 2.3 ka and some 2.24 ka ago. Those events resulted into wide and thick successions of pumice-rich, pyroclastic deposits, which include charcoal rich layers, which is evidence of previous vegetation in times of volcanic activity. The most prominent outcrops with charcoal rich layers are situated on the southeastern side of the Pululahua dome complex, along the Monjas river.

A big part of the western mountain flank of the city of Quito, occupies the PVC, which is composed of five successive volcanoes, of which the first four are extinct reaching ages of 1.1 Ma to 4 ka. The El Cinto basal edifice (1.1 to 0.9 Ma) is followed by the Rucu Pichincha stratovolcano (850 to 150 ka), Guagua Pichincha stratocone (60 to 11 ka), Toaza volcanic dome complex (11 to 4 ka) within the collapsed, avalanche amphitheater of Guagua Pichincha and finally the presently active Cristal volcanic dome complex (3,700 years to present day) within the Toaza caldera. The Cristal volcanic dome complex gave rise of repeated growth and collapse of volcanic domes, which occurred in the period of 1998 to 2001 (Monzier *et al.*, 2002; Robin *et al.*, 2010).

Results and discussion

Pyroclastic flows and pyroclastic surges produced by directed, sub-plinian explosions of the outer caldera of Pululahua situated older domes, whose activity represents the second phase of its eruptive period, occurred some 12-10 ka ago. Close-by to the La Marca dome, prominent charcoal deposits of a fluvial-lagoon environment along the Monjas river have been identified and dated, correspond to this time period and event.

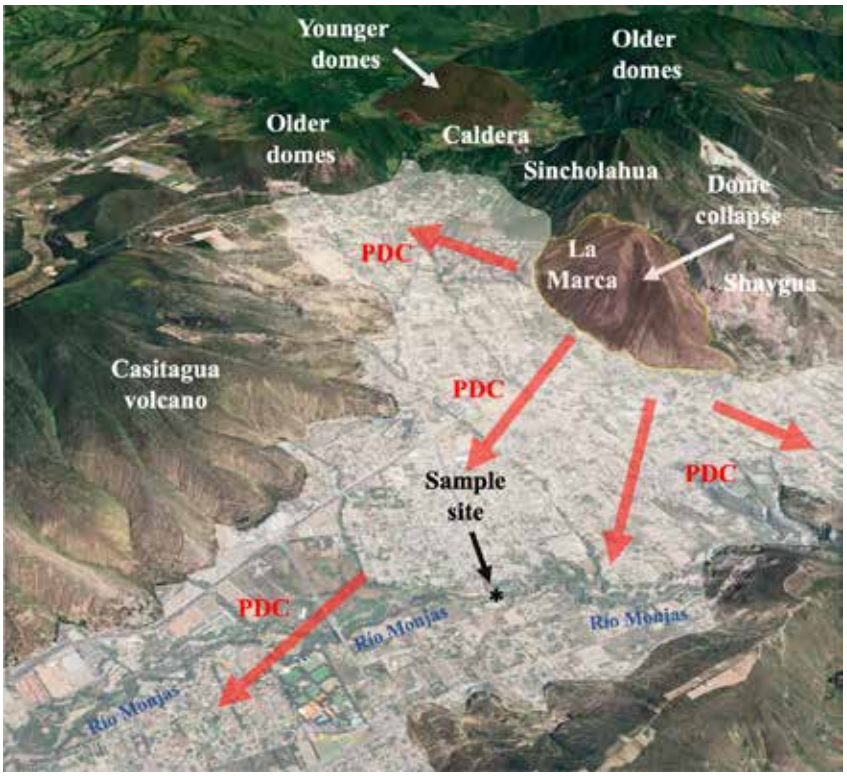


Fig. 1. South (left) to north (right) panoramic, bird-view of the result of the directed blast situation of the older collapsed domes of the Pululahua caldera and dome complex, generating pyroclastic density currents (PDC), which cover a vast area of the Inter-Andean Valley, forming what is now the base of the San Antonio de Pichincha village.



Fig. 2. Charcoal horizons of the Río Monjas type section (A-D). Note that the most prominent charcoal deposit is of about 65 cm thick (A: 45 cm plus 20 cm of the basal part), while others are mixed with pumaceous ash particles (B). Furthermore, there appear charcoal lenses within the pyroclastic deposits (C). Uppermost charcoal layers above an erosional contact (D).

We analyzed and characterized the charcoal deposits and encountered microorganisms such as benthic diatoms, saprophytic fungi and nitrogen-fixing bacteria, as well as herbaceous vascular plants such as horsetails, lycopods, bamboos, ferns, and small shrubs. These identified organisms originated from temperate and cold ecosystems, probably from flooded or seasonally flooded areas. The charcoal fragments perfectly preserved by the favorable conditions suggest that the original ecosystems of the Pululahua paleoflora correspond to areas of humid and lacustrine environments typical of swampy ecosystems, humid mountains and Andean moorlands.

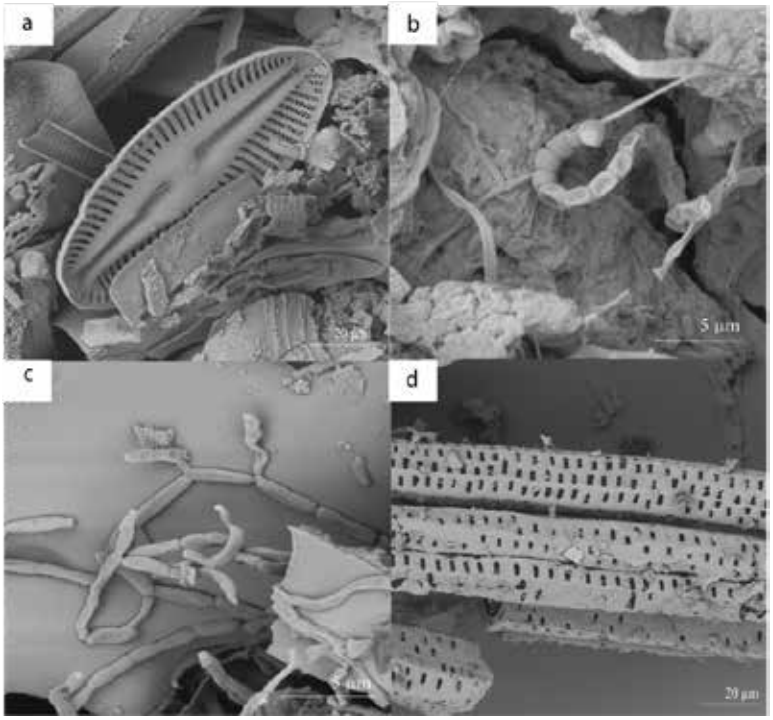


Fig. 3. SEM photomicrographs: a. Diatom Bacillariophyceae, valves oval, elongated, symmetrical, with raphe. Linear, marked transverse striations; b. Streptomyces well-developed filamentous vegetative hyphae; c. Bacillus sp., rods in branched chains; and d. Polypodiophyta, Equisetaceae adjacent nodal metaxylem tracheids.

In the coastal area of Ecuador, close to the city of Portoviejo, at the site called Papayita, an ash layer which includes charcoal pebbles (fossilized wood), with an impressive thickness of 85 centimeters was encountered above an underlying paleosol. A fact that is striking when considering that the closest volcano with sufficient eruptive power to produce such ash volumes, Quilotoa, is around 165 km away in a direct line. Nonetheless, provenance analysis based on geochemistry analysis and mineralogy revealed that the volcano responsible for the high amounts of the expelled material must have been the PVC with a distance of some 225 km in a SW direction. The stratigraphic sequence at Papayita is of significant interest, with a base consisting of geological material layer, succeeded by a paleosol and a cultural layer. The latter contains several discernible activity areas, including a hearth and small midden areas. Two separate features contained human remains associated with the Valdivia ceramics found at the site.

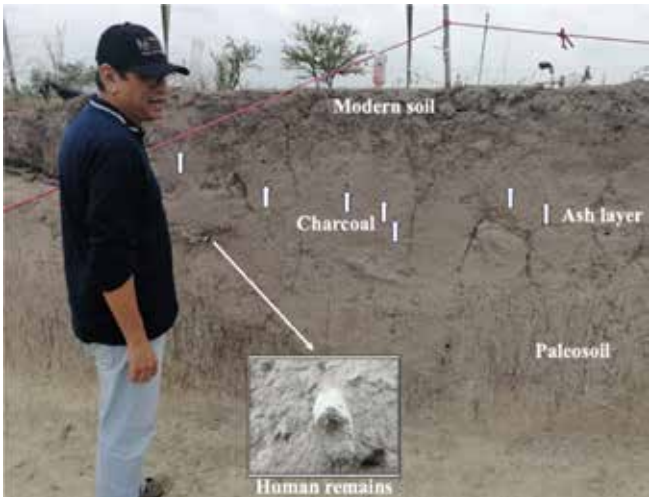


Figure 4. Exposed machine cut due to farmer's construction of a traditional water reservoir. It provided a pro file that indicates the main stratigraphic components of the Papayita site. The most important sections of the profile sequence being (from bottom to top): the paleosol, the ash layer, and the modern soil or plow zone. The position of the human remains and other artifacts, as well as several charcoal fragments, can be discerned in the profile.

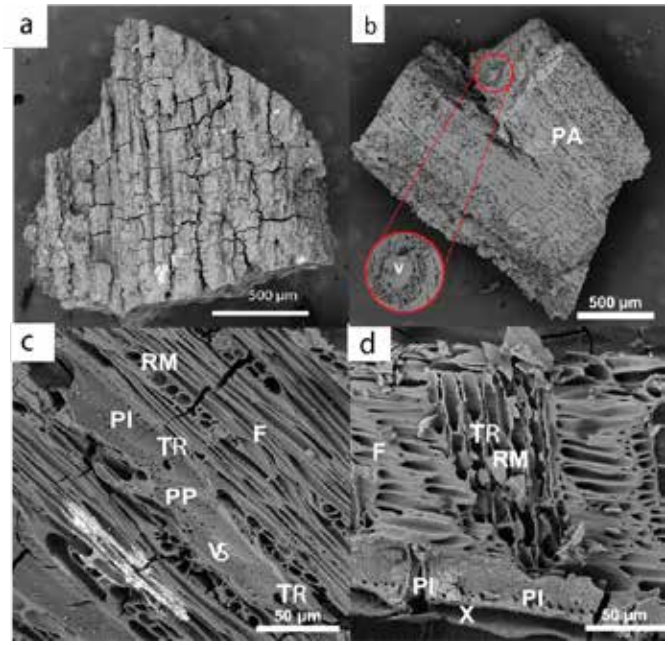


Figure 5. SEM photomicrographs of charred plant material, anatomical features of charcoal samples: A. Elongated and fusciform cells, tangential section, vascular system with septa without points, own to gymnosperms (VS), simple perforation plates (PP), medullary radius (RM), intervascular pits (PI), fibers (F) and tracheids (TR); B. Tangential cut: intervascular pits (PI), simple perforation plates (PP), medullary radius (RM), fibers (F), and xylem (X). C. Woody vascular system (VS), showing woody tracheid (TR), axial parenchyma (PA); B. Fragment of charred wood.

Interestingly, the cultural layer is sealed by a significant, uninterrupted deposit of volcanic ash reaching 85 centimeters in thickness. The features discovered, as well as the artifacts' angles of deposition suggest that this ashfall occurred while living activity at Papayita was ongoing. In other words, the site had not been abandoned at the moment the ashfall event began. The evidence of human activity after the ashfall is minimal and there is, so far, no indication of further human occupation until modern times. The mineralogical and geochemical data coincide with the geochronological outcome of the charcoal which yielded an age of 3530 ±30 years, identical to the 3560 ±70 years BP, 3540 ±30 years BP and 3549 ±30 years BP ages of previous studies (Zeidler, 1994; Zeidler, 2016; Robin *et al.*, 2008; Robin *et al*., 2010). The fossilized wood fragments collected in Papayita, were identified, thanks to their perfectly preserved anatomical structure, as a plant from the Gymnosperm group, of the Podocarpaceae family, being vegetation from temperate or cold climates in the foothills of the Andes (Páez-Barrera et al., 2024).

Conclusion

A dome collapse of the Pululahua caldera and dome complex some 10k ago, was able to cover and preserve an ancient fluvio-lagunar environment. Based on this volcanic event, it has been possible to identify several dozens of microorganisms, such as plants, diatomens, fungi and bacteria allowing to reconstruct the paleo-environment shortly after glaciation and just prior human settlements.

The species belonging to the Podocarp family inhabit temperate and cold areas of the Andes with an altitudinal distribution range between 1900 and 3800 m a.s.l., meaning that the volcanic activity of the PVC transported Podocarpus wood from a cloud forest of the high Andean zone to the Papayita site located in a coastal environment near the sea level where it was preserved. The vast ashfall and the subsequent charcoal-laden ash layer, coupled with the ensuing environmental disturbances, were probable key contributors to the ending of human occupation at the Papayita settlement and may have played a part in the termination or final metamorphosis of the Valdivia cultural tradition in this region ~3500 years ago.

References

Andrade, S. D., Müller, A. V., Vasconez, F. J., Beate, B., Aguilar, J., & Santamaría, S. (2021). Pululahua dome complex, Ecuador: eruptive history, total magma output and potential hazards. Journal of South American Earth Sciences, 106, 103046.

Ayala-Usma, D. A., Lozano-Gutiérrez, R., Orejuela, C., Pérez-Ángel, L. C., Montes, C., & González-Arango, C. (2024). Exceptionally preserved subfossil woods from late Pleistocene volcanic deposits from the Northern Andes of Colombia. Review of Palaeobotany and Palynology, 324, 105090.

Cadena, E. A., & Román-Carrión, J. L. (2018). A review of the fossil record of Ecuador, with insights about its challenges and future development. Ameghiniana, 55(5), 571-591.

Monzier, M., Samaniego, P., Robin, C., Beate, B., Cotten, J., Hall, M. L., ... & Toulkeridis, T. (2002, September). Evolution of the Pichincha volcanic complex (Ecuador). In Proceedings of fifth international symposium on Andean geodynamics, Toulouse (pp. 429-432).

Páez-Barrera, G. T., Vizuete, K., Ortiz-Aguilu, J. J., Castro, G., Debut, A., & Toulkeridis, T. (2024). Characterization and chronology of charcoal found in the volcanic ashfall that impacted a late Valdivia community in coastal Ecuador. Acta Palaeobotanica, 35-50.

Robin, C., Samaniego, P., Le Pennec, J.L., Mothes, P., Van Der Plicht, J., 2008. Late Holocene phases of dome growth and Plinian activity at Guagua Pichincha volcano (Ecuador). Journal of Volcanol- ogy and Geothermal Research 176(1), 7–15.

Robin, C., Samaniego, P., Le Pennec, J. L., Fornari, M., Mothes, P., & van Der Plicht, J. (2010). New radiometric and petrological constraints on the evolution of the Pichincha volcanic complex (Ecuador). Bulletin of volcanology, 72, 1109-1129.

Svoboda, J., Krejčí, O., Krejčí, V., Dohnalová, A., Sázelová, S., Wilczyński, J., & Wojtal, P. (2019). Pleistocene landslides and mammoth bone deposits: The case of Dolní Věstonice II, Czech Republic. Geoarchaeology, 34(6), 745-758.

Toulkeridis, T., & Zach, I. (2017). Wind directions of volcanic ash-charged clouds in Ecuador–implications for the public and flight safety. Geomatics, Natural Hazards and Risk, 8(2), 242-256.

Ukraintseva, N., Leibman, M., Streletskaya, I., & Mikhaylova, T. (2014). Geochemistry of plant-soil-permafrost system on landslide-affected slopes, Yamal, Russia as an indicator of landslide age. Landslides in cold regions in the context of climate change, 107-131.

Vallé, F., Morelli, C., Krainer, K., Roghi, G., & Kustatscher, E. (2024). Depositional environments and plant communities in the exceptional context of the Kungurian megacaldera of the Athesian Volcanic Group (Southern Alps, N-Italy). Review of Palaeobotany and Palynology, 324, 105083.

Zeidler, J.A., 2016. Modeling cultural responses to volcanic disaster in the ancient Jama–Coaque tradition, coastal Ecuador: A case study in cultural collapse and social resilience. Quaternary International 394, 79–97.

Zeidler, J., 1994. Archaeological Testing in the Middle Jama Valley. In: Zeidler, J., Pearsall, D. (eds), Regional Archaeology in Northern Manabí, Ecuador, Volume 1: Environment, Cultural Chronology, and Prehistoric Subsistence in the Jama River Valley. University of Pittsburgh Memoirs in Latin American Archaeology 8, pp. 71–98. Ediciones Libri Mundi.

17th INTERNATIONAL CONGRESS of the Geological Society of Greece

BULLETIN OF THE GEOLOGICAL SOCIETY OF GREECE, SP. PUBL.

EXTENDED ABSTRACT 235

Foreshock-aftershock discrimination in real-time during the 2025 seismic cluster near Santorini volcano, Greece, based on earthquake statistics and complex networks theory

Papadopoulos G.A.[1], Triantafyllou I.[2], Siettos C.[3], Spiliotis K.[4]

(1) Hellenic Mediterranean University, 71410 Heraklion, Greece, gerassimospapadopoulos2@gmail.com (2) Institute of Physics of the Earth's Interior and Geohazards, Hellenic Mediterranean University Research Center, 73133 Chania, Greece, ioannatriantafyllou@hmu.gr (3) Dipartimento di Matematica e Applicazioni "Renato Caccioppoli", Università degli Studi di Napoli "Federico II", Naples, Italy, constantinos.siettos@unina.it (4) School of Civil Engineering, Democritus University of Thrace, Greece, spiliotiskos@gmail.com

Introduction / Background

Foreshocks, aftershocks and swarms are the most common types of space-time seismicity clusters (Mogi, 1963). The real-time discrimination between foreshocks and other types of clusters is of great importance for the short-term hazard assessment but it is a challenging issue. Therefore, only *a posteriori* solutions have been proposed. During January-March 2025 a space-time seismicity cluster was recorded between Santorini and Amorgos islands, South Aegean, with the largest earthquake (M_L=5.3) occurring on 10 February 2025. This case offered a good opportunity to decipher the type of the ongoing seismic cluster based on the daily re-evaluation of the seismicity state. We utilized tools from the earthquake statistics and the complex networks theory and were able to discriminate beforehand the foreshock-aftershock nature of the ongoing cluster. Our findings were documented on time with internal reports as well as with public reports and statements.

Methods

The real-time characterization of the type of the ongoing seismicity cluster near Santorini was based on the daily monitoring of the 3D seismicity changes, i.e. in the dimensions of space, time and magnitude. Real-time means that the evaluation of a data set retrieved from the earthquake catalogue up to time t, was completed at time t+1 days. The onset of the cluster has been considered to occur on 30 January 2025 which corresponds to t=1 day. The 3D changes detected were compared with the 3D state of background seismicity (BS) in the same area in the time interval from January 2015 to January 2025. This procedure was followed up to 12 March 2025 when we realized that the cluster activity was already at very low level. The implementation of our method has been made possible thanks to the open availability of earthquake data by the Institute of Geodynamics of the National Observatory of Athens (https://bbnet.gein.noa.gr/HL/seismicity/real-time-seismicity/last-24-hours), which provides real-time updating of the national earthquake catalogue.

In the magnitude domain the monitoring of the seismicity state was performed by calculating the variation of the critical geophysical parameter b, which is the slope of the straight line in the Frequency Magnitude Distribution (FMD) well-known as G-R law expressed by (1) (Gutenberg and Richter, 1944):

$$\log N = a - b\,M \qquad (1)$$

N is the discrete or cumulative number of events of magnitude ≥M±ΔM, and a, b are parameters determined by the data. For global seismicity b is about 1 (e.g., Schorlemmer *et al.*, 2005). However, in regional and local seismic zones the b-value is sensitive in many factors the most important being the stress loading conditions (Mogi, 1963) and the crustal heterogeneity (e.g., Abercrombie and Mori, 1996). Therefore, the b-value has been considered as a stress-meter within the crustal material (e.g., Schorlemmer *et al.,* 2005). The methods of Maximum Curvature and of Fixed-M_c, both incorporated in the z-map toolbox (Wiemer, 2001), were utilized to calculate the completeness magnitude threshold, M_c, and the b-value during the BS as well as during the 2025 cluster. The significance of the b-value changes was tested with the test of Utsu (1966).

In the domain of space, we were based on the spatial distribution of the betweeness centrality (BC), which is a topological metric that quantifies the number of times a node (surface patch or earthquake epicenter) acts as a bridge along the shortest path between two other nodes. Bridging nodes that connect disparate parts of the network often have high BC value. Such nodes greatly participate in the flow of information in the network. In earthquake processes high BC indicates persistent seismic activity. From the first few days of the cluster it became obvious that the earthquake epicenters gradually migrated from SW to NE, which is the direction of the main tectonic faults in the area. Since M_c=2.9 was found for the first days of the cluster, for the monitoring of the seismicity migration we considered as zero point the epicenter of the first earthquake of M_L ≥2.9 at time t=1 day. Then we measured from

that point the mean distance, D, of epicenters of the subsequent earthquakes with an ensemble of 100 earthquakes in each measurement step. In the domain of time we analyzed the seismicity rate, r, in terms of r=n/T or r=N/T, where n=discrete number of earthquakes, N=cumulative number of earthquakes and T is a constant time interval.

Results

At time t=4 days (2 February 2025) after the initiation of the seismic cluster, we were able to recognize that the cluster was characterized by the basic properties of the foreshock sequences, i.e. acceleration of the seismicity rate, r, gradual increase of the earthquake magnitudes and significant drop of the b-value as time goes on towards the mainshock occurrence (Jones and Molnar, 1979, Papadopoulos and Minadakis, 2017). This pattern was evident until the largest earthquake (M_L=5.3) on 10 February 2025. The earthquake epicenters migrated from SW to NE towards the epicentral area of the M_L=5.3 mainshock. The maximum distance of D~25 km was found for the mainshock epicentral area. The foreshock move towards the mainshock epicenter has also been observed in other foreshock sequences. The maximum migration velocity was on the order of 3 km/day. On the 13th February we detected important drop in both the number and the magnitudes of the earthquakes. The gradual decrease of r followed power-law and was consistent with the well-known Omori aftershock decay. At the same time, a gradual increase of the b-value was detected, which was an additional evidence of aftershock activity. On the other hand, the betweeness centrality (BC) metric showed that during the stage of background seismicity although the activity was important and persistent in the Santorini-Amorgos area only weak seismicity hubs were detected in the Nea Kammeni (Santorini) and the Kolumbo volcanoes. From the first days of the 2025 seismic cluster the BC metric became quite strong in the Santorini-Amorgos seismic cluster but no seismicity hubs appeared in the two volcanic centers. This picture did not change until 12 March 2025.

During the seismic cluster in Santorini-Amorgos our findings were periodically transmitted by one of us (GP) to the competent state authorities, i.e. the Ministry for Climate Change and Civil Protection, including the Earthquake Planning and Protection Organization, and were communicated through reports (Triantafyllou and Papadopoulos, 2025) and statements in mass and social media, thus documenting beforehand the real-time foreshock-aftershock discrimination during the ongoing cluster.

Conclusions

The 2025 seismic cluster in Santorini-Amorgos area is a good example of real-time discrimination between foreshocks, aftershocks and swarms. The foreshock nature of the cluster was detected as early as the 4th day of the cluster and was verified by daily seismicity monitoring until the occurrence of the mainshock (M_L=5.3) on 10 February 2025. A few days later the aftershock sequence following the mainshock was also detected. These results disfavor the interpretation of the 2025 seismicity cluster as a swarm case. The gradual migration of epicenters with maximum velocity of ~3 km/day does not account for hydraulic diffusion and favors a cascade failure process. The findings of our analysis were documented in many ways beforehand during the ongoing seismic cluster. The area between Santorini and Amorgos acts as a long-term seismicity hub and stress concentrator.

References

Abercrombie, R. E., Mori, J., 1996. Occurrence patterns of foreshocks to large earthquakes in the western United States. Nature 381, 303–307.

Jones, L.M., Molnar, P., 1979 Some characteristics of foreshocks and their possible relationship to earthquake prediction and premonitory slip on faults. J. Geophys. Res. 84, 3596–3608.

Mogi, K., 1963. Some discussion on aftershocks, foreshocks and earthquake swarms – the fracture of a semi-infinite body caused by an inner stress origin and its relation to the earthquake phenomena (3rd paper). Bull. Earthq. Res. Inst. Univ. Tokyo 41, 615–658.

Gutenberg, B. and Richter, C.,1944. Frequency of earthquakes in California. Bull. Seism. Soc. Am. 34, 185–188.

Papadopoulos, G.A., Minadakis, G., 2016. Foreshock Patterns Preceding Great Earthquakes in the Subduction Zone of Chile. Pure Appl. Geophys., https://doi.org/10.1007/978-3-319-51529-8_3.

Schorlemmer, D., Wiemer, S., Wyss, M., 2005. Variations in earthquake-size distribution across different stress regimes. Nature 437, 539–542.

Triantafyllou, I., Papadopoulos, G.A., 2025. A unique seismic cluster near Santorini, Greece, foreshadows a strong earthquake? https://www.emsc.eu/Special_reports/, 3 p. (uploaded on 6 February 2025).

Utsu, T., 1966. A statistical test of the difference in b-value between two earthquake groups. J. Physics Earth 14, 37–40.

Wiemer, S., 2001. A software package to analyze seismicity: ZMAP. Seismol. Res. Lett. 72, 374-383.

17th INTERNATIONAL CONGRESS of the Geological Society of Greece

BULLETIN OF THE GEOLOGICAL SOCIETY OF GREECE, SP. PUBL.

EXTENDED ABSTRACT 236

Image-based grain size analysis of coastal sediments

Papadopoulos Th.[1], Pechlivanidou S.[1], Foumelis M.[1], Pennos Ch.[1]
(1) Department of Physical & Environmental Geography, School of Geology, Aristotle University of Thessaloniki, Thessaloniki, Greece

Abstract

In this study we show that image-based grain size analysis, could under appropriate conditions, replace the traditional grain size analysis in the laboratory, providing reliable results, especially for coarse-grained samples.

Coasts are dynamic systems affected both by natural and anthropogenic factors. Over the last few decades, the impact of climate change in coastal areas has become increasingly evident, with accelerated erosion significantly altering shorelines, threatening ecosystems, and endangering human settlements. Grain size analysis of coarse sediments (i.e. coarser than silt) traditionally held with the sieving method, remains one of the basic tools for studying coastal processes. However, this approach can be time-consuming and requires strategic sampling, particularly in extensive areas, along with a thorough understanding of geological principles. New methods, such as the use of satellite imagery and high-resolution photographs from drones or smartphones, provide faster solutions, although they often require further validation and comparison with laboratory-based grain size analysis to ensure accuracy.

Here, we investigate the effectiveness and accuracy of Buscombe's (2013) code in photographic grain size analysis techniques, both on-site and in the laboratory. We compare the grain size results obtained from this method with those from traditional sieving to draw reliable conclusions, while assessing the technical specifications and external factors affecting the accuracy of the method. The aim is to save time and resources to improve coastal zone research.

Buscombe's code is a Python algorithm that speeds up grain size analysis using sediment photos (Buscombe, 2013). It relies on Morlet wavelet to estimate the grain size distribution, by analyzing selected regions of the image to reduce computational load. This algorithm identifies patterns and frequencies in the image that correspond to different grain sizes. The results are presented as Power Spectrum Density (PSD) and, through interpolation, a complete grain size distribution is generated, eliminating the need for further adjustments.

Sampling took place in the coastal area of Kalamaria, Thessaloniki, Greece. The site was carefully selected to avoid interference from swimmers or municipal equipment. Sediment samples were collected from six different locations, based on visual observation of grain size distribution. The samples were first dried in the oven at 100°C and then sieved using 0.5Φ sieves in the Sedimentology Laboratory, at the Aristotle University of Thessaloniki. Processing of the grain size results performed using Gradistat software (Blott & Pye, 2001) following Folk and Ward method (Folk & Ward, 1957).

To evaluate the accuracy of the method for obtaining automated grain size results, we took high-resolution photographs (12MP and 108MP) of the samples in the laboratory using a Xiaomi Redmi Note 11S smartphone. Photographs were processed using the Buscombe's code and the results were compared with those from sieving. The comparison included the whole sediment samples as well as specific grain size fractions (i.e., 0 Φ).

After testing the accuracy of the code on laboratory photographs, we applied the same approach to photographs taken in the field, where external factors, such as lighting and shadows, could influence the results. Field photographs were taken of three samples (i.e., samples NOΘ-201, NOΘ-202, and NOΘ-203) in the afternoon under mild natural lighting with some shadows, and two samples (i.e., samples NOΘ-301 and NOΘ-302) at noon with strong natural lighting with minimal shadows. The grain size results from field photographs were then compared to those of the same samples photographed in the laboratory.

Table 1. Grain size results using the Buscombe's code (2013) for sediment samples sieved at 0 Φ (1 mm)

Sample	Mean grain size (mm) using Buscombe's with 108MP camera resolution	% Difference	Mean grain size (mm) using Buscombe's with 12MP camera resolution	% Difference
NOΘ-2P	0.61	39%	0.69	31%
NOΘ-3P	0.89	11%	0.89	11%
NOΘ-4P	0.94	6%	0.82	18%
NOΘ-5P	0.91	9%	0.92	8%
NOΘ-6P	0.98	2%	0.87	13%

Table 1 shows the mean grain size results for the 0 Φ fractions using the Buscombe code on photographs with 108MP and 12MP resolution. The percentage deviations range from 2% to 39% with the 108MP resolution photos and from 8% to 31% with the 12MP ones, indicating that higher resolution provides slightly more accurate results. The NOΘ-6P sample displays the smallest deviation (2%), while the NOΘ-2P sample demonstrates the largest (39% for the 108MP resolution photos and 31% for the 12MP resolution photos). Overall, both analyses yield comparable results, with the 108MP resolution offering a slight advantage in precision.

Table 2. Grain size results using the Buscombe's code (2013) for the whole sediment samples

Sample	Camera Analysis	Mean grain size (mm) using Buscombe code	Grain Size results from sieving (mm)	% Difference
NOΘ-1P	12MP	1.19	0.38	213%
NOΘ-1P	108MP	1.14	0.38	202%
NOΘ-3P	12MP	1.78	0.98	82%
NOΘ-3P	108MP	1.57	0.98	59%

Table 2 presents the mean grain size results for whole sediment samples analyzed using Buscombe's code, along with the differences compared to sieving results. For the fine-grained sample NOΘ-1P (i.e., 0.38 mm), discrepancies are substantial, reaching 213% with 12MP resolution photos and 202% with108MP resolution photos. In contrast, for the coarser-grained NOΘ-3P sample (i.e., 0.98 mm), discrepancies decrease significantly to 82% with 12MP resolution photos and 59% with 108MP resolution photos. These results suggest that the accuracy of the Buscombe code improves with higher resolution images and coarser-grained samples are used, while it exhibits greater errors with finer-grained samples.

Table 3. Comparison of the grain size results using the Buscombe's code (2013) on lab and field photos

Sample	Grain Size (mm) Lab	Grain Size (mm) Field	% Difference
NOΘ – 201	1.08	2.36	118%
NOΘ – 202	1.14	2.68	135%
NOΘ – 203	1.15	2.76	141%
NOΘ – 301	0.99	1.74	76%
NOΘ – 302	1.09	1.17	8%

Table 3 highlights variations in grain size between laboratory and field photographs, which range from 8% to 141%. Samples NOΘ-201, NOΘ-202 and NOΘ-203, photographed under less favorable lighting conditions and shadows, show the largest differences, ranging from 118% to 141%. Conversely, samples NOΘ-301 and NOΘ-302, captured under more favorable conditions with adequate lighting, show significantly smaller discrepancies, with NOΘ-302 having the smallest difference at just 8%. These findings indicate that the shooting conditions play a crucial role in the accuracy of the particle size analysis. Despite these variations, sediment classifications based on the Wentworth chart (Wentworth, 1922) differ by only one class. For samples NOΘ-201, NOΘ-202, and NOΘ-203, results from the field photos are classified as very fine gravel, while results from the lab photos as classified as very coarse sand. Similarly, samples NOΘ-301 and NOΘ-302, show even smaller discrepancies, with samples being classified as very coarse sand in both field and lab photos.

Our results show that the application of the Buscombe code to 0 Φ grain size fraction has satisfactory accuracy, when compared to the sieving data. However, in the whole sediment samples, the deviations are higher, especially in the finer grain sizes, reaching up to 200%, highlighting the need for method optimization. In the coarse grain sizes, the discrepancies decreased, with the use of high-resolution (108MP) photographs enhancing accuracy. Overall, the code proved to be effective for larger grain sizes, while its accuracy is significantly affected by the resolution of the photograph and the homogeneity of the sample.

Comparison of field and laboratory photographs highlighted the importance of external factors, such as lighting and shadows. Field photographs under good lighting conditions showed smaller differences compared to photos taken under unfavorable conditions. Coarse-grained samples showed better convergence between methods, while the use of high-resolution photographs improved the results.

Acknowledgements

Sincere gratitude is extended to the doctoral candidates, surveyors Ion and Kostas, for dedicating their valuable time to ensure the accurate and scientific acquisition of field photographs.

References

Blott, S.J. and Pye, K., 2001. GRADISTAT: a grain size distribution and statistics package for the analysis of unconsolidated sediments. Earth Surface Processes and Landforms, 26(11), pp.1237-1248.

Buscombe, D., 2013. Transferable wavelet method for grain□size distribution from images of sediment surfaces and thin sections, and other natural granular patterns. Sedimentology, 60(7), pp.1709-1732.

Folk, R.L. and Ward, W.C., 1957. Brazos River bar [Texas]; a study in the significance of grain size parameters. Journal of Sedimentary Research, 27(1), pp.3-26.

Wentworth, C.K., 1922. A scale of grade and class terms for clastic sediments. *The Journal of Geology*, 30(5), pp.377-392.

17th INTERNATIONAL CONGRESS of the Geological Society of Greece

BULLETIN OF THE GEOLOGICAL SOCIETY OF GREECE, SP. PUBL.

EXTENDED ABSTRACT 237

Development of a cartographic web application for monitoring the Corinth Canal using UAV data

Papadopoulou Ermioni Eirini[1], Proestakis Stavros[2], Anagnostopoulos Christos Nikolaos[3], Soulakellis Nikolaos[2]

(1) Department of Civil Engineering and Geomatics, School of Engineering and Technology, Cyprus University of Technology, Lemesos 3603, Cyprus, e.papadopoulou@cut.ac.cy

(2) Department of Geography, University of the Aegean, 81100 Mytilene, Greece

(3) Department of Cultural Technology, University of the Aegean, 81100 Mytilene, Greece

Introduction / Background

The Corinth Canal is a landmark of immense historical, cultural, and industrial significance, bridging the Saronic and Corinthian gulfs. It serves as a symbol of engineering ingenuity and a vital transportation route (Manolopoulou, 2024). The Corinth Canal cuts through the isthmus of Corinth, a geologically dynamic area characterized by sedimentary rock formations, tectonic activity, and steep slopes (Anagnostopoulos et al., 1991). The canal, approximately 6.4km long and 25m wide, exposes a cross-section of the region's stratigraphy, offering a unique opportunity for geological study. However, its steep walls, composed primarily of loose conglomerates and marls, are prone to erosion, landslides, and structural instability. These risks are compounded by the area's seismic activity, necessitating continuous monitoring and management. The Corinth Canal has been mapped using modern 3D mapping techniques, such as UAVs data processing and Structure-from-Motion (SfM) photogrammetry, enabling the creation of highly accurate 3D models and orthomosaics (Saroglou et al., 2019). Additionally, the canal's deformation is being monitored using SBAS (Small Baseline Subset) Interferometric Synthetic Aperture Radar (InSAR) and GNSS (Global Navigation Satellite Systems) techniques (Yaragunda and Oikonomou, 2024). These techniques have been applied to recent landslides, providing valuable insights into slope geometry, stability analysis, and risk assessment. Despite the advanced mapping efforts, a dedicated online platform for aggregating and unifying the mapping data has not yet been developed. This presents a significant opportunity to create a unified web-based mapping application that would enhance access to and utilization of these data by the scientific community and relevant stakeholders. To address these needs, this study, in collaboration with Corinth Canal S.A (A.E.DI.K) aimed to create a detailed geospatial archive of the canal through advanced UAV (Unmanned Aerial Vehicle) technologies. The initiative combined cutting-edge data collection techniques and a robust flight planning strategy to support sustainable management, promote its historical value, and enable continuous monitoring of its condition.

Objectives.

The study had three interlinked objectives:

i. **Developing high-resolution geospatial data products**: These included 3D point clouds, textured models, orthomosaics, and digital elevation models (DEMs), capable of capturing the canal's intricate details with spatial resolutions of 10-20 cm.

ii. **Implementing precise flight planning for optimized data acquisition**: A systematic and carefully designed flight plan was crucial to ensure comprehensive coverage, minimize data gaps, and maintain high geometric accuracy.

iii. **Creating a web-based mapping platform**: This platform integrates the collected datasets, enabling spatiotemporal monitoring of the canal's slopes, assessing structural stability, and supporting effective management strategies.

Methods

The data collection process between October 23-29, 2023, utilized UAVs equipped with RGB cameras, thermal sensors, and GNSS receivers. To ensure systematic coverage, the canal was divided into nine segments. Each segment was mapped using three meticulously planned flight patterns: vertical (nadir), east-west oblique, and north-south oblique. This design minimized data voids and ensured optimal image overlap (90% frontal and 80% lateral). Flight paths were pre-designed using DJI's Pilot 2 software, considering terrain variability, safety parameters, and the need for uniform data quality. The flights captured high-resolution imagery at height of flights ranging from 120 meters for general mapping, to 3-10 meters for detailed thermal scans and panoramic images at specific points of interest. Between October 23 and 29, 2023, UAV flights systematically captured high-resolution geospatial data of the

Corinth Canal. Employing UAV models such as the Mavic 3E and Matrice 300, the project utilized RGB and thermal sensors for diverse imaging needs. Each flight was executed with specific gimbal angles—typically -90° for vertical (nadir) and -70° for oblique imagery—ensuring precise coverage and minimizing data voids. The captured images featured resolutions ranging from 3.22 to 3.45 cm/pixel for general mapping to less than 1 cm/pixel for specific locations. This meticulous planning facilitated the creation of comprehensive datasets, later integrated into a web-based cartographic platform to enhance monitoring and management efforts.

Table 1: Characteristics of Flights Conducted for the 3D Mapping of the Corinth Canal

Date	October 23, 2023	October 24, 2023	October 25, 2023	October 28, 2023	October 29, 2023
Number of Flights	6	14	7	4	3
UAV Model	Mavic 3E	Mavic 3E	Mavic 3E	Mavic 3E	Matrice 300
Sensor Type	RGB Camera	RGB Camera	RGB Camera	RGB Camera	RGB + Thermal Sensors
Gimbal Angle	-90° (vertical), -70° (oblique)	-90° (vertical), -70° (oblique)	-90° (vertical), -70° (oblique)	360° Panoramic	Various
Image Resolution	3.22–3.45 cm/pixel	3.22–3.45 cm/pixel	3.22–3.45 cm/pixel		5–10 cm/pixel
Flight Patterns	Vertical (nadir), oblique east-west	Vertical (nadir), oblique east-west	Vertical (nadir), oblique east-west	Panoramic and detailed imaging	Vertical, oblique imaging

The collected data were processed using photogrammetric algorithms such as Structure from Motion (SfM) and Multi-View Stereo (MVS) (Westoby et al., 2012), producing dense point clouds, DEMs, and orthomosaics. Geometric accuracy was further validated by comparing the results with existing topographic diagrams. The photogrammetric outputs were then enhanced with thermal data to supporting the identification of potential structural vulnerabilities.

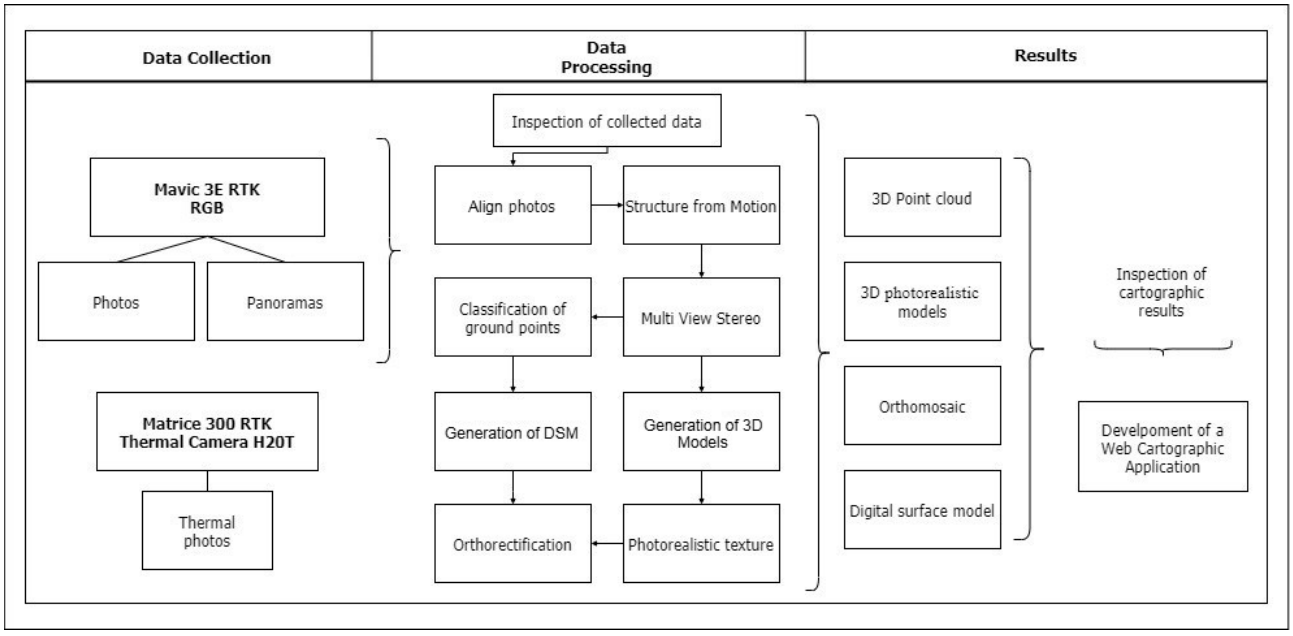


Figure 1. Flow diagram of the methodology

A key aspect of the study was the development of the “Corinth Canal” web mapping platform. This platform integrates all spatial datasets into a user-friendly interface, enabling stakeholders to visualize and interact with the canal’s digital representation. The platform was developed using GIS-based tools, such as ArcGIS Online and customized web applications, to provide functionalities including spatial analysis (distance, area, and slope measurement), thematic comparisons, and annotation capabilities. Special emphasis was placed on supporting multitemporal monitoring of the canal’s slopes, with tools designed to track changes over time, enabling early detection of risks such as landslides or structural instability.

Results

The study successfully delivered a comprehensive suite of geospatial products that offer detailed insights into the Corinth Canal's current condition. Seven georeferenced 3D models and point clouds were created, covering the entire canal and its individual segments, alongside high-resolution orthophotos, digital elevation models (DEMs), and thermal imagery. The results demonstrated high accuracy, with spatial resolutions ranging from 10-20 cm, and were validated through comparisons with existing topographic diagrams. This process confirmed the reliability of UAV-based data collection as a highly precise and efficient method for documenting such complex structures.

The integration of thermal imagery further enriched the dataset, enabling the identification of potential structural vulnerabilities, such as hotspots indicative of material stress or instability. These thermal findings, combined with detailed 3D models and DEMs, provide critical information for assessing the canal's geotechnical and structural health.

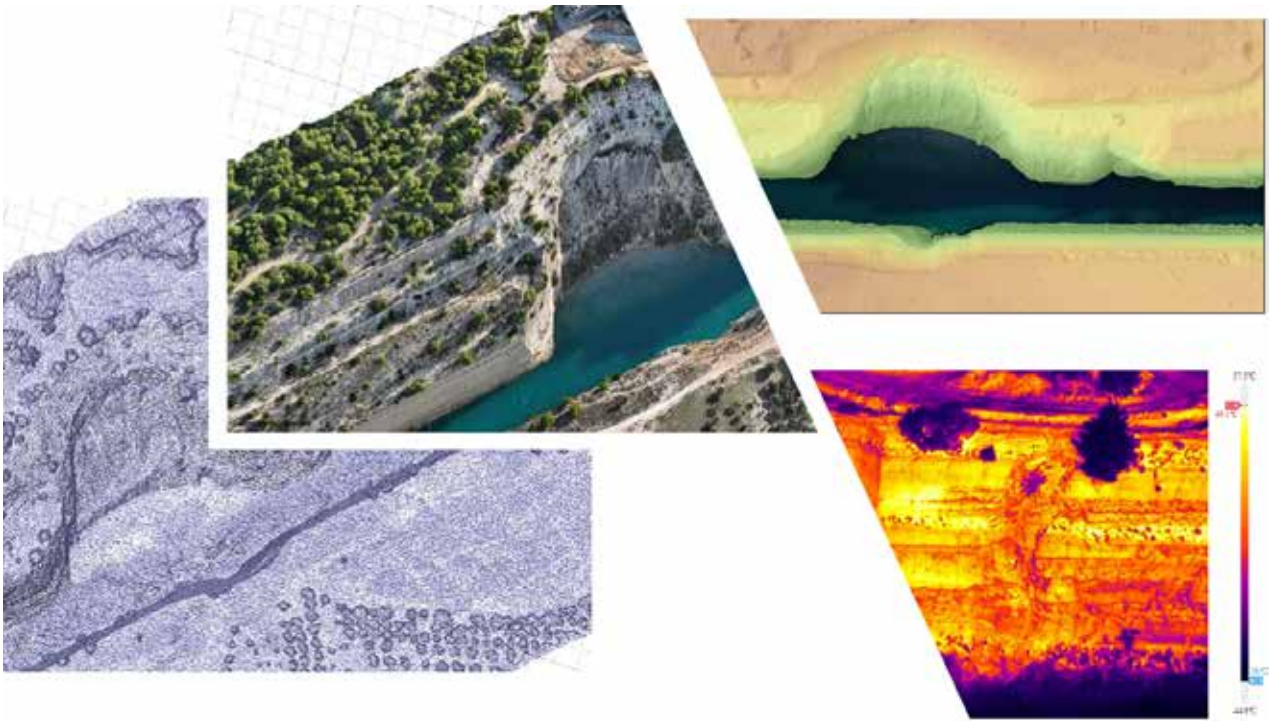


Figure 2. 3D photorealistic model, mesh of an irregular triangular network, DEM and a thermal photo of the 4th section of the Corinth Canal.

A significant outcome of the study was the development of the cartographic web application named "Corinth Canal". This interactive tool consolidates all spatial datasets, offering a user-friendly interface for visualizing and analyzing the canal's digital representation. The platform includes a variety of tools tailored to the needs of stakeholders:

- **Measurement Tools**: Users can perform distance, area, and slope calculations directly within the platform, enabling precise spatial analysis for maintenance and planning activities.
- **Thematic Comparisons**: Layers such as thermal imagery, 3D models, and orthophotos can be overlaid and compared, facilitating the identification of changes or inconsistencies over time.
- **Annotation and Note-Taking**: Users can add annotations and comments to specific areas, enhancing communication among teams and stakeholders involved in the canal's management.

The platform's design emphasizes accessibility and ease of use, ensuring that both technical and non-technical users can interact effectively with the data. Moreover, it enhances operational workflows by providing centralized access to critical geospatial information, streamlining decision-making processes. By bridging advanced UAV-based data collection with modern GIS technology, this study has laid the foundation for a sustainable, data-driven approach to the monitoring and management of the Corinth Canal. The web application not only supports day-to-day operations but also contributes to long-term preservation efforts, offering a scalable model for similar cultural and industrial heritage sites worldwide.



Figure 3: "Corinth Canal" cartographic web application.

Conclusions

The development of the "Corinth Canal" web mapping platform stands as a pivotal achievement in this study, offering an innovative and user-friendly tool for visualizing and managing the canal's digital representation. By integrating high-resolution spatial datasets—including 3D models, orthomosaics, DEMs, and thermal imagery—the platform provides stakeholders with the capability to monitor and assess the canal's structural stability in a dynamic and accessible manner. Designed with tools for distance and area measurement, thematic comparisons, and annotation, the platform supports multitemporal analysis, enabling early detection of risks such as landslides or structural instability. This interactive application not only streamlines operational workflows but also serves as a scalable model for preserving and monitoring similar cultural/industrial heritage sites or critical infrastructures worldwide.

This study underscores the transformative potential of UAV technologies in cultural heritage management. By employing precise flight planning and advanced photogrammetric methods, we achieved a comprehensive and high-resolution geospatial archive of the Corinth Canal. The integration of thermal data enriched the analysis, enabling the identification of structural vulnerabilities such as material stress and instability. UAV-based mapping it is considered a reliable and efficient method for documenting complex geological and structural settings, with centimeter-level accuracy that surpasses traditional methods in both speed and cost-effectiveness.

Future work could focus on integrating machine learning algorithms with the collected UAV data to automate the detection of structural vulnerabilities, such as cracks or erosion patterns, along the canal's slopes. Additionally, expanding the monitoring system to include real-time data acquisition using UAVs equipped with advanced sensors (e.g., LiDAR or hyperspectral imaging) could enhance the multitemporal analysis of geological and structural changes. Finally, collaborative efforts could explore creating a shared digital twin of the canal, enabling global access for research, education, and cultural preservation initiatives.

Acknowledgements

This work was supported by the sub-contract action "3D Geometric Documentation of the Corinth Canal and Digitization of the Cultural Content of the Corinth Canal Museum," which is part of the project "Promotion and Exploitation of the History and Cultural Value of the Corinth Canal and Digital Promotion of the Industrial Museum," under the OPERATIONAL PROGRAMME COMPETITIVENESS, ENTREPRENEURSHIP, AND INNOVATION 2014-2020 framework, funded by Greece and the EU.

Special thanks are extended to George Zouglis, General Manager of Corinth Canal S.A. (A.E.DI.K), and Dimitrios Roussis for their continuous support, collaboration, and technical assistance

References

Anagnostopoulos, A.G., Kalteziotis, N., Tsiambaos, G.K., Kavvadas, M., 1991. Geotechnical properties of the Corinth Canal marls. Geotech. Geol. Eng. 9, 1–26. https://doi.org/10.1007/BF00880981

Manolopoulou, A.-R., 2024. Museum of the Isthmus of Corinth--History with a view. Technische Universität Wien.

Saroglou, C., Kallimogiannis, V., Bar, N., Manousakis, G., Zekkos, D., 2019. Analysis of slope instabilities in the Corinth canal using UAV-enabled mapping. Proc. Int. Conf. Nat. Hazards Infrastruct.

Westoby, M.J., Brasington, J., Glasser, N.F., Hambrey, M.J., Reynolds, J.M., 2012. “Structure-from-Motion” photogrammetry: A low-cost, effective tool for geoscience applications. Geomorphology. https://doi.org/10.1016/j.geomorph.2012.08.021

Yaragunda, V.R., Oikonomou, E., 2024. Monitoring the Los (Line of Sight) Deformation of the Corinth Canal, Greece Using SBAS and GNSS Techniques. IGARSS 2024 - 2024 IEEE Int. Geosci. Remote Sens. Symp. 11056–11061. https://doi.org/10.1109/igarss53475.2024.10642704

17th INTERNATIONAL CONGRESS of the Geological Society of Greece

BULLETIN OF THE GEOLOGICAL SOCIETY OF GREECE, SP. PUBL.

EXTENDED ABSTRACT 238

An integrated approach using Remote Sensing and the Environmental Seismic Intensity Scale ESI 2007 for three major earthquakes in the Aegean region

Papadopoulou E.[1], Chatzipetros A.[1]

(1) Department of Structural, Historical and Applied Geology, School of Geology, Aristotle University of Thessaloniki, Greece, epapadoas@geo.auth.gr

Introduction / Background

The study of earthquake impacts on the environment is important for understanding seismic hazards and reducing associated risks. Remote sensing, particularly through Sentinel-1 satellite imagery, offers an effective method for detecting ground displacement and mapping fault systems. The Environmental Seismic Intensity Scale (ESI 2007) provides a robust framework for evaluating earthquake effects on the environment (Michetti et al., 2007) with high precision (Papanikolaou & Melaki, 2017). This study combines Sentinel-1 remote sensing techniques with the ESI 2007 scale to assess seismic hazards and disaster potential by analysing recent seismic events in the Aegean region, focusing on the Kozani-Grevena 1995, Lesvos 2017 and Samos 2020 earthquakes. On 1995 May 13, Kozani and Grevena were struck by an Ms = 6.6 (Mw 6.5) earthquake, causing extensive damage. Meyer et al. (1996) reported surface ruptures over 8 km comprising open fissures and scarps on the pre-existing Palaeochori Fault striking N70◦E. It was preceded by foreshocks, causing significant impacts to buildings, and triggered environmental effects such as rockfalls, landslides, liquefaction, and surface ruptures (Meyer et al., 1998, Hatzfeld et al. 1995, Pavlides et al. 1995, Chatzipetros 1998). On June 12, 2017, a Mw 6.3 earthquake struck southeastern Lesvos Island, causing disasters to the natural environment, buildings, and infrastructure, particularly in southeastern Lesvos. The earthquake's epicentre was offshore, with a depth of ~13 km, and was associated with a NW-SE striking (Papadimitriou et al., 2017), SW-dipping normal fault along the northern margin of the offshore Lesvos basin (Chatzipetros, et. al, 2013). It triggered secondary earthquake environmental effects (EEE) (Lekkas et al., 2017) such as ground cracks, slope movements, and a tsunami in Plomari port, likely caused by offshore landslides (Karamvasis et al., 2017 Vlachakis et al., 2020). The 2020 Samos earthquake, with a magnitude of 7.0, struck the eastern Aegean Sea on October 30th, significantly impacting Samos Island, Greece, and Izmir, Turkey. Caused by normal faulting along the North Aegean Trough, it triggered substantial ground deformation (Mavroulis et al., 2020), including co-seismic uplifts and displacements and produced surface ruptures, landslides, liquefaction, coastal changes, and hydrological anomalies (Foumelis et al., 2021, Ganas et al., 2021, Sakkas, 2021). The Samos earthquake serves as a focal point in such studies.

Methods

The methodology integrates advanced remote sensing techniques and field-based analyses to investigate ground displacement and environmental effects caused by seismic events. Sentinel-1 Synthetic Aperture Radar (SAR) data were utilized for pre- and post- seismic periods, with differential interferometric SAR (DInSAR) processing, employed to measure co-seismic deformation. The analysis involved co-registering SAR images, removing the topographic phase using Shuttle Radar Topographic Mission (SRTM) data, unwrapping phase data using SNAP Desktop software. Vertical (up-down) displacement component was calculated from ascending and descending LOS data and was visualized within a GIS environment. Using published and field information about the distribution and magnitude of surface effects and the ESI 2007 scale, the study evaluates environmental impact, such as uplifts, surface ruptures, slope failures, and liquefaction, by mapping and digitizing these data in GIS, producing isoseismal maps with the method of kriging that illustrate intensity patterns. The final step involves an analysis of remote sensing data and traditional field measurements to validate their consistency and potential data overlap.

Results and Conclusions

The analysis of ascending Sentinel-1 data (Fig. 1 and Fig. 3) and descending Sentinel-1 SAR data (Fig. 2 and Fig. 4) for the Lesvos and Samos earthquakes demonstrated significant ground displacement, accurately captured through interferometric synthetic aperture radar (InSAR). Moreover, the ascending and descending Sentinel-1 data showed similar results for both seismic events. Field measurements used for the ESI 2007 scale and the seismic intensities ranged from IV to IX, which are broadly in agreement with other studies (Lekkas et al., 2017, Papanikolaou & Melaki, 2017, Mavroulis et al., 2021), reflecting the widespread impacts of all three events. Moreover, the use of the Environmental Seismic Intensity (ESI-07) scale demonstrated its effectiveness in evaluating primary and secondary earthquake environmental effects (EEEs), such as slope failures, liquefaction, and ground cracks, particularly in inaccessible areas.

The maps (Fig. 1, 2, 3, 4) of surface co-seismic deformation fields obtained by analysis of interferometric synthetic aperture radar (InSAR) images have significantly improved the description of earthquake effects. The seismic intensity was visualized in isoseismal maps to illustrate the spatial distribution of impacts for the Kozani-Grevena (for which no InSAR data was available Fig. 5), Lesvos (Fig. 6) and Samos (Fig. 7) earthquakes present the spatial distribution of seismic intensity and highlighted areas

of heightened risk, enhancing seismic hazard assessment and disaster preparedness for future applications. This integrated approach offered valuable insights into the environmental impacts of seismic events and improved hazard assessment. It also emphasized the complementary roles of remote sensing in covering inaccessible areas and field data for high-resolution, localized studies. The multidisciplinary response shown in these studies demonstrates the growing integration of advanced geospatial technologies, field observations, and historical data in seismic risk assessment.

In conclusion, this study underscores the effectiveness of combining Sentinel-1 SAR imagery with the ESI 2007 scale to assess environmental impacts of strong earthquakes. It enhances our understanding of seismic risks by detecting concealed faults and quantifying ground displacement, especially in remote or inaccessible areas. The findings contribute to the ESI 2007 database and highlight the critical role of remote sensing in earthquake research. This integrated framework has the potential to strengthen disaster preparedness and response strategies, providing a foundation for future advancements in seismic risk assessment.

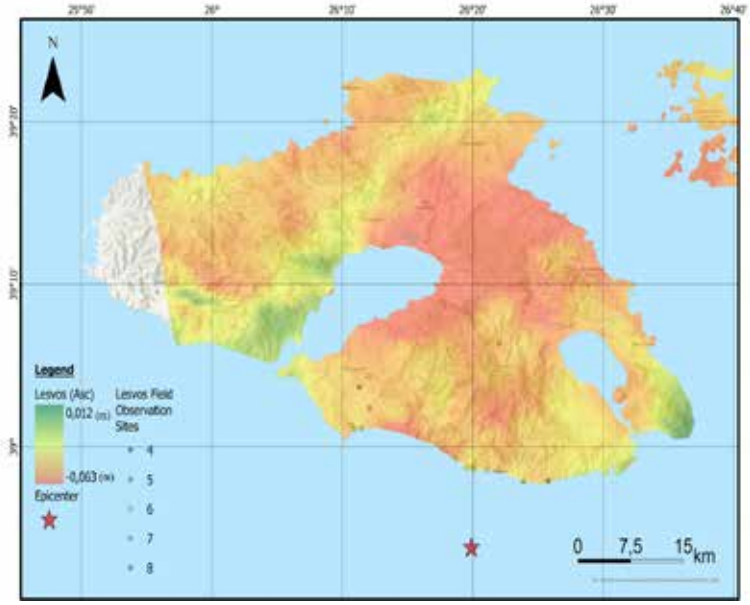


Figure 1. Ground displacement map in meters after the Lesvos earthquake in 2017 using Ascending Sentinel-1 orbit data.

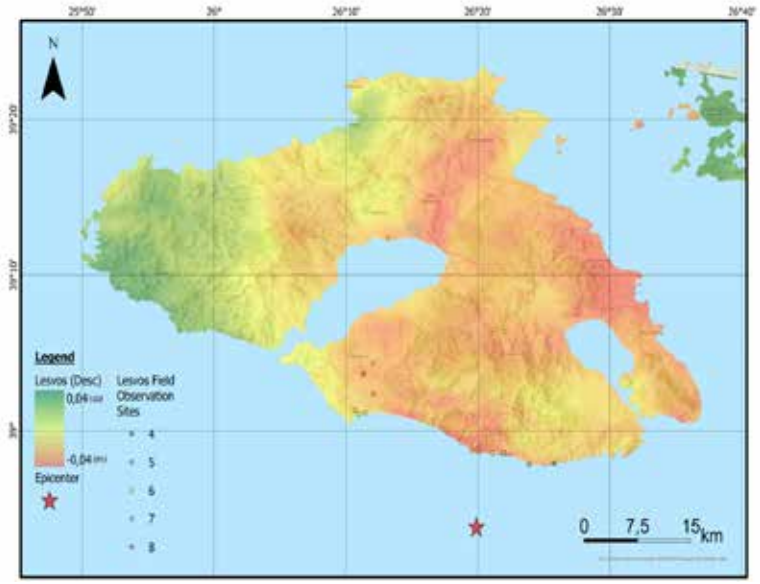


Figure 2. Ground displacement map in meters after the Lesvos earthquake in 2017, using Descending Sentinel-1 orbit data.

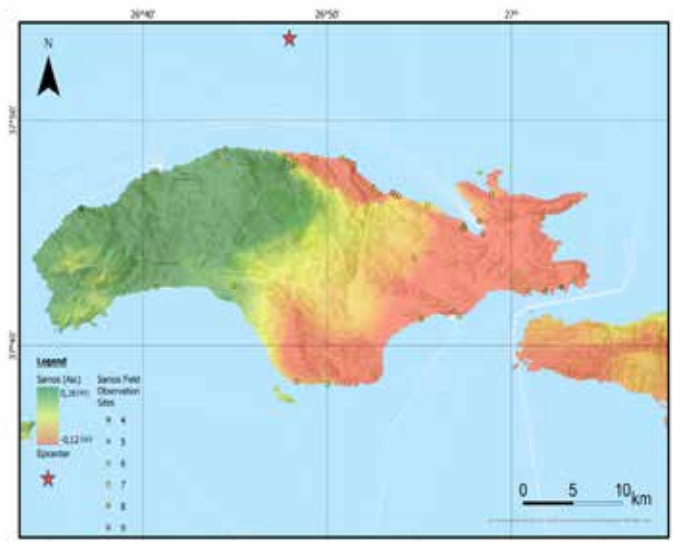


Figure 3. Ground displacement map in meters after the Samos earthquake in 2020, using Ascending Sentinel-1 orbit data.



Figure 4. Ground displacement map in meters after the Samos earthquake in 2020, using Descending Sentinel-1 orbit data.

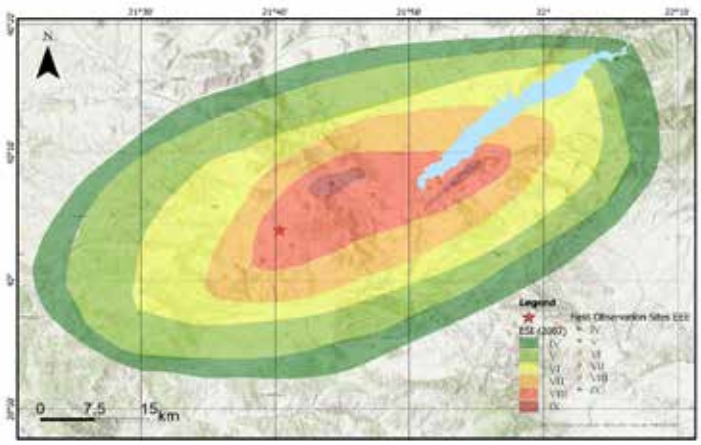


Figure 5. Isoseismal map of the Kozani-Grevena earthquake in 1995, using field survey data.

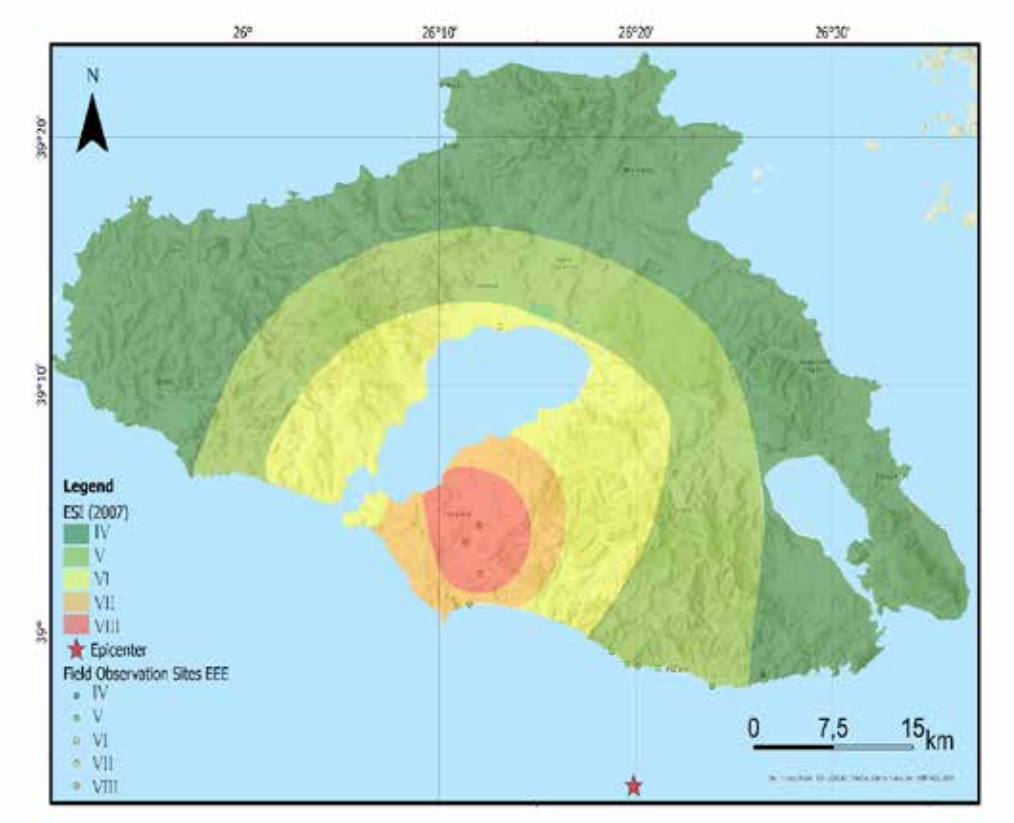


Figure 6. Isoseismal map of the Lesvos earthquake in 2017, using field survey data.

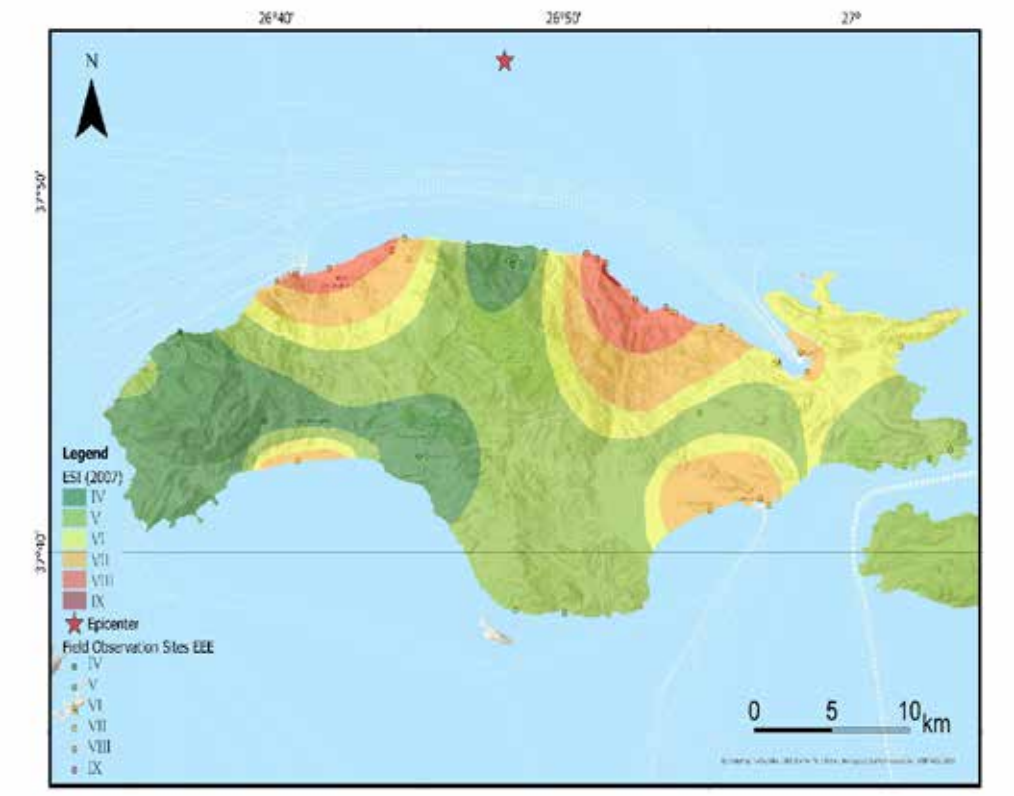


Figure 7. Isoseismal map of the Samos earthquake in 2020, using field survey data.

Acknowledgements
The authors would like to express thank to ESA and Copernicus for providing access to SAR images. The figures were created using SNAP Desktop and ArcGIS Pro Geographic Information System.

References

Chatzipetros, A.A., 1998. Palaeoseismological and Morphotectonic Study and Mechanical Behavior of Active Fault Systems in Mygdonia, Eastern Chalkidiki, Kozani - Grevena. Ph.D. Dissertation, Department of Geology, Aristotle University of Thessaloniki, Thessaloniki, Greece.

Chatzipetros, A., Kiratzi, A., Sboras, S., Zouros, N., Pavlides, S. 2013. Active faulting in the north-eastern Aegean Sea Islands. Tectonophysics 597-598, 106-122.

Foumelis, M., Papazachos, C., Papadimitriou, E., Karakostas, V., Ampatzidis, D., Moschopoulos, G., Kostoglou, A., Ilieva, M., Minos-Minopoulos, D., Mouratidis, A. and Kkallas, C., 2021. On rapid multidisciplinary response aspects for Samos 2020 M7. 0 earthquake. Acta Geophysica, 69, pp.1025-1048.

Ganas, A., Elias, P., Briole, P., Valkaniotis, S., Escartin, J., Tsironi, V., Karasante, I. and Kosma, C., 2021. Co-seismic and post-seismic deformation, field observations and fault model of the 30 October 2020 Mw= 7.0 Samos earthquake, Aegean Sea. Acta Geophysica, 69(3), pp.999-1024.

Hatzfeld, D., Nord, J., Paul, A., Guiguet, R., Briole, P., Ruegg, J.-C., Cattin, R., Armijo, R., Meyer, B., Hubert, A., Bernard, P., Karakostas, V., Papaioannou, C., Papanastassiou, D., Veis, G., 1995. The Kozani-Grevena (Greece) earthquake of May 13, 1995, Mw = 6.6: Preliminary results of a field multidisciplinary survey. Seismological Research Letters 66, 61–70.

Karamvasis, K. and Karathanassi, V., 2017. Deformation effects of dams on coastal regions using sentinel-1 iw tops time series: The west Lesvos, Greece case. The International Archives of the Photogrammetry, Remote Sensing and Spatial Information Sciences, 42, pp.91-96.

Lekkas, E., Mavroulis, S., Skourtsos, E., Andreadakis, E., Antoniou, V., Kranis, C., Soukis, K., Lozios, S., Alexoudi, V., 2017. Earthquake environmental effects induced by the 2017 June 12, Mw 6.3 Lesvos (North Aegean Sea, Greece) earthquake. Department of Dynamic Tectonic Applied Geology, Faculty of Geology and Geoenvironment, School of Sciences, National and Kapodistrian University of Athens, Athens, Greece.

Mavroulis, S., Triantafyllou, I., Karavias, A., Gogou, M., Katsetsiadou, K.N., Lekkas, E., Papadopoulos, G.A. and Parcharidis, I., 2021. Primary and secondary environmental effects triggered by the 30 October 2020, Mw= 7.0, Samos (Eastern Aegean Sea, Greece) earthquake based on post-event field surveys and InSAR analysis. Applied Sciences, 11(7), p.3281.

Meyer, B. et al., 1996. The 1995 Grevena (Northern Greece) earthquake: fault model constrained with tectonic observations and SAR interferometry, Geophys. Res. Lett., 23, 2677–2680.

Meyer, B., Armijo, R., Massonnet, D., de Chabalier, J.B., Delacourt, C., Ruegg, J.C., Achache, J. & Papanastassiou, D., 1998. Comment on 'Geodetic investigation of the 13 May Kozani-Grevena (Greece) earthquake' by Clarke et al., Geophys. Res. Lett., 25, 129–l30.

Michetti, A.L.E.S.S.A.N.D.R.O., Audemard, F., Azuma, T., Clague, J., Comerci, V., Esposito, E., Guerrieri, L., Grpinar, A., McCalpin, J., Mohammadioun, B. and Mrner, N.A., 2007. Environmental Seismic Intensity Scale 2007-ESI 2007.

Papadimitriou, P., Tselentis, G.A., Voulgaris, N., Kouskouna, V., Lagios, E., Kassaras, I., Kaviris, G., Pavlou, K., Sakkas, V., Moumoulidou, A. and Karakonstantis, A., 2017. Preliminary report on the Lesvos 12 June 2017 Mw= 6.3 earthquake. Euro-Med Seismological Centre (EMSC).

Papanikolaou, I. and Melaki, M., 2017. The Environmental Seismic Intensity Scale (ESI 2007) in Greece, addition of new events and its relationship with magnitude in Greece and the Mediterranean; preliminary attenuation relationships. Quaternary International, 451, pp.37-55.

Pavlides, S.B., Mountrakis, D.M., Chatzipetros, A.A., Zouros, N.C., Kostopoulos, D.S., 1995. The Grevena - Kozani (May 13, 1995) earthquake, western Macedonia, Greece: seismogenic faulting in an "aseismic" area. Department of Geology and Physical Geography, Aristotle University of Thessaloniki, GR-54006, Thessaloniki, Greece.

Sakkas, V., 2021. Ground deformation modelling of the 2020 Mw6. 9 Samos earthquake (Greece) based on InSAR and GNSS data. Remote Sensing, 13(9), p.1665.

17th INTERNATIONAL CONGRESS of the Geological Society of Greece

BULLETIN OF THE GEOLOGICAL SOCIETY OF GREECE, SP. PUBL.

EXTENDED ABSTRACT 239

Expertise on Specifications – Evaluation Criteria and Design of a Special Label for Local Agrotourism Products and Services: a cooperation for the benefit of four Greek UNESCO Global Geoparks!

Papadopoulou P.[1], Fassoulas, Ch.[2], Iliopoulos, G.[1,3], Kitsaki, G.[4], Kolendrianou, M.[2], Mikroulea, E.[5], Papaioannou, Ch.[4], Pattakos, D.[6], Perakis, V.[7], Tsoni, M.[3], Tsimpri, I.[8]

(1)Laboratory of Palaeontology and Stratigraphy, Geology Department, University of Patras, Patras, Greece, penelpapadop@upatras.gr (2) Psiloritis UNESCO Global Geopark, Anogia, Greece (3) Management Unit of Chelmos - Vouraikos National Park and Protected Areas of Northern Peloponnese, Natural Environment and Climate Change Organization, Chelmos Vouraikos UNESCO Global Geopark, Kalavryta, Greece (4) Epirus Developmental S.A., Vikos-Aoos UNESCO Global Geopark, Ioannina, Greece (5) Lassithi Developmental S.A., Agios Nikolaos, Lasithi, Greece (6) Psiloritis Developmental S.A., Anogia, Greece (7) Sitia UNESCO Global Geopark, Sitia, Greece (8) Achaia S.A., Kalavryta, Greece

Introduction

The purpose of this work is to study the specifications required for developing or improving a quality label for products and services offered by businesses in the regions of the four collaborating geoparks (Vikos-Aoos UNESCO Global Geopark, Sitia UNESCO Global Geopark, Chelmos Vouraikos UNESCO Global Geopark, Psiloritis UNESCO Global Geopark).

The project involves the design of a special label for local agrotourism products and services in the cooperating areas, based on global market quality standards and UNESCO principles for Global Geoparks. Additionally, it includes the design of the specifications and evaluation criteria for the products and services of each region, which will carry this special label, in alignment with UNESCO's principles for Global Geoparks.

This expertise is conducted within the framework of the Interterritorial Cooperation Plan entitled "EMPOWERMENT, PROMOTION, AND NETWORKING OF UNESCO GEOPARKS" and, more specifically, as part of the project "Expertise on Specifications – Evaluation Criteria and Design of a Special Label for Local Agrotourism Products and Services."



Fig.1: Presentation of the project partners

The Interterritorial Cooperation Plan is implemented under the local CLLD/LEADER program, Submeasure 19.3 of Measure 19 of the Rural Development Program (RDP) 2014–2020, by the coordinating Local Action Group (LAG) ACHAIA S.A. – DEVELOPMENTAL ANONYMOUS COMPANY OF LOCAL AUTHORITIES, in collaboration with the following participating partners: EPIRUS DEVELOPMENTAL S.A. – Developmental Organization of Local Authorities, LASSITHI DEVELOPMENTAL S.A. – Developmental Organization of Local Authorities, AKOMM – PSILORITIS DEVELOPMENTAL S.A. – Developmental Organization of Local Authorities (Fig.1).

Methodology

The design of the quality label and the proposals for improving the existing ones (Psiloritis and Sitia UGGps) were based on several aspects:

- Study of Criteria and Application of 1st Generation Quality Labels: Examination of standards like AGRO (Hellenic Agricultural Organization–DIMITRA) and the EU's Eco-Label for environmental certification of products and services.

- Study of 2nd Generation Quality Labels: Investigation on labels such as the certification for the Samaria National Park, the "CRETE" quality label, local cultural support agreements like the Epirus Ancient Theaters Cultural Route, the PINDOS quality pact (no longer in effect), and the Special Quality Label for Greek Cuisine (E.S.P.E.K.).
- Study of Quality Labels for Geoparks: Analysis of existing labels from participating geoparks (Sitia and Psiloritis) and international geopark labels such as "Naturtejo Geopark Geoproduct," "Qualità parco" from Adamello Brenta Geopark, and "Naturally Tasty" from Beigua Geopark.
- Study of GEOfood Label Standards: Inspection of the guidelines and specifications of the GEOfood label.
- Review of Literature including research on the history and philosophy of quality label development, as well as other public surveys (e.g. Ilbery and Kneafsey, 1998; Henchion and McIntyre, 2000; Eckardt, 2007; Marques, 2007; Carpenter and Larceneux, 2008; Lorenzini, 2011; Ramos and Garrido, 2014; Košičiarová Kajima et al., 2016; 2017; Hutagalung et al., 2024 and other).
- Discussions with Project Partners and Geopark Representatives Five online meetings were held, including one kickoff meeting and four individual meetings with each partner. These meetings focused on expectations and challenges regarding quality label use.
- Online meeting with Lassithi Developmental S.A., Sitia Geopark, and Local Businesses: Local businesses shared their experiences, challenges, benefits, and suggestions for improving the label's operation. A survey conducted by the Psiloritis Geopark also provided insights from businesses using its quality label.
- Contractor's experience and discussions with local businesses and geopark representatives
- Designing of a customized questionnaire (Google Forms) aiming on a) obtaining general information about the participating businesses, information about the promotion methods and sustainable practices they use and information about their level of knowledge about geoparks and quality labels in general and b) in assessing the intentions of geoparks that do not implement certification as well as to evaluate the experiences of already certified businesses. The questionnaire was distributed to relevant businesses in all four areas and the results were analysed and validated.

An analysis of the needs of the co-operating partners was also conducted.

Results

The research resulted in proposals regarding the improvement of the already existing quality labels and the drafting of a regulation which sets out the conditions that must be followed by beneficiaries who wish to use this quality mark. The aim of granting this quality mark is to certify the suitability of the product-service to represent the geopark area as a genuine expression of its identity.

Additional objectives for applying the quality mark to products and businesses are:

- To certify the locality of the product-service
- To create added value to the product-service by providing or enriching the identity of the region and leveraging participation in the UNESCO Global Geoparks Network
- To connect the products-services with the geodiversity elements of the geopark area
- To provide differentiation to the products-services in relation to similar products by leveraging the uniqueness of the region and the experiences provided
- To enhance the credibility of the product/service
- To promote local products-services at a national and international level
- To strengthen relationships between producers, entrepreneurs and other interested parties
- To ultimately strengthen the local economy either directly or indirectly.
- To enhance the feeling of "belonging" in the collaborating businesses

The quality mark is aimed at businesses related to agro tourism, agriculture and rural tourism.

Eligibility criteria

The eligibility criteria are divided into general criteria, specific criteria and proportional coverage criteria. The general criteria are applied in their entirety to all enterprises and regard the legality, locality and mode of operation of the enterprise. The specific criteria are applied per type of enterprise (catering and accommodation businesses, manufacturing businesses -inside or outside the geopark area-, tourist-ecotourism offices, use of organic products etc.). The proportional coverage criteria constitute a set of criteria, the application of which can substantially contribute to the achievement of the objectives of the certification but are more specialized and difficult to apply practices (e.g. ISO or other certifications, minimizing the consumption of natural resources and waste in at least one way etc). For this reason, it is not recommended to cover all of these criteria, but it is required to cover at least 5 of them.

The coverage of the required criteria is confirmed by the presentation of the corresponding supporting documents.

Code of conduct

The "identity" of a region is not shaped solely by measurable characteristics, and for this reason, granting the current certification requires, in addition to meeting specific criteria by the interested businesses, a commitment to a set of **ethical rules**. This involves a collection of principles and rules that the parties involved must fully adopt as a way of life. These cannot function as criteria because their evaluation by individuals is inherently subjective. The signing of a **Code of Conduct** is proposed as a way to operate with integrity and commit to common values.

The proposed quality label regulation also determines obligations of both the participating businesses and geoparks, as well as of the certification process (application, evaluation, inspections and audit, issuance and monitoring) and proposes actions in order to maximize the impact of the quality label.

Discussion and Conclusions

The establishment of a quality label for geopark products and services represents a significant step towards promoting sustainable development and the responsible management of natural and cultural resources. Through this initiative, the high quality of offered products and services is ensured, while simultaneously the visibility of geoparks as exemplary areas that integrate tourism, education, and environmental protection os enhanced.

The implementation of the quality label can make a crucial contribution to the economic development of local communities by offering incentives for innovation while protecting and showcasing the unique natural wealth of geoparks. Strict adherence to the criteria established for the quality label will guarantee its reliability and strengthen the trust of visitors and consumers.

Finally, collaboration among various stakeholders—such as local communities, producers, management bodies, and educational institutions—serves as the foundation for the successful implementation and continuous improvement of the quality label. This will enhance the sustainability and uniqueness of geoparks in the long term.

References

Carpenter, M., Larceneux, F., 2008. Label equity and the effectiveness of values-based labels: an experiment with two French Protected Geographic Indication labels. International Journal of Consumer Studies, 32(5), pp.499-507.

Eckardt, C., 2007. Creating economic benefit by regional and international networking in the Global and European Geopark Bergstrasse-Odenwald, Germany. Abstracts of 7th European Geopark Network Open Conference, NW Highlands Geopark 10,

Henchion, M., McIntyre, B., 2000. Regional Imagery and Quality Products: the Irish Experience. British Food Journal, 102(8), 630-644,

Hutagalung, P.M., Nasution, Z., Ginting, N., 2024. The role of geological relationship and brand of geoproduct on regional development in Samosir Island of Geopark Caldera Toba with mediating method. GeoJournal of Tourism & Geosites, 52(1),

Ilbery, B., Kneafsey, M., 1998. Promoting Quality Products and Services in the Lagging Rural Regions of the European Union. European Urban and Regional Studies, 5(4), 329-341.

Kajima, S., Tanaka, Y., Uchiyama, Y., 2017. Japanese sake and tea as place-based products: a comparison of regional certifications of globally important agricultural heritage systems, geopark, biosphere reserves, and geographical indication at product level certification. Journal of Ethnic Foods, 4(2), 80-87.

Košičiarová, I., Nagyová, Ľ., Holienčinová, M., Rybanská, J., 2016. Quality Label as the Guarantee of Higher Quality of Food–A Case Study of Slovak Food Market. Procedia-Social and Behavioral Sciences, 220, pp.200-209.

Lorenzini, E., 2011. Territory branding as a strategy for rural development: experiences from Italy.

Marques, R. T., 2007. Sustainable tourism and certification in Geopark Naturtejo: A case study. Paper presented at 7th European Geopark Network Open Conference, HighLands Geopark, NW.

Ramos, E., Garrido, D., 2014. Towards a" 2nd Generation" of Quality Labels: a Proposal for the Evaluation of Territorial Quality Marks. Cuadernos de desarrollo rural, 11(74), pp.101-123.

17th INTERNATIONAL CONGRESS of the Geological Society of Greece

BULLETIN OF THE GEOLOGICAL SOCIETY OF GREECE, SP. PUBL.

EXTENDED ABSTRACT 240

West Akrocheiras section: a pilot multi-proxy palaeoenvironmental analysis

Papadopoulou P.[1], Iliopoulos, G[1], Bendle, J.[2], Christanis, K.[1], Kalaitzidis, S.[1], Liapi, E.[3], Perleros, K.[1], Soulakelis, N.[3], Tzortzi, M.[1], Zouros, N.[3,4]

(1) Department of Geology, University of Patras, Patras, Greece, penelpapadop@upatras.gr (2) School of Geography, Earth and Environmental Sciences, University of Birmingham, Birmingham, UK (3) Department of Geography, University of the Aegean, Mytilene, Greece (4) Natural History Museum of the Lesvos Petrified Forest, Sigri, Greece

Introduction / Background

The Lesvos Petrified Forest is a geological heritage site of global significance, featuring silicified tree trunks, fossil leaves and volcanic deposits dated back to the lower Miocene. Initially brought to scientific attention in 1844, it gained broader recognition in late 19th and early 20th centuries, with pivotal research in the 1990s elucidating its formation processes (e.g. Velitzelos & Zouros, 1997). Designated as one of the first European Geoparks in 2000, and Global Geopark in 2004, the Lesvos Petrified Forest is the main geological heritage area of international significance for the recognition of Lesvos island as an UNESCO Global Geopark in 2015 (https://www.lesvosmuseum.gr/en/node). Recognized as one of the first 100 IUGS geological heritage sites in 2022, the Lesvos Petrified Forest is a hub for research, education, and sustainable tourism.

Recent construction works of the Kalloni-Sigri road brought to the light new fossiliferous localities hosting thousands of fossils including fossilized trees and leaves (Zouros et al., 2022). The road cuts at the new fossiliferous sites enable detailed stratigraphic analysis of the Sigri pyroclastic rocks and a reevaluation of the area's stratigraphy and palaeoenvironmental evolution. This study focuses on the analysis of West Akroheiras section (39.230107°, 25.905465°, 320 m section length, Fig. 1) following a pilot multi-proxy approach and aiming to establish the most effective methods for palaeoenvironmental reconstruction of the Lesvos Petrified Forest monument.

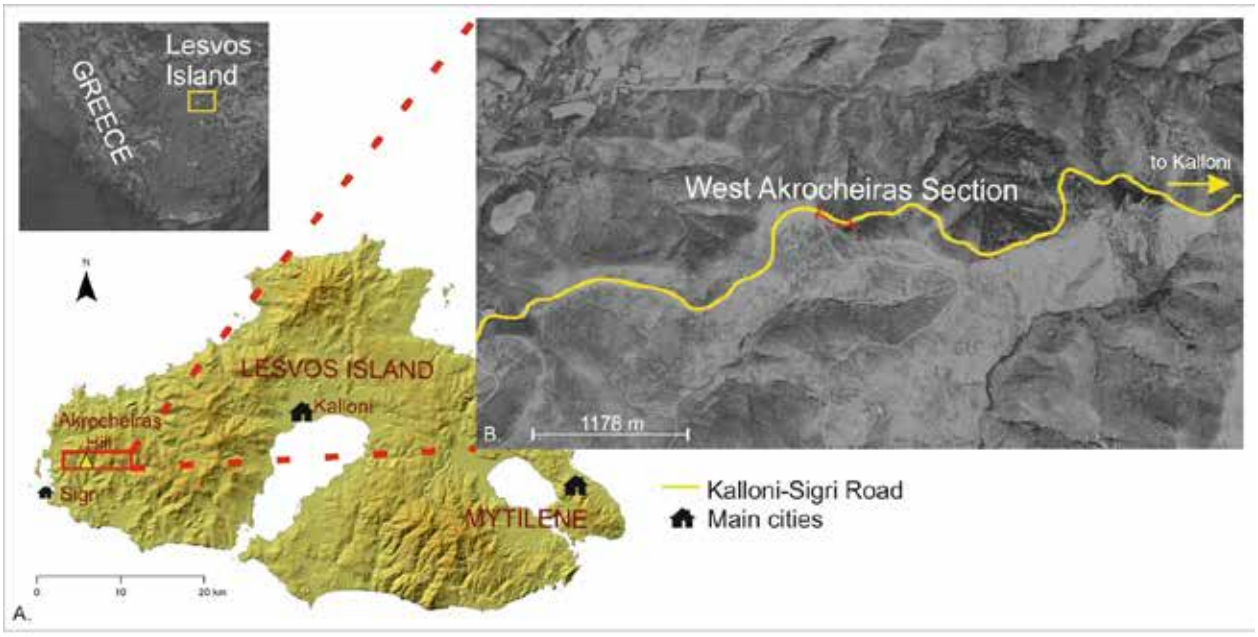


Fig. 1: A. DEM image of Lesvos Island. Main cities and main points of interest are noted. The study area is noted with the red rectangle. B. Satellite image of the study area, where the studied section (red line) is noted.

Geological setting

The volcanic rocks of Lesvos have been extensively studied and mapped, with notable contributions from researchers such as Hecht (1972, 1974a,b), Pe-Piper (1978, 1980) and Pe-Piper et al. (2019), who established the stratigraphic framework and identified key volcanic structures. These formations lie at the top of Permian schists (Katsikatsos et

al., 1982) and marbles, and include the Sigri Pyroclastic Formation, which features pyroclastic and volcaniclastic deposits rich in silicified tree trunks and fossilized leaves (Velitzelos & Zouros, 1997, Zouros, 2021). The Sigri pyroclastics derived from an early Miocene stratovolcano chain (Hecht, 1972; 1974a, b; Pe□Piper, 1980), dating between 21.5 and 18.4 Ma ago (Pe-Piper et al., 2019), with stratigraphic divisions inferred from adjacent geological formations. The volcanic chain follows a NNE-SSW orientation influenced by the dextral strike-slip tectonic regime of the Aegean-Anatolian microplate (Yilmaz et al., 2000). Over geological time, this regime evolved, giving rise to various fault systems, including dextral, sinistral and normal faults during Neogene and Quaternary times. These findings highlight the complex tectonic and volcanic history of the island, contributing to a deeper understanding of its geological evolution.

Material and Methods

Stratigraphic logging was performed in several places of the studied section as the lateral continuity of the layers was interrupted by faults, in addition to the many lateral changes in the nature of the pyroclastic material. The lithological characterisation of the pyroclastic rocks followed Fisher & Schmincke (1984) and Francis & Oppenheimer (2003). The most prominent fallen or standing tree trunks and fossil leaf horizons were noted along with basic sedimentological characteristics. Taphonomic observations of the fossil leaves were made in situ. Bed by bed sampling was also conducted.

Generalised stratigraphic cross sections containing the most important features (characteristic horizons, major faults etc.) were compiled and photos were taken. The sections were digitised later on (using CorelDRAW Graphics Suite), and the respective stratigraphic columns were drawn (using Strater 5 software) (Figs 2 and 3) and correlated. Moreover, very high-resolution Images acquired through Unmanned Aerial Vehicles were used to generate: i. a 2D orthophotomap and ii. 3D textured model, both used for digital stratigraphic measurements (e.g. layer thickness).

A number of rock samples were picked up for selected pilot analysis methods (XRD, organic petrography, micropalaeontologic analyses, and organic geochemistry, as well as systematics and taphonomy of fossil leaves). Powder XRD analysis was conducted on three palaeosoil samples (B6, B13, B23; Fig. 2) in the Department of Geology, University of Patras. Organic petrographical analysis was conducted on five samples (B3, B6 and B12; Fig. 2) also at the Department of Geology, University of Patras. Micropalaeontological analysis for aquatic organism remains (e.g. ostracods, diatoms) was conducted in fifteen samples (A1, A2, A3, A4, A5, B1, B2, B9, B10, B12, B13, D1, D2, Fig. 2) (Department of Geology, University of Patras). Samples B1, B6, B9, B12, B13, B19, B20 and D1 (Fig. 2) were subjected to organic geochemistry analysis at the Birmingham University. The systematic classification of the fossil leaves was based on their macro-morphological characteristics and was performed at the Natural History Museum of the Lesvos Petrified Forest.

Results

West Akrocheiras section consists mainly of coarse tuffs, lapilli tuffs and less of tuff breccia layers intercalated with palaeosoil horizons, with a total thickness of 22 m (Figs 2 and 3, columns C8.1-C8.13). Volcaniclastic layers are also included. Several strike slip faults exist with vertical displacements < 2 m, uplifting the western parts of the section. After correlating the stratigraphic data from the combined study of several sections along the Akrocheiras Hill roadcuts, seven palaeosoil horizons have been recorded in this section (Figs. 2 and 3, PS8.1-PS8.7), separating it in eight units (Units 8.1-8.8, Figs 2 and 3).

Standing fossil trunks were recorded in three palaeosoil horizons (Figs. 2 and 4 - PS8.3, Fig. 3 - PS8.5 and PS8.6). Fossil leaves were recorded in great numbers in many horizons throughout this section (units U8.1, U8.3 and U8.4), both as leaf litter between different layers and also oriented in different directions, mixed with the pyroclastic materials. The lower part of the section (units U8.1-U8.4) exhibits intense volcaniclastic characteristics (conglomerate lenses mostly at the western part).

Unit U8.2 possibly represents deposition of volcaniclastic material in a water body, as implied by the massive unconsolidated pyroclastic coarse ash layer with thickness around 1 m (column C8.1, Fig. 2). In this unit transported coal were found (column C8.2). Unit U8.4 bears a series of pyroclastic flows with leaf litter in at least five horizons (columns C8.2 and C8.3).

XRD analysis in the soil samples revealed that they consist mostly of crystalline intermediate feldspars and clay minerals or/and zeolites. Amorphous inorganic or/and organic material is also included.

Maceral analysis of sample B3 (unit 8.2) obtained from the 1-m-thick coarse pyroclastic ash layer at the bottom of the sequence, proved containing partially charred biomass derived from fresh and/or slightly peatified organic matter, probably of arboreal origin. Several organic fragments display a gelified texture and are heat-affected, as the relatively high mean random vitrinite reflectance values (0.47-2.0%) and the cracks indicate. These partially or totally-

carbonised peaty, and woody fragments may be air-borne transported from the surroundings and deposited there. Sample B6 (unit 8.2) represents a thin black layer, which contains charred particles (semifusinite and degradofusinite) with plasticized edges and displays a mean reflectance of 0.85%. In the same strata, charred particles with thin cell walls (pyrofusinite) are also common, with reflectance values ranging up to 1.4%. Interestingly, several particles display a pre-charring gelification, whereas the in-situ growth of the precursor plants is evident by the included charred corpohuminite particles. Sample B12 (unit 8.3) is characterized as a carbonaceous or sapropelic coaly layer (i.e. elevated liptinite content), with limited thermal affection and VR of 0.5%; the mode of deposition seems to be in a short-lasted water-logged limnic/limnotelmatic environment; an epigenetic thermal influence is evident only by some cracks.

All the samples that were micropalaeontologically examined, were barren. This implies either a non-aquatic environment, unfavorable life conditions (e.g. anoxic) or/and unfavorable preservation conditions (e.g. low pH values).

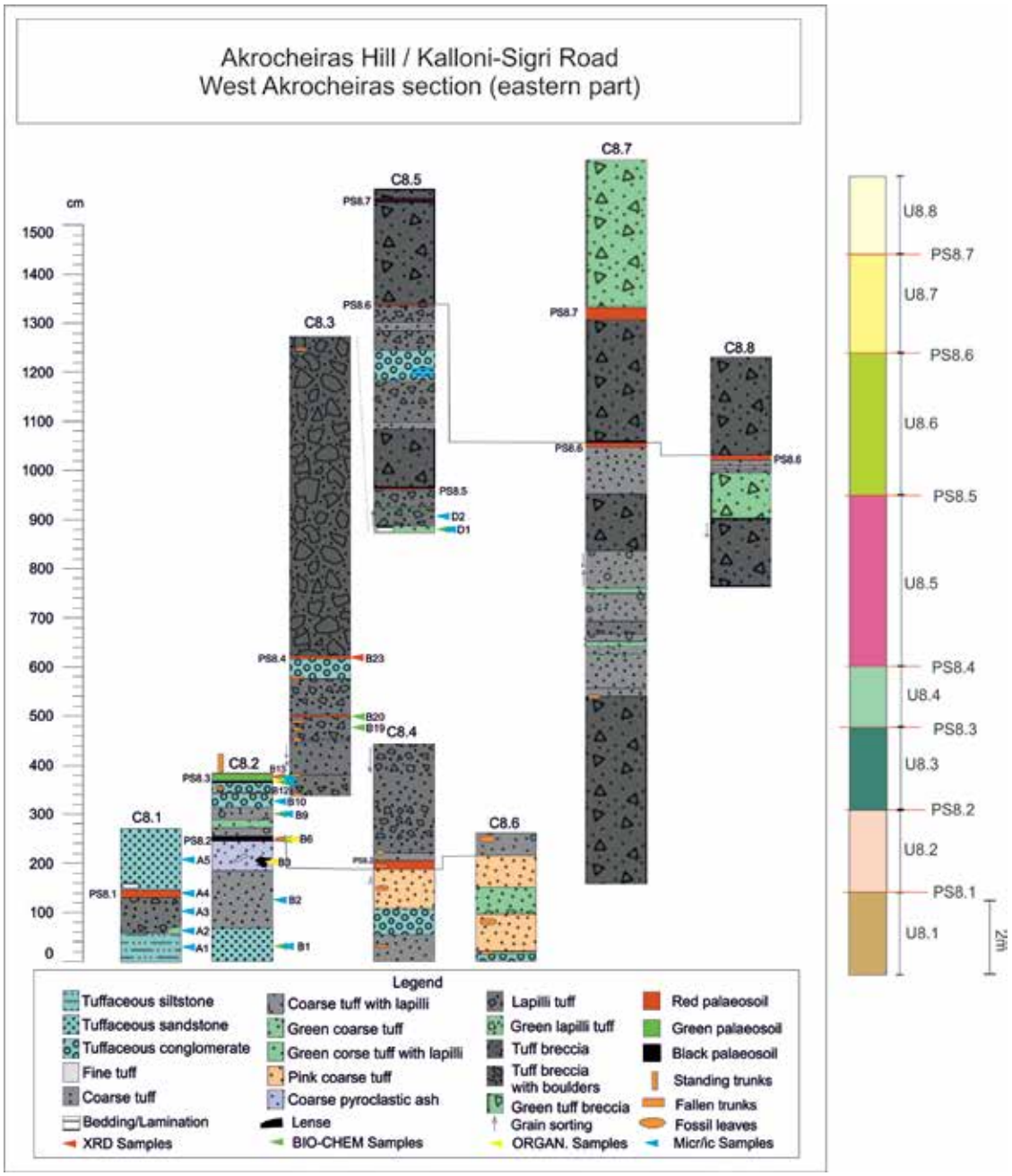


Fig. 2: Stratigraphic columns presenting the logged sequences from the eastern part of West Akrocheiras section. On the right, the units are schematically presented.

Pilot biomarker analyses of the eight samples revealed that the majority of them have plant wax n-alkanes in with only one showing an absence of these compounds. Some samples show some signs of thermal/diagenetic impact (B1), but overall the samples show high potential for organic geochemical work, including sufficient concentrations for compound specific isotope analyses. Some samples appear exquisitely well preserved, comparable with extract leaf matter of modern or very recent age (Holocene). Alkane response varies from 0-91% (samples D1 and B1/B20, respectively). Total Lipid content (TLE) varies from 0.6 mg (sample B19) to 5.8 mg (sample B9). No correlation was found between TLE and the abundance of n-alkanes in the samples. Sample B20 shows a very distinctive pattern where alkanes are persistent but a cluster of broad peaks is observed around C26-C29 alkane response time.
To date, the systematic taxonomy of the fossil leaves has revealed more than 55 plant taxa from West Akrocheiras. The palaeoflora consist of bryophytes, ferns and several angiosperms (including herbaceous and woody monocots, dicots). Among the identified plant taxa, *Daphnogene polymorpha* (A. Braun) Ettingshausen, *Laurophyllum* sp., *Phoenicites* sp., *Rosa* sp., *Nerium* sp., *Myrtophyllum* sp., *Pungiphyllum cruciatum* (A.Braun) Frankenhäuser & V.Wilde and members of Fagaceae family are abundant floristic elements.

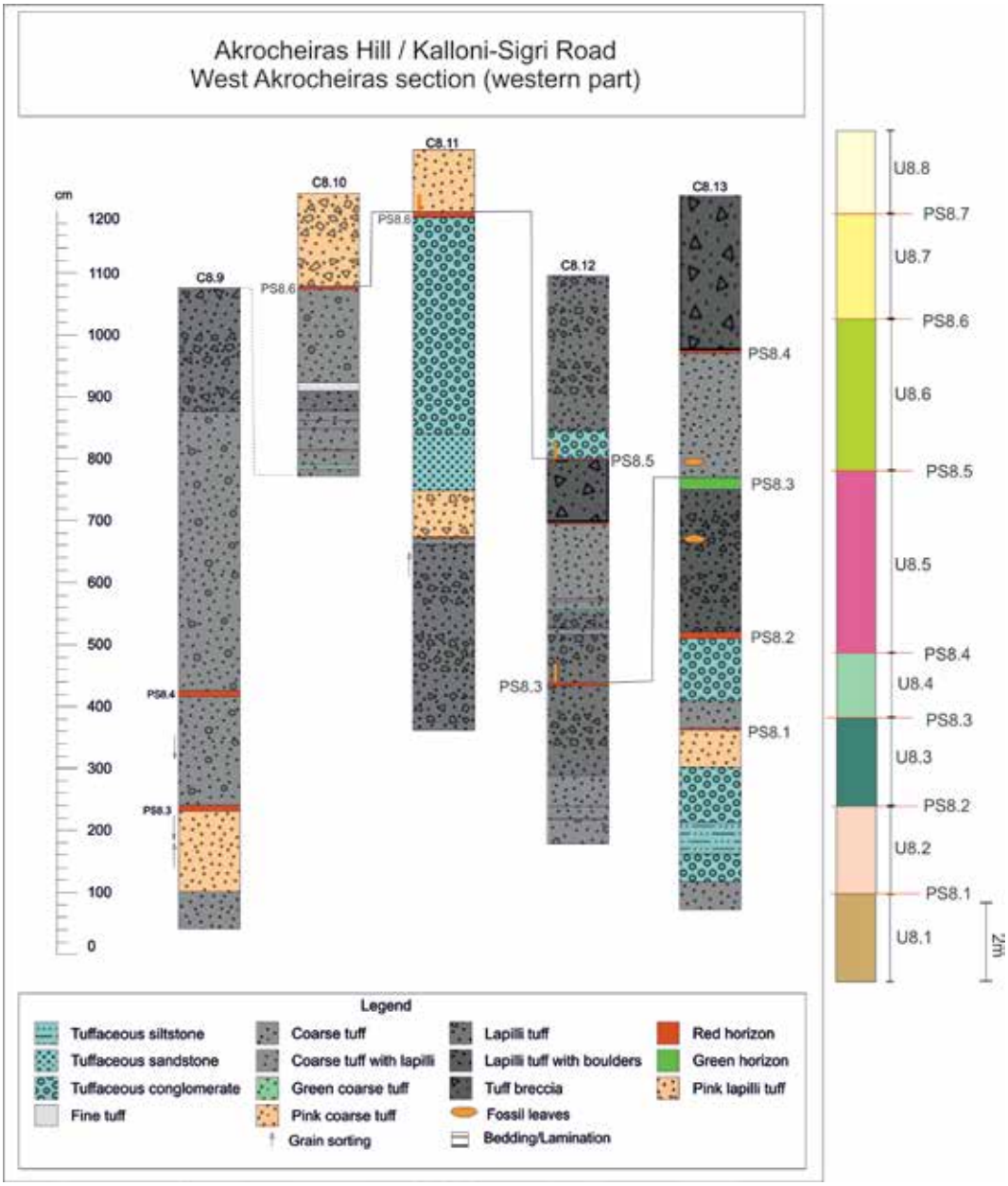


Fig. 3: Stratigraphic columns presenting the logged sequences from the western part of West Akrocheiras section. On the right the units are schematically presented.

Discussion

Palaeosoil horizons were examined in order to distinguish the different eruption phases. In West Acroheiras section at least 8 different eruption phases have been recognized corresponding to units U8.1- U8.8 (Figs 2 and 3).

The pilot studies on the palaeoenvironmental evolution of West Acroheiras section gave encouraging results. The lithology of some layers of the lower part (units 8.1 and 8.2) provides evidence of a water body (layer of samples B1-B2), nevertheless, the micropalaeontological analysis gave no results implying unfavorable life or preservation conditions. The organic geochemical analysis of sample B1 revealed high content of thermally matured organic matter, possibly rapidly deposited under anoxic conditions. Thus, if there was a water body there, then a hot pyroclastic flow must have entered it. This is in agreement with the results of the organic petrography analysis for sample B3, which reveals organic matter charred in various degrees, representing roots and arboreal plants, possibly deriving from a nearby peat-forming environment. The combined analysis of sample B6 from palaeosoil horizon PS8.2 (which marks the end of unit 8.2) reveals a palaeoenvironment with high organic matter content, partially affected by thermal alteration and buried rapidly under anoxic conditions. The very good preservation conditions of alkanes can be also attributed to clay minerals as was shown by the XRD analysis of the same sample.

Unit 8.3 shows volcaniclastic lithological characteristics. The fossil leaves scattered in the layer, reveal the deposition of transported material. Both organic petrography and organic geochemistry analyses of palaeosoil horizon PS8.3 show preservation of organic material (samples B12/B23). The palaeoenvironment is characterized as water-logged with limited thermal affection. On this palaeosoil horizon a remarkable fossilized standing tree trunk has been preserved (possibly a giant *Sequoia* tree, typically thriving on soils with good moisture retention). It is worth mentioning that the layers of units 1-3 show limited lateral continuity.



Fig. 4: Fossil giant *Sequoia* trunk standing on palaeosoil horizon PS8.3 in West Akrocheiras section.

Unit 8.4 bears a lot of fossiliferous layers. Fossilized leaf litter (fossil leaves laid on fine-grained horizons) were found at various levels along with transported fossilized leaves and trunks scattered in the pyroclastic material. Organic geochemical analysis of sample B19, deriving from a lapilli tuff layer with scattered fossilized leaves and trunks, gave low values of alkane response and TLE relatively to samples from palaeosoil horizons such as sample B20 but still includes organic remains. According to Retallack (1984), the preservation of leaves and wood in non-calcareous environments is only possible in water-logged environments with $0<Eh<200$ mV and pH 2-5. Thus, the pyroclastic flow that generated this specific layer contained a sufficient amount of acidic water for the preservation of fossilized plant material and thus the depositional environment was anoxic. Sample B20, from a small palaeosoil horizon, gave evidence for a dry climate and a terrestrial environment (where waxy coatings on plants were more prominent) possibly consisted of vascular plants, trees, shrubs and herbaceous elements.

The systematic taxonomy of fossil leaves indicates a rich flora dominating different habitats such as riparian and mesophytic forests in the lowlands and adjacent surroundings. Several plant taxa including ferns, diverse palms (e.g, *Phoenicites* sp.), *Daphnogene polymorpha* suggest proximity to a water source, while others such as *Laurophyllum* sp., *Nerium* sp. and Fagaceae spp. are indicative of well-drained soils.

Units 8.5 to 8.8 present more thick and coarse-grained, organic matter-lean layers.

Conclusions

- The stratigraphic analysis of West Akroheiras section allowed the identification of at least eight different eruption phases recorded in the layers of this section (units 8.1-8.8). Based on standing fossil trunks at

least three forests had developed on some of the palaeosoil horizons of this section. Detailed stratigraphic analysis of the volcaniclastic sequence serves as a basis for the synthesis of the results from all methods and for palaeoenvironmental reconstruction.

- The taxonomy of the fossil leaves so far has revealed a mosaic of habitats such as riparian and mesophytic forests occurring in the broader area. The high alkane response and/or TLE implies decomposition and chemical transformation of organic matter (plants, algae or/and microrganisms) and favourable conditions for organic matter preservation (e.g. anoxic conditions, rapid burial and presence of clay minerals).
- The preservation of leaves and wood in non-calcareous environments is only possible in water-logged environments with 0<Eh<200 mV and pH 2-5 (acidic environments). Thus, evidence for the physicochemical conditions of the water-saturated layers is provided.
- Organic petrography on palaeosoil horizons gave evidence for water-logged environments amongst others.

The diverse methods revealed that there is a great potential in clarifying the Miocene palaeoclimatic and palaeoenvironmental conditions of the Lesvos Petrified Forest and this potential is multiplied when these methods are applied in combination. In the future more systematic and detailed analyses are needed in order to fully unravel the history of the area, its palaeoclimatic and palaeoenvironmental evolution.

Acknowledgements
We would like to sincerely thank Ass. Prof. Lambropoulou Paraskevi for the XRD analysis.

References

Fischer, R., Schmincke, H.U., 1984. Pyroclastic Rocks, Springer-Verlag Berlin Heidelberg.
Francis, P., Oppenheimer, C., 2003. Volcanoes. Oxford University Press.
Hecht, J.,1972: Geological map Plomari-Mytilene sheet. 1:50000. IGME, Athens.
Hecht, J., 1974a: Geological map Mithimna sheet. 1:50000. IGME, Athens
Hecht, J., 1974b: Geological map Polychnitos sheet. 1:50000. IGME, Athens.
Katsikatsos, G., Mataragas, D., Migiros, G., Triandafillou, E., 1982. Geological study of Lesbos island, Special Report, IGME, Athens.
Pe-Piper, G., 1978. The Cenozoic volcanic rocks of Lesbos (Greece), unpublished readership thesis, University of Patras.
Pe- Piper, G., 1980. The Cenozoic Volcanic Sequence of Lesvos, Greece. Z. dt. geol. Ges., 131, 889- 901.
Pe-Piper, G., Piper, J.W.D., Zouros, N., Anastasakis, G., 2019. Age, stratigraphy, sedimentology and tectonic setting of the Sigri Pyroclastic Formation and its fossil forests, Early Miocene, Lesbos, Greece. Basin Research 2019, DOI: 10.1111/bre.12365.
Retallack, G., 1984. Completeness of the rock and fossil record: some estimates using fossil soils. Paleobiology, 10(1), pp.59-78.
Velitzelos, E., Zouros, N., 1997. The petrified forest of Lesvos–Protected natural monument. Proc. Internat. Sympos. On Engineering Geology and the Environment, Athens, 3037-304.
Yılmaz, Y., Genç, Ş. C., Gürer, F., Bozcu, M., Yılmaz, K., Karacik, Z., … Elmas, A., 2000. When did the western Anatolian grabens begin to develop? Geological Society, London, Special Publication, 173, 353–384. https://doi.org/10.1144/GSL.SP.2000.173.01.17.
Zouros, N.C., 2021. The Miocene petrified forest of Lesvos, Greece: Research and geoconservation activities. Geoconservation Research. 4(2), 635–649.
Zouros,N., Soulakellis,N.,Valiakos,I., Bentana,K., Theodorou,E., Zgournios,E., Antonakis,E. and Lamprakopoulos,A.: Enhancement and promotion of the new fossiliferous sites along the new Kalloni Sigri road.-An example of good practice in geoconservation in Lesvos Isl. UNESCO Global Geopark Greece. Bulletin of Geological Society of Greece Sp. Publ. 10, pp. 849-850.

17th INTERNATIONAL CONGRESS of the Geological Society of Greece

BULLETIN OF THE GEOLOGICAL SOCIETY OF GREECE, SP. PUBL.

EXTENDED ABSTRACT 241

Comparing broadband and strong-motion data using collocated sensors in the HP network, Greece

Papageorgiou A.[1,2], Ktenidou O.-J.[1], Pikoulis E.-V.[1], Sokos E.[2]

[1] *National Observatory of Athens, Greece*

[2] *University of Patras, Greece*

Introduction and motivation

High-quality seismic data is of great importance in a wide range of seismological applications and studies, whether focusing on the source, path or site effect. Errors related to the sensors (calibration, orientation, or installation issues) or erroneous metadata may produce unreliable data that do not reflect true ground motion, either in all or in part of the frequency range of interest. We select stations of the Hellenic Unified Seismic Network (HUSN), and in particular the two networks that possess a significant number of co-located broadband and strong-motion sensors, namely HL (National Observatory of Athens; DOI:10.7914/SN/HL) with 24 co-located stations, and HP (University of Patras, DOI:10.7914/SN/HP) with 11 co-located stations. Our aim is to scrutinize their data over their frequency band during all periods of joint operation, in order to understand to what extent, the data from the two sensors agree and investigate potential discrepancies. In the abstract at hand, we focus on the HP network (Figure 1. black diamonds represent the collocated stations of HP network).



Figure 1. Map of collocated stations in Greece. HP stations appear as black diamonds.

Methodology

To perform a detailed analysis, we developed a targeted in-house code for data processing. We compiled a dataset of more than 1000 recordings from a total of 11 collocated sensors for the time period 2012-2023. Our records are of events with magnitudes M4 or larger, out to distances depending on magnitude. Our starting point was the NGA-West2 and NGA-East processing protocols by PEER, UC Berkeley (Kishida et al 2016) and the recent automated processes of Cauzzi et al. (2022). After inspecting the raw waveforms and identifying clipped data, we manually process them in the time and frequency domain, considering both horizontal components per event.

First, in the time domain we: perform visual inspection and detect issues such as lags (Figure 2. left) or amplitude discrepancies (Figure 2. right) in the time domain, manually pick P and S arrivals to select signal and noise windows, calculate peak-to-peak ratios (Figure 2. bottom) and inspect them with time. After that, in the frequency domain we perform visual inspection of S-wave and noise FAS (Fourier Amplitude Spectrum) of acceleration, examine the usable bandwidths, and calculate FAS ratios (Figure 3.).

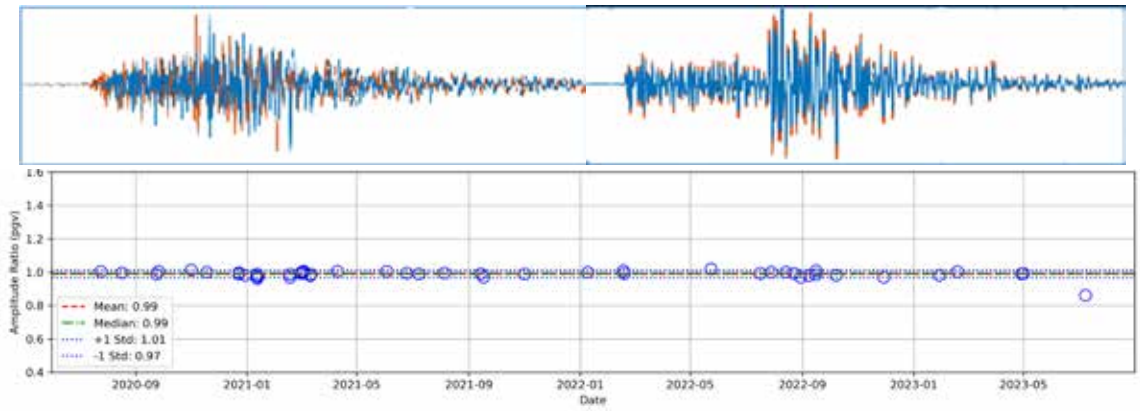


Figure 2. Top: Comparison of waveforms and problem detection in time (left) and amplitude (right). Bottom: peak amplitude ratio for a single component with time: no discrepancy observed.

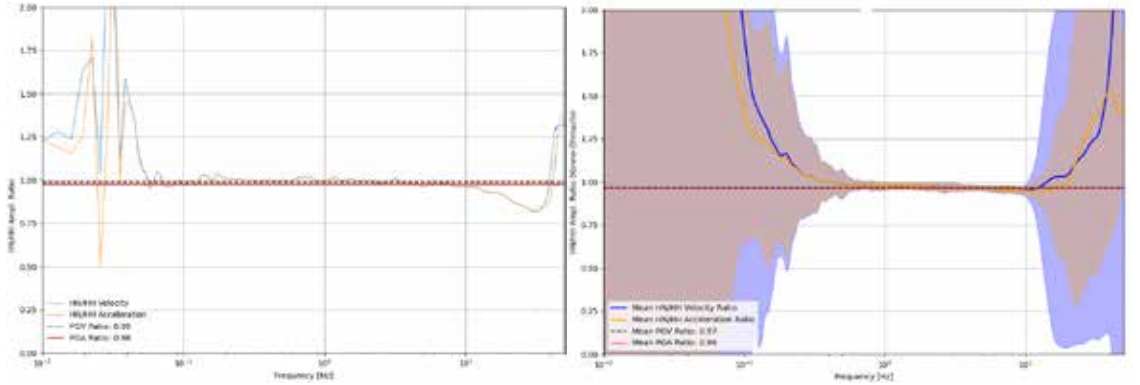


Figure 3. FAS ratios (SM/BB) for a single event (left) and average ratios for a station (right).

Results and conclusions

In this work we attempted a careful visual inspection of data from the collocated stations of the HP network in both the time and frequency domain, with the aim of compiling parameters that describe and assess data usability. By examining the observed discrepancies, we identify and amend certain underlying errors in sensor response. We compare the usable frequency between channels, per station, and assess data reliability and usability in the frequency domain. We calculate peak amplitude ratios for the 2 sensors per component and investigate if this deviates from unity, either persistently or sporadically. We identified GPS problems (time lags), component errors (amplitude discrepancies due to hardware), and metadata issues. Issues detected are fed back to the operator, so these findings contribute to network health monitoring and highlight potential for system improvement. Studies such as this one can help underline the potential impact that amplitude or time issues may have on several methods, including event location, tomographic studies, source analysis (moment tensor, slip inversion, etc.), as well as strong-motion applications, shakemaps, and dynamic analyses of structures.

References

Cauzzi C., Bindi D., Buscetti M., Cambaz D., Carrilho F., Custodio S., Clinton J., Felicetta C., Evangelidis Ch., Kalafat D. and Gallovic F. (2022). Comparison of Velocity and Acceleration Earthquake Records as a Quality Assessment Tool for European Co-Located Seismic Stations. 3rd European Conference on Earthquake Engineering & Seismology, Bucharest, Romania, 2022.

Kishida T., Ktenidou O-J., Darragh R.B. and Silva W.J. (2016). Semi- Automated Procedure for Windowing Time Series and Computing Fourier Amplitude Spectra for the NGA-West2 Database. PEER Report, Pacific Earthquake Engineering Research Center, UC Berkeley

17th INTERNATIONAL CONGRESS
of the Geological Society of Greece

BULLETIN OF THE GEOLOGICAL SOCIETY OF GREECE, SP. PUBL.

EXTENDED ABSTRACT 242

Groundwater changes and induced seismicity influencing surface deformation in post-mining landscapes

Papageorgiou E.[1], Foumelis M.[1], Dominique P.[2], Bonatis P.[1], Raucoules D.[2], De Michele M.[2], Papadimitriou E.[1]

(1) Aristotle University of Thessaloniki, Thessaloniki, Greece, elenpapageo@geo.auth.gr (2) French Geological Survey (BRGM), Orléans, France

Introduction

In this study, we employed advanced interferometric time series analysis to explore the relationship between water level variability, seismicity, and induced surface motion over the Gardanne coalfield (Figure 1), while also accounting for potential long-term contributions. A spatio-temporal investigation of surface motion measurements was therefore conducted using data from the Copernicus Sentinel-1 mission, ultimately aiming to attribute the observed motion to a deformation mechanism.

The Gardanne coalfield, located in southern France between Marseille and Aix-en-Provence, was mined from the 17th century until 2003. Different techniques were employed along the basin with the deepest exploitation reaching up to 1300 m depth to the west of the basin (Dominique *et al*., 2022). The gradual progression of the mine workings to the west of the basin was affected by groundwater flow and pumping was considered essential to lower the water level and allow access to deeper levels. After mining ceased in 2003, the ending of pumping led to the flooding of the mine, with groundwater levels stabilizing around 2010. Since then, water level is relatively stable by pumping, with annual fluctuations of about twenty meters (Dominique, 2016).

With the gradual rise of the underground water level microseismicity was felt by the population in 2010 and a strong seismic swarm occurred in November 2012. Since then, swarming seismic activity lasting a few days has been re-appearing periodically in the same area, especially in November 2012, December 2014, November 2016 - March 2017 and August 2017. Prior analysis of seismic data revealed apparent connection of seismic activity with seasonal changes of underground water level in the mine, as well as with pumping rates (Dominique, 2016). Further analysis showed that swarming activity is related to the reactivation of minor fault segments being favorably oriented with respect to the local tectonic stress field (Dominique *et al*., 2022). However, no impact on the surface has been observed in post mining period that would indicate collapses of underground mining works (Namjesnik *et al*. 2022).

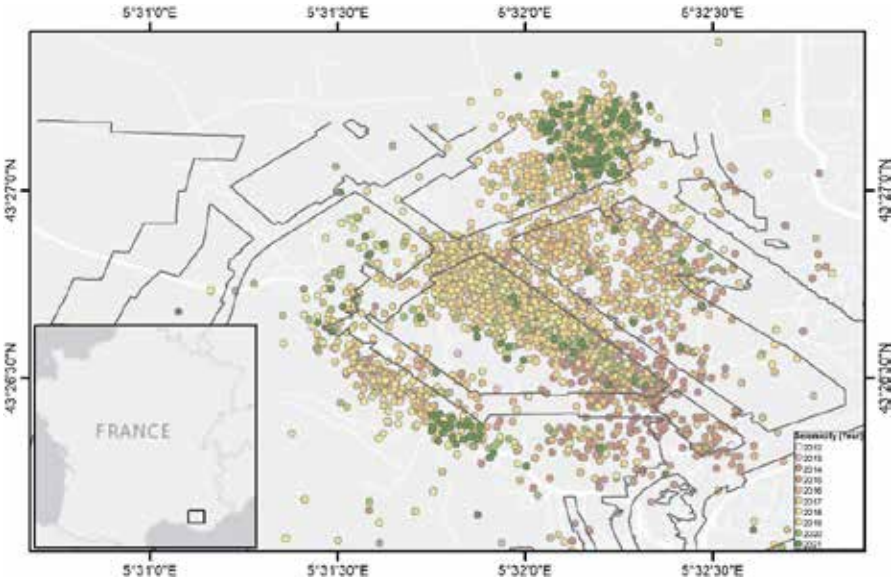


Figure 1. Gardanne coal mine area with observed seismicity (Ineris, BRGM). In the background the coal mine workings are depicted with black lines.

Methods / Results

Post-mining surface deformation detected from multi-temporal interferometric processing for the period from April 2015 to December 2022 via the SNAPPING service (Foumelis *et al*., 2022) revealed deformation patterns spatially correlated with the epicentral area of the 2016-2017 Gardanne micro-seismic activity (Figure 2). The temporal evolution of surface motion shows a signal attributed to induced seismicity, evidenced by a clear change in the displacement time series during this specific period.

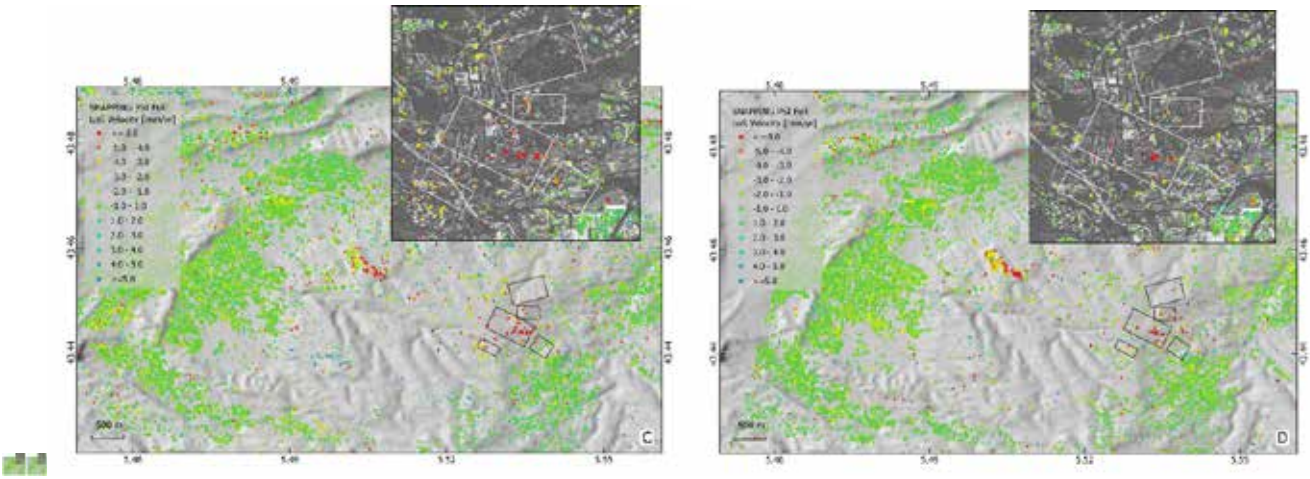


Figure 2. Surface motion rate along the LoS considering the period 2015-2022 and SNAPPING PSI processing schemes for ascending (a) and descending (b) satellite tracks. The rectangles outline the clusters of seismicity.

Geometric decomposition of the ascending and descending LoS measurements confirms the above observation, showing prevailing vertical motion with a negligible E-W component. This is also consistent with the focal mechanisms of major recorded events, which indicate normal faulting, typical of post-mining sites.

To investigate the relationship between seismicity locations and observed surface motion, we performed spatial clustering of micro-seismicity using the k-means algorithm. This process resulted in 5 distinct clusters (Figure 2), which accounted for ~80% of the total number of events in the catalogue within the epicentral area. It is apparent that seismic activity increased after each pumping phase, with a notable correlation between the magnitude of water table lowering and the frequency of seismic events. The consecutive drops in the water table during 2015 and 2016 contributed to the largest seismic swarm of late 2016 - early 2017, also coincided with the largest surface motion signal. An overall consistency was observed between the timing of micro-seismic events and the occurrence of surface displacements across the various seismic clusters.

Although the interpretation of the measurements until early 2017 is straightforward, it becomes more complex when examining the seismic activity and related surface motion for the August 2017 swarm. This signal seems to extend well beyond the main epicentral region, representing a seasonal subsidence component observed in the inter-annual displacement time series from 2015 to 2022. This seasonal signal might mask the maximum motion, potentially impacting the assessment of deformation caused by post-mining seismic activity during this period.

Conclusions

Our findings suggest that the observed surface motion is likely a result of energy released by both seismicity and aseismic motion caused by fluctuations of the mine's water table. The onset and variability of surface motion may also be controlled by the heterogeneity of the mine workings, such as differences in the gallery dimensions and the lithological composition of the overlying lithology.

Acknowledgements

This work is a contribution to the Research Fund for Coal and Steel (RFCS 2019) by the European Commission -Directorate - General for Research and Innovation under the Grant agreement (899192) – PostMinQuake and to Research Fund for Coal and Steel (RFCS 2023) by the European Commission -Directorate - General for Research and Innovation under the Grant agreement (101157400) - SIRIMA

References

Dominique, P., 2016. Microseismicity in a mining context-The Gardanne coal basin (Bouches-du-Rhône), 1280–1287. JNGG_ Nancy_2016_miscrosismicite_Gard.pdf Accessed 2025–01–25 [in French]

Dominique, P., Aochi, H., Morel, J., 2022. Triggered seismicity in a flooded former coal mining Basin (Gardanne Area France). Mine Water Environ 41(2):1–18.

Foumelis, M., Delgado Blasco, J.M., Brito, F., Pacini, F., Papageorgiou, E., Pishehvar, P., Bally, P., 2022. SNAPPING Services on the Geohazards Exploitation Platform for Copernicus Sentinel-1 Surface Motion Mapping. Remote Sens., 14, 6075. https://doi.org/10.3390/rs14236075.

Namjesnik, D., Kinscher, J., Contrucci, I., Klein, E., 2022. Impact of past mining on public safety: seismicity in area of flooded abandoned coal Gardanne mine, France. Int J Coal Sci Technol 9, 90. https://doi.org/10.1007/s40789-022-00558-1.

17th INTERNATIONAL CONGRESS of the Geological Society of Greece

BULLETIN OF THE GEOLOGICAL SOCIETY OF GREECE, SP. PUBL.

EXTENDED ABSTRACT 243

Hydrochemical characterization of multi-layer porous aquifer of Larissos system, Peloponnese

Papailiopoulou Maria., Apostolopoulou P., Stavropoulou V., Pouliaris C., Kazakis N. and Zagana E.
(1) University of Patras, Faculty of Natural Sciences, Department of Geology, Greece; m.papailiopoulou@ac.upatras.gr; up1065363@ac.upatras.gr; vstavropoulou@ac.upatras.gr; christospouliaris@gmail.com; nkazakis@upatras.gr; zagana@upatras.gr
**Correspondence: m.papailiopoulou@ac.upatras.gr*

Introduction

The groundwater system of Larissos has poor chemical status due to human activities in the area. Due to the high-water needs of the population, aquifers have been underused for many years and have degraded the quality and quantity of groundwater. As a result, aquifers have been in a state of over pumping for decades, which has led to a reduction in the water table, which has reached negative absolute altitudes, and to the occurrence of seawater intrusion, particularly in the northern and north-eastern part of the region. In addition, the aquifers are also affected by the agricultural activity taking place in the study area, resulting in locally elevated nitrate (NO_3^-) values. Through sampling and chemical analyses carried out in the laboratory, these phenomena of seawater intrusion and increased nitrate values are observed and are shown in the graphs. Chemical analyses were carried out for the determination of major cations (Ca^{2+}, Mg^{2+}, Na^+ and K^+ and major anions (HCO_3^-, SO_4^{-2}, Cl^-, NO_3^-, NO_2^-, NH^{4+} and PO_4^{2-}). In the Laboratory of Hydrogeology of the Department of Geology at the University of Patras, all analyses were carried out in accordance with the suggested procedures and standards. The Na^+, K^+, Ca^{2+}, Mg^{2+} were measured using a Perkin Elmer atom absorption spectrometer. The HCO_3^- were determined by indicator H_2SO_4 titration. The other main anions were measured by a Hach® DR 4000 spectrophotometer.

Study Area

The study area is located in northwestern Peloponnese, and specifically in the prefecture of Achaia, and occupies an area of approximately 163 km^2. The main river in the study area is the Larissos river. The main riverbed of Larissos is 19,5 km long, originating from mountain Movri and emptying into the Prokopou lagoon. It is one of the most important sources of surface runoff in the area and collects water from various streams along its course. In addition, the river also receives overflows and excess water from the irrigation ditch from the Pinios river. The Larissos groundwater system is mainly developed in deposits dating back to the Neogene and Quaternary periods.

According to data from the “River basin management plan”, the groundwater system of Larissos is estimated to have an average annual supply of approximately $26 \cdot 10^6$ m^3/y and the total annual water withdrawal is $33 \cdot 10^6$ m^3/y. These quantities are used to fill the supply needs of irrigation and water supply. Furthermore, the hydraulic characteristics of the system, such as hydraulic conductivity and storage coefficient, also have been calculated and equal $3{,}5 \cdot 10^{-5}$m/sec και 5-8% respectively.

Geology

The Larissos groundwater system is structured by rock formations of the tectonostratigraphic zone of Ionian and is mostly covered by sediments dating back to Neogene and Quaternary periods. In particular, the Ionian zone includes limestones of Upper Jurassic to Palaeocene age and Eocene flysch. The postalpine sediments include sands, screes, recent cones of scree, eluvial formations, terrestrial and torrential deposits and alluvial deposits dating from Quaternary period and friable sandstones, sandy clays and yellowish to grey clayey marls from the Neogene (Figure 1). Geomorphologically, the study area is divided into flat zone (79,23%), semi-mountainous zone (13,42%), hilly zones (4,95%) and lagoons (2,40%). It is observed that the transition from flat to the hilly and mountainous zones is gentle and smooth (Stavropoulos, X., 1992).

Hydrogeology

In the study area there are two types of aquifers, the first is found in carbonate rocks and the second in sediments that are dating in Neogene and Quaternary periods (Stavropoulos, X., 1992). The hydropermeability of geological formations depends on the porosity, the size, the shape and the distribution of the grains. The geological formations of the area are classified into three categories based on their hydro-lithological behavior. The first category concerns hydropermeable formations which allow water to penetrate and circulate and include formations of the Holocene age such as scree, recent cones of scree and alluvial deposits. The second category includes semi-hydropermeable formations which have low permeability and can store and allow water to flow but at a low rate. These include formations dating from the Pleistocene and contain pebbles, sandstones, clays and clay marls. The third category includes impermeable formations, such as flysch, which do not allow the flow of water.

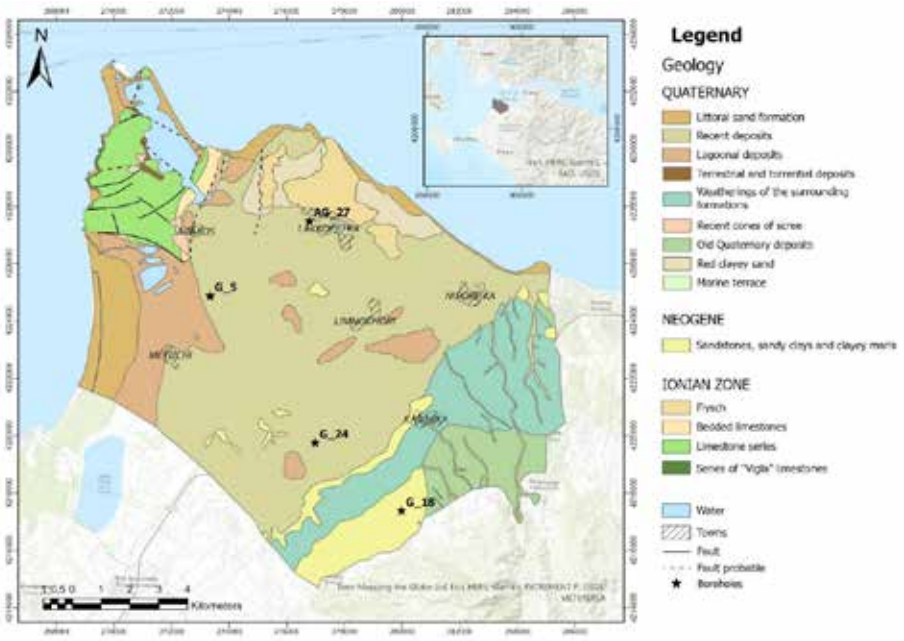


Figure 1. Geological map of study area (modified from I.G.M.E., 1977-1980)

Results and Discussion

Characteristics of groundwater hydrochemistry

Table 1 indicates the physicochemical characteristics of water samples. Especially, the electrical conductivity depends on the temperature and the amount of dissolved salts in the water. When high values of electrical conductivity occur then there is likely to be water pollution (Kazakis N., 2013). It is observed by Figure 2 that in boreholes G_24, G_5 and G_18 the values of electrical conductivity range from 630 μS/cm to 1600 μS/cm, while in borehole AG_27 the values are very high and exceed 2000 μS/cm. The pH expresses the concentration of hydroxide cations (H3O+) in an aqueous solution. The solution is neutral when pH = 7, acidic when pH < 7 and alkaline when pH > 7. It is observed that in boreholes G_24, G_5 and G_18 the pH values increase with depth and the water solution can be classified from acidic to alkaline, while in borehole AG_27 there is a decrease in pH values. The Oxidation Reduction Potential (ORP) gives information about the oxidation state of the elements in an aqueous solution. The water is called reductive when the values are negative and oxidative when it shows positive values (Mandhlaras, D., 2005). It is observed that borehole G_24 shows negative values, borehole G_5 has both positive and negative values and boreholes G_18 and AG_27 have positive values. Dissolved Oxygen (DO) provides informations on the exposure of groundwater to atmospheric air. When the values are zero or very low then the water is old and non-renewable. It is observed that all boreholes have low values ranging from 1.5 mg/l to 5.8 mg/l. The total dissolved solids are a parameter that related to electrical conductivity and depends on the type of rock through which the water and its flow velocity. For values of TDS<1000 mg/l the water is classified as fresh (Davis – DeWiest, 1966). It is observed that in boreholes G_24, G_5 and G_18 the values of TDS range from 270 to 575 mg/l, while in borehole AG_27 the values reach 857 mg/l. The increase in calcium ions is associated with the initial stages of salinization where cations are exchanged as Ca^{+2} is released and Na^{+}, Mg^{+} and K^{+} are absorbed from seawater (Walraevens et al. 1993). It is observed that all boreholes show high values and in borehole AG_27 the values reach 310 mg/l. Sodium ions are associated with the infiltration of seawater and its mixing with fresh water. The concentration of Na^{+} increases with the continuous pumping of aquifers. It is observed that boreholes G_24 and G_18 have values ranging between 20 mg/l and 32 mg/l, while boreholes G_5 and AG_27 have higher values up to 134 mg/l (Figure 3). Cloride ions are associated with seawater infiltration and their high value indicates high pumping conditions. It is observed that in boreholes G_5 and AG_27 the values are >100 mg/l and in boreholes G_24 and G_18 they range between 40 mg/l and 51 mg/l (Figure 4). Nitrate ions in groundwater are associated with agricultural activities that cause contamination of the aquifer (Figure 5). It is observed that all boreholes have high nitrate values while boreholes G_18 and AG_27 have the highest. The Revelle factor is a parameter for the identification of salinization. For seawater it takes values >150 and for good water the index has values <1 (Kalergis, G., 2000). It is observed that the water of boreholes G_24, G_18 and AG_27 is good while the water of borehole G_5 is slightly contaminated.

	Sampling date	Sampling depths (m)	EC (μS/cm)	T (°C)	pH	ORP	DO (mg/l)	TDS (mg/l)	Ca^{+2} (mg/l)	Mg^{+2} (mg/l)	Na^{+} (mg/l)	K^{+} (mg/l)	HCO_3^{-} (mg/l)	SO_4^{-2} (mg/l)	Cl^{-} (mg/l)	NO_3^{-} (mg/l)	NO_2^{-} (mg/l)	NH_4^{+} (mg/l)	PO_4^{-3} (mg/l)	F^{-} (mg/l)
G_24	14/11/2024	46	840	19.1	7.08	-155.9	1.58	457	86	13.90	30	3.7	298.9	0	44.3	51.2	0		0	0
		49	831	19.1	6.86	-142.3	2.38	312	84.8	15.61	24	3.6	381.86	0	42.4	49.3	0.028		0.11	0
		52	641	19.1	7.25	-162	2.28	314	72	13.66	20	3.9	336.72	1	41.7	48.8	0		0.12	0.11
G_5	14/11/2024	30	697	20	7.39	-38.4	3.38	294	58.4	17.56	58	3.3	145.18	6	98.8	48.6	0.021	0.742	0.15	0.24
		45	697	19.9	7.48	-8.4	3.1	269	56	16.58	54	3.2	186.66	5	97.7	47.8	0	0.911	0.15	0.31
		60	700	19.9	7.61	9.5	3.2	272	58.8	14.39	58	3.2	197.64	4	102	48.4	0.003	0.574	0.14	0.28
		75	1512	19.9	7.47	98.4	3.94	569	94	41.22	108	7.4	185.44	21	339	48.3	0.054	1.72	0.16	0.42
		90	1505	19.9	7.49	174.2	3.54	575	90.4	48.05	112	8.4	219.6	19	351	49	0.062	1.867	0.09	0.38
		105	1467	20	7.5	16.5	2.92	567	91.6	47.56	116	8.4	176.9	19	352	16.8	0.002	1.914	0.05	0.47
G_18	14/11/2024	40	1034	18.9	7.4	102.8	4.36	396	159.2	3.17	30	0.6	392.84	81.3	49.4	83.4	0.017	0.032	0.44	0
		50	1038	18.8	7.43	161.1	5.36	394	130.4	14.15	30	0.6	363.56	82.8	50.9	184.4	0.021	0.13	0	0.05
		60	1042	18.7	7.43	158.3	4.39	407	131.2	13.66	32	0.6	372.1	84.7	50.8	127	0.03	0.042	0.11	0.07
AG_27	14/11/2024	20.7	2010	19.7	7.04	243.2	4.83	839	310.4	10.73	126	1.5	397.72	500	156	108	0.026	0.047	0.09	0.51
		21.9	2018	22.4	7.02	221.6	5.78	857	282.4	22.93	134	1.5	384.3	540	162	96.4	0.033	1.23	0.04	0.71

Table 1. Physicochemical characteristics of water samples

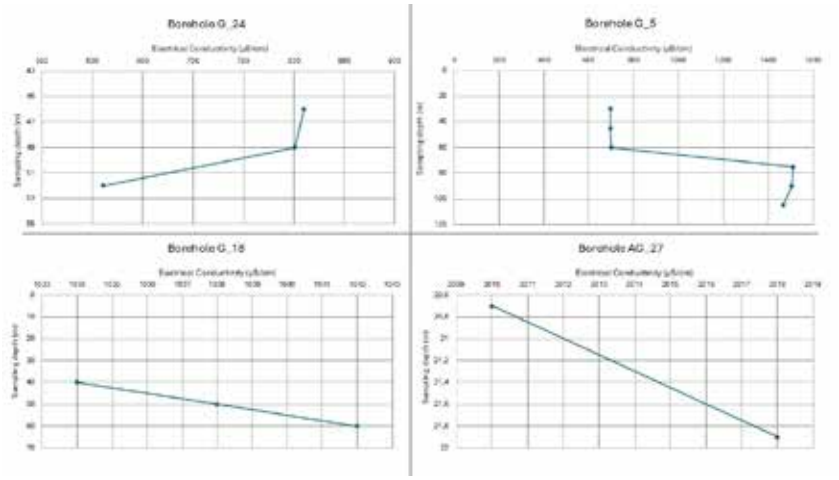


Figure 2. Profiling of EC (μS/cm) in the four boreholes of study area

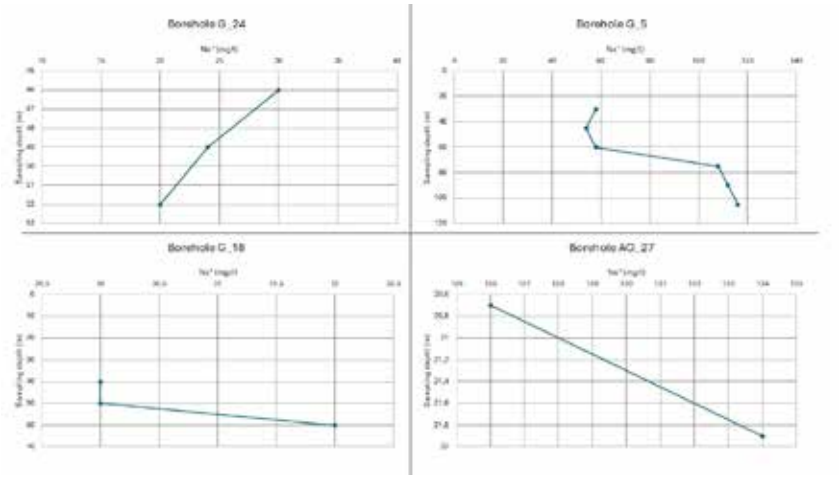


Figure 3. Profiling of Na^{+} in the four boreholes of study area

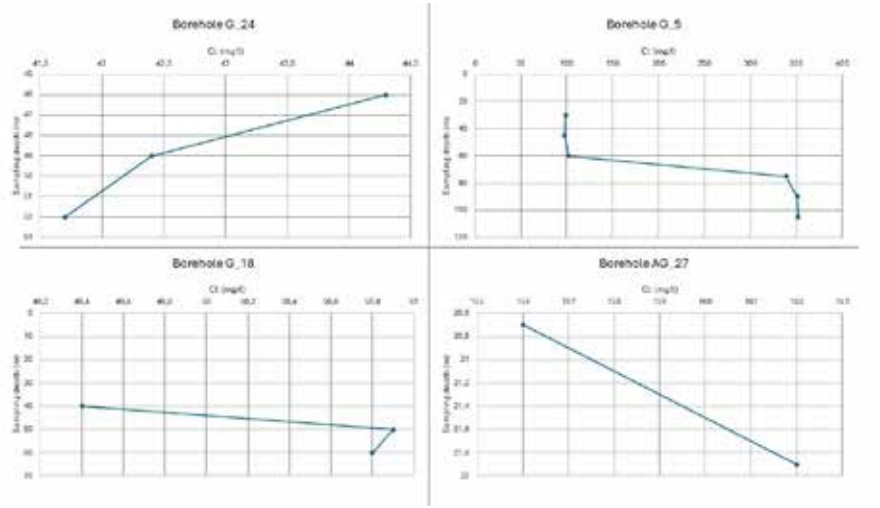


Figure 4. Profiling of Cl^- in the four boreholes of study area

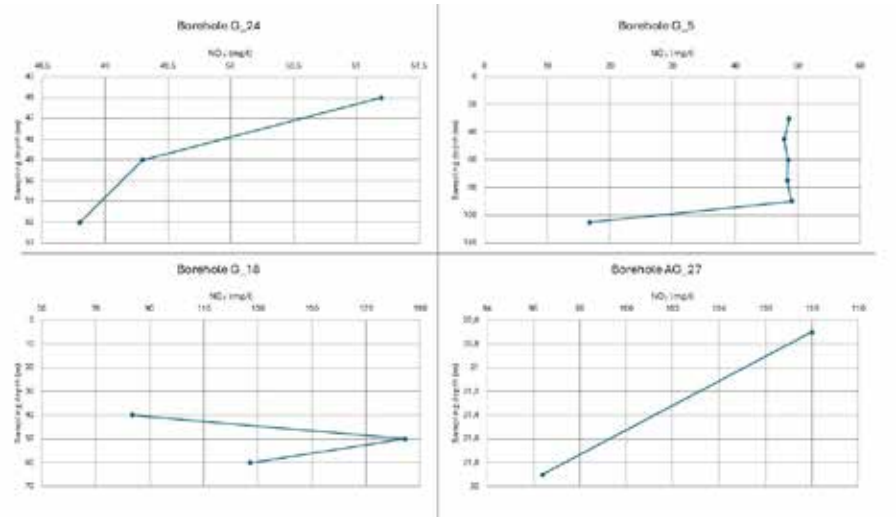


Figure 5. Profiling of NO_3^- in the four boreholes of study area

Study of hydrochemical facies

With respect to the main cations and anions in solution, it was determined that the hydrochemical facies changed from the low salinity Ca^{2+}-HCO_3^- type to the Na^+-Cl^- type as salinity increased (Mahlknecht et al., 2017). Typically, samples with higher salinity have been identified close to the coast or in areas that had been severely affected by the hydraulic gradient inversion, while samples with lower salinity were found further from the coast (Tamez-Meléndez et al., 2016). The Piper diagram at Figure 6 (a) shows the two main water chemical types of Ca-HCO_3 and Ca-Mg-Cl. Also, the samples from boreholes G_18 and three samples from G_5 is mainly dominated by type Ca-Mg-HCO_3 or types of Mg-Ca-HCO_3. The samples from boreholes AG_27 and the other samples from G5 appear to be enriched in Cl. According to the results figure 6 (b) shows the Schoeller Berkaloff diagram. This diagram shows the groundwater samples in different depths of mains cations and anions respectively. Moreover, in the Schoeller diagram the water samples show high concentrations of Ca, Na, Cl, and NO_3 in relation to low concentrations of SO_4 and Mg. For borehole G_24 the diagram shows that with increasing depth the concentrations of the elements decrease. Also, in borehole G_5 the lines of the samples in depths 30, 45 and 60 m appear almost parallel. In addition, in relation to the next three sampling depths 75, 90 and 105 m the samples are enriched in all elements. Regarding borehole G_18, the concentrations of the elements are low at the depth of 40 m compared to the next two depths, and specifically the NO_3 at the depth of 50 m are increased compared to the depth of 60 m. In addition, all major ions except nitrate increase with increasing depth.

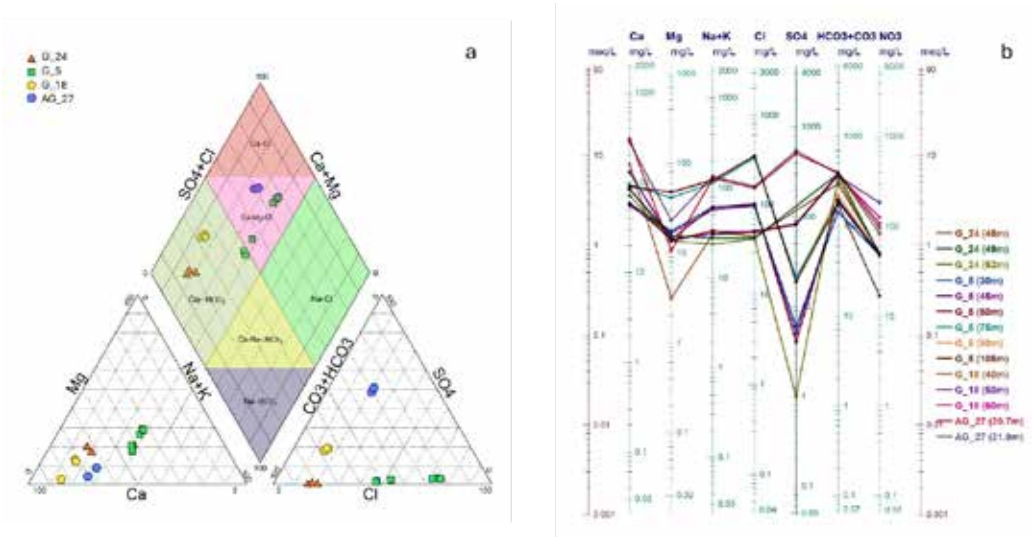


Figure 6. (a) Piper diagram showing the water type; (b) Schoeller Berkaloff diagram

Conclusions

The samples were collected from different depths and analyzed for physicochemical parameters, major cations, and anions. The interpretation was carried out using Piper and Schoeller–Berkaloff diagrams. During the cation exchange phenomena with seawater intrusion, the hydrochemical facies of groundwater evolves from Ca–HCO_3 to Na–Cl. Ion exchange is one of the fundamental geochemical processes occurring during the salinization of groundwater. The seawater intrusion leads to an increase in Na^+, Mg^{2+}, and SO_4^{2-} concentrations due to ion exchange. The geochemical processes controlling groundwater chemistry in the research area include ion exchange, carbonate production, mineral precipitation, and seawater intrusion (Salem and Osman, 2017). Moreover, the dissolution of gypsum in coastal aquifers containing gypsum beds results in more complex water–rock interactions when freshwater mixes with saline fluids or seawater (Campana and Fidelibus, 2015). Two groups of groundwater were identified on the Larissos groundwater system of Ca-HCO_3 and Ca-Mg-Cl according to Piper diagram. As the above results show that the borehole AG_27 faces the most serious problem regarding seawater intrusion. The borehole AG_27 exhibited high electrical conductivity values, with elevated concentrations of Na^+, Cl^-, and SO_4^{2-}, indicating possible influence from seawater intrusion or interaction with evaporate formations. In contrast, borehole G_5 showed dominance of Ca^{2+} and HCO_3^-, classifying it as a Ca–HCO_3 type, particularly at lower depths. At greater depths, however, an evolution toward a mixed Ca–Mg–Cl type was observed. The gradual increase in ion concentrations with depth in borehole G_5 can be attributed to the fact that deeper groundwater has a longer residence time within the aquifer and comes into contact with rock formations richer in soluble components, leading to ion enrichment in the water. The sudden decrease in electrical conductivity was created at lower depths in G_24. Borehole G_24 exhibits stable physicochemical parameters, with minor variations among the samples collected at depths of 46, 49, and 52 meters. The major ions show consistent concentrations, with a dominance of Ca^{2+} and HCO_3^-, classifying the water as Ca–HCO_3 type. The concentrations of Na^+, Cl^-, and SO_4^{2-} are low, with no indication of seawater intrusion. Moreover, in all boreholes, the concentration of NO_3 decreases with respect to the depth, except for the borehole G_18, where at the intermediate depth their concentration is increased. In addition, the concentration of Cl increases in relation to the depth of the borehole, and in particular the boreholes which are located near to the coast have high concentrations of Cl. Consequently, the borehole sample logging helps to find out the interactions of freshwater and saltwater in coastal areas. This strategy is expected to support a much wider range of coastal aquifer research. The study highlighted the importance of vertical sampling and multiparametric analysis in understanding the qualitative evolution of aquifers and identifying zones of contamination or salinization. The results contribute to the management of groundwater resources in areas with complex geological and hydrogeological conditions.

Acknowledgments

The present work was financially supported by the «Andreas Mentzelopoulos Foundation»

References

Campana, C., Fidelibus, M.D., 2015. Reactive-transport modelling of gypsum dissolution in a coastal karst aquifer in Puglia, southern Italy. Hydrogeol J 23, 1381–1398. https://doi.org/10.1007/s10040-015-1290-x.

Davis, S.N., DeWiest, R.J.M., 1966 : Hydrogeology . 2nd edition, Wiley, New York, pp.463.

I.G.M.E., 1978 - 1980. Geological Map of Greece, Scale 1:50.000. Nea Manolas and Patrai, Sheets.

Kalergis, G., 2000. Applied – Environmental Hydrogeology. 2nd edition, volume B, Techical Chamber of Greece, Athens.

Kazakis, N., 2013. Assessment of the risk of external groundwater pollution: Application to the Anthemounta river basin. PhD Dissertation, Department of Geology, Aristotle University of Thessaloniki, Greece.

Mandhlaras, D., 2005. Environmental – hydrogeological research in the Glafkos basin. University of Patras, Department of Geology, Division of Applied Geology and Geophysics, Laboratory of Hydrogeology – Technical Geology.

Salem, Z.E.-S., Osman, O.M., 2017. Use of major ions to evaluate the hydrogeochemistry of groundwater influenced by reclamation and seawater intrusion, West Nile Delta, Egypt. Environ Sci Pollut Res 24, 3675–3704. https://doi.org/10.1007/s11356-016-8056-4.

Specific Secretariat for Water, 2013. River Basin Management Plan. Management Plan for the River Basins of North Peloponnese River Basin District.

Stavropoulos, X., 1992. Hydrogeological conditions of a wide area of Kato Achaia – Manolados (NW Peloponnese). PhD Dissertation, Department of Mining and Metallurgical Engineering, National Technical University of Athens.

Warlaevens, K., Lebbe, L., Ceukelaire, M.D., Houtte, E.V., Greuck, W.D., (1993): Influence on groundwater quality of the Paleozoic Brabant Massif in Belgium due to overexploitation. Groundwater Quality Management (Proceedings of the GQM 93 Conference held at Tallinn, September 1993). IAHS Publ. no. 220, 1994.

17th INTERNATIONAL CONGRESS of the Geological Society of Greece

BULLETIN OF THE GEOLOGICAL SOCIETY OF GREECE, SP. PUBL.

EXTENDED ABSTRACT 244

Assessment of the groundwater vulnerability using DRASTIC method in Larissos watershed, Greece

Papailiopoulou Maria., Chrisanthakopoulou K., Stavropoulou V., Pouliaris, C., Kazakis, N. and Zagana, E.

(1) Faculty of Natural Sciences, Department of Geology, University of Patras, Greece

Introduction

Especially in the world's arid areas, groundwater provides the only source of water because of its extensive supply, low sensitivity to pollution compared to surface water, and storage capacity (Zghibi et al., 2016). In addition, as groundwater is the primary supply of drinking water, it is crucial to determine how vulnerable it is to anthropogenic contamination (Iqbal et al., 2015). Therefore, nitrate contamination of groundwater due to agricultural practices and an important increase in the use of fertilizers is becoming an increasingly serious problem (Zghibi et al., 2016). The probability with which a contaminant introduced into the ground surface might enter and spread throughout groundwater due to human activity is known as inherent vulnerability having consideration given to the region under research's natural geological, hydrological, hydrogeological, and hydrogeochemical characteristics (Zghibi et al., 2016). In most parts of the world, groundwater reservoirs are the only supply of water that is drinkable, yet they are rapidly transforming into a resource that is not renewable (Udosen et al., 2024). Aquifer vulnerability has been evaluated using DRASTIC, a reliable and validated vulnerability model (Aller, n.d.) (Kazakis and Voudouris, 2015). The acronym DRASTIC originates from the parameters that the model is intended to assess: depth to groundwater (D), net recharge rate (R), aquifer media (A), soil media (S), topography (T), impact of vadose zone (I) and hydraulic conductivity rating (C). The study proposes to develop and carry out an assessment tool that uses a geographic information system (GIS) and the DRASTIC model to control the groundwater vulnerability of the watershed of Larissos in Greece. Assessing the relative importance of the DRASTIC criteria for determining aquifer vulnerability is an additional objective of this study.

Study area

The study area is located in the north-west part of Peloponnese, which is located in Greece (Fig.1). The mean annual precipitation is approximately 781 mm, and the temperature it is observed in the months of July and August reaches approximately 27.4°C, while the minimum is placed at month of January with rising around 10.2°C is 10.2 °C these values were estimated based on five years of records (2020–2024) which collected in the study area. The study area is characterized to numerous rivers, from east to west with the main river being the Larissos. Characteristic of the Ionian series in the Lower Cretaceous is the plunge of the watershed that originated due to the taphrogenesis and the deposition along it of Vigla limestones-rich in planktonic organisms-due to the high rate of sedimentation (Karakitsios, 1995). Also, the overlay of "Pantokrator" limestones is found from the Vigla limestones, a fact attributed to a large extent erosion of the stratigraphic sequence. In the deposition phase of limestones of the Upper Senonian, the conditions of carbonate sedimentation they are homogenous until the Eocene, with characteristic features the low rate of sedimentation and the partial supply of material from the Pro-Apulias to the west and Gavrovou-Tripoli to the east, favorable for him formation of micro-breccia and micro-conglomerate limestones with Nummulitidae. Finally, like any sequence, likewise the sequence of Ionia Zone ends with the presence of the flysch. These are clay exchanges, marls, sandstones, siltstones and conglomerates, starting from their deposition in the Eocene, which also reflects its change sedimentation from carbonate to clastic (appearance of Pliocene deposits and Quaternary deposits). It is observed that a wide range of faults in its northwestern and southeastern parts of study area with dominant directions W-E, N-S and SW-NE respectively. The majority of faults occurring within the boundaries of our study area are recorded in the carbonate series and in alluvial deposits.

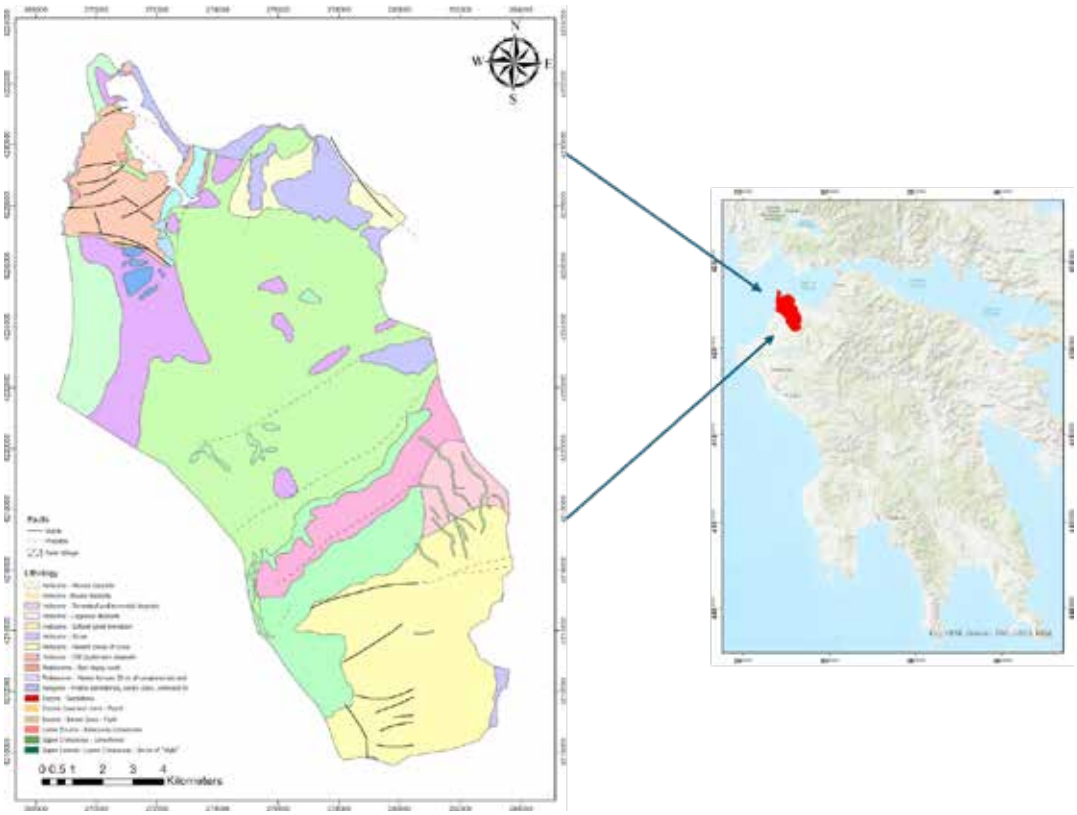


Figure 1. Geological map of study area (modified from I.G.M.E., 1977-1980)

Materials and methods

This is one of the most important parameters in the methodology DRASTIC (Table 1) as it determines the time required until the pollutant reaches the aquifer. Great depth of groundwater indicates a long-time transport interval of the contaminant in the groundwater and sufficient thickness of it unsaturated zone resulting in the weakening of the pollutant and the greater aquifer protection. The hydrological parameters that are widely used for the application of the method in areas with granular formations is seven in number and are also the acronyms of the term DRASTIC and are as follows:

The DRASTIC index is calculated as follows:

DI=DrDw+RrRw+ArAw+SrSw+TrTw+IrIw+CrCw

r index is the value of the parameter

w index is the weight of each parameter

Table 1. DRASTIC weighting and ratings for every DRASTIC parameter (Aller et al., 1987)

Parameters	Interval	Rating	Weight
D (m)	0-1,5	10	5
	1,5-4,5	9	
	4,5-9	7	
	9-15	5	
	15-23	3	
	23-30,5	2	
	>30,5	1	
R (mm/year)	>254	9	4
	178-254	8	
	102-178	6	
	51-102	3	
	0-51	1	

A	Massive shale	2	3
	Metamorphic/Igneous Weathered	3	
	Metamorphic/Igneous Glacial Till	4	
	Bedded Sandstone	5	
	Limestone and Shale sequences	6	
	Massive Sandstone	6	
	Massive Limestone	6	
	Sand and Gravel	8	
	Basalt	9	
	Karst Limestone	10	
S	Thin or absent	10	5
	Gravel	10	
	Sand	9	
	Laterite / peat	8	
	Shrinking and/ or aggregated clay	7	
	Sandy loam	6	
	Loam	5	
	Silty Loam	4	
	Clay Loam	3	
	Muck	2	
	Non-shrinking and non-aggregated clay	1	
T (%)	0-2	10	3
	2–6	9	
	6–12	5	
	12–18	3	
	>18	1	
I	Karstified limestone	10	3
	Βασάλτης	9	
	Sand and gravel	8	
	Άμμοι και χαλίκια με σημαντικό ποσοστό ιλύος και αργίλου	6	
	Στρωματώδης ασβεστόλιθος, ψαμμίτης σχιστή άργιλος	6	
	Sandstone	6	
	Limestones	6	
	Μεταμορφωμένα/ Πυριγενή	4	
	Σχιστή άργιλος	3	
	Clay	2	
	Confined aquifer	1	
C (m/day)	>81,6	10	2
	40,8-81,6	8	
	28,56-40,8	6	
	12,24-28,56	4	
	4,08-12,24	2	
	0,04-4,08	1	

Results and discussion

This work analyzed the DRASTIC model to accurately and effectively assess groundwater vulnerability (Ozegin et al., 2024). The primary factor influencing aquifer vulnerability is water table depth, which is the height between the thickness of subsurface earth components and the water level (Rahman, 2008). The distribution of the parameter in the bounded area differs from point to point, as seen in the groundwater depth thematic map (fig. 2a). Low values of the depth are observed in the NE part of the area, while the high values of this dominate the SW side of the watershed. Moreover, high recharge indicates a higher

vulnerability to contamination. This is due to the fact that increased internal water movement could transport more pollutants (Jesiya and Gopinath, 2019). High values of recharge dominate in the NW part of the watershed, on both sides the lagoon Kalogria, characterized by gentle slopes and the heavy rains (fig. 2b). Conversely, low values of R occur in the NE, NW and N part of the study area, with its prevailing large slopes and small amounts of rain. Aquifer media are different kinds of geological formations that serve as pathways for the transmission and storage of water. The aquifer's media shows a lower vulnerability to groundwater when the grain size is smaller (Saha and Alam, 2014). The distribution map of parameter A the prevailing type of aquifer in the study area is lithological consisting of sand and gravels (fig. 2c). As most of the area consists of the specific combination of materials, the study area calibrated mainly with 8. However, the study area indicates different aquifer material. In the NW part of the watershed karstified limestone and sandstone layers are noted and limestones with layers of clay in the southern part of it. The study area at these positions is rated with 10 and 6 respectively. The soil media affect the area's replenishment and have a greater impact on the movement of contaminants across the geologic layers (Bhuvaneswaran and Ganesh, 2019). In the case of this parameter, the data is not sufficient and consequently the map of soil cannot be carried out. An inclined gradient angle increases the intensity of water discharge and reduces pollution susceptibility, but a small slope angle supports significant contaminat migration with water, which is absorbed through a vertical channel (Ozegin et al., 2024). According to the map of the T parameter the study area in almost its entire extent is represented by gradients >18%, so it is rated as 10 (fig. 2d). However, the distribution of slopes it is different in the NW and SE part of the watershed and in a limited part of that in the NE, because of the increase in altitude. Also, with the territory of gentle slopes favoring active infiltration. The domain that extends before the water table and is an aeration zone is known as the vadose zone (Ahmed et al., 2015). For the study area, in the case where clay minerals dominate in the unsaturated zone and its thickness is large, the length of time the contaminant remains in the unsaturated zone increases and this results in its weakening and preventing the infiltration to the groundwater. According to the results are observed 3 different lithologies (fig. 2e). Almost completely the unsaturated zone in the watershed of Larissos consists of sand and gravel with significant percentage of silt and clay. Also at the center of it are places where the unsaturated zone consists of sand and gravel and the value of parameter is 8. On the contrary, to the west of the watershed is observed the value 3, indicating that the material of the unsaturated zone is detailed. By indicating the aquifer's capacity to transport water, C affects the rate at which contaminated material moves through the groundwater system (Aller et al., 1987). In addition, the size of an unconsolidated aquifer's pores and the interconnected of its intergranular void spaces affect its hydraulic conductivity. As particle size increases, hydraulic conductivity decreases (Ozegin et al., 2024). High water values hydraulic conductivity corresponds to high values of water permeability. The different calibration of values is shown in while the distribution of the parameter in the watershed is shown with the distribution map (fig. f).

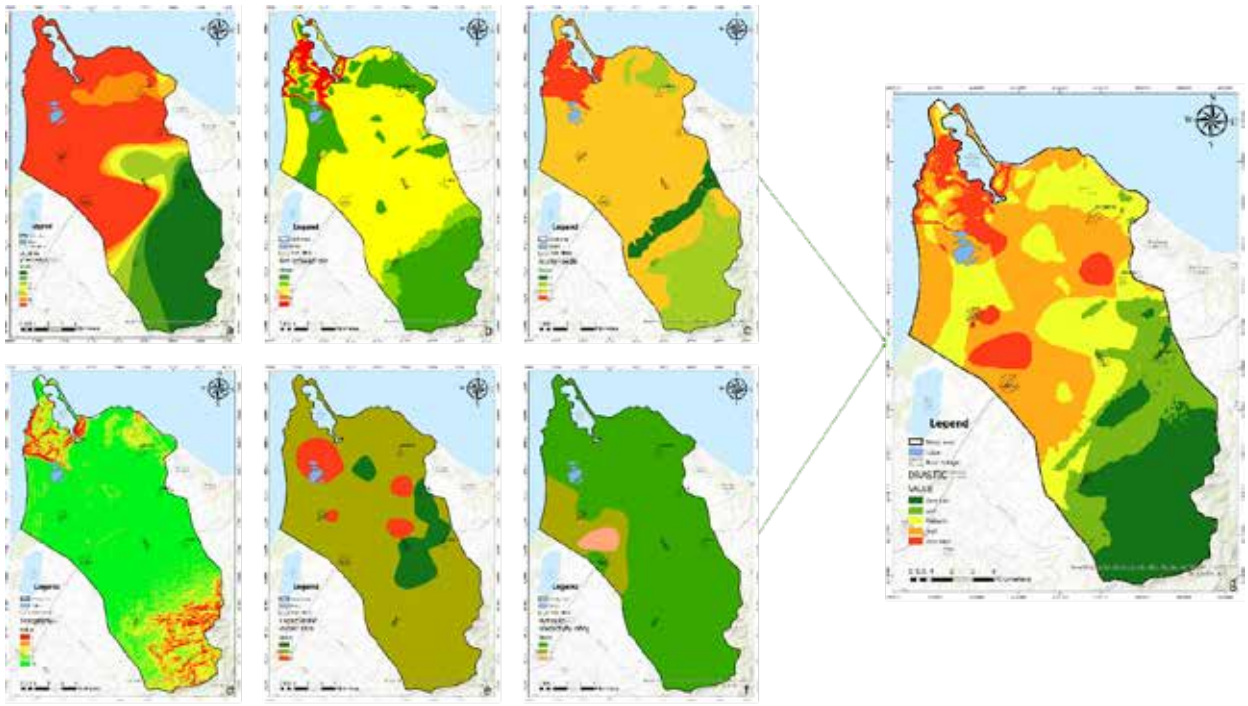


Figure 2. (a) Map of depth to groundwater; (b) Map of net recharge rate; (c) Map of aquifer media; (d) Map of topography; (e) Map of impact of the vadose zone; (f) hydraulic conductivity rating; (g) Map of DRASTIC method

Conclusions

It is crucial and necessary for investigation into the vulnerability of aquifers, which are groundwater resource systems. Throughout the research area, aquifer formations are still in risk from pollutants that are both naturally occurring and caused by humans. The results of six distribution maps, which correspond to the six parameters of the DRASTIC methodology contributed to the drafting of the final DRASTIC map (fig. 1g) that indicates the distribution of its vulnerabilities study area in terms of external pollutant. The maps were produced using the ArcGIS Pro program as well as the value of the gravity of each parameter. According to the final vulnerability map almost completely the SW part of the watershed it appears in green as the least sensitive part of the study area. This is reasonably explained as this section characterized by a large depth of the aquifer, high slopes, low rainfall and clay material that is impermeable, preventing the infiltration of the pollutant. Instead, highly vulnerable positions within it defined area are in red in the NW part of it, on both sides of the Kalogria lagoon, and in some places in the central part of the basin, which are characterized by gentle slopes, shallow depth of groundwater, intense rainfall and the presence of karstic limestone. The above features favor active recharge and the infiltration of pollutants. Finally, the other areas in the central and NW extent of the study area are characterized by high to moderate vulnerabilities as well present intermediate characteristics. Due to its ability to adapt to specific hydrogeology and human (land use) factors, this model-based technique can be used to study and manage groundwater resources. The pollution hazard map provides the data sets and model predictions required for land use and water resource management and strategic planning.

References

Ahmed, I., Nazzal, Y., Zaidi, F.K., Al-Arifi, N.S.N., Ghrefat, H., Naeem, M., 2015. Hydrogeological vulnerability and pollution risk mapping of the Saq and overlying aquifers using the DRASTIC model and GIS techniques, NW Saudi Arabia. Environ Earth Sci 74, 1303–1318. https://doi.org/10.1007/s12665-015-4120-5

Aller, L., n.d. DRASTIC: A STANDARDIZED SYSTEM FOR EVALUATING GROUND WATER POLLUTION POTENTIAL USING HYDROGEOLOGIC SETTINGS.

Aller, L., Lehr, J.H., Petty, R., Bennett, T., 1987. Drastic: A Standardized System to Evaluate Groundwater Pollution Potential using Hydrogeologic Setting. Journal Geological Society of India 29, 23–37. https://doi.org/10.17491/jgsi/1987/290112

Bhuvaneswaran, C., Ganesh, A., 2019. Spatial assessment of groundwater vulnerability using DRASTIC model with GIS in Uppar odai sub-watershed, Nandiyar, Cauvery Basin, Tamil Nadu. Groundwater for Sustainable Development 9, 100270. https://doi.org/10.1016/j.gsd.2019.100270

Iqbal, J., Gorai, A.K., Katpatal, Y.B., Pathak, G., 2015. Development of GIS-based fuzzy pattern recognition model (modified DRASTIC model) for groundwater vulnerability to pollution assessment. Int. J. Environ. Sci. Technol. 12, 3161–3174. https://doi.org/10.1007/s13762-014-0693-x

Jesiya, N.P., Gopinath, G., 2019. A Customized FuzzyAHP - GIS based DRASTIC-L model for intrinsic groundwater vulnerability assessment of urban and peri urban phreatic aquifer clusters. Groundwater for Sustainable Development 8, 654–666. https://doi.org/10.1016/j.gsd.2019.03.005

Kazakis, N., Voudouris, K.S., 2015. Groundwater vulnerability and pollution risk assessment of porous aquifers to nitrate: Modifying the DRASTIC method using quantitative parameters. Journal of Hydrology 525, 13–25. https://doi.org/10.1016/j.jhydrol.2015.03.035

Ozegin, K.O., Ilugbo, S.O., Adebo, B., 2024. Spatial evaluation of groundwater vulnerability using the DRASTIC-L model with the analytic hierarchy process (AHP) and GIS approaches in Edo State, Nigeria. Physics and Chemistry of the Earth, Parts A/B/C 134, 103562. https://doi.org/10.1016/j.pce.2024.103562

Rahman, A., 2008. A GIS based DRASTIC model for assessing groundwater vulnerability in shallow aquifer in Aligarh, India. Applied Geography 28, 32–53. https://doi.org/10.1016/j.apgeog.2007.07.008

Saha, D., Alam, F., 2014. Groundwater vulnerability assessment using DRASTIC and Pesticide DRASTIC models in intense agriculture area of the Gangetic plains, India. Environ Monit Assess 186, 8741–8763. https://doi.org/10.1007/s10661-014-4041-x

Udosen, N.I., George, N.J., Ekanem, A.M., 2024. Aquifer vulnerability valorization via DRASTIC index-based assessment within litho-facies of a coastal environment. Results in Earth Sciences 2, 100033. https://doi.org/10.1016/j.rines.2024.100033

Zghibi, A., Merzougui, A., Chenini, I., Ergaieg, K., Zouhri, L., Tarhouni, J., 2016. Groundwater vulnerability analysis of Tunisian coastal aquifer: An application of DRASTIC index method in GIS environment. Groundwater for Sustainable Development 2–3, 169–181. https://doi.org/10.1016/j.gsd.2016.10.001

17th INTERNATIONAL CONGRESS of the Geological Society of Greece

BULLETIN OF THE GEOLOGICAL SOCIETY OF GREECE, SP. PUBL.

EXTENDED ABSTRACT 245

RescueME, a Research Action that focuses on the enhancement of the resilience of coastal cultural landscapes in Europe. The case study of Psiloritis UGGp, Crete, Greece

C.Papailiou[1], M. Kolendrianou[2] C. Fassoulas[1,3]

(1) Psiloritis UGGp, Crete, Greece, cpapailiou@psiloritisgeopark.gr , (2) Psiloritis UGGp, Crete, Greece, info@psiloritisgeopark.gr , (3) Natural History Museum, Univ. of Crete, Crete, Greece, bfassoulas@gmail.com

Research highlights

How can we protect European cultural heritage from climate change, natural hazards and other stressors such as pollution and over-tourism?

Introduction

RescueME (Resilient Cultural Landscapes) is a Research project funded by the Horizon Europe programme where five Resilience Landscape Laboratories (R-labscapes) are working with 12 consortium research and technology partners to create new approaches of protecting coastal cultural heritage and landscapes, implementing innovative resilience solutions and culture-focused strategies. The project started in February 1st, 2023, lasts for 42 months and focuses on the enhancement of the resilience of coastal cultural landscapes (CLs) in Europe.

The five case studies (Psiloritis UGGp in Greece, the island of Neuwerk in Germany, Portovenere, Cinque Terre & the Islands in Italy, L'Horta in Spain, and the city of Zadar in Croatia) have been selected carefully as complementary representatives of European coastal landscapes. They act as resilience landscape laboratories (R-labscapes) to validate the results and ensure their replicability. For these five target areas, RescueME is going to produce digital tools and innovative solutions for climate change adaptation and natural disaster risk management.

Regarding Psiloritis UGGp located at the island of Crete, Greece, planned actions focus on shielding of its northern coast (parts of the Municipalities of Mylopotamos & Rethymnon) from the impacts of extreme weather phenomena such as heatwaves, droughts, water shortages and, secondarily, floods. Also, Psiloritis UGGp has set as priority to enhance heritage resilience, raise awareness among local stakeholders and make RescueME project results actionable in the local framework.

Common heritage is a central element of our communities and economies, and a principal but vulnerable dimension of our common identity as Europeans. It has been proven that cultural heritage contributes to well-being, social cohesion, identity, local economy, territorial attractiveness, and environmental sustainability (European Commission, 2021), but the climate crisis and natural hazards threaten this heritage. RescueME is going to take immediate action to demonstrate how an innovative data-driven, community-based and heritage-centric actionable landscape approach for resilience enhancement can protect our cultural heritage and landscapes, while supporting the transition toward a green society and economy that sustains resilient, cohesive, nature-connected communities. RescueME proposes a call for broadening the scope, triggering actions, untapping and mobilizing resources, engaging actors, and facilitating the decision making and the implantation of co-created just resilience solutions to protect our common heritage.

RescueME is developing, testing and demonstrating the effectiveness of an Actionable Framework based on the Resilient Historical Landscape approach (RHL) complemented by data, models, methods, and tools able to assess risks and opportunities, co-develop inclusive and just resilience strategies and innovative solutions to protect European cultural heritage and cultural landscapes from climate change, disaster risk, as well as other stressors (such as pollution and over-tourism) with special focus on European coastal landscapes (FUNDACION TECNALIA RESEARCH & INNOVATION, 2023).

Methodology



Figure 1: Map of RescueME area. This area applies to the semi-mountainous and lowland part of the Municipality of Mylopotamos as well as part of the old Municipality of Arkadi of the current Municipality of Rethymno.

For project implementation, the study area of Psiloritis UGGp (Figure 1) has been determined as well as the main hazards the area faces due to climate change, while stakeholder task forces have been set. These, comprise of local CCSIs (Creative & Cultural Sectors and Industries) and other businesses, experts with local knowledge, researchers as well as civil society, and participate in the co-creation process of the project that entails the collaborative engagement of diverse local stakeholders in the development of resilience measures and strategies in the R-labscape.

For the purpose of co-creation of local measures and solutions, these local stakeholders have already been engaged in an intensive Resilience Baseline Assessment for a better understanding of the local knowledge/awareness. The assessment has been conducted via a questionnaire of 78 quantitative and qualitative questions which was distributed amongst targeted users as well as stakeholders based on the RescueME indicator approach. This approach implements a GLOCAL (global and local) strategy blending global and local factors alongside top-down and bottom-up approaches, as well as the adoption of the concepts of Socio-Ecological Systems (SES) and a landscape approach, as described in the Deliverable “Actionable framework for resilient historic landscapes”. By this way, weak spots and strong points have been identified in Psiloritis R-labscape and the most appropriate approach is going to inform the co-creation of resilience measures.

Stakeholders have also participated in two “impact chain” workshops (Impact Chains) to address the impacts from heatwaves and temperature rise and possible adaptive measures, on the sectors of agriculture and tourism. At a first step, these impact chains identified first the main hazards that threat the R-labscape, analyzed the potential capitals (build, natural, cultural, economic, social etc.) that might be affected, and determined the specific impacts that might occur. In a second step, the focus was concentrated on the impacts in tourism and agricultural activities, identifying the vulnerabilities, the weaknesses and the potential drivers for enhancing local resilience.

Based on the Impact Chains, a predictive impact model which is going to be defined to model and quantify the impacts of the considered hazards and stressors, specifically addressing the aspects of ecosystems services and local heritage values. Especially in Psiloritis UGGp, the model is going to focus on the impact of changes in temperature and precipitation patterns on agriculture and tourism. As a start, a Multiscale risk and resilience assessment of the

R-labscape has been developed through a questionnaire and bilateral meetings with the R-labscape in order to analyze the possibilities of the development of the final model. Following, local quantitative data have been selected, such as the population number of the area, tourism turnover in euros and agricultural area in m^2 etc., in order to have a selection of indicators for the spatial analysis of the impact model.
After thorough analysis of the results obtained by the Impact Chains, the Resilience Baseline Assessment and the Multiscale risk and resilience assessment a long list of issues and common findings between them was created by the relevant work package leaders which were categorized in capitals and key elements according to the SES Framework. This list was validated by the R-labscape in order to understand what matters most and what needs to be addressed urgently to enhance resilience. Currently, resilience issues have been further categorized in a reduced list and prioritized via a prioritization exercise by assessing their impact on resilience, complexity and effort required to address them. By this way, the Psiloritis UGGp focuses on the most critical issues when co-creating resilience measures and solutions.
Moreover, a RescueME resilience meta-repository as well as local policy tools have been created which show existing knowledge and solutions on community- or system-based resilience in order to define measures, solutions and conditions to guide Cultural Landscapes in building their transformative resilience strategies. Also, RescueME research partners are starting the development of the first steps of a social innovation and co-creation tool, the Resilient Landscapes Serious Game for resilience strategy development. By this way, compatible solutions are going to be adapted in a local context with in-person workshops with local stakeholders. Currently, the structure of the game Board mock-up game, game steps, resilience strategy objectives and possible scenarios are being built.
RescueME aims, also, to deliver a set of advanced digital solutions, easily accessible through a single application portal (RescueME One-stop Shop). The design and development of all foreseen digital solutions will follow a human-centred approach, based on a common set of definitions, including a comprehensive multi-scale data model. The digital solutions will include a geospatial and interoperable Data Lake, a geospatial Data Intelligent Platform for heterogeneous data aggregation, processing, and visualization, and a set of AI-based tools and solutions (crowdsourcing, satellite mapping, AR app). Currently, in order to deliver a set of advanced digital solutions, social media posts are being analyzed and available local actionable data sources are being gathered to be inserted in a Data Lake of AI based tools. Also, already calculated by Psiloritis UGGp geographical, demographic and, economic data at the Multiscale risk and resilience assessment phase, are going to be selected and displayed through the Geospatial Data Intelligent Platform, to allow the users further use of such data sources if necessary.
Last but not least, the project is going to produce a digital One-Stop-Shop (OSS) that will include advanced tools for the protection and promotion of coastal cultural landscapes of Europe.

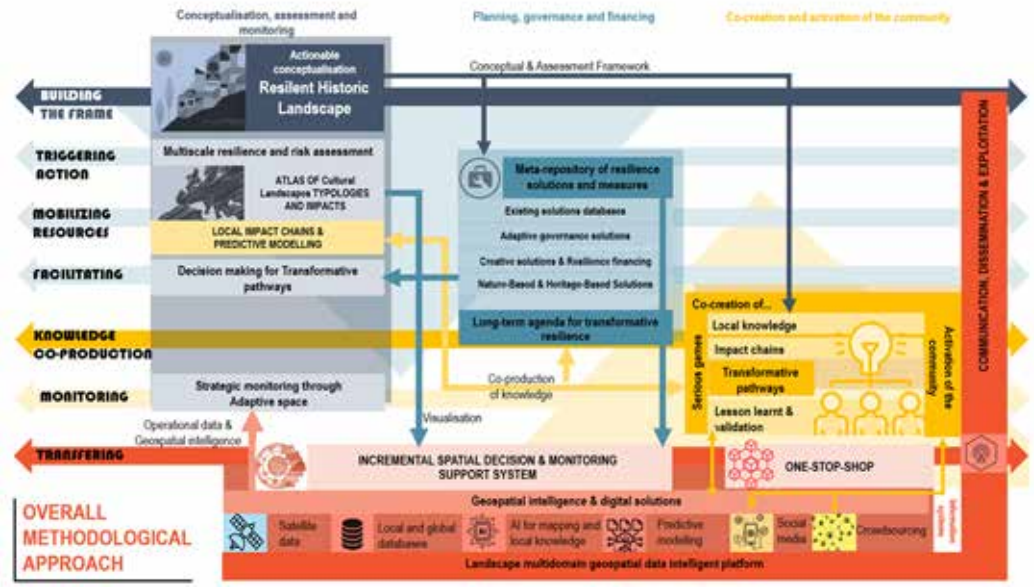


Figure 2: RescueME methological approach

For all the above, the RescueME methodological approach (Figure 2) interconnects the conceptualisation of approaches and quantification of values and impacts with the development of resilience solutions and measures to create long-term transformative strategies. From a bottom-up approach, these strategies are being co-created with the R-labscapes and for the top-down approach, they are implemented in the decision-making tools to facilitate the transference.

Results

Key conclusions have been drawn by the local stakeholders at the two local Impact Chains. In specific, on 11th October 2023, at the 1st Impact Chain, 13 local stakeholders from the public and private sector gathered at Panormos in Crete in an interactive group session to discuss how they perceive the existing and potential future climate-related hazards in the region. The workshop's results revealed how the selected area's climate-related hazards, such as the rise of winter temperatures, may cause impacts on agriculture, culture, ecosystems, infrastructure, people, tourism and Crete's economy. At the same time, the participants' discussions explored how the impacts are affected by exposed elements of the Cultural Landscape, apparent sensitivities and capacities in these sectors. Therefore, the workshop concluded in an effort by the stakeholders to propose potential adaptation measures. For instance, the rise of winter temperatures may cause diseases that affect both livestock and agricultural production as well as public health. As a sub-effect, less products are available on the market, the income is getting lower, the welfare state gets weakened and rural communities are being abandoned. At the same time, there is an apparent sensitivity: the lack of civic engagement and participation of citizens in planning & implementation. Workshops/seminars were, therefore, proposed for good practice exchange at the local level.

On 2nd February 2024, at Aggeliana in Crete, a deeper review and analysis of the same topic was made by 12 different local stakeholders from targeted sectors. This time, the focus of 2nd Impact Chain was only on agriculture and tourism, since these are the main driving forces in the economy of Crete. At that workshop, new adaptation measures were also addressed. For instance, climate related hazards such as heat waves may increase the time spent inside hotel units, the energy and water consumption but also reduce travel agencies income due to the lack of tourist mobility. The promotion of off-season alternative tourism could be one of the adaptation measures.



Figure 3: Impact Chain Workshop 2

This task supported the next steps of the project along with the results obtained by the Resilience Baseline Assessment and the Multiscale risk and resilience assessment developing the list of all related resilience issues. As a result, the prioritized list of issues has been created in order to focus on the issues which are most critical for the co-creation of resilience measures and solutions, having in mind the main co-creation aims of Psiloritis UGGp (enhancing heritage resilience, raising awareness among stakeholders and making RescueME project results actionable in the local framework). Examples of those issues include the lack of agricultural training which may pose challenges in terms of implementing sustainable farming practices, adopting modern agricultural techniques and ensuring the long-term viability of traditional farming methods. This is of relatively high impact but also feasible to address. Also, climate impacts on crop productivity and water resources may pose concerns regarding water availability and management, highlighting vulnerabilities to drought and over-pumping with significant risks to agricultural productivity and livelihoods, a challenge highly complex but also with a high impact if addressed. Lastly, facing the reduced attractiveness of the destination for tourists due to the impacts of natural hazards on the cultural landscape (e.g. coastal erosion), human health (heatwaves) and recreational outdoor activities, may become a "Big Project" having relatively high impact, requiring also to address quite intensive resource efforts.

All these actions are part of a long co-creation and decision-making process that is taking place with the collaboration of project partners and local actors in order to enhance the common heritage resilience from climate change, natural hazards and other stressors.

Acknowledgements
This study is funded under the EU's Horizon Europe, key funding programme for research and innovation, with title: "Equitable RESilience solutions to strengthen the link between CUltural landscapEs and coMmunitiEs", Grant agreement ID: 101094978. We would like to thank all those technical and research partners of the project who make a vast contribution for the success of this on-going research.

References

European Commission, 2021, Culture and the Sustainable Development Goals: Challenges and Opportunities [Voices of Culture Brainstorming Report]

FUNDACION TECNALIA RESEARCH & INNOVATION, 2023, "Equitable RESilience solutions to strengthen the link between CUltural landscapEs and coMmunitiEs", Grant Agreement ID: 101094978, – RescueME - Part B – 7 [Research Project under EU's Horizon Europe funding programme]

17th INTERNATIONAL CONGRESS of the Geological Society of Greece

BULLETIN OF THE GEOLOGICAL SOCIETY OF GREECE, SP. PUBL.

EXTENDED ABSTRACT 246

Innovative Efforts in Geotourism: The Vikos-Aoos UNESCO Global Geopark

Haritakis Papaioannou[1], Christos Stergiou[2], Spiros Staridas[1], Aristotelis Stagkikas[1], *Georgia Kitsaki[1]*

[1]Vikos-Aoos UGGP – Development Agency of Epirus S.A. (EPIRUS S.A.), 45332, Ioannina, Greece, h.papaioannou@epirussa.gr; [2]School of Geology, Aristotle University of Thessaloniki, 54124, Thessaloniki, Greeece

Introduction

To enhance geotourism and public awareness, the Vikos-Aoos Geopark launched the "Enhancement of Geosites and Geological Formations" project (2022–2024). This initiative integrates modern technology and infrastructure to improve visitor experience and promote sustainable tourism. Key components include a mobile app offering interactive geological and cultural content, visitor centers providing in-depth interpretation, and outdoor viewing platforms showcasing geosites through strategic placements and aerial imagery. Additionally, a visitor tracking system at eight major sites has provided valuable data on geotourism trends. These efforts strengthen conservation-focused tourism and serve as a model for balancing heritage preservation with visitor engagement.

Methods

The Vikos-Aoos Geopark, in collaboration with the Hellenic Ministry of Environment and Energy, has undertaken a comprehensive initiative to enhance geotourism, visitor engagement, and public awareness of its geological heritage. This project, titled "Enhancement of Geosites and Geological Formations and Evaluation of Visitability of Geosites and Landscapes of High Aesthetic Value in Vikos-Aoos UNESCO Global Geopark", is funded by the Natural Environment & Climate Change Agency (N.E.C.C.A.) under the framework of a cooperation memorandum signed between N.E.C.C.A. and the Hellenic UNESCO Global Geoparks Forum in 2022. Spanning from 2022 to 2024, the project implements a strategic, multi-faceted approach to improving visitor services and sustainable tourism development.

The first major action (Action 1) of the project focused on enhancing information and geosite interpretation services through the development of a web-based digital mapping application. Designed for use both within visitor centers and on mobile devices, this platform allows for interactive exploration of the Geopark's geological, environmental, and cultural heritage. The application provides dynamic, user-friendly access to geosite data, enabling visitors to engage with scientific information through maps, multimedia content, and interactive tools.

The second action (Action 2) centered on the installation of Outdoor Viewing Spots (OVS) at carefully selected locations within the Geopark. These platforms were strategically placed to highlight key geosites and landscapes of high aesthetic value, offering visitors enhanced vantage points to appreciate and understand the region's unique geomorphology. This intervention not only improves the geotourism experience but also reinforces the Geopark's educational mission by making significant geological formations more accessible and visually interpretable.

The third action (Action 3) involved the installation and operation of a visitor counting system, aimed at collecting real-time data on tourist activity within the Geopark. By monitoring visitor numbers across key sites, this system provides valuable insights into seasonal tourism trends, site popularity, and the overall impact of geotourism initiatives. The collected data supports future planning efforts, ensuring that conservation strategies align with sustainable tourism growth. Together, these actions contribute to a more immersive and informative visitor experience while supporting the long-term management and conservation goals of the Vikos-Aoos UNESCO Global Geopark.

Results

Action 1 was titled "Improvement of Information and Geosite Interpretation Services" and was implemented to enhance the educational and awareness-raising capacity of the Vikos-Aoos Geopark, two modern Information Centers were established (Action 1.1) in the municipalities of Zagori (Vitsa) and Konitsa. These centers serve as key hubs for visitors, providing structured insights into the Geopark's geological, environmental, and cultural heritage. Their design prioritizes accessibility and engagement, utilizing modern technology to improve visitor interaction with geosite information. By centralizing interpretive resources, these centers strengthen the Geopark's role as an educational destination, promoting geotourism and fostering appreciation for natural landscapes.

A web-based digital mapping application was developed (Action 1.2) to complement the Information Centers and extend accessibility to geosite data (Figure 1a-d). This interactive platform presents the entirety of the Geopark's

geological, cultural, and environmental assets through a user-friendly, two-dimensional map. Accessible via web browsers on desktop and mobile devices, the application allows users to navigate geosites, explore categorized information on geoheritage, culture, and geotourism, and interact with multimedia content. Developed in collaboration with geologists, biologists, and historians, the platform ensures scientifically accurate and engaging content delivery. Its digital format modernizes geosite interpretation, allowing visitors to plan their routes, visualize geodiversity, and interact with the Geopark's rich heritage beyond the physical boundaries of the information centers.

To maximize the effectiveness of these digital tools, specialized IT equipment was installed (Action 1.3) at both Information Centers (Figure 1a,b). In Konitsa, a digital presentation screen wall system, an interactive info kiosk, and a dedicated computer provide visitors with dynamic, on-demand access to geosite information (Figure 1a,b). Similarly, the Vitsa Information Center features a digital screen wall system, a smart interactive table, and a computer, fostering an immersive educational experience (Figure 1c,d). These installations modernize the visitor experience by integrating smart technology into geotourism services, enabling real-time exploration of geological data and supporting sustainable tourism development in the Geopark.



Figure 1. Examples of the specialized IT equipment installed in the Informations Centers at Konitsa and Vitsa. a, b. The digital screen wall systems installed at Konitsa projecting the web-based digital mapping application developed for the Vikos-Aoos Geopark. c. Top view of the smart interactive table at Vitsa. d. The smart interactive table during installation at Vitsa.

To enhance visitor engagement and raise awareness about the geological and geomorphological features of the Vikos-Aoos Geopark, a series of outdoor viewing areas were installed at carefully selected locations, under Action 2: "Installation of Outdoor Viewing Areas at Significant Geosites in Landscapes of High Aesthetic Value". These viewing platforms were designed to provide strategic vantage points where visitors could appreciate geosites, geological formations, and landscapes of exceptional beauty while simultaneously accessing educational interpretative panels. The primary goal of this initiative was to merge the aesthetic appreciation of these landscapes with scientific knowledge, helping visitors understand the forces that shaped the region.

Each outdoor viewing area features a specialized prefabricated canopy structure equipped with exhibit panels that highlight key geological, environmental, and cultural aspects of the surrounding landscape. The structures maintain a uniform design, but the content of each panel is tailored to the specific geosite, ensuring site-specific interpretation. The panels, measuring three meters in length, present information in both Greek and English and include photographs, diagrams, and explanatory texts. The selection of these locations was based on their scientific, educational, and touristic value, ensuring that visitors have access to some of the most iconic geological features within the Geopark. Three major outdoor viewing areas were established at critical geosites, two in the eastern-southern section of the Geopark (Municipality of Zagori) and one in the western-northern section (Municipality of Konitsa). Each location was selected to showcase significant geological formations, offering visitors an immersive experience that blends scenic beauty with

scientific exploration.

The first outdoor viewing area, located at Kapesovo fault (geosite 12) and the Stone Stairway of Vradeto, provides a remarkable perspective of the Kapessovo fault and its role in shaping the regional geomorphology. The mountainous landscape of Tymfi, composed primarily of limestone formations dating from 145 to 15 million years ago, is revealed through aerial photographs and diagrams. The interpretative panel at this site highlights nine distinct geological features, including the effects of glacial activity during the Pleistocene epoch, which sculpted the area's characteristic U-shaped valleys (Telbisz *et al.,* 2019). Visitors can gain insight into the tectonic and erosional forces that shaped the terrain while admiring the rugged beauty of the surrounding cliffs and gorges.

The second viewing area, is related to the Voïdomatis river Valley and Astraka Fault (geosite 9), offers a spectacular panoramic view of the Vikos Gorge and the surrounding mountain formations. The Towers of Papigo, a striking set of vertical limestone formations, dominate the landscape, shaped by the Astraka fault and karstic erosion processes (Chatzipetros *et al.,* 2024). This site also provides insight into the hydrological system of the Voidomatis river, which emerges from the karst springs of Mount Tymfi before flowing towards its confluence with the Aoos river. The exhibit panel at this location presents nine key geological features, allowing visitors to explore the interplay between faulting, river dynamics, and mountain-building processes.

The third viewing area, positioned at Prophet Elias Hill (1071 m) near Konitsa fault (geosite 8), provides an unparalleled panoramic view of the Konitsa plain and the surrounding mountain ranges. This location offers vistas of Lapatos, Trapezitsa, Gamila, and Astraka, with the Aoos river flowing through the valley, shaping the landscape through continuous erosion and sediment deposition. Visitors can trace the 24-km long Konitsa fault and learn about the structural features of this active seismogenic fault (Chatzipetros *et al.,* 2024). Furthermore, they can explore the sedimentary processes of the Aoos river, learn about the sulfur caves of Sarantaporos river valley and admire the Smolikas (2497 m) and Gamila (2497 m) peaks (Lazaridis *et al.,* 2024). The panel here showcases seven distinct geological features, explaining how the tectonic forces responsible for the formation of the Konitsa fault have influenced the region's topography. From this vantage point, visitors can also observe the Nemerçika mountain range, marking the natural border between Greece and Albania, as well as the ophiolite peaks of Smolikas (2637 m), Greece's second highest mountain.

These outdoor viewing areas provide an unparalleled opportunity to connect with the geological past while enjoying breathtaking landscapes. Visitors gain a deeper appreciation of the region's dynamic geological history, from ancient fault movements and glacial sculpting to modern river systems and ongoing erosional processes. By merging scientific interpretation with stunning natural beauty, these installations reinforce the Geopark's mission of education, conservation, and sustainable geotourism, offering an immersive and enriching outdoor experience.

The third action implemented under this project was tilted "Installation and Operation of a Visitor Counting System at Geosites". Its scope was to effectively manage visitor traffic and ensure sustainable tourism in the Vikos-Aoos Geopark. A visitor counting system was installed at key geosites and geomorphological formations (Figure 3a-c). This system aims to collect data on the number of hikers in specific areas, such as the Vikos and Aoos Gorges and the Dragon Lakes of Tymfi and Smolikas. By analyzing visitor numbers and movement patterns, park authorities can develop informed strategies for conservation, infrastructure planning, and visitor experience enhancement. The system utilizes passive infrared sensors to count visitors discreetly. Counters were placed at eight strategic locations along major hiking trails, ensuring coverage of high-traffic areas like the Vikos Gorge and its branches, the Aoos Gorge, and popular scenic viewpoints such as the Oxya (Stone Forest) in Monodendri. These bidirectional sensors not only track the number of hikers but also identify their direction of movement (Figure 4a). Additionally, the counting data can be co-evaluated in relation with real time weather and extract information on how weather may affect or not visitor traffic (Figure 4b). The collected data is transmitted to a central unit, where it is processed using specialized software for further analysis. The placement of the sensors was carefully designed to minimize their visual impact on the natural landscape while maintaining accurate and reliable data collection (Figure 3a,c).

A significant example of the system's effectiveness is the monitoring of visitor numbers at the Agkastromeni Spring (geosite 4), located at the exit of the Vikos Gorge (Figure 4a). This site marks the main springs of the Tymfi karst system, where water emerges from limestone and dolomitic limestone formations with black chert. The spring, formed due to the Astraka fault, has an intermittent flow that varies with seasonal water availability. Nearby, an 18th-century church, once a monastery, serves as a cultural landmark and a resting point for hikers. The results from the counter at this site indicate that approximately 16,000 visitors pass through annually, with a steady flow throughout the year. The highest visitor numbers occur on weekends and holidays, peaking during the summer and early autumn months, particularly in August, when around 4,000 hikers visit the site.

The implementation of the visitor counting system provides invaluable insights into hiking trends and seasonal variations in visitor traffic. This data will help park managers maintain a balance between accessibility and conservation, ensuring the long-term protection of the geopark's natural and cultural heritage while enhancing the visitor experience.



Figure 2. a. The interpretive panel at viewpoint located opposite to the Kapesovo fault and the participants of the Vikos-Aoos Geopark re-evaluation (July, 2024).



Figure 3. a. Detail of the counting system that was installed at key geosites and geomorphological formations. b. Field work photograph during the installation of the system. c. Detail of the rugged case protecting the logging-transmitting digital apparatus.

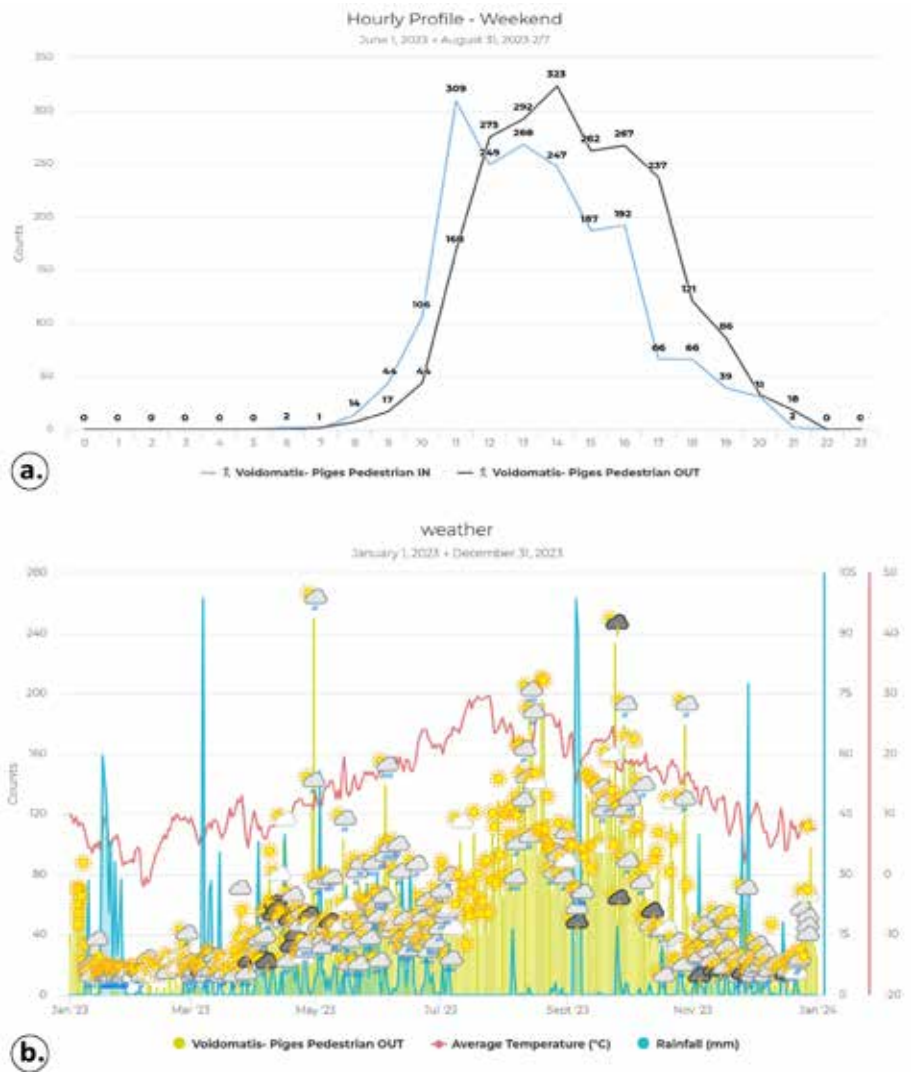


Figure 4. a. Diagram showing the hourly allocation of incoming and out coming visitors to the Agkastromeni spring of Voidomatis river. b. Visitors counts coupled with weather conditions from January 2023 to January 2024.

Conclusions

The implemented actions in the Vikos-Aoos Geopark enhance visitor experience while promoting geoconservation and awareness. The outdoor viewing areas provide panoramic insights into key geosites, while the new interpretation panels educate visitors on geological processes shaping the landscape. Additionally, the visitor counting system enables sustainable management by monitoring foot traffic across major trails. These efforts contribute to preserving the park's natural and cultural heritage while fostering appreciation for its geological significance. Through these initiatives, the Geopark strengthens its role as a model for responsible geotourism and environmental stewardship.

Acknowledgements

Authors would like to thank the Natural Environment and Climate Change Agency (NECCA) for founding the project.

References

Chatzipetros, A., Stergiou, C.L., Papaioannou, H., 2024. Seismic hazard in an actively uplifting area: the case of Vikos-Aoos UNESCO Global Geopark, NW Greece, in: Pellicer, M.X., Aytac, A., Amorfini, A., Delaby, S. (Eds.), Geohazards in European Geoparks, Akademisyen Yayınevi Kitabevi, Ankara, Turkey, pp.150-153.

Lazaridis, G.T., Melfos, V., Papadopoulou, L., Onac, B.P., Stergiou, C.L., Maravelis, A.G., Voudouris, P., Dora, D., Fitros, M., Papaioannou, H., Vouvalidis, K., 2024. Sulfuric acid speleogenesis in Greece. Acta Carsologica 53, 127–144.

Telbisz, T., Stergiou, C.L., Mindszenty, A., Chatzipetros, A., 2019. Karst features and related social processes in the region of the Vikos Gorge and Tymphi Mountain (Northern Pindos National Park, Greece), Acta Carsologica 48, 29-42.

17th INTERNATIONAL CONGRESS
of the Geological Society of Greece

BULLETIN OF THE GEOLOGICAL SOCIETY OF GREECE, SP. PUBL.

EXTENDED ABSTRACT 247

Volcanism and the metamorphic core complexes of Rhodope and Cyclades

Papanikolaou D.[1], Nomikou P.[1] & Lambridou D.[1]
(1) Department of Geology and Geoenvironment, National and Kapodistrian University of Athens, Greece

The four active volcanic centres of the Aegean arc and another ten inactive volcanic centres, activated during Oligocene – Middle Pleistocene, following its southward migration are described with emphasis on their tectonic signature. They are all localized within tectonic grabens, resulting from the back-arc extension of the Hellenic arc throughout its Late Eocene – Present evolution. Our study was based on geological maps and the transverse tectonic profiles both onshore and offshore. The material presented is either from our own publications (usually modified) or new. The orientation of the tectonic grabens depends on the extensional stress field of each period and region. The existence of Late Miocene granitic rocks in the Cyclades without outcrops of Late Miocene volcanics is probably due to the considerable uplift of the Cycladic metamorphic core complex that has denudated the upper geological formations together with the volcanic rocks. The volcanic activity is observed within the arc parallel marine molasse of the North Aegean – Rhodope back arc basin during Oligocene – Early Miocene and within the Plio-Quaternary marine arc parallel tectonic grabens/basins of the South Aegean. Middle-Late Miocene volcanic rocks are observed within continental tectonic grabens/basins only in the lateral margins of the Cycladic metamorphic tectonic window.

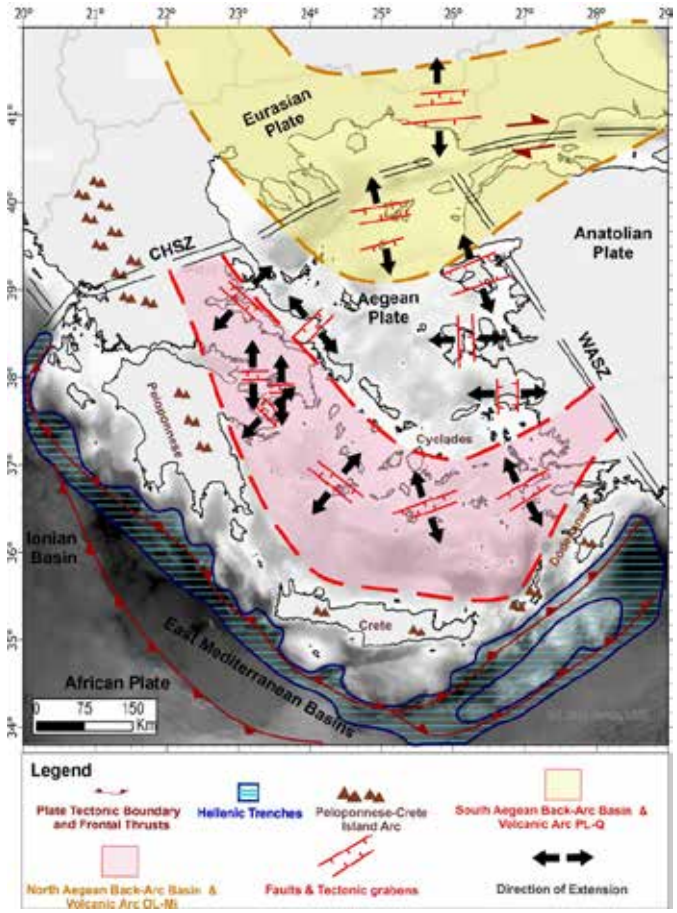


Fig. 1. Map showing the dominant tectonic trend and stress orientation in the 14 volcanic fields studied in this paper. The volcanism during Oligocene – early Miocene is observed within the molassic back arc basin of Rhodope – North Aegean Sea (No 11, No 12, No 13, No 14) whereas the Plio-Quaternary volcanism is observed in marginal marine basins along the northern border of the present back arc Cretan Basin (No 1, No 2, No 3, No 4, No 6). Exceptions are observed in the eastern Aegean islands (No 8, No 9) with N-S tectonic trend during the Middle – Late Miocene and W. Attica-Corinth (No 5, No 7) with E-W tectonic trend during Late Pliocene – Early Pleistocene.

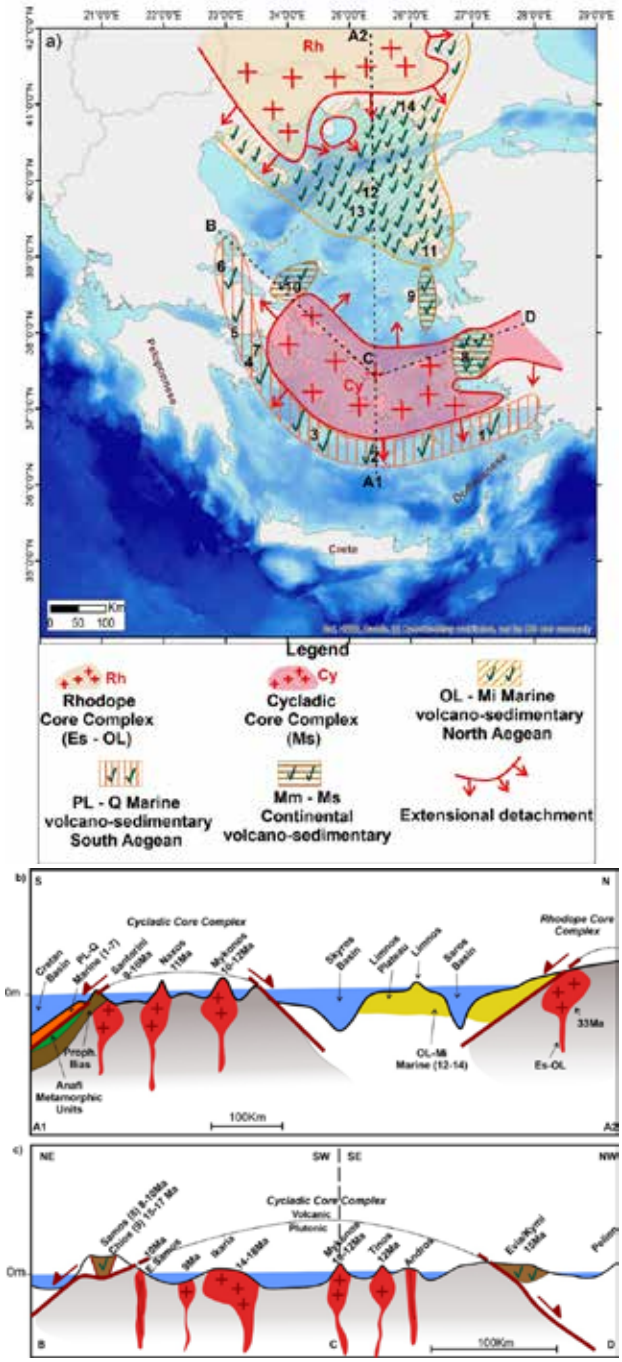


Fig. 2. a) The location of the 14 studied volcanic outcrops of the Hellenic arc within the Aegean tectonic structure. The volcanic outcrops are related to the Rhodope and Cycladic metamorphic core complexes with marine outcrops in the molassic basin of the North Aegean during Oligocene – Early Miocene and marine outcrops during Late Pliocene - Quaternary along the southern border of the Cycladic belt. Middle – Late Miocene continental outcrops are observed at the margins of the Cycladic core complex in Evia and Samos-Chios. b) N- S- schematic cross section A1-A2 through the Aegean Sea showing the volcanic outcrops in relation to the two metamorphic core complexes. Miocene granites of the Cyclades are indicated in Mykonos, Naxos and Santorini. c) Longitudinal schematic section B-C-D along the Cycladic core complex from Pelion – Northern Evia to Samos. The Miocene granitic rocks are shown within the core complex (Samos, Ikaria, Mykonos, Tinos) and the volcanic rocks within Miocene continental sedimentary basins at the two margins (Evia/Kymi and Samos, Chios).

Conclusions

In conclusion, almost all volcanic outcrops of the evolving Hellenic arc throughout the Late Eocene – Present are related to extensional tectonic graben structures associated with sedimentary basins, either marine or continental. Exceptions to this rule are very few, such as the Skyros andesite of Middle Miocene age about 15 Ma (Fytikas et al., 1980), which intruded the Alpine basement rocks of marbles, tectonically emplaced ophiolites and Cretaceous limestones. The role of the metamorphic core complexes in the distribution of the magmatic and volcanic products of the evolving Hellenic arc is documented and it is shown that the overall image of the upwelling magmas can be obtained only by combining the plutonic with the volcanic products.

References

Papanikolaou, D., Nomikou, P. & Lambridou, D. 2024. Tectonic grabens and volcanism in the Aegean, Greece. Geological Society of London, Special Publications, accepted.

17th INTERNATIONAL CONGRESS
of the Geological Society of Greece

BULLETIN OF THE GEOLOGICAL SOCIETY OF GREECE, SP. PUBL.

EXTENDED ABSTRACT 248

The influence of stratigraphy for the generation of surface evidence of liquefaction phenomena; case study Piniada, Greece

Papathanassiou G.[1], Valkaniotis S.[1], Taftsoglou M.[2]
(1) School of Geology, Aristotle University of Thessaloniki, Greece, gpapatha@geo.auth.gr
(2) Department of Earth Science, University of Ferrara, Italy

Introduction / Background

The present study focuses on the assessment of liquefaction potential in an area where numerous liquefaction phenomena were triggered by the 2021 Damasi, Greece, earthquake. The liquefaction features were reported during a field survey conducted few hours after the event along the Piniada Valley (Papathanassiou et al. 2022). They were classified as i) sand craters, as singular features as well as aligned ones, ii) ground fissures, from where a mixture of water and fine sandy and silty material was ejected, and iii) lateral spreading phenomena. According to eyewitnesses, the phenomena occurred during the March 3rd mainshock, locally caused mixed fluid fountaining as high as 1 m from the topographic surface. The total area covered by the ejected material (sand blow) at Piniada Valley was estimated as 0.0325 km^2, approximately 0.5% of the zone that is delimited by the village Piniada, to the north, and the present-day river channel of river Pinios, to the south (Papathanassiou et al. 2022).

This area is covered by Holocene sediments deposited along the meandering fluvial system of Pinios. The characteristic evolution of Pinios River dictates the depositional process of the sediments and contributed to the lateral and vertical heterogeneity of the surficial soil material. That was clearly shown during the 2021 event since liquefaction phenomena preferred to concentrate in specific location forming clusters of liquefaction-induced ground disruption such as sand boils, craters and ground fissures (Valkaniotis et al. 2024). In addition, it is highlighted that within a short distance, the severity of ejecta was totally different.

Methodology

For the purposes of this research, we investigated the role of the stratification of soil deposits for the generation (or not) of liquefaction-induced surface evidence and to the relevant ejecta severity. In order to achieve this, we used data derived by six CPTu tests conducted on an area where liquefaction phenomena were mapped. The liquefaction potential at each site was estimated following the method proposed by Hutabarat and Bray (2022), who concluded that the layer stratification can lead to not producing ejecta.

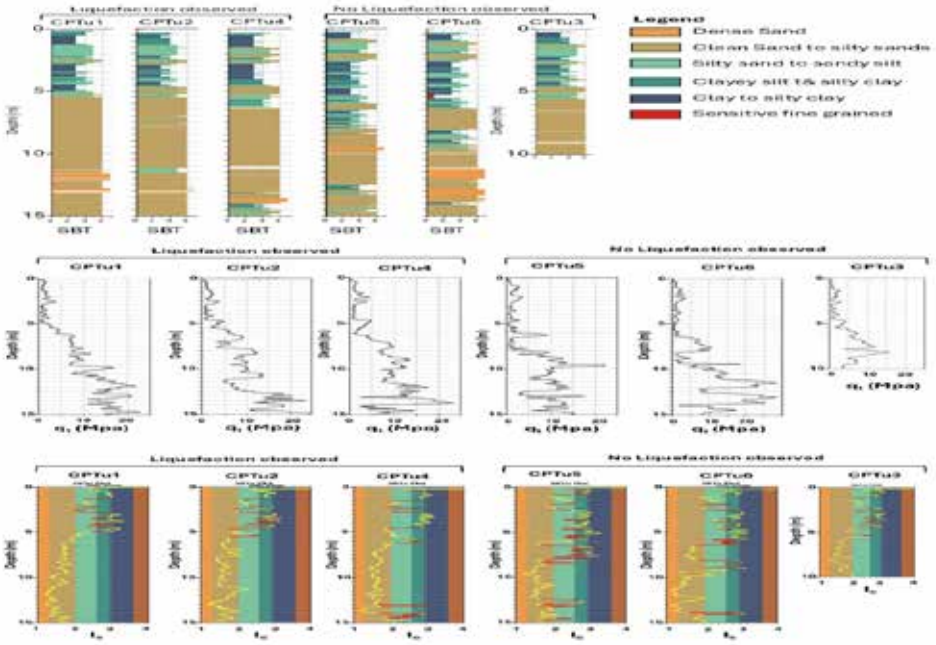


Figure 1. Soil stratigraphy of investigated sites, classified as liquefaction and non-liquefaction ones (Papathanassiou et al. 2025)

Thus, they developed a methodology aiming to address the prediction of the liquefaction-induced ejecta severity by quantifying two new factors: the liquefaction ejecta demand (L_D) and the crust layer resistance (C_R). The former considers the soil layer beneath the crust layer that may contribute to ejecta production and captures the hydraulic conductivity contrast, while the latter one (C_R) is related to the non-liquefiable crust layer that prevents liquefied material to eject and is estimated by taking into account the shear strength and thickness of this surficial stratum. According to Hutabarat and Bray (2022), this new method considers the system response of the soil column and captures the liquefaction-induced upward seepage that can erode the crust layer resulting in the generation of ejecta.

Conclusions

The outcome arisen by our study is that partially or highly stratified soil deposits are not expected to generate artesian flow pressure capable of producing liquefaction surface evidence, i.e. ejecta. This is due to the fact that i) the thickness of liquefiable sand-like layers is usually too small to produce large value of excess hydraulic head h_{exc}, while ii) in case this happens, the interbedded low-k_v soil layers impede the upward seepage. On the other hand, soil deposits where thick continuous sand-like material is encountered, are expected to produce excess hydraulic head that can lead the soil-water mixture onto the surface, i.e., ejecta. It is pointed out that this type of soil deposit can produce ejecta even when the thickness of the crust layer is larger than 4 m.

Acknowledgements

This study was financially supported by the Research Committee of Aristotle University of Thessaloniki. We would like to thank Dr. John Ioannidis for providing the software CLiq 3.0, the GEOT.ER. DIDASKALOU S.P. for conducting the in-situ tests (CPTu), the residents of Piniada village for their contribution and support, and especially Themistoklis Raptis and Christos Giannakos for permitting access to their properties during the geotechnical and geophysical surveys.

References

Hutabarat D, Bray JD (2022) Estimating the severity of liquefaction ejecta using the cone penetration test. J Geotech Geoenviron Eng 148(3):04021195. https://doi.org/10.1061/(ASCE)GT.1943-5606.0002744

Papathanassiou G, Valkaniotis S, Ganas A, Stampolidis A, Rapti D, Caputo R (2022) Floodplain evolution and its influence on liquefaction clustering: the case study of March 2021 Thessaly, Greece, seismic sequence. Eng Geol 298:106542. https://doi.org/10.1016/j.enggeo.2022.106542

Papathanassiou G., Fikos Il., Valkaniotis S., Stampolidis Al., Rapti D., Taftsoglou M., Caputo R. (2025). Response of stratified soil deposits to the severity of liquefaction phenomena: the Piniada Valley, Greece, case study, Bulletin of Engineering Geology and the Environment, under review

Valkaniotis, S., Rapti, D., Taftsoglou, M., Papathanassiou G., Caputo R. (2024). Geomorphological mapping for liquefaction likelihood: the Piniada Valley case study (central Greece). Bull Earthquake Eng 22, 5451–5474 (2024). https://doi.org/10.1007/s10518-024-01993-y

17th INTERNATIONAL CONGRESS of the Geological Society of Greece

BULLETIN OF THE GEOLOGICAL SOCIETY OF GREECE, SP. PUBL.

EXTENDED ABSTRACT 249

Monitoring the Santorini Volcano for 3 decades (1995-2025) by ISMOSAV and its role for the early detection of the 2011-2012 and 2024-2025 intra-caldera unrests

C. Papazachos[1], G. Vougioukalakis[3], S. Bitharis[2], Ch. Pikridas[2], M. Foumelis[1], Ch. Ventouzi[1], Ch. Kkallas[1], E. Karagianni[1], D. Vamvakaris[1], and E. Papageorgiou[1]

(1) Aristotle University of Thessaloniki, School of Geology, Thessaloniki, Greece (kpapaza@geo.auth.gr)

(2) Aristotle University of Thessaloniki, School of Rural and Surveying Engineering, Thessaloniki, Greece

(3) Institute for the Study and Monitoring of Santorini Volcano, Santorini, Greece

Introduction

The Institute for the Study and Monitoring of Santorini Volcano (ISMOSAV) was established in 1995 as a non-profit entity, with the main purpose of continuing the operation of the Volcanological Observatory and the volcano monitoring networks (seismological, geodetic, geophysical and geochemical) in 1993 in the framework of a European research program. A secondary objective of ISMOSAV was to promote volcanological research in Santorini, contributing significantly to the improved assessment of volcanic hazard and improving the ability to predict any volcanic activity or unrest in a timely manner. In this way, ISMOSAV has filled the gap left by the lack of a public body in Greece (e.g. research institute, etc.) that is responsible for the study and management of volcanic hazard, striving to protect Santorini by maintaining a reliable monitoring system that increases the likelihood of early warning of the volcano's reactivation, while also refuting, when necessary, any unfounded rumors and/or speculation. As a result, over the past 30 years and mainly with the support of the island's local authorities, ISMOSAV has managed to overcome several problems related to the lack of permanent research infrastructure on the island, maintaining and upgrading installed networks, replacing obsolete equipment, and processing real-time and near-real time information.

We present information on the early detection of the 2011-2012 and 2024-2025 volcano-tectonic intra-caldera unrests in Santorini. The presented results verify the critical role of ISMOSAV for the identification of these unrests, as well as on the measures that were taken to handle them. Moreover, they strongly suggest the need to establish the first permanent Volcanological Observatory on the island, operated by a local or other state authority, that will rely on and "assimilate" the existing ISMOSAV infrastructure, as well as monitoring sensors operated by other institutes, allowing to continue and expand on the ISMOSAV's 30-year legacy.

Data and Analysis

During the first 15 years of operation, ISMOSAV mainly relied on monitoring microseismicity to assess volcanic activity. This was mainly performed in collaboration with the Seismological Station of the Aristotle University of Thessaloniki (AUTh), gradually evolving and improving on the initial network of 5 analogue seismological stations. The recordings of the first analogue seismological network, initially recorded on paper in a local acquisition facility in Profitis Ilias, where later locally digitized and transmitted via the internet to AUTh. Until 2010 (Figures 1) these data showed continuous but relatively low seismic activity, mainly in the area of the submarine volcano of Koloumbo, as well as in several tectonic faults to the north and northeast of Santorini (e.g., an **M**5.1 sequence in June 2009), but also along the active tectonic line Koloumbos-Anydro-Amorgos area (e.g., Dimitriadis et al., 2005). These results, which showed little variability between 1995 and 2010, were in agreement with the findings of local seismological networks periodically installed on the island, as well as in the broader Santorini area (e.g. Bohnhoff et al., 2006; Dimitriadis et al., 2009).

As a result of this monitoring, ISMOSAV was able to detect the 2011-2012 volcanic unrest as early as February 2011. Figure (2) depicts the very early intra-caldera seismicity distribution, as presented in a confidential report submitted to the Earthquake Planning and Protection Organization in March 2011. From

this map, it was evident that the seismic activity began in January 2011 on the NE coast of Nea Kameni and expanded towards the NE (and less towards the SW) in February, continuing both to the northeast (Firostefani-Imerovigli) and southwest (Palaia-Nea Kameni area) in March 2011. From these early results it was evident that the activity was mainly concentrated at depths of 2-6 km, with shallower depths (2-4 km) in Palaia and Nea Kameni, increasing towards the mainland (Firostefani). The small hypocentral errors (0.7 km and 1.4 km for the horizontal and vertical coordinates) showed that this unusual seismicity was a reliable feature. This unrest was further supported by the temporal evolution of this low magnitude seismicity (Figure 3), that showed clear indications of significant temporal variations, increasing in late February 2011, as well as independent data (sea temperature increase, sea level changes, etc.).

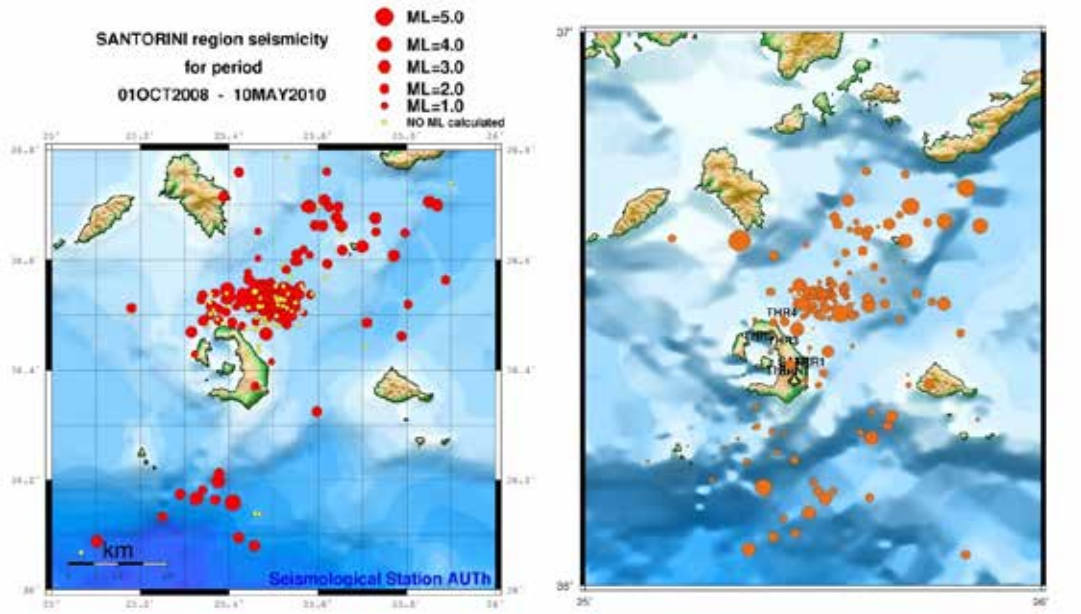


Figure 1. Seismic activity in the volcanic center of Santorini between October 2008 and May 2010 (left) and January 2006 and October 2008 (right).

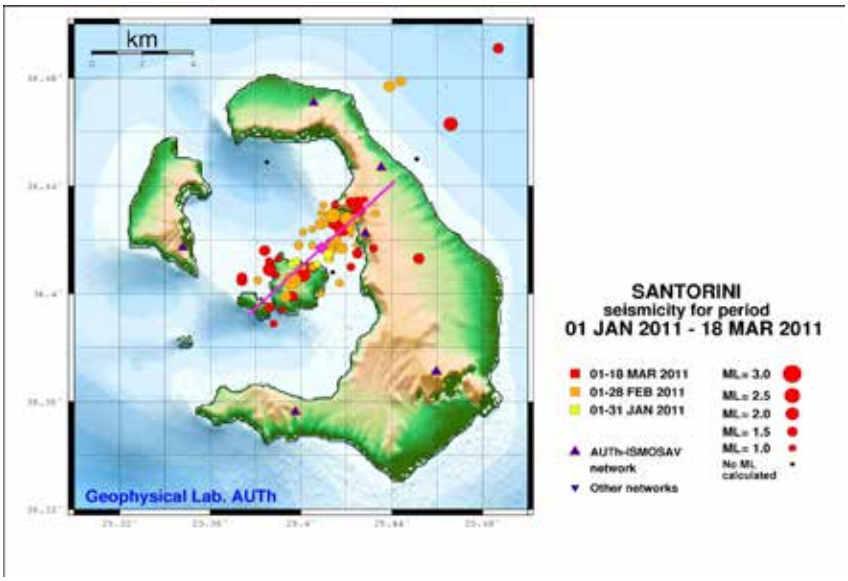


Figure 2. Seismic activity in the volcanic center of Santorini between January 9 and March 18, 2011, as originally reported in March 2011.

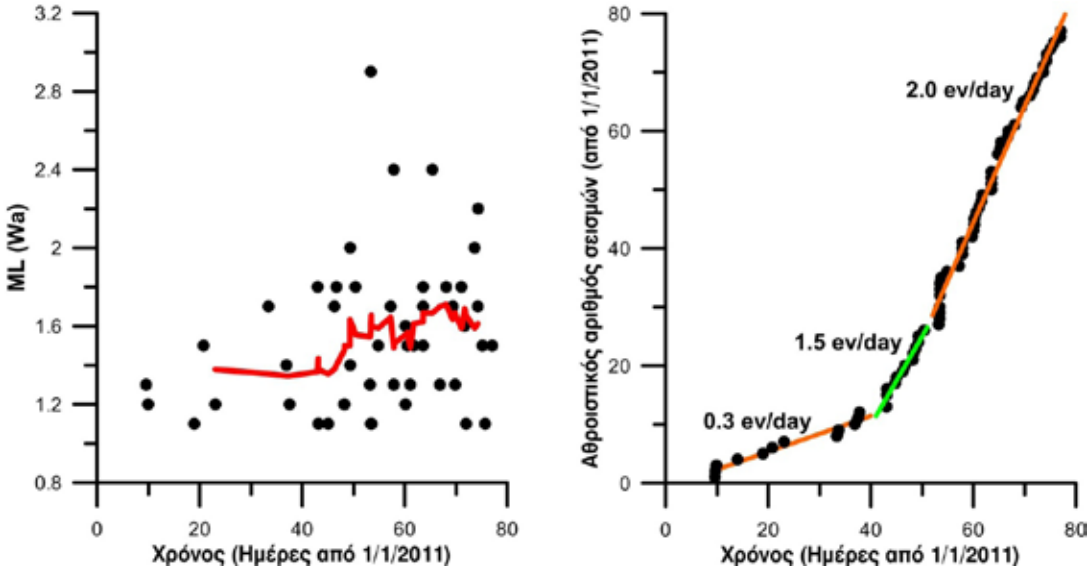


Figure 3. Temporal variation of the local earthquake magnitude for events with M_L>1.1 (left) and cumulative number of earthquakes (right) for the seismic sequence shown in Fig. 2. The moving average is shown by a red line for the left figure, while colored lines depict the rate (number of events per day) in the right figure.

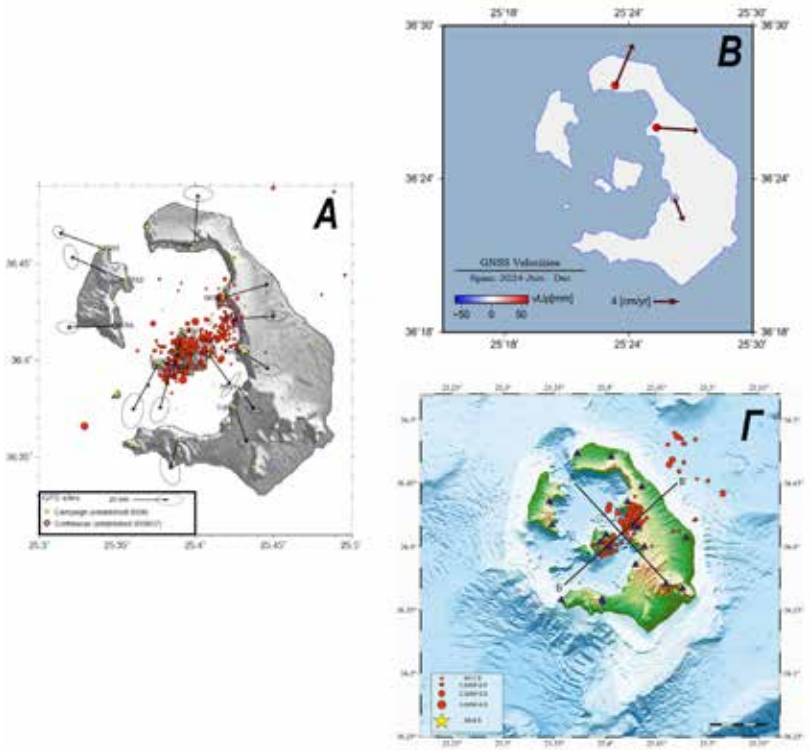


Figure 4. A) Earthquakes (red circles) in the Kameni fault and related displacements from GPS data in the Santorini caldera during the 2011–2012 seismic–volcanic crisis (Newman et al., 2012). B) Relative movements in the Santorini caldera from late June to early December 2024 for the three real-time GPS stations of ISMOSAV. Γ) Best located epicenters of earthquakes with magnitude M_L≥1.1 in the Santorini caldera during the second half of 2024 (mid-September-19 Dec. 2024).

While the 2011-2012 unrest was later extensively studied using a combination of earthquake, GPS, InSAR and geochemical data (e.g. Newman et al., 2012; Foumelis et al., 2013; Parks et al., 2012, 2013, 2015; Saltogianni et al., 2014; Tassi et al., 2013, Papadimitriou et al., 2015 among others), and while a large number of instruments were additionally installed during the unrest, within a few years the monitoring of the island returned to its previous state, with a small number of permanent seismographs and a single GPS station operating in real-time after 2016. To handle this situation, ISMOSAV installed three new GNSS receivers along with the corresponding ancillary equipment in October 2919, establishing a new modern geodetic network to monitor changes in the Earth's relief caused by possible volcanic activity. Furthermore, it continued to monitor seismicity, improving the network coverage and quality. Finally, it also relied on the use of the SNAPPING PSI operational service for InSAR data to further monitor surface deformation. This platform is integrated into ESA's Geohazards Exploitation Platform (GEP) and has been used for automated updates at regular intervals, providing an additional monitoring option for the volcano.

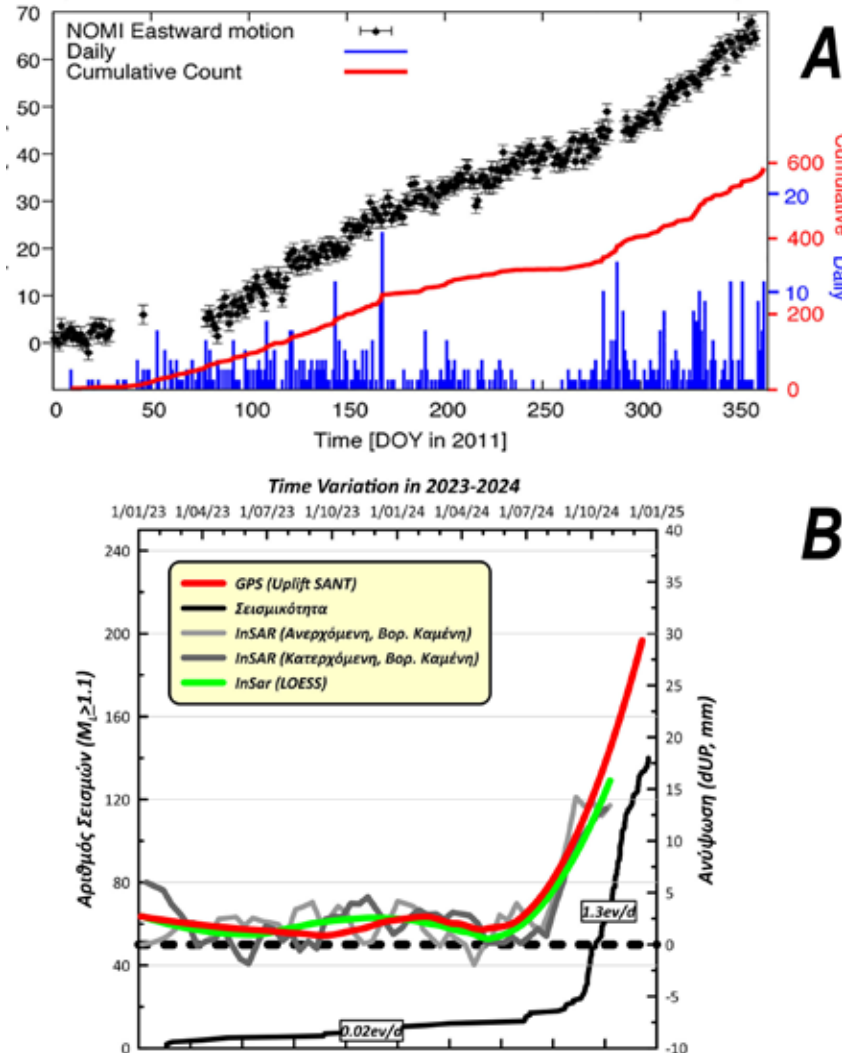


Figure 5. A) Eastward motion of GPS station NOMI station (black circles) and seismicity at the Santorini caldera from the 2011-2012 earthquake-volcanic crisis (Newman et al., 2012). B) Relative elevations at GNSS station SANT station and the northern segment of Nea Kameni (InSAR data) and seismicity rate at the Santorini caldera since January 2023, as originally reported by ISMOSAV. The island's caldera uplift is evident from June 2024 and seismicity has increased by almost 2 orders of magnitude during the period September-December 2024.

This persistent and systematic monitoring has allowed ISMOSAV to detect and inform the Greek government (Civil Protection, Earthquake Planning and Protection Organization) on January 2, 2025, for the on-going (at the time) intra-caldera unrest, as this was identified by seismicity, GNSS and InSAR data (Figures 4 and 5). More specifically, the ISMOSAV network detected since mid-September 2024 an anomalous seismic activity on the central fault of Kameni (Figure 4Γ). Analysis of geodetic data (Figure 4B) confirmed that this activity was accompanied by strong deformation, which started earlier (end of June 2024). This activity was almost identical to the 2011-2012 unrest, where more than 15 million cubic meters of magma rose to a depth of ~3-4 km, north of Nea Kameni. As shown by Figure 4, the displacements detected in northern Santorini and the relative seismic activity from mid-September 2024 were almost identical to the corresponding 2011-12 activity. This was verified by Figure (5), which presents the variation of seismic activity and relative deformation from GPS and InSAR data, as well as its comparison with similar data from the 2011-2012 crisis. From these figures it became evident that from the end of June 2024 (for deformation) and from mid-September 2024 (for seismicity) an unrest very similar to the 2011-12 phenomenon was evolving in Santorini.

Discussion and Conclusions

It is worth noticing that the continuous (for more than 3 decades) monitoring of the Santorini volcano by ISMOSAV did not only lead to the identification of the important 2011-2012 and 2024-2025 unrests, which had a significant impact on the island, but also led to important developments in volcanic risk management in Greece. These developments involved the publication of the TALOS Civil Protection plan for volcanic hazard in Santorini, as well as the creation of a Permanent Scientific Committee for the monitoring of the Greek Volcanic Arc under the auspices of the Earthquake Planning and Protection Organization, both motivated and realized after the 2011-2012 unrest. It is evident that the recent 2024-2025 caldera unrest should also be used as a platform to further strengthen and support the development of the necessary volcanic hazard policy in Greece. As noted in the Jan 2, 2025, letter of ISMOSAV to the Civil Protection and EPPO, this can be realized by adopting several measures, such as:

a) Strengthening of the role of the Permanent Scientific Committee for the Monitoring of the Greek Volcanic Arc of EPPO by creating permanent working research groups, with appropriate support for the volcanic arc monitoring and evaluation.

B) The allocation of the necessary resources (financial and other) for the permanent improvement (upgrading) and densification of the monitoring networks in Santorini, to improve the scientific and operational response, especially if there is an adverse evolution of tecto-volcanic activity.

C) The review and refinement of the TALOS plan, especially with respect to other volcanic centers (Koloumbo), as well as regarding the possible actions that will be required for the residents and visitors of Santorini in case of unrest or eruption.

D) Establishment of a permanent Volcanological Observatory of Santorini supported by the state. This observatory, for which a suitable site has been already selected and allocated by the Municipality of Thera, could “assimilate” existing monitoring networks to provide continuous volcano monitoring and reliable assessment of the associated volcanic hazard and risk, especially in periods of unrest.

Acknowledgements

The authors would like to acknowledge the help of Geothira MAE, the Municipality of Thera, EPPO, Greek Civil Protection, as well as ISMOSAV members and Santorini locals for their continuous support during the 30+ years of Santorini volcano monitoring by ISMOSAV. We would also like to thank a) Metrica SA for the donation of 3 GNSS stations that are permanently installed on Santorini, b) the Research Committee of the Aristotle Univ. Thessaloniki for partly funding 4 wide-band seismological and 1 GNSS stations, that are also permanently installed on Santorini, c) the IRIS technical company operating in Santorini, for providing valuable assistance regarding the permanent ISMOSAV network maintenance during the last 10+ years.

References

Bohnhoff, M., Rische, M., Meier, T., Becker, D., Stavrakakis, G., Harjes, H., (2006). Microseismic activity in the Hellenic Volcanic Arc, Greece , with emphasis on the seismotectonic setting of the Santorini – Amorgos zone. Tectonophysics, 423, 17–33

Dimitriadis, I. M., Panagiotopoulos, D. G., Papazachos, C. B., Hatzidimitriou, P. M., Karagianni, E. E., & Kane, I. (2005). Recent seismic activity (1994-2002) of the Santorini volcano using data from local seismological network. In: Developments in Volcanology (Vol. 7, pp. 185-203), Elsevier.

Dimitriadis, I., Karagianni, E., Panagiotopoulos, D., Papazachos, C., Hatzidimitriou, P., Bohnhoff, M., ... & Meier, T., (2009). Seismicity and active tectonics at Coloumbo Reef (Aegean Sea, Greece): Monitoring an active volcano at Santorini Volcanic Center using a temporary seismic network. Tectonophysics, 465(1-4), 136-149.

Foumelis, M., Trasatti, E., Papageorgiou, E., Stramondo, S., & Parcharidis, I. (2013), Monitoring Santorini volcano (Greece) breathing from space, Geoph. J. Int., 193(1), 161-170, https://doi.org/10.1093/gji/ggs135

Newman, A.V., Stiros, S., Feng, L., Psimoulis, P., Moschas, F., Saltogianni, V., Jiang, Y., Papazachos, C., Panagiotopoulos, D., Karagianni, E., & Vamvakaris, D. (2012), Recent geodetic unrest at Santorini Caldera, Greece. Geophys. Res. Lett., 39, L06309.

Papadimitriou, P., Kapetanidis, V., Karakonstantis, A., Kaviris, G., Voulgaris, N., & Makropoulos, K. (2015). The Santorini Volcanic Complex: A detailed multi-parameter seismological approach with emphasis on the 2011–2012 unrest period. J. Geodyn., 85, 32-57, https://doi.org/10.1016/j.jog.2014.12.004

Parks, M. M., Biggs, J., England, P., Mather, T. A., Nomikou, P., Palamartchouk, K., ... & Zacharis, V. (2012), Evolution of Santorini Volcano dominated by episodic and rapid fluxes of melt from depth. Nature Geoscience, 5(10), 749-754.

Parks, M.M., S Caliro, G Chiodini, DM Pyle, TA Mather, K Berlo, M Edmonds, J Biggs, P Nomikou, & C Raptakis, (2013). Distinguishing contributions to diffuse CO2 emissions in volcanic areas from magmatic degassing and thermal decarbonation using soil gas 222Rn-δ13C systematics: application to Santorini volcano, Greece. Earth and Planetary Science Letters, 377-378, 180-190, https://doi.org/10.1016/j.epsl.2013.06.046

Parks, M. M., Moore, J. D., Papanikolaou, X., Biggs, J., Mather, T. A., Pyle, D. M., ... & Nomikou, P. (2015). From quiescence to unrest: 20 years of satellite geodetic measurements at Santorini volcano, Greece. J. Geoph. Res.: Solid Earth, 120(2), 1309-1328.

Saltogianni, V., Stiros, S.C., Newman, A.V., Flanagan, K., & Moschas, F (2014), Time-space modeling of the dynamics of Santorini volcano (Greece) during the 2011-2012 unrest, Journal of Geophysical Research, 119, 8517-8537, https://doi.org/10.1002/2014JB011409

Tassi, F., Vaselli, O., Papazachos, C.B., Giannini, L., Chiodini, G., Vougioukalakis, G.E., Karagianni, E., Vamvakaris, D., & Panagiotopoulos, D., (2013). Geochemical and isotopic changes in the fumarolic and submerged gas discharges during the 2011-2012 unrest at Santorini caldera (Greece). Bull. Volcanol., 75, 711, https://doi.org/10.1007/s00445-013-0711-8

17th INTERNATIONAL CONGRESS of the Geological Society of Greece

BULLETIN OF THE GEOLOGICAL SOCIETY OF GREECE, SP. PUBL.

EXTENDED ABSTRACT 250

Effects of boiling and seawater mixing on hyper-enrichment of antimony in active polymetallic seafloor massive sulfide hydrothermal diffusers at the Aegean Kolumbo volcano

Papoutsa A.[1], Kilias S.[1], Zegkinoglou N.[1], Pletsas V.[1], Avoukatou R.[1,] Nomikou P.[1], Polymenakou P. [2], Somogyi A.[3], Ahmad Q.[4]

(1) National and Kapodistrian University of Athens, Athens, Greece, angpapou@geol.uoa.gr
(2) Hellenic Centre for Marine Research, Heraklion Crete, Greece
(3) Synchrotron Soleil, Saint-Aubin, Gif-sur-Yvette, France
(4) Centre de Recherches Petrographiques et Geochimiques (CRPG), Universite de Lorraine, Nancy, France

Highlights

Coupled to magmatic degassing of metal (loid)- and volatile-rich fluids, boiling, and fluid-seawater mixing mechanisms are responsible for Sb hyper-enrichment in the Kolumbo SMS mineralization. Our results raise the possibility of (sub) seafloor Sb-rich mineralization at Kolumbo and other submarine volcanoes along the 500 km of the Hellenic Volcanic Arc.

Introduction / Background

Antimony (Sb) is a metalloid of Critical Raw Materials (CRMs) that are both of great economic importance for the EU and of high supply risk (European Commission, 2023). Therefore, its sustainable supply greatly depends on understanding the Sb-ore precipitation mechanisms, especially stibnite (Sb_2S_3), the worldwide major source of Sb. A target setting to secure sustainable access to CRMs, including Sb and related metal(loid)s (Au, Ag, Ga, Ge, Te), is sea-floor massive sulfide (SMS) deposits worldwide. Recent advances in understanding Sb solubility and transportation in hydrothermal ore-fluids on land, showed mainly aqueous species of thioantimonite ($H_2Sb_2S_4$) and hydroxothioantimonite [$Sb_2S_2(OH)_2$], while vein-type stibnite precipitation was controlled by: boiling-related solubility reduction of $H_2Sb_2S_4$, and subsequent cooling-induced solubility decrease of $Sb_2S_2(OH)_2$ (Yu *et al*., 2023). Recently, Kodera *et al.* (2024), and Kaufmann *et al.* (2024), have suggested that hydrothermal fluid temperature decrease has been the main mechanism for stibnite precipitation in vein-type epithermal deposits on land (Slovakia). However, whether these phenomena can cause Sb mineralization (i.e., stibnite and Sb-bearing sulfosalts) in submarine hydrothermal systems, remains incompletely known. To our knowledge only Dekov *et al*. (2022) have dealt with the physicochemical conditions of stibnite precipitation at the Daiyon-Yonaguni Knoll (Okinawa Trough) hydrothermal barite deposits, and suggested that precipitation at ~80◦C, low $\log_{10}a$ of $Sb_2S_4^{2-}$ and Eh<0), from sub-seafloor phase separated fluids. Driven by the scarce knowledge on Sb enrichment (i.e., stibnite, Sb-sulfosalts) processes at seafloor hydrothermal conditions, we investigated the Sb-rich, polymetallic, SMS mineralization of modern CO_2-degassing, SMS diffuser vents, of Kolumbo submarine volcano, Hellenic volcanic arc [hereafter "Kolumbo CO_2 diffusers" ("KCO_2Ds")]. These rare actively forming Sb- and Au-rich polymetallic (As, Ag, Tl, Pb, Zn, Hg) SMS SMS deposits comprising pyrite, marcasite, sphalerite, chalcopyrite, galena, Pb-Sb sulfosalts, stibnite, orpiment/realgar and barite (Kilias *et al*., 2013). The KCO_2Ds display a distinct mineral zonation, grading from a pyrite-dominated, barite-polymetallic sulfide inner part (ISSC), through a thin sphalerite-dominated sulfide zone, to a barite-sulfide outer layer, and finally to an orpiment-dominated exterior (OAsL) locally covered by $Fe3^+$-(hydrated)-oxyhydroxides (SFeC) (Kilias *et al*. 2013). Importantly, pyrite occurs erratically within, and throughout, the KCO_2Ds, and occurs as compositionally zoned colloform pyrite 1 (Py1) that is overgrown by aggregated anhedral pyrite 2 (Py2), and coarse-grained euhedral pyrite 3 (Py3) (see Fig. 1 and Kilias *et al*., 2022). Samples came from KCO_2Ds that vent nearly pure CO_2 boiling fluids at 265°C (Kilias *et al*., 2013; Zegkinoglou *et al*., 2023). Hence, the Kolumbo system represents an optimum natural laboratory to decipher the effect of boiling and cooling due to fluid-seawater mixing, on stibnite composition, and Sb hyper-enrichment associated with SMS mineralization.

Materials and Methods

- **Sampling**

Sulfide samples were retrieved with Remotely Operated Vehicles (ROVs) from the northern part of the Kolumbo crater. Detailed descriptions on sampling and preparation methods are presented in Kilias *et al*. (2013) and in HCMR's "SeaBioTech Report 2013".

- **Optical microscopy and Mineral Analyses**

All samples were petrographically examined via transmitted and reflected light microscopy. The quantitative analyses of the main sulfide-sulfosalt phases were conducted by Energy Dispersive Spectroscopy (EPMA-EDS) using a JEOL JXA-8600 Superprobe. The S contents were determined by EPMA analysis. Trace element analysis was performed by laser ablation-inductively coupled plasma-mass spectrometry (LA-ICP-MS) using a New Wave Research-ESI 213 nm laser unit attached to a ThermoScientific ICAP-Q quadrupole ICP-MS. Analytical precision and accuracy were monitored by the repeated analysis of FeS-1 and MASS-1 (United States Geological Survey-USGS). Trace element concentrations were processed by the Iolite software package (https://iolite-software.com).

- **Raman spectroscopy**

Raman spectroscopy was performed using a Renishaw inVia Raman confocal microscope. Spectra were obtained using the 785 nm laser and a grating of 1200 groves per mm, with a power range between 0.5 and 0.05 mW, due to the varying stability and fluorescence of the analysis spots. Samples were exposed to the laser through a long-focal distance, 50X objective lens with 0.55 numerical aperture, and with the measured spectral range extended from 100 to 3200 cm-1. The obtained spectra were then processed by the WiRE software for Windows. Background noise was reduced by the subtraction of a polynomial baseline, and cosmic ray removal corrections were performed for all spectra.

- **Synchrotron X-ray fluorescence (μ-XRF)**

Polished thin sections of selected representative samples were analyzed using scanning μ-XRF at the Nanoscopium hard X-ray CX3-scanning spectromicroscopy beamline of Synchrotron Soleil (France). A monochromatic X-ray beam, with an energy range of 11.8–20 keV, was focused on the sample area using a Kirkpatrick–Baez nano-focusing mirror. To achieve micrometer resolution in elemental mapping of mm²-sized sample areas, the fast-continuous scanning (FLYSCAN) technique was employed.

Results

- **Mineralogy, textures and paragenesis of stibnite (Sb_2S_3) and Sb-sulfosalts**

Antimony phases include thin, needle-like stibnite crystals mainly in the OBL (Fig. 1A) and OAsL and individual Sb-bearing sulfosalt phases, such as semseyite and meneghinite, throughout the KCO_2Ds (see below and Kilias *et al*., 2022). Sb-bearing sulfosalts, relatively abundant in the ISSC, mostly occur as dendritic fishbone-like crystals (Figs. 1B, C), as intergrowths with barite rimming pyrite successions (Fig. 1D), and as overgrowths on Py1 (Fig. 1E). Sb-bearing sulfosalts may also occur as colloform-like phases (Fig. 1F) rimming As-sulphides, such as orpiment. Replacement of Sb-bearing sulfosalts by orpiment has also been observed, resulting in a porous and inclusion-rich (Pb-Sb sus) As-sulphide. The As-sulfide overgrowth precipitates from hydrothermal solution, indicating boiling-induced Coupled Dissolution Reprecipitation (CDR) processes (Fig. 1G). Moreover, a progressive transition of Pb-Sb sulfosalts to orpiment-like As-sulfides resembling frutexites-like microstomatolites with branching and outgrowths formed by cyclic growth has also been detected. The alternating banding consists of Pb-Sb sulfosalts progressively transitioning to orpiment-like As-sulphides (Fig. 1H). Rare stibnite occurs as independent needle-like crystals in open space, as inclusions in prismatic barite, or as intergrowths with Pb-Sb sulfosalts and orpiment of the OAsL (Figs. 1I, J, K respectively). Stibnite has also been found as a tube-like core in orpiment filamentous structures (Fig. 1L).

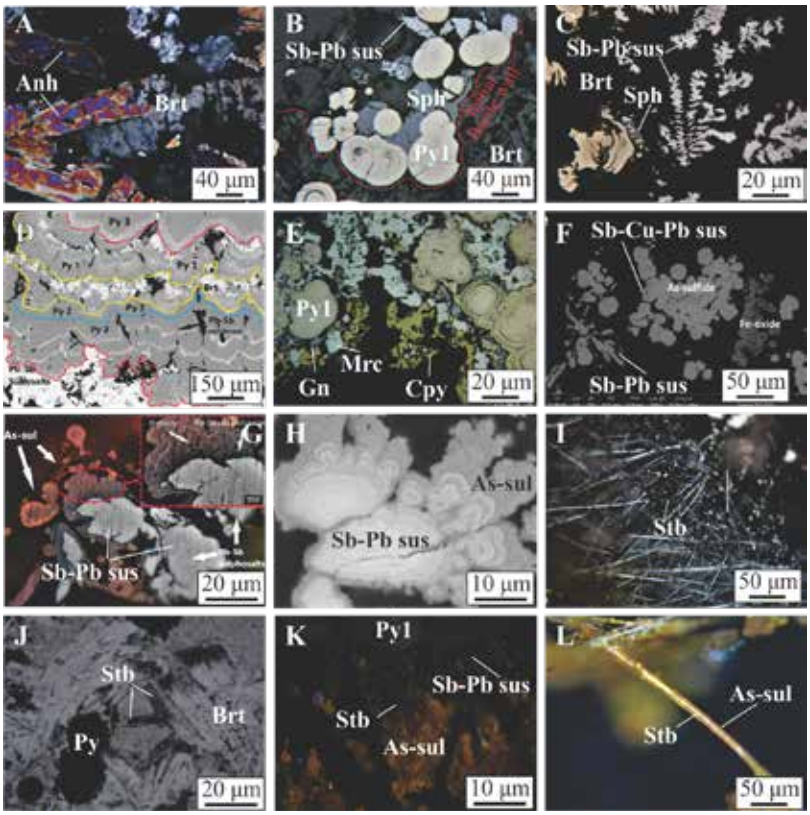


Figure 1. Reflected photomicrographs (A, B, C, F, I, G, K, L) and BSE images (D, G, H), showing textural features of stibnite, semseyite and meneghinite and other KCO2Ds minerals. (A) Replacement of anhydrite (Anh) by barite. (Brt) Colloform Py1 intergrown with sphalerite (Sph) and semseyire (Pb-Sb sus) on pore space of the barite "mound". (C) Dendritic texture of semseyite, with pyrite and sphalerite on barite substrate. (D) Repeated cycles (separated by colored dotted lines) of successive and subparallel colloform-crustiform micronscale bands of Py1, 2, and 3, interbanded with barite; semseyite is intergrown with barite (lower left). (E) Chalcopyrite lining channel edge, with marcasite, galena and Py1; (F) Colloform meneghinite (Sb-Cu-Pb sus) intergrown with As-sulfides, associated with semseyite and Fe oxyhydroxides. (G) Semseyite (Pb-Sb sus) sulfosalt partially replaced by orpiment (As-sul) with trace metal(loid)-rich Pb-Sb sulfosalt inclusions, indicating CDR processes; (H) Frutexites-like stromatolitic structure showing a CDR reaction of fine Pb-Sb sulfosalt laminae alternating with, and gradually replaced by As-sulfide laminae. (I) Needle-like, radiating stibnite (Stb) crystals, filling cavities and covering barite surface. (J) Radial and random needle-like stibnite crystals within transparent crystals of barite; (K) Intergrowth of barite, pyrite 1, semseyite (Sb-Pb sus), stibnite (Stb) and orpiment (As-sul). (L) Core-shell filamentous structure including core of stibnite and shell of orpiment.

- **Spectral characterization of Sb-bearing phases**

The majority of the obtained Raman spectra indicate that the dominant Sb-bearing phases in the KCO_2Ds are stibnite (Sb_2S_3) and semseyite ($Pb_9Sb_8S_{21}$). Stibnite exhibits sharp, characteristic Raman peaks, with decreasing intensity, at 312, 283, 240, 192, 156 and 129 cm^{-1}. Semseyite, presents a dominant Raman peak at 217 cm-1, with a broad shoulder at 176 cm^{-1}. Raman peaks of lesser intensity are present at 335, and 120 cm^{-1}. A less abundant, Sb-bearing sulfosalt that has been identified through Raman spectroscopy is meneghinite ($Pb_{13}CuSb_7S_{24}$), presenting a dominant Raman peak at 212 cm^{-1} with a shouldering peak at 248 cm^{-1}, and a secondary but intense peak at 328 cm^{-1}.

- **Mineral chemistry and Sb enrichment (LA-ICP-MS)**

LA-ICP-MS spot analyses show a unique enrichment in Sb in all the mineral phases present at the KCO_2Ds (Fig. 2). Galena exhibits a strong Sb enrichment with maximum concentration of 98000 ppm. Py1 is the most common sulfide mineral in the system and displays high Sb concentrations, up to 111192 ppm. The concentration of Sb in Py2 reaches up to 36100 ppm, whereas Py3 is the most depleted generation of pyrite, with maximum concentration of 79000. Sphalerite is also highly enriched in Sb concentration, reaching up to 98000 ppm. Marcasite and chalcopyrite are moderately enriched in Sb ranging up to 7730 ppm, and 16100 ppm, respectively. Lastly, the Sb concentration in orpiment is measured up to 16100 ppm.

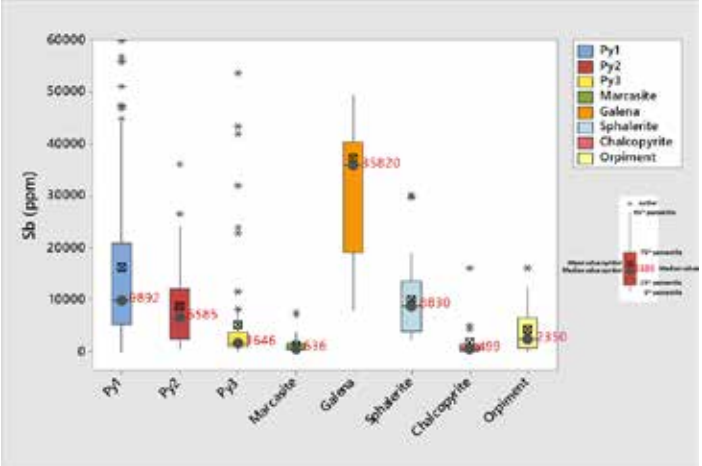


Figure 2. Box and whisker plots of Sb concentration in sulfide minerals present at the KCO2Ds analyzed by LA-ICP-MS. Mean values (black squares) are calculated using the entire dataset (including outliers), and might plot outside the respective box, whereas median values (gray dots, red numbers) are based solely on data within the box (25th to 75th percentile).

To better understand the sequestration of trace metals and especially Sb, in the main mineral phases, LA-ICP-MS depth profiles were thoroughly examined. The smooth parts of LA-ICP-MS time resolved spectra indicate structurally bound metal(loid)s while the irregular and spiky parts of the profiles signify the presence of micro/nanoparticles in the structure (George *et al*., 2019). The LA-ICP-MS depth profiles in stibnite display irregular parts for most trace elements (Zn, Ag, Au, Tl) implying that these elements are incorporated as nanoparticles in the structure of stibnite (Fig. 3A, 3B). The depth profiles for Sb in pyrite exhibit both smooth and spiky parts indicating that Sb precipitates both as nanoparticles along with other metal(loid)s and as lattice bounded in the structure of pyrite (Fig. 3C). Pb-Sb sulfosalts depth profiles appear spiky with respect to As, Cu, Ag, Zn and Au suggesting the incorporation of those metal(loid)s as inclusions (Fig. 3D).

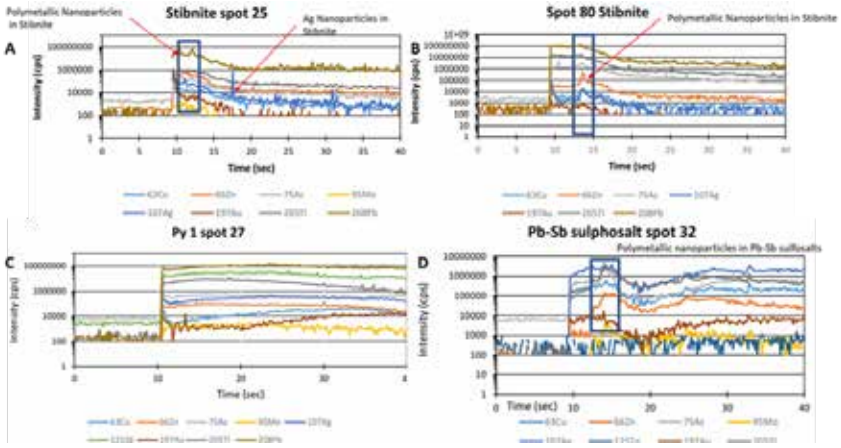


Figure 3. Time resolved spectra of metal(loid)s in pyrite and stibnite. A., B. LA-ICP-MS irregular depth profiles in stibnite. Note the presence of spikes in the same wavenumber for different trace elements, indicating the existence of polymetallic inclusions in stibnite. C. Smooth Sb LA-ICP-MS depth profile in Py1, signifying the sequestration of antimony in solid solution. D. Spiky depth profiles in Pb-Sb sulfosalts exhibiting polymetallic inclusions.

- **Synchrotron X□ray fluorescence (μ□XRF)**

Multi-scale length elemental maps on Py1 demonstrate that metal(loids) do not exhibit a homogeneous distribution, but rather a concentric chemical zoning. Elements such as Fe and Pb exhibit oscillatory chemical zoning at the inner part of the pyrite (Fig. 4A, E), whereas Zn, Cu, and As tend to enrich the outer zones of the crystal (Fig. 4B, C, F). Antimony, on the other hand (Fig. 4D) demonstrates oscillatory zoning rimwards. Core-to-rim traverse on Py1 indicates that the Sb, Pb and Tl concentrations have been affected predominately by boiling processes (Fig, 5A). The spatial distribution of Sb/Pb ratios with values less than 0.5, which are characteristic of boiling-induced precipitation (Falkenberg *et al*.,

2021) demonstrate an alternation of boiling-dominated, and likely seawater mixing-dominated regions (Fig. 5B), that coincide with the oscillatory chemical zoning of Sb (Fig, 4D).

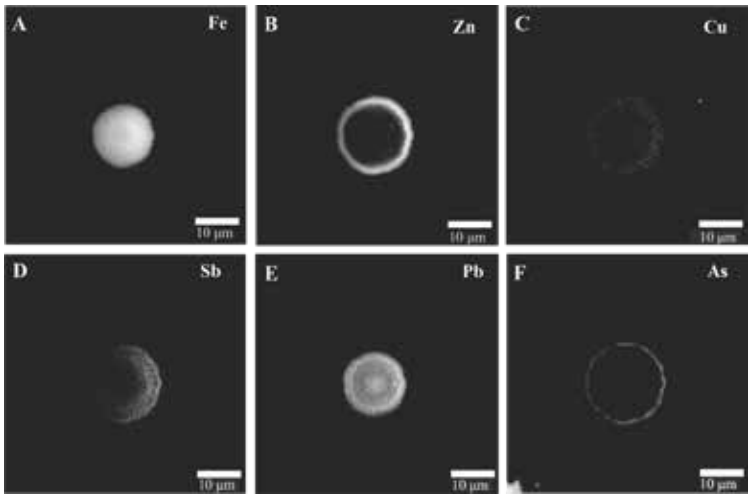


Figure 4. Synchrotron μ-XRF elemental maps of spheroidal pyrite from KCO_2Ds, illustrating the spatial distribution patterns of A) Fe, B) Zn, C) Cu, D) Sb, E) Pb, F) As.

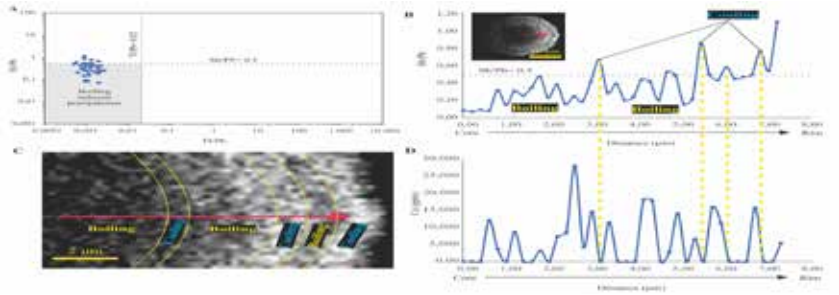


Figure 5. Synchrotron-obtained data from Py1 showing: (A) Sb/Pb vs. Tl/Pb (modified from Falkenberg et al., 2021) demonstrating boiling-induced precipitation, (B) a core-to-rim traverse in Py1 showing the alternation of boiling-dominated and likely non-boiling or fluid-seawater mixing (cooling) dominated regions

Discussion and Conclusions

Kolumbo is a submarine arc volcano that hosts a complex and dynamic magmatic-hydrothermal system with constantly evolving fluid chemistry through space and time (Zegkinoglou *et al.*, 2023; Patten *et al.*, 2024; Hector *et al.*, 2024. Geochemical and micro-textural evidence shows that the Kolumbo SMS mineralization has been formed by fluids undergoing multiple recurrent intense boiling and/or flashing or gentle and/or non-boiling events (Fig. 5); moreover, the high contents of Sb, along with As, Hg, and Tl in the KCO_2 Ds (Figs. 2 and 3) support boiling and zone refining processes, as these metal(loid)s are easily mobilized in the vapor phase (see Zegkinoglou *et al.*, 2023). The Kolumbo pyrite has recorded critical information related to boiling vs. non-boiling: The features displayed by Py1(±Py2) that occurs erratically distributed within the KCO_2Ds, reflect multiple episodes of vigorous boiling to flashing, whereas Py2 that occurs mostly in the inner KCO_2D parts, it is spatially concurrent with chalcopyrite lining narrow channels (Fig. 1E), has features that suggest precipitation from hot (>250°C) gently boiling to non-boiling fluids (Zegkinoglou *et al.*, 2023). Thus, pyrite can provide key information for the interpretation of associated Sb mineralization (stibnite, semseyite and meneghinite) forming conditions, and conditions of Sb incorporation in pyrite, during the 3-stage KCO_2Ds growth model (Berkenbosch *et al.*, 2012; Zegkinoglou *et al.*, 2023; Roman *et al.*, 2019; Falkenberg *et al.*, 2021). Vigorous boiling events have coincided with periods of intense magmatic degassing of volatiles and metal(loid)s (i.e., Cu, Au, Sb), and increase of the proportion of magmatic fluids into the Kolumbo hydrothermal system. In addition, the evolving Kolumbo magmatic-hydrothermal system could include periods of magmatic quiescence that results in a seawater-dominated hydrothermal fluid (Zegkinoglou *et al.*, 2023; Hector *et al.*, 2024).

At Kolumbo, textural (Fig. 1) and chemical variations of multiple pyrite (colloform, microcrystalline, crustiform banding, euhedral), chalcopyrite (linings), Pb-Sb sulfosalt (semseyite, meneghinite) (dendrites, colloform and subhedral crystals)

generations, are indicative for sulfide-sulfosalt precipitation during repeated cycles of progression from a young low-temperature <150–200°C) seawater-dominated, to a more "refined" system with a higher temperature (up to 300-350°C) upwelling of phase separated liquid-, or vapor-, dominated fluid flux and less seawater mixing (Falkenberg *et al.*, 2021). The close association of dendritic semseyite ($Pb_9Sb_8S_{21}$) (Fig. 1C), with adjacent concentrically layered colloform Py1, and anhedral sphalerite, occupying pore space of the Stage 1 barite substrate (Fig. 1B), suggests an early semseyite formation due to rapid precipitation and undercooling at temperatures <150–200°C, due to mixing of upwelling boiling, liquid- or vapor-dominated fluids, with seawater, in seawater-dominated inner KCO_2Ds (ISSC) zones (Berkenbosch *et al*., 2012; Falkenberg *et al*., 2021). In addition, semseyite that is interbanded with barite layers associated with colloform-crustiform banded Py1 (Fig. 1D), suggests that semseyite was synchronous with the development of barite and Py banding, and resulted from rapid precipitation due to boiled off hydrothermal fluid-seawater mixing-cooling cycles (Berkenbosch *et al*., 2012; Roman *et al*., 2019). Similarly, semseyite associated with orpiment [highly enriched in Sb (≤1.23 wt%)-unpublished data)] (Fig. 1F,G,H), on the outer chimney wall (OBL, OAsL), indicates a genetic linkage to low-temperature (≤100 °C) As and Sb-rich boiled off vapor input and vapor-seawater mixing (Dekov *et al*., 2013). The replacement and recrystallization of massive, or stromatolite-like, semseyite to colloform As-sulfides (i.e., orpiment) (Figs. 1G, H) probably represent a low-temperature (100 to 150°C) overprint and coupled dissolution and reprecipitation (CDR) processes based on zone refining (Berkenbosch *et al*., 2012; Falkenberg *et al*., 2021).

The trace element incorporation mechanisms in the Kolumbo stibnite, semseyite, and pyrite, also depends on variable degrees of fluid-seawater mixing and fluid boiling precipitation. For example, intensity spikes in time-integrated LA-ICP-MS spectra (Fig. 3D) are likely related to microscale polymetallic inclusions in stibnite and semseyite (Fig. 3A,B). Such inclusions may well reflect hydrothermal fluid supersaturation in Cu, Ag, Sb, and Pb, caused either by abrupt cooling because of abundant fluid-seawater mixing, or boiling that caused destabilization of metal(loid) complexes (Falkenberg *et al.*, 2021). These notions are supported by chemically zoned Py1 spheroids that exhibit low Sb/Pb and Tl/Pb ratios, and decoupled zoning between trace metal(loids), indicating boiling-induced precipitation (Fig. 5A). In this paper, we have documented that additional to magmatic volatile degassing, boiling- and seawater mixing-induced processes, may be responsible for hyper-enrichment of Sb in the Kolumbo SMS mineralization.

Acknowledgements

We thank Daniel Smith (University of Leicester) and Manuel Keith (Friedrich-Alexander-Universitat) for their assistance in the LA-ICP-MS analyses.

References

Berkenbosch H. A., de Ronde C. E. J., Gemmell J. B., McNeill A. W., Goemann K., 2012. Mineralogy and Formation of Black Smoker Chimneys from Brothers Submarine Volcano, Kermadec Arc. Economic Geology 107, 1613–1633.

Falkenberg, J.J., Keith, M., Haase, K.M., Bach, W., Klemd, R., Strauss, H., Yeo, I.A., Rubin, K.H., Storch, B., Anderson, M.O., 2021. Effects of fluid boiling on Au and volatile element enrichment in submarine arc-related hydrothermal systems. Geochimica et Cosmochimica Acta 307, 105-132.

Hector, S., Patten, C.G., Beranoaguirre, A., Lanari, P., Kilias, S., Nomikou, P., Peillod, A., Eiche, E., Kolb, J., 2024. Magmatic evolution of the Kolumbo submarine volcano and its implication to seafloor massive sulfide formation. Mineralium Deposita 59, 1229-1248.

George, L.L., Biagioni, C., Lepore, G.O., Lacalamita, M., Agrosi, G., Capitani, G.C., Bonaccorsi, E., d'Acapito, F., 2019 The speciation of thallium on (Tl,Sb,As)-rich pyrite. Ore Geology Reviews 107, 364-380.

Kaufmann, A.B., Lazarov, M., Weyer, S., Števko, M., Kiefer, S., Majzlan, J., 2024. Changes in antimony isotopic composition as a tracer of hydrothermal fluid evolution at the Sb deposits in Pezinok (Slovakia). Mineralium Deposita 59(3), 559-575.

Koděra, P., Mathur, R., Zhai, D., Milovský, R., Bačo, P. and Majzlan, J., 2024. Coupled antimony and sulfur isotopic composition of stibnite as a window to the origin of Sb mineralization in epithermal systems (examples from the Kremnica and Zlatá Baňa deposits, Slovakia). Mineralium Deposita, pp.1-17.

Patten, C.G.C., Hector, S., Kilias, S., Ulrich, M., Peillod, A., Beranoaguirre, A., Nomikou, P., Eiche, E., Kolb, J., 2024. Transfer of sulfur and chalcophile metals via sulfide-volatile compound drops in the Christiana-Santorini-Kolumbo volcanic field. Nature Communications, 15(1), 4968.

Roman N., Reich M., Leisen M., Morata D., Barra F., Deditius A. P., 2019. Geochemical and micro-textural fingerprints of boiling in pyrite. Geochimica et Cosmochimica Acta 246, 60–85.

Yu, H.C., Qiu, K.F., Simon, A.C., Wang, D., Mathur, R., Wan, R.Q., Jiang, X.Y., Deng, J., 2023. Telescoped boiling and cooling mechanisms triggered hydrothermal stibnite precipitation: Insights from the world's largest antimony deposit in Xikuangshan China. American Mineralogist, 108(7), 1213-1223.

Zegkinoglou, N.N., Ryan, M., Kilias, S.P., Godfrey, L., Pletsas, V., Nomikou, P., Zaronikola, N., 2023, Boiling-induced extreme Cu isotope fractionation in sulfide minerals forming by active hydrothermal diffusers at the Aegean Kolumbo volcano: Evidence from in situ isotope analysis. Geology 51,1072–1076.